Probing the Beyond the Standard Model Higgs Sector using the ATLAS Detector

Guillermo Nicolas Hamity

Department of Physics and Astronomy

The University of Sheffield

Supervisor: **Dr Trevor Vickey**

A thesis submitted in partial fulfilment of the requirements for the degree of

Doctor of Philosophy

January 2020

To Giselle, Amaia and Leila.

Declaration

I hereby declare that except where specific reference is made to the work of others, the contents of this dissertation are original and have not been submitted in whole or in part for consideration for any other degree or qualification in this, or any other University. This dissertation is the result of my own work and includes nothing which is the outcome of work done in collaboration, except where specifically indicated in the text.

Guillermo Nicolas Hamity
January 2020

Acknowledgements

First and foremost I would like to acknowledge my supervisor, Dr Trevor Vickey, who has supported my academic career from the time I was a masters student at the University of Witwatersrand. I am thankful for the invaluable mentorship and support you have provided over the years, without which my research would not have been possible.

I would like to thank the University of Sheffield for providing me with the means to undertake my PhD through the Teaching Scholarship. Schemes which provide funding for non-European students to undertake study in Europe are sparse, and their importance cannot be overstated.

I need to acknowledge all the collaborators from the ATLAS experiment that I have had the privilege of working with, of which there are too many to mention here. There are a handful of individuals with whom I have worked nights and weekends, and who have made a notable impact on me as a researcher. In no particular order I would like to make special mention of: Lei Zhang, Lorenz Hauswald, Dirk Duschinger, Will Davey, and Pawel Jan Klimek.

I would like to thank my friends: German Carrillo Montoya, whose knowledge, patience, curiosity and genuine excitement as a researcher have been a vital influence to me as a young scientist; Josefina Alconada, for showing me the power that comes from wielding a good text editor.

Calum Macdonald, Vangelis Kourlitis, and Harry Moss, from the group in Sheffield. Our time together as PhD candidates was a genuine pleasure to me. Our countless discussions about physics, among other things, have kept me semi-sane over the years.

I want to thank my parents, who did everything they could to provide Ayelen, Diego and I with the best possible start to life at tremendous sacrifice to themselves. My late father, Guillermo, had an intoxicating dedication to strive for perfection that continues to motivate me. My mother, Monica, is the pillar on which we all lean.

The unwavering support from my partner and true love, Giselle Bronwyn Lowe, has been constant throughout. The sacrifices made over these last few years have been endured by us both. Building a life with you and our young family, Amaia and Leila, is my deepest joy.

Abstract

A Higgs boson with a measured mass of 125 GeV has been observed by both the ATLAS and CMS experiments and found to be compatible with the predictions from the Standard Model (SM). The now consolidated Higgs sector has become a topic of considerable study as a potential portal to new physics. Several models beyond the SM (BSM) exist with non-trivial Higgs sectors and predict the existence of additional Higgs bosons yet to be observed. One such type of model is the Two-Higgs-Doublet-Model (2HDM) which extends the SM Higgs sector in a minimal way, while another type which considers supersymmetry is the Minimal Supersymmetric Standard Model (MSSM). The implications of both models are considered in the thesis.

This thesis presents two searches for additional Higgs bosons predicted by BSM models. One search is for heavy neutral Higgs bosons decaying to a pair of tau leptons. The second search is for charged Higgs bosons decaying to a tau lepton and a neutrino. No significant excess is observed in either analysis and regions of the parameter space of the MSSM are excluded.

This thesis also presents a reinterpretation of the measurement of the 125 GeV Higgs boson cross-section in the context of the 2HDMs and MSSM. The measured 125 GeV Higgs boson cross-sections are found to be compatible with the predictions of the SM, and are used to constrain the 2HDM and MSSM parameter space.

Results from the direct searches, in terms of model-independent cross-section limits, and the 125 GeV Higgs boson cross-section measurements are shown to provide complementary constraints on the MSSM parameter space.

Table of contents

Author's Contributions

This thesis presents two searches: one for neutral [1], and one for charged [2], Higgs bosons. This thesis also presents constraints on beyond the Standard Model (BSM) physics from precise measurements of the discovered 125 GeV Higgs boson [3]. The material presented is a collaborative effort performed by members of the ATLAS collaboration. The thesis is composed into four parts, with the content and author's contributions summarised below.

Part I introduces the theoretical foundations of the Standard Model (SM) and the BSM theories described in this thesis. Chapter 1 introduces the details of the SM and the phenomenology of the SM Higgs boson at the Large Hadron Collider (LHC). Chapter 2 starts by motivating the use of the Higgs sector as a portal to new physics. Two BSM models with extended Higgs sectors are described: the Two-Higgs-Doublet-Model (2HDM) and the Minimal Supersymmetric extension to the Standard Model (MSSM). The phenomenology of the additional Higgs bosons predicted by these models at the LHC is presented. The section concludes by summarising the corresponding legacy results by ATLAS during Run-1 of the LHC data-taking period.

The author made contributions to producing the theoretical calculations of the neutral MSSM Higgs cross-sections used throughout this thesis. In particular the author was involved in creating, maintaining and validating the ROOT files which contain theoretical cross-section, branching fraction and mass calculations for neutral Higgs bosons in the context of the MSSM. Additionally, the author implemented the theoretical uncertainties in the calculations of the p_{T} reweighting scheme documented in Appendix A.1.

Part II is devoted to the experimental methodology. The discussion in Chapter 3 presents a description of the LHC, followed by a discussion of the ATLAS experiment and its detectors. The ATLAS data model is discussed in Chapter 4 with emphasis on object reconstruction, which is intended as a resource for analysis chapters: in particular with regards to the selection of data events and the determination of uncertainties of the analyses. Part II concludes with

Chapter 5 dedicated to the statistical analysis of data, which is of particular importance to the work the author conducted in this thesis.

In the context of the ATLAS detector, the author was involved in the commissioning of silicon strip sensors for the new ATLAS Inner Tracker (ITk) which will be installed in time for the High Luminosity Large Hadron Collider (HL-LHC). This work was included into Ref. [4] and is not detailed in the thesis. The author was also involved in the monitoring of the inner detector (ID) during several data-taking shifts in the ATLAS control room during data-taking periods.

Part III documents three analyses. Chapter 6 presents a search for neutral heavy Higgs bosons which decay to a pair of tau leptons within the ATLAS detector. Chapter 7 presents a search for charged Higgs bosons which decay to a tau lepton and a neutrino within the ATLAS detector. The details pertaining to the analysis in Chapter 7 are kept brief and an emphasis is placed on the work by the author, as many details are similar to those described in Chapter 6. Both searches are interpreted in the context of the MSSM. In both searches the author was involved in the implementation of the statistical model used to extract the results, in particular: the determination of the impact of uncertainties on the results, the determination of the final event distributions and cross-section limits, and the implementation of the interpretation of results in the BSM models. Additionally the author contributed to the generation of event samples and maintaining of analysis code for early results from the analysis in Chapter 6. The author was also involved in additional interpretations of this analysis in the context of a Z' search documented in Ref. [1], but which is not detailed in the thesis.

Chapter 8 presents the reinterpretation of the precision measurements of the 125 GeV Higgs couplings in the context of both the 2HDM and MSSM. The interpretation is dependant on Higgs cross-section and branching fraction measurements, which are summarised. Here the author contributed to the validation of the statistical framework used in the cross-section measurements and the breakdown of uncertainties which impact the result. The primary contribution is with regards to implementing and validating the BSM parameterisation and extracting the constraints for BSM models from the Higgs boson measurements.

Part IV is the conclusion. The results from the Higgs searches and the Higgs precision measurements are summarised and presented on an equal footing in the context of the MSSM. A prospect study of the di-tau search at the HL-LHC concludes the discussion, for which the author provided updated theory predictions and contributed to the analysis code.

Part I

Theory

Chapter 1

The Standard Model of particle physics

The Standard Model (SM) of particle physics is the theory which describes the fundamental particles of the universe and their interactions [5–8]. Up to this point, it has been shown to be void of significant experimental inconsistencies. It is, however, considered to be an incomplete theory, as it does not include the gravitational force or account for astrophysical phenomena like dark matter or dark energy. Furthermore, its derivation is as a result of a tapestry of theories which developed alongside experimental observations. Therefore, the SM was not determined by some irreducible fundamental principles, and it falls short of being a complete theory of everything. The high-energy physics community has spent enormous effort in the search for hints of physics lying outside the predictions of the SM theory which points in the direction of a more fundamental theory. No smoking gun has been found as of yet.

A particularly interesting area of the current research is in the Higgs sector of the SM [9–13]. The recently discovered Higgs boson remained elusive for decades after its prediction, and the properties of the particle are still being explored at the Large Hadron Collider (LHC) [14]. As a consequence, exploring the Higgs sector as a portal to new physics is an alluring prospect. In particular, searches for additional Higgs bosons that result from an extended Higgs sector are actively conducted by the A Toroidal LHC Apparatus (ATLAS) [15] and Compact Muon Solenoid (CMS) [16] experiments at the LHC. Furthermore, the discovered Higgs boson is actively probed for signs of new physics [17]. The SM and Higgs mechanism are introduced in this chapter.

1.1 Overview of the Standard Model

The SM of particle physics is a theory that classifies the fundamental particles of matter and describes their interactions [5, 6]. Its current structure was formulated in the 1970s after the unification of the weak and electromagnetic (EM) interactions [18–20], and the incorporation of the Brout-Englert-Higgs (BEH) mechanism [9–13] (sometimes referred to as the *the Higgs mechanism*). The SM can currently account for practically all experimental data from high-energy physics experiments. The theory is defined in the language of Quantum Field Theory (QFT), in which particles are quanta of corresponding fields. The details of the particle content of the SM are summarised in this section[1]. Natural units are used throughout this thesis, such that the reduced Plank's constant ($\hbar$) and the speed of light (c) are equal to unity, $\hbar = c = 1$. The elementary EM charge unit (e) is set to $e = \sqrt{4\pi\alpha}$, where $\alpha \approx \frac{1}{137}$ is the fine structure constant. Quoted charges should be considered to be in units of e and the unit symbol will be omitted in the text.

All matter in the SM is built from spin-$\frac{1}{2}$ particles known as *fermions*. The fermions are grouped into six *quarks*: up (u), down (d), charm (c), strange (s), top (t) and bottom (b); and six *leptons*: electron (e) and electron-neutrino (ν_e), muon (μ) and muon-neutrino (ν_μ), and tau (τ) and tau-neutrino (ν_τ). Table 1.1 lists the fermion particle content of the SM, along with representative quantum numbers that are defined in the discussion to follow[2]. Each fermion has a corresponding anti-particle with inverted quantum numbers. Force interactions between matter particles are described through the interchange of spin-1 particles, known as the *gauge bosons*. The SM incorporates three fundamental forces via the interaction of gauge bosons: the EM, weak, and strong force. The SM gauge bosons are summarised in Table 1.2.

The electroweak (EW) theory of the SM unifies both EM and weak interactions. The EM interactions are between particles with EM charge (Q) through the exchange of massless *photons* (γ). The corresponding coupling strength of interactions is α, which is proportional to the probability amplitude of an EM process. The weak interactions occur between fermions which have non-zero *weak-isospin* charge (I_W). Left-handed fermions in the SM have half-integer weak-isospin, with longitudinal component $I_W^{(3)}$ taking values of either $\frac{1}{2}$ or $-\frac{1}{2}$. Left-handed fermions are arranged into weak-isospin doublets,

$$\begin{pmatrix} u \\ d \end{pmatrix}, \begin{pmatrix} c \\ s \end{pmatrix}, \begin{pmatrix} t \\ b \end{pmatrix}, \begin{pmatrix} \nu_e \\ e \end{pmatrix}, \begin{pmatrix} \nu_\mu \\ \mu \end{pmatrix}, \begin{pmatrix} \nu_\tau \\ \tau \end{pmatrix}, \tag{1.1}$$

[1] The discussion on the SM follows the literature in Refs. [5, 6], while many of the details pertaining to the SM and beyond the Standard Model (BSM) Higgs mechanism follow the details in Refs. [7, 8].

[2] The quantum numbers presented here is not an exhaustive list, but have been chosen as they are relevant for subsequent discussion.

Table 1.1 The Standard Model fermions, listed with representative quantum numbers as described in the text. The masses quoted are mean values from Ref. [21].

Fermions (spin-$\frac{1}{2}$)								
Quarks								
					Left-handed		Right-handed	
Gen	Name	Mass	C	Q	$I_W^{(3)}$	Y	$I_W^{(3)}$	Y
I	u	2.2 MeV	$R/G/B$	$\frac{2}{3}$	$\frac{1}{2}$	$\frac{1}{3}$	0	$\frac{4}{3}$
	d	4.7 MeV	$R/G/B$	$-\frac{1}{3}$	$-\frac{1}{2}$	$\frac{1}{3}$	0	$-\frac{2}{3}$
II	c	1.27 GeV	$R/G/B$	$\frac{2}{3}$	$\frac{1}{2}$	$\frac{1}{3}$	0	$\frac{4}{3}$
	s	96 MeV	$R/G/B$	$-\frac{1}{3}$	$-\frac{1}{2}$	$\frac{1}{3}$	0	$-\frac{2}{3}$
III	t	173.21 GeV	$R/G/B$	$\frac{2}{3}$	$\frac{1}{2}$	$\frac{1}{3}$	0	$\frac{4}{3}$
	b	4.18 MeV	$R/G/B$	$-\frac{1}{3}$	$-\frac{1}{2}$	$\frac{1}{3}$	0	$-\frac{2}{3}$
Leptons								
I	ν_e	< 2.2 eV	—	0	$\frac{1}{2}$	-1	0	0
	e	0.511 MeV	—	-1	$-\frac{1}{2}$	-1	0	-2
II	ν_μ	< 0.17MeV	—	0	$\frac{1}{2}$	-1	0	0
	μ	105.7 MeV	—	-1	$-\frac{1}{2}$	-1	0	-2
III	ν_τ	< 18.2 MeV	—	0	$\frac{1}{2}$	-1	0	0
	τ	1.776 GeV	—	-1	$-\frac{1}{2}$	-1	0	-2

Table 1.2 The Standard Model bosons: vector bosons mediate the gauge interactions in the SM, while the Higgs boson is attributed to the BEH mechanism that gives particles their mass. The masses quoted are mean values from Ref. [21].

Bosons			
Vector (spin-1)			
Interaction	Mediator	Mass	Q
Strong	gluon (g)	0	0
EM	photon (γ)	0	0
Weak	$W^\pm$	80.39 GeV	± 1
	Z	91.19 GeV	0
Scalar (spin-0)			
BEH mechanism	Higgs boson H	125.09 GeV	0

where the upper and lower components have $I_W^{(3)} = \frac{1}{2}$ and $I_W^{(3)} = -\frac{1}{2}$, respectively, and are separated by a unit of electric charge. The upper and lower components of weak-isospin doublets are referred to as up-type and down-type particles, respectively. Right-handed fermions have zero weak-isospin and are arranged into weak-isospin singlets. As a consequence, the only fermions that interact via the weak force are left-handed fermions (and right-handed anti-fermions). In the unified EW theory, the EM charge associated with a particle is related to $I_W^{(3)}$ and a quantum number known as *hypercharge* (Y) via,

$$Q = I_w^{(3)} + \frac{Y}{2}. \tag{1.2}$$

Quarks have an electric charge of $Q = \frac{2}{3}$ (up-type) or $Q = -\frac{1}{3}$ (down-type) while down-type leptons have $Q = 1$ and neutrinos have $Q = 0$. Their charge conjugate states represent the corresponding anti-particles.

The weak interactions in the quark and lepton sector occur though the interchange of massive charged ($W^{\pm}$) or neutral (Z) bosons. The associated coupling strength of the weak interaction (α_{W}) is $\sim 10^{-6}$ at distances larger than approximately the width of a proton. The Cabibbo–Kobayashi–Maskawa (CKM) matrix [22] provides the relationship between mass eigenstates of quarks and their weak interaction eigenstates, allowing for up-type to down-type transitions across quark generations. Similarly, the Pontecorvo–Maki–Nakagawa–Sakata (PMNS) matrix [23] provides the relationship between mass eigenstates of neutrinos and their weak interaction eigenstates.

Quantum Chromodynamincs (QCD) is the theory describing the strong nuclear force, where interactions occur between fermions which have colour charge (C, which can take one of three values, green G, red R, or blue B), mediated by eight massless coloured gluons (g). The only fermions which are coloured in the SM are the quarks. In QCD the gluons themselves have colour charge and self-interact. All coupling strengths for the forces in the SM are *running*, meaning that their values are dependant on the energy scale of the interaction. Due to the gluon self-interactions, the coupling constant of the strong force (α_{S}) at low energy scales (large distances) is large, $\alpha_{\mathrm{S}} \sim 1$, driving the confinement of quarks into colourless baryons. At high-energy scales (small distances) α_{S} is reduced, leading to the *asymptotic freedom* of the bare colour charge.

Lastly, in the formulation of the SM, particle masses stem from their interactions with the vacuum of a scalar field, know as the Higgs field. The quanta of this field is the scalar Higgs boson, whose properties are listed in Table 1.2. Much of the remainder of this chapter is dedicated to establishing the Higgs boson as an essential component of the SM.

1.2 Particle interactions via local gauge invariance

The QFTs utilised to establish the SM are required to be invariant under particular symmetries associated with the SM interactions. These symmetries are defined precisely for the strong, described by the transformations from the group $SU(3)_C$, and EW, described by the transformations from the product group $SU(2)_L \times U(1)_Y$, interactions. The QFT of the SM is a gauge theory in that it is required to be invariant under *local* gauge symmetry transformations. Imposing this requirement on the Dirac equation for *spinors* (defined below) will result in the desired vector bosons which mediate the SM interactions. The details surrounding this formulation are discussed in this section, and lead us naturally to a discussion surrounding mass terms in the SM Lagrangian.

Interactions in the theory are between spin-$\frac{1}{2}$ fermions which can be described mathematically by *spinors*,

$$\psi(x) = \begin{pmatrix} \psi(x)_1 \\ \psi(x)_2 \\ \psi(x)_3 \\ \psi(x)_4 \end{pmatrix}, \tag{1.3}$$

composed of four complex fields, dependant on the space-time[3] four-vector x, describing the spin and momentum state of a particle/anti-particle. The Lagrangian of a spinor satisfying the free-particle Dirac equation[4] is,

$$\mathscr{L}_D = \underbrace{i\bar{\psi}\gamma^\mu \partial_\mu \psi}_{\text{kinetic}} - \underbrace{m\bar{\psi}\psi}_{\text{mass}}, \tag{1.4}$$

where the first term is related to the kinetic energy, while the second is related to the mass of the fermion.

Imposing local gauge invariance on the Dirac Lagrangian generally results in having to redefine the covariant derivative $\partial_\mu \to D_\mu$ by introducing a new gauge field with accompanying gauge strength.

For example, imposing local gauge invariance generated by a U(1) symmetry requires the covariant derivative $\partial_\mu \to D_\mu = \partial_\mu + iqA_\mu$. Here a new gauge field A_μ with coupling strength q is introduced, which transforms as $A_\mu \to A'_\mu = A_\mu - \frac{1}{q}\partial_\mu \chi(x)$ under local gauge transformations.

[3] $x \equiv x^\mu$ where the indices represent space-time components, $\mu = 0, 1, 2, 3$, with $\mu = 0$ being the time component.

[4] γ^μ are the four gamma matrices, $\bar{\psi} \equiv \psi^\dagger \gamma^0$ is the adjoint spinor, and ∂_μ is the covariant four-derivative.

In the SM, local gauge invariance is imposed for transformations from the product of groups $\mathrm{SU}(3)_C \times \mathrm{SU}(2)_L \times \mathrm{U}(1)_Y$ [6–8]. In order to impose local gauge invariance for $\mathrm{SU}(3)_C \times \mathrm{SU}(2)_L \times \mathrm{U}(1)_Y$, the covariant derivative is defined as [8],

$$D_\mu = \partial_\mu + \overbrace{\underbrace{ig'YB_\mu}_{\mathrm{U}(1)_Y} + \underbrace{igT^aW_\mu^a}_{\mathrm{SU}(2)_L}}^{\mathrm{SU}(2)_L \times \mathrm{U}(1)_Y} + \underbrace{ig_s t^A G_\mu^A}_{\mathrm{SU}(3)_C}. \tag{1.5}$$

Introduced here is a vector field B_μ from the $\mathrm{U}(1)_Y$ interactions acting on hypercharge Y with coupling strength g'. From the $\mathrm{SU}(2)_L$ symmetry, three gauge fields are introduced: W_μ^k with $k = 1,2,3$. The generators T^k with $k = 1,2,3$ are the three 2×2 Pauli matrices. The weak interaction has coupling strength g, and acts only on left-handed fermions, i.e., associated with weak-isospin ($I_W = \frac{1}{2}$), which are arranged into weak-isospin doublets: $I_W^{(3)} = (\frac{1}{2}, -\frac{1}{2})$.

Under the combined $\mathrm{SU}(2)_L \times \mathrm{U}(1)_Y$ symmetry the required B_μ and W_μ^k fields can be related to physical observables. For the charged currents, $W_\mu^\pm = \frac{1}{\sqrt{2}}(W_\mu^1 \mp iW_\mu^2)$, where the superscripts are indices. For the neutral currents,

$$\begin{pmatrix} A_\mu \\ Z_\mu \end{pmatrix} = \begin{pmatrix} \cos\theta_W & \sin\theta_W \\ -\sin\theta_W & \cos\theta_W \end{pmatrix} \begin{pmatrix} B_\mu \\ W_\mu^3 \end{pmatrix}, \tag{1.6}$$

where the physical photon (A_μ) and Z boson (Z_μ) fields are expressed as linear combination of W_μ^3 and B_μ via the weak mixing angle θ_W, where $\tan\theta_W = \frac{g'}{g}$. This follows from the relation of EM charge Q, hypercharge and weak-isospin in Eq. (1.2).

The $\mathrm{SU}(3)_C$ group which acts on colour charge C is generated by the eight Gell-Mann matrices t^A with coupling strength g_s. Eight gluon fields are required and invariant under local gauge transformations, denoted G_μ^A.

Replacing ∂_μ in Eq. (1.4) with the D_μ of Eq. (1.5) generates the interaction terms of the fermion spinors with the respective force carriers. Ignoring the fermion mass terms, the kinetic Lagrangian for fermions can be expressed as,

$$\begin{aligned} \mathscr{L}_{\text{fermion, kin.}} &= i\bar{\psi}\gamma^\mu D_\mu \psi \\ &= \underbrace{i\bar{\psi}\gamma^\mu \partial_\mu \psi}_{\text{kinetic}} \\ &\quad + \underbrace{i\bar{\psi}\gamma^\mu (ig'YB_\mu + igT^aW_\mu^a + ig_s t^A G_\mu^A)\psi}_{\text{interaction}}, \end{aligned} \tag{1.7}$$

where a term is included for each fermion field: excluding right-handed neutrinos and with right-handed fermions arranged into weak-isospin singlets. Furthermore, the new fields required by the local gauge invariance from $SU(3)_C \times SU(2)_L \times U(1)_Y$ symmetry introduce corresponding kinetic energy terms for the gauge bosons in the Lagrangian[5].

It should be noted at this point that although the local gauge invariance imposed on Eq. (1.4) necessitates introducing gauge boson fields, these fields are not given a respective mass term. In the case of the gluon and photon propagators this is not a problem. However, since the weak bosons are known to be massive, terms of the form $m^2 W_\mu W^\mu$ need to be introduced. These terms however violate local gauge invariance when introduced by hand into the Lagrangian. Similarly, under the asymmetry between left- and right-handed fermions in $SU(2)_L \times U(1)_Y$, the $m\bar{\psi}\psi$ terms also violate the local gauge invariance. In the SM these two issues are rectified by the BEH mechanism [9–13, 24], which generates the mass for both the massive gauge bosons and fermions without violating gauge invariance.

1.3 The BEH mechanism

The BEH mechanism is introduced here as applied in the context of requiring a U(1) local gauge symmetry, in which a massless gauge boson will acquire a mass. This will introduce the concepts which are needed when applying the BEH mechanism in the $SU(2)_L \times U(1)_Y$ local gauge symmetry (following the description in Refs. [6–8]) required of the SM. It will then be applied to generate fermion masses.

1.3.1 Symmetry breaking for the U(1) group

We assume that there exists a complex scalar field $\phi(x)$ which can be written as the complex combination of two constituent fields: $\phi(x) = \frac{1}{\sqrt{2}}(\phi_1(x) + i\phi_2(x))$. The Lagrangian $\mathscr{L}$ of the scalar field can be expressed as,

$$\mathscr{L} = (\partial_\mu \phi)^* (\partial^\mu \phi) - V(\phi), \tag{1.8}$$

[5]The gauge boson kinetic energy ($F_{\mu\nu}$) terms are derived using to the commutator of the covariant derivative in Eq. (1.5), $[D_\mu, D_\nu] = -igF_{\mu\nu}$.

where the first term is representative of the kinetic energy of a scalar particle, and the potential energy of the field is assumed to be of the form,

$$V(\phi) = \mu^2(\phi^*\phi) + \lambda(\phi^*\phi)^2, \tag{1.9}$$

where $(\phi^*\phi)$ and $(\phi^*\phi)^2$ terms are identified as mass and self-interaction terms, respectively. The parameters μ and λ are constants which describe the shape of the potential.

The Lagrangian in the form in Eq. (1.8) is not invariant under a U(1) local gauge transformation: $\phi(x) \to \phi'(x) = e^{ig\chi(x)}\phi(x)$. This is due to the ∂_μ derivatives acting on the now space-time dependant $\chi(x)$. In order to attain local gauge invariance, the derivative in the Lagrangian is replaced by $D_\mu = \partial_\mu + igA_\mu$, where A_μ is a new gauge field required to transform as $A_\mu \to A'_\mu = A_\mu - \partial_\mu\chi(x)$, and g is the gauge coupling strength. Rewriting Eq. (1.8) in the gauge covariant form with associated new field A_μ,

$$\mathscr{L} = (D_\mu\phi)^*(D^\mu\phi) - \frac{1}{4}F^{\mu\nu}F_{\mu\nu} - \mu^2(\phi^*\phi) - \lambda(\phi^*\phi)^2, \tag{1.10}$$

where the kinetic energy associated with the new field is expressed in the term of the form $F^{\mu\nu}F_{\mu\nu}$, with the tensor $F^{\mu\nu} = \partial^\mu A^\nu - \partial^\nu A^\mu$.

In order to apply perturbation theory to the Lagrangian in Eq. (1.10), a finite minimum in the potential is required, in which case λ is required to be positive. The parameter μ^2 would represent a mass term whilst it is positive. This is however not a requirement, and setting $\mu^2 < 0$ yields a minimum point in the potential where $\phi \neq 0$. Figure 1.1 is representative of the scalar potential $V(\phi)$ in Eq. (1.9) with $\mu^2 < 0$. The minimum of the potential lies on a circle in the complex plane with,

$$\phi_1^2 + \phi_2^2 = \frac{-\mu^2}{\lambda} = v^2, \tag{1.11}$$

where v is the non-zero vacuum expectation value (VEV) of the field. In the BEH mechanism a particular point on the circle is chosen as the physical VEV of the field. This process is known as *spontaneous symmetry breaking*. Without any loss of generality, the VEV can be chosen to be on the positive real component of the field, $(\phi_1, \phi_2) = (v, 0)$, depicted in Figure 1.1 as the red point.

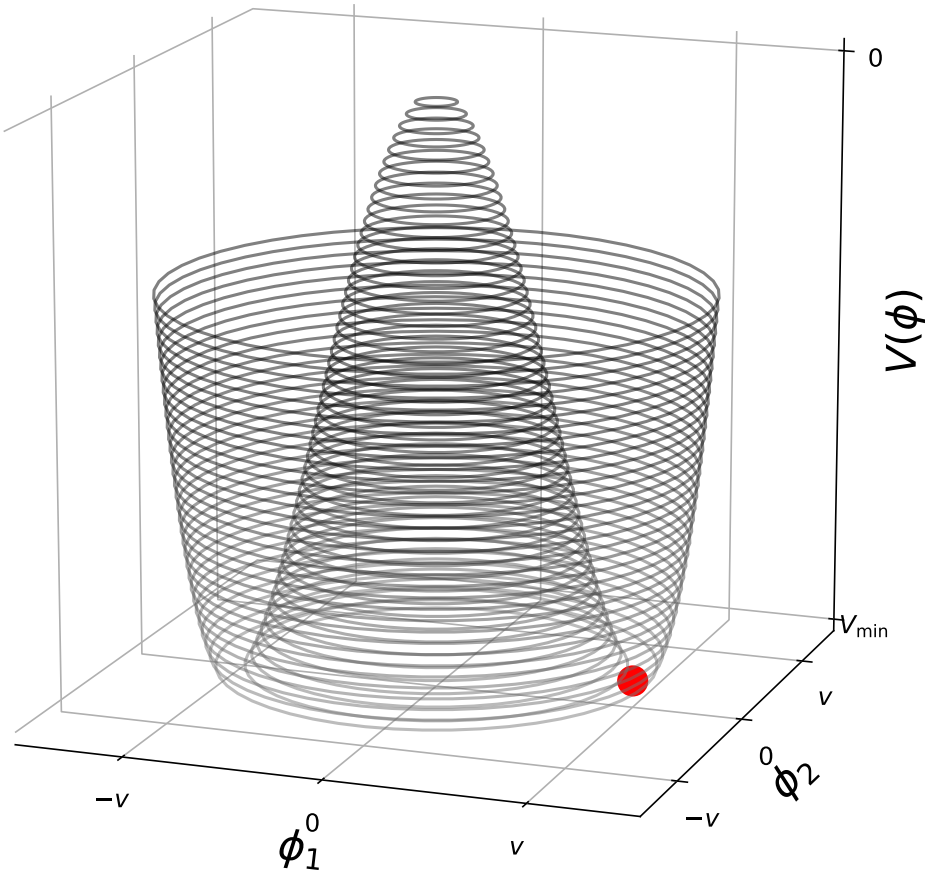

Figure 1.1 The potential energy of the complex field $\phi = \phi_1 + i\phi_2$ as defined in Eq. (1.9) with $\mu < 0$. The red point is representative of choosing the physical vacuum expectation value (VEV) in the positive real direction.

If we rewrite the field ϕ as a perturbation about its minimum, $\phi = \frac{1}{\sqrt{2}}(v + h(x) + i\xi(x))$, and expand the covariant derivative D_μ, the Lagrangian becomes,

$$\begin{aligned}\mathscr{L} =& \frac{1}{2}(\partial_\mu h)^*(\partial^\mu h) - \lambda v^2 h^2 \\ & - \frac{1}{4}F^{\mu\nu}F_{\mu\nu} + \frac{1}{2}g^2 v^2 A_\mu A^\mu \\ & + \frac{1}{2}(\partial_\mu \xi)^*(\partial^\mu \xi) + gvA_\mu(\partial^\mu \xi) - V_{\text{int.}},\end{aligned} \tag{1.12}$$

where three and four-point interaction terms between expansion fields h and ξ, and the vector field A_μ, have been collected into in the $V_{\text{int.}}$ term. Taking a closer look at the Lagrangian in Eq. (1.12), the expansion of ϕ about its minimum after symmetry breaking has lead to three important consequences: the massless gauge boson has picked up a mass term, with mass gv, providing a mechanism which gives mass to vector bosons; the real component scalar field h has become massive, with mass $\sqrt{2\lambda}v$; there is a massless h field attributed to the imaginary component of the expansion about the VEV, referred to in the literature as the Goldstone boson. The Goldstone boson has a direct coupling with the massive boson ($gvA_\mu\partial^\mu h$) which seems to imply that the massive vector boson can spontaneously convert into a massless scalar. However, this coupling is ultimately not physical, and can be eliminated by choosing the correct gauge transformation, $\phi(x) \to \phi'(x) = e^{-i\xi(x)/v}\phi(x)$, referred to as the *unitary* gauge. This choice eliminates the Goldstone boson, and is equivalent to choosing the field ϕ to be real: $\phi = \frac{1}{\sqrt{2}}(v+h(x))$. Choosing the unitary gauge yields,

$$\begin{aligned}\mathscr{L} = &\underbrace{\frac{1}{2}(\partial_\mu h)^*(\partial^\mu h)}_{\text{Higgs kinetic}} - \underbrace{\lambda v^2 h^2}_{\text{Higgs mass}} \\ &- \underbrace{\frac{1}{4}F^{\mu\nu}F_{\mu\nu}}_{\text{gauge boson kinetic}} + \underbrace{\frac{1}{2}g^2v^2A_\mu A^\mu}_{\text{gauge boson mass}} \\ &+ \underbrace{g^2vA_\mu A^\mu h + \frac{1}{2}g^2A_\mu A^\mu h^2}_{\text{Higgs and gauge boson interaction}} - \underbrace{\lambda vh^3 - \frac{1}{2}\lambda h^4}_{\text{Higgs self interaction}} \quad . \end{aligned} \tag{1.13}$$

This Lagrangian describes interactions of massive field h with an associated real physical boson, the Higgs boson, with a now massive gauge boson attributed to requiring U(1) local gauge symmetry. The scalar and vector boson mass terms are still present: $m_h = \sqrt{2\lambda}v$ and $m_A = gv$. The $A_\mu A^\mu h$ and $A_\mu A^\mu h^2$ terms indicate three and four-point interaction vertices between the vector and scalar boson. The h^3 and h^4 terms indicate the Higgs boson self-interaction vertices. The coefficients in these interactions are related to their respective coupling strengths.

In summary, starting with a theory for a complex scalar boson and requiring U(1) local gauge symmetry lead to a required massless gauge boson, which becomes massive after spontaneous symmetry breaking— *the BEH mechanism*. The initial and final degrees of freedom (DOFs) of the theory remain the same: initially there are two DOFs for the real and complex components of the field, and two for the polarisation of the massless boson. After the boson acquires mass, its polarisation has three DOFs (i.e., -1, 0, $+1$), while the complex

field has been absorbed by choosing the unitary gauge, resulting in four DOFs. The Higgs boson mass is determined by v and λ, meaning that it needs to be ascertained experimentally: the parameter v is present in the vector boson mass term, and can therefore be determined by the observed boson mass, but the λ parameter defines the shape of scalar potential, and needs to be measured. Additionally, the interaction terms of h with the vector boson (and later bosons and fermions) do not depend on λ, so their strength is known, while the Higgs boson self-interaction terms depend on λ and must be determined experimentally.

1.3.2 Electroweak symmetry breaking

In order to generate mass terms for the SM massive gauge bosons, $W^{\pm}$ and Z, spontaneous symmetry breaking needs to be applied to the EW sector, $\mathrm{SU}(2)_L \times \mathrm{U}(1)_Y$, also referred to as electroweak symmetry breaking (EWSB). The BEH mechanism follows in much the same way as described above, but now requiring the covariant derivative D_μ from the $\mathrm{SU}(2)_L \times \mathrm{U}(1)_Y$ term of Eq. (1.5). Two complex scalar fields are arranged into a weak-isospin doublet,

$$\Phi = \begin{pmatrix} \phi^+ \\ \phi^0 \end{pmatrix} = \begin{pmatrix} \frac{\phi_1 + i\phi_2}{\sqrt{2}} \\ \frac{\phi_3 + i\phi_4}{\sqrt{2}} \end{pmatrix}, \tag{1.14}$$

with the usual one unit of electric charge separating the up and down components. Here, ϕ^+ and ϕ^0 are complex scalar fields, each composed of two real scalar fields, leading to four DOFs. There are also four accompanying massless fields, W_μ^k (where $k = 1, 2, 3$) and B_μ, each with two polarisation DOFs: in total 12 DOFs. The corresponding scalar Lagrangian for the complex scalar doublet is,

$$\mathscr{L} = (D_\mu \Phi)^\dagger (D^\mu \Phi) - \mu^2 (\Phi^\dagger \Phi) - \lambda (\Phi^\dagger \Phi)^2. \tag{1.15}$$

The minima of the potential with $\mu^2 < 0$, lies on a complex hyper-sphere,

$$(\phi_1^2 + \phi_2^2 + \phi_3^2 + \phi_4^2) = \frac{-\mu^2}{\lambda} = v^2. \tag{1.16}$$

The symmetry is spontaneously broken by requiring the minimum to be in the real positive field direction, $\phi_3 = v^2$. This choice is made as the neutral field must acquire a non-zero VEV in order for the photon to be massless. As before, we can expand the fields about this minimum, resulting in three Goldstone bosons, which are eliminated by choosing the unitary

gauge, i.e.,

$$\Phi = \frac{1}{\sqrt{2}}\begin{pmatrix} 0 \\ h(x)+v \end{pmatrix}. \tag{1.17}$$

Using this form of the scalar doublet, the resulting kinetic terms in Eq. (1.15) yield mass terms for the W_μ^k and B_μ fields defined in Section 1.2. Specifically, the mass terms for the W_μ^k and B_μ fields appear as,

$$\begin{aligned} &\frac{1}{8}(gv)^2(W_\mu^1 W^{1\mu} + W_\mu^2 W^{2\mu}) \\ &+\frac{v^2}{8}\begin{pmatrix} W_\mu^3 & B_\mu \end{pmatrix}\begin{pmatrix} g^2 & -gg' \\ -gg' & g'^2 \end{pmatrix}\begin{pmatrix} W^{3\mu} \\ B^\mu \end{pmatrix}, \end{aligned} \tag{1.18}$$

which in terms of physical bosons yields the relations,

$$m_{W^\pm} = \frac{gv}{2}, \quad m_Z = \frac{gv}{2\cos\theta_W}, \quad \text{and } m_A = 0. \tag{1.19}$$

Along with the vector boson masses, terms appear for interactions between the Higgs and vector boson fields, which are of the form VVh and VVh^2 for the three and four-point vertices, respectively. There are also terms for the Higgs boson self-interactions: h^3 and h^4. An example of the VVh and h^2 Feynman diagrams are shown in Figures 1.2 (a) and (c). Counting the resulting DOFs, three per massive boson, two for the massless photon, and one real Higgs field, we end up with the twelve DOFs we started with, where the DOFs from Goldstone bosons are said to have been *eaten* by the massive gauge bosons.

Experimental measurements of m_W and g places the VEV of the Higgs field at a value of $v \sim 246$ GeV [21]. This immediately gives the coupling strengths for the hWW (gm_W) and hZZ ($gm_Z/\cos\theta_W$) vertices.

1.3.3 Yukawa interactions

In the SM, fermions also acquire their mass through the BEH mechanism. Representing the mass term in Eq. (1.4) in terms of left and right-handed chiral components, $-m(\bar{\psi}_R\psi_L + \bar{\psi}_L\psi_R)$ is not invariant under $\mathrm{SU}(2)_L \times \mathrm{U}(1)_Y$ gauge transformations. To give fermions their mass, *Yukawa* terms are added to the Lagrangian,

$$\mathscr{L}_{\text{Yukawa}} = -Y_f(\bar{\psi}_R\Phi^\dagger\psi_L + \bar{\psi}_L\Phi\psi_R), \tag{1.20}$$

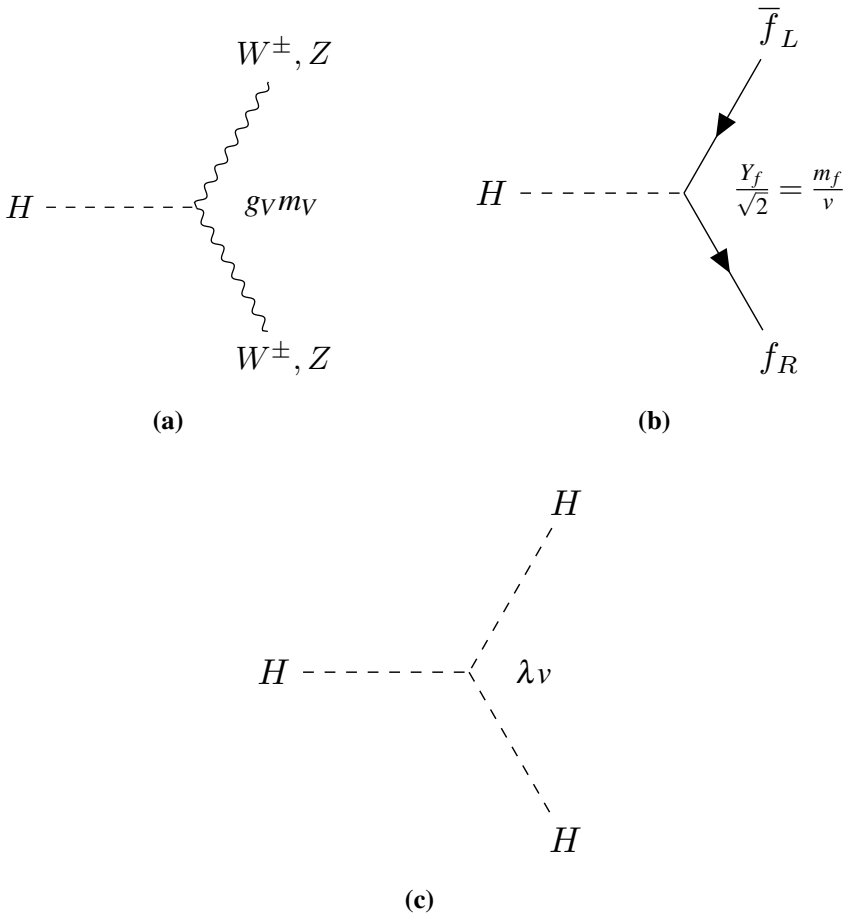

Figure 1.2 Examples of Feynman diagrams for Higgs boson three-point vertices for (a) vector boson, (b) Yukawa, and (c) Higgs self couplings with their respective coupling strengths in the SM.

where a coupling strength Y_f of the fermion to the Higgs doublet is introduced. After EWSB the down-type component of the Higgs doublet acquires a nonzero field $v+h$, while the up-type is zero. In this case, only the down-type fermions (ψ_d) acquire mass, i.e., charged leptons and down-type quarks,

$$\mathscr{L}_{\text{Yukawa}} = -\underbrace{\frac{Y_d v}{\sqrt{2}}\bar{\psi}_d\psi_d}_{\text{fermion mass}} - \underbrace{\frac{Y_d h}{\sqrt{2}}\bar{\psi}_d\psi_d}_{\text{Higgs-fermion vertex}}. \tag{1.21}$$

Generating mass terms for up-type fermions can be achieved in a similar manner by introducing a conjugate complex scalar doublet[6]. In either case the Yukawa coupling Y_f can be expressed in terms of the fermion mass,

$$Y_f = \frac{\sqrt{2}m_f}{v}, \tag{1.22}$$

which will define the coupling strength of the Higgs-fermion vertex. The Higgs-fermion interaction vertex is shown if Figure 1.2 (b).

1.4 The SM Higgs boson

As discussed in the previous section, the Higgs field generates mass for fermions and massive vector bosons in the SM. The Higgs boson couplings to a SM particle are defined by the VEV and are proportional to the mass of the particle. However, the mass of the Higgs boson is a free parameter of the theory, and needs to be measured experimentally. A Higgs boson was discovered in 2012 by the ATLAS and CMS experiments [25, 26] at the LHC [14]. Experimental measurements of the discovered boson [27–31] have placed its mass at $m_H = 125.09 \pm 0.24$ GeV [21] and has been found to be consistent with a neutralscalar required by the SM Higgs boson [9–13, 24]. The SM predictions for the cross-sections and branching fractions of the production and decay modes of a 125 GeV Higgs boson produced at the LHC are detailed in this section.

1.4.1 Higgs boson production and cross-sections

Figure 1.3 (a) shows state of the art predictions of the cross-section modes for a SM Higgs boson produced in pp collisions for a range of centre-of-mass energies ($\sqrt{s}$) at the LHC. Figure 1.3 (b) shows the Higgs boson production cross-sections at a fixed centre-of-mass energy of $\sqrt{s} = 13$ TeV as a function of the Higgs boson mass. The dominant production mechanism for a $m_H \approx 125$ GeV at the LHC is gluon-fusion (ggF), shown in Figure 1.4 (a) at leading-order (LO). Though the gluon is massless, the ggF process dominates through virtual top-quark loops, which couple strongly to the Higgs boson due to the large Y_t. The cross-section of this process is approximately 20–50 pb for $\sqrt{s} = 8$–13 TeV with theoretical

[6]Neutrinos are known to have small mass due to the observation of their oscillations. The way in which their masses are generated is yet unknown: they may be Dirac, in which case their masses are generated as the up-type quarks, or Mayorana, in which case they are their own anti-particle, or a mixture of the two, where their masses may be generated by the seesaw mechanism [6].

uncertainties on the order of 7%. The next dominant production is that of vector-boson-fusion (VBF), shown in Figure 1.4 (b) at LO. This process has a cross-section of $O(10^{-1})$ that of ggF. It has a distinct signature as it will produce two quark jets along the beam-line (forward jets). The next dominant production mechanism is vector-boson associated Higgs boson production (VH), with either an associated Z or $W^{\pm}$, shown in Figure 1.5. The next highest Higgs boson cross-section is via Higgs boson production with associated third generation quarks. The t-associated Higgs boson production ($t\bar{t}H$) and b-associated Higgs boson production ($b\bar{b}H$) have comparable cross-section at $\sqrt{s} = 13$ TeV (~ 0.5 pb). The convention is to denote b-associated production as $b\bar{b}H$ since single b-associated Higgs boson production (bH) is negligible[7] [32]. Single t-associated Higgs boson production (tH) is produced with an EW vertex in the Feynman diagram, as shown in Figure 1.7, and has a low cross-section of ~ 90 fb at $\sqrt{s} = 13$ TeV.

ATLAS has observed several Higgs boson production processes and continues to provide higher degrees of precision of their cross-sections. Most recent is the observation of $t\bar{t}H$ production [33] with an observed statistical significance of 6.3 σ (standard deviations). The CMS experiment has likewise recently observed $t\bar{t}H$ production with an observed significance of 5.2 σ [34]. The latest combination of Higgs boson measurements by ATLAS is presented in Section 8.1.2 for different production modes, the results of which are summarised in Table 8.4, in which the ggF, VBF and VH productions are observed with a statistical significance of over 5 σ. CMS has performed a similar analysis in Ref. [35] with results compatible with the SM predictions. Higgs boson production via $b\bar{b}H$ and tH are yet to be directly observed.

Although the Higgs boson cross-section increases as a function of the centre-of-mass energy of the pp collisions, the increase in discovery sensitivity does not. This is due to the cross-sections of other process also increasing. In particular, $t\bar{t}$ production at the LHC dominates the total cross-section and generates a large source of background for Higgs boson measurements and searches. Figure 1.8 shows a comparison of the measured cross-sections of several processes by ATLAS at different centre-of-mass energies ($\sqrt{s} = 7, 8, 13$ GeV). The total ggF Higgs boson cross-section is shown compared to other processes. The state of the art cross-section predictions agree with observations within uncertainties. In most all cases, the experimental uncertainties dominate.

[7] Inverting the roles of t- and b-quarks in Figures 1.7 (b)–(d) requires an initial-state t-quark, making this process highly suppressed, while the process in Figure 1.7 (a) would still be attributed to single top-quark production.

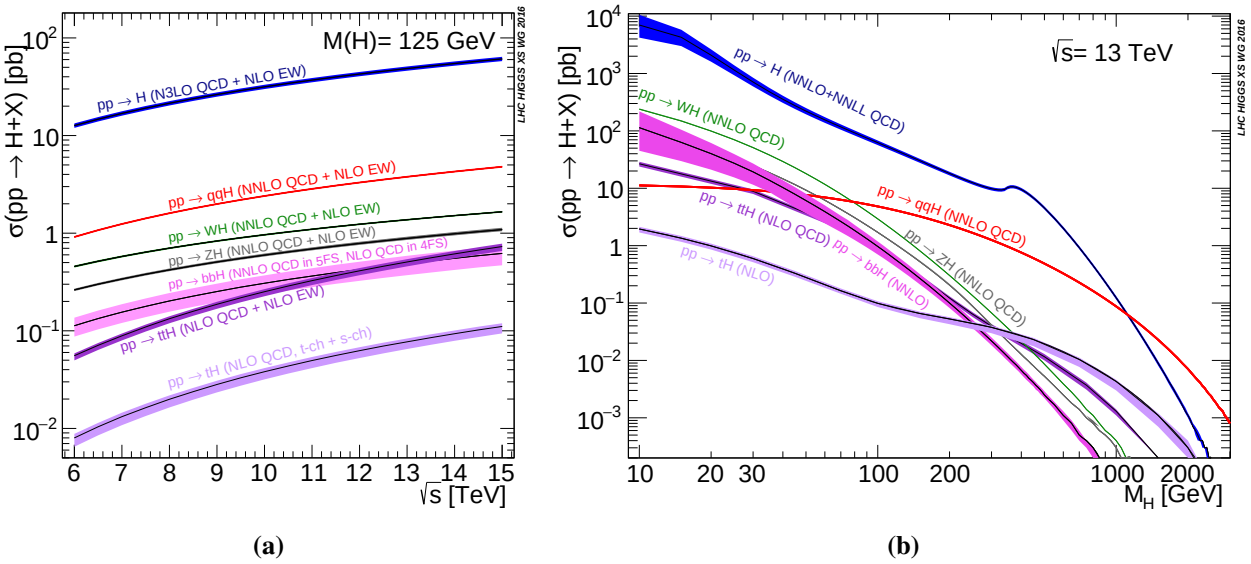

(a) **(b)**

Figure 1.3 Production mode cross-section of a SM Higgs boson with mass $m_H = 125$ GeV at (a) varying pp collision energies, and (b) with varying mass m_H at fixed pp collision energy $\sqrt{s} = 13$ TeV [36].

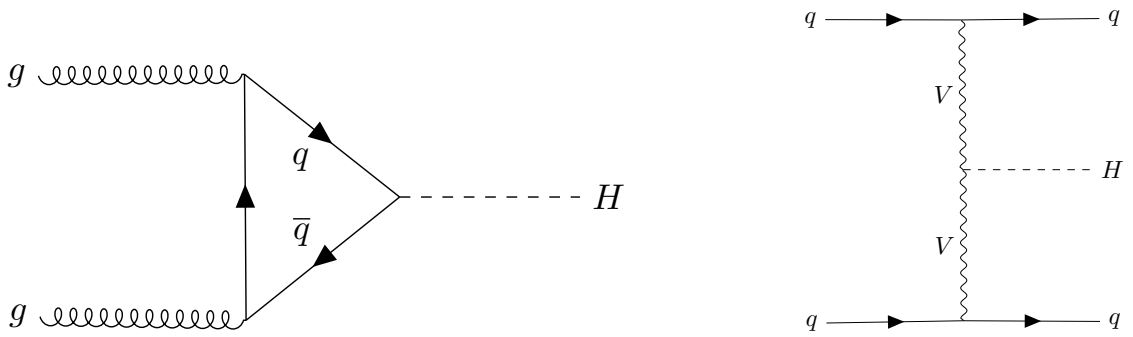

(a) **(b)**

Figure 1.4 Examples of leading-order Feynman diagrams for Higgs boson production via (a) gluon-fusion (ggF) and (b) vector-boson-fusion (VBF).

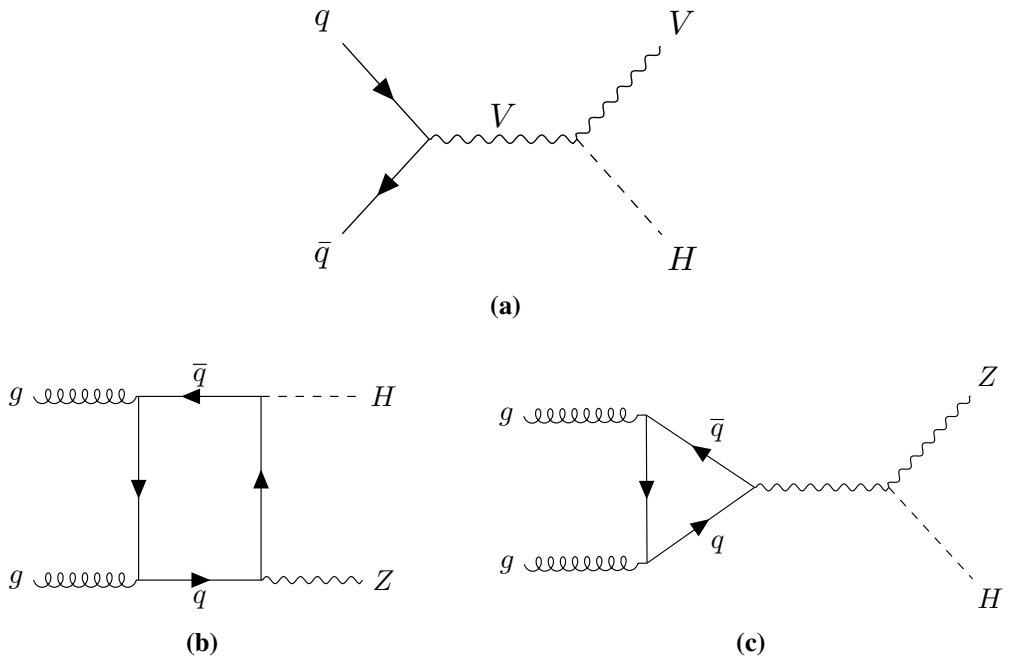

Figure 1.5 Examples of leading-order Feynman diagrams for Higgs boson production via vector-boson associated Higgs boson production (VH) with associated (a) $W^{\pm}$ or Z, or (b, c) Z bosons.

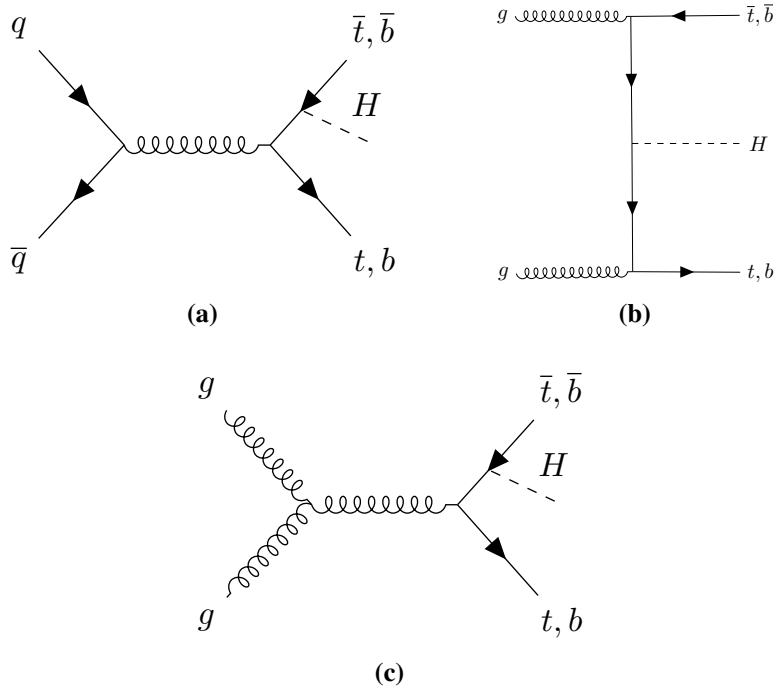

Figure 1.6 Examples of leading-order Feynman diagrams for Higgs boson production via t-quark associated $t\bar{t}H$ or b-quark associated $b\bar{b}H$ production.

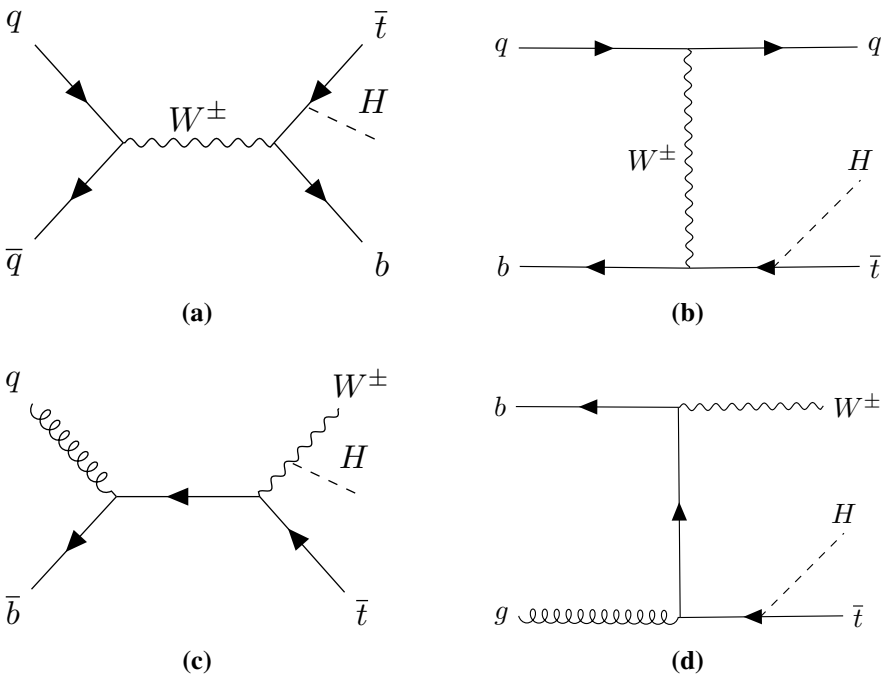

Figure 1.7 Examples of leading-order Feynman diagrams for Higgs boson production via single t-quark associated production tH, along with an associated (subfigures a and b) light quark or (subfigures c and d) $W^{\pm}$ boson.

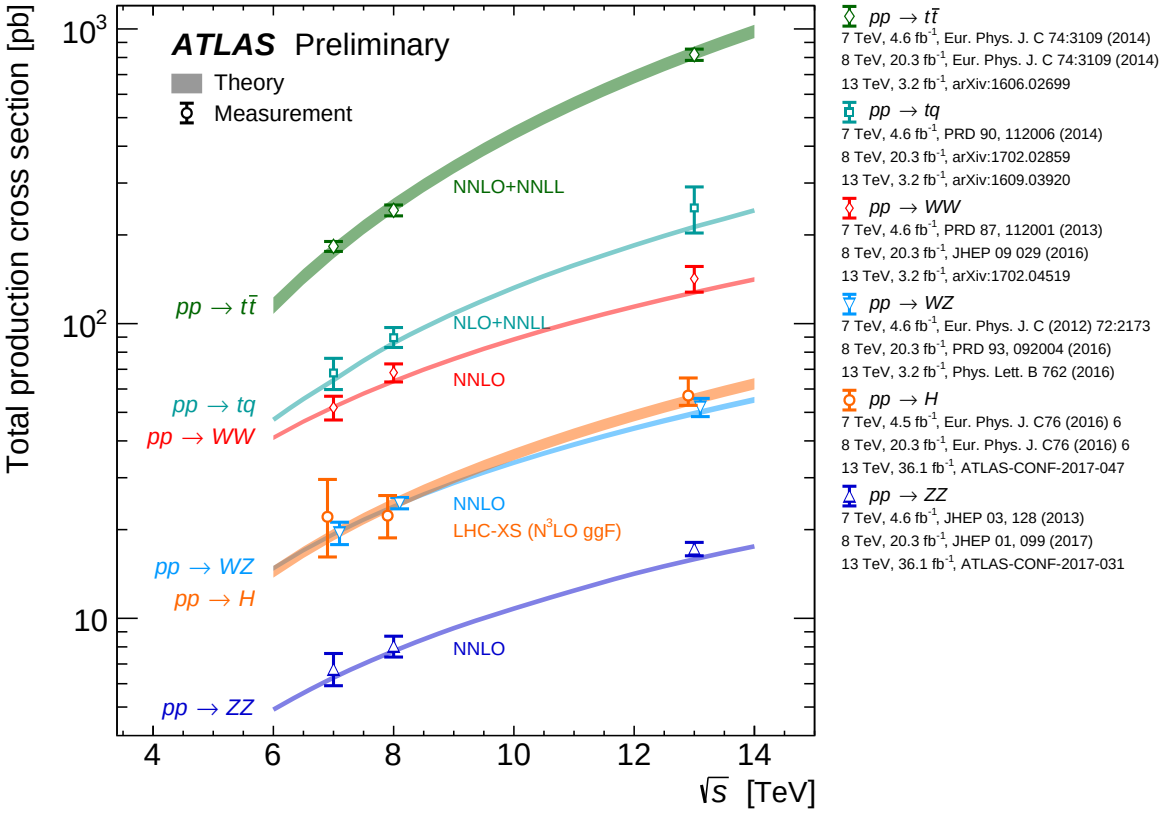

Figure 1.8 Summary of measurements, from ATLAS data-taking periods with $\sqrt{s} = 7, 8$, and 13 TeV pp collisions, of the total production cross-sections for some SM processes [37]. Some markers are displaced horizontally for better visibility. Respective references are shown in the legend.

1.4.2 Higgs boson decay widths and branching fractions

In the SM, the Higgs boson branching fractions for decays to SM particles are proportional to a given particle's mass. As was noted in Section 1.3, the Higgs boson coupling strengths to vector bosons are of the form gm_W and $\frac{gm_W}{\cos\theta_W}$ for the $W^{\pm}$ and Z interactions, respectively. The fermionic Higgs boson coupling strengths are of the form m_f/v. The branching fractions are shown in Figure 1.9 (a) [36, 38] for a Higgs boson with mass ~ 125 GeV, and in Figure 1.9 (b) for a wide range of Higgs boson masses. The dominant branching fraction for a 125 GeV Higgs boson is $H \to b\bar{b}$ ($\sim 58\%$). This signature is however very difficult to probe due to the overwhelming QCD background. Although they have suppressed branching fractions, the two most sensitive decay channels are the $H \to \ell\ell\ell\ell$ ($\sim 0.01\%$ with $\ell \neq \tau$) and $H \to \gamma\gamma$ ($\sim 0.2\%$) due to their final-states providing clean signatures. The $H \to \gamma\gamma$ decay cannot occur directly as the photons have no mass, and do not couple to the Higgs boson directly. The $H \to \gamma\gamma$ decay occurs in the SM through quark and vector-boson loops, as shown in Figure 1.10. It is sometimes convenient to express such loop interactions as an effective coupling, as shown in Figure 1.11. The latest results by ATLAS measuring coupling strengths of the Higgs boson to SM particles will be presented in Section 8.2 as part of the work towards this thesis. In particular, Figure 8.5 gives a direct comparison of the measured coupling strengths, which should scale linearly, in the case of fermions, and quadratically, in the case of vector bosons, with the particle mass. All measurements are found to be consistent with the SM prediction.

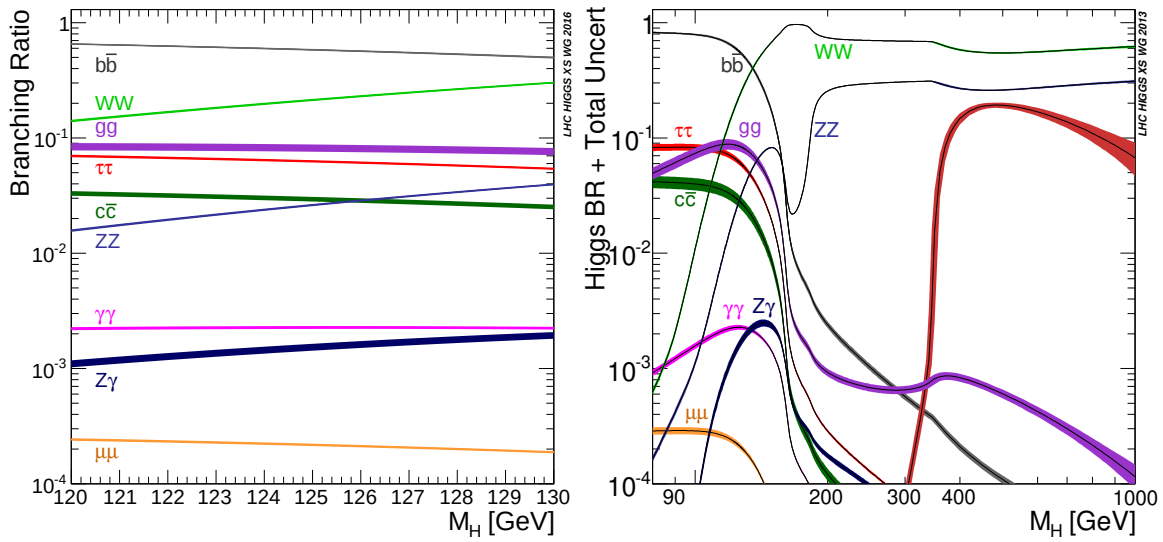

(a) **(b)**

Figure 1.9 Branching ratios of a SM Higgs boson with mass (a) $m_H \approx 125$ GeV [36], and (b) $m_H \in [80, 1000]$ GeV [38].

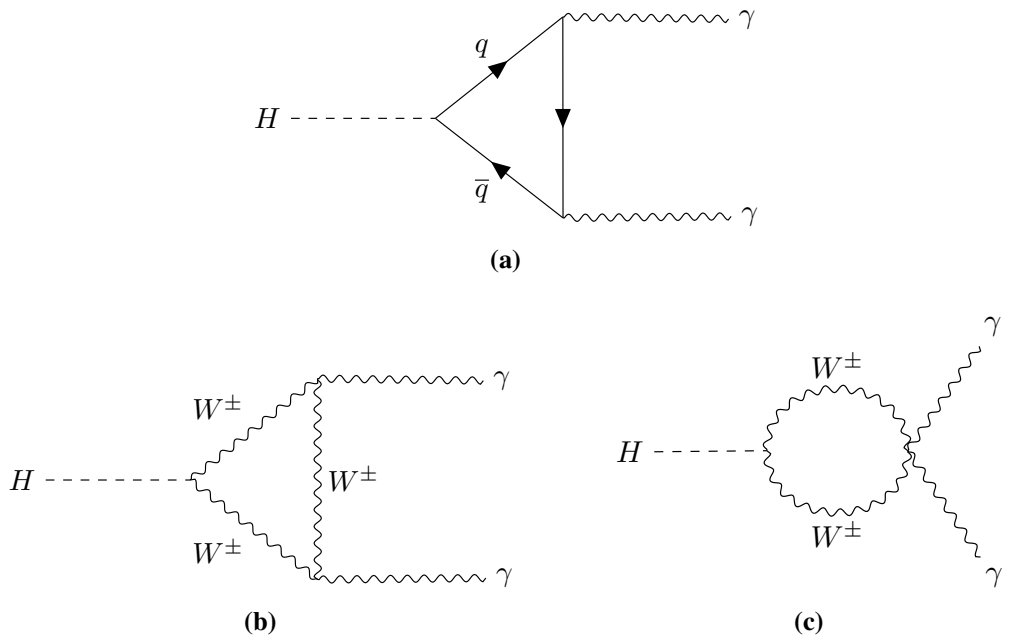

Figure 1.10 Examples of leading-order Feynman diagrams for Higgs boson decay to $\gamma\gamma$ via (a) quark and (b, c) $W^{\pm}$ boson loops.

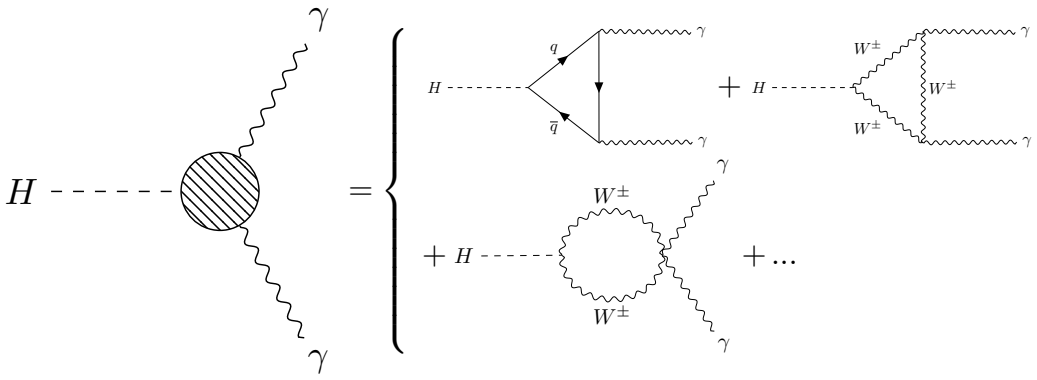

Figure 1.11 Representation of Feynman diagrams for the effective Higgs boson decay to $\gamma\gamma$.

Chapter 2

The Higgs sector beyond the Standard Model

2.1 Shortcomings of the Standard Model

There are several open questions left by the SM which suggest that a theory beyond the Standard Model (BSM) may exist [6]: including open questions about the nature of the flavour sector, the forms of the CKM and PMNS matrices, the process in which the neutrinos acquire mass, and the source of matter/anti-matter asymmetry in the universe after *baryogenesis*. The discussion here only focuses on three potential shortcomings with the SM without attempting to be absolute. The first is dark matter, which is a well established cosmological observation that does not have an adequate particle candidate in the SM. Approximately 85% of the mass of the visible universe is estimated to be composed of dark matter, with the remaining $\sim 15\%$ being visible matter [39]. The second problem in the SM is referred to as the *hierarchy problem*. Corrections to the Higgs boson mass stem from fermionic loops (in particular from the massive t-quark) which would make its mass huge, up to the Planck scale. In order to have a light Higgs boson (as the discovered 125 GeV Higgs) these corrections need to cancel, which in the SM requires a fine tuning of over 30 orders of magnitude. Another observation which may suggest a theory exists beyond the SM is that of the running of strong and EW couplings. It is observed that the EM and weak force are two components of the electroweak force ($\mathrm{SU}(2)_L \times \mathrm{U}(1)_Y$). In a similar manner one might expect the strong force to unify with the electroweak force. Indeed the coupling constants of the SM theory seem to suggest that the EM, weak and strong couplings might align at some high-energy scale, the Grand

Unified Theory (GUT) scale. This hints at the SM being an effective theory of some more fundamental theory which unifies the forces at high-energy.

The Higgs sector is a relevant place to search for answers to these shortcomings. For one, dark matter has mass, and if it obtains it via the BEH mechanism as in the SM, the Higgs boson would directly couple to it. Given that the Higgs sector as defined in the SM, with a single Higgs doublet, is the simplest possible structure required by the theory to acquire massive particles, it seems appropriate to consider extensions of the Higgs sector. The minimal[8] approach to expanding the Higgs sector is to consider adding an additional Higgs doublet, in so called Two-Higgs-Doublet-Models (2HDMs) [7, 40]. The additional DOFs in these models will result in additional Higgs bosons, one of which would be the discovered 125 GeV Higgs. The flexibility of the scalar mass spectrum introduced in Two-Higgs-Doublet-Models (2HDMs) can contain additional sources of charge conjugation and parity violation (CP-violation) required by *baryogenesys*.

An additional motivation for considering 2HDMs comes from supersymmetry (SUSY) [41–43]. In SUSY models each fermionic degree of freedom has a supersymmetric spin-0 partner. Similarly each gauge boson in the SM has a supersymetric spin-$\frac{1}{2}$ partner that is a fermion. SUSY models require two Higgs doublets in order to generate mass terms for all particles in the theory. SUSY also may provide answers to the three shortcomings in the SM discussed above. The simplest possible SUSY model consistent with the SM is the Minimal Supersymmetric extension to the Standard Model (MSSM). Even for the simplified case of the MSSM, it is highly complex model with the most general form boasting up to 120 free parameters. It is therefore common practice for the MSSM to be considered within specified benchmark models, in which specific values of these parameters are chosen, to provide a framework which is practical for interpreting results.

The proton has been observed to be stable with a proper lifetime greater than 2.3×10^{33} years [44]. In a general MSSM the proton is allowed to decay. This issue can be averted by the requirement of conservation the R-parity quantum number [43], defined as,

$$R = (-1)^{2S+3B+L}, \tag{2.1}$$

where S, B and L are spin, baryon, and lepton quantum numbers of a particle. Requiring that R-parity be conserved leads to stable protons. It also results in the lightest supersymmetric particle (LSP) being stable, providing a suitable dark matter candidate. The MSSM models dealt within this thesis are R-parity conserving.

[8] Adding the fewest number of additional parameters.

In the MSSM, SUSY partners to the fermions provide corrections to the Higgs boson mass term that naturally cancel the problematic terms in the SM, and hence, no fine tuning is required. The most important parameters in the correction stem from the stop sector. More details on the Higgs mass in the MSSM are presented in Sections 2.3 and 2.3.1.

Finally, the additional particles provided by SUSY alter the running of the couplings in a way that they converge approximately at the GUT scale. When additional particles from the MSSM are included into the evolution of the running coupling constants, they appear to unify at a singular point at $O(10^{16})$ GeV, as shown in Figure 2.1.

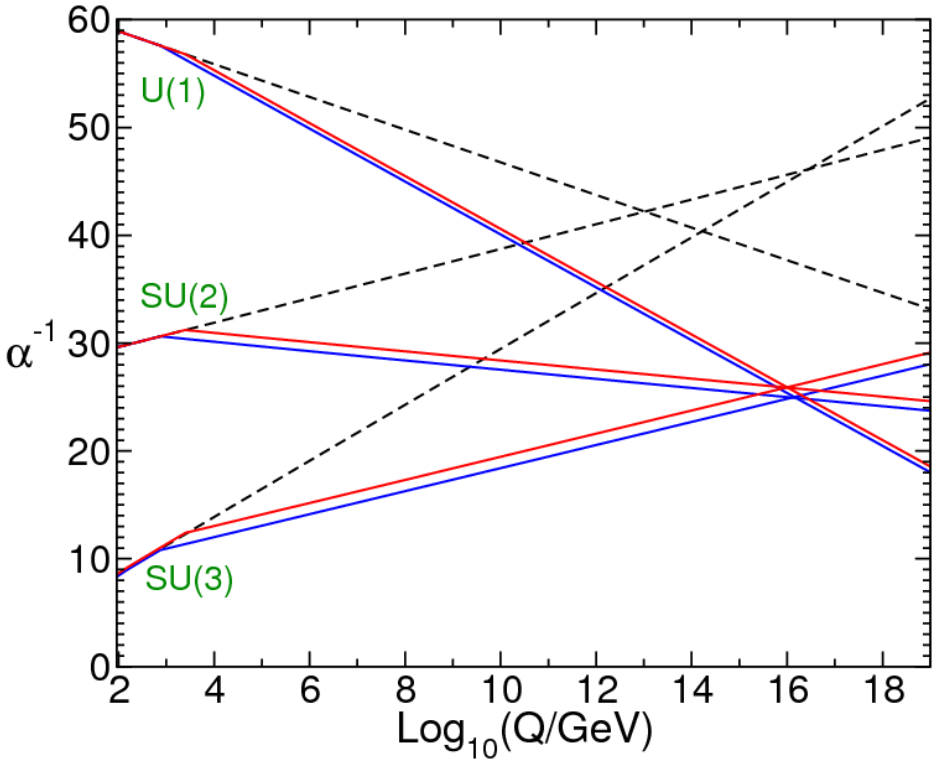

Figure 2.1 Two-loop renormalisation group evolution of the inverse gauge couplings α^{-1} in the Standard Model (dashed lines) and the MSSM (solid lines) [43]. In the MSSM case, two limiting lines are shown for varying sparticle masses.

The study of the minimal extensions to the SM offer a fruitful phenomenology which is motivated by the solutions to problems in the SM as stated above. The remainder of this chapter will focus on introducing 2HDMs and the MSSM, both of which are used to interpret Higgs boson precision measurements and Higgs boson searches in this thesis.

2.2 Two-Higgs-Doublet-Models

Following the discussion in the previous section, it is worth considering a non-minimal Higgs sector. A minimal extension to the SM Higgs sector is that of a 2HDM. In general, the additional complexity in the Higgs sector allows for flavour-changing neutral currents (FCNCs) at tree-level, which are experimentally disfavoured. The phenomenology of several 2HDMs which allow sufficiently suppressed tree-level FCNCs are discussed in Ref. [40]. A simplified approach to studying 2HDMs is by using the result by Glashow and Weinburg [45], which found that Higgs boson mediated FCNCs are absent, at tree-level, if all fermions of a particular charge couple to only one Higgs doublet. Hence FCNCs can be explicitly eliminated from the models by choosing appropriate Higgs-fermion couplings. Additionally, in the simplified models, the Higgs sector is considered to conserve CP. Assuming two Higgs doublets (Φ_1 and Φ_2), and the most general scalar potential[9] $V(\Phi_1,\Phi_2)$ satisfying the simplifications above, the VEVs of each doublet (denoted as v_1 and v_2, respectively) can each be assumed to be real and positive, with $v=\sqrt{v_1^2+v_2^2}\approx 246$ GeV. After EWSB the complex doublets can be written about their minimum,

$$\Phi_a = \begin{pmatrix} \phi_a^+ \\ (v_a+\rho_a+i\chi_a)/\sqrt{2} \end{pmatrix}, \text{ for } a=(1,2), \tag{2.2}$$

where ϕ_a^+ are complex fields, and ρ_a and χ_a are real fields. There are eight DOFs in this Higgs sector, three of which are absorbed by the longitudinal polarisation of the three massive gauge bosons (after choosing the correct gauge). The remaining five DOFs are physical scalar Higgs fields with respective scalar bosons: two charged Higgs ($H^\pm$), one neutral CP-odd Higgs (A^0), and two neutral CP-even Higgs (h^0 and H^0, where by convention $m_{h^0}<m_{H^0}$). There are six free parameters in the 2HDM Higgs sector, four Higgs masses (since $m_{H^+}=m_{H^-}$), the ratio of the VEVs ($\tan\beta\equiv\frac{v2}{v1}$), and the mixing angle of the neutral CP-even Higgs bosons (α). The physical mass eigenstates of the Higgs fields can be written as linear combinations of the above fields,

$$h^0 = \rho_1\sin\alpha-\rho_2\cos\alpha, \tag{2.3}$$
$$H^0 = -\rho_2\sin\alpha-\rho_1\cos\alpha, \tag{2.4}$$
$$A^0 = \chi_1\sin\beta-\chi_2\cos\beta, \tag{2.5}$$
$$H^\pm = \phi_1^\pm\sin\beta-\phi_2^\pm\cos\beta. \tag{2.6}$$
$$\tag{2.7}$$

[9] The full form of the potential is given in Ref. [40].

As with the SM the fermion and vector boson masses are defined by their relation to the VEV, e.g., $m_W^2 = \frac{g^2 v^2}{2} = \frac{g^2(v_1^2+v_2^2)}{2}$. Similarly, the coupling strengths are given by the respective interaction terms of particle fields with the Higgs fields. In the vector boson sector, neutral couplings of the form h^0VV, H^0VV, ZA^0h^0, and ZA^0H^0, are allowed. Notably missing from the Lagrangian are A^0VV terms. As a consequence, the strength of the Higgs di-boson vertex can be expressed relative to the SM coupling strength g_{HVV}^{SM} irrespective of the Higgs boson mass,

$$\xi_{VV}^{H^0} \equiv \frac{g_{H^0VV}}{g_{HVV}^{\mathrm{SM}}} = \cos(\beta-\alpha), \tag{2.8}$$

$$\xi_{VV}^{h^0} \equiv \frac{g_{h^0VV}}{g_{HVV}^{\mathrm{SM}}} = \sin(\beta-\alpha), \tag{2.9}$$

where ξ has been defined as a scale factor to the Higgs-gauge coupling strength relative to the SM. If h^0 is assumed to be the discovered 125 GeV SM-like Higgs, H^0 becomes gauge-phobic at $\cos(\beta-\alpha) \approx 0$ (Eq. (2.8)), giving the SM limit where the h^0VV vertex has the SM coupling strength. The zero superscript is dropped from h^0, H^0 and A^0, i.e., h denotes the SM-like Higgs, H the heavy CP-even Higgs, and A the CP-odd, unless otherwise stated.

As discussed above, one way of guaranteeing no tree-level FCNCs from the Higgs sector can be imposed by carefully coupling fermions with the same quantum numbers to the same Higgs doublets. This allows for four such choices, which by themselves fix the Higgs-fermionic couplings. The first choice is referred to as *Type-I* 2HDM, where all fermions couple to one scalar doublet, Φ_2 by convention, while vector bosons couple to the other, Φ_1. In *Type-II* 2HDM, all down-type fermions couple to Φ_1, while up-type quarks couple to Φ_2. In both cases, all down-type fermions couple to the same Higgs doublet. The additional two choices invert this requirement. In the *Lepton-specific* model, the up- and down-type quarks couple to Φ_2, while down-type leptons couple to Φ_1. The last type is where down-type leptons and up-type quarks couple to Φ_2, while down-type quarks couple to Φ_2, referred to as the *Flipped* 2HDM. The models are summarised in Table 2.1.

Table 2.1 Coupling of 2HMD Higgs doublets to SM fermions in the four models without FCNCs [40].

Model	Type-I	Type-II	Flipped	Lepton-specific
vector bosons	Φ_1	Φ_1	Φ_1	Φ_1
up-type quarks	Φ_2	Φ_2	Φ_2	Φ_2
down-type quarks	Φ_2	Φ_1	Φ_1	Φ_2
leptons	Φ_2	Φ_1	Φ_2	Φ_1

With the above four models defined, the 2HDM Yukawa couplings can be expressed in terms of the SM Yukawa couplings Y_f of Eq. (1.22). In the neutral Higgs sector[10] the Yukawa coupling terms are [7, 40],

$$\mathscr{L}_{\text{Yukawa}}^{\text{2HDM (neutral)}} = -\frac{Y_f}{\sqrt{2}}(\xi_h^f \bar{f} f h + \xi_H^f \bar{f} f H - \xi_A^f \bar{f} \gamma^5 f A), \tag{2.10}$$

where f are summed over fermion spinors, and ξ_ϕ^f are scale factors for $\phi = h, H, A$: they are defined in Table 2.2, where ξ_{up}^ϕ, ξ_{down}^ϕ, and ξ_ℓ^ϕ are for up-type quarks, down-type quarks, and leptons, respectively.

The ξ factors scale the corresponding coupling strengths of the 2HDM Higgs bosons to SM particles with respect to the SM Higgs boson couplings. The terms will translate into $\propto \xi^2$ scaling of the Higgs boson cross-sections and partial widths. However, determining precisely the 2HDM Higgs boson cross-sections and branching fractions is dependant on the Higgs boson mass spectrum, and the kinematically allowed processes. In general there are no tight restrictions on the relative masses of the 2HDM Higgs bosons and the calculation has to be performed for several reference values, as was done in Ref. [40]. However, if we intend to explain the observed 125 GeV Higgs boson with such a model, we should assign this boson to one of the CP-even neutral Higgs bosons. As stated above, it is usually assumed that the lighter h is the discovered 125 GeV Higgs boson[11]. Since the h Higgs couplings to SM particles are well defined in 2HDM, measurements of the 125 GeV Higgs boson cross-section and branching fractions can be used to constrain the parameter space. This is done in the coupling modifier framework in Sections 2.5 and 8.3, where the scale factors in Table 2.2 directly scale the Higgs boson cross-section and branching fraction. Although this is a simplified picture, since one should also consider modifications to the total cross-section from processes like a heavy Higgs decaying to a pair of 125GeV Higgs bosons, $H \to hh$, and higher order loop corrections, it is found be adequate at the SM limit, i.e., $\cos(\beta - \alpha) \approx 0$. The validation of this approximation is performed in Section 8.3.1.1.

[10] The charged Higgs boson introduces flavour-changing charged currents (FCCCs) to the Higgs Yukawa terms, with their strengths dependant on ξ_{up}^A, ξ_{down}^A, and ξ_ℓ^A. The quark terms include CKM matrix-elements. The full expression can be found in Ref. [40] and is not repeated here.

[11] For one, no lighter scalar boson has as of yet been discovered. Secondly, it avoids the additional complication of having H as the 125 GeV boson: effects from decays like $H \to hh$ and $H \to ZA$, which are highly mass dependant, would need to be considered.

Table 2.2 Relative coupling strength of the 2HDM Higgs-fermion Yukawa couplings [40].

Model	Type-I	Type-II	Flipped	Lepton-specific
		Light CP-even h		
ξ^h_{up}		$\cos\alpha/\sin\beta$		
ξ^h_{down}	$\cos\alpha/\sin\beta$	$-\sin\alpha/\cos\beta$	$\cos\alpha/\sin\beta$	$-\sin\alpha/\cos\beta$
ξ^h_{ℓ}	$\cos\alpha/\sin\beta$	$-\sin\alpha/\cos\beta$	$-\sin\alpha/\cos\beta$	$\cos\alpha/\sin\beta$
		Heavy CP-even H		
ξ^H_{up}		$\sin\alpha/\sin\beta$		
ξ^H_{down}	$\sin\alpha/\sin\beta$	$\cos\alpha/\cos\beta$	$\sin\alpha/\sin\beta$	$\cos\alpha/\cos\beta$
ξ^H_{ℓ}	$\sin\alpha/\sin\beta$	$\cos\alpha/\cos\beta$	$\cos\alpha/\cos\beta$	$\sin\alpha/\sin\beta$
		CP-odd A		
ξ^A_{up}		$\cot\beta$		
ξ^A_{down}	$-\cot\beta$	$\tan\beta$	$-\cot\beta$	$\tan\beta$
ξ^A_{ℓ}	$-\cot\beta$	$\tan\beta$	$\tan\beta$	$-\cot\beta$

2.3 The Minimal Supersymmetric Standard Model

SUSY is a well motivated extension to the SM[41, 42]. It relates fermionic and bosonic particle states via a space-time symmetry, resulting in super-multiplets containing particles and their superpartners (*sparticles*). In SUSY models, each fermionic (bosonic) degree of freedom in the SM has a boson (fermion) superpartner with the same quantum numbers. This leads to several additional particles. For example, every quark in the SM can be either left- or right-handed, so there are two spin-0 *squarks* (denoted[12] $\tilde{q}_{\text{L}}$ and $\tilde{q}_{\text{R}}$). Similarly there are spin-0 superpartners for the down-type leptons and up-type neutrinos, the *sleptons* and *sneutrinos*. For the SM vector bosons the superpartners are spin-$\frac{1}{2}$ *gauginos*, i.e., *gluino*, *bino* and *wino*. Additionally, for each Higgs boson there is a spin-$\frac{1}{2}$ *higgsino*. The *neutralinos* ($\tilde{\chi}^0$) and *charginos* ($\tilde{\chi}^{\pm}$) are mass eigenstates of the mixtures of neutral and charged gauginos and higgsinos.

If SUSY is not a broken symmetry, the superpartners described above would be found with the same masses as their corresponding SM particles. In this case, the fine tuning corrections needed to keep the Higgs boson mass at the EW scale is not needed: particle loop corrections to the Higgs boson mass would naturally cancel with their corresponding sparticle loops. However, since sparticles are not observed with the same mass as particles, SUSY is required to be a broken symmetry. For SUSY to solve the hierarchy problem as discussed above, the SUSY breaking scale needs to be of $O(1\text{ TeV})$ [6–8]. Beyond this

[12]The $\tilde{q}_{\text{L}}/\tilde{q}_{\text{R}}$ notation refers to the chiral state of their superpartner particles. The squark itself is spin-0 and does not have a chiral state.

scale, fine tuning of loop cancellations are again needed. Most recently, several searches for sparticles have been performed at ATLAS and CMS [46, 47], placing constraints on TeV scale sparticle masses. In several SUSY models the LSP candidate is stable and weakly interacting, and is a suitable candidate for dark matter.

The Minimal Supersymmetric extension to the Standard Model (MSSM) [48] contains two Higgs doublets H_d ($I = \frac{1}{2}, Y = 1$) and H_u ($I = \frac{1}{2}, Y = -1$) each with corresponding vacuum expectation values, $v_d = v\cos\beta$ and $v_u = v\sin\beta$, where $\tan\beta = \frac{v_u}{v_d}$. The supersymmetric scalar potential in the MSSM can be considered as a special case of the Type-II 2HDM. As with Type-II 2HDM, one doublet (H_u) couples to up-type quarks, while the other (H_d) couples to down-type fermions. Goldstone bosons give mass to the massive gauge bosons, resulting in an additional five scalar Higgs boson mass eigenstates, h, H, A, and $H^{\pm}$. Under CP-conservation the two CP-even Higgs fields are allowed to mix with mixing angle α. This angle diagonalises the mass matrix of h and H and is explicitly dependant on β, and the scalar and Z boson masses [48],

$$\cos 2\alpha = -(\frac{m_A^2 - m_Z^2}{m_H^2 - m_h^2})\cos 2\beta, \tag{2.11}$$

$$\sin 2\alpha = -(\frac{m_H^2 + m_h^2}{m_H^2 - m_h^2})\sin 2\beta. \tag{2.12}$$

Subsequently, the Higgs boson mass spectrum at tree-level can be described by a choice of two free parameters, usually m_{A} and $\tan\beta$ [7, 48],

$$m_{H^{\pm}}^2 = m_{\mathrm{A}}^2 + m_W^2, \tag{2.13}$$

$$m_H^2 = \frac{1}{2}(m_{\mathrm{A}}^2 + m_Z^2 + \sqrt{(m_{\mathrm{A}}^2 + m_Z^2)^2 - 4m_Z^2 m_{\mathrm{A}}^2\cos^2(2\beta)}), \tag{2.14}$$

$$m_h^2 = \frac{1}{2}(m_{\mathrm{A}}^2 + m_Z^2 - \sqrt{(m_{\mathrm{A}}^2 + m_Z^2)^2 - 4m_Z^2 m_{\mathrm{A}}^2\cos^2(2\beta)}). \tag{2.15}$$

The resulting predicted Higgs boson mass spectrum places lower limits on the heavy CP-even, CP-odd, and charged Higgs bosons: $m_{H^{\pm}} \geq m_W$, $m_H \geq m_Z$ and $m_{\mathrm{A}} \geq m_h$, making them heavy. There is also an important upper limit on the lightest CP-even Higgs [7, 48]: $m_h \leq m_Z|\cos(2\beta)|$, i.e., m_h is required to be lighter than m_Z at tree-level. However, radiative corrections to m_h push the upper limit to ~ 135 GeV, consistent with the 125 GeV Higgs. The most important parameters to the radiative corrections come from the SUSY sector: in particular the stop mixing parameter (X_t), and the stop masses ($m_{\tilde{t}_1}$ and $m_{\tilde{t}_2}$) usually expressed as $M_{\mathrm{SUSY}} = \sqrt{m_{\tilde{t}_1} m_{\tilde{t}_2}}$.

At the decoupling limit ($m_{\mathrm{A}} \gg m_Z$) the lightest Higgs boson h attains couplings that are SM-like. In particular, this limit corresponds to $\alpha \approx \beta - \frac{\pi}{2}$ for which the hVV couplings approach their SM values (as in Eq. (2.8)). Accordingly the HVV coupling vanishes. At this limit the masses of the heavy Higgs bosons become almost degenerate: $m_{\mathrm{A}} \simeq m_H \simeq m_{H^\pm}$. In the fermion sector, the resulting down-type couplings are proportional to $\tan\beta$, while up-type couplings are proportional to $\cot\beta$. As a result, the production of MSSM Higgs bosons via b-associated Higgs boson production, and decaying to down-type quarks or leptons (e.g., $b\bar{b}$ or $\tau^+\tau^-$), is enhanced compared to the SM in large portions of the parameter space.

In the SM the production of Higgs bosons in association with b-quarks is suppressed by ~ 2 orders of magnitude when compared to the dominant gluon fusion process, putting direct $b\bar{b}H$ observations out of reach of the current experiment. However, dominant production modes for the neutral Higgs bosons in the MSSM are gluon-fusion (ggF) and b-associated Higgs boson production, the latter of which is enhanced at large values of $\tan\beta$. These production modes are discussed in the context of the MSSM in Sections 2.4.1 and 2.4.2. Although at tree-level the MSSM Higgs boson mass spectrum is well defined without explicitly selecting SUSY parameters, it is not possible to ignore the large radiative corrections needed to relax the upper bound on m_h. These corrections, stemming from SUSY masses and mixing parameters, need to be defined. This results in several benchmark scenarios in the MSSM, discussed in Section 2.3.1.

2.3.1 MSSM benchmark scenarios

In order to accommodate the measured 125 GeV Higgs, proposed MSSM scenarios should provide a candidate Higgs boson with this mass. The 125 GeV Higgs boson is commonly considered to be the lightest CP-even Higgs, where MSSM scenarios provide light Higgs bosons with $m_h \sim 125$ GeV. As discussed earlier, corrections to m_h from loop contributions in the MSSM are crucial for attaining $m_h \sim 125$ GeV. In most scenarios the SUSY parameters are constrained by requiring them to produce a Higgs mass of $m_h = 125 \pm 3$ GeV [36]. The 3 GeV range is attributed to the uncertainty with which the Higgs boson masses are predicted in the MSSM. In general: $M_{\mathrm{SUSY}} = 1$ TeV provides m_h in this range with maximal X_t for $\tan\beta \gtrsim 10$; while at $\tan\beta \lesssim 10$, m_h vanishes at tree-level and larger values of M_{SUSY} are generally needed [36].

The $m_{\mathrm{h}}^{\mathrm{max}}$ scenario [49] was originally defined in order to provide conservative bounds on $\tan\beta$ at the Large Electron-Positron Collider (LEP) [50, 51] and predates the Higgs boson discovery: the mixing parameter X_t is defined at each $\tan\beta$ value so as to maximise m_h.

This scenario is still used for interpretations in Run-2 of the LHC to serve as a comparison to previous results, and to provide conservative constraints for the MSSM. The scenario is updated [52] with higher precision experimental measurements of m_{t}, and increased gluino masses in accordance with updated $m_{\tilde{g}}$ search lower limits. The resulting region not excluded by experiment and compatible with $m_h = 125.09 \pm 3$ GeV is at values of $\tan\beta < 10$ (see Figure 6.33 (b) for details).

The $m_{\mathrm{h}}^{\mathrm{mod+}}$ scenario [52] is a modified version of $m_{\mathrm{h}}^{\mathrm{max}}$, defined in light of the discovered Higgs boson at 125 GeV. While the $m_{\mathrm{h}}^{\mathrm{max}}$ maximised m_h, tweaking the mixing parameter X_t can easily produce values in the desired range of m_h. There are two such variations, $m_{\mathrm{h}}^{\mathrm{mod+}}$ and $m_{\mathrm{h}}^{\mathrm{mod-}}$, depending on the chosen sign of X_t. Due to this definition they provide a wide range of parameter space withing the allowed m_h range (see Figures 6.33 (c) and (d)).

Interpretations in the $m_{\mathrm{h}}^{\mathrm{mod+}}$, $m_{\mathrm{h}}^{\mathrm{mod-}}$ and $m_{\mathrm{h}}^{\mathrm{max}}$ are presented in the context of the heavy Higgs boson to di-tau search of Chapter 6 as part of the work for this thesis. In these scenarios most SUSY particles are relatively heavy, while having relatively light neutralinos and charginos (~ 200 GeV) which reduce the heavy neutral Higgs boson branching fractions to SM particles. Additional MSSM scenarios have been proposed, and are summarised here, but are not used for interpretation in this thesis. Recently Ref. [53] introduced updated benchmark scenarios intended to be used for the final Run-2 searches. The main updates are from higher precision measurements of the 125 GeV Higgs boson total cross-section and mass, as well as updated limits on SUSY particle masses. Most importantly, the precision in the MSSM calculations of m_h has improved, requiring a more constrained range on m_h ($\sim$ 1–2 GeV). Additional MSSM models have been defined with different light SUSY particles, such as the *light-stop*, and *light-stau* scenarios [52]. The *tau-phobic* scenario [52] reduces the neutral Higgs boson branching fraction to down-type fermions, and also predicts low-mass staus, with possible $H \to \tilde{\tau}_1\tilde{\tau}_2$ decays. These scenarios have also been revisited in light of new experimental constraints and higher precision calculations [53]. Scenarios with light charginos, neutralinos or staus are provided, with the *light-stop* and *tau-phobic* scenarios no longer valid in light of the most recent experimental constraints. A new scenario dubbed m_h^{125} sets all superpartners at high masses, providing a 2HDM-like model with MSSM inspired couplings [53]. Ref. [53] also introduces *alignment* scenarios in which either h or H are compatible with the measured Higgs boson cross-sections and branching fractions, irrespective of the other MSSM Higgs boson masses, i.e., without assuming the decoupling limit ($m_{\mathrm{A}} \gg m_Z$), allowing for valid parameter space at lower Higgs boson masses. A scenario which allows CP-violation in the Higgs sector [53] is also provided for the first time.

The final benchmark discussed takes a different approach to those defined above, and is also used in interpretations in this thesis. As stated above, as $\tan\beta$ approaches unity m_h vanishes and the SUSY masses are required to be much larger than $O(1\text{ TeV})$ in order to attain corrections resulting in $m_h \sim 125$ GeV. Precise calculations in this case require an Effective Field Theory (EFT) approach which is presently an area of active research [53]. An alternative to attaining predictive calculations at low $\tan\beta$ is by using the hMSSM scenario [36, 54, 55]. This scenario is used in interpretations for both the MSSM Higgs boson searches (Sections 6.5.4 and 7.5) and the SM Higgs boson coupling reinterpretation (Section 8.3.2.2) documented in this thesis. In the hMSSM, $m_h = 125.09$ GeV is considered as a fixed parameter of the model. In this implementation, instead of searching for SUSY parameters that provide the radiative corrections needed to yield $m_h \sim 125$ GeV, these corrections are determined from the fixed m_h value. Several simplifications are made in the hMSSM in order for this to be possible. All SUSY particles are assumed to be too massive to affect the production (except for squark loop contributions) and decays of the Higgs boson. Only the leading radiative corrections to tree-level masses are considered to be relevant: those from stop and top loops. This treatment allows one to express the entire Higgs sector in terms of m_A, $\tan\beta$ and m_h, where the radiative corrections are now also expressed in terms of these parameters. If it is assumed that this approximation is valid even for large M_SUSY, the hMSSM avoids any dependence on additional SUSY parameters. However, it should be noted that at values of $\tan\beta \lesssim 1.5$ and $m_\text{A} \lesssim 200$ GeV, requiring $m_h = 125$ GeV may translate to M_SUSY at the GUT scale, yielding an undesirable MSSM[13]. Additionally, although it is true that stop and top radiative corrections are dominant in the majority of the phase-space, this assumption can break down at low values of $\tan\beta$ [53].

Calculations for the Higgs masses, cross-sections, and branching fractions, are determined in the context of the benchmark scenarios following the prescription in Ref. [36]. The masses and Yukawa coupling of the Higgs bosons are computed with FEYNHIGGS [56–61] and their resulting branching fractions calculated by combining calculations from HDECAY [62, 63], FEYNHIGGS and PROPHECY4f [64, 65]. This is done for all scenarios with the exception of the hMSSM, for which the Higgs masses and branching fractions are computed using HDECAY only. Higgs boson cross-sections and branching fractions to SM particles are shown in Figures 2.2 and 2.3 for neutral Higgs bosons in the hMSSM and $m_\text{h}^{\text{mod}+}$, respectively. For the $m_\text{h}^{\text{mod}+}$ the branching fractions to the LSP are also shown. The dominant cross-sections for neutral Higgs boson production are ggF and b-associated production ($b\bar{b}\phi$) which are discussed in Sections 2.4.1 and 2.4.2. An increase in the A boson cross-section via ggF is seen at $m_A = 2 \times m_t$ due to on-shell top-quarks entering the production, and is more pronounced

[13] The fine tuning of the Higgs boson mass is again required.

at lower values of $\tan\beta$ where ggF is enhanced. The undulations in branching fractions at particular values of m_A correspond to the mass points where decay modes such as $A \to Zh$, $H \to hh$, $H \to Zh$ and $H \to WW$ (not shown in Figures 2.2 and 2.3) become kinematically available. The dominant production mode for charged Higgs boson production is dependant on $m_{H^\pm}$ and is discussed in Section 2.4.3.

2.4 BSM Higgs boson production

2.4.1 Neutral Higgs boson production via gluon-fusion

The ggF production of a neutral Higgs boson, $\phi = h/H/A$, in the MSSM is predominantly though virtual quark and squark loops as shown in Figure 2.4. The cross-sections for ggF production are calculated using SUSHI [66], which includes next-to-leading-order (NLO) supersymmetric-QCD corrections [67–72] predominantly due to stop and sbottom production loops. Next-to-next-to-leading-order (NNLO) QCD corrections for the top quark [73–77], as well as light-quark EW effects [78, 79], are also included.

In the heavy Higgs boson to di-tau search in Chapter 6, the ggF samples are generated assuming SM couplings and this underestimates the loop contributions from b-quarks at high $\tan\beta$. This can ultimately impact the Higgs boson p_{T} spectrum and subsequent signal acceptance. As discussed in Ref. [36], at the limit where $p_{\mathrm{T}}^{\phi} \to 0$, a resummation procedure is needed in order to obtain accurate results. An accurate calculation of the differential Higgs boson p_{T} cross-section is obtained by calculating top-quark-only and bottom-quark-only loop contributions separately at appropriate scales [36, 80], $Q_t(m_\phi)$ and $Q_b(m_\phi)$, and then adding the top-bottom loop interference calculation, which is performed at an interference scale $Q_{\mathrm{int}}(m_\phi)$. There are currently plans to provide a tool to perform the Higgs boson p_{T} reweighting for ggF signal samples. Details of the reweighting scheme are documented in Appendix A.1. Appropriate choices for the scales are shown in Figure A.1. A Higgs p_{T} distribution which takes into account the interference effects is shown in Figure A.2. The individual contributions are reweighted by the respective Yukawa coupling in the MSSM. These effects were not included in the results of Chapter 6 as they were found to cause negligible impact on the final discriminant and signal acceptance within the mass range considered, i.e., $m_{\mathrm{A}} \geqq 200$ GeV. The resummation procedure is utilised by a more recent CMS search for heavy Higgs bosons decaying to di-tau [81], where the area in which the final limits were effected is found to be below $m_{\mathrm{A}} \sim 130$ GeV.

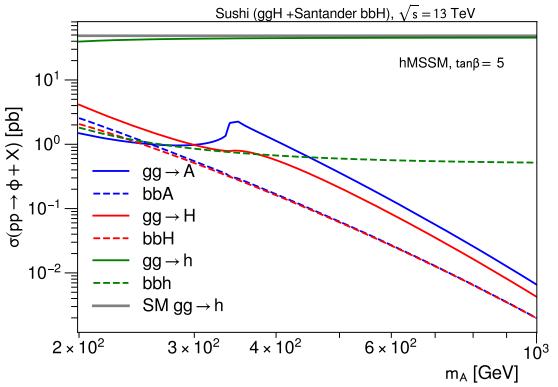

(a) $\sigma, \tan\beta = 5$

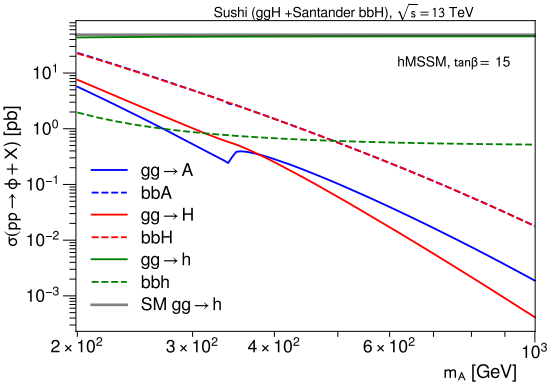

(b) $\sigma, \tan\beta = 15$

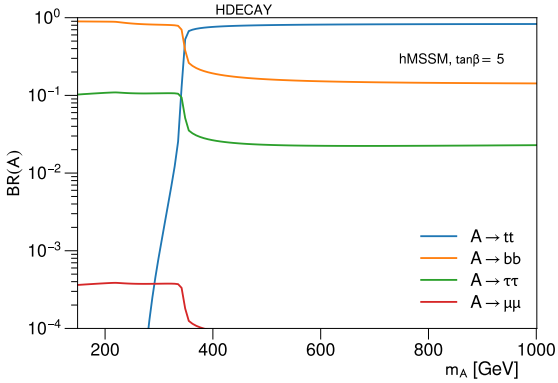

(c) $BR(A), \tan\beta = 5$

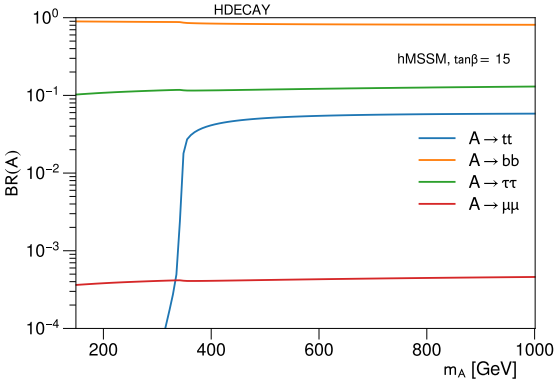

(d) $BR(A), \tan\beta = 15$

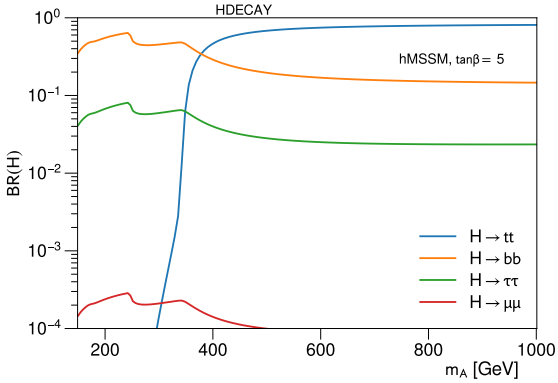

(e) $BR(H), \tan\beta = 5$

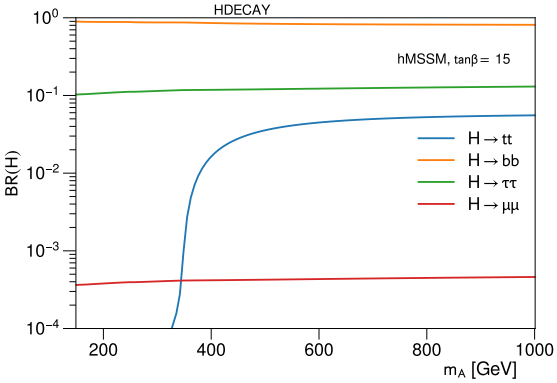

(f) $BR(H), \tan\beta = 15$

Figure 2.2 Higgs boson cross-section and branching fractions in the hMSSM scenario. Shown are h, H and A cross-sections via ggF and $b\bar{b}\phi$ at (a) $\tan\beta = 5$ and (b) $\tan\beta = 15$. The respective branching fractions are shown for A at (c) $\tan\beta = 5$ and (d) $\tan\beta = 15$ and for H at (e) $\tan\beta = 5$ and (f) $\tan\beta = 15$. The hMSSM has no predicted LSP branching fraction.

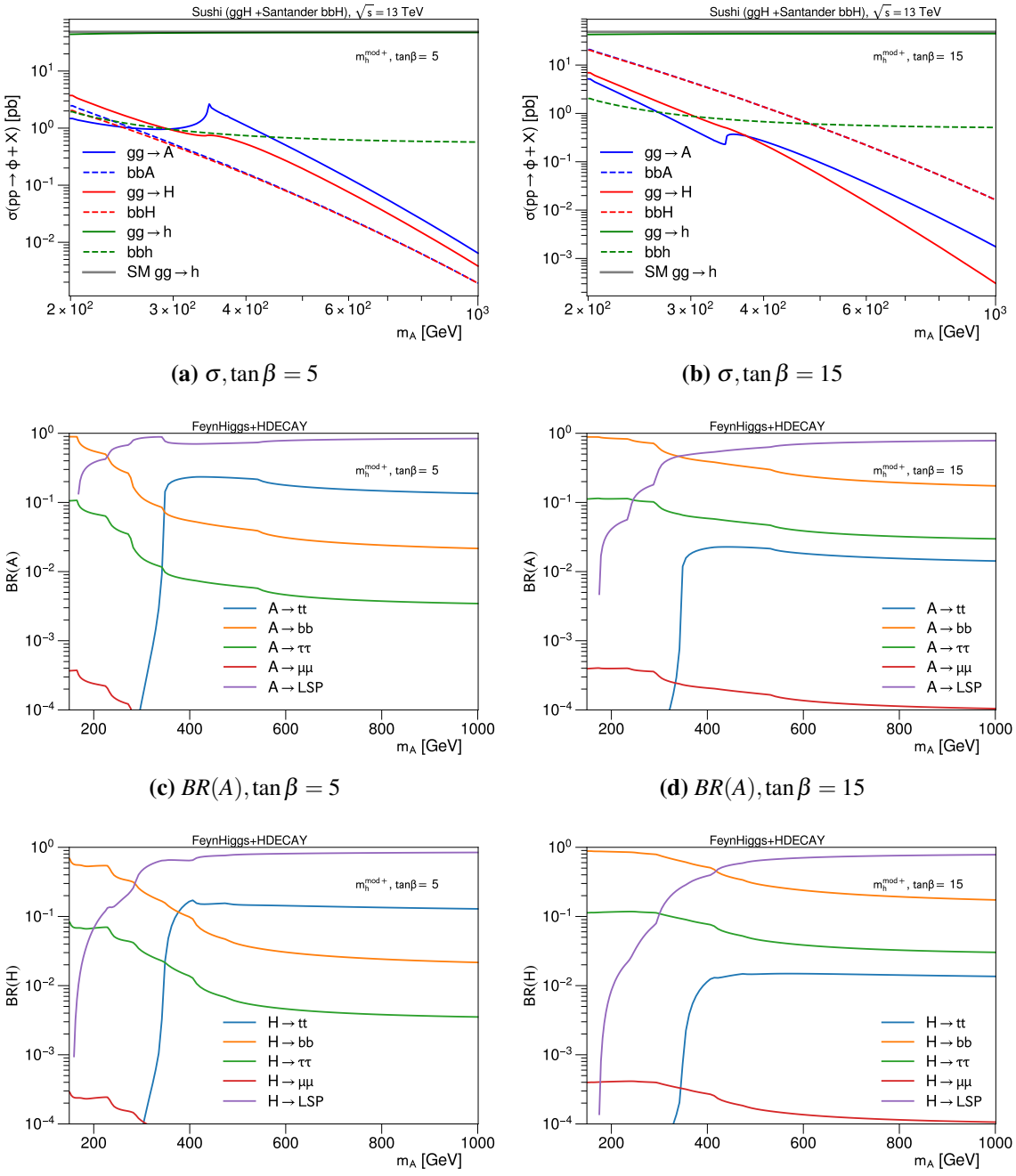

(a) $\sigma, \tan\beta = 5$ **(b)** $\sigma, \tan\beta = 15$

(c) $BR(A), \tan\beta = 5$ **(d)** $BR(A), \tan\beta = 15$

(e) $BR(H), \tan\beta = 5$ **(f)** $BR(H), \tan\beta = 15$

Figure 2.3 Higgs boson cross-section and branching fractions in the $m_{\mathrm{h}}^{\mathrm{mod+}}$ scenario. Shown are h, H and A cross-sections via ggF and $b\bar{b}\phi$ at (a) $\tan\beta = 5$ and (b) $\tan\beta = 15$. The respective branching fractions are shown for A at (c) $\tan\beta = 5$ and (d) $\tan\beta = 15$ and for H at (e) $\tan\beta = 5$ and (f)$\tan\beta = 15$. The branching fractions to LSP are shown.

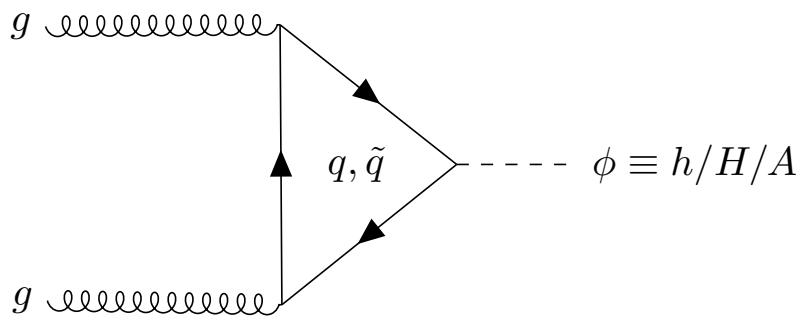

Figure 2.4 Leading-order Feynman diagram for a MSSM neutral Higgs boson produced via gluon-fusion (ggF).

2.4.2 Neutral Higgs boson production in association with a b-quark

The enhancements of Higgs boson couplings to down-type fermions in 2HDM and MSSM will enhance the $b\bar{b}H$ production cross-section with respect to the SM. Under certain conditions (e.g., high values of $\tan\beta$ in MSSM), $b\bar{b}H$ may even become the dominant production process, warranting proper modelling and evaluation of its theoretical cross-section and associated uncertainties. The four-flavour scheme (4FS) and five-flavour scheme (5FS) are two methods for calculating the $b\bar{b}\phi$ cross-section at different limits of the hard-scatter scale [82]. A description and comparison of these two schemes, as well as solutions for consolidating their differences, follows.

The production of $b\bar{b}\phi$ in pp collisions involves the energy scale of the hard interaction (Q). In the case where the hard-scatter scale is at the order of the mass of the b-quark, $Q \sim m_b$, it becomes convenient to perform cross-section calculations in which the b-quark does not appear in the initial-state partonic process. Calculations in this limit are therefore known to be in the 4FS: they exclude the 5th quark flavour from initial-state partons. Instead, final-state b-quarks in $bb\phi$ production are produced by gluons splitting into $b\bar{b}$. The LO processes for $b\bar{b}\phi$ in the 4FS are shown in Figure 2.5. They involve gluon-gluon (Figure 2.5 (a)) or quark-antiquark (Figure 2.5 (b)) initial-state interactions. The initial-state quark-antiquark interactions in Figure 2.5 (b) is exclusively between light quarks. Both diagrams show $g \to b\bar{b}$ splitting responsible for generating final-state b-quarks. The 4FS has the advantage of having well defined final-state b-quark observables involving 0, 1, or 2 b-tagging events, due to the final-state b-quark multiplicity of the LO diagrams (Figure 2.5). However, at scales where $Q >> m_b$, collinear divergences break down of the predictive power of calculations in the 4FS [82].

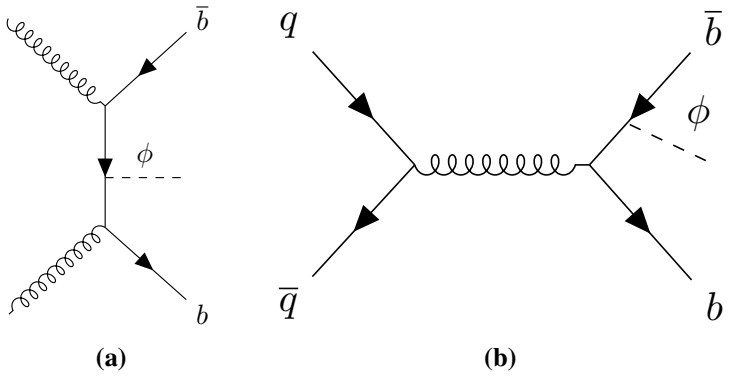

Figure 2.5 Feynman diagrams of the LO $b\bar{b}\phi$ production for the four-flavour scheme with (a) gluon-gluon and (b) quark-antiquark initial interactions.

The divergences at high values of Q in the 4FS are remedied in the 5FS where the b-quarks are assumed to be massless and can therefore be treated in the same way as light initial-state quarks in the partonic process [82]. The LO $b\bar{b}\phi$ process in the 5FS is shown in Figure 2.6 (a). This $2 \rightarrow 1$ process has the benefit of being much simpler than the 4FS LO processes, and hence it is feasible to calculate its radiative corrections beyond NLO (Figure 2.6 (b)) and NNLO (Figure 2.6 (c)), while on the other hand the state of the art 4FS calculations are limited to NLO precision. The level of simplicity of the 5FS does come at the cost of final-state kinematics. Information of observables with non-zero b-tagged multiplicities become available only at NLO and NNLO , which ultimately incurs additional uncertainties in the kinematics and tagging of the b-quark.

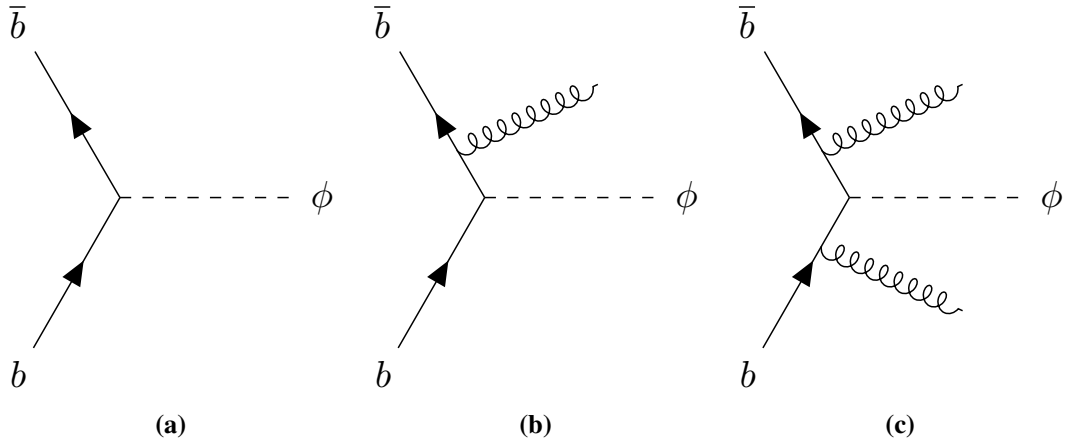

Figure 2.6 Feynman diagrams of the (a) LO, (b) NLO and (c) NNLO $b\bar{b}\phi$ production for the five-flavour scheme

Calculations of the $b\bar{b}\phi$ cross-section are performed in the 5FS using SUSHI based on BBH@NNLO [83]. In the 4FS cross-sections are taken from the SM calculations and reweighted by the corresponding MSSM Yukawa coupling vales as described in [84, 85]. Calculations of the $b\bar{b}H$ cross-section at a particular Higgs boson mass m_H in the SM are directly applicable to the cross-sections of all neutral Higgs [36] (i.e., $b\bar{b}\phi$ for $\phi = h, H, A$) in a 2HDM, and to a good approximation in MSSM, by reweighting with the respective Yukawa scale factors for the model.

Following the discussion above, the 4FS and 5FS have arguments which work for and against either scheme. The 4FS prescription is valid up to $Q \sim m_\phi/4$, after which large collinear logarithms become important, and the 5FS provides better predictive power. The Santander matching technique described in Ref. [82] proposes a pragmatic interpolation between the two asymptotic limits at very light and heavy Higgs boson masses. It uses a reweighting which combines the 4FS and 5FS, converging on using the 5FS at $m_\phi \to \infty$ and the 4FS at the low limit $m_\phi \sim m_b$. The lower mass limit from which the 5FS begins to take affect needs to be chosen at the point when logarithmic corrections become sizeable. The choice of $\log(m_\phi/m_b) = 2$ is made, and leads to an equal weighting of the two schemes at moderate values of $m_\phi \sim 100$ GeV, where the two schemes yield the most similar inclusive cross-sections. It leads to the following formula for the inclusive $b\bar{b}\phi$ cross-section ($\sigma^{\text{Santander matched}}_{b\bar{b}\phi}$) [82],

$$\sigma^{\text{Santander matched}}_{b\bar{b}\phi} = \frac{1}{1+\omega}(\sigma^{4FS}_{b\bar{b}\phi} + \omega\sigma^{5FS}_{b\bar{b}\phi}) \tag{2.16}$$

where

$$\omega = log\frac{m_\phi}{m_b} - 2 \tag{2.17}$$

Included here as an example is the effect of Santander matching in the hMSSM, calculated as described in Ref. [36]. The total inclusive cross-sections of the Santander matched $b\bar{b}\phi$ production for the neutral Higgs bosons (h, H, A), along with the individual cross-sections from 4FS and 5FS, are shown in Figure 2.7. Since in the hMSSM the SM-like Higgs boson is $m_h = 125$ GeV at all valid values of m_A, $\sigma_{b\bar{b}h}$ is evaluated only at values considered to be moderate in Santander matching. Therefore the Santander matched SM-like Higgs boson cross-section in the hMSSM will resemble an average of the two schemes, $\sigma_{b\bar{b}h} \approx (\sigma^{4FS}_{b\bar{b}h} + \sigma^{5FS}_{b\bar{b}h})/2$. For H and A bosons, where $m_A \sim m_H$, the matching shows the $b\bar{b}\phi$ cross-section of at moderate ($m_A \sim 200$ GeV) as an average of 4FS and 5FS cross-sections, while for higher values of m_A the calculation converges on the 5FS.

Santander matching is currently used as the default inclusive cross-section prediction for $b\bar{b}\phi$ in MSSM interpretations by analysis at the LHC. One should note however that the Santander matching scheme is by no means theoretically rigorous. Newer prescriptions from the Large Hadron Collider Cross Section Working Group (LHCXSWG) recommend the use of fully matched 4FS and 5FS prescription as documented in Refs. [86] and [87]. The prescription combines the complete NLO 4FS calculation including top-loop interference contributions with the resummation of the collinear logarithms presented in the 5FS. It has been found to give slightly larger $b\bar{b}\phi$ cross-sections with smaller uncertainties with respect to Santander matching, although their central values do match within 1σ. The current interpretations from limits on the $b\bar{b}\phi$ cross-section can therefore be viewed as conservative in regions where the $b\bar{b}\phi$ cross-section dominates. The end of Run-2 analysis will have updated recommendations from the LHCXSWG with the fully matched $b\bar{b}\phi$ cross-section calculations.

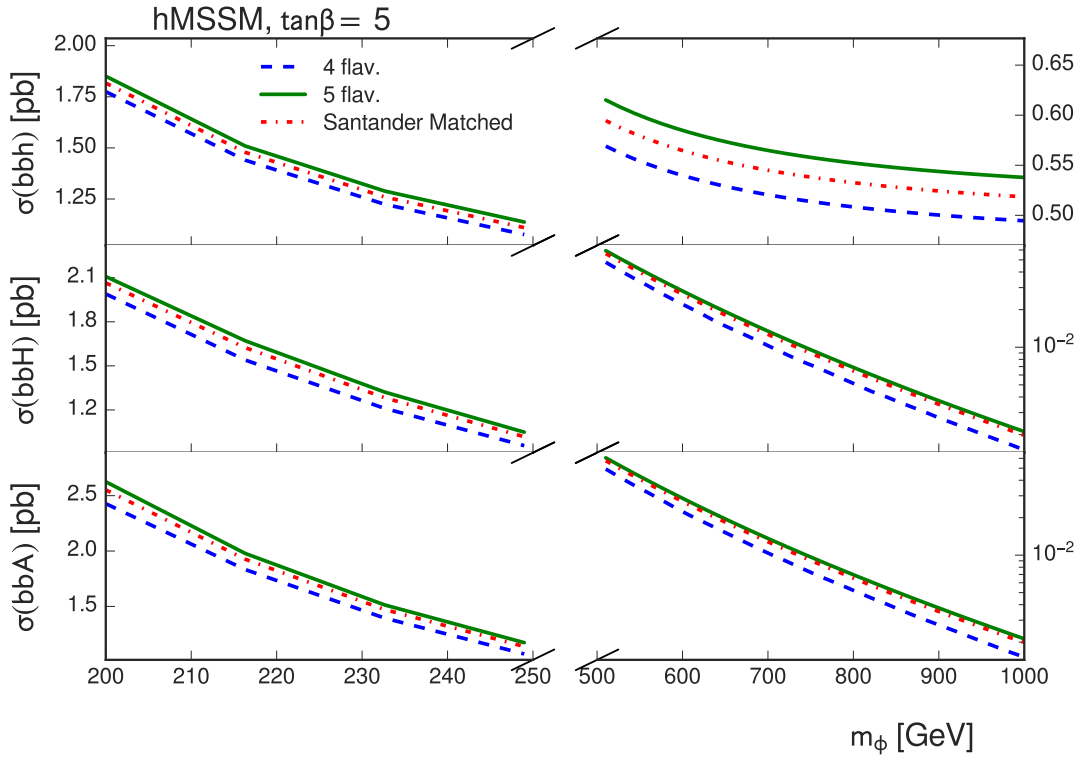

(a)

Figure 2.7 Total cross-section of the neutral Higgs bosons (h, H, A) via b-quark associated production at $\tan\beta = 5$ and as a function m_A in the hMSSM model. Shown is a comparison of the different b-quark associated four- and five-flavour cross-section calculations, along with the Santander matched cross-section. The m_A axis is split into lower and higher m_A so as to compare the cross-sections at different scales.

2.4.3 Charged Higgs boson production

The leading production process of the charged Higgs boson at the LHC is dependant on its mass $m_{H^\pm}$ and can be classified into three regions. If $m_{H^\pm}$ is light enough the primary production will be through the decay of the top-quark, $t \to H^+ b$, as shown in Figure 2.8 (a). At low enough mass range, $m_{H^\pm} \lesssim 160$ GeV, top-quark off-shell effects can be neglected, and the $H^\pm$ cross-section can be simply determined from the $t\bar{t}$ cross-section multiplied by the predicted $t \to H^+ b$ branching fraction, where both top-quarks are considered on-shell. In the high-mass range, $m_{H^\pm} \gtrsim 200$ GeV, the dominant production is in association with a top-quark, as shown in Figure 2.8 (b). Here there is no associated $W^\pm$ at LO and the final-state is $pp \to \bar{t}bH^+$. Here the heavy charged Higgs boson total cross-section calculation can be performed in the 4FS and 5FS which are Santander matched [36, 88–91]. At the mass range around the top mass, 145 GeV $\lesssim m_{H^\pm} \lesssim 200$ GeV, effects from non-resonant (Figure 2.8 (c)), single-resonant, and double-resonant top-quarks play an important part and the full $pp \to H^\pm W^\mp b\bar{b}$ process needs to be considered [92]. The recent work of Ref. [92] provides cross-section calculations in the intermediate mass region performed at NLO precision. The total cross-section for a charged Higgs boson from Type-II 2HDM is shown in Figure 2.9. In order to obtain MSSM cross-sections for different scenarios, the 2HDM NLO cross-sections are corrected by MSSM Yukawa coupling terms, as calculated with FEYNHIGGS, to take into account SUSY-QCD effects. As with the neutral Higgs, the charged Higgs boson branching fractions are calculated with FEYNHIGGS and/or HDECAY. The dominant decay mode for $H^\pm$ at low-mass in the hMSSM and $m_{\mathrm{h}}^{\mathrm{mod}+}$ is $H^\pm \to tb$, shown in Figure 2.10 as a function of $m_{H^\pm}$. In both models the $H^\pm \to \tau\nu$ decay mode is important at higher values of $\tan\beta$. In the $m_{\mathrm{h}}^{\mathrm{mod}+}$ benchmark, decays to SUSY particles become dominant at high-mass. Also shown is the branching ratio to the light Higgs boson with an associated $W^\pm$, which tends to be increase at low $\tan\beta$ but remains with a small branching fraction.

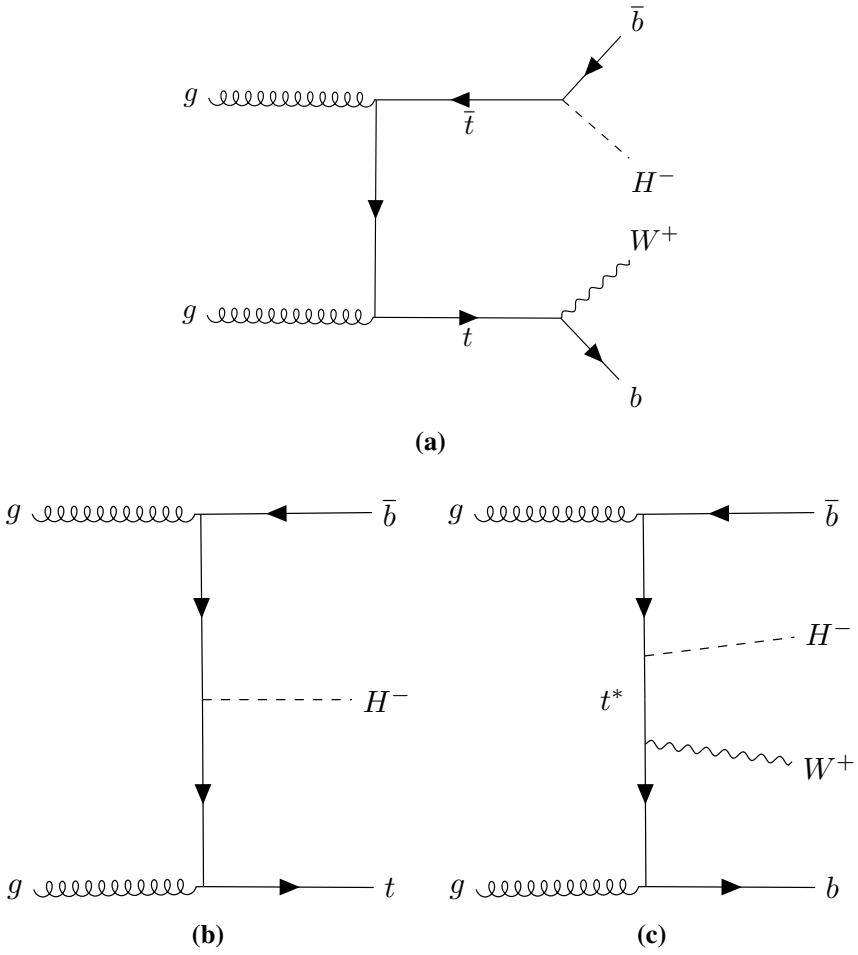

Figure 2.8 Feynman diagrams of the LO charged Higgs boson production for the (a) light (b) heavy and (c) intermediate (with non-resonant top-quark) mass range.

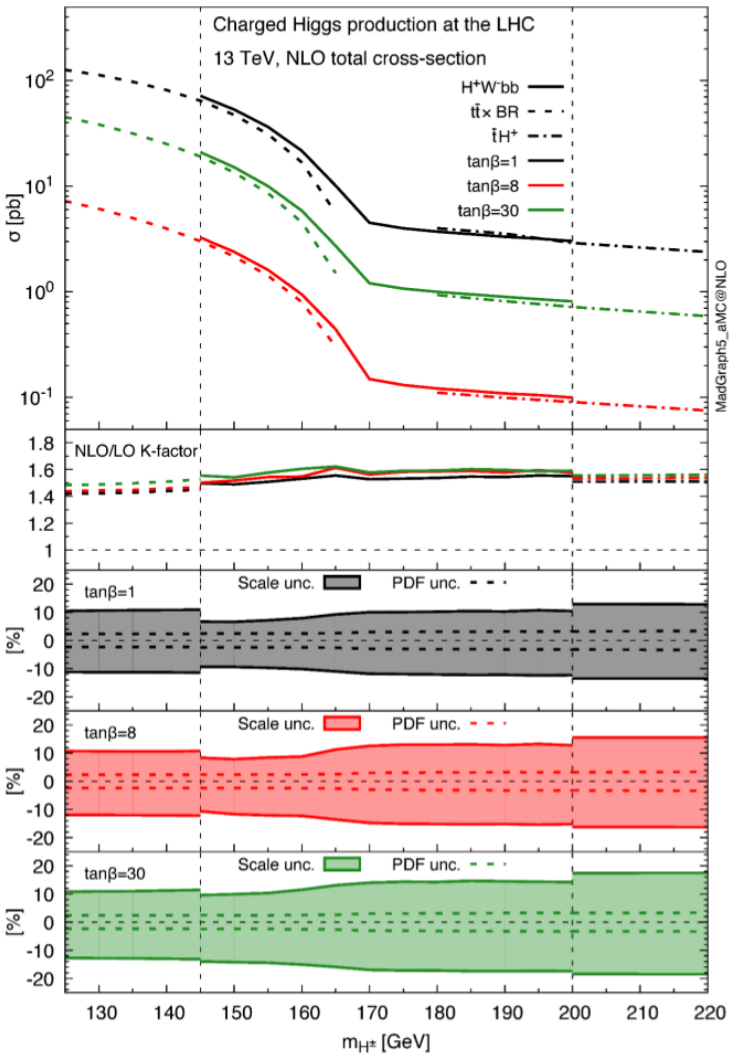

Figure 2.9 Total cross-section at NLO precision for a charged Higgs boson from a Type-II 2HDM at different values of $\tan\beta$, showing the low, intermediate and high-mass range [92].

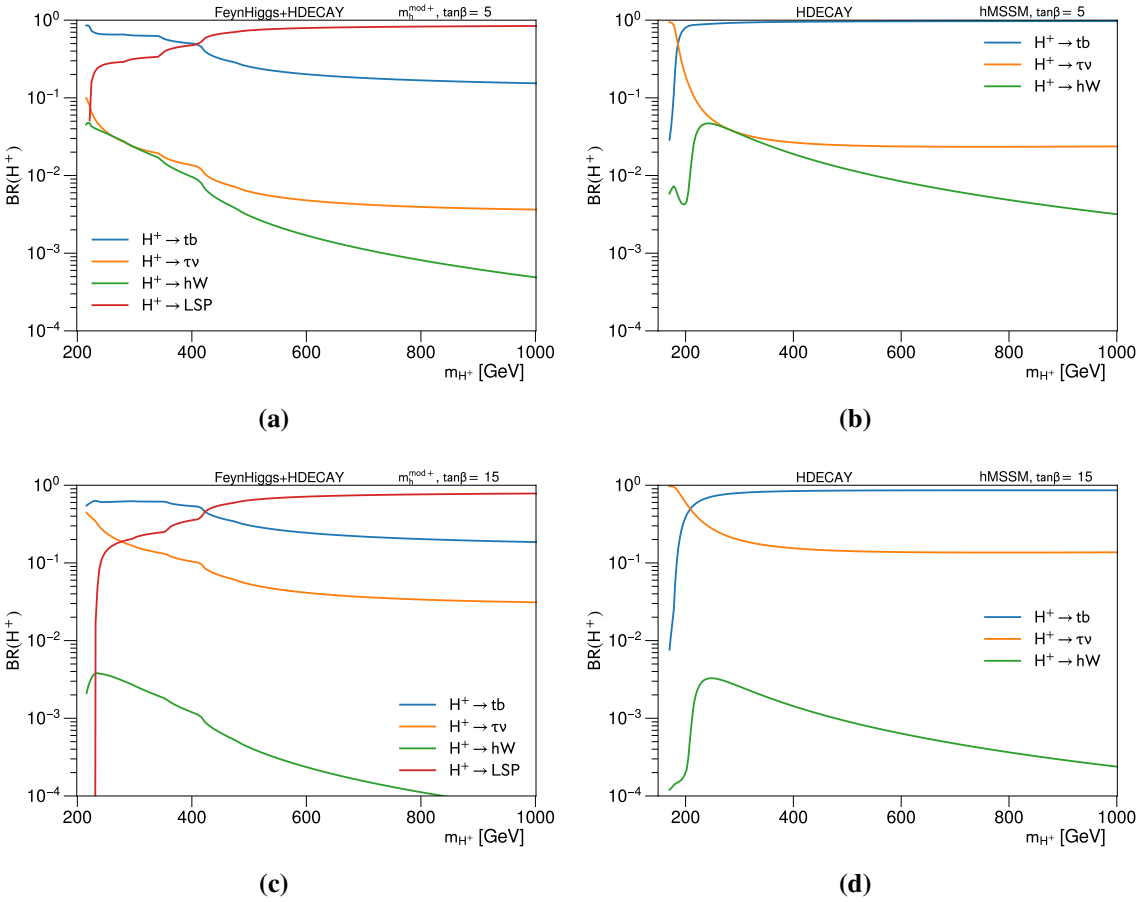

Figure 2.10 Charged Higgs boson branching fractions in the $m_{\mathrm{h}}^{\mathrm{mod}+}$ and hMSSM scenario for the most sensitive decay processes with $m_{H^\pm} > 200$ GeV.

2.5 Constraints on BSM Higgs bosons in Run-1 of the LHC

Although the extended Higgs sector described above for 2HDMs and MSSM are minimal extensions and are somewhat simplified models, they provide signatures which can be readily probed at the LHC. Both the 2HDM and MSSM require additional Higgs bosons which are directly searched for. Several searches for additional scalars have been performed in ATLAS with the Run-1 and Run-2 datasets, and limits have been set on the cross-section of the additional scalar bosons. These limits can then be compared to state of the art cross-section predictions such as those described in the previous sections. As an example, Figure 2.11 (a) show 95% confidence level (CL) limits from Run-1 in the hMSSM m_{A}–$\tan\beta$ plane. Shown are constraints from direct heavy Higgs boson searches with up to $\sqrt{s} = 8$ TeV pp collisions and 20.3 fb^{-1} data: $A/H \to \tau\tau$ [93], $A \to hZ$ [94], $H \to VV$ [95, 96] and $H^{\pm} \to \tau\nu$[97]. Furthermore, the 2HDM and MSSM models become constrained via indirect measurements, such as the 125 GeV Higgs boson coupling, which are incompatible with certain regions of phase-space. The compatibility of the measured 125 GeV Higgs boson couplings to SM particles was probed in Run-1 and used to place constraints on several BSM models [17]. Figure 2.11 (a) shows the limit placed in Run-1 on the hMSSM from reinterpretation of the 125 GeV Higgs boson coupling measurement. Figure 2.11 (b) shows the constraints from the same Higgs coupling measurement on the Type-II 2HDM phase-space.

It is clear that to fully probe the BSM Higgs sector one relies on both SM measurements and direct searches. This work has continued in Run-2. Direct searches for $A/H \to \tau\tau$ and $H^{\pm} \to \tau\nu$ with 36.1 fb^{-1} Run-2 at $\sqrt{s} = 13$ TeV pp collisions are presented in this thesis. Indirect limits on 2HDM and hMSSM from the latest 125 GeV coupling measurements with up to 80 fb^{-1} Run-2 data is also presented. A total of 147 fb^{-1} of integrated luminosity was recorded by ATLAS in Run-2 and is still being analysed at the time of writing.

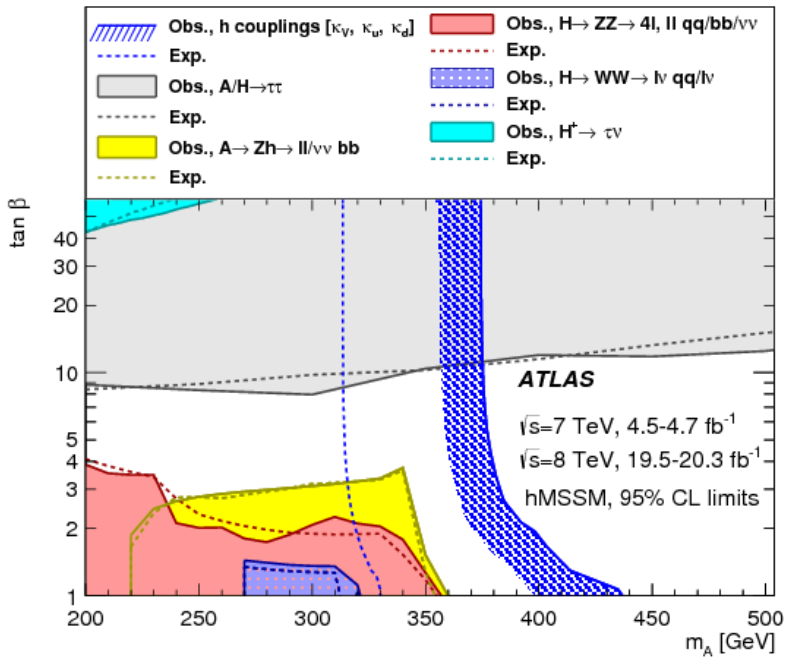

(a)

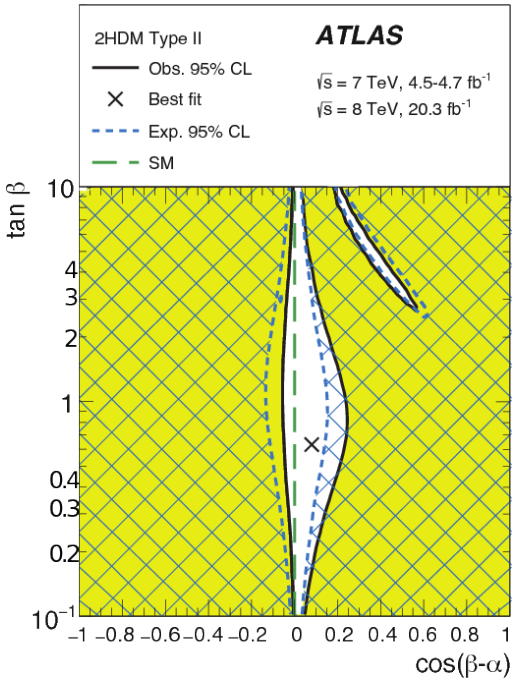

(b)

Figure 2.11 Run-1 expected and observed exclusion limits at 95% CL in the (a) hMSSM from direct heavy Higgs boson searches and 125 GeV Higgs boson coupling measurement, and (b) Type-II 2HDM from the 125 GeV Higgs boson coupling measurement [17].

Part II

Experimental method

Chapter 3

Overview of the ATLAS Experiment

ATLAS [15] is one of the four main detectors at the four collision points around the Large Hadron Collider (LHC) [14] at the European Organization for Nuclear Research (CERN). This chapter briefly describes the LHC, the ATLAS detector, and its component detectors and sub-systems.

3.1 The Large Hadron Collider

The LHC [14] at CERN near Geneva, Switzerland, is the world's most powerful man-made particle accelerator. It is designed to collide proton beams (pp collisions) with up to a 14 TeV centre-of-mass energy and a peak instantaneous luminosity of 10^{34} cm^{-2}s^{-1}. It is also designed to collide heavy ion beams with an energy of up to 2.8 TeV per nucleon. The LHC houses two high luminosity general purpose detectors, ATLAS [15] and the Compact Muon Solenoid (CMS) [16], designed to take advantage of the full instantaneous luminosity delivered by the LHC. There are two additional experiments situated at LHC collision points: the Large Hadron Collider beauty experiment (LHCb) [98] is dedicated to searches for new physics by probing rare b-quark decays; A Large Ion Collider Experiment (ALICE) [99] is designed to probe the quark-gluon plasma created in heavy-ion collisions. The LHC surpassed its design instantaneous luminosity in 2017, with ATLAS reporting a peak delivered instantaneous luminosity of 2.1×10^{34} cm^{-2}s^{-1} by the end of Run-2 data-taking in 2018 [100].

During pp collisions two proton beams are accelerated up to 7 TeV each[14], in clockwise and anti-clockwise directions around a ring of circumference $\sim 27\,\text{km}$, and made to collide at the four interaction points. Proton beams are made up of proton bunches spaced $25\,\text{ns}^{-1}$ apart, with $\sim 10^{11}$ protons in each bunch. The main LHC ring is injected with protons that have been accelerated in pre-accelerators as shown in Figure 3.1. Protons are accelerated to 1.4 GeV by a Linear Accelerator (LINAC) and the Proton Synchrotron Booster (PSB) before passing to the Proton Synchroton (PS) where they are accelerated to 26 GeV. Protons are injected into the Super Proton Synchroton (SPS) where they are accelerated to 450 GeV before being injected into the main LHC ring. The LHC makes use of 1300 dipole magnets at 8.7 TeV to ramp the proton energy up to 7 TeV, while quadrupole magnets focus the proton bunches.

The first operational run of the LHC (Run-1) lasted from late 2009 till early 2013. During that time, ATLAS recorded 4.7 fb^{-1} at $\sqrt{s} = 7$ TeV, and 20.1 fb^{-1} at $\sqrt{s} = 8$ TeV, centre-of-mass pp collision data deemed good for physics analysis. The LHC then went on its planned first long shutdown (LS1) to undertake upgrades in preparation for subsequent running at a higher centre-of-mass energy. During the second operational run (Run-2), from mid 2015 till late 2018, the LHC provided pp collisions with a centre-of-mass energy of $\sqrt{s} = 13$ TeV. A cumulative distribution of the total integrated luminosity recorded by ATLAS during Run-2 is shown in Figure 3.2 (a), in which a total of 139 fb^{-1} of data is considered good for physics analysis.

When two proton bunches are made to collide at the interaction point, several interactions will occur between the component protons. The profile of the number of interactions per event (pileup) recorded by ATLAS for different years during Run-2 data-taking is shown in Figure 3.2 (b). An average of 33.7 pileup interactions per event are observed.

The LHC began its second long shutdown (LS2) in 2019 in which planned upgrades to both the LHC and its detectors will take place, with the Run-3 period of data-taking scheduled for 2021. During Run-3, the LHC is planning to run with centre-of-mass energy of between 13 TeV and 14 TeV till the third long shutdown (LS3) at the end of 2023. Upgrades for the High Luminosity Large Hadron Collider (HL-LHC) [101] are planned during LS3. The HL-LHC is scheduled to commence in 2026 and is planned to increase the instantaneous luminosity of collisions by up to seven times the design value of the LHC, and is expected to be operational till 2038. A total of 3000–4000 fb^{-1} of data is projected to be derived by the combined LHC and HL-LHC running periods.

[14]This is the design energy. The highest energy ever reached per proton beam at the LHCis 6.5 TeV.

The two Higgs boson searches presented in this thesis (Chapters 6 and 7) are performed with an integrated luminosity of 36.1 fb^{-1} of pp collision data at $\sqrt{s} = 13$ TeV, recorded by ATLAS during 2015 and 2016. The Higgs boson cross-section measurements presented in Chapter 8 include Run-2 data recorded during 2015, 2016 and 2017, with up to 79.8 fb^{-1} of data. The full Run-2 data are currently being analysed at the time of writing. A prospect study with the full expected HL-LHC dataset is presented in the concluding Chapter 9.

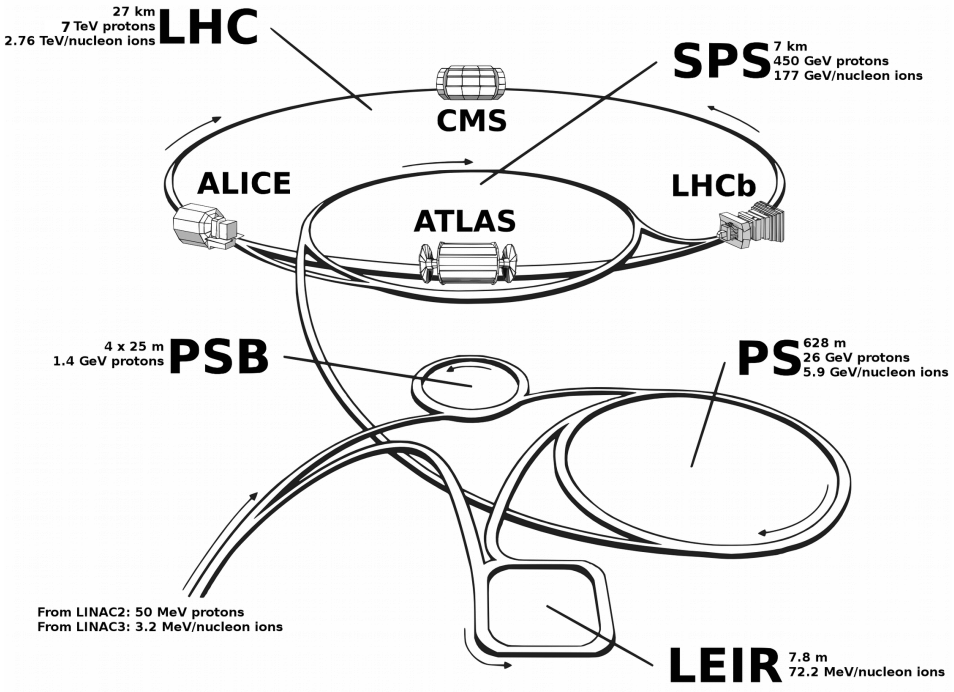

Figure 3.1 A schematic representation of the LHC accelerator complex [102], including the main accelerators which ramp up the proton energy before being injected into the LHC.

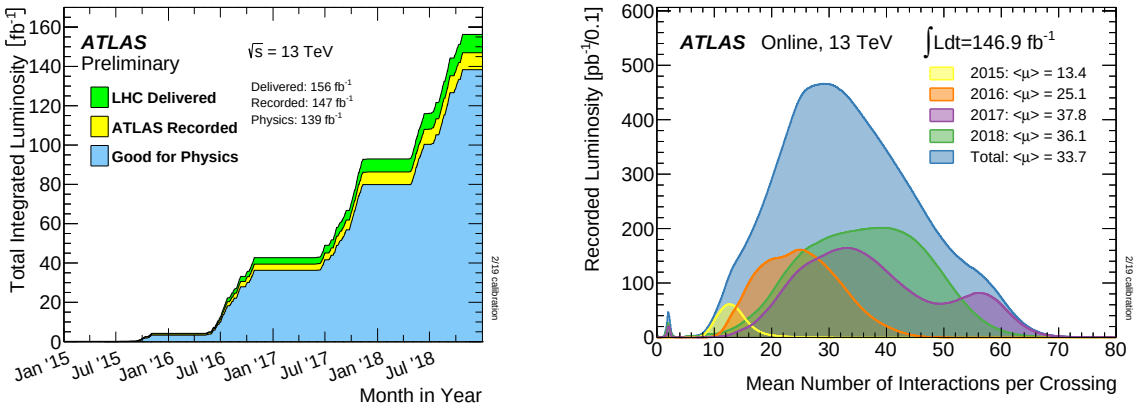

(a) **(b)**

Figure 3.2 The (a) integrated luminosity and (b) mean number of interactions per event (pileup) recorded by ATLAS during pp collisions in the Run-2 data-taking period [100].

3.2 The ATLAS Detector

The ATLAS detector [15] is a general purpose particle detector designed to provide excellent tracking and energy measurements of particles stemming from the interaction point, where protons beams from the LHC collide. The physics goals for which it was designed include the search for the SM Higgs boson, and searches for BSM physics like SUSY. Driven by its ambitious physics agenda, ATLAS was designed to meet several requirements, including: fast and radiation-hard electronics and sensors, a large detector acceptance, good tracking and vertexing of charged particles, high-resolution calorimetry for precise energy measurements, good muon identification and momentum resolution, and a highly efficient triggering system with high levels of background suppression. It meets these goals by comprising a modular design with several independent sub-detectors and systems which are shown in Figure 3.3.

ATLAS uses a right-handed coordinate system with its origin at the nominal interaction point at the centre of the detector. The x-axis points in the direction to the centre of the LHC ring, and the y-axis points upwards. ATLAS is comprised of several sub-detectors arranged as concentric cylinders around the interaction point. A cylindrical coordinate system is generally used, with radius r and azimuthal angle ϕ used in the transverse plane, where ϕ is measured around the z-axis. The pseudorapidity is defined in terms of the polar angle θ, measured from the positive z-axis, as $\eta = -\ln\tan(\theta/2)$. Angular distance is measured in units of $\Delta R \equiv \sqrt{(\Delta\eta)^2 + (\Delta\phi)^2}$.

The inner detector (ID) [104, 105] is the innermost detector and designed to provide high-precision momentum resolution and reconstruction of charged particles in a high luminosity

environment. The ID is surrounded by a solenoid magnet which provides in a 2 T magnetic field, bending the trajectories of charged particles. The ID is a combination of the silicon pixel sensor (Pixel) [106] and the semiconductor tracker (SCT) [104, 105] in the inner part of the ID, with the straw-tube transition radiation tracker (TRT) [107] comprising the outer layer. Energy measurements are provided by the electromagnetic calorimeter (EM-Cal) and hadronic calorimeter (Had-Cal) found outside of the solenoid magnet, each made from different technologies depending on their position in the detector. Liquid-argon (LAr) sampling calorimeters [108] make up the EM-Cal, providing a coverage of $|\eta| < 3.2$. The barrel Had-Cal is a scintillator-tile calorimeter [109] with a large barrel and two extended barrel cylinders, providing a coverage of $|\eta| < 1.7$. Hadronic calorimetry is provided by LAr calorimeters in the end-caps, covering a pseudorapidity range of $1.5 < |\eta| < 3.2$. Forward LAr calorimeters provide both hadronic and electromagnetic calorimetry up to $|\eta| < 4.9$. The calorimeters are surrounded by the muon spectrometer [110] comprised of high-precision tracking and triggering chambers. A system of toroidal magnets provides strong bending power which allows for precision muon momentum measurements. A Trigger and Data Acquisition (TDAQ) [111, 112] system is used to identify and record interesting events in a

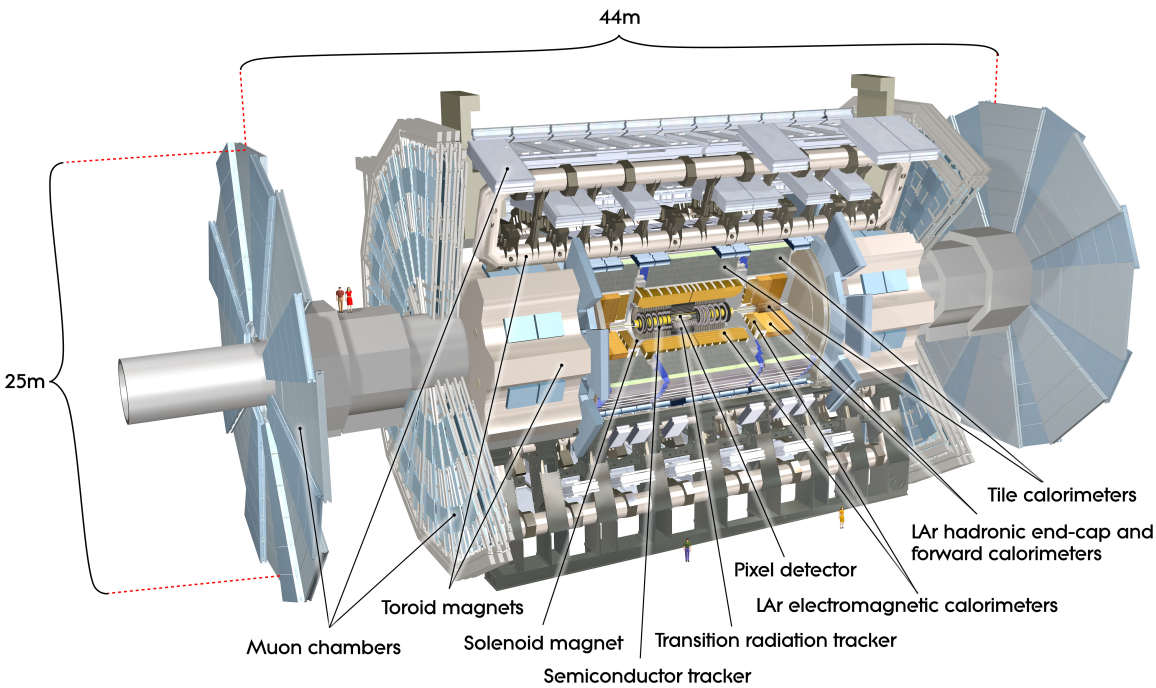

Figure 3.3 An computer generated cut-away view of the ATLAS detector [103], showing the main sub-detectors and magnets.

high-rate environment. These systems are briefly described in the following sections, while more details can be found in Ref. [15].

3.2.1 The inner detector (ID)

The inner detector (ID) [104, 105] measures the properties of charged particles and reconstructs their trajectories (tracking) up to a pseudorapidity of $|\eta| < 2.5$ [15, 113]. It is made up of independent sub-detectors, the Insertable B-layer (IBL) [113–115], the Pixel, SCT and TRT, each arranged as concentric cylinders around the beam axis in the barrel region, and as disks perpendicular to the beam axis in the end-cap regions, as shown in Figure 3.4 (a). A zoomed in view of the barrel layers of the Pixel, SCT, and TRT detectors are shown in Figure 3.4 (b).

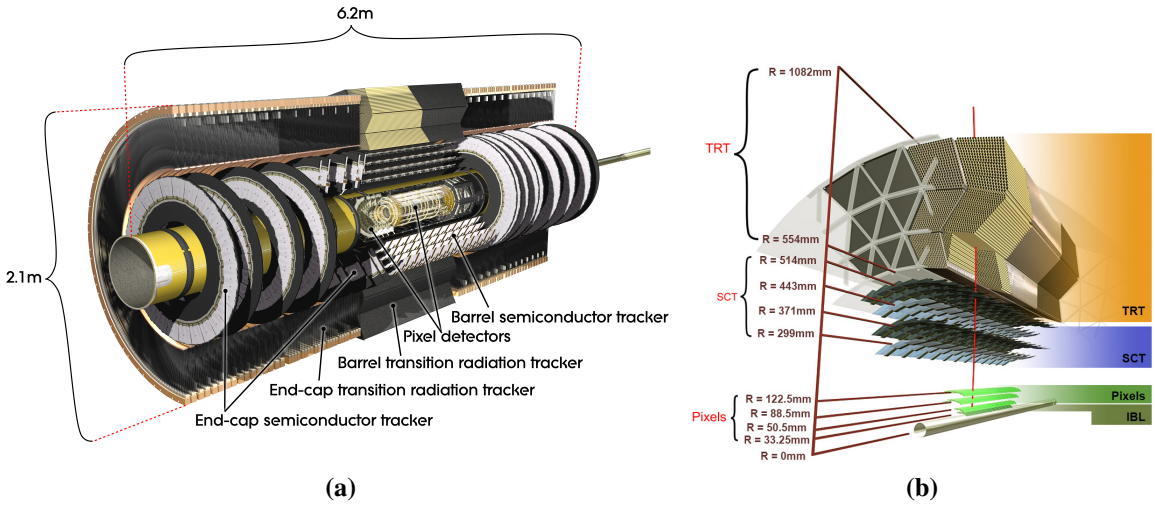

(a) **(b)**

Figure 3.4 A cut-away image of the ATLAS ID, where (a) shows both barrel and end-cap detectors [116], and (b) shows a zoomed in view of the layers of the barrel ID [113], showing the IBL.

3.2.1.1 The silicon pixel sensor (Pixel)

The Pixel detector [106] is required to have high-resolution capabilities in a highly dense particle environment at small radii from the interaction point. It achieves this by housing a high density of pixel sensors channels. In Run-1 the Pixel detector was made up of three barrel layers, located at radii of 50.5 mm (B-Layer), 88.5 mm (Layer 1), and 122.5 mm (Layer 2) centred around the beam axis, and two end-caps with three disc layers each. This

included of total of 1744 modules which read out 80 million pixel sensors, each having a typical pixel size of 50×400 μm^2 and thickness 250 μm. The spatial resolution provided by the pixel sensors are typically 10 μm in R–ϕ and 115 μm in z (R) in the barrel (disc). During LS1 the Insertable B-layer (IBL) [113–115] was installed at a radius of 33.25 mm, adding an additional 12 million pixel sensors of dimension 50×250 μm^2. It improves tracking by providing an additional measurement point, and mitigates the possible loss of hits expected with higher instantaneous luminosity [113]. The radii of the four Pixel barrel layers are shown in Figure 3.4 (b).

3.2.1.2 The semiconductor tracker (SCT)

The SCT [104, 105] consists of 4088 modules of silicon strip detectors arranged in four concentric barrels and two end-caps of nine disks each, covering a total surface area of 60 m^2. A single barrel silicon strip sensor is a p-on-n silicon sensor with 768 read-out strips each with 80 μm pitch. Each barrel sensor has a total surface area of 6.36×6.40 cm^2. Two such sensors are wire-bonded together to form 12 cm long strips, making up a single side of a SCT module. An example of a SCT barrel module is shown in Figure 3.5, made up of two back-to-back layers, each with a pair of strip sensors. The layers are rotated with a stereo angle of 40 mrad with respect to each other to provide position measurements in R–ϕ. End-cap sensors are more complicated in design due to their required layout on discs. The pitch of the readout strips of a end-cap sensor will vary depending on its position in the SCT. Like the barrel sensors, each end-cap sensor has 768 read-out strips. The SCT typically provides four space points (with two hits per module) per track and offers a total coverage of $|\eta| < 2.5$. In total the SCT has approximately 6.3 million channels, and provides a spatial resolution of 17 μm in R–ϕ and 580 μm in z (R) in the barrel (disc) modules.

3.2.1.3 The transition radiation tracker (TRT)

The TRT [107] is made up of drift tubes of 4 mm diameter of length 144 cm (37 cm) for the barrel (end-caps) filled with a xenon or argon based gas mixtures. The walls of the straw tubes are made from Kapton films coated with carbon-polyimide, aluminium and polyurethane layers. Charged particles crossing TRT straws ionise the active gas mixture, producing electrons which drift towards a 31 μm diameter gold-plated tungsten wire. The anode wire collects a detectable signal current which is amplified, shaped and discriminated on. In the barrel, straws are placed parallel to the beam-line and cover a radius from 554 mm to 1082 mm. The end-cap straws are arranged perpendicular to the beam-line and cover

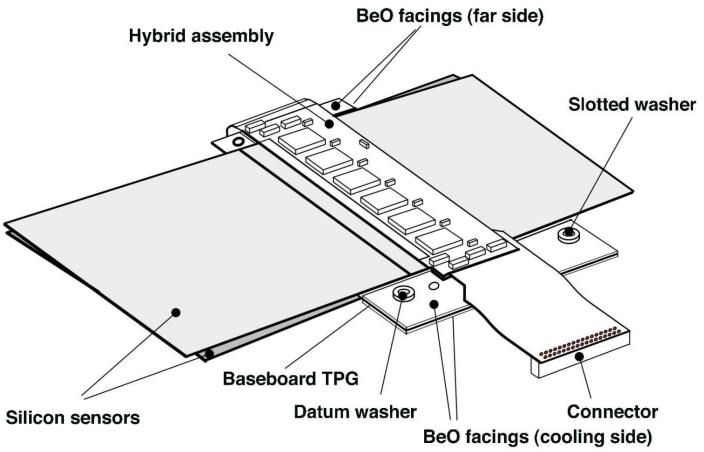

Figure 3.5 Schematic view of an SCT barrel module [117]. Two silicon strip sensors per side are wire-bonded to create 12 cm long strips. The hybrid assembly houses the read-out chips of the module.

827 mm $< |z| <$ 2774 mm and a radius from 617 mm to 1106 mm. The TRT provides a total coverage of $|\eta| < 2$ with $\sim$ 30 space points per track, with $\sim$ 130 μm resolution.

3.2.1.4 Tracking and vertexing in the inner detector (ID)

Tracking in the ID [118, 119] is comprised of many components working together to provide charged-track flight-path information and momentum measurements. The tracking software in the ID has a modular design comprised of features like track extrapolation, fitting and vertexing. The tracking logic can be divided into different steps. The first step is data pre-processing: raw data from signals in the ID are converted into geometrical information. Hits in the silicon detectors are then clustered, where clusters from the two-sided SCT modules are converted into a single space-point. Timing information from the TRT is used to create calibrated drift circles. A track finder is then run, having different strategies for different applications. The default track finding looks for combinations of space points in the Pixel layers and first SCT layer, and extrapolates track candidates into the remaining layers of the SCT [120]. The track candidates undergo a fit, with quality selection being used to prune ambiguities, outlier clusters, and fake tracks. The remaining tracks are extrapolated into the TRT and refit. The primary vertex is determined from an iterative χ^2 fit of tracks associated within a region in z along the beam line [121]. Algorithms are run on the final tracks to reconstruct secondary vertices and photon conversions.

A variety of track-defining variables are provided at the user end, that include local track coordinates from individual detector modules. The most relevant track-defining variables

Table 3.1 Track reconstruction efficiencies and absolute systematic uncertainties for both `loose` and `tight` tracks in Run-2 data, adapted from Ref. [122].

Track Selection	`loose`		`tight`	
η Range	$\lvert\eta\rvert < 0.1$	$2.3 \leq \lvert\eta\rvert \leq 2.5$	$\lvert\eta\rvert < 0.1$	$2.3 \leq \lvert\eta\rvert \leq 2.5$
Track efficiency (%)	91	73	86	63
Systematic uncertainty (%)	.4	2.2	.5	2.6

for subsequent discussions are: the transverse impact parameter (d_0), which is the transverse plane distance from the closest point of the track to the z-axis; the longitudinal z position of the closest point of the track to the z-axis (z_0); the polar (θ) and azimuthal (ϕ) angles of the associated track vector; and the charge-signed curvature of the track ($\frac{q}{p}$).

Tracking performance in early Run-2 data [122] is studied for tracks having $p_{\mathrm{T}} > 400$ MeV, $|\eta| < 2.5$ and passing either a `loose` or `tight` selection criteria. The selection criteria depends on requirements on the number of hits associated to a given track in each of the sub-detectors of the ID. The track reconstruction efficiencies for `loose` or `tight` tracks are shown in Table 3.1 for regions in which track efficiencies are associated with their lowest ($|\eta| < 0.1$) and highest ($2.3 \leq |\eta| \leq 2.5$) systematic uncertainties. The resolution of the track impact parameter in Run-2 is shown in Figure 3.6 compared to that of Run-1. The observed d_0 resolution [122] is $\lesssim 120$ μm for tracks with $p_{\mathrm{T}} \sim 1$ GeV and $|\eta| \sim 2.5$, improving to ~ 20 μm for central tracks with $p_{\mathrm{T}} \gtrsim 6$ GeV. Similarly the resolution of the longitudinal impact parameter (z_0) is ~ 70 μm for $p_{\mathrm{T}} \gtrsim 6$ GeV, increasing to $\lesssim 700$ μm for low p_{T} and large $|\eta|$.

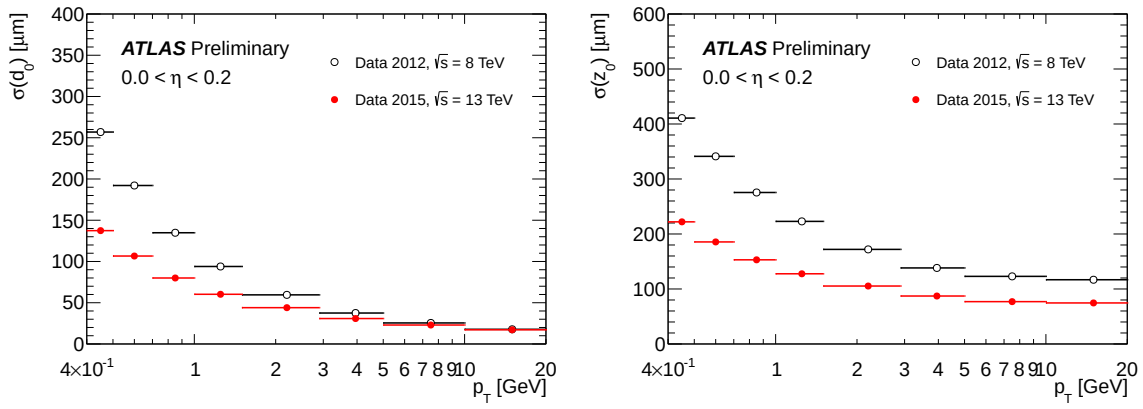

Figure 3.6 Comparison of the Run-1 and Run-2 (a) transverse and (b) longitudinal impact parameter resolution in the central region of the detector as a function of track p_{T} [123].

3.2.2 Calorimetry

Both the EM-Cal and Had-Cal are sampling calorimeters [108, 109], in which high density layers of absorbing material prompt particle showers which are measured in active detector layers. The EM-Cal makes use of layers of lead to prompt bremsstrahlung ($e \rightarrow e\gamma$) or pair production ($\gamma \rightarrow ee$), producing cascading EM showers which are characterised by the radiation length (X_0) of the material involved. The Had-Cal uses high density material which prompts strong nuclear interactions to occur, producing cascading particle showers which have wider spreads than that of the EM showers, and have interaction lengths an order of magnitude greater than X_0. The calorimeters cover a range of $|\eta| < 4.9$, with high granularity EM calorimeters used in a range that matches the coverage of the ID, so as to optimise the reconstruction of electrons and photons. Coarser granularity is used in the rest of the coverage as is sufficient to satisfy the requirements for jet and missing transverse energy ($E_{\mathrm{T}}^{\mathrm{miss}}$) reconstruction. The layout of the ATLAS calorimeter is shown in Figure 3.7. The typical resolution of the calorimeter component are shown in Table 3.2.

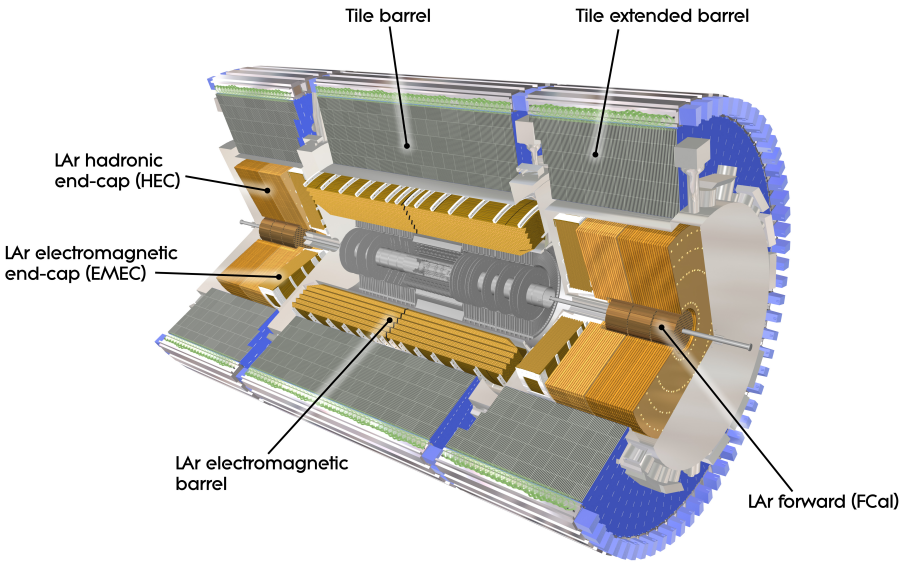

Figure 3.7 A computer generated view of the ATLAS calorimeter [124], showing the different components of the EM-Cal and Had-Cal.

Table 3.2 Typical calorimeter component resolution, adapted from Ref. [125].

Calorimeter	Resolution (%)
EM-Cal	$\sigma(E) = \frac{10}{\sqrt{E}} \oplus 0.7$
Had-Cal	$\sigma(E) = \frac{50}{\sqrt{E}} \oplus 3$
forward calorimeter (FCal)	$\sigma(E) = \frac{100}{\sqrt{E}} \oplus 10$

3.2.2.1 The electromagnetic calorimeter (EM-Cal)

The EM-Cal is divided into the electromagnetic barrel calorimeter (EMB-Cal) ($|\eta| < 1.475$), with a small gap in coverage (4 mm) at $z = 0$, and two electromagnetic end-cap calorimeters (EME-Cals) ($1.375 < |\eta| < 3.2$), each divided into outer ($1.375 < |\eta| < 2.5$) and inner ($2.5 < |\eta| < 3.2$) barrels. The EM-Cal is made up of lead absorber plates separated by layers of LAr detectors which operate at a temperature of ~ 90 K. The LAr detectors are made from accordion-shaped kapton gaps filled with LAr and provide a continuous symmetry in coverage over ϕ. Ionised gas in the gaps is collected by copper electrodes to produce a signal. In the range of $|\eta| < 2.5$ the EM-Cal is segmented into three active layers, shown in Figure 3.8, and provides a higher granularity than in the region $2.5 < |\eta| < 3.2$ which only has two active layers. A pre-sampler is placed in the region of $|\eta| < 1.8$ to correct for the energy lost in the material before the calorimeter, also shown in Figure 3.8. The channels of the EM-Cal are individual cells with varying geometry, as shown in the figure. EM calorimetry in the range $3.1 < |\eta| < 4.9$ is provided by the FCal described in the next section.

3.2.2.2 The hadronic calorimeter (Had-Cal)

The bulk of the Had-Cal consists of scintillator tile calorimeters which are divided into a barrel ($|\eta| < 1$) and two extended barrels ($0.8 < |\eta| < 1.7$). The tile calorimeter makes use of steel absorbing layers separated by active plastic scintillating tiles, covering a range which extends from 2.28 m to 4.25 m radially with a total of 500 000 tiles. The hadronic end-cap calorimeter (HEC) consists of two wheels of LAr calorimeters situated behind the EME-Cal at each end-cap. The HEC has a coverage of $1.5 < |\eta| < 3.2$ providing some overlap with both the tile and forward calorimeters. The HEC is made from copper plate layers separated by 8.5 mm gaps with LAr which provides the active sampling material. The FCal provides both hadronic and EM calorimetry in the range $3.1 < |\eta| < 4.9$. At this extreme forward region the FCal is required to be able to deal with high radiation densities. The FCal is

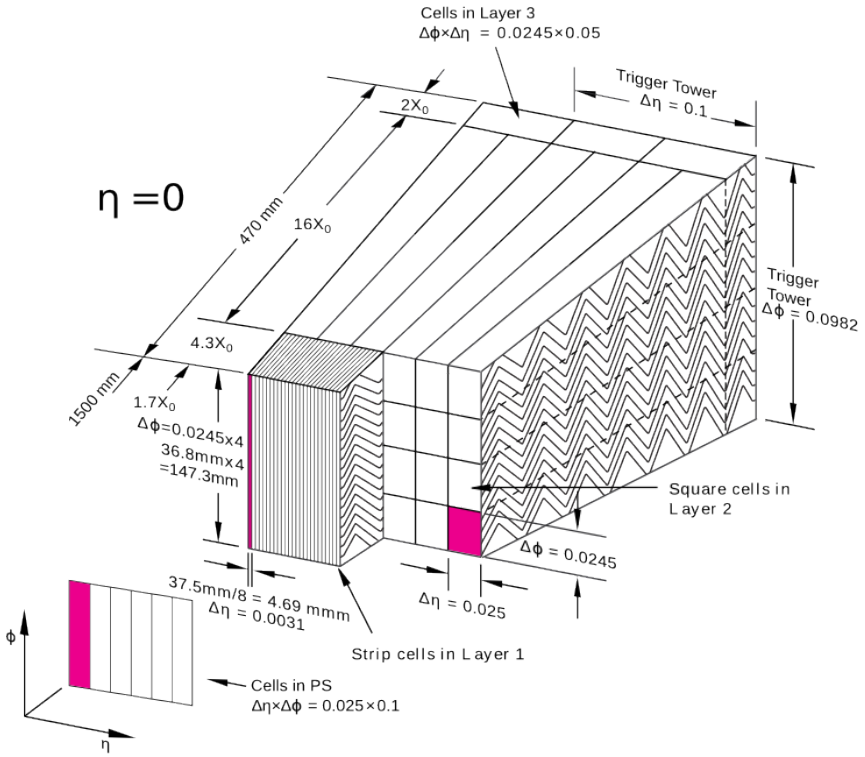

Figure 3.8 A schematic representation of a section of the LAr EM-Cal barrel region, showing different layers and the radiation length (X_0) of their material, as well as their constituent cells and their coverage in $\eta \times \phi$ [15].

made from a matrix of copper plates with drilled holes housing an electrode structure. The electrodes are made from a copper tube with a co-axial rod. The gap between the rod and tube is filled with LAr which is the active sampling material. The FCal is split into three modules. The innermost module provides EM energy measurements as the rods are made from copper. Tungsten rods are used in the two subsequent modules, providing a material with higher absorption length, suitable for hadronic energy measurements.

3.2.2.3 Clustering

Signals from calorimeter cells are used to create clusters of energy deposits in the calorimeter in order to provide information about candidate particles. Two main clustering algorithms are used: a sliding window algorithm which forms a cluster by summing cells within a clustering window, and topological cell clustering [126] which iteratively sums adjacent cells. Both methods are discussed in more detain in the context of the High-Level trigger (HLT) in Section 3.2.5.2 (page 68).

3.2.3 The muon spectrometer (MS)

A layout of the muon spectrometer (MS) [110] is shown in Figure 3.10. The MS is instrumented by triggering and high-precision tracking chambers. Muon tracks are deflected by the superconducting barrel toroid magnets in the range $|\eta| < 1.4$, while two smaller end-cap toroid magnets deflect tracks in the range of $1.6 < |\eta| < 2.7$. The transition region muons ($1.4 < |\eta| < 1.6$) are deflected by both barrel and end-cap toroid magnets. The precision measurement of muon tracks is provided by two types of muon chambers. In the barrel region, track measurements are made in chambers arranged into three cylindrical layers around the beam axis. Three layers of chambers are arranged perpendicular to the beam axis per end-cap side. A total of 354 240 Monitored Drift Tubes (MDTs) are grouped into chambers which are used over almost the entire $|\eta| < 2.7$ range to provide precision tracking. Each tube has a resolution of 80 μm. The exception is the innermost barrel layer where the $2.0 < |\eta| < 2.7$ range is covered by Cathode Strip Chambers (CSCs) which can withstand the demanding rates. The CSCs offer a resolution of 60 μm. The triggering chambers cover a range of $|\eta| < 2.4$. Resistive Plate Chambers (RCPs) are used in the barrel region while Thin Gap Chambers (TGCs) cover the end-cap regions. The triggering capabilities of the muon chambers are discussed in Section 3.2.5.

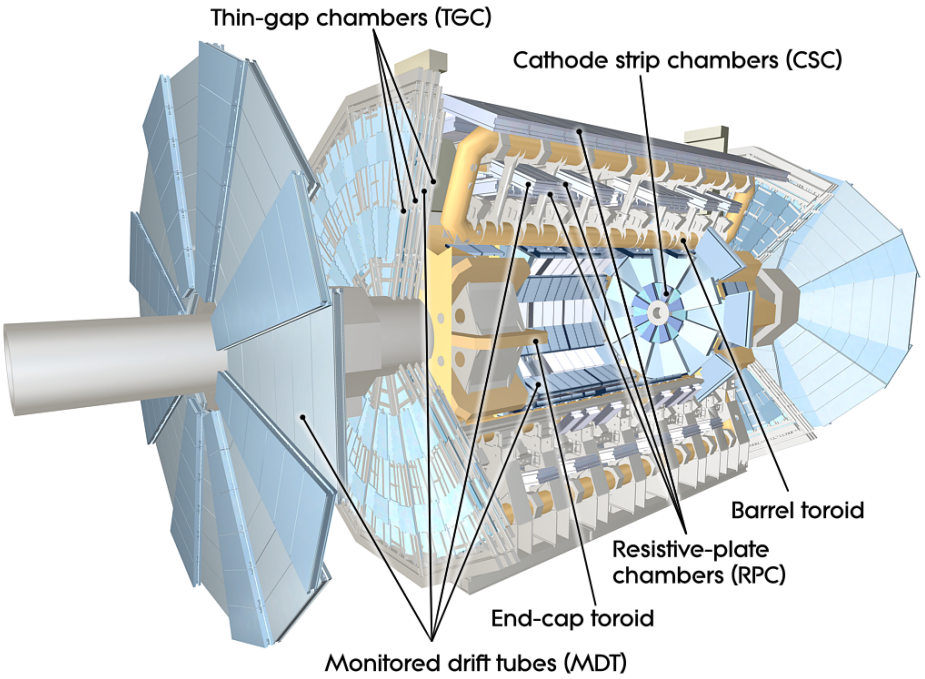

Figure 3.9 A computer generated view of the ATLAS muon system [15], showing the different components of the MS and the toroid magnets.

3.2.4 Magnet systems

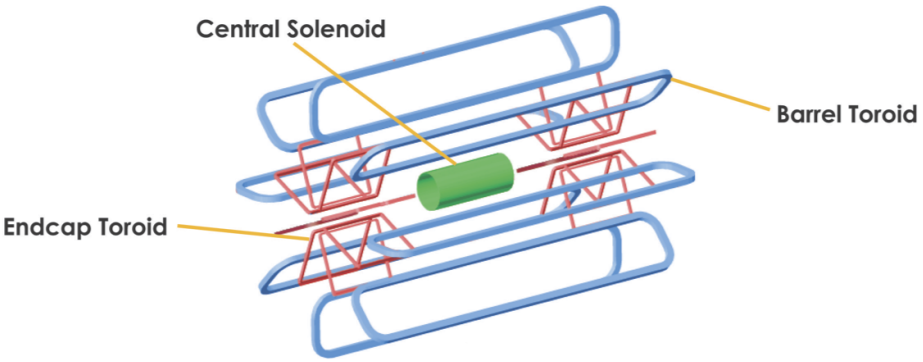

Figure 3.10 A schematic view of the ATLAS magnetic system [127], showing the solenoid (green), and barrel (blue) and end-cap (red) toroids.

The magnet systems in ATLAS provide a bending plane for the trajectories of charged particles, from which their momentum can be deduced. The magnetic system is made up of two primary components each running at a temperature of ~ 4.5 K. The first is the solenoid magnet which surrounds the ID. It is just 45 mm thin so as to minimise the radiative thickness prior to the calorimeters. The solenoid is 5.3 m long and 2.5 m in diameter and weighs 5.4 tonnes, storing an energy of 40 MJ, and providing a 2 T axial magnetic field to the ID. This allows for the precise measurement of charged particles with a p_{T} of up to ~ 100 GeV.

The second component of the magnetic system is that of the toroid magnets, which can be split into a barrel and two end-cap regions. Each region has eight coils, radially assembled around the beam axis. The axial length of each barrel coil is 25.3 m while the end-cap coils are 5 m. The toroid system has an average field of 0.6 T and allows for the measurements of muons with p_{T} up to 6 TeV.

3.2.5 Trigger and data acquisition

The TDAQ system [111, 112] is responsible for the triggering of events considered interesting for physics analysis in the ATLAS detector while maintaining manageable rates of data acquisition. A schematic overview of the TDAQ is shown in Figure 3.11. It consists of a two stage process: a hardware-based Level-1 trigger (L1), and a subsequent software-based High-Level trigger (HLT). In Run-2 the read-out rate of the L1 trigger is constrained to a maximum of 100 kHz (240 GB/s), while HLT runs on average at 1000 Hz (2.4 GB/s). Regions-of-Interest (RoIs), that are identified at L1, are passed on to the HLT where additional algorithms are run. The L1 trigger is composed of the Level-1 calorimeter trigger (L1Calo)

and Level-1 muon trigger (L1Muon), that feed into the Central Trigger Processor (CTP). The CTP is responsible for applying preventative dead-time (a window of time during which no data is collected). *Simple dead-time* is applied to avoid overlapping read-out windows by limiting the minimum time allowed to pass between two consecutive L1 accepts. The nominal *simple dead-time* in Run-2 is[15] set to 100 ns. To avoid the on-detector front-end (FE) read-out electronics from being overwhelmed, the number of L1 accepts per number of bunch crossings is limited, known as *complex dead-time*. Upon receiving a L1 acceptance signal, data from the FE read-out electronics are parsed to their detector-specific Read-Out Drivers (RODs) for processing, and subsequently collected by the Read-Out System (ROS). Events are buffered at the ROS and processed by the HLT. Events passing the HLT are collected in on-site local storage and exported to Tier-0 for offline reconstruction. Both the L1 and HLT can be assigned *prescale* factors that disable the triggers for a certain fraction of accepts. The trigger prescale factors can be varied during data-taking to accommodate for different rate constraints at a particular instantaneous luminosity. Further details of the L1 and HLT are provided in what follows.

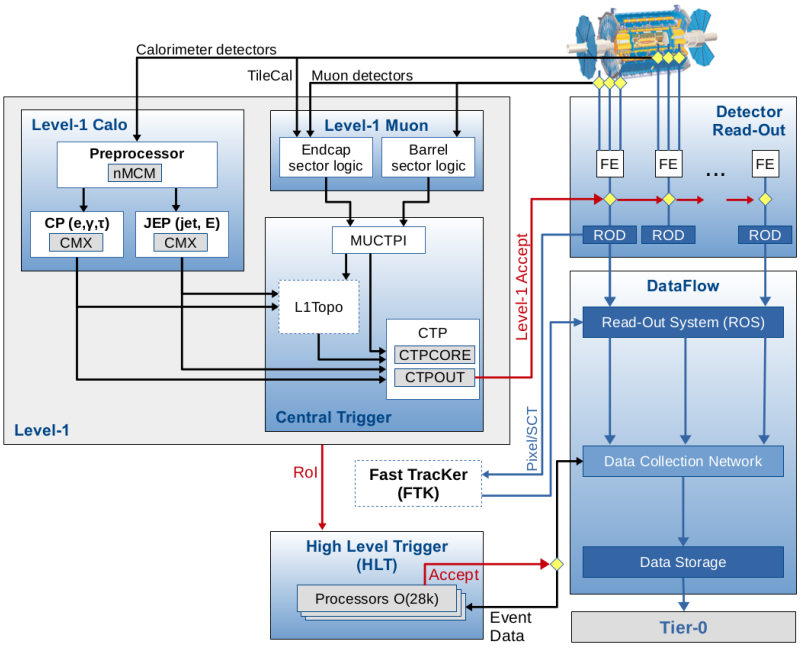

Figure 3.11 The ATLAS TDAQ system in Run 2, highlighting the triggering and data-flow [112].

A description of the triggering algorithms used for particular physics objects are described in the respective subsections of Section 4.3. The trigger rates from different groups of trigger objects are shown in Figure 3.12 from a representative run recorded in July 2016 as a function

[15]Equivalent to four bunch crossings, since the nominal bunch spacing in Run-2 is 25 ns.

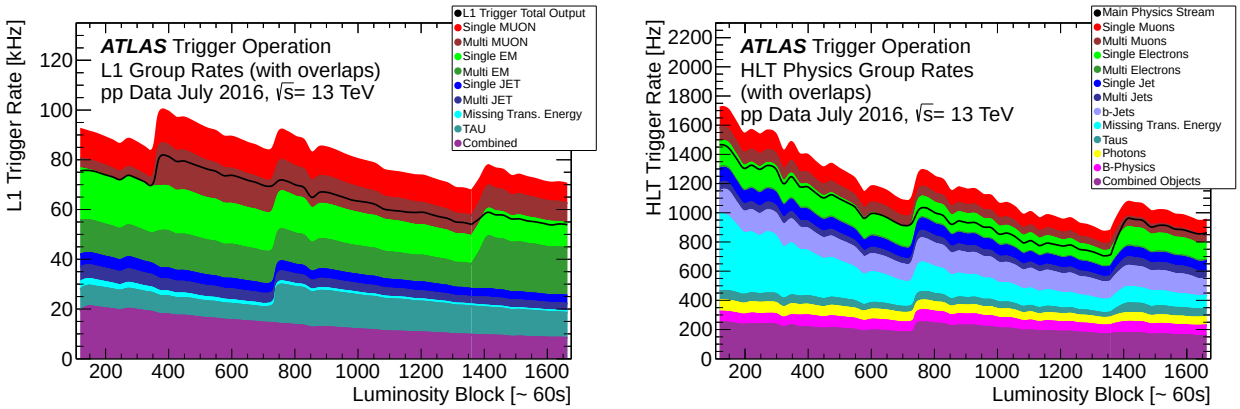

Figure 3.12 Physics trigger group rates at (a) L1 and (b) HLT as a function of the number of luminosity blocks which correspond to on average 60s per luminosity block in a representative run taken in July 2016 [128]. Overlaps between trigger groups are included in the total rate.

of the recorded luminosity block. Each luminosity block corresponds to approximately 60 s of data-taking. Rates decay exponentially with decreasing luminosity during an LHC fill, while periodically increasing due to change in the trigger prescales used to optimise the bandwidth usage. Due to energy resolution effects, triggers have a region in which they are not fully efficient, referred to as a turn-on curve, right around their online p_{T} requirements. Examples of trigger turn-on curves can be seen for single electron, single muon, and single tau lepton triggers in Figure 4.2 (b), Figure 4.3 (b) and Figure 4.5, respectively. Within this region, the efficiency of the data recorded is reduced. Scale factors are provided to match the efficiency of triggers modelled in simulation to those observed in data. Although these trigger scale factors still serve to match the efficiency in simulation to data before the turn-on curve, they tend to carry large uncertainties in this region due to the low statistics. Therefore it is common practice to select objects that are on the efficiency plateau of the trigger, as done in the analyses in this thesis.

3.2.5.1 Level-1 trigger (L1)

The L1 trigger is seeded by L1Calo and L1Muon, which are trigger systems based on the calorimeters and muon spectrometers, respectively. The L1Calo is seeded by analogue signals from ∼7000 trigger towers in the calorimeters, each with a granularity of $\phi \times \eta = 0.1 \times 0.1$. Figure 3.13 shows a schematic representation of trigger towers, input to the L1Calo. Analog signals from the trigger towers are digitised and calibrated in a pre-processor and transmitted in parallel to both the Clustering Processor (CP) and the jet/$\sum E$ processor (JEP). Here $\sum E$

refers to the total summed energy. The CP is responsible for identifying electron/photon and hadronic tau candidates based on energy thresholds and isolation conditions. A RoI in the CP is identified as a 2×2 trigger tower cluster in the EM-Cal, as shown in Figure 3.13, where one combination of two nearest neighbour towers exceeds a predefined energy threshold. The isolation ring in the EM-Cal surrounding the RoI, and core and isolation Had-Cal towers directly behind the RoI, can be used to place isolation criteria at trigger level. RoIs are identified by the JEP as 4×4 or 8×8 trigger tower clusters with a $\sum E$ from the EM-Cal and Had-Cal above a predefined threshold. A 2×2 cluster with maximum energy is identified as the cluster's core. They are used to seed jet triggers and calculate the global $\sum E$ used in $E_{\mathrm{T}}^{\mathrm{miss}}$ triggers.

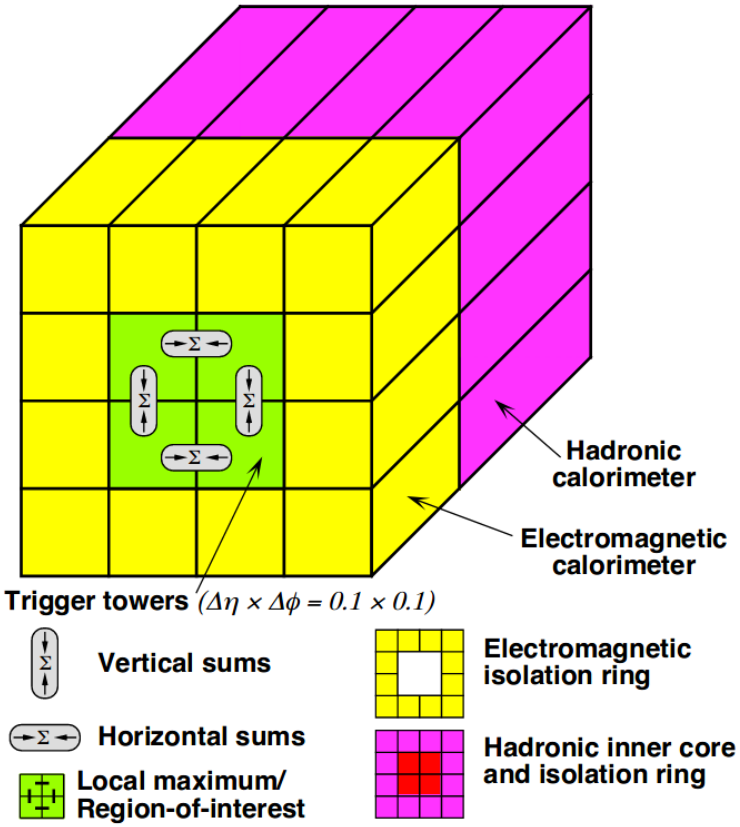

Figure 3.13 Schematic representation of a trigger tower that seeds the L1Calo algorithms [112]. Shown are the RoI and isolation regions in the EM-Cal, as well as the respective inner core and isolation regions in the Had-Cal.

The L1Muon is seeded from the RCPs and TGCs in the barrel and end-cap regions, respectively, that provide triggering and position information for muons. In Run-1 a significant fraction of the L1Muon accepts in the end-cap region where attributed to events

with slow particles originating at large z along the beam pipe, as shown in Figure 3.14. A new coincidence requirement that takes into account end-cap inner and forward inner TGCs, introduced in Run-2 [111, 112], mitigate these background sources.

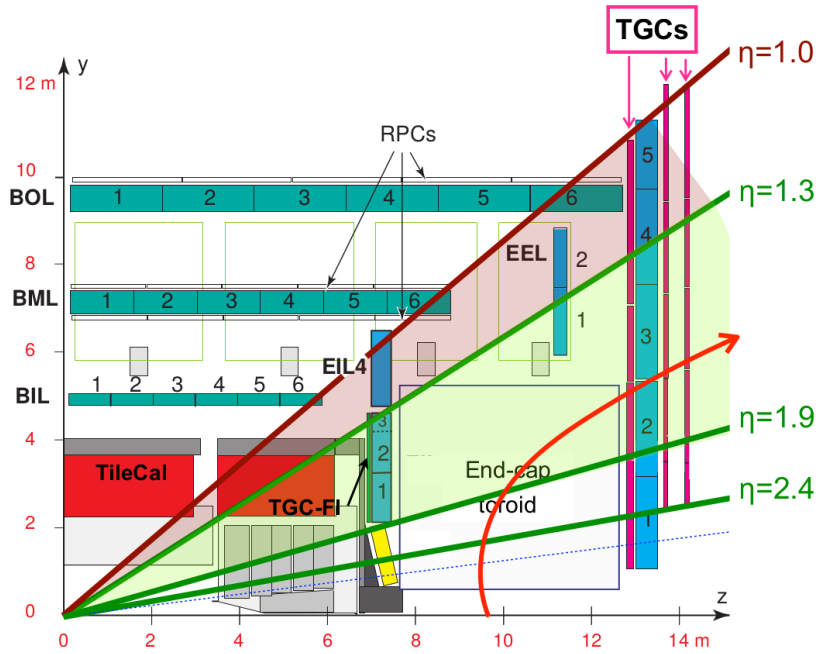

Figure 3.14 Schematic representation of the MS with different η sections being highlighted. The RCPs and TGCs that seed the L1Muon are shown. A source of background to L1Muon are from slow particles originating at large z along the beam pipe, an example of that is shown by the red arrow [112].

Both the L1Calo and L1Muon accepts are parsed to a Level-1 topological trigger (L1Topo) that was introduced in Run-2 [111]. L1Topo identifies interesting events based on the kinematic and geometric attributes of the input, motivated by physics-based signatures. It includes refined calculations of global quantities, such as $E_{\mathrm{T}}^{\mathrm{miss}}$. Events passing the L1Calo, L1Muon, and/or L1Topo are parsed to the CTP that makes the final L1 trigger decision based on the dead-time requirements.

3.2.5.2 High-Level trigger (HLT)

The HLT is a software-based trigger that provides fast-object and event reconstruction in order to refine trigger decisions. The time that it takes the HLT to process an event depends on the pileup conditions of the event and the trigger menu used at the time. Generally the HLT is split into two stages: an initial fast-reconstruction stage that eliminates a large

portion of events, and a second slower more precise reconstruction stage. During the HLT processing, several algorithms dedicated to tracking in the ID and MS, and clustering in the calorimeters, are implemented and tuned to their target signature. Some brief description of these algorithms is presented below. The HLT reconstruction can be performed on a RoI or full-event basis, depending on the final topology targeted. All events passing the HLT trigger that are intended for physics analysis are written to a dedicated event stream called `Main`. Additional streams dedicated to calibration, monitoring, and detector performance.

Fast track reconstruction in the ID, at the level of the HLT, consists of pattern recognition algorithms tuned for the particular trigger; precision tracking borrows heavily from the offline track reconstruction techniques. Tracking is a computationally expensive process and takes up on average 40% of the HLT CPU time. As such, tracking algorithms are mostly applied to RoIs and not performed on the full event. The tracking dedicated to hadronic tau lepton and b-jet triggers are run on larger RoIs than that of the muon and electron triggers. Both hadronic tau lepton and b-jet tracking in the HLT therefore use multi-stage tracking to moderate CPU processing time. The details of the tau and b-jet tracking used for triggering are discussed in more detail in Sections 4.3.6 and 4.3.5.

In the HLT, calorimeter information is reconstructed into cells and clusters in order to provide information about candidate particles. Since the HLT has access to the full detector granularity, the algorithms improve the accuracy of energy and position measurements performed at L1. The first stage of the HLT reconstruction in the calorimeter is the conversion of raw calorimeter data into a collection of cells. For well-separated objects (electrons, photons, muons, taus) cell reconstruction is performed within RoIs identified at L1. The full calorimeter raw data is unpacked for the reconstruction of calorimeter cells for jets and $E_{\mathrm{T}}^{\mathrm{miss}}$ objects. In either case, the calorimeter data is accessed from the data collection buffer, as needed. Cells are used as inputs to clustering algorithms, which create clusters of energy deposits in the calorimeter. Two such clustering algorithms are used. A sliding window algorithm forms a cluster by summing cells within a clustering window. The algorithm scans a grid of cell towers and aligns the window with an orientation that provides a local maximum of transverse energies. A barycentre at each layer in the calorimeter is calculated and all cells within a fixed window of its position are included in the cluster. An alternative clustering method is that of topological cell clustering [126]. This method is seeded by a single calorimeter cell, and iteratively adds cells, satisfying energy threshold conditions, to form a cluster. Seed cells are identified by satisfying energy thresholds significantly above that of the expected noise. Topological cell clustering provides performance similar to the clustering in the offline reconstruction, although it is significantly slower that the

sliding window algorithm. The resulting topo-clusters are used for tau, jet and $E_{\mathrm{T}}^{\mathrm{miss}}$ object reconstruction in the HLT.

The HLT muon track reconstruction is split into fast- and precision-reconstruction stages [112]. The fast reconstruction is seeded from RoIs defined at L1. Drift time and position information from the MDTs chambers in the RoI are used to fit MS-only tracks using muon track look-up tables. These tracks are extrapolated back to match tracks in the ID and are refit to provide a *combined* muon candidate. The precise tracking starts from the MS-only and combined muon candidates identified in the previous stage. A tracking algorithm, similar to the one used in the offline muon track reconstruction, makes use of information from additional trigger chambers and precision muon chambers within the respective RoI. An extrapolation of MS-only tracks back into the ID is again used to match ID tracks. If the matching fails, an inside-out approach is tried where ID tracks are extrapolated to the MS and matched to MS tracks. This second attempt at combined muon reconstruction is significantly slower than the outside-in approach, and is used to recover a fraction of muon objects ($\sim 5\%$). Muon trigger menus generally make use of combined muon candidates, although MS-only muons are also triggered since they can be useful for exotic signatures.

Chapter 4

ATLAS Data

Collision events are observed in the ATLAS detector as electronic signals that are later reconstructed into charged tracks and neutral energy deposits and subsequently classified as belonging to physics objects. This chapter describes the data chain of recorded and simulated data events in the ATLAS detector, and the reconstruction algorithms used in subsequent analysis chapters.

4.1 Distributed computing and the ATLAS data model

The ATLAS experiment makes use of the Worldwide LHC Computing Grid (WLCG) which provides most of the computational resources the experiment requires [129]. The WLCG is a network of computer centres from across the world comprised into a hierarchical multi-tier computing infrastructure. Computing centres are categorised into four Tiers, depending on the role that they play. The ATLAS Tier-0 site [130] is the local CERN data centre through which all of the recorded data from the experiment passes. Within ATLAS, the Tier-0 centre is mainly responsible for prompt processing of the raw data coming from the online TDAQ system, writing of raw and reconstructed data to tape, and distributing the data to off-site Tier-1 centres. Tier-1 sites are primarily used to archive raw data, reprocess data, and provide access to processed versions of the data. They also provide some computing resources to analysis groups for data analysis. Tier-2 sites provide additional storage and computing resources and are used for generating event simulation samples. Tier-3 sites are primarily comprised of local institute clusters and provide local user-end storage and computing resources.

The raw event data recorded by the TDAQ system are initially in a byte-stream (RAW) format. The RAW data format is reconstructed at Tier-0 into a representation of physics objects, as described in Section 4.3, and stored in the Event Summary Data (ESD) format. The ESD format contains sufficient information to allow for the re-calibration of the event reconstruction: track re-fitting, jet calibration, particle identification, etc.. The ESD format is subsequently reduced into the Analysis Object Data (AOD) format which contains a summary of the reconstructed event, and contains sufficient information for common analysis tasks. The AOD format is compatible with the ROOT [131] data framework commonly used for data storage and analysis by the particle physics community.

4.2 ATLAS simulation

In order to generate simulated data, i.e., Monte Carlo (MC), the data model requires additional steps. The simulation of events from a particular physics process is performed by event generators which simulate the incident parton interactions and subsequent showering of final-state particles. The event simulation process is further described below. The resulting simulated events are stored in the Event Data (EVNT) format, and contains the particle information as produced by the MC generator. This information is commonly referred to as MC truth level information. EVNT data are then processed through the detector simulation step, either full (GEANT 4 [132]) or fast (ATLFASTII [133]) simulation, simulating the detector acceptance and response, and producing a collection of interactions, or hits, with the detector. The data is stored in the HITS data format. This format subsequently undergoes digitisation in order to convert detector hits into the electronic signals read out by the TDAQ system, resulting in a similar RAW format (also containing MC truth information) to that used in the online data-taking. The RAW format is then reconstructed into ESD and AOD formats.

4.2.1 Event generators

The role of a MC event generator is to simulate events produced from the interactions occurring in the particle detector. The discussion here focuses on the description of pp collisions within the ATLAS detector. In a high-energy pp collision, a parton from each of the two approaching protons are involved in an interaction with large momentum transfer, referred to as the hard-scatter process. The hard-scatter process determines the main characteristics of the event and produces outgoing final-state particles. Short lived intermediate particles

can be created in the hard-scatter, and need to be considered. Additionally, partons from the protons which are not involved in the hard interaction may also undergo soft scattering or radiate partons and produces final-state particles. This process, comprising of the final-state particles not directly involved in the hard-scatter, is referred to as the underlying event (UE). Due to QCD confinement, final-state quarks and gluons are not directly observable within the detector, and undergo hadronisation: the fragmentation of coloured partons into colour-neutral hadrons, and the decay of unstable hadrons. Similarly, Quantum Electrodynamincs (QED) radiation from initial or final-state partons will be produced. This results in parton showers (PSs): cascades of particles such as hadrons, photons and electrons which traverse the detector.

There are many event generators available for simulating high-energy pp interactions. These generators make use of parton distribution functions (PDFs) to define the flavour and momentum probability distributions of the partons from the incoming protons. The cross-section of a particular interaction is determined from the matrix-element (ME) calculation of the initial and final-state interaction and the proton PDFs. The simulation of subsequent showering of final-state partons is performed by simulating QED and QCD radiation, and making use of fragmentation models. In practice, different event generators have varying performance when simulating different physics processes, and need to be tested and cross-checked against data. It is not uncommon for the ME calculations and PS to be performed separately with different generators. The specific generators used to model particular processes in the analysis chapters will be mentioned therein.

4.3 Object reconstruction

The raw ATLAS data (and event simulation) is a collection of digitised signals from different detector systems. The signals need to be reconstructed into physics objects (a representation of detector signals as particles) so that they can be conveniently used for physics analyses. Large fractions of data available to ATLAS include well understood processes that are not of interest. In order to record interesting events, a dedicated TDAQ system is in place to control the data acquisition rates (Section 3.2.5). The TDAQ system is reliant on fast object reconstruction in order to make decisions on which events are interesting and should be recorded. This is referred to as online reconstruction. Recorded data is subsequently reconstructed by the offline reconstruction algorithms at Tier-0 where the reconstruction algorithms are not constrained by the latency requirements of the TDAQ.

When measuring event rates and cross-sections a thorough understanding of the efficiency with which physics objects are reconstructed, within the detector, is vital. The efficiency of a certain object is composed of several components, associated with the object's reconstruction $\varepsilon_{\text{reco.}}$, identification $\varepsilon_{\text{id.}}$, isolation $\varepsilon_{\text{iso.}}$, and triggering $\varepsilon_{\text{trig.}}$ efficiencies. Several working groups within ATLAS are tasked with the development of object reconstruction, identification, triggering, etc., with groups dedicated to objects such as electrons, muons, photons, jets, tau leptons (*taus* for short), and missing transverse energy. The working groups also provide the measurement of the object efficiencies, and their respective uncertainties, to be used by analyses within ATLAS. They will also provide recommended calibrations and corrections that can be used to address object mis-modelling.

The details of the reconstruction, identification, isolation and triggering of physics objects used in subsequent physics analysis chapters are discussed here. A schematic representation of the different layers of the ATLAS detector used to reconstruct different physics objects is shown in Figure 4.1.

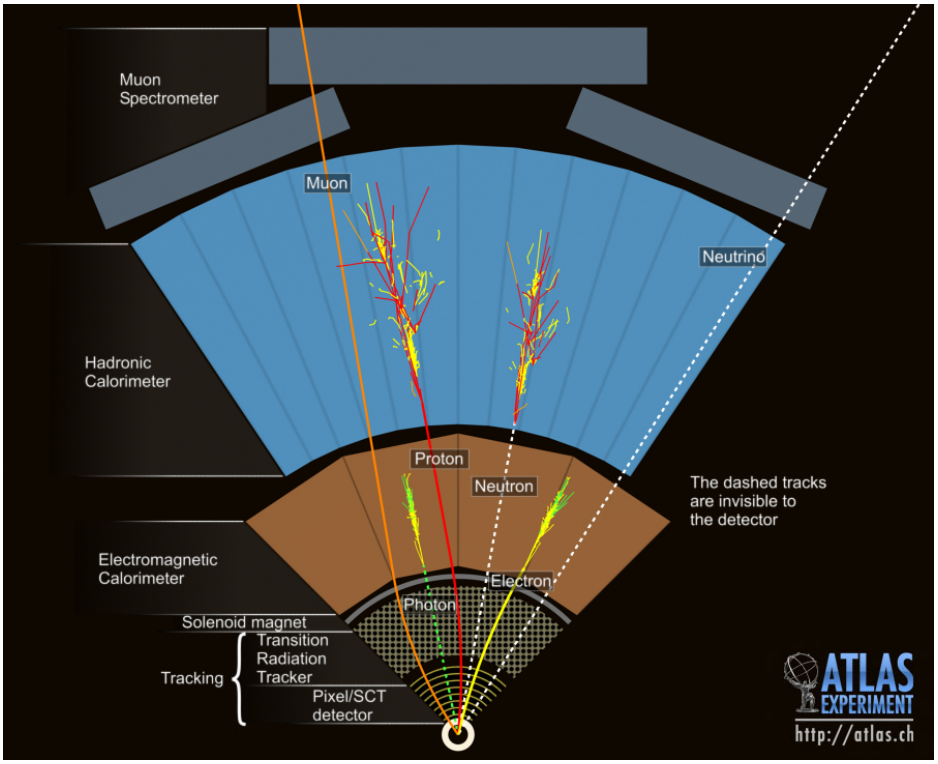

Figure 4.1 A computer generated view of the ATLAS detector showing the active detector layers used for particle reconstruction [134].

4.3.1 Electrons

Electron candidates, referring to objects which are candidates for either e^+ or e^-, are selected by matching EM-Cal clusters to tracks fit from hits in the ID [135]. Clusters in the EM-Cal are seeded by a sliding window search in $\eta \times \phi$ for longitudinal towers which have a total cluster transverse energy of $E_{\mathrm{T}} > 2.5$ GeV. Qualifying clusters then provide RoIs within which ID tracking algorithms are run. Tracks are reconstructed by using pattern recognition based on hits in the ID, where the pattern finding algorithm allows for energy loss in subsequent layers of the ID. Tracks are fit from several ID hits using a χ^2 fit. The resulting tracks are extrapolated into the EM-Cal. The tracks and calorimeter clusters are then matched by considering the distance in $\eta \times \phi$ between the track position in the middle layer of the EM-Cal, and the barycentre of a EM-Cal cluster. The electron candidate is then the resulting matched track and EM-Cal cluster [16]. Electron candidates are removed if they fail to have any precision silicon hits and are considered as photon candidates. The experimental effects on the cluster energy are taken into account by performing an energy calibration using simulated events. The electron four-momentum is then computed from the energy from the calibrated cluster and the primary track associated with the original cluster.

General sources of backgrounds to reconstructed electrons include non-prompt electrons, from photon conversion or heavy flavour hadronic decays, and charged hadronic particles[17], like $\pi^{\pm}$'s. Consequently, dedicated identification algorithms are used to assess the quality of the electron candidates. The baseline electron identification algorithm makes use of a likelihood based multivariate method[18]. Signal and background probability distribution functions (PDFs) are built for a set of discriminating variables which are sensitive to the separation of signal and background reconstructed electrons. An electron candidate is then assigned a probability of being either a signal or background object, calculated from a likelihood ratio derived from the candidate's properties. Three working points are provided, listed here in order of increasing background rejection, `loose`, `medium` and `tight`. The working points are all based on the same likelihood discriminant. Events selected by the `tight` (`medium`) working point are a subset of events selected by the `medium` (`loose`) working point (i.e., `loose` $\supseteq$ `medium` $\supseteq$ `tight`). The signal efficiency for an electron candidate with $E_{\mathrm{T}} = 25$ GeV is in the range of approximately 75% to 90%, depending on

[16] When several tracks are matched to a single cluster, the ambiguity is resolved by identifying a primary track based on the cluster-track distance, and number and location of pixel hits

[17] The TRT offers good discrimination from charged hadrons through the detection of transition radiation photons.

[18] An alternative electron identification, using a cut based method as opposed to the likelihood method, is also provided—with respective `loose`, `medium`, `tight` working points—although it is not used in Run-2 analyses and generally reserved for cross checks.

the working point, and increases as a function of E_{T}. Figure 4.2 (a) shows the electron reconstruction and identification efficiencies for different working points as a function of E_{T}, measured for data and MC in $Z \to ee$ events. The difference between the data and MC efficiencies is provided as a scale factor to correct MC.

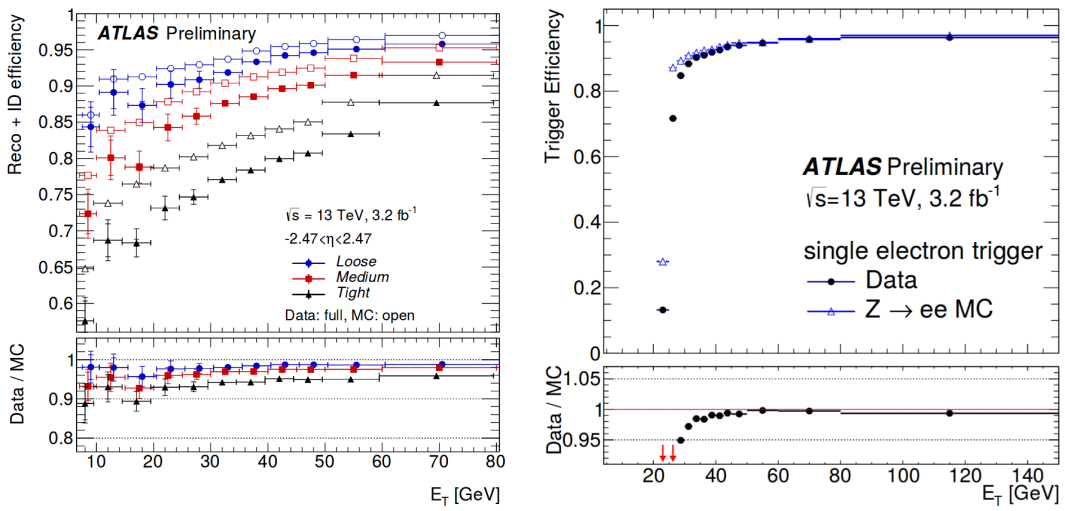

(a) **(b)**

Figure 4.2 Measured efficiency in $Z \to ee$ events for data and MC of (a) the electron reconstruction and identification at different working points, and (b) the 24 GeV `medium` electron trigger [135].

Along with the electron identification requirements introduced above, electron isolation techniques are designed to provide additional background rejection. Analyses targetting prompt electrons in the final-state can benefit from requirements on the electron isolation in order to further discriminate against converted photons and hadronic electron sources. Variables which quantify the isolation of the electron are based on either calorimeter or tracking information in a cone around the electron. Working points for the electron isolation requirements are defined on a fixed basis (i.e., with a constant threshold on the discriminating variables) or varying with the electron E_{T}. The `gradient` isolation working point provides approximately 90(99)% efficiency for electrons with $E_{\mathrm{T}} = 25(60)$ GeV.

Reconstructed electrons are used at the decision level in the HLT, seeded by calorimeter RoIs at L1. Figure 4.2 (b) shows the efficiency in $Z \to ee$ events of the $E_{\mathrm{T}} = 24$ GeV `medium` electron trigger for data and MC.

4.3.2 Photons

Photons yield similar signatures in the EM-Cal to that of electrons, i.e., sliding window clusters matched to tracks in the ID, and their reconstruction proceeds in parallel [136]. Prompt photons in ATLAS are identified as electromagnetic showers in the EM-Cal which are isolated from other particles in the event [136]. Due to the possible photon conversion into electron-positron pairs ($\gamma \rightarrow e^+e^-$) within the ID, photon candidate EM-Cal clusters are matched to tracks originating from a conversion vertex. These photons are identified as *converted photons*. Alternatively a prompt photon reaching the EM-Cal (*unconverted photons*) will have a signature shower without an associated track in the ID.

The energy of reconstructed photons is measured from deposited clusters in the EM-Cal, calibrated to take into account energy loss in the ID layers, as well as the energy leakage into the Had-Cal. The calibration is performed using a combination of simulation and data-driven studies. The calibrated energy of the photon candidate, and the position of the barycentre of clusters within the RoI in the second EM-Cal layer, is used to calculate the E_{T} of the candidate photon.

Photon identification algorithms [136] are used in order to identify prompt photons from other sources, such as from hadronic decays, or QCD jets, which can mimic prompt photon signatures. Prompt photons tend to produce narrower energy deposits in the EM-Cal compared to jet backgrounds. Additionally, jet showers misidentified as photon candidates tend to have higher levels of leakage into the Had-Cal, compared to those from prompt photons. Sources of non-prompt photons are rejected by the photon identification algorithm, which uses EM shower shape information to discriminate sources of background to prompt photons. Isolation and identification working points are available, though they are not explicitly relevant to the subsequent discussion in this thesis and are not detailed here.

4.3.3 Muons

Muons have an average proper lifetime of 2.2 μs and are stable within the detector material of ATLAS. They are charged leptons and their trajectories can be mapped by the tracking systems within ATLAS. Due to their large mass, above three orders of magnitude that of the electron mass, they produce minor deposits of energy in the calorimeters. The MS described in Section 3.2.3 is responsible for reconstructing muon trajectories outside of the calorimeters. Muon candidates are therefore composed of tracks determined from hits in the MS, which tend to be matched to tracks in the ID. The muon reconstruction [137] starts with a search

for hits in MS layers aligned with the trajectory of a muon in the bending plane. Precise momentum and η measurements are provided by the MDTs and CSCs, with the triggering detectors providing (η, ϕ) position measurements. Muon track candidates are built from χ^2 fits of hits from segments in the different layers. Hits with large χ^2 contributions are excluded and refit until the tracks pass predefined qualifying criteria.

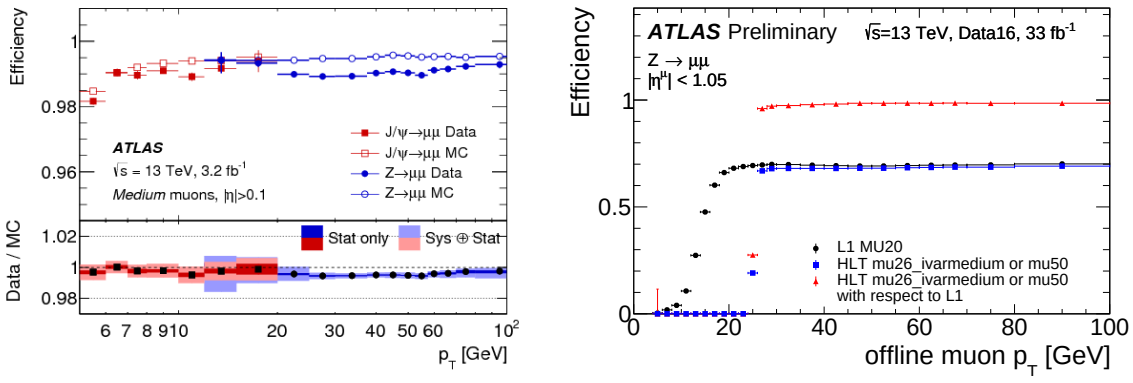

(a) **(b)**

Figure 4.3 Measured efficiency in (a) $Z \to \mu\mu$ and J/ψ events for data and MC of the muon reconstruction efficiency for the `medium` identification working point [137], and (b) $Z \to \mu\mu$ and J/ψ events for data with the 2016 unprescaled muon L1 and HLT trigger in the barrel region [112].

Four types of reconstructed muons are provided in Run-2 [137]. Only those relevant to this thesis are commented on here. The bulk of muons are *combined muons* where a global fit of ID and MS tracks is performed by extrapolating MS tracks back into the ID, i.e., an outside-in approach. Muon candidates without ID tracks, which are compatible with originating from the interaction point, are reconstructed as *extrapolated muons*. They are used to extend the muon acceptance at high η where the ID coverage is limited.

The muon identification [137] aims to identify prompt muons from non-prompt muon backgrounds, such as muons decaying from charged hadrons. In particular, muons from charged hadronic decays inside the ID will produce signature kinked tracks that tend to have poor fit quality, and incompatible momentum and charge dispersion in the ID and MS. As such, the muon identification relies on applying quality requirements on muon candidates. In particular, the quality and number of ID and MS hits associated to muon candidate tracks are used to select high quality candidates. Additionally, several variables are used for muon identification, including variables associated to the spread of the candidate's charge and momentum in the ID and MS, and the quality of the χ^2 fit. Three working points are provided

for the nominal muon identification, `loose`, `medium` and `tight`[19]. The `medium` working point is the nominal selection for muons in most analyses, and is optimised to reduce sources of uncertainty associated with muon reconstruction and calibration; only combined and extrapolated muons are considered. The efficiency in data and MC of the `medium` muon working point is shown in Figure 4.3 (a).

In addition to the muon identification described above, further background rejection for prompt muons originating from heavy resonances is provided by isolation requirements on muon candidates. Isolation variables are constructed in isolation regions surrounding the muon candidates, by removing energy (or momentum) contributions attributed to the muon and taking into account pileup and UE effects. The tracking isolation variable $p_{\mathrm{T}}^{\mathrm{iso}}$ sums the p_{T} of tracks within a cone which shrinks as a function of the total muon (p_{T}^{μ}), $\Delta R = \min(10\ \mathrm{GeV}/p_{\mathrm{T}}{}^{\mu}, 0.3)$. The calorimeter isolation variable $E_{\mathrm{T}}^{\mathrm{iso}}$ has a fixed isolation region of $\Delta R = 0.2$. Seven isolation working points are identified for Run-2 [137], applying selections on $p_{\mathrm{T}}^{\mathrm{iso}}$ and $E_{\mathrm{T}}^{\mathrm{iso}}$ which depend on p_{T}^{μ} and efficiency requirements of the working point. The `loose` and `tight` isolation working points are defined to have fixed 99% and 96% efficiency, respectively. The `gradient` and `gradient-loose` working points provide varying efficiencies with respect to p_{T}^{μ}, with $> 90\%$ and $> 95\%$ efficiency for $p_{\mathrm{T}}^{\mu} = 25$ GeV, respectively, increasing to 99% for $p_{\mathrm{T}}^{\mu} = 60$ GeV. The remaining three working points are defined by either using fixed cuts on the isolation variables (`fixed-cut-loose`), using only the track based isolation (`loose-track-only`), or both (`fixed-cut-tight-track-only`).

Muon triggers have already been described in Section 3.2.5.2. The efficiency of the L1 and HLT muon trigger with `medium` identification is shown in Figure 4.3 (b) as measured in $Z \to \mu\mu$ events. The L1 muon trigger efficiency is $\sim 70\%$ in the barrel region compared to $\sim 90\%$ in the end-caps due to material from toroid magnets and the support structure.

4.3.4 Jets

Due to colour confinement in QCD, coloured final-state partons in pp collisions, i.e., gluons and quarks, are observed experimentally as colourless hadrons. This process is referred to as parton showering and results in collimated sprays of colourless particles, known as *jets*. It is modelled via fragmentation models. How a jet is defined within an experiment is dependant on the algorithms used to group particles into jets and define their combined momentum. Sequential clustering algorithms are currently preferred to define jets as they are they are

[19] An additional working point which is optimised for heavy resonant W' and Z' searches to high p_{T} muons is also provided. It targets muon candidates with $p_{\mathrm{T}} > 100$ GeV.

infra-red and collinear (IRC) safe [138]: under collinear splitting, or soft emission, of partons, the resulting jets identified do not change. Sequential clustering algorithms cluster particles from initial candidates, and iteratively add additional particles into the jet. The default jet definition used in ATLAS Run-2 reconstruction makes use of the anti-k_t algorithm [139] with radius parameter $R = 0.4$. The algorithm uses the distances d_{ij} and d_{iB} defined as,

$$d_{ij} = \min\left(\frac{1}{(p_{\mathrm{T}}^{i})^2}, \frac{1}{(p_{\mathrm{T}}^{j})^2}\right) \times \frac{\Delta R_{ij}^2}{R^2},$$
$$d_{iB} = \frac{1}{p_{\mathrm{T}}^{i}}, \tag{4.1}$$

where ΔR_{ij} is the angular distance between particles i and j, and p_{T}^{i} is the transverse momentum of particle i. The algorithm constructs all d_{ij} and d_{iB} combinations and finds the minimum quantity. If a d_{ij} is found as the minimum, the set of particles ij are combined. If a d_{iB} is found as the minimum, particle i is identified as a jet and removed from the algorithm. The process is repeated until all particles have been clustered into a jet, or the desired number of jets are found. From Eq. (4.1) it can be seen that this algorithm will prefer to cluster around high p_{T} (hard) objects first, and will iteratively add softer objects into the jet. The resulting anti-k_t jets are circular jets, of varying circumference, that tend to be clustered around hard particles. They are robust against soft jets from UE and pileup due to their hard particle dependence, but are poor at resolving jet substructure.

In Run-2 reconstruction, jet objects are seeded from topological cell clusters[20] in the calorimeter [126]. The reconstruction of topo-clusters is calibrated to account for the expected noise levels in Run-2 conditions. Their energies are calculated at the EM scale, defined as the calibrated energy scale of EM particles. The resulting clusters are used as input into the anti-k_t algorithm, implemented in the FastJet package [140], which reconstructs jet objects. At this stage, the energy associated with a reconstructed jet does not correspond to the true energy of the particle jet, and a dedicated calibration of the jet energy scale (JES) is required to correct for experimental effects. The difference in the reconstructed and true jet energy can be quantified by measuring the jet energy response, which is the average ratio of the reconstructed jet energy over the true jet energy, determined from MC simulation experiments. There are several effects that need to be accounted for when calibrating JES. The reconstructed jet energy needs to take into account the energy loss in the inactive detector regions, due to jet components falling outside the detector acceptance, and due to soft jet components that are skipped by the clustering algorithm due to threshold

[20] See Section 3.2.5.2

requirements. Additionally, the calorimeters have different energy responses for hadronic and electromagnetic showers. The jet energy response is also dependant of pileup conditions. Since additional particles from pileup will be included into jet reconstruction, the result will on average be an increase in the reconstructed jet energy. To account for these effects the JES calibration is done in several steps [141]. First the jet direction is corrected to point to the hard-scatter vertex, and the four-momentum of the jet is recalculated. Next, per-event level pileup subtraction is used to remove the average excess energy within the area of the jet [142], with a residual pileup correction determined from MC studies. The resulting jet energy response is made to be independent on the number of primary vertices in the event. The absolute JES calibration is then performed from MC truth studies to correct the jet four-momentum to that of the truth jets. Tracking, jet shape and MS information is used to reduce flavour dependence of the response and improve jet resolution. Finally, a residual scale factor is applied to the reconstructed jet energy so as to match the reconstructed MC jet energy resolution.

While the effects from pileup are on average subtracted on an event-by-event basis, as discussed above, local fluctuations may result in reconstructed jets which originate from pileup. Tracking based variables are defined and used in a multivariate discriminant in order suppress reconstructed jets from pileup. In particular, the fraction of the total p_{T} from tracks associated to the jet which originate from the primary vertex, as well as the jet energy (post JES calibration), provide an effective handle for pileup background suppression. The resulting multivariate discriminant is known as the jet vertex tagger (JVT) [143] and provides pileup jet suppression with hard-scatter jet efficiencies which are stable with respect to pileup conditions.

There are several additional background sources which may deposit energy in the calorimeters and be reconstructed as jets. These include upstream beam backgrounds, cosmic-ray showers and calorimeter noise. A dedicated jet cleaning tool [144] is provided in order to veto events which are suspected to have sources of *bad* jets. This is done with predefined `loose-bad` and `tight-bad` working points, the former providing high event efficiency while the latter provides high jet purity. Jet cleaning is applied at analysis level after the objects selection and overlap conditions have been applied, and prior to calculation of $E_{\mathrm{T}}^{\mathrm{miss}}$.

The nominal jet reconstruction for jet triggers at the HLT resembles that of the offline reconstruction. The jet reconstruction at the HLT is highly flexible, and can be performed on a RoI basis and/or without the different components of JES calibration. Common triggers provided include different jet multiplicities passing a variety of energy thresholds.

4.3.5 *b*-jets

Many important signatures from SM and BSM physics have final-state *b*-quarks. The resulting hadrons have a mean lifetime of $\sim 1.5\,\text{ps}$ and will therefore generally travel several millimetres within the ATLAS detector volume before subsequently decaying. This results in a secondary vertex displaced from the primary interaction point, characterised by tracks with large transverse and longitudinal impact parameters. Additionally, a *b*-hadron tends to have a large invariant mass with respect to its decay products, resulting in decay products with high p_{T} and subsequently wider jets and higher track multiplicities than those associated with light quark hadrons. These features are used to identify jets from *b*-hadrons (*b*-jets) using dedicated *b*-tagging algorithms [145, 146]. The *b*-tagging algorithms are seeded from reconstructed jets, and make use of reconstructed tracks and the position of the primary vertex. The identification of *b*-jets was improved substantially in Run-2 by the inclusion of the IBL [114]. One such algorithm, `MV2` [146], combines the output of several *b*-tagging classifiers in a boosted decision tree (BDT) regression. It is trained on simulated $t\bar{t}$ events, with resulting *b*-jets as the signal, and *c*-jets and light quark jets considered as background. Variations of the regression discriminant exist as `MV2cXX`, where the trailing `XX` are numbers which indicate the fraction of *c*-jets in the background sample used for training. For example, `MV2c10` is trained against a sample comprised of 10% *c*-jets, and 90% light quark jets[21]. Several working points are provided which offer a varying performance in *b*-jet efficiency and background rejection. The recommended algorithm for Run-2 is `MV2c10`, whose working points and performance are shown in Table 4.1 [146]. The *b*-jet triggers used in Run-2 adopt the same *b*-tagging algorithms used offline.

Table 4.1 Working points for the `MV2C10` *b*-tagging algorithm, showing the expected *b*-jet efficiency, and background rejection, estimated from $t\bar{t}$ events [146].

BDT Cut Value	*b*-jet Efficiency [%]	*c*-jet Rejection	Light-jet Rejection	τ Rejection
0.9349	60	34	1538	184
0.8244	70	12	381	55
0.6459	77	6	134	22
0.1758	85	3.1	33	8.2

[21] This naming scheme was defined in Ref. [147]. However, for the more recent versions, which are used in the subsequent analyses, the fractions only match approximately. For example, in `MV2c10` in Ref. [146] the training background sample was set at 7% *c*-jets and 93% light quark jets.

4.3.6 Taus

Taus (τ-leptons) are an important signature to many SM and BSM analyses. The short lifetime of taus results in a proper decay length of $\sim$80 μm, decaying within the LHC beam pipe and well before reaching the IBL [21]. Taus decay $\sim 65\%$ of the time into hadrons, predominantly neutral (π^0) and charged pions ($\pi^\pm$) of several multiplicities. Due to charge conservation, most hadronically decaying taus decay with 1 or 3 charged particles (or prongs), subsequently denoted as $\tau_{\text{1-prong}}$ and $\tau_{\text{3-prong}}$, respectively. The remaining 35% are attributed to leptonic decay modes, i.e., electrons ($\tau^- \to e^- \bar{\nu}_e \nu_\tau$) and muons ($\tau^- \to \mu^- \bar{\nu}_\mu \nu_\tau$)[22], distributed approximately evenly between the two modes. Hadronically decaying taus are denoted as τ_{had}, while leptonically decaying taus are τ_{lep}, with τ_{e} and τ_μ denoting decays to electrons and muons, respectively. Table 4.2 shows the individual decay channels of taus and their respective decay rates. In practice τ_{lep} candidates are indistinguishable from prompt electrons and muons from the interaction point. Therefore, ATLAS analyses rely on muon and electron reconstruction algorithms in order to identify τ_{lep} candidates. Tau reconstruction within ATLAS exclusively refers to the reconstruction of τ_{had}. In practice, the energy associated with the accompanying neutrino in hadronic decays is lost as missing energy, and only the visible decay products are used in the reconstruction. The reconstructed tau candidate is therefore usually referred to as $\tau_{\text{had-vis}}$, to allude to the fact that the invisible component is not taken into account, while the τ notation is reserved for the true tau lepton.

All anti-k_t jet candidates are initially considered as $\tau_{\text{had-vis}}$ candidates and seed the $\tau_{\text{had-vis}}$ reconstruction algorithm [148, 149]. Jets associated with τ_{had} decays have particular features which can be used to distinguish them from other jet sources. In particular, they tend to produce energy deposits which are culminated and have low-multiplicities of associated tracks. The tau reconstruction is seeded by jets which are required to have $p_{\text{T}} > 10$ GeV and $|\eta| < 2.5$ with a veto on transition region jets ($1.37 < |\eta| < 1.52$). A tau vertex is chosen from a selection of vertices from candidate tracks within a cone of $\Delta R < 0.2$ of the jet candidate. The vertex from the track with highest momentum fraction is chosen as the tau vertex. The tracks must pass quality criteria and have a transverse plane distance $d_0 < 1\,\text{mm}$, as well as be within $|\Delta z_0 \sin(\theta)|$ of the tau vertex[23]. Isolation ($0.2 < \Delta R < 0.4$) and core ($\Delta R < 0.2$) regions are defined as cones around the resulting tau candidate. The vector sum of topo-clusters within the tau core region is used to define the tau direction with respect to

[22] Leptonic tau decays are a flavour changing processes induced though a virtual $W^\pm$ boson, i.e.,

$$\tau^- \to W^- \nu_\tau \to \ell^- \bar{\nu}_\ell \nu_\tau$$

.

[23] See Section 3.2.1.4

Table 4.2 Average tau lepton decay branching fractions (B) in percentage [21]. Charged hadrons are represented by $h^{\pm}$ and are either pions or kaons.

Decay mode	$B[\%]$
Total τ_{lep}	35.2
$\tau^- \to e^- \bar{\nu}_e \nu_\tau$	17.8
$\tau^- \to \mu^- \bar{\nu}_\mu \nu_\tau$	17.4
Total τ_{had}	64.8
$\tau^- \to h^- \nu_\tau$	11.5
$\tau^- \to h^- \pi^0 \nu_\tau$	26.0
$\tau^- \to h^- \pi^0 \pi^0 \nu_\tau$	9.5
$\tau^- \to h^- h^+ h^- \nu_\tau$	9.8
$\tau^- \to h^- h^+ h^- \pi^0 \nu_\tau$	4.8
Other τ_{had}	3.2

the tau vertex. A correction to the tau energy response is applied by using the local cluster energy calibration of topo-clusters associated with the tau, and subtracts an amount of energy which is proportional to the number of reconstructed interaction vertices in the event, in order to compensate for the expected energy contribution from pileup. As with the jet calibration, the energy response is corrected to visible tau energy from MC truth events—excluding neutrino decays. The calibration is done in bins of $|\eta|$ and number of prongs. The full tau energy scale (TES) calibration [149] includes additional correction scale factors which are extracted through a tag-and-probe analysis in $Z \to \tau_\mu \tau_{\text{had}}$ events, where the reconstructed m_Z distribution is matched to simulation by correcting the tau energy. This is done independently for $\tau_{\text{1-prong}}$ and $\tau_{\text{3-prong}}$ candidates.

The tau identification algorithm [149] is an important tool which can be used to reject backgrounds from quark- and gluon-initiated jets. It employs the use of a BDT to create a multivariate regression discriminant that can be subsequently used to attain certain levels of tau efficiency and purity. Input variables to the BDT are corrected so as to not be pileup dependent. The variables used include variables related to the candidate's calorimeter cells, clusters, shower shape and tracks. Additionally, a method which provides the reconstruction of the individual constituent particles of the tau decay, i.e., charged and neutral hadrons, known as tau particle flow (TPF) [150], is used to provide variables related to reconstructed pions and their respective energies. The BDT is trained on $Z/\gamma^* \to \tau\tau$ simulated signal samples against multijet background samples from data. Three working points are provided, `loose`, `medium`, and `tight`, which are defined to provide tau efficiencies which are constant with respect to the tau p_{T}. The targeted combined reconstruction and identification efficiencies for $\tau_{\text{1-prong}}$ ($\tau_{\text{3-prong}}$) candidates are 60% (50%), 55% (40%), and 45% (30%)

for `loose`, `medium`, and `tight` working points, respectively, as shown in Figure 4.4. A dedicated electron discrimination is also provided in order to reject jets from electrons faking tau candidates [149]. Here, $\tau_{\text{1-prong}}$ candidates which have a reconstructed electron within their isolation cone are vetoed. The electron has to pass an identification working point requirement which is tuned to yield 95% efficiency for hadronic taus.

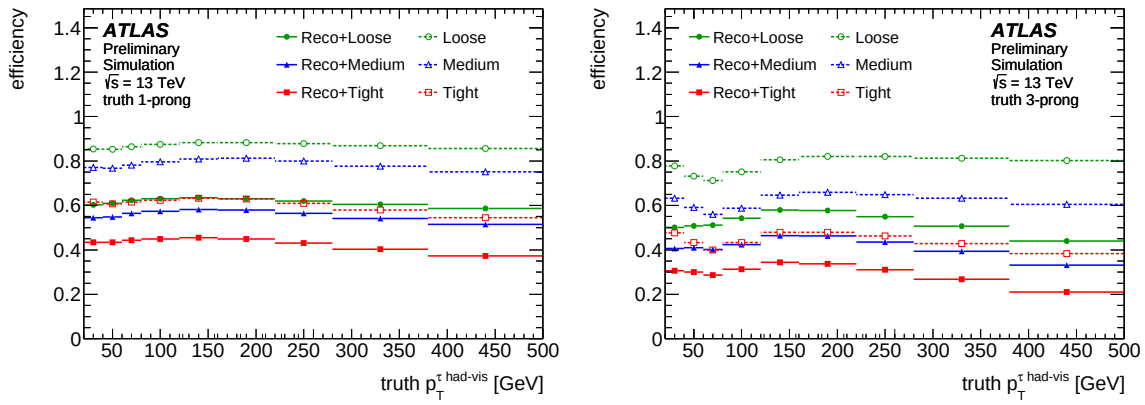

(a) **(b)**

Figure 4.4 Measured $\tau_{\text{had-vis}}$ identification efficiencies, and combined identification and reconstruction efficiencies, in MC for (a) $\tau_{\text{1-prong}}$ and (b) $\tau_{\text{3-prong}}$ passing different identification working points as a function of the $\tau_{\text{had-vis}}$ p_{T} [151].

At L1, tau candidates are triggered by identifying RoIs in clusters of 2×2 trigger towers in the EM-Cal, as discussed in Section 3.2.5.1 [112]. Isolation requirements are placed on the L1 tau triggers, with $E_{\text{T}} < 60$ GeV, to yield a 98% efficiency when run on simulation. The large number of jets having similar properties to τ_{had} decays makes moderating tau trigger rates very challenging. At the HLT a $\Delta R < 0.2$ cone is paced around the L1 RoI direction. A tau energy calibration scheme is used to calculate the energy from topo-clusters of calorimeter cells within the cone. Energy threshold requirements are then applied on the tau candidates. A fast multiple stage tracking is then used to reconstruct ID tracks. The multiple stage tracking offers a way to moderate the high CPU time required to perform tracking in the large RoIs required by effective tau triggering. The fast tracking is followed by the nominal precision tracking described in Section 3.2.5.2. Reconstructed tau candidate variables are defined analogous to the ones used in the offline tau identification classifier. These variables are used in a BDT regression to provide a single score used for tau identification. The same trained BDT is used on offline and online tau reconstruction to preserve the correlations between different tau identification working points. The BDT is trained separately for tau candidates with 1 and 3 associated charged tracks. The primary tau triggers used for physics analysis

include single tau triggers with high E_{T} thresholds, or tau triggers with an accompanying electron, muon, tau, or $E_{\mathrm{T}}^{\mathrm{miss}}$ trigger accept. The measured efficiencies in data and MC for a single $\tau_{\text{had-vis}}$ trigger with a p_{T} threshold of 25 GeV is shown in Figure 4.5.

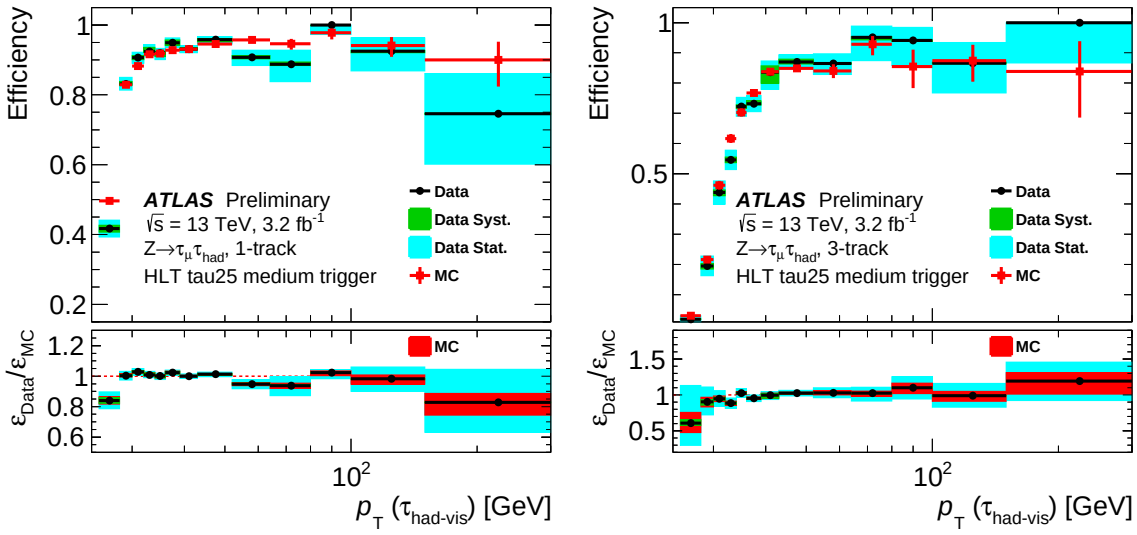

(a) **(b)**

Figure 4.5 Measured $\tau_{\text{had-vis}}$ trigger efficiencies in data and MC for (a) $\tau_{\text{1-prong}}$ and (b) $\tau_{\text{3-prong}}$ passing a HLT with a $\tau_{\text{had-vis}}$ p_{T} threshold of 25 GeV [149].

4.3.7 $E_{\mathrm{T}}^{\mathrm{miss}}$ reconstruction

In the pp collisions in ATLAS the individual partons of crossing protons carry varying fractions of the proton energy. As such, the longitudinal component of the energy of a hard parton collision will vary. On the other hand, the transverse energy fraction carried by partons is minimal compared to the collision energy. Therefore, the transverse components of the energy of all objects that arise from a parton collision are expected to be zero, or very close to it. In practice, however, the energies from particles which escape detection in ATLAS (such as neutrinos) are missed, in which case this sum can be significantly larger than zero. The reconstruction of missing transverse energy ($E_{\mathrm{T}}^{\mathrm{miss}}$) is therefore an important proxy for measuring the energy of particles that escape detection.

In ATLAS the $E_{\mathrm{T}}^{\mathrm{miss}}$ reconstruction [152, 153] has to take into account the full event information, in which all reconstructed particle objects described in Sections 4.3.1– 4.3.6 are considered. The default $E_{\mathrm{T}}^{\mathrm{miss}}$ reconstruction is the track soft-term (TST) $E_{\mathrm{T}}^{\mathrm{miss}}$ and is comprised of two components: a *hard-term* composed of fully reconstructed and calibrated

objects, i.e., electrons, photons, muons, taus and jets; and a *soft-term*, which is composed of tracks which are not associated to the hard-term objects, but which have a coincidence with the hard-scatter vertex[24]. The vector definition $\mathbf{E}_{\mathrm{T}}^{\mathrm{miss}}$ is,

$$\mathbf{E}_{\mathrm{T}}^{\mathrm{miss}} = -\sum_{i\in\text{hard objects}} \boldsymbol{p}_{\mathrm{T}}^{i} \quad -\sum_{j\in\text{soft tracks}} \boldsymbol{p}_{\mathrm{T}}^{j}. \tag{4.2}$$

The first sum in Eq. (4.2) is a vector sum of all reconstructed (hard) objects in the event, meeting some predefined quality criteria. In order to avoid double counting of detector signals, a procedure which removes overlapping objects is in place. In particular, all reconstructed particles, with the exception of muons, will have some ambiguity with a defined jet object [25]. The $E_{\mathrm{T}}^{\mathrm{miss}}$ reconstruction therefore requires a sequence in which objects are included into the calculation. In a default reconstruction, priority is given first to reconstructed muons, then electrons, then photons, followed by hadronic taus, and finally jets. At each step, objects which belong to two or more classes are assigned the object definition with highest priority, while their overlapping objects are removed. The second term in Eq. (4.2) is the vector sum of the soft components of $E_{\mathrm{T}}^{\mathrm{miss}}$. This component is intended to capture energy from soft emission from hard objects, as well as objects which do not satisfy the threshold requirements of the reconstructed particles. For the TST $E_{\mathrm{T}}^{\mathrm{miss}}$ it is composed of the vector sum of the p_{T} from all tracks not associated with hard objects included in $\mathbf{E}_{\mathrm{T}}^{\mathrm{miss}}$ which stem from the hard-scatter vertex. Both hard- and soft-terms have little pileup dependence. For the hard-term this is as a result of being constructed from calibrated objects, which already account for pileup effects. For the soft-term it is as a result of the hard-scatter vertex association, which to a large extent removes effects from additional interactions in the same bunch crossing. The default $E_{\mathrm{T}}^{\mathrm{miss}}$ reconstructions outlined above is not intended to be a blanket $E_{\mathrm{T}}^{\mathrm{miss}}$ definition, and flexible support is provided for analysis level $E_{\mathrm{T}}^{\mathrm{miss}}$ definitions.

$E_{\mathrm{T}}^{\mathrm{miss}}$ triggers are seeded from the L1 JEP as described in Section 3.2.5 with dedicated algorithms which reconstruct calo-based $E_{\mathrm{T}}^{\mathrm{miss}}$ from cells, jets, or topo-clusters.

[24]The hard-scatter vertex is considered to be the primary vertex in an event with the highest scalar p_{T} sum of associated tracks.

[25]Only combined muon candidates are considered in the $E_{\mathrm{T}}^{\mathrm{miss}}$ calculation. Due to their signals in the MS, they can be readily distinguished from jet signals

Chapter 5

Statistical Methods

High-energy physics is reliant on the ability to test different hypotheses. An experiment aiming to make a measurement of an observable, or discover or exclude the existence of a new particle, must design analysis in a way that allows the testing of different hypotheses. In the simplest example one can test a null hypothesis $\mathbb{H}_{\text{null}}$ versus an alternative hypothesis $\mathbb{H}_{\text{alt}}$. For the purpose of discovering a new particle not predicted by the SM, the null hypothesis would be identified as the SM prediction. To establish a discovery one would need to reject $\mathbb{H}_{\text{null}}$ in favour of an alternative hypothesis, in this case some BSM prediction. This is done by defining a test statistic, a quantity dependant on parameters related to the hypothesis[26] which quantifies the probability of observing a particular dataset. Predefined conditions of the test statistic have to be defined in order to either fail to reject $\mathbb{H}_{\text{null}}$, or reject $\mathbb{H}_{\text{null}}$ in favour of $\mathbb{H}_{\text{alt}}$. The condition pertaining to a discovery is when $\mathbb{H}_{\text{null}}$ is rejected at a statistical significance (referred to in the following as just the *significance*) of 5σ or above[27]. In the presence of a lack of evidence for the alternate hypothesis, $\mathbb{H}_{\text{alt}}$ is excluded at 95% CL[28]. In the section that follows, the test statistics and inference methods used within the analyses discussed in Sections 6–8 are presented. Concepts belonging to the validation of fitting likelihood functions, the estimation of uncertainties for measurements and cross-section limits, and the Asimov dataset are also described.

[26]This is following a frequentist definition of the test statistic, giving a probability of observing a dataset based with respect to a given hypothesis. An alternative approach is based on Bayesian hypothesis testing, where inference is made on the probability of the hypothesis given the data. Although Bayesian statistics are widely used in particle physics they are not relevant in the analyses discussed in the text. The preceding discussion will be limited to discussing the frequentist treatment.

[27]Significance level is defined by the quantile of a normal Gaussian distribution and is defined in Eq. (5.12).

[28]CL is defined as $\alpha = 1 - p$-value, defined in Eq. (5.11)

5.1 The likelihood function

The test statistic for both searches and measurements are based on the likelihood function. The binned likelihood $\mathscr{L}(\boldsymbol{x}|\mu)$ for a dataset $\boldsymbol{x}$ is the probability of observing $\boldsymbol{x}$ for a given hypothesis $\mathbb{H}_\mu$[29]. Here $\boldsymbol{x} = \{x_i\}$ is the set of the number of events in all considered bins of the desired distributions. For any given bin in a distribution, the expected number of signal and background events are determined by the corresponding cross-sections and integrated luminosity (taking into account the detector response). The total number of events, n, for a particular process is then given by,

$$n = L \cdot \sigma \cdot \varepsilon \cdot A, \tag{5.1}$$

where L is the integrated luminosity delivered by the accelerator, σ is the predicted cross-section of the process, and ε and A are the efficiency and geometrical acceptance of the detector. It is common practice to parameterise the total expected number of events in the i-th bin of a distribution as,

$$n_i = \mu \cdot s_i + b_i, \tag{5.2}$$

where s_i and b_i is the expected number of signal and background events in the i-th bin, respectively, and μ is the signal strength parameter which globally scales the signal, given by,

$$\mu = \frac{\sigma_{obs}}{\sigma_{SM}}, \tag{5.3}$$

where σ_{SM} is the signal cross-section as predicted by the SM [30] and σ_{obs} is the observed cross-section. The binned likelihood is defined as the product of the Poisson distribution for each bin,

$$\mathscr{L}(\boldsymbol{x}|\mu) = \prod_{i \in \text{bins}} e^{-n_i} \frac{n_i^{x_i}}{x_i!} \tag{5.4}$$

$$= \prod_{i \in \text{bins}} e^{-(\mu \cdot s_i + b_i)} \frac{(\mu \cdot s_i + b_i)^{x_i}}{x_i!}. \tag{5.5}$$

[29] In a likelihood function the dataset $\boldsymbol{x}$ remains fixed, and it is the hypothesis parameters which vary. The notation $\mathscr{L}(\boldsymbol{x}|\mu)$ chosen here is commonly used and reads as: the likelihood of $\boldsymbol{x}$ under the hypothesis $\mathbb{H}_\mu$

[30] For measurements or searches where the signal is defined by the SM this definition results in agreement with the SM where $\mu = 1$. For searches of BSM particles there is of course no σ_{SM}. For such a case one could define μ in terms of an expected BSM cross-section, σ_{BSM}. This does not introduce a dependence on a particular BSM model as the cross-sections in Eq. 5.1 and Eq. 5.3 cancel. The BSM signal MC templates are usually normalised to represent the number of events expected with $\sigma_{BSM} = 1$pb, and the signal strength is directly interpretable as a multiplicative factor, i.e., $\sigma_{BSM}(\mu = X) = X$pb.

In the case where we are interested in measuring the signal strength, μ can be considered to be the parameter of interest (POI). The likelihood function will in general also depend on additional parameters which are not of immediate interest, referred to as nuisance parameters (NPs), but which must be accounted for in the analysis. In the presence of a set of NPs, $\boldsymbol{\theta} = \{\theta_j\}$, the likelihood function takes on additional terms attributed to different sources of uncertainty. NPs are generally, although not exclusively, parameterised in terms of Gaussian probability distributions with an expected value θ_j^0 and standard deviation $\sigma_{\theta_j^0}$ determined via an auxiliary measurement. The true value of any $\theta_j \in Gauss(\theta_j^0, \sigma_{\theta_j^0})$ is not considered to be known *a priori* but is estimated[31] from $\boldsymbol{x}$. In the presence of NPs the binned likelihood function is written as,

$$\mathscr{L}(\boldsymbol{x}, \boldsymbol{\theta}^0 | \mu, \boldsymbol{\theta}) = \prod_{i \in \text{bins}} e^{-n_i(\mu,\boldsymbol{\theta})} \frac{\mu_i^{n_i(\mu,\boldsymbol{\theta})}}{x_i!} \times \prod_{j \in \text{systs}} e^{\frac{(\theta_j - \theta_j^0)^2}{\sigma_{\theta_j}}} \tag{5.6}$$

$$= \prod_{i \in \text{bins}} Poisson(x_i | \mu \cdot s_i(\boldsymbol{\theta}) + b_i(\boldsymbol{\theta})) \times \prod_{j \in \text{systs}} Gauss(\theta_j^0 | \theta_j, \sigma_{\theta_j}), \tag{5.7}$$

where *Poisson* and *Gauss* represent Poisson and Gaussian distributions, respectively. In the interest of readability and brevity the implicit dependence on the dataset and nuisance parameters will be omitted from the following text, such that $\mathscr{L}(\mu, \boldsymbol{\theta})$ implies $\mathscr{L}(\boldsymbol{x}, \boldsymbol{\theta}^0 | \mu, \boldsymbol{\theta})$[32].

Maximising the likelihood function in terms of its free parameters μ and $\boldsymbol{\theta}$ yields their estimated values with respect to a particular dataset. An unconditional[33] global[34] fit of the likelihood function of the dataset $\boldsymbol{x}$ and set of NPs $\boldsymbol{\theta}^0$ is at the points $\hat{\mu}$ and $\hat{\boldsymbol{\sigma}}$, also known as the maximum-likelihood estimators (MLEs) of the parameters. Alternatively, by using a conditional fit where a subset of parameters is set to particular values, the MLEs of the remaining parameters serve as their best estimates under those conditions.

[31] These estimates are extracted by maximising the likelihood of the data with respect to a set of parameters, the details of which will be discussed later in the text.

[32] The expanded form will henceforth be limited in use to cases where different sets of $\boldsymbol{x}, \boldsymbol{\theta}^0$ are used, and the explicit form is beneficial to the reader.

[33] The term unconditional refers to all parameters being allowed to vary in the fit. Conversely a fit where one or several parameters are fixed to specific values is considered to be a conditional fit.

[34] The term global refers to all regions and bins of interest being considered in the fit. Conversely a fit where one or several bins or regions are not included is referred to as being local.

5.2 Test statistics and hypothesis testing

The Neyman-Person lemma [154] states that the likelihood-ratio test

$$q^{NP} = -2\log\frac{\mathscr{L}(\mathbb{H}_{\text{alt}})}{\mathscr{L}(\mathbb{H}_{\text{null}})} \tag{5.8}$$

is the most powerful hypothesis test one can perform when comparing two hypotheses, $\mathbb{H}_{\text{null}}$ vs. $\mathbb{H}_{\text{alt}}$. For testing the hypothesis $\mathbb{H}_\mu$ we turn to test statistics based on the profile likelihood ratio, $\lambda(\mu)$ [155],

$$\lambda(\mu) = \frac{\mathscr{L}(\mu, \hat{\hat{\boldsymbol{\theta}}})}{\mathscr{L}(\hat{\mu}, \hat{\boldsymbol{\theta}})}, \tag{5.9}$$

where the $\hat{\mu}$ and $\hat{\boldsymbol{\theta}}$ in the denominator represent the MLEs of μ and $\boldsymbol{\theta}$ after performing an unconditional fit, while the $\hat{\hat{\boldsymbol{\theta}}}$ in the numerator are the MLEs of $\boldsymbol{\theta}$ from a conditional fit with μ fixed. Since the denominator corresponds to the maximum value of the likelihood function it follows that $0 \leq \lambda(\mu) \leq 1$, where $\lambda(\mu) \to 1$ implies some good agreement of $\mathbb{H}_\mu$ with the data. Several test statistics are defined for different purposes related to hypothesis testing in high-energy physics [155].

5.2.1 Hypothesis testing for the purpose of measurement

The test statistic t_μ is defined as,

$$t_\mu = -2\log\lambda(\mu), \tag{5.10}$$

where $\lambda(\mu)$ is the profile likelihood ratio defined in Eq. (5.9). With t_μ one can test the compatibility of different values of a POI, μ. Higher values of t_μ correspond to an incompatibility of $\mathbb{H}_\mu$ with the data. To quantify the level of disagreement with data for a particular value of μ a p-value is defined as,

$$p_\mu = \int_{t_{\mu,obs}}^{\infty} f(t_\mu|\mu)dt_\mu, \tag{5.11}$$

where $t_{\mu,obs}$ is the observed value of the test statistic t_μ from the data, and $f(t_\mu|\mu)$ is the probability distribution function (PDF)[35] of t_μ under the assumption of $\mathbb{H}_\mu$. An inference test can then be performed by defining a particular threshold value α for which any hypothesis $\mathbb{H}_\mu$ with $p_\mu < \alpha$ can be rejected. One usually converts the p-value into an equivalent significance

[35] More on how the PDFs are constructed is given in Section 5.3

value, Z, via,

$$Z = \Phi^{-1}(1-p), \tag{5.12}$$

where Φ^{-1} is the quantile of the standard Gaussian distribution. Under this definition the 5σ significance required for a discovery translates to a p-value[36] of $p = 2.87 \times 10^{-7}$. For the exclusion of a signal hypothesis, a p-value of 0.05 (95% CL) is usually used, corresponding to $Z = 1.64$.

The test statistic t_μ is a simplified case of test statistics based on the profile likelihood function. It is primarily used for testing two-sided measurements of the POI μ, where both $\mu < \hat{\mu}$ or $\mu > \hat{\mu}$ may result in small p-values, showing incompatibility with data. In cases where the presence of signal can only increase the mean event rate to what is expected from background processes, i.e., $\mu \geq 0$, downward fluctuations of the data are not considered evidence for rejecting $\mathbb{H}_{\text{null}}$. An alternate test statistic for positive signal, $\tilde{t_\mu}$ is defined as,

$$\tilde{t}_\mu = -2\log\tilde{\lambda}(\mu), \tag{5.13}$$

where,

$$\tilde{\lambda}(\mu) = \begin{cases} \frac{\mathscr{L}(\mu,\hat{\hat{\boldsymbol{\theta}}})}{\mathscr{L}(\hat{\mu},\hat{\boldsymbol{\theta}})} & \hat{\mu} \geq 0 \\ \frac{\mathscr{L}(\mu,\hat{\hat{\boldsymbol{\theta}}})}{\mathscr{L}(0,\hat{\boldsymbol{\theta}})} & \hat{\mu} < 0 \end{cases}. \tag{5.14}$$

Under the definition of $\tilde{t}_\mu$ a negative value of the MLE $\hat{\mu}$ will result in the denominator of $\tilde{\lambda}(\mu)$ to be taken as the conditional maximum likelihood at $\mu = 0$.

5.2.2 Hypothesis testing for the purpose of exclusion

For statistical exclusion of the background-only hypothesis, i.e., $\mu = 0$ so that $\mathbb{H}_0 \equiv \mathbb{H}_{\text{null}}$, in favour of an alternate hypothesis with positive signal, $\mu \geq 0$, the test statistic q_0 is used,

$$q_0 = \begin{cases} -2\log\lambda(0) & \hat{\mu} \geq 0 \\ 0 & \hat{\mu} < 0 \end{cases}, \tag{5.15}$$

with $\lambda(0)$ as defined in Eq. (5.9). This is a special case of the test statistic $\tilde{t}_\mu$ with $\mu = 0$. Like with $\tilde{t}_\mu$, the data shows lack of agreement with the hypothesis only for upward fluctuations of the signal strength, $\hat{\mu} > 0$.

[36] The probability with which the observed data can be attributed with a fluctuation under the $\mathbb{H}_{\text{null}}$.

The test statistic q_μ is defined for setting upper limits on the signal strength parameter μ, namely,

$$q_\mu = \begin{cases} -2\log\lambda(\mu) & \hat{\mu} \leq \mu \\ 0 & \hat{\mu} > \mu \end{cases} . \tag{5.16}$$

Larger values of q_μ would be related to higher levels of discrepancy between the data and the hypothesis $\mathbb{H}_\mu$. There is an upper bound on μ, $\hat{\mu} > \mu$, below which the test statistic $q_\mu = 0$. This ensures that upward fluctuations of the data well above the tested value of μ do not serve as evidence against $\mathbb{H}_\mu$. This condition on q_μ (when testing $\mathbb{H}_\mu$) is complimentary to that set on q_0 (when testing $\mathbb{H}_0$) in Eq. (5.15). The p-value p_0 is associated with q_0, given as,

$$p_0 = \int_{q_{0,obs}}^{\infty} f(q_0|0)dq_0, \tag{5.17}$$

while p_μ corresponds to q_μ, given as,

$$p_\mu = \int_{q_{\mu,obs}}^{\infty} f(q_\mu|\mu)dq_\mu. \tag{5.18}$$

Here $f(q_0|0)$ denotes the PDF of the test statistic q_0 under the assumption of $\mathbb{H}_0$, while $f(q_\mu|\mu)$ denotes the PDF of the test statistic q_μ under the assumption of $\mathbb{H}_\mu$. An alternate test statistic for exclusion of $\mathbb{H}_\mu$ for positive signals, $\mu > 0$, is $\tilde{q}_\mu$, defined to be,

$$\tilde{q}_\mu = \begin{cases} -2\log\frac{\mathscr{L}(\mu,\hat{\hat{\boldsymbol{\theta}}})}{\mathscr{L}(0,\hat{\boldsymbol{\theta}})} & \hat{\mu} < 0 \\ -2\log\lambda(\mu) & 0 \leq \hat{\mu} \leq \mu \\ 0 & \hat{\mu} > \mu \end{cases} . \tag{5.19}$$

Finally, when considering exclusion limits, the *CLs* method [156] is recommended[37]. It has an added advantage over q_μ (and $\tilde{q_\mu}$) as it avoids exclusion in background dominated regimes. It does this by taking into account the p_0 value in a test statistic, CL_s, defined as,

$$CL_s = \frac{CL_{b+s}}{1 - CL_b}, \tag{5.20}$$

where CL_{b+s} and C_b are p-values attributed to the signal-plus-background and background-only hypotheses, respectively[38]. The CL_s is then tested against a particular confidence level

[37] As long as there is no clear evidence for $\mathbb{H}_\mu$, exclusion limits using *CLs* are recommended [156].

[38] This is just a different convention of notation for the p-values attributed to q_0 and q_μ. Equivalently, $CL_s = \frac{p_\mu}{1-p_0}$.

α. The *CLs* prescription serves as a conservative approximation of limits placed with CL_{b+s} (e.g., q_μ) with *CLs* converging the CL_{b+s} in the limit of negligible backgrounds.

5.3 The asymptotic approximation

Section 5.2 introduced the p-values used for hypothesis testing. The p-values defined in Eqs. (5.11), (5.17) and (5.18) are all dependant on the PDFs of their respective test statistic under a particular hypothesis. The PDFs $f(t_\mu|\mu)$, $f(q_0|0)$ and $f(q_\mu|\mu)$ can each be determined by running an ensemble of toy experiments[39]. Each toy experiment will provide a single point measurement of the test statistic. By running several thousand toy experiments we can construct the required PDF. However, this approach is very often not a viable technique as generating thousands of toys to obtain a single PDF is computer intensive. Furthermore the technique becomes even less attractive for exclusion limits, where several $\mathbb{H}_\mu$ hypotheses are tested, or under increasingly complex models, such as those used in combinations of analyses channels.

When the determination of PDFs via toy experiments is not realistically possible (or desirable) one can use the asymptotic approximation [155], leading to analytic forms of the PDFs [155]. Generally one would like to be able to obtain the analytic form of $f(q_\mu|\mu')$ for cases where μ' is not necessarily equal to μ: the test statistic q_μ under the assumption that the true distribution pertains to μ'. An equivalent statement can be made for $f(t_\mu|\mu')$ and $f(q_0|\mu')$. The asymptotic approximations are based on results from Wilks [157] and Wald [158] which gives the analytic form of the test statistic at the large sample limit,

$$-2\log\lambda(\mu) = \frac{(\mu-\hat{\mu})^2}{\sigma^2} + O(1/\sqrt{N}). \tag{5.21}$$

Here N is the dataset size and $\hat{\mu}$ is a Gaussian distribution with mean μ' and standard deviation σ. Eq. (5.21) leads to analytic forms for the PDFs of test statistics in Section 5.2, as well as for p-values. Details are outlined in Ref. [155], of which the main results are summarised here.

[39] A particular toy experiment would constitute generating a random data set within the predefined likelihood model, $\boldsymbol{x}_{toy}$. One would then compute the test statistic (e.g., q_μ^{toy}) via performing the respective fits in the profile likelihood ratio.

At the large sample limit the cumulative distribution of $f(t_\mu|\mu)$ is[40],

$$F(t_\mu|\mu) = 2 \times (\int_{-\infty}^{t_\mu} f(t_\mu|\mu) dt_\mu - \frac{1}{2}) \tag{5.22}$$

$$= 2\Phi(\sqrt{t_\mu}) - 1, \tag{5.23}$$

where Φ is the cumulative distribution of a Gaussian with unit variance and zero mean. The p-value is therefore given as,

$$p_\mu = 1 - F(t_\mu|\mu) = 2(1 - \Phi(\sqrt{t_\mu})). \tag{5.24}$$

A similar approximation can be found for the positive signal test-statistic $\tilde{t}_\mu$ [155]. Under the asymptotic approximation the test statistics t_μ and $\tilde{t}_\mu$ become χ^2 distributed with n number of DOF equal to the number of POIs. This allows us to place confidence intervals at $1-\alpha$ CL, defined as the region where,

$$-2\log\lambda(\mu) < F^{-1}_{\chi^2_n}(1-\alpha), \tag{5.25}$$

where $F^{-1}_{\chi^2_n}$ is the quantile of the χ^2 distribution with n-DOF.

For the purpose of discovery the asymptotic approximation yields a cumulative distribution,

$$F(q_0|0) = \Phi(\sqrt{q_0}), \tag{5.26}$$

with p-value

$$p_0 = 1 - F(q_0|0), \tag{5.27}$$

from which one can obtain a simple formula for the significance for excluding $\mathbb{H}_0$, $Z_0 = \sqrt{q_0}$. The cumulative and p-value functions for the test statistic for exclusion limits, q_μ, has the same form as Eqs. (5.26) and (5.27) when using the large sample approximation, leading to the significance $Z_\mu = \sqrt{q_\mu}$. Excluding $\mathbb{H}_\mu$ is achieved at $1-\alpha$ CL when the p-value is found below a specified threshold α. The upper limit on μ is the largest p_μ found such that $p_\mu \leq \alpha$. Hence the upper limit μ_{up} can be found numerically as the value of for which $p_\mu = \alpha$,

$$\mu_{up} = \hat{\mu} + \sigma\Phi^{-1}(1-\alpha), \tag{5.28}$$

[40] Two sided bands.

where σ is the variance of $\hat{\mu}$. The exclusion test statistic for positive signals $\tilde{q}_\mu$ has a similar approximation to that of q_μ [155].

5.4 The Asimov dataset

It is usually desirable to quote the expected sensitivity of an analysis. This can be useful when making projections for prospective experiments, such as those performed in Part IV for the HL-LHC, or when comparing the measured significance to an expected median significance. The expected sensitivity and variance of a result under a hypothesis $\mathbb{H}_\mu$ from a dataset generated with $\mathbb{H}_{\mu'}$ can be extracted using a representative dataset known as the Asimov dataset.

The Asimov dataset is an artificial dataset defined to yield the true parameter values when used to evaluate the estimators of all parameters in the model. Practically the Asimov dataset is created by the following procedure: One performs a unconditional fit to an observed dataset and extracts the MLEs[41]. The signal strength parameter μ is then set to the desired data hypothesis[42] μ'. The effect of setting all parameters to their post fit values, as well as $\mu = \mu'$, is propagated into the observable distributions. The Asimov dataset is then extracted from these distributions. A subsequent unconditional fit to the Asimov dataset should[43] then return $\hat{\mu} = \mu'$. The profile likelihood ratio with respect to an Asimov dataset is therefore [155],

$$\lambda_A(\mu) = \frac{\mathscr{L}_A(\mu, \hat{\hat{\boldsymbol{\theta}}})}{\mathscr{L}_A(\hat{\mu}, \hat{\boldsymbol{\theta}})} = \frac{\mathscr{L}_A(\mu, \hat{\hat{\boldsymbol{\theta}}})}{\mathscr{L}_A(\mu', \hat{\boldsymbol{\theta}})}, \tag{5.29}$$

where $\mathscr{L}_A(\mu) = \mathscr{L}(\boldsymbol{x}_{\mu'}|\mu)$ is the likelihood of the Asimov dataset, $\boldsymbol{x}_{\mu'}$, given hypothesis $\mathbb{H}_\mu$.

The Asimov dataset discussed above can be used for several purposes, summarised here from Ref. [155]. Firstly it can be used to estimate the median significance of a test statistic. The median significance $\text{med}[Z_0|\mu']$ of the discovery test statistic q_0 assuming a signal strength μ' is given as,

$$\text{med}[Z_0|\mu'] = \sqrt{q_{0,A}}, \tag{5.30}$$

[41] In the case where there is no observed dataset, such as in prospect studies, the Asimov dataset is extracted by performing an unconditional fit to the nominal values of all parameters, $\boldsymbol{\theta}^0$. This may result in constraints of the uncertainties $\sigma_{\boldsymbol{\theta}}$ due to the expected statistics, although the post fit values of the parameters will remain unchanged from their nominal values.

[42] In general one may wish to not only set μ to a particular value, but also some subset of $\boldsymbol{\theta}$. However the usual case is to test different values of μ.

[43] This is not necessarily the case when there is no significant sensitivity of measure μ accurately.

where $q_{0,A} = -2\log\lambda_A(0)$. For upper limits, where one excludes $\mathbb{H}_\mu$, the median exclusion significance assuming $\mu' = 0$ is,

$$\text{med}[Z_\mu|0] = \sqrt{q_{\mu,A}} \qquad \text{for } q_{\mu,A}, \text{ and} \tag{5.31}$$

$$\text{med}[Z_\mu|0] = \sqrt{\tilde{q}_{\mu,A}} \qquad \text{for } \tilde{q}_{\mu,A}, \tag{5.32}$$

with $q_{\mu,A} = -2\log\lambda_A(\mu)$ and $\tilde{q}_{\mu,A} = -2\log\tilde{\lambda}_A(\mu)$. Under statistical fluctuations the significance obtained from data is not necessarily the median significance in Eqs. (5.30) and (5.31). It is therefore also useful to quote uncertainty bands on the median significance corresponding to $\pm N\sigma$ variation on $\hat{\mu}$, where σ is the variance of $\hat{\mu}$. Uncertainty bands on the median discovery significance are given as,

$$Z_0(\mu' + N\sigma) = \text{med}[Z_0|\mu'] + N, \tag{5.33}$$

$$Z_0(\mu' - N\sigma) = \max[\text{med}[Z_0|\mu'] - N, 0]. \tag{5.34}$$

using Eqs. (5.28) and (5.31) the median for the upper limit μ_{up} at $1-\alpha$ CL can be written as,

$$\text{med}[\mu_{up}|\mu'] = \mu' + \sigma\Phi^{-1}(1-\alpha), \tag{5.35}$$

with the $\pm N\sigma$ uncertainty bands are given as,

$$\text{band}_{N\sigma} = \mu' + \sigma(\Phi^{-1}(1-\alpha) \pm N). \tag{5.36}$$

The variance σ of $\hat{\mu}$ with data from hypothesis μ' can be obtained from the Asimov dataset, either by using the second derivatives of $\mathscr{L}_A(\mu)$, or by using the approximation $\sigma = \frac{\mu^2}{q_{\mu,A}}$.

5.5 Fit results and diagnostics

As described in Section 5.2, hypothesis testing in the context of many high-energy physics searches and measurements is reliant of fits of likelihood functions. By extracting MLEs the fits are used to obtain results and their respective uncertainties. Running diagnostics of the fits is an important part of validating the results, and one is usually interested in understanding the flexibility of the likelihood model, and its success in fitting the data. In the analysis chapters of this thesis the statistical models are implemented in workspaces: files in a ROOT [131] data format which house a collection of RooStats [159] based data

structures, primarily used for working with statistical models, such as likelihood functions. A workspace can house several statistical models, including their categories, likelihoods, histogram templates, NPs, POIs, etc. Aspects regarding the determination of results and uncertainties, and performing fit diagnostics, are summarised here so that they may be referenced in later chapters.

5.5.1 Types of nuisance parameters

Sources of systematic uncertainties in likelihood functions are parameterised as NPs, as shown in Eq. (5.6). In a binned likelihood this is done by building template histograms of the discriminating distributions for $\pm 1\sigma$ of the pre-fit systematic effect. In general a systematic uncertainty is depicted as a single number θ_j which can describe the effect of the systematic uncertainty on the final discriminating distribution. In the case where one is only interested in the effect of θ_j as a normalisation uncertainty, the parameterisation is intuitive: a change in the value of θ_j translates to a difference in the total number of events of any process affected by θ_j. When also considering the shape effects of the systematic uncertainty θ_j, the effect is usually parameterised as the morphism between template histograms from $\pm 1\sigma$ of θ_j. A particular value of θ_j then corresponds to some interpolation between these two histograms, whereby both normalisation and shape effects are taken into account[44]. The template histograms from which systematic effects are derived are susceptible to statistical fluctuations, and it is not uncommon to smooth the systematic effect over several bins of the template. It is also common practice to prune systematic effects which have negligible variation [45].

Normalisation factors are NPs which are free (unconstrained) parameters, in the same way as the POI. These are multiplicative factors affecting some background or signal process with no attached prior. Their uncertainties are usually heavily constrained post-fit by statistics in the dataset. In some cases specific regions are designed to specifically target constraining normalisation NPs.

MC statistics affect the signal and background template histograms with a corresponding statistical uncertainty. These uncertainties are implemented as an additional NP in the k-th template bin, γ_k, which scales the total background in that bin.

[44] One may also choose to only consider shape effects of a systematic uncertainty, where the total number of events would be held constant.

[45] In the analyses in Sections 6 and 7, uncertainties are pruned when the maximum difference of (θ_j) from the nominal template is less than 1%.

5.5.2 Pulls, constraints and correlations

The unconditional and conditional likelihood fits will produce a set of MLEs for all parameters which are profiled in the fit. The pull $\Delta\theta_j$ of a particular NP θ_j is defined as the difference of its MLE from the its initial value θ_j^0 over its standard deviation σ_{θ_j},

$$\Delta\theta_j = \frac{\hat{\theta}_j - \theta_j^0}{\sigma_{\theta_j}}. \tag{5.37}$$

One would expect the pull $\Delta\theta_j$ to be non-zero when θ_j is responsible for correcting the model to fit the dataset in question. However, one does not expect very large pulls, generally greater 1σ, in models which are flexible enough to model the dataset adequately. Large pulls in a particular NP may require some additional investigation. Some examples of pull plots can be found throughout this thesis, e.g., in Figure 6.19

The post-fit uncertainty σ_{θ_j} is calculated from the covariance matrix, which includes correlation coefficients. A matrix of parameter correlations is usually used to understand which parameters parameterise the degrees of freedom within the model in a similar way (see Figure 6.21 for an example). In the presence of sufficient statistics, the uncertainties of parameters may become constrained. (Anti-)Correlation of parameters can further result in reduced post-fit uncertainties.

The impact of a NP of the measurement $\hat{\mu}$ can be determined in order to rank the set of NPs in terms of their effect on the result. Each NP is fixed to their $\pm 1\sigma$ pre-fit and post-fit values. A conditional fit is done where this NP is held constant and the impact is extracted as the difference in the central value of μ,

$$\text{impact}(\theta_j) = \Delta\mu^{\pm} = \hat{\hat{\mu}}_{\theta_j^0 \pm \sigma_{\theta_j}} - \hat{\mu}, \tag{5.38}$$

where $\hat{\hat{\mu}}_{\theta_j^0 \pm \sigma_{\theta_j}}$ is the MLE where all parameters except θ_j have been profiled. It is common practice in measurements of μ to summarise the impacts of dominant NPs in a *ranking* plot. Ranking plots are used in the Higgs combination to quantify the importance of NPs, as in Figure 8.3.

When quoting a final set of results of the measurement $\hat{\mu}$, the impact of NPs on the result tend to be summarised by quoting the *breakdown* of groups of similar NPs. The procedure here is different to that of the ranking plots described above. Here we fix a sub-group of NPs, $\boldsymbol{\theta}_g \subset \boldsymbol{\theta}$, to their nominal post-fit values and repeat the fit. One then takes the quadratic difference of the total error on μ from the conditional and unconditional fit as the impact

of $\boldsymbol{\theta}_g$ on the result. The total statistical uncertainty is obtained in the same way by fixing all systematic uncertainty based NPs in the fit (e.g., Table 8.5). Similarly, when quoting the effect of $\boldsymbol{\theta}_g$ on the exclusion upper limit μ_{up} the upper limit is recalculated while holding the set $\boldsymbol{\theta}_g$ fixed to their nominal values (e.g., Figure 6.30).

Part III

Analysis

Chapter 6

Search for a heavy Higgs boson decaying to a pair of tau leptons

The coupling of the 125 GeV Higgs boson to the fermionic sector has been established with the observation of $H \to \tau\tau$ at ATLAS and CMS with Run-1 data [31, 160, 161], and more recently with Run-2 data [162–164]. The $H \to \tau\tau$ analysis has also been used to constrain the CP quantum numbers of the Higgs boson, found to be consistent with the SM expectation [165]. However, it remains possible that the discovered Higgs boson is part of an extended Higgs sector. The search for a heavy resonant scalar to a pair of tau leptons (di-tau) is well motivated. As described in Section 2, large portions of the 2HDM and MSSM parameter space have a Higgs sector with increased couplings to down-type fermions. The extended Higgs sector has three neutral (h, H, A), and two charged ($H^{\pm}$) Higgs bosons (see Section 2). Several searches for heavy neutral Higgs bosons decaying to a pair of tau leptons ($H/A \to \tau\tau$) have been performed by ATLAS and CMS with Run-1 data [93, 166] with no deviations to the SM prediction found. In Run-2, the CMS experiment searched for heavy ($m_{\mathrm{A}} > 90$GeV) and low-mass (25 GeV $< m_{\mathrm{A}} <$ 70 GeV) $H/A \to \tau\tau$ at $\sqrt{\mathrm{s}} = 13$ TeV pp collisions with an integrated luminosity of 35.9 fb^{-1}[81, 167]. In both cases no evidence of a scalar resonance was observed.

This chapter details the latest search for a neutral Higgs boson to a pair of tau leptons, as detailed in Ref. [1], using 36.1 fb^{-1} of pp collision data at a centre-of-mass energy of 13 TeV using the ATLAS detector. The search is performed for a Higgs with a mass within the range of 0.2–2.25 TeV. The dominant production modes for the neutral Higgs ($h/H/A$) in the 2HDM and MSSM is gluon-fusion (ggF) and b-associated production. The b-associated production will be referred to in the following as $b\bar{b}\phi$, but should be considered to be inclusive

of single-bottom production, i.e., $b\phi$. The production processes are detailed in Sections 2.4.1 and 2.4.2. The leading-order Feynman diagrams are shown in Figure 2.4 (page 39) for ggF and Figures 2.5 and 2.6 (page 40) for $b\bar{b}\phi$. While the 2HDM production modes are not dependant on SUSY particles, squark loop contributions are relevant in the MSSM.

The final-state tau leptons can decay either hadronically or leptonically[46]: their branching fractions are shown in Table 4.2 (page 83). In the analysis, the di-tau final-state is considered to decay fully hadronically ($\tau_{\text{had}}\tau_{\text{had}}$), or semi-leptonically ($\tau_{\text{lep}}\tau_{\text{had}}$). The fully leptonic ($\tau_{\text{lep}}\tau_{\text{lep}}$) decay mode is not considered. Events are also categorised as those with zero (b-veto) or at least one (b-tagged) b-jet, in order to increase the sensitivity to $b\bar{b}\phi$ production. The search for the di-tau final-state is used to place cross-section limits on a ggF and $b\bar{b}\phi$ produced heavy resonance decaying to di-tau, which are interpreted in the context of the MSSM.

In this chapter the event samples used in the analysis, including recorded data or simulated events, are detailed in Section 6.1. The object and event selection of the analysis are detailed in Section 6.2. The background estimation techniques are presented in Section 6.3 and the uncertainties related to the analysis are presented in Section 6.4. The results are presented in Section 6.5. Subsidiary material can be found in Appendix B.

6.1 Event samples

Data with events within luminosity blocks that are recorded while all detector subsystems are operating in good conditions is considered. The luminosity blocks considered are filtered using a recommended good run list (GRL) which includes the 2015 and 2016 data-taking periods with a total integrated luminosity of 36.1 fb^{-1} [168]. Jet cleaning is applied on an event-by-event basis [144] in order to exclude events which are suspected of having reconstructed jets which do not originate from the interaction point, i.e., attributed to hardware problems, cosmic showers, or beam induced backgrounds. Any event which is flagged with the `loose-bad` jet cleaning working point is excluded. The primary vertex of each event is chosen as the vertex candidate with the highest sum of the squared transverse momenta of all associated tracks. Only events which contain at least one primary vertex with at least two associated tracks are included.

[46] Already introduced in Section 4.3.6 is the notation τ_{lep}, which represents a τ-lepton decay to an electron or a muon and neutrinos, and τ_{had}, which represents the decay to one or more hadrons and a neutrino.

Several sources of background are present in the final selection of the analysis. Both the $\tau_{\text{lep}}\tau_{\text{had}}$ and $\tau_{\text{had}}\tau_{\text{had}}$ channels have sizeable contributions from multijet events which pass the event selection. The multijet contribution in both channels is estimated from data-driven techniques. Additionally, several sources of background are attributed to non-multijet events. This includes backgrounds in which a quark- or gluon-initiated jet is misidentified as a reconstructed hadronic tau, $\tau_{\text{had-vis}}$ (see Section 4.3.6), predominantly from W+jets and $t\bar{t}$. They are modelled via a data-driven technique in the $\tau_{\text{lep}}\tau_{\text{had}}$ channel, and simulation with data-driven corrections in the $\tau_{\text{had}}\tau_{\text{had}}$ channel. The remaining background contributions, which have real $\tau_{\text{had-vis}}$ objects in their final-state, arise from Z/γ^*+jets, W+jets, $t\bar{t}$, single top-quark and di-boson (WW, WZ and ZZ). These sources are estimated from simulation events normalised to their theoretical cross-sections as summarised in the following.

Z/γ^*+jets events are generated using the POWHEG-BOX v2 [169–172] event generator and the CT10 PDF set [173]. Final-state partons are interfaced with PYTHIA 8 [174, 175] to model the parton shower (PS), using the AZNLO [176] set of tune parameters and the CTEQ6L1 [177] PDF set. The photon emission from charged particles are modelled with PHOTOS++ 3.52 [178]. The samples are re-scaled to their estimated cross-sections: calculated at NNLO in QCD with VRAP 0.9 [179] and the CT14NNLO [180] PDF set, with NLO EW corrections calculated with MCSANC 1.20 [181] and MRST2004QED PDF set [182].

W+jets events in the $\tau_{\text{had}}\tau_{\text{had}}$ channel are modelled using up to NLO matrix-elements using COMIX [183] and OPENLOOPS [184], and are generated with the SHERPA 2.2.0 [185, 186] event generator. The PS is modelled with SHERPA using the ME+PS@NLO recommendation [187]. In the $\tau_{\text{lep}}\tau_{\text{had}}$ channel, the W+jets is generated using the same prescription as the Z/γ^*+jets: using the POWHEG-BOX v2 generator with PYTHIA 8 PS. The W+jets cross-section is determined at NNLO precision with FEWZ [179, 188, 189].

Background with top-quarks originate from single top-quark or pair produced $t\bar{t}$ processes. Single top-quark production can occur via s-channel or t-channel processes, or in association with a $W^{\pm}$ (Wt-channel)[47]. Events from $t\bar{t}$, and single top-quark s-channel and Wt-channel, are modelled using the POWHEG-BOX v2 event generator with the CT10 PDF set. Single top-quark t-channel events are modelled with the POWHEG-BOX v1 event generator with the CT10F4 PDF set. The PS for all top backgrounds is modelled with PYTHIA 6.428 using the Perugia set of tune parameters [191] and the CTEQ6L1 PDF. The $t\bar{t}$ normalisation is calculated at NNLO with next-to-next-leading-logarithm (NNLL) precision using the TOP++2.0 [192] program. The total single top-quark cross-section used are calculated at

[47] Feynman diagrams for these processes can be found in Ref. [190].

NLO for the t- and s-channel from Ref. [193, 194], and at NLO+NNLL for the Wt-channel from Ref. [195].

Di-boson background is generated at up to NLO using SHERPA 2.1.1 using the CT10 PDF set and interfaced with with the SHERPA for PS modelling by following the ME+PS@NLO recommendation. The event yield from the resulting samples is used, corrected with regards to the recommended α_{QED} value [21].

Gluon-fusion (ggF) produced Higgs boson events are generated at NLO using POWHEG-BOX v2 with the CT10 PDF set. Events are interfaced with PYTHIA 8.210 [196] for the PS modelling using the AZNLO set of tune parameters and the with the CTEQ6L1 PDF set. The simulation of $b\bar{b}\phi$ events is done at NLO in the four-flavour scheme (4FS) using MADGRAPH5_aMC@NLO 2.1.2 [197, 198] with the CT10NLO_NF4 PDF set [180]. Events are interfaced with PYTHIA 8.210 for the PS modelling using the A14 [199] set of tune parameters and the with the NNPDF2.3LO PDF set [200]. Signal samples are generated for 15 different Higgs mass points, from 200 GeV to 2.25 TeV: [200 GeV, 250 GeV, 300 GeV, 350 GeV, 400 GeV, 500 GeV, 600 GeV, 700 GeV, 800 GeV, 1000 GeV, 1200 GeV, 1500 GeV, 1750 GeV, 2000 GeV, 2250 GeV].

All simulated events are overlaid with simulated minimum-bias event in order to model the effect of pileup. The minimum-bias events are generated with PYTHIA 8, using the A2 set of tune parameters [201] and the MSTW2008LO PDF set [202]. All generated samples, with the exception of the $b\bar{b}\phi$ signal samples, undergo full simulation through the ATLAS detector using GEANT 4 [132, 203]. The $b\bar{b}\phi$ signal samples are simulated using the ATLFASTII [133] fast simulation. All simulated events undergo the object reconstruction outlined in Section 4.3.

6.2 Analysis strategy

6.2.1 Baseline selection

Particles are reconstructed following the descriptions given in Section 4.3, with particular details related to identification, isolation, selection, and $E_{\text{T}}^{\text{miss}}$ reconstruction procedures provided in this section. The object preselection is mostly common to both the $\tau_{\text{lep}}\tau_{\text{had}}$ and $\tau_{\text{had}}\tau_{\text{had}}$ channels, with a few differences in the combinatorials of the selected objects. Refined channel dependent selection criteria are discussed in their specific sections. To get the correct efficiency of the object selection in MC, the recommended scale factors from

subsidiary measurements for object reconstruction, identification, isolation and triggering are applied.

The analysis makes use of reconstructed leptons. As is common practice within ATLAS, the term *leptons* here is used to refer to reconstructed electrons and muons, and excludes reconstructed taus[48]. Reconstructed electron candidates are selected with $E_{\mathrm{T}} > 15$ GeV and pseudorapidity $|\eta| < 2.47$, to ensure quality reconstruction. Electrons that are reconstructed in the transition region between the barrel and end-cap calorimeters ($1.37 < |\eta| < 1.52$) are not included; they result in large uncertainties related to the rate that electrons are misclassified as (or *fake*) taus. Electrons which fake tau candidates are referred to as $e \to \tau_{\text{had-vis}}$ fakes. All reconstructed electrons must satisfy the `loose` likelihood-based identification working point. Muon candidates are required to have a $p_{\mathrm{T}} > 7$ GeV and to be within the detector acceptance ($|\eta| < 2.5$). Only muons which pass the `loose` identification requirement are considered. All reconstructed leptons which pass the baseline selection up to this point are considered as objects used in the overlap removal procedure discussed below. In the $\tau_{\text{lep}}\tau_{\text{had}}$ channel the selected reconstructed lepton candidate is additionally required to pass a `medium` likelihood-based identification working point[49] as well as the `gradient` isolation requirement.

Jet candidates are reconstructed using the anti-k_t algorithm and calibrated at the EM scale with JES corrections described in Section 4.3.4. Only jets with $p_{\mathrm{T}} > 20$ GeV and $|\eta| < 2.5$ are considered. A requirement on the JVT discriminant is applied for jets with $p_{\mathrm{T}} < 60$ GeV and $|\eta| < 2.4$ to provide suppression of background pileup jets. All jets passing the aforementioned criteria are considered as potential b-jet candidates. Jets stemming from b-quarks are identified by the b-tagging algorithm `MV2c10` [146]. A jet with a `MV2c10` regression discriminant score ($w_{\texttt{MV2c10}}$) greater than 0.824 is classified as a b-jet. This working point provides an average b-jet efficiency of 70% in $t\bar{t}$ events and rejects c-jets, τ_{had} fakes, and light quark jets at approximately 13:56:380 parts per every b-jet accepted, respectively [146].

Reconstructed $\tau_{\text{had-vis}}$ candidates are required to have a $p_{\mathrm{T}} > 25$ GeV and $|\eta| < 2.5$, with taus falling in the transition region between the barrel and end-cap calorimeters being vetoed. The tau candidates must have either one or three associated tracks and an associated electric charge of ± 1. In the $\tau_{\text{had}}\tau_{\text{had}}$ channel the transverse mass requirement for $\tau_{\text{had-vis}}$ candidates is increased to $p_{\mathrm{T}} > 45$ GeV, in order to be closer to the p_{T} requirements from the lowest

[48] This is due to the tau leptons not being observed directly within the detector material, i.e., decaying prior to reaching the detector.

[49] In the case that the selected lepton is a muon, this imposes the requirement that it must be a combined or extrapolated muon (see Section 4.3.3).

p_{T} unprescaled tau trigger used in this channel. Taus which fail the electron veto criteria are rejected. The $\tau_{\text{had-vis}}$ candidate in the $\tau_{\text{lep}}\tau_{\text{had}}$ channel is selected as the one with highest p_{T}, sometimes referred to in the following as τ_1. The two $\tau_{\text{had-vis}}$ candidates in the $\tau_{\text{had}}\tau_{\text{had}}$ channel are the two candidates with highest (*leading*) and second highest (*sub-leading*) p_{T}, referred to here as τ_1 and τ_2, respectively. All remaining tau candidates are considered to be jets. The $\tau_{\text{had-vis}}$ candidates selected at this point are used in the overlap removal procedure outlined below. The τ_1 is required to pass the `medium` tau identification criterion, and the τ_2 in the $\tau_{\text{had}}\tau_{\text{had}}$ channel must pass the `loose` tau identification.

Any ambiguity in the object selection above is resolved by a dedicated overlap removal procedure. Objects with a geometric overlap are removed in the following order: jets within a $\Delta R = 2.0$ cone of the selected $\tau_{\text{had-vis}}$ candidates are removed; jets within a $\Delta R = 4.0$ cone of an electron or muon are removed; any $\tau_{\text{had-vis}}$ within a $\Delta R = 2.0$ cone of an electron or muon is removed; electrons within a $\Delta R = 2.0$ cone of a muon are excluded. The size of the $\Delta R = 4.0$ cone for the jet-lepton overlap requirement was selected based on the ΔR distribution at the baseline selection.

All selected objects are used in the $E_{\mathrm{T}}^{\text{miss}}$ calculation which includes the track soft term, as discussed in Section 4.3.7. A special case is that of the anti-isolation region in the $\tau_{\text{lep}}\tau_{\text{had}}$ channel, in which the lepton isolation requirements are inverted. In this case the nominal $E_{\mathrm{T}}^{\text{miss}}$ calculation would calibrate the anti-isolated lepton as a jet. The $E_{\mathrm{T}}^{\text{miss}}$ calculation in this region is therefore re-run to consider the anti-isolated leptons with the lepton energy scale instead, so as to not bias the $E_{\mathrm{T}}^{\text{miss}}$ calculation in this region.

6.2.2 Ditau mass reconstruction

An important discriminant in the search for a heavy resonance is related to the invariant mass of the object. In ATLAS pp collisions, an unknown portion of the energy of the incoming hadrons will be lost in down the beam line, i.e., the z-component. However, by design, the vector sum of transverse components of energy are expected to cancel under energy and momentum conservation laws. In the case of a heavy resonance ϕ with mass m_ϕ decaying to a pair of particles, a transverse mass variable m_{T} can be defined which is invariant under Lorentz boost, i.e., m_{T} is identical in both the lab- and ϕ-frame. If ϕ decays into daughter particles d_1 and d_2 with invariant mass m_{d_1} and m_{d_2} and transverse energy and momentum

$(E_{\mathrm{T}}^{d_1}, \boldsymbol{p}_{\mathrm{T}}^{d_2})$ and $(E_{\mathrm{T}}^{d_2}, \boldsymbol{p}_{\mathrm{T}}^{d_1})$, the transverse mass is defined as [21],

$$\begin{aligned} m_{\mathrm{T}} &= \sqrt{(E_{\mathrm{T}}^{d_1} + E_{\mathrm{T}}^{d_2})^2 - (\boldsymbol{p}_{\mathrm{T}}^{d_1} + \boldsymbol{p}_{\mathrm{T}}^{d_2})^2} \\ &= \sqrt{m_{d_1}^2 + m_{d_1}^2 + 2(E_{\mathrm{T}}^{d_1} E_{\mathrm{T}}^{d_2} - \boldsymbol{p}_{\mathrm{T}}^{d_1} \cdot \boldsymbol{p}_{\mathrm{T}}^{d_2})}. \end{aligned} \tag{6.1}$$

In the relativistic limit $E^2 \approx \boldsymbol{p} \cdot \boldsymbol{p}$ and $m_{d_1} \sim m_{d_2} \sim 0$ such that m_{T} can be written as,

$$m_{\mathrm{T}} = \sqrt{2 p_{\mathrm{T}}^{d_1} p_{\mathrm{T}}^{d_2} (1 - \cos\Delta\phi(d_1, d_2))}, \tag{6.2}$$

where $p_{\mathrm{T}}^{d_1}$ and $p_{\mathrm{T}}^{d_2}$ are scalar magnitudes of the transverse momentum, and $\Delta\phi(d_1, d_2)$ is the angular separation of the daughters in the transverse plane. Eq. (6.2) is the m_{T} definition used throughout this analysis, often denoted as $m_{\mathrm{T}}(d_1, d_2)$ which denotes the corresponding objects being used. Eq. (6.2) has the property that two objects which have large angular separations in the transverse plane will yield lower values of m_{T}.

The final discriminating variable in the $\phi \to \tau\tau$ search presented here is the total transverse mass $m_{\mathrm{T}}^{\mathrm{tot}}$, defined as,

$$m_{\mathrm{T}}^{\mathrm{tot}} = \sqrt{m_T^2(E_{\mathrm{T}}^{\mathrm{miss}}, \tau_{\mathrm{vis}}^1) + m_{\mathrm{T}}^2(E_{\mathrm{T}}^{\mathrm{miss}}, \tau_{\mathrm{vis}}^2)) + m_{\mathrm{T}}^2(\tau_{\mathrm{vis}}^1, \tau_{\mathrm{vis}}^2)}, \tag{6.3}$$

where τ_{vis}^1 and τ_{vis}^2 are the visible tau decay products (in the case of $\tau_{\mathrm{lep}}\tau_{\mathrm{had}}$ channel, one of these terms will relate to the lepton candidate) and $E_{\mathrm{T}}^{\mathrm{miss}}$ is the missing transverse energy of an event. Alternate mass reconstruction techniques exists and were also investigated. An additional variable that can be used is the total visible mass m_{vis}, which is the vector sum of $\boldsymbol{p}^{\tau_{\mathrm{vis}}^1}$ and $\boldsymbol{p}^{\tau_{\mathrm{vis}}^2}$. The m_{vis} variable does not take into account important information provided by $E_{\mathrm{T}}^{\mathrm{miss}}$ which is related to the energy carried by neutrinos in tau decays, and does not provide optimal separation against background. It is however still a useful variable for providing information on the event topology, and used in the $\tau_{\mathrm{lep}}\tau_{\mathrm{had}}$ channel to suppress $Z \to \ell\ell$ background events.

Additionally, dedicated mass reconstruction algorithms, which attempt to recover the invisible components of the tau decay, were investigated. The Missing Mass Calculator (MMC) [204] is an algorithm, tuned on SM ($m_H = 125$ GeV) $H \to \tau\tau$ simulation, that parameterises the resonant mass (m_{MMC}) based on the visible tau decay products and the $E_{\mathrm{T}}^{\mathrm{miss}}$ of the event. The Matrix-element Oriented Sampling Calculator (MOSAIC) [205] is another such algorithm, which uses a matrix-element based technique to achieve similar results as the MMC. Both algorithms were explored but subsequently abandoned in favour

of $m_{\mathrm{T}}^{\mathrm{tot}}$. For one, while $m_{\mathrm{T}}^{\mathrm{tot}}$ is computationally trivial to calculate, the MMC and MOSAIC algorithms are CPU intensive. When considering that the reconstructed mass would have to be recalculated, per event and for every systematic variation in the analysis, they caused substantial delays in the analysis turn-around time. In addition to this, the algorithms do not have full coverage of event topologies, and fail to produce results in a few cases (although this is only at a level of $\sim 1-3\%$). More importantly, m_{MMC} and $m_{\texttt{MOSAIC}}$ did not offer any improvement to the analysis sensitivity. The reason being that $m_{\mathrm{T}}^{\mathrm{tot}}$ has the property that it tends to reconstruct the mass of events with jets misclassified as taus (referred to as jet $\rightarrow \tau_{\text{had-vis}}$ fakes) at a lower values, yielding a larger signal separation to this type of background than what m_{MMC} and $m_{\texttt{MOSAIC}}$ provide.

6.2.3 Event selection

6.2.3.1 Event selection in the $\tau_{\text{lep}}\tau_{\text{had}}$ channel

Events in the $\tau_{\text{lep}}\tau_{\text{had}}$ channel are selected by single lepton triggers. The triggers considered are the lowest p_{T} unprescaled triggers with varying isolation and identification requirements, and are different for the 2015 and 2016 data-taking periods. The single lepton triggers used in the 2015 and 2016 data-taking periods are shown in Table 6.1 [112, 206]. An event is required to pass any trigger in the set of its respective period. In order to mimic the different trigger conditions for 2015 and 2016 in MC, each simulated event is assigned a random run number for which the running trigger menu is considered, and the event is applied a scale factor to mimic the running time of the trigger.

Events must have at least one identified $\tau_{\text{had-vis}}$ candidate and one electron or one muon candidate. Events with more than one lepton passing the baseline criterion are rejected (*dilepton veto*) in order to reduce $Z/\gamma^* \rightarrow \ell\ell$ background events. The electron or the muon in the event are required to match geometrically with the HLT object that triggered the event. In order to ensure that the triggered objects are on their trigger efficiency plateau, offline objects are required to have slightly higher p_{T} than their geometrically matched trigger object. For the different muon p_{T} triggers considered, the offline matched object is required to have $p_{\mathrm{T}} > 55$ GeV, if the muon is matched to `mu50`, or $p_{\mathrm{T}} > 30$ GeV, if the muon is matched to `mu20_iloose_L1MU15` or `HLT_mu26_ivarmedium` (see Figure 4.3 (b) on page 77). For each set of electron triggers, the high p_{T} triggers are intended to recover efficiency of the lowest p_{T} electron trigger. It is therefore sufficient to require that the matched electron has $p_{\mathrm{T}} > 30$ GeV in order to be on the efficiency plateau (see Figure 4.2 (b) on page 75).

The final selection in the $\tau_{\text{lep}}\tau_{\text{had}}$ signal region (SR) proceeds as follows: For the $\tau_{\text{had-vis}}$candidate selected in the baseline selection, a $|\eta| < 2.3$ selection is applied in order to reduce $e \to \tau_{\text{had-vis}}$ fakes background. The lepton (ℓ) and τ_{had} candidates are required to have opposite sign charge, and must have an angular separation in the transverse plane, $\Delta\phi(\ell, \tau_{\text{had-vis}}) > 2.4$. The $\Delta\phi(\ell, \tau_{\text{had-vis}})$ requirement ensures that the decay products are back-to-back, as would be expected from the heavy resonant signal. Since in the $\tau_{\text{lep}}\tau_{\text{had}}$ channel the lepton is associated with an additional neutrino decay, e.g., $\tau^- \to \nu_\tau \ell^- \bar{\nu}_\ell$, the $\mathbf{E}_{\text{T}}^{\text{miss}}$ is expected to be aligned with the lepton. The SR therefore imposes a requirement on the transverse mass $m_{\text{T}}(\boldsymbol{p}_{\text{T}}^{\ell}, \mathbf{E}_{\text{T}}^{\text{miss}})$ (Eq. (6.2)) to be less than 40 GeV. This requirement results in the lepton and $\mathbf{E}_{\text{T}}^{\text{miss}}$ directions being approximately aligned in the transverse plane, and reduces backgrounds stemming from W+jets and $t\bar{t}$ processes. In order to reduce $e \to \tau_{\text{had-vis}}$ fakes stemming from $Z \to ee$ events, a veto on events where m_{vis} is between 80 and 110 GeV is applied in the $\tau_{\text{e}}\tau_{\text{had}}$ channel. A summary of the $\tau_{\text{lep}}\tau_{\text{had}}$ signal region selection is shown in Table 6.3 on page 118.

Table 6.1 Trigger list for the $\tau_{\text{lep}}\tau_{\text{had}}$ analysis corresponding to the lowest unprescaled triggers in 2015 and 2016 data [112, 206].

Period	Single electron triggers	Single muon triggers
2015	`e24_lhmedium_L1EM20VH` **OR** `e60_lhmedium` **OR** `e120_lhloose`	`mu20_iloose_L1MU15` **OR** `mu50`
2016	`e26_lhtight_nod0_ivarloose` **OR** `e60_lhmedium_nod0` **OR** `e140_lhloose_nod0`	`mu26_ivarmedium` **OR** `mu50`

6.2.3.2 Event selection in the $\tau_{\text{had}}\tau_{\text{had}}$ channel

The preselection in the $\tau_{\text{had}}\tau_{\text{had}}$ channel is defined in such a way that is orthogonal to the $\tau_{\text{lep}}\tau_{\text{had}}$ channel by rejecting events which contain an electron or a muon passing the `loose` identification. Events are triggered by the lowest p_{T} unprescaled single tau triggers used during the 2015 and 2016 data-taking periods [112, 206]. They are shown in Table 6.2. In data, events are required to pass the lowest unprescaled trigger used at the time. In MC events, events are weighted with respect to the integrated running time of each lowest unprescaled trigger during the data taking periods considered. The τ_1 candidate is required to be geometrically matched (within $\Delta R < 0.2$) to the object that fired the trigger. Additionally, its transverse momentum, $p_{\text{T}}^{\tau_1}$, is required to be at least 5 GeV above the online p_{T} requirement of the matched trigger. The offline $p_{\text{T}}^{\tau_1}$ requirement of the respective single tau trigger, as well

as their approximate contribution to the total luminosity recorded in the analysis, are shown in Table 6.2. The $p_{\mathrm{T}}^{\tau_2}$ is required to be greater than 65 GeV. Leading and sub-leading $\tau_{\text{had-vis}}$ candidates must have a back-to-back topology in the transverse plane, $\Delta\phi(\tau_1,\tau_2) > 2.7$, and have opposite charge.

Table 6.2 Trigger list for the $\tau_{\text{had}}\tau_{\text{had}}$ analysis corresponding to the lowest unprescaled triggers in 2015 and 2016 data [112, 206]. The approximate relative contribution to the total luminosity, in which the trigger was used as the lowest unprescaled trigger, is also shown.

Single tau triggers	Offline $p_{\mathrm{T}}^{\tau_1}$ [GeV]	Fraction of total luminosity [%]
HLT_tau80_medium1_tracktwo_L1TAU60	> 85	15
HLT_tau125_medium1_tracktwo	> 130	25
HLT_tau160_medium1_tracktwo	> 165	60

6.2.3.3 Final categorisation

The final categorisation in the $\tau_{\text{lep}}\tau_{\text{had}}$ and $\tau_{\text{had}}\tau_{\text{had}}$ channels is the split of events with at least one (b-tagged category) or zero (b-veto category) b-tagged jets. This split is to increase the sensitivity to MSSM neutral Higgs boson which can either be produced via ggF or b-associated production.

6.2.3.3.1 Distributions for the final selection The $\tau_{\text{lep}}\tau_{\text{had}}$ SR $m_{\mathrm{T}}^{\text{tot}}$ distributions are shown in Figure 6.1 for the b-veto and b-tagged categories before being fit to data (pre-fit). In the $\tau_{\text{lep}}\tau_{\text{had}}$ channel, important sources of backgrounds are W+jets in the b-veto and $t\bar{t}$ in the b-tagged categories. The contribution from jet $\rightarrow \tau_{\text{had-vis}}$ fakes (referred to as *fakes* in the plots) is determined from the data-driven estimates described in Section 6.3.1. Also shown are backgrounds which are modelled with MC, including[50] $Z \rightarrow \ell\ell$, $Z \rightarrow \tau\tau$, di-boson and $t\bar{t}$, and the heavy Higgs signal. The total systematic uncertainties related to MC, detector, and data-driven estimates are shown. There is some over-estimation of the data compared to MC. The MC distributions are however shown pre-fit, and the background yield is expected to be corrected after the distributions have been fit to data (post-fit).

An important contribution in the b-tagged region is the contribution of real ℓ and $\tau_{\text{had-vis}}$ backgrounds from $t\bar{t}$ events. The $t\bar{t}$ background has large theoretical uncertainties which are implemented as differences in the choice of generator, scale and showering used (see

[50]The contribution of W+jets background with true $\tau_{\text{had-vis}}$ is negligible.

Section 6.4.3 for details). In light of the large uncertainties, an additional top control region is introduced (CR-T), which is included in the final statistical fits in order to constrain the $t\bar{t}$ uncertainties. The CR-T is defined in the same way as the $\tau_{\text{lep}}\tau_{\text{had}}$ b-tagged SR, with a high m_{T} selection in order to increase the $t\bar{t}$ contamination: $m_{\text{T}}(\boldsymbol{p}_{\text{T}}^{\ell}, \mathbf{E}_{\text{T}}^{\text{miss}}) > 110(100)$ GeV in $\tau_{\text{e}}\tau_{\text{had}}(\tau_{\mu}\tau_{\text{had}})$ categories. Figure 6.2 shows the $m_{\text{T}}^{\text{tot}}$ distributions in CR-T for the $\tau_{\text{e}}\tau_{\text{had}}$ and $\tau_{\mu}\tau_{\text{had}}$ categories.

Figure 6.3 shows the $m_{\text{T}}^{\text{tot}}$ distribution of the b-tagged and b-veto regions in the $\tau_{\text{had}}\tau_{\text{had}}$ channel. In both cases the dominant background is attributed to events with two jet$\rightarrow \tau_{\text{had-vis}}$ fakes, from the multijet background. In the b-veto category there are contributions from W+jets ($W(\rightarrow \tau\nu)$+jets, in which one $\tau_{\text{had-vis}}$ is real, while the other is a jet $\rightarrow \tau_{\text{had-vis}}$ fake) and $Z \rightarrow \tau\tau$, with some small contributions from $t\bar{t}$ events. In the b-tagged category there is a considerable $t\bar{t}$ component. The normalisation mis-modelling in this region can therefore be corrected post-fit, after the $t\bar{t}$ uncertainties have been constrained. There is also a sample category ("Other") which is inclusive of the remaining backgrounds, which includes $W(\rightarrow \ell\nu)$+jets, $Z(\rightarrow \ell\ell)$+jets and di-boson.

6.2.3.3.2 Signal acceptance and efficiency The detector acceptance (A) and acceptance times efficiency ($A \times \varepsilon$) for a scalar boson of varying mass, produced via ggF or $b\bar{b}\phi$, are shown in Figure 6.4. Also shown are the fraction of ggF and $b\bar{b}\phi$ events which have a b-tagged jet. The detector acceptance is determined by a MC truth level (page 71) analysis of the resulting events reconstructed in simulation. The signal efficiency is determined from the final number of simulated signal events in the SR after applying the object and event selection. The $\tau_{\text{lep}}\tau_{\text{had}}$ channel is found to have a larger acceptance at low m_{ϕ}, while at higher mass the $\tau_{\text{had}}\tau_{\text{had}}$ channel is dominant, as it has a higher branching fraction. The signal efficiency increases as a function of m_{ϕ} as the signal moves away from the selection thresholds. There is minimal contamination of ggF in the b-tagged category, while around 50% to 75% of $b\bar{b}\phi$ events end up in the b-veto category. There is a slight decrease in efficiency at very large m_{ϕ} as the di-tau objects are merged into a single jet object: the current selection requires two isolated tau objects. Uncertainties on the signal acceptance are discussed in Section 6.4.3.

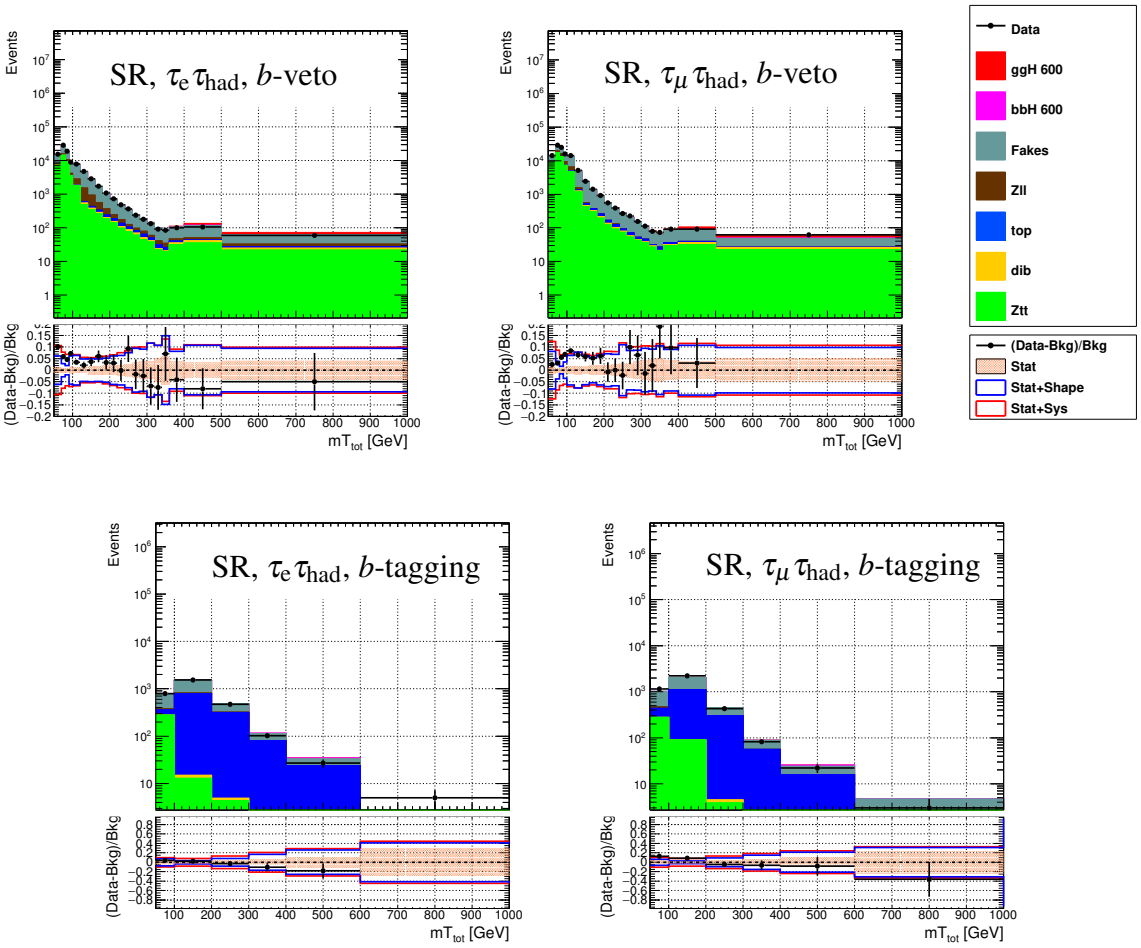

Figure 6.1 Distributions of m_T^{tot} variable in the b-veto (a) $\tau_e\tau_{had}$ and (b) $\tau_\mu\tau_{had}$ and b-tagged (c) $\tau_e\tau_{had}$ and (d) $\tau_\mu\tau_{had}$ SRs [207]. Shown are the data, the different background components, the heavy Higgs signal normalized to 1 pb, and the respective uncertainties. The *fakes* background component refers to the data-driven background estimate. Backgrounds which are modelled with MC are shown: $Z \to \ell\ell$, $Z \to \tau\tau$, di-boson and $t\bar{t}$.

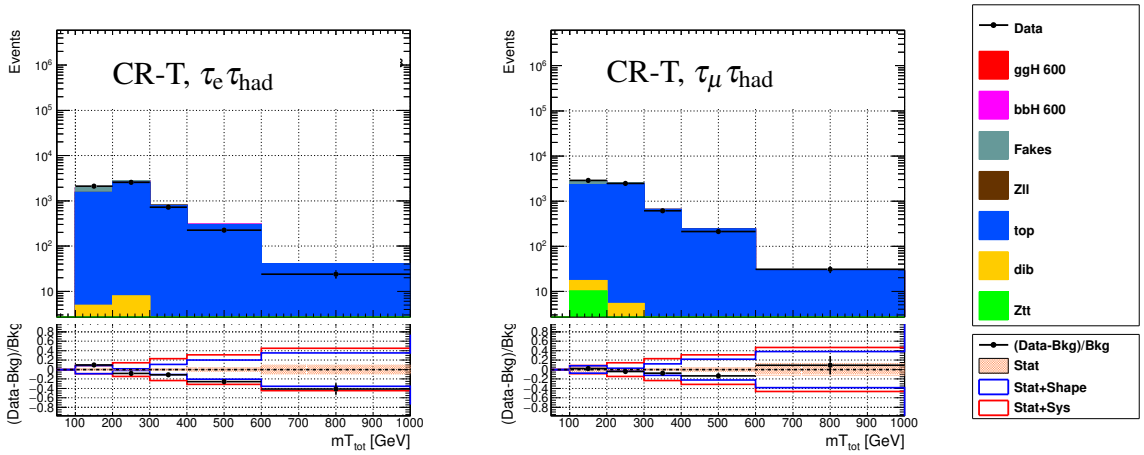

Figure 6.2 Distributions of the $m_{\mathrm{T}}^{\mathrm{tot}}$ variable in the $\tau_e\tau_{had}$ and $\tau_\mu\tau_{had}$ CR-T [207]. Shown are the data, the different background components, the heavy Higgs signal normalized to 1 pb, and the respective uncertainties. The *fakes* background component refers to the data-driven background estimate. Backgrounds which are modelled with MC are shown: $Z \to \ell\ell$, $Z \to \tau\tau$, di-boson and $t\bar{t}$.

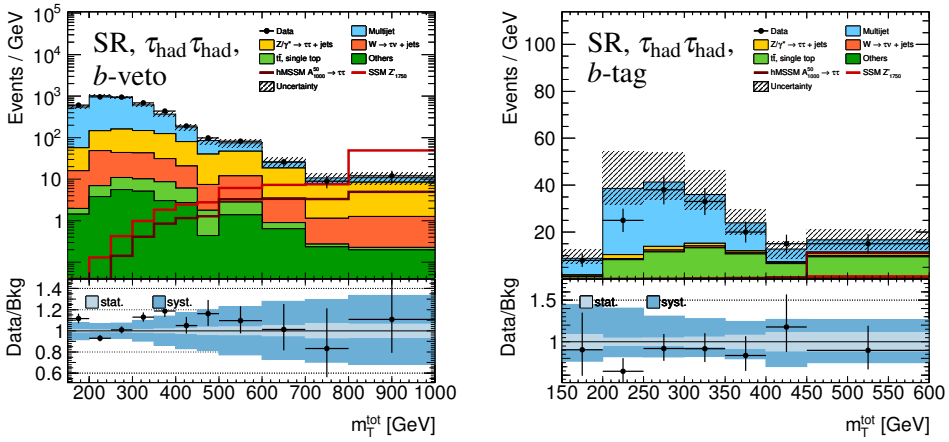

Figure 6.3 Distributions of the $m_{\mathrm{T}}^{\mathrm{tot}}$ variable in the $\tau_{had}\tau_{had}$ (a) b-veto and (b) b-tagged SR [208]. Shown are the data, the different background components, the heavy Higgs signal normalised to 1 pb, and the respective uncertainties. The multijet background component refers to the data-driven background estimate. Backgrounds which are modelled with MC are shown: $Z \to \tau\tau$, W+jets, $t\bar{t}$ and others ($W(\to \ell\nu)$+jets, $Z(\to \ell\ell)$+jets and di-boson). The multijet background is estimated from the data-driven fake-factor method. The full statistical and systematic uncertainties are shown.

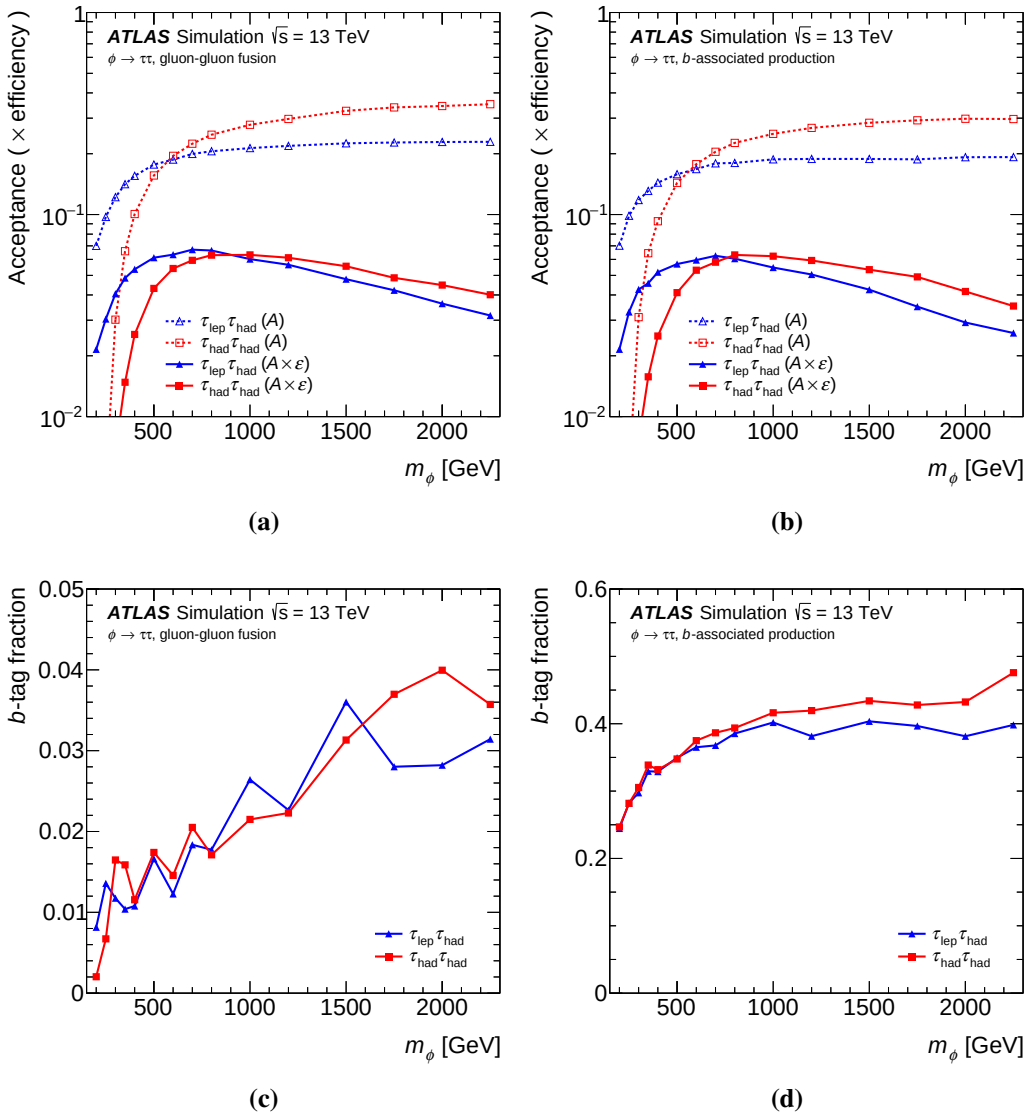

Figure 6.4 Acceptance (A) and acceptance times efficiency ($A \times \varepsilon$) for a scalar boson produced via (a) gluon–gluon fusion and (b) b-associated production and the fraction of events entering the b-tagging category for (c) gluon–gluon fusion and (d) b-associated production [1]. The acceptance is calculated with respect to the full di-tau branching fraction.

6.3 Background estimation

The background contributions in the $\tau_{\text{lep}}\tau_{\text{had}}$ and $\tau_{\text{had}}\tau_{\text{had}}$ SRs can be thought of as falling into one of two categories. The first category is the background contribution from sources with real prompt taus (and leptons for the $\tau_{\text{lep}}\tau_{\text{had}}$ channel) that are successfully reconstructed and pass the aforementioned selection criteria. In the $\tau_{\text{lep}}\tau_{\text{had}}$ and $\tau_{\text{had}}\tau_{\text{had}}$ analyses, these backgrounds are estimated from MC simulation, with scale factors and data-driven corrections applied in order to correct mis-modelling. The second category is attributed to objects that fake the reconstructed taus or leptons. Here the modelling of rates at which simulated objects are misidentified as taus and leptons have varying degrees of performance, and the analyses turn to data-driven estimations for these backgrounds. The composition of real and fake backgrounds are different in the $\tau_{\text{lep}}\tau_{\text{had}}$ and $\tau_{\text{had}}\tau_{\text{had}}$ SRs, and the estimation of these backgrounds are therefore performed independently in each channel. The estimation of real and fake backgrounds are detailed in Sections 6.3.1 and 6.3.2 for the $\tau_{\text{lep}}\tau_{\text{had}}$ and $\tau_{\text{had}}\tau_{\text{had}}$ channels, respectively.

Common amongst the background estimation techniques is the definition of control regions (CRs), which are designed to select events with a high purity of the background being studied. From the CRs the background composition is studied, and *fake-factors* or *fake-rates* (which will be defined later) are measured and used to estimate the background contribution in the SR.

6.3.1 $\tau_{\text{lep}}\tau_{\text{had}}$ background estimation

The dominant source of background in the $\tau_{\text{lep}}\tau_{\text{had}}$ channel is attributed to events with jet $\rightarrow \tau_{\text{had-vis}}$ fakes. These events can be divided into those where the reconstructed lepton comes from a real lepton, predominantly stemming from W+jets ($t\bar{t}$) in the b-veto (b-tagged) category, and those where the reconstructed lepton comes from a misidentified jet (jet $\rightarrow \ell$ fakes), predominantly stemming from multijet events. These backgrounds have dedicated selection criteria designed to suppress their contributions in the $\tau_{\text{lep}}\tau_{\text{had}}$ SR. The BDT based tau identification requirement on the leading-$\tau_{\text{had-vis}}$ (`medium`) suppresses the jet $\rightarrow \tau_{\text{had-vis}}$ fakes. Furthermore, the isolation requirement on the lepton candidate (`gradient` isolation) is intended to suppress jet $\rightarrow \ell$ fakes. To the opposite end, one can create orthogonal regions to the SR by inverting these requirements. For example, inverting the tau identification results in a region which is expected to be enriched with jet $\rightarrow \tau_{\text{had-vis}}$ fakes, and similarly inverting the lepton isolation will provide a region enriched with jet $\rightarrow \ell$ fakes. A data-driven *combined fake-factor* method is developed for the $\tau_{\text{lep}}\tau_{\text{had}}$ channel, in which these orthogonal regions

are used to study the background composition and extract an estimation of fake background sources. Several CRs are defined to this end.

An important component of the background contribution in the $\tau_{\text{lep}}\tau_{\text{had}}$ SR and CRs are sources of backgrounds with real tau and lepton candidates. The main contributions are from $Z \to \tau\tau$ in the b-veto category, and $t\bar{t}$ in the b-tagged category, with smaller contributions from $Z \to \ell\ell$, diboson, and single top-quark processes. Their contributions in the SR and CRs are estimated from simulation. A simulated event is only considered if the reconstructed tau and lepton are both *truth matched*: attributed to a real tau and lepton by the MC truth level information (page 71). All recommended scale factors relating to object reconstruction, identification, energy resolution, triggering, etc., are applied to the events. Other sources of backgrounds which are determined from simulation include $\mu \to \tau_{\text{had-vis}}$ and $e \to \tau_{\text{had-vis}}$ fakes: The former make a small contribution and are sufficiently well modelled by simulation. The latter have recommended scale factor corrections (determined in $Z \to \ell\ell$ events) that are applied to MC events where the $\tau_{\text{had-vis}}$ candidate is matched to an electron at truth level.

In order to estimate the contribution of jet $\to \tau_{\text{had-vis}}$ fakes in the $\tau_{\text{lep}}\tau_{\text{had}}$ SR, a CR (referred to as CR-1) is defined with the same selection criteria as the SR, but with an inverted tau identification criteria. The selected tau candidate in CR-1 must have a tau identification BDT score ($w_{\text{tau-id-bdt}}$) of > 0.35, referred to here as the `very-loose` tau identification, and fail the `medium` tau identification working point. This `very-loose` requirement ensures that the quark- and gluon-initiated jet composition and the kinematics in the CR are not too dissimilar to that in the SR. Events in CR-1 can be converted into an estimation of the jet $\to \tau_{\text{had-vis}}$ background in the SR by determining a transfer rate in an orthogonal *fakes region*. However, as mentioned above, the jet $\to \tau_{\text{had-vis}}$ background events in the $\tau_{\text{lep}}\tau_{\text{had}}$ channel will either have an accompanying real or fake (jet $\to \ell$) lepton, predominantly from W+jets and $t\bar{t}$ (collectively referred to here as non-multijet) or multijet backgrounds, respectively. These sources have different compositions of quark- and gluon-initiated jets, with higher fractions of gluon-initiated jets in multijet backgrounds. Since quark-initiated jets are typically narrower and produce fewer hadrons than gluon-initiated jets, they tend to fake $\tau_{\text{had-vis}}$ candidates more frequently, resulting in significantly different fractions of jet $\to \tau_{\text{had-vis}}$ fakes. As such, the contributions of multijet and non-multijet backgrounds in the jet $\to \tau_{\text{had-vis}}$ estimation are performed separately.

The definitions of all control and fakes regions used to extract background templates and transfer rates are shown in Table 6.3. A schematic representation of the combined fake-factor method as used in the $\tau_{\text{lep}}\tau_{\text{had}}$ channel is shown in Figure 6.5. The details of the method, and the relative regions, are described in the following sections. The combined

fake-factor technique is outlined by the following: The jet $\rightarrow \tau_{\text{had-vis}}$ transfer rates (referred to as *fake-factors*) are determined in two fake regions (multijet and non-multijet components), and applied to events in CR-1 in order to estimate the jet $\rightarrow \tau_{\text{had-vis}}$ background in the SR. The relative contribution of the multijet background in CR-1 is determined by applying a jet $\rightarrow \ell$ fake-factor, calculated from an additional fakes region, to events from a multijet pure CR (referred to as CR-2). The relative component of multijet and non-multijet is determined from the fraction of data-driven multijet events in CR-1 with regards to data, also known as r_{QCD}. The multijet and non-multijet fake-factors are weighted with respect to r_{QCD} to produce a combined fake-factor that is applied to events in CR-1 to estimate jet $\rightarrow \tau_{\text{had-vis}}$ fakes in the SR.

6.3.1.1 Backgrounds with jet $\rightarrow \ell$ (and $\tau_{\text{had-vis}}$) fakes (multijet)

In order to estimate the number of events from multijet background in the SR ($N^{\text{SR}}_{\text{multijet}}$) from that in CR-1 ($N^{\text{CR-1}}_{\text{multijet}}$), a multijet fakes region (MJ-FR) is defined, as shown in Figure 6.5. The MJ-FR follows the same event selection as the union of the SR and CR-1, i.e., without any requirement on the `medium` $\tau_{\text{had-vis}}$ identification, with the exception that the selected lepton is required to fail the `gradient` isolation criterion. The lepton isolation is inverted in order to increase the purity of the jet $\rightarrow \ell$ fakes, attributed to multijet background in the analysis. Within the MJ-FR, a CR is defined (CR-2), where events are required to fail the `medium` $\tau_{\text{had-vis}}$ identification. The selection for MJ-FR and CR-2 are summarised in Table 6.3 and Figure 6.5.

In order to estimate the contribution of multijet background in CR-1, a lepton fakes region (L-FR) is defined. Any event in the L-FR must satisfy the following selection: Exactly one lepton is selected, as with the SR selection, which is trigger matched. However, no requirement on the offline lepton isolation is imposed on the candidate. The event must contain at least one (two, not counting the b-tagged jet) selected jets for the b-veto (b-tagged) categories. The event must not have any $\tau_{\text{had-vis}}$ candidates passing the `loose` $\tau_{\text{had-vis}}$ identification. The transverse mass $m_{\text{T}}(\ell, E_{\text{T}})$ of the event must be less than 30 GeV. The m_{T} requirement eliminates contributions from W+jets and $t\bar{t}$ events, and shifts the L-FR closer to the SR. Similarly the requirement on the multiplicity of additional jets also rejects true lepton backgrounds in favour of multijet events.

The multijet background contribution in the SR is calculated as follow, see Figure 6.5: First, a multijet background estimation in CR-1 ($N^{\text{CR-1}}_{\text{multijet}}$) is determined by applying the lepton fake-factor (f_{L}) to data events in CR-2. The contribution from events from non-

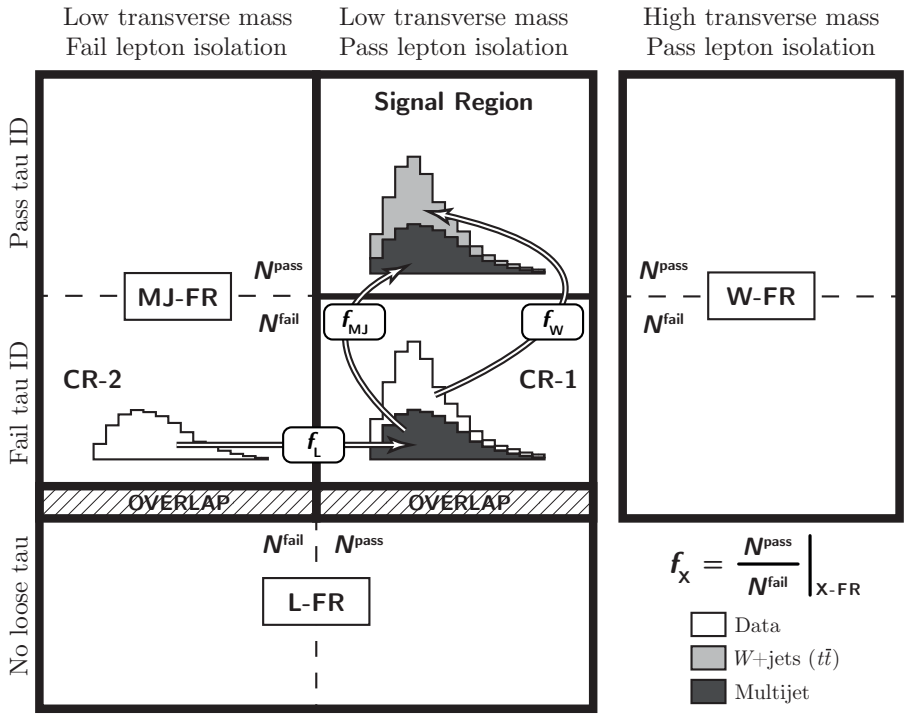

Figure 6.5 Schematic of the fake-factor background estimation in the $\tau_{\text{lep}}\tau_{\text{had}}$ channel [1]. The fake-factors, f_{MJ}, f_{W} and f_{L}, are defined as the ratio of events in data that pass/fail the specified selection requirements, measured in the fakes regions MJ-FR, W-FR and L-FR, respectively, as defined in the text.

Table 6.3 Definition of signal, control and fakes regions used in the analysis [1]. The symbol ℓ represents the selected electron or muon candidate and τ_1 (τ_2) represents the leading (sub-leading) $\tau_{\text{had-vis}}$ candidate.

Channel	Region	Selection
$\tau_{\text{lep}}\tau_{\text{had}}$	SR	ℓ (trigger, isolated), τ_1 (medium), $q(\ell)\times q(\tau_1)<0$, $\lvert\Delta\phi(\ell,\tau_1)\rvert>2.4$, $m_{\text{T}}(\mathbf{p}_{\text{T}}^{\ell},\mathbf{E}_{\text{T}}^{\text{miss}})<40\,\text{GeV}$, veto $80<m(\mathbf{p}^{\ell},\mathbf{p}^{\tau_1})<110\,\text{GeV}$ ($\tau_{\text{e}}\tau_{\text{had}}$channel only)
	CR-1	Pass SR except: τ_1 (very-loose, fail medium)
	CR-2	Pass SR except: τ_1 (very-loose, fail medium), ℓ (fail isolation)
	MJ-FR	Pass SR except: τ_1 (very-loose), ℓ (fail isolation)
	W-FR	Pass SR except: $70\,(60)<m_{\text{T}}(\mathbf{p}_{\text{T}}^{\ell},\mathbf{E}_{\text{T}}^{\text{miss}})<150\,\text{GeV}$ in $\tau_{\text{e}}\tau_{\text{had}}(\tau_{\mu}\tau_{\text{had}})$ channel
	CR-T	Pass SR except: $m_{\text{T}}(\mathbf{p}_{\text{T}}^{\ell},\mathbf{E}_{\text{T}}^{\text{miss}})>110\,(100)\,\text{GeV}$ in the $\tau_{\text{e}}\tau_{\text{had}}(\tau_{\mu}\tau_{\text{had}})$ channel, b-tagging category only
	L-FR	ℓ (trigger, selected), jet (selected), no loose $\tau_{\text{had-vis}}$, $m_{\text{T}}(\mathbf{p}_{\text{T}}^{\ell},\mathbf{E}_{\text{T}}^{\text{miss}})<30\,\text{GeV}$

multijet backgrounds in CR-2 are taken into account by subtracting the expected number of simulation events ($N^{\text{CR-2}}_{\text{non-multijet}}$) from data ($N^{\text{CR-2}}_{\text{data}}$),

$$N^{\text{CR-1}}_{\text{multijet}} = f_{\text{L}} \times (N^{\text{CR-2}}_{\text{data}} - N^{\text{CR-2}}_{\text{non-multijet}}). \tag{6.4}$$

The f_{L} fake-factor is determined in the L-FR by calculating the ratio,

$$f_{\text{L}} = \frac{N^{\text{L-FR, pass-}\ell\text{-iso}}_{\text{data}} - N^{\text{L-FR, pass-}\ell\text{-iso}}_{\text{non-multijet}}}{N^{\text{L-FR, fail-}\ell\text{-iso}}_{\text{data}} - N^{\text{L-FR, fail-}\ell\text{-iso}}_{\text{non-multijet}}}, \tag{6.5}$$

where $N^{\text{L-FR, pass-}\ell\text{-iso}}_{\text{data}}$ ($N^{\text{L-FR, pass-}\ell\text{-iso}}_{\text{non-multijet}}$) and $N^{\text{L-FR, fail-}\ell\text{-iso}}_{\text{data}}$ ($N^{\text{L-FR, fail-}\ell\text{-iso}}_{\text{non-multijet}}$) are the number of events in data (non-multijet MC) that pass and fail the lepton isolation, respectively. The lepton fake-factor is determined in Section 6.3.1.1.1.

The relative component of multijet events in CR-1 is determined by the factor r_{QCD},

$$r_{\text{QCD}} = \frac{N^{\text{CR-1}}_{\text{multijet}}}{N^{\text{CR-1}}_{\text{data}} - N^{\text{CR-1}}_{\text{true-}\tau\text{ MC}}}, \tag{6.6}$$

where $N^{\text{CR-1}}_{\text{true-}\tau\text{ MC}}$ is the true $\tau_{\text{had-vis}}$ MC in CR-1. Thus, the data-driven multijet contribution is scaled with respect to total expected jet $\rightarrow \tau_{\text{had-vis}}$ fake background in CR-1. The multijet fraction is determined in Section 6.3.1.1.2.

The multijet fake-factor (f_{MJ}) is determined in the ML-FR and weighted by r_{QCD} before being applied to events in CR-1 (after true background subtraction) in the combined fake-factor. The f_{MJ} fake-factor is determined in the MJ-FR by calculating the ratio,

$$f_{\text{MJ}} = \frac{N^{\text{MJ-FR, pass-}\tau\text{-id}}_{\text{data}} - N^{\text{MJ-FR, pass-}\tau\text{-id}}_{\text{non-multijet}}}{N^{\text{MJ-FR, fail-}\tau\text{-id}}_{\text{data}} - N^{\text{MJ-FR, fail-}\tau\text{-id}}_{\text{non-multijet}}}, \tag{6.7}$$

where $N^{\text{MJ-FR, pass-}\tau\text{-id}}_{\text{data}}$ ($N^{\text{MJ-FR, pass-}\tau\text{-id}}_{\text{non-multijet}}$) and $N^{\text{MJ-FR, fail-}\tau\text{-id}}_{\text{data}}$ ($N^{\text{MJ-FR, fail-}\tau\text{-id}}_{\text{non-multijet}}$) are the number of events in data (non-multijet MC) that pass and fail the $\tau_{\text{had-vis}}$ `medium` identification, respectively. The multijet fake-factor is determined in Section 6.3.1.1.3.

6.3.1.1.1 Calculation of the lepton fake-factor The lepton fake-factors are calculated in the L-FR by first subtracting the contribution of real lepton backgrounds in MC from data templates. The data templates are parametrized in terms of the lepton $|\eta|$. This is chosen as f_{L} is expected to vary as a function of η, with varying performance of the muon or

electron isolation at different regions of the detector. The lepton fake-factors are calculated independently in b-tagged and b-veto categories. Furthermore, they are separated into two lepton p_{T} bins for the $\tau_{\mu}\tau_{\mathrm{had}}$ channel, high ($p_{\mathrm{T}} > 55$ GeV) and low ($p_{\mathrm{T}} < 55$ GeV) muon p_{T}, in order to account for the separate p_{T} muon triggers used. Since the electron trigger scale factors are provided as a combined scale factor, this is not done in the $\tau_{\mathrm{e}}\tau_{\mathrm{had}}$ channel.

Uncertainties in the calculation of f_{L} factors include the statistical uncertainties attributed to limited statistics in the data and simulation (used in MC subtraction), although this effect is considerably small. Further uncertainties on the true lepton background subtraction are taken into account by varying the normalisation of MC in the L-FR by 20%. An uncertainty in which the m_{T} threshold value used to define the L-FR is also considered. The corresponding f_{L} factors are shown in Figure 6.6 for $\tau_{\mathrm{e}}\tau_{\mathrm{had}}$ channel, with the corresponding envelope uncertainties. The total uncertainty in f_{L} is found to be between 5–50%.

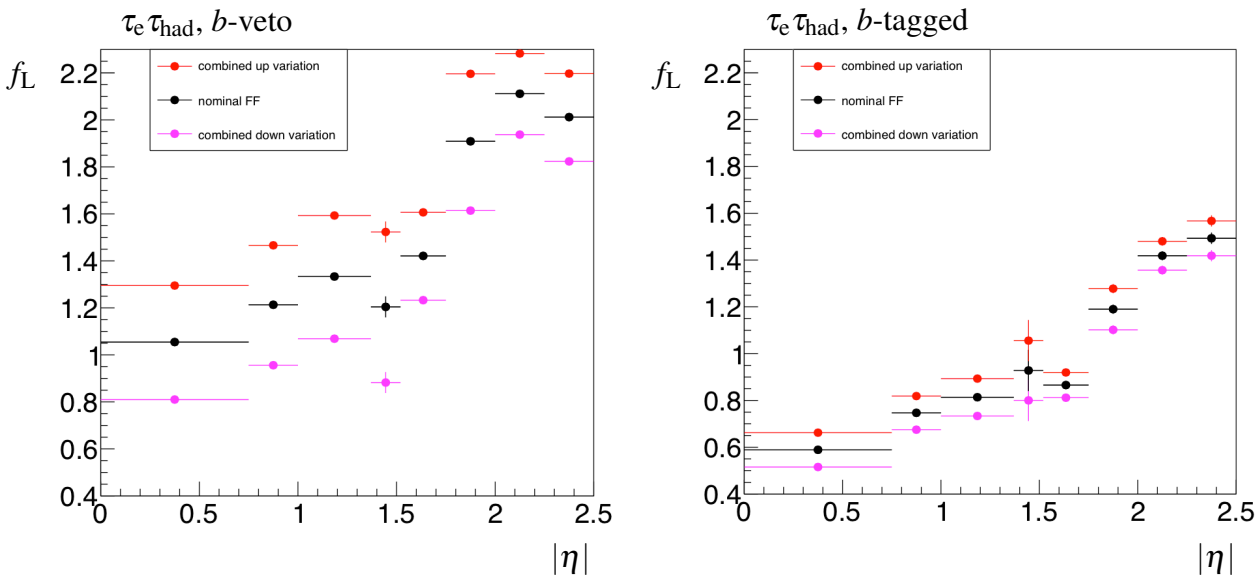

Figure 6.6 Fake-factors (f_{L}) from the $\tau_{\mathrm{e}}\tau_{\mathrm{had}}$ [207], determined in the L-FR, as a function of lepton $|\eta|$ in (a) b-tagged and (b) b-veto categories.

To predict the multijet events in CR-1, f_{L} is applied to events in CR-2 (Eq. (6.4)), as shown in Figure 6.5. The contribution in CR-2 from real muon and electron backgrounds is very small, and subtracted as in Eq. (6.4). The resulting estimate of the multijet backgrounds in CR-1 is show in Figure 6.7 for the $\tau_{\mathrm{e}}\tau_{\mathrm{had}}$ channel as a function of the tau p_{T} ($p_{\mathrm{T}}^{\tau_{\mathrm{had\text{-}vis}}}$). The corresponding distributions for the $\tau_{\mu}\tau_{\mathrm{had}}$ channel are shown in Figure 6.7. The multijet component is labeled as (QCD) in the plot. The non-multijet backgrounds are, at this stage,

estimated from simulation. Without the data-driven estimate of the non-multijet background, mis-modelling of the data is seen in high p_{T} tails. The uncertainties shown are only statistical so the effect seen here is exaggerated.

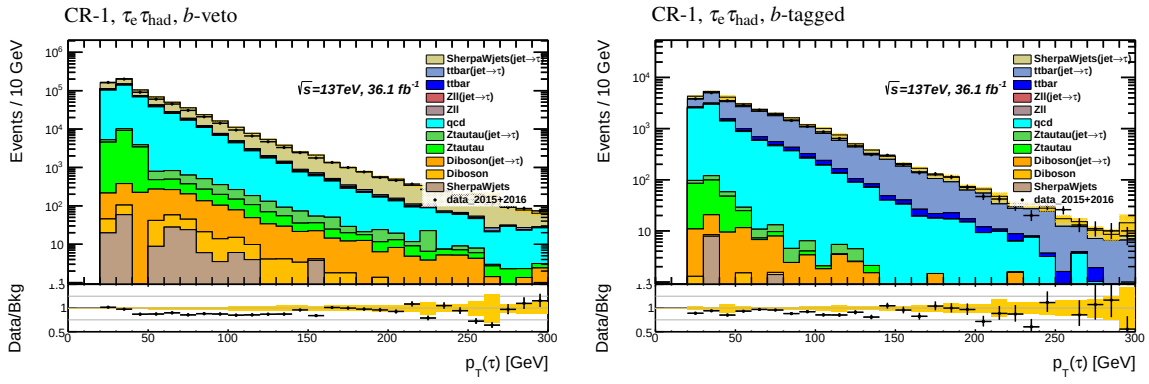

(a) **(b)**

Figure 6.7 Distributions of $\tau_{\text{had-vis}}$ p_{T} for the (a) b-veto and (b) b-tagged categories in the $\tau_e\tau_{had}$ CR-1 [207]. The multijet background (QCD) is estimated using the lepton fake-factors on events in CR-2. The only uncertainties shown are the statistical uncertainties of the sample.

6.3.1.1.2 Calculation of the multijet fraction In order to predict r_{QCD}, the fraction of events that arise from multijet, a prediction of the multijet background contribution is performed in CR-1. The r_{QCD} fraction is then determined as a function of the $p_{\mathrm{T}}^{\tau_{\text{had-vis}}}$, separately for b-tagged and b-veto categories, as well as for the $\tau_e\tau_{had}$ and $\tau_\mu\tau_{had}$ channels. For the calculation of this fraction, simulation is used to predict the number of events with a true τ_{had}, and the lepton fake-factor data-driven method is used to predict the contribution of multijet events. In each bin of the two paramaterizing variables (p_{T} and number of tracks), the factor is defined as in Eq. (6.6). Uncertainties from the f_{L} factor used to derive the multijet estimation in CR-1 are propagated into uncertainties on r_{QCD}. Additionally, the uncertainties from the statistics and MC systematics in the data and simulation in CR-1 are also included. The combination of all sources of uncertainties to r_{QCD} are symmetrized, and are constrained to so that $0 \leq r_{\mathrm{QCD}} \leq 1$. The r_{QCD} factors are shown in Figure 6.8 as a function of the $p_{\mathrm{T}}^{\tau_{\text{had-vis}}}$ for the $\tau_e\tau_{had}$ channel, along with their respective envelope uncertainties.

6.3.1.1.3 Calculation of the multijet fake-factor The multijet fake-factor is measured in the MJ-FR, which has an inverted lepton isolation criteria that of the signal region. The f_{MJ}

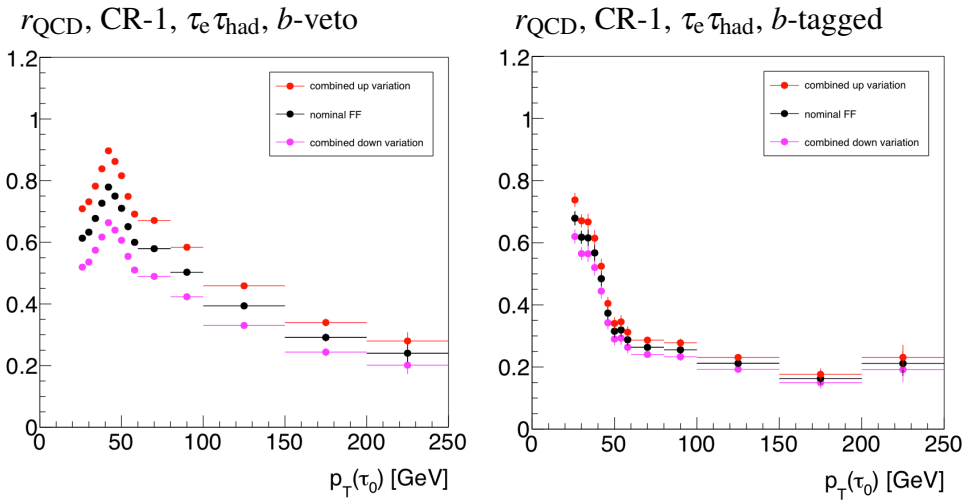

(a) **(b)**

Figure 6.8 Distribution of the multijet factor, r_{QCD}, as a function of the $p_T^{\tau_{had\text{-}vis}}$ for the (a) b-veto and (b) b-tagged categories in the $\tau_e\tau_{had}$ channel, along with the total up and down shifts for the uncertainties [207].

factor is determined with Eq. (6.7), much in the same way as was outlined for the calculation of f_L. The fake-factors here are parametrized in terms of the number of prongs and the p_T of the tau candidate (as with r_{QCD}). The parameterisation is also split into 2015 and 2016 data periods. This is due to the isolation requirement in lepton trigger in 2015 being more loose than their 2016 counterparts, whereby the data failing the offline lepton isolation will be higher. Additionally, different pileup conditions between 2015 and 2016 lead to different fake-factors. As such, the composition of multijet fakes can be different in each case, in which case an inclusive fake-factor would bias the background estimation.

The uncertainties on f_{MJ} are attributed to the MC subtraction of non-multijet backgrounds in the MJ-FR. This background contributes very minimally to this region. The normalisation of the background is varied by 50% with respect to the nominal MC estimation. This is a conservative approach, and is used since the modelling of leptons failing isolation (as in MJ-FR) are not as robustly studied as events that pass lepton isolation. An additional source of uncertainty is derived by estimating the fake-factors when varying the lepton anti-isolation criteria used to define MJ-FR. A CR where the $\tau_{had\text{-}vis}$ and lepton have the same sign (SS) charge is used to calculate fake-factors with varying lepton anti-isolation definitions. The difference between these fake-factors and the nominal f_{MJ} is taken as an uncertainty on f_{MJ}. An additional variation on the multijet fake-factor is also determined in a SS CR with events passing the nominal lepton isolation. A 20% uncertainty on the nominal distribution

is considered as the uncertainty of the f_{MJ}, which is found to envelop approximately 68% of the variations.

Since f_{MJ} is parameterised as a function of $p_{\text{T}}^{\tau_{\text{had-vis}}}$ only, due to the limited statistics, it could lead to imperfections in the modelling some other variables in the SR. A closure test is performed by applying f_{MJ} back to the same MJ-FR where it has been derived, and a trend is observed in the angular separation between the $\tau_{\text{had-vis}}$ candidate and the $E_{\text{T}}^{\text{miss}}$. Figure 6.9 shows the distribution in $|\Delta\phi(\tau_1, E_{\text{T}}^{\text{miss}})|$ for the ratio of events passing over failing the `medium` $\tau_{\text{had-vis}}$ identification after applying f_{MJ} in MJ-FR for the b-veto category. A trend in the fake-factors for low p_{T} taus ($p_{\text{T}} < 60$ GeV) is visible in Figure 6.9. The same closure test performed for high p_{T} taus shows a consistency with unity (within uncertainties). Additionally, the b-tagged region is also consistent with unity. Therefore, a correction is applied to f_{MJ} in b-veto events with low $p_{\text{T}}^{\tau_1}$ by weighting events in bins of $|\Delta\phi(\tau_1, E_{\text{T}}^{\text{miss}})|$. The uncertainty on this correction is taken by halving the correction. This uncertainty is also applied to the b-tagged, and high p_{T} b-veto, region, although no correction is applied to these cases.

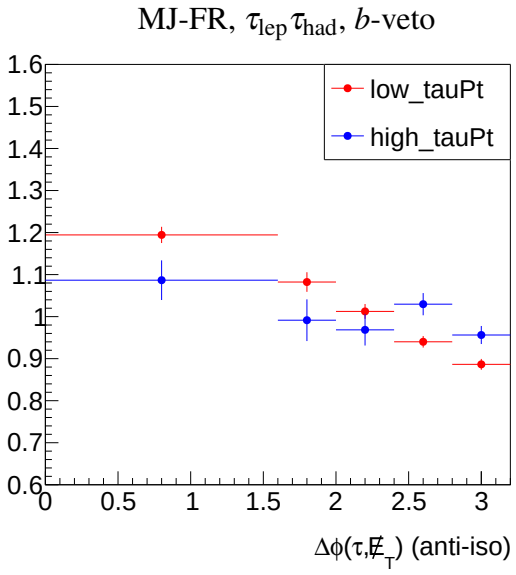

Figure 6.9 Distribution in b-veto events of the ration of taus passing over failing the $\tau_{\text{had-vis}}$ identification in the MJ-FR as a function of $|\Delta\phi(\tau_1, E_{\text{T}}^{\text{miss}})|$ after applying f_{MJ} [207]. A trend is visible in events with low p_{T} $\tau_{\text{had-vis}}$ ($p_{\text{T}} < 60$ GeV).

6.3.1.2 Backgrounds with only jet $\rightarrow \tau_{\text{had-vis}}$ fakes (non-multijet)

The background from non-multijet sources (W+jets in b-veto and $t\bar{t}$ in b-tagged), are studied in the fakes region W-FR. This is defined with the same selection as the $\tau_{\text{lep}}\tau_{\text{had}}$ SR with some differences (see Figure 6.5): Firstly, for the $\tau_{\text{had-vis}}$ candidate the `very-loose` identification criteria are used, i.e., $w_{\text{tau-id-bdt}} > 0.35$, introducing a higher level of contamination from jet $\rightarrow \tau_{\text{had-vis}}$ fakes. Secondly, a selection on the transverse mass is applied, $60(70)$ GeV $< m_{\text{T}}(\ell, E_{\text{T}}^{\text{miss}}) < 150$ GeV in the $\tau_\mu\tau_{\text{had}}$ ($\tau_{\text{e}}\tau_{\text{had}}$) channel. The low end of the m_{T} selection increases the purity of real lepton backgrounds: multijet contamination, where jet $\rightarrow \ell$ fakes are prominent, is reduced. The high end of the m_{T} selection is to reduce the contribution from sources of true $\tau_{\text{had-vis}}$ backgrounds from top quarks, which dominates at high m_{T}. The selection is summarised in Table 6.3.

Figure 6.10 show the background composition in W-FR for the $\tau_{\text{e}}\tau_{\text{had}}$ channel as a fucntion of $m_{\text{T}}(\ell, E_{\text{T}}^{\text{miss}})$. Contributions of each physics process are presented: all true $\tau_{\text{had-vis}}$ and jet$\rightarrow \tau_{\text{had-vis}}$ fakes are modelled with MC simulation, while the multijet contribution is estimated using the fake-factors technique described in Section 6.3.1.2. Shown are both b-tagged and b-veto categories, as well as the distributions before and after applying the `medium` $\tau_{\text{had-vis}}$ identification. Several features relating to the background composition are displayed, and are discussed here with relation to the $\tau_{\text{e}}\tau_{\text{had}}$ channel, with the same conclusions holding for the $\tau_\mu\tau_{\text{had}}$ channel. In Figure 6.10 (a) it is shown that the composition of background in the b-veto category is largely attributed to W+jets with jet$\rightarrow \tau_{\text{had-vis}}$ fakes. Although all backgrounds are substantially reduced after applying the `medium` $\tau_{\text{had-vis}}$ identification (Figure 6.10 (b)), the jet$\rightarrow \tau_{\text{had-vis}}$ fakes contribution remains dominant. Additionally the contribution from the true $\tau_{\text{had-vis}}$ $t\bar{t}$ background is relatively increased. In the b-tagged category in Figure 6.10 (c) the contribution from W+jets events becomes minor, both true and fake $\tau_{\text{had-vis}}$ backgrounds being predominantly attributed to $t\bar{t}$. After applying the `medium` $\tau_{\text{had-vis}}$ identification (Figure 6.10 (d)) the jet$\rightarrow \tau_{\text{had-vis}}$ fakes from $t\bar{t}$ are largely reduced, and the dominant background can be attributed to $t\bar{t}$ events with a real $\tau_{\text{had-vis}}$. In all distributions shown, there is large disagreement between data and MC prediction. In particular, after applying `medium` $\tau_{\text{had-vis}}$ identification, which is a selection which is close to the $\tau_{\text{lep}}\tau_{\text{had}}$ SR, there is and evident mis-modelling, showing that one should not rely on simulation for the fake $\tau_{\text{had-vis}}$ background.

The non-multijet fake-factors (f_{W}) are derived from events in the W-FR. The multijet fake-factor method described in the previous section is performed in the high m_{T} region to derive the multijet background in this region. Backgrounds from true ℓ and $\tau_{\text{had-vis}}$ events are

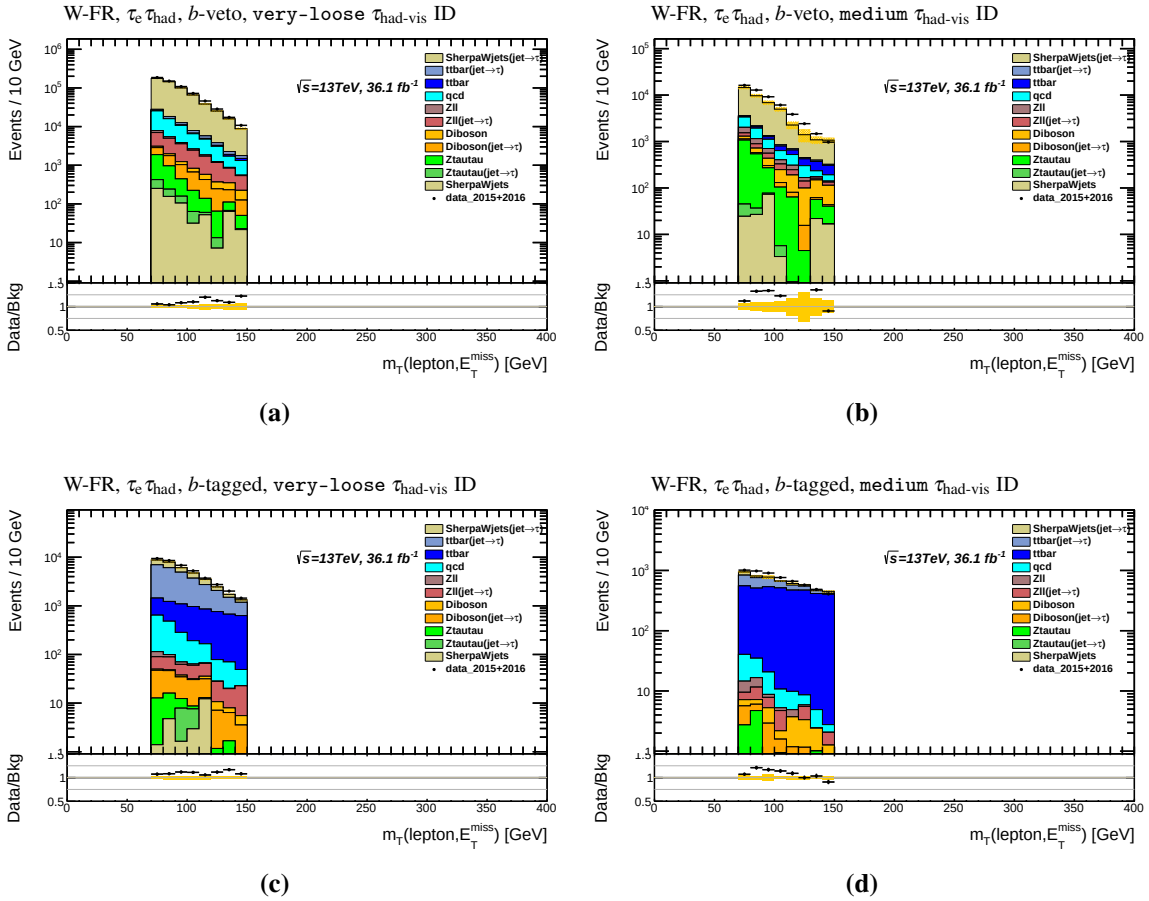

Figure 6.10 Distribution of $m_T(\ell, E_T^{miss})$ in the W-FR $\tau_e\tau_{had}$ channel [207] in the b-veto category (a) before and (b) after applying the medium $\tau_{had\text{-}vis}$ identification, and the b-tagged category (c) before and (d) after applying the medium $\tau_{had\text{-}vis}$ identification. All backgrounds are estimated from simulation, with the exception of multijet (here reffered to as QCD) which is derived used the multijet data-driven method described in Section 6.3.1.2.

estimated using simulation. The f_W fake-factor is calculated as,

$$f_W = \frac{N_{\text{data}}^{\text{W-FR, pass-}\tau\text{-id}} - N_{\text{other bkg.}}^{\text{W-FR, pass-}\tau\text{-id}}}{N_{\text{data}}^{\text{W-FR, fail-}\tau\text{-id}} - N_{\text{other bkg.}}^{\text{W-FR, fail-}\tau\text{-id}}}, \tag{6.8}$$

where $N_{\text{data}}^{\text{W-FR, pass-}\tau\text{-id}}$ ($N_{\text{other bkg.}}^{\text{W-FR, pass-}\tau\text{-id}}$) and $N_{\text{data}}^{\text{W-FR, fail-}\tau\text{-id}}$ ($N_{\text{other bkg.}}^{\text{W-FR, fail-}\tau\text{-id}}$) are the number of events from data (simulation and data-driven estimates) that pass and fail the $\tau_{had\text{-}vis}$ identification. They are parametrized in terms of $\tau_{1\text{-prong}}$ and $\tau_{3\text{-prong}}$, and $p_T^{\tau_{had\text{-}vis}}$. As with the multijet fake-factor, the composition of fakes can be dependent of the number of associated b-tagged jets in the selection. Therefore, f_W is determined separately in b-tagged and b-veto

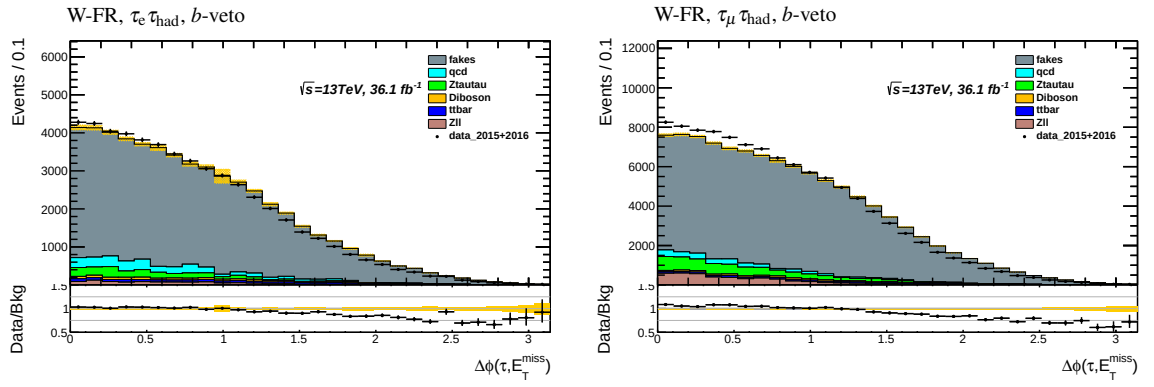

(a) **(b)**

Figure 6.11 $|\Delta\phi(\tau_1, E_{\mathrm{T}}^{\mathrm{miss}})|$ distribution when applying f_W factors back into the W-FR for (a) $\tau_e\tau_{had}$ and (b) $\tau_\mu\tau_{had}$ in the b-veto category [207]. The resulting uncertainties displayed are statistical.

categories. However, as can be seen in Figure 6.10 (d), the b-tagged category passing the $\tau_{\text{had-vis}}$ identification suffers from very low statistics after the subtraction of the real and multijet background components. The determination of a p_{T} dependent fake-factor in this region is therefore not possible, as it would be plagued by very large uncertainties. Instead, the $p_{\mathrm{T}}^{\tau_{\text{had-vis}}}$ shape in the b-tagged category is extracted from the b-veto estimate, with the normalisation of this estimate determined in a single bin distribution in the b-tagged region. The b-tagged correction factor is determined to be 0.8 ± 0.10 and 0.66 ± 0.17, for $\tau_{\text{1-prong}}$ and $\tau_{\text{3-prong}}$, respectively, with the uncertainties taken as half of the respective correction. As with multijet fake-factors, a correction is derived in $|\Delta\phi(\tau_1, E_{\mathrm{T}}^{\mathrm{miss}})|$ in order to correct mis-modelling in distributions which are not used to calculate the fake-factors. Figure 6.11 shows the resulting $|\Delta\phi(\tau_1, E_{\mathrm{T}}^{\mathrm{miss}})|$ distribution when applying f_W factors back into the W-FR, and illustrates the need for this correction. As with f_{MJ}, this correction is only found to be needed in b-veto events, and is not applied in the b-tagged category. The $|\Delta\phi(\tau_1, E_{\mathrm{T}}^{\mathrm{miss}})|$ correction is divided into different tau $p_{\mathrm{T}}^{\tau_{\text{had-vis}}}$ bins and the difference between the p_{T} binned and nominal corrections is used to determine the uncertainty of the correction, found to be approximately 30%.

The definition of W-FR assumes that the fake-factors calculated in the high-$m_{\mathrm{T}}(\ell, E_{\mathrm{T}}^{\mathrm{miss}})$ region can be used, as they are, for the low-$m_{\mathrm{T}}(\ell, E_{\mathrm{T}}^{\mathrm{miss}})$ signal region. This assumption is tested in a validation region which lies between the SR and W-CR in m_{T}: 40 GeV $< m_{\mathrm{T}}(\ell, E_{\mathrm{T}}^{\mathrm{miss}}) < 60(70)$ GeV in the $\tau_\mu\tau_{had}$ ($\tau_e\tau_{had}$) channel. The disagreement between the modelling and data in the $p_{\mathrm{T}}^{\tau_{\text{had-vis}}}$ distribution is taken as an extrapolation uncertainty into the SR.

6.3.1.3 The combined fake-factor for jet→ $\tau_{\text{had-vis}}$ fakes

The final estimate of jet → $\tau_{\text{had-vis}}$ in the $\tau_{\text{lep}}\tau_{\text{had}}$ SR is determined by applying a combined fake-factor to all data events in CR-1 after MC subtraction. The combined fake-factor takes into account the expected fraction of multijet events, determined as r_{QCD} in CR-1. The final combined fake-factor $f_{\text{fake }\tau}^{\text{combined}}$ is given as,

$$f_{\text{fake }\tau}^{\text{combined}} = f_{\text{W}} \times (1 - r_{\text{QCD}}) + f_{\text{MJ}} \times r_{\text{QCD}}. \tag{6.9}$$

The final multijet and non-multijet fake-factors used in the analysis are summarised in Figure 6.12

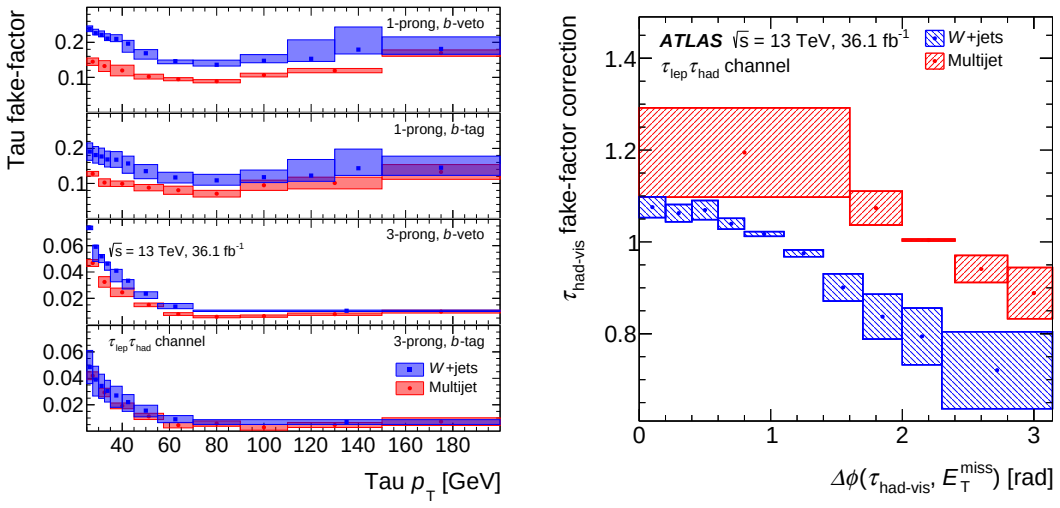

(a) **(b)**

Figure 6.12 The multijet and W+jets (non-multijet) fake-factors for jet → $\tau_{\text{had-vis}}$ fake background (a) and b-veto $|\Delta\phi(\tau_{\text{had-vis}}, E_{\text{T}}^{\text{miss}})|$ correction (b) in the $\tau_{\text{lep}}\tau_{\text{had}}$ channel[1]. All uncertainties are included. Only the 2016 multijet fake-factors are shown.

6.3.2 $\tau_{\text{had}}\tau_{\text{had}}$ background estimation

In the $\tau_{\text{had}}\tau_{\text{had}}$ channel, the dominant background is multijet, that has a cross-section several orders of magnitude higher than the signal processes. Despite the big suppression of this background due to the event selection, a sizeable contribution remains. Multijet events in the SR are attributed to events where two jets are misidentified as $\tau_{\text{had-vis}}$. This background is estimated using a data-driven method similar to the one described in the $\tau_{\text{lep}}\tau_{\text{had}}$ fake-

Table 6.4 Definition of signal, control and fakes regions used in the $\tau_{\text{had}}\tau_{\text{had}}$ analysis. The symbol ℓ represents the selected electron or muon candidate and τ_1 (τ_2) represents the leading (sub-leading) $\tau_{\text{had-vis}}$ candidate.

Channel	Region	Selection
$\tau_{\text{had}}\tau_{\text{had}}$	SR	τ_1 (trigger, medium), τ_2 (loose), $q(\tau_1)\times q(\tau_2)<0$, $\lvert\Delta\phi(\tau_1,\tau_2)\rvert>2.7$
	CR-1	Pass SR except: τ_2 (fail loose)
	DJ-FR	jet trigger, τ_1+τ_2 (no identification), $q(\tau_1)\times q(\tau_2)<0$, $\lvert\Delta\phi(\tau_1,\tau_2)\rvert>2.7$ $p_{\text{T}}^{\tau_2}/p_{\text{T}}^{\tau_1}>0.3$
	W-FR	μ (trigger, isolated), τ_1 (no identification), $\lvert\Delta\phi(\mu,\tau_1)\rvert>2.4$ $m_{\text{T}}(\mathbf{p}_{\text{T}}^{\mu},\mathbf{E}_{\text{T}}^{\text{miss}})>40\,\text{GeV}$, b-vetocategory only
	T-FR	Pass W-FR except: b-tagging category only

factors. Fake-factors are derived in a di-jet fakes region (DJ-FR) and applied to a anti-tau identification CR (CR-1). This technique is described in detail in Section 6.3.2.1.

The remaining backgrounds are all estimated using MC techniques. A significant and irreducible background contribution arises from $Z/\gamma^*\to\tau\tau$. Due to the lepton veto, $Z\to\ell\ell$ decays have a very minor contribution. A background contribution comes from $W(\to\tau\nu)$+jets events, where one of the additional jets is misidentified as a $\tau_{\text{had-vis}}$. Other backgrounds from W decays arise when the muon or electron and one additional jet in $W(\to\ell\nu)$+jets are misidentified as hadronically decaying tau leptons. Due to the electron and muon veto this background is highly suppressed. Both $t\bar{t}$ as well as single top-quark production can pass the event selection with real and fake $\tau_{\text{had-vis}}$ objects. Both $W(\to\tau\nu)$+jets and $t\bar{t}$ backgrounds comprise jet $\to\tau_{\text{had-vis}}$ fakes. This happens when both top quarks in $t\bar{t}$ have true $\tau_{\text{had-vis}}$ final-states or due to misidentified leptons or jets. There is also a fraction from di-boson production, in which true and misidentified $\tau_{\text{had-vis}}$ can also emerge. The contamination of non-multijet backgrounds with a jet $\to\tau_{\text{had-vis}}$ fake in the SR amounts to $\sim 1.6\%(\sim 7.0\%)$ in the b-veto (b-tagged) channel, and does not require a dedicated fake-factor method. In order to estimate the non-multijet fake background contribution, MC events with a fake $\tau_{\text{had-vis}}$ are weighted by corrections derived in a W+jets fakes region (W-FR) for b-veto and $t\bar{t}$ fakes region (T-FR) for b-tagged channel. This technique is detailed in Section 6.3.2.2. Table 6.4 shows the definitions of the SR, CR and fakes regions in the $\tau_{\text{had}}\tau_{\text{had}}$ channel. An additional region where the multijet fake-factor method is validated, is defined in the same way, but requiring that the two tau candidates have same sign charge (SS).

6.3.2.1 Data-driven QCD background estimation

To estimate the amount of multijet background in the $\tau_{\text{lep}}\tau_{\text{had}}$ signal region, a control region CR-1 is defined. CR-1 has the same selection as the SR except that the `loose` tau identification requirement on the τ_2 candidate is inverted, i.e., τ_2 must fail the `loose` tau identification. The multijet estimate in the SR is derived from events in CR-1, after subtraction of non-multijet background, multiplied by the di-jet fake-factors (f_{DJ}). The f_{DJ} factors are derived in the DJ-FR. The DJ-FR is designed to be close to the SR, while having relatively low $\tau_{\text{had-vis}}$ contamination. Events are selected by requiring any of the following single jet triggers [112, 206]: `HLT_j460`, `HLT_j440`, `HLT_j420`, `HLT_j400`, `HLT_j380`, `HLT_j360`, `HLT_j320`, `HLT_j300`, `HLT_j260`, `HLT_j200`, `HLT_j175`, `HLT_j150`, `HLT_j110`, `HLT_j85`, `HLT_j60`. The $p_{\text{T}}^{\tau_1}$ candidate must exceed the online p_{T} thresholds by at least 10 %. Events are required to contain at least two tau candidates with $p_{\text{T}} > 65$ GeV. The leading tau is defined as the *tag* and the sub-leading as the *probe*. The tag is required to have $p_{\text{T}} > 85$ GeV. The tag and probe jet have to be back-to-back ($\Delta\phi > 2.7$). The transverse momentum of the *probe* jet has to be at least 30 % of the p_{T} of the tag jet. The f_{DJ} factors are defined as the number of probe-jets that pass the `loose` identification, $N^{\text{pass }\tau-\text{ID}}$, divided by the number that fail, $N^{\text{fail }\tau-\text{ID}}$, parametrized in terms of the $p_{\text{T}}^{\tau_2}$ and number of tracks ($N_{\text{track}}^{\tau_2}$),

$$f_{\text{DJ}} = \frac{N^{\text{pass }\tau-\text{ID}}(p_{\text{T}}^{\tau_2}, N_{\text{track}}^{\tau_2})}{N^{\text{fail }\tau-\text{ID}}(p_{\text{T}}^{\tau_2}, N_{\text{track}}^{\tau_2})}. \tag{6.10}$$

All backgrounds (Z + jets, W + jets, single top-quark, $t\bar{t}$ and di-boson) are subtracted before computing the fake-factors to avoid possibles biases in the estimation. The dominant non-multijet backgrounds in the DJ-FR are attributed to $t\bar{t}$, in the b-tagged, and W + jets, in the b-veto region.

Several sources of uncertainties enter in the calculation of f_{DJ}. Firstly the statistical uncertainty of the data and MC simulations are propagated through the calculation of the fake-factors. The fraction of background contamination is found to be largest for events with $\tau_{\text{3-prong}}$ tau candidates and ranges up to 7.4%. The total statistical uncertainty on the background is smallest in the $\tau_{\text{1-prong}}$ opposite sign pass-ID region for the b-veto category (6.6%) and is largest for the $\tau_{\text{1-prong}}$ same sign fail-ID region b-veto category (33.7%). Additionally, the systematic uncertainties from the experimental nuisance parameters are derived from the recommended MC uncertainties. The uncertainties are generally small when compared to the statistical components and the total systematic uncertainty is used, derived by adding individual components in quadrature. In order to reduce the impact of the choice of binning, a linear interpolation of nominal values and uncertainty bands is

used. The fake-factors are derived and compared for b-tagged and b-veto, as well as an inclusive category (no selection on the number of b-tagged jets). The f_{DJ} factors do not show large differences in most p_{T} regions between the b-tagged and b-veto, therefore the final fake-factors are derived in the inclusive b-jet region. This reduces the large uncertainties in the b-tagged fake-factors, caused due to lack of statistics in the category.

In Figure 6.13 the fake-factors are shown (for $\tau_{\text{1-prong}}$ and $\tau_{\text{3-prong}}$) in the b-veto and b-tagged categories, both of which are just the inclusive region fake-factors, with the b-tagged fake-factors having an additional uncertainty. This additional systematic uncertainty is derived from the difference of the nominal fake-factors between the inclusive and b-tagged regions, to account for the fact that the fake-factors used in the b-tagged region are heavily based on statistics from the b-veto region. Also shown are the different components to the total uncertainty. In general the largest impact on the total uncertainty is coming from the data statistics, although the MC statistical uncertainty in some high p_{T}-bins is larger. In the low p_{T}-bins in the b-tagged region, there is a large uncertainty attributed to using the inclusive fake-factors. The multijet fake-factor method is validated in the SS signal region, which is predominantly multijet background, and is found to provide good modelling, as shown in Figure 6.14.

6.3.2.2 Modelling of fake taus in MC backgrounds

The contribution from MC background with at least one jet $\rightarrow \tau_{\text{had-vis}}$ fake is non-negligible in the SR. However, unlike in the $\tau_{\text{lep}}\tau_{\text{had}}$ channel, this background is sufficiently suppressed to not require a fake-factor method. Instead, data-driven corrections on non-multijet MC backgrounds with jet $\rightarrow \tau_{\text{had-vis}}$ fakes are applied. The main contributions for this background are from single top-quark, $t\bar{t}$ and $W(\rightarrow \tau\nu)$+jets. In general the quark/gluon-induced jet fraction for the W+jets and top backgrounds are different, with a higher fraction of gluon-induced jets expected in the W+jets compared to top backgrounds. The rate at which jet $\rightarrow \tau_{\text{had-vis}}$ fakes occur in either background are therefore different. The modelling of fake tau rates from non-multijet background is checked in two fakes regions, one for selecting top (T-FR) and one for W (W-FR) backgrounds. Both regions are defined by selection events that pass a single lepton trigger `HLT_mu50`, with exactly one offline muon with $p_{\mathrm{T}} > 55$GeV and `medium` identification that is matched to the trigger. The muon is required to pass the `gradient` isolation, in order to reduce multijet background. Additionally to the baseline criteria described for the $\tau_{\text{had}}\tau_{\text{had}}$ channel, the requirement on the p_{T} of tau candidates is increased to 50GeV. No identification criteria is applied to the tau candidate, avoiding biases on the fake rate. Only events with at least one $\tau_{\text{had-vis}}$ candidate are considered. As with the

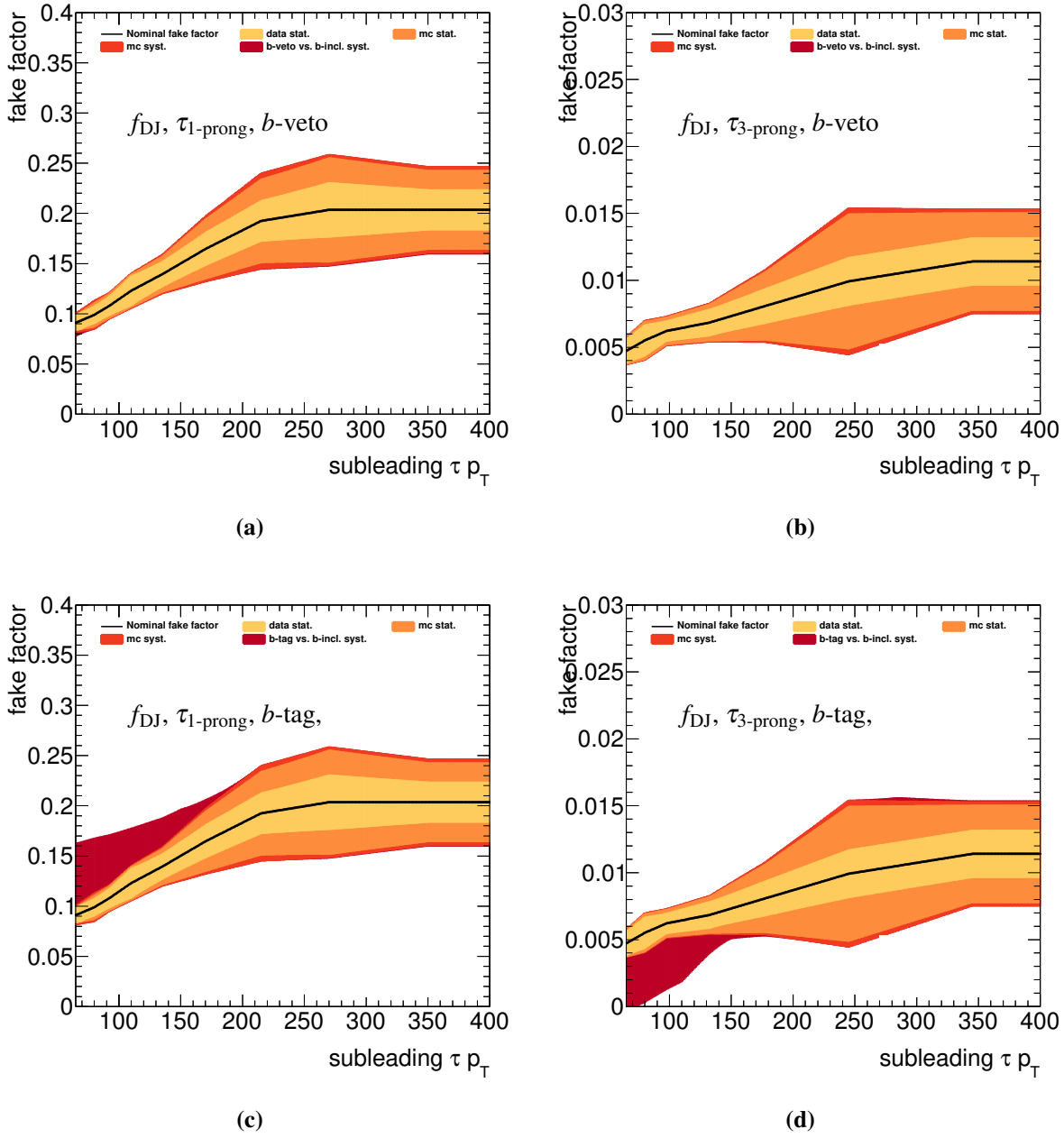

Figure 6.13 Multijet fake-factors as a function of pt^{τ_2} and $N^{\tau_2}_{\text{track}}$ [208]. Shown is the comparison of b-tagged, b-veto and inclusive fake-factors (top). The fake-factors for the b-veto (middle) and b-tagged (bottom) are displayed, both of which use the inclusive fake-factors, but the b-tagged has an additional uncertainty applied. Statistical and systematic uncertainties are added in quadrature to derive the total uncertainties of the method.

$\tau_{\text{lep}}\tau_{\text{had}}$ channel, a selection on the m_{T} distribution of the lepton and $E_{\text{T}}^{\text{miss}}$ further reduces the multijet contribution, and increases the W+jets and $t\bar{t}$ purity: $m_{\text{T}}(\boldsymbol{p}_{\text{T}}^{\mu}, \mathbf{E}_{\text{T}}^{\text{miss}}) > 40\,\text{GeV}$.

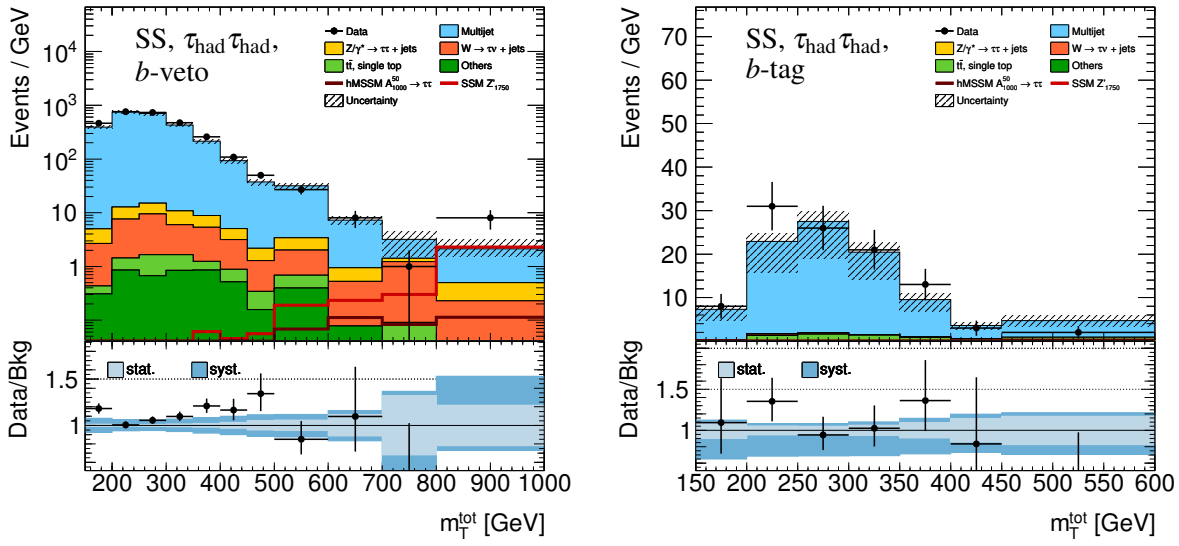

Figure 6.14 $m_{\text{T}}^{\text{tot}}$ distributions in the same-sign control region of the (a) b-veto and (b) b-tag category [208].

To obtain a similar kinematic region as for the SR, a selection on $\Delta\phi(\mu,\tau) > 2.4$ is applied. Finally, the W-FR (T-FR) is defined by requiring zero (at least one) b-jets in the event. The selection results in a purity of 92% for $W(\to \mu\nu)$+jets in the W-FR and 82% for top background in the T-FR. The MC from other sources is subtracted in each region before calculating the fake-rates.

The data-correction to non-multijet MC in the SR is performed by applying fake-rates for the leading and sub-leading $\tau_{\text{had-vis}}$ candidate. The fake-rate for the sub-leading $\tau_{\text{had-vis}}$ is derived in the W-FR ($r_{\text{W}}^{\tau_2}$) or T-FR ($r_{\text{T}}^{\tau_2}$) as the ratio of the number of $\tau_{\text{had-vis}}$ candidates that pass the `loose` tau identification, over the total number of $\tau_{\text{had-vis}}$ candidates. Similarly, the fake-rate for the leading $\tau_{\text{had-vis}}$ is derived in the W-FR ($r_{\text{W}}^{\tau_1}$) or T-FR ($r_{\text{T}}^{\tau_1}$) as the ratio of the number of $\tau_{\text{had-vis}}$ candidates that pass the `medium` tau identification and are matched to a single tau trigger (from Table 6.2), over the total number of $\tau_{\text{had-vis}}$ candidates. The fake-rates which are applied to top backgrounds ($t\bar{t}$ and single top-quark) are calculated in the T-FR, while those applied to non-top (i.e., $W(\to \tau\nu)$+jets and others) are derived in the W-FR. The fake-rates are measured using the leading $\tau_{\text{had-vis}}$ candidate in the fakes region and are parametrized in terms of $p_{\text{T}}^{\tau_1}$ and N_{track}.

The correction of MC in the SR proceeds as follows. Any MC event which passes the $\tau_{\text{had}}\tau_{\text{had}}$ and which does not contain a truth matched $\tau_{\text{had-vis}}$ candidate is applied the corresponding fake-rate. MC events which do not contain a truth matched $\tau_{\text{had-vis}}$ candidate and fail the either tau identification or the trigger requirement (p_{T} and matching) are not

discarded. This increases the statistics of these fake backgrounds and allowing for a more precise description, especially in the high p_{T} tails of the distributions. In the case that the leading tau is not truth matched, the `medium` $\tau_{\text{had-vis}}$ identification and trigger match requirement are dropped, and the event is multiplied by the corresponding fake-rate: $r_{\mathrm{W}}^{\tau_1}$ or $r_{\mathrm{T}}^{\tau_1}$. In the case that the sub-leading tau is not truth matched, the `loose` $\tau_{\text{had-vis}}$ identification is not used, and the $r_{\mathrm{W}}^{\tau_2}$ or $r_{\mathrm{T}}^{\tau_2}$ rates are applied as an event weight. Figure 6.15 shows the fake-rates for the leading and sub-leading $\tau_{\text{had-vis}}$ used in the OS and SS SR. The fake-rates are all derived from data, and are found to have good compatibility with the same fake-rates when derived from MC events. The exception is in the case of the $\tau_{\text{3-prong}}$ OS top fake-rate, which is calculated in a region which is very limited in data statistics. In this case, the fake-rates derived in data are not compatible with those in MC. Some of the fake-rate bins in data where observed to be zero, an observation which is not trusted to reflect the expected fake-rate. In this case, fake-rates derived in MC are instead used.

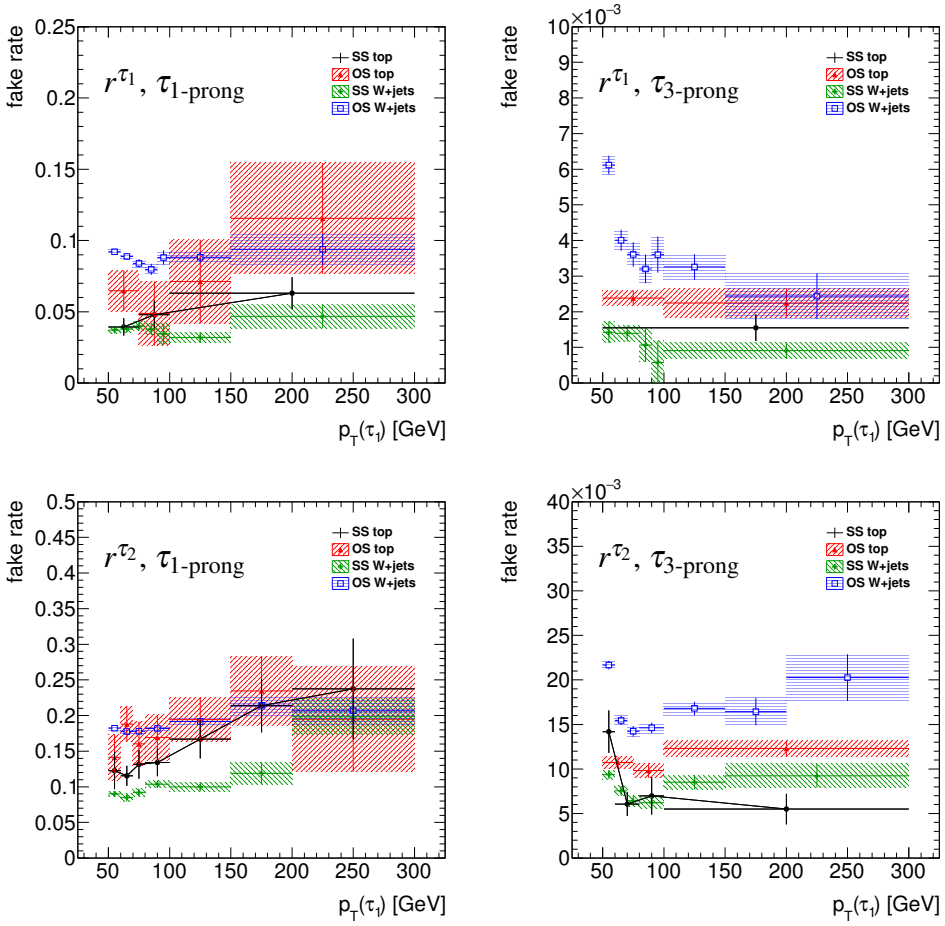

Figure 6.15 Fake-rates measured in the W-FR and T-FR for the leading (r^{τ_1}) and sub-leading (r^{τ_2}) $\tau_{\text{had-vis}}$ candidate in terms of the $\tau_{\text{had-vis}}$ p_{T} and number of prongs [208]. Uncertainties shown are due to data and MC statistics.

6.4 Systematic Uncertainties

Uncertainties from statistical limitations, detector effects, MC modelling, and data-driven background estimations, are propagated into the final $m_{\text{T}}^{\text{tot}}$ distributions as nuisance parameters (NPs). Each uncertainty will contribute to the total uncertainty in the workspaces used in the final fits in Section 6.5, which are generally considered to both affect the normalisation and shape of a particular sample in the $m_{\text{T}}^{\text{tot}}$ distribution: the normalisation effect is attributed to the variation in the total number of events, while for the shape effect, the variation histograms are renormalised to the nominal number of events, and a ratio of the variation over the nominal describes the shape of the distribution. Shape histograms are further smoothed, in order to reduce the effect of statistical fluctuations: neighbouring bins are merged until

two bins are left, describing the trend of the shape effect on the distribution. Many of the uncertainties propagated to the final distribution turn out to be inconsequential in the final fit, and NPs with negligible contributions are pruned in order to improve the performance of the fitting machinery. This is done for normalisation uncertainties which have a total uncertainty less than 1%, and for shape uncertainties which have no single bin with $> 1\%$ uncertainty. The different sources of uncertainties are summarised in this section. The data-driven uncertainties have already been discussed in the previous section, where the more detailed discussion of these uncertainties is presented, but are again summarised here for completeness. The final pre-fit uncertainties (before fitting to data) are summarised in Tables 6.7–6.12 for each of the four $\tau_{\text{lep}}\tau_{\text{had}}$ and two $\tau_{\text{had}}\tau_{\text{had}}$ SRs. The tables for the $\tau_{\text{lep}}\tau_{\text{had}}$ T-CR are found in Appendix B.1.

6.4.1 Experimental uncertainties

Uncertainties related to the detector simulation are included for signal and for backgrounds that are estimated using simulated samples. These systematics include uncertainty associated with:

- the pileup reweighting procedure
- the τ_{had} reconstruction and identification efficiencies,
- the τ_{had} trigger scale factor,
- the electron and muon trigger, reconstruction and identification efficiencies,
- jet, electron, muon and τ_{had} energy scales,
- jet energy resolution,
- calibration of the $E_{\text{T}}^{\text{miss}}$,
- jet flavour tagging systematics,
- jet vertex tagging scale factor systematics.

The naming conventions used for the different sets of detector related uncertainties can be deduced form Tables 6.7–6.12. Any systematic effect on the overall normalisation or shape of the $m_{\text{T}}^{\text{tot}}$ distribution in the signal region and control regions is considered. These uncertainties

are also taken into account for simulated samples that are used in the development of data-driven methods. The tau reconstruction and identification uncertainties contain additional high-p_{T} uncertainties. ATLFASTII [133] simulation has been used for the detector simulation of the $bb\phi$ samples and corresponding detector uncertainties have been used.

6.4.2 Background cross-section and modelling uncertainties

An uncertainty on the integrated luminosity (`ATLAS_LUMI`) of 3.2% is applied to all signal and background processes [168], with the exception of data-driven backgrounds. The cross-section uncertainties for $t\bar{t}$, single top-quark and di-boson production are taken from the working group recommendations as 6%, and applied to events modelled with MC. The $W+$jets cross-section uncertainties are negligible in the $\tau_{\mathrm{had}}\tau_{\mathrm{had}}$ channel, while the $W+$jets samples are not used in the $\tau_{\mathrm{lep}}\tau_{\mathrm{had}}$ channel, so no cross-section uncertainty is used on the $W+$jets samples.

For the Z/γ^*+jets backgrounds, mass dependant correction k-factors [209] are used to correct NLO Z/γ^*+jets to NNLO . The uncertainties on the k-factors (`ATLAS_LPXKFACTOR`) include PDF, PS modelling, and α_{S}- and EW-scale choice. An additional uncertainty on the Z/γ^*+jets background is considered to originate from potential mis-modelling of heavy flavour jets, the effect of which is checked by applying a very large uncertainty on Z/γ^*+jets MC events. A normalisation uncertainty on the Z/γ^*+jets background of $^{+100}_{-50}$% is considered, and observed to only impact the final limit by 0.48% in the most extreme case (at the 400 GeV mass point). Since the impact is very small, the additional uncertainty is not introduced to the statistical model.

In Figure 6.16 the $W+$jets background modelling is checked in the $\tau_{\mathrm{had}}\tau_{\mathrm{had}}$ channel W-FR and T-FR at with $p_{\mathrm{T}}^{\mu} > 110$ GeV, to increase the purity of $W+$jets, and shows good modelling of the data. An additional check is performed by assessing the impact of adding a 20% uncertainty to the $W+$jets samples. This uncertainty is motivated by a study with 8 TeV $W \to \tau\nu$ `Sherpa` samples, where PDF and renormalisation and factorisation scales are varied and found to yield an uncertainty of $\sim 15\%$ [210]. The 20% uncertainty used is therefore slightly conservative, and is found to impact the final result by $\sim 0.5\%$, so it is not included in the analysis.

Uncertainties related to $t\bar{t}$ modelling are associated with the hard-scatter, hadronisation, and PS modelling. In order to assess their impact, variation samples are generated and compared to the nominal $t\bar{t}$ MC. The uncertainty in the hadronisation modelling is assessed by comparing $t\bar{t}$ events generated in POWHEG-BOX 2 interfaced with Herwig++

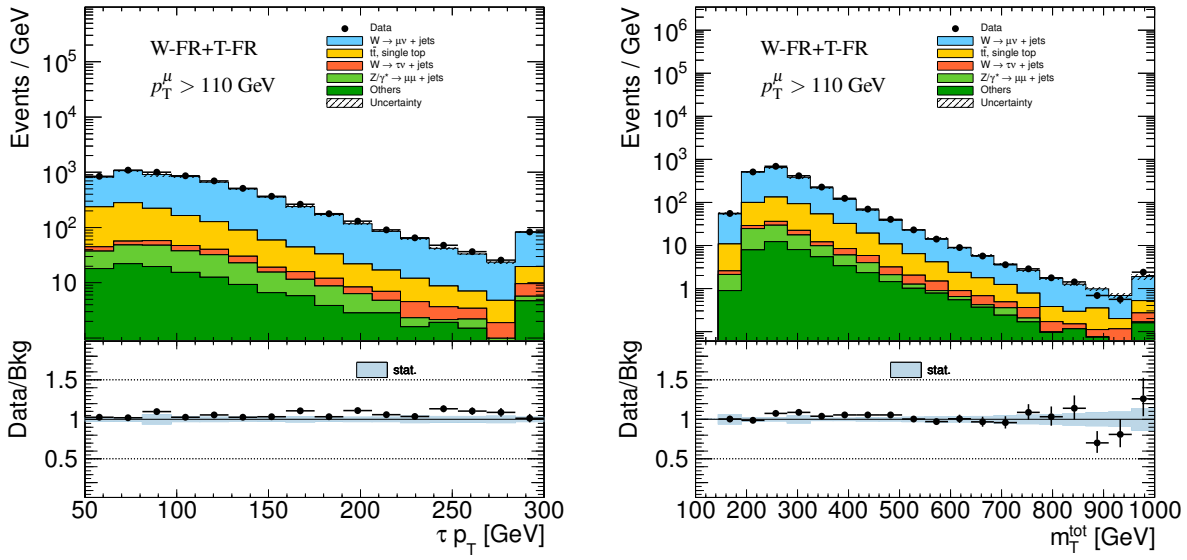

Figure 6.16 Distributions for tau p_{T} (a) and $m_{\mathrm{T}}^{\mathrm{tot}}$ (b) in the W-FR+T-FR in the $\tau_{\mathrm{had}}\tau_{\mathrm{had}}$ channel, with $p_{\mathrm{T}}^{\mu} > 110$ GeV, for checking W+jets modelling. Fake rates have not been applied. The uncertainty band includes statistical uncertainties only.

or PYTHIA 6 for the PS. The hard-scatter uncertainties are estimated by comparing samples generated with MADGRAPH5_aMC@NLO or POWHEG and interfaced with Herwig++ showering. The generator and showering uncertainties are enveloped into a single variation (`ATLAS_TTBAT_SHOWERGEN`) and shown in Figure 6.17 (a). Radiation uncertainties are assessed by varying the renormalisation and factorisation scales, and varying the `hdamp` parameter in POWHEG-BOX which controls the amount of radiation produced by the PS (`ATLAS_TTBAR_RADIATION`). The resulting radiation uncertainties are shown in Figure 6.17 (b). In the $\tau_{\mathrm{had}}\tau_{\mathrm{had}}$ channel, these uncertainties are not found to have shape effect, and are applied as a flat uncertainty on the normalisation. Additionally, the low statistics of $t\bar{t}$ in the $\tau_{\mathrm{had}}\tau_{\mathrm{had}}$ b-veto channel yields uncertainties which are very statistically limited. A 50% (and 100%) normalisation uncertainty is introduced to the $t\bar{t}$ MC to assess the impact of additional uncertainties on the $t\bar{t}$ modelling in the $\tau_{\mathrm{had}}\tau_{\mathrm{had}}$ channel, shown in Table 6.5. The impact on the final cross-section limits (as calculated in Section 6.5.2) is observed to be small for $m_\phi < 1$ TeV. The impact on the limit is non-negligible for larger mass points ($\sim 1.5\%$). However, when the $\tau_{\mathrm{had}}\tau_{\mathrm{had}}$ is fit including the T-CR, designed to constrain $t\bar{t}$ uncertainties, the impact on the expected limit is less than 1%. An additional uncertainty on the $t\bar{t}$ normalisation is therefore not included.

Table 6.5 Impact on the expected limit of an additional ad-hoc 50% and 100% uncertainty on the top background normalisation in the $\tau_{\text{had}}\tau_{\text{had}}$ b-veto category, with and without the $\tau_{\text{lep}}\tau_{\text{had}}$ T-CR.

	Top norm. sys.	Exp. limit [pb]	Impact [%]	Exp. limit [pb]	Impact [%]	Exp. limit [pb]	Impact [%]
	m_H [GeV]	300		400		700	
$\tau_{\text{had}}\tau_{\text{had}}$ b-veto	nominal	1.40669		0.38686		0.0831	
	50%	1.40684	-0.011	0.38717	-0.08	0.08316	-0.068
	100%	1.40765	-0.069	0.38906	-0.57	0.08342	-0.376
$\tau_{\text{had}}\tau_{\text{had}}$ b-veto with T-CR	nominal	0.84583		0.20159		0.04299	
	50%	0.84595	-0.014	0.20163	-0.018	0.04301	-0.045
	100%	0.84595	-0.014	0.20163	-0.019	0.04301	-0.047
	m_H [GeV]	1000		1200		1500	
$\tau_{\text{had}}\tau_{\text{had}}$ b-veto	nominal	0.03015		0.01978		0.01571	
	50%	0.03026	-0.344	0.01983	-0.27	0.01575	-0.207
	100%	0.03066	-1.685	0.02005	-1.35	0.01588	-1.056
$\tau_{\text{had}}\tau_{\text{had}}$ b-veto with T-CR	nominal	0.01732		0.01145		0.0087	
	50%	0.01733	-0.016	0.01145	-0.007	0.0087	-0.004
	100%	0.01733	-0.017	0.01145	-0.007	0.0087	-0.004

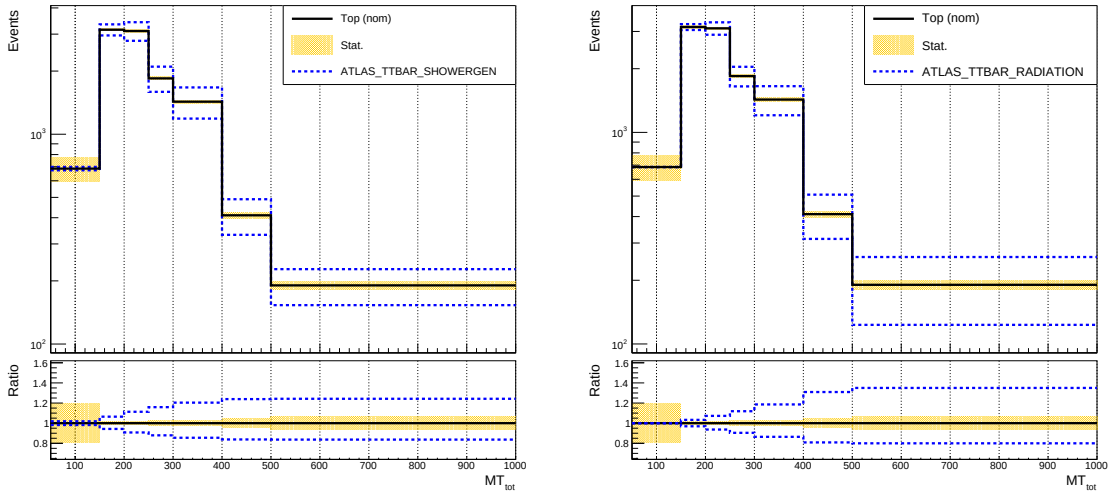

(a) **(b)**

Figure 6.17 $m_{\mathrm{T}}^{\mathrm{tot}}$ distribution of top background with uncertainties related to (a) parton shower and hard-scatter modelling, and (b) radiation modelling in the $\tau_{\mathrm{lep}}\tau_{\mathrm{had}}$ T-CR.

6.4.3 Uncertainties on signal modelling

The signal modelling uncertainties are determined for three components: the QCD scale, the tune of the generator, and the PDF set used. To estimate the uncertainties related to factorisation and renormalisation scales, the scales are varied by a factor of two in either direction, including correlating and anti-correlating the variations. These are implemented at the ME level, for aMC@NLO for $b\bar{b}\phi$ and POWHEG for ggF, and stored as event weights in the sample, to be later used to determine the uncertainty. The largest deviation in each direction of the nominal is taken as the final scale uncertainty.

To estimate the uncertainty due to PDF in ggF, weights for every PDF in `PDF4LHC15_nlo_100` [211] are generated. For $b\bar{b}\phi$ the `LHAPDF` [212] package was used to determine weights for each PDF in the `PDF4LC15_nlo_nf4_30` [211] set. To estimate uncertainties due to UE, initial-state radiation (ISR) and final-state radiation (FSR) modelling, PYTHIA 8 A14 [213] and AZNLO [214] tune variations are used for $b\bar{b}\phi$ and ggF, respectively.

A truth level selection is applied to the generated samples in order to assess the uncertainty on the signal acceptance after applying the weight variations. The uncertainty due to a particular variation is estimated by comparing the weighted number of events before or after the selection. For the $\tau_{\mathrm{had}}\tau_{\mathrm{had}}$ channel the event must have at least two $\tau_{\text{had-vis}}$ with $p_{\mathrm{T}} > 40\,\mathrm{GeV}$ with opposite sign charge. The leading $\tau_{\text{had-vis}}$ must have $p_{\mathrm{T}} > 85\,\mathrm{GeV}$ with

sub-leading $\tau_{\text{had-vis}}$ $p_{\text{T}} > 65\,\text{GeV}$. Both $\tau_{\text{had-vis}}$ candidates must be back-to-back: $\Delta\phi > 2.7$. A lepton veto is applied on the event. The single tau trigger weighting scheme is applied to emulate the running time of the lowest un-prescaled trigger. For the $\tau_{\text{lep}}\tau_{\text{had}}$ channel an event must have at least one $\tau_{\text{had-vis}}$ with $p_{\text{T}} > 25\,\text{GeV}$, and exactly one muon or one electron with $pt > 30\,\text{GeV}$. The tau lepton candidate must be back-to-back ($\Delta\phi > 2.4$), opposite charge and satisfy the m_{T} and m_{vis} selection of the signal region. Overlap removal is applied to both channels as implemented in the signal selection. Weights are applied to each event corresponding to their probability to be *b*-tagged.

None of the acceptance uncertainties discussed here caused significant shape effect on the $m_{\text{T}}^{\text{tot}}$ distribution and are considered as normalisation uncertainties only. All of the total up and down variations of the groups (scale, tune, or PDF) are summed in quadrature. The resulting up and down variations are then symmetrised. The uncertainties are determined for three representative mass points, and a conservative parameterisation is used to interpolate or extrapolate to different mass points. The resulting uncertainties are shown in Table 6.6.

Table 6.6 Acceptance uncertainties on ggF and $b\bar{b}\phi$ signal samples in percent [%]. Measured uncertainties are determined as described in the text. The uncertainties applied are parameterised in terms of the sample m_ϕ (divided by 1 GeV).

		gluon fusion production							
		b-veto				*b*-tagged			
	m_{A}	200 GeV	500 GeV	1 TeV	> 1 TeV	200 GeV	500 GeV	1 TeV	> 1 TeV
$\tau_{\text{lep}}\tau_{\text{had}}$	measured [±%]	4.22	2.21	1.48	-	15.70	7.33	7.36	-
	applied [±%]	$4.91 - 0.00343 \times m_\phi$			1.0	$17.79 - 0.0104 \times m_\phi$			7.0
	m_{A}	400 GeV	700 GeV	1 TeV	> 1 TeV	400 GeV	700 GeV	1 TeV	> 1 TeV
$\tau_{\text{had}}\tau_{\text{had}}$	measured [±%]	1.22	1.32	1.08	-	9.41	7.51	8.48	-
	applied [±%]	1.5				10			
		b-associated production							
		b-veto				*b*-tagged			
	m_{A}	200 GeV	500 GeV	1 TeV	> 1 TeV	200 GeV	500 GeV	1 TeV	> 1 TeV
$\tau_{\text{lep}}\tau_{\text{had}}$	measured [±%]	2.72	1.34	1.46	-	3.87	2.0	1.04	-
	applied [±%]	$3.04 - 0.00158 \times m_\phi$			1.4	$4.58 - 0.00354 \times m_\phi$			1.0
	m_{A}	400 GeV	700 GeV	1 TeV	> 1 TeV	400 GeV	700 GeV	1 TeV	> 1 TeV
$\tau_{\text{had}}\tau_{\text{had}}$	measured [±%]	1.70	1.30	0.79	-	2.04	1.28	0.94	-
	applied [±%]	$2.23 - 0.00133 \times m_\phi$			0.9	$2.73 - 0.00183 \times m_\phi$			0.9

6.4.4 Uncertainties on data-driven background estimations

In the $\tau_{\text{lep}}\tau_{\text{had}}$ channel, the data-driven uncertainties are described in detail in Section 6.3.1. Uncertainties which impact the multijet and W+jets fake-factors are implemented as `ATLAS_Fakes_shape_QCD` and `ATLAS_Fakes_shape_Wjets`, respectively, and are parameterised in terms of the fake-factor distributions and decorrelated for the $\tau_\mu\tau_{\text{had}}$ and $\tau_{\text{e}}\tau_{\text{had}}$ channels. The uncertainty on the r_{QCD} (`ATLAS_Fakes_shape_rQCD`) and $|\Delta\phi(\tau_1, E_{\text{T}}^{\text{miss}})|$ correction (`ATLAS_Fakes_Dphi`) are also decorrelated into $\tau_\mu\tau_{\text{had}}$ and $\tau_{\text{e}}\tau_{\text{had}}$ channels. An uncertainty related to using the b-inclusive W+jets fake-factor in the b-tagged channel (`ATLAS_Fakes_shape_WJetsBtag`) is correlated amongst the $\tau_{\text{lep}}\tau_{\text{had}}$ channels.

In the $\tau_{\text{had}}\tau_{\text{had}}$ channel, several sources of uncertainty enter in the calculation of the f_{DJ} factor, discussed in Section 6.3.2. In order to account for the statistical limitation in the DJ-FR, `QCDFF_stat` uncertainties are introduced, which are decorrelated into tau prong and p_{T} bins, in which the fake-factor is derived. The uncertainties from the detector systematic effects are fully propagated into the estimation (`QCDFF_sysmc`), but are pruned since they do not have sufficient shape effects. The additional uncertainties with respect to using the b-inclusive fake-factors being used in the b-tagged SR (`QCDFF_BTAG_syst`) are implemented. An extrapolation uncertainty from CR-1 to the SR is derived in the SS region, shown in Figure 6.18, where a 6% normalisation uncertainty (`ATLAS_QCDFF_EXTRAPO`) on multijet background is applied to cover the difference between the distributions. The uncertainties on the fake-rates (`HHFAKERATE`) are dominated by data statistics in the W-FR.

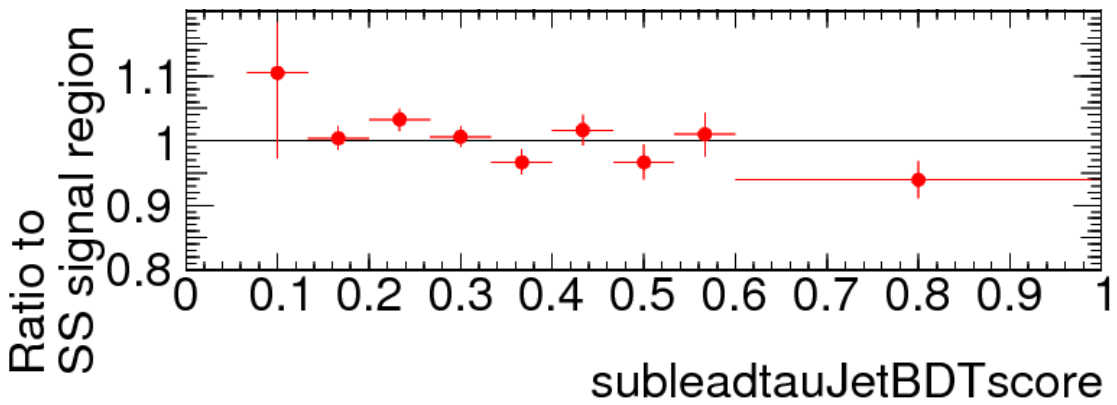

Figure 6.18 Ratio of data minus MC in the in the CR-1 over the SR as a function of the BDT score of the sub-leading tau candidate in the SS $\tau_{\text{had}}\tau_{\text{had}}$ channel [208]. The data minus MC distributions are compared for the SR and CR-1, but with the SS charge, selection. Events in the final bin fall into the numerator of the fake-factors, where a 6% difference is observed.

Table 6.7 Pre-fit uncertainty (in [%]) of NPs for the $m_{\mathrm{T}}^{\mathrm{tot}}$ distribution in the $\tau_{\mathrm{e}}\tau_{\mathrm{had}}$ b-veto SR, as they are in the final workspace after smoothing and pruning. Shown are the total normalisation uncertainty, with † representing that a shape uncertainty is also considered. The normalisation effect is pruned if the uncertainty is below 1%, while shape effects are pruned if they do not have sufficient variations in neighbouring bins.

Type	Sample NP	Z+jets [%]	DYZ [%]	Diboson [%]	Fakes [%]	Top [%]	bbH300 [%]	ggH300 [%]
Signal	ATLAS_AU_bbH300	-	-	-	-	-	±2.57	-
	ATLAS_AU_ggH300	-	-	-	-	-	-	±3.88
XS	ATLAS_LPXKFACTORALPHAS	±2.58 †	±2.56	-	-	-	-	-
	ATLAS_LPXKFACTORPDF	±3.80	±3.72	-	-	-	-	-
	ATLAS_LPXKFACTORPI	†	-	-	-	-	-	-
	ATLAS_LUMI	±3.20	±3.20	±3.20	-	±3.20	±3.20	±3.20
	ATLAS_xsec_Diboson	-	-	±6.00	-	-	-	-
	ATLAS_xsec_Top	-	-	-	-	±6.00	-	-
Data driven	ATLAS_Fakes_Dphi_QCD_eh	-	-	-	±2.45 †	-	-	-
	ATLAS_Fakes_Dphi_Wjets_eh	-	-	-	±3.15	-	-	-
	ATLAS_Fakes_shape_QCD_eh	-	-	-	±5.13 †	-	-	-
	ATLAS_Fakes_shape_Wjets_eh	-	-	-	±2.90	-	-	-
	ATLAS_Fakes_shape_rQCDehad	-	-	-	±2.00 †	-	-	-
Tau	ATLAS_TAUIDAFII	-	-	-	-	-	±3.00	-
	ATLAS_TAUIDHighPt	†	-	-	-	-	-	-
	ATLAS_TAUIDTotal	±5.87	-	±5.49	-	±5.62	±5.83	±5.86
	ATLAS_TAURECOAFII	-	-	-	-	-	±5.00	-
	ATLAS_TAURECOEleEleOLR	-	±1.83	-	-	-	-	-
	ATLAS_TAURECOHighPt	†	-	-	-	-	-	-
	ATLAS_TAURECOTauEleOLR	†	-	-	-	±1.06	±1.31	±1.27
	ATLAS_TAURECOTauEleOLRAFII	-	-	-	-	-	±2.23	-
	ATLAS_TAURECOTotal	±4.02 †	-	±3.11	-	±2.92 †	±2.52 †	±2.52
	ATLAS_TESAFII	-	-	-	-	-	±3.79 †	-
	ATLAS_TESDETECTOR	†	-	$^{+3.92}_{-2.73}$	-	$^{+3.04}_{-2.42}$	±3.14	±3.06
	ATLAS_TESINSITU	±4.43 †	-	±1.06 †	-	±1.71 †	†	-
	ATLAS_TESMODEL	±1.57	-	-	-	-	-	-
b-tagging	ATLAS_btagEffSfEigen_B_0	-	-	-	-	±8.54	±2.36	-
	ATLAS_btagEffSfEigen_B_1	-	-	-	-	±1.75 †	-	-
	ATLAS_btagEffSfEigen_B_2	-	-	-	-	±1.06	-	-
Top (excl. XS)	ATLAS_TTBAR_RADIATION	-	-	-	-	±4.81 †	-	-
	ATLAS_TTBAR_SHOWERGEN	-	-	-	-	±6.71 †	-	-
Other	ATLAS_EGRESO	-	-	-	-	-	†	-
	ATLAS_EGSCALE_ALLCORR	-	†	-	-	-	-	-
	ATLAS_JERNP1	±1.09	±1.65	±2.17	-	-	±2.31	±1.70
	ATLAS_JETNP1	±2.60 †	$^{+2.42}_{-1.91}$	-	-	$^{+2.86}_{-1.81}$	$^{+3.89}_{-1.86}$ †	±2.57
	ATLAS_METSoftTrkResoPara	-	±1.12	†	-	±1.78 †	-	±1.11 †
	ATLAS_METSoftTrkResoPerp	-	†	†	-	†	†	†
	ATLAS_METSoftTrkScale	-	±1.32	-	-	-	†	-
	ATLAS_PRW	$^{+5.17}_{-4.02}$ †	$^{+3.76}_{-2.72}$	$^{+3.12}_{-1.75}$	-	$^{+1.94}_{-1.08}$ †	†	†

Table 6.8 Pre-fit uncertainty (in [%]) of NPs for the $m_{\mathrm{T}}^{\mathrm{tot}}$ distribution in the $\tau_{\mathrm{e}}\tau_{\mathrm{had}}$ b-tagged SR, as they are in the final workspace after smoothing and pruning. Shown are the total normalisation uncertainty, with † representing that a shape uncertainty is also considered. The normalisation effect is pruned if the uncertainty is below 1%, while shape effects are pruned if they do not have sufficient variations in neighbouring bins.

Type	Sample NP	Z + jets [%]	DYZ [%]	Diboson [%]	Fakes [%]	Top [%]	bbH300 [%]	ggH300 [%]
Signal	ATLAS_AU_bbH300	-	-	-	-	-	±3.52	-
	ATLAS_AU_ggH300	-	-	-	-	-	-	±14.67
XS	ATLAS_LPXKFACTORALPHAS	±2.58	±2.45	-	-	-	-	-
	ATLAS_LPXKFACTORPDF	±3.82	±3.63	-	-	-	-	-
	ATLAS_LUMI	±3.20	±3.20	±3.20	-	±3.20	±3.20	±3.20
	ATLAS_xsec_Diboson	-	-	±6.00	-	-	-	-
	ATLAS_xsec_Top	-	-	-	-	±6.00	-	-
Data driven	ATLAS_Fakes_Dphi_QCD_eh	-	-	-	±4.67	-	-	-
	ATLAS_Fakes_Dphi_Wjets_eh	-	-	-	±1.59	-	-	-
	ATLAS_Fakes_shape_QCD_eh	-	-	-	±3.85	-	-	-
	ATLAS_Fakes_shape_WjetsBtag	-	-	-	±9.18	-	-	-
	ATLAS_Fakes_shape_Wjets_eh	-	-	-	±5.70	-	-	-
	ATLAS_Fakes_shape_rQCDehad	-	-	-	±1.52 †	-	-	-
Tau	ATLAS_TAUIDAFII	-	-	-	-	-	±3.00	-
	ATLAS_TAUIDTotal	±5.82	-	±5.55	-	±5.59	±5.82	±5.81
	ATLAS_TAURECOAFII	-	-	-	-	-	±5.00	-
	ATLAS_TAURECOEleEleOLR	-	±1.71	-	-	-	-	-
	ATLAS_TAURECOTauEleOLR	-	-	-	-	-	±1.36	±1.09
	ATLAS_TAURECOTauEleOLRAFII	-	-	-	-	-	±2.29	-
	ATLAS_TAURECOTotal	±4.13	-	±2.70	-	±2.92	±2.53	±2.39
	ATLAS_TESAFII	-	-	-	-	-	$^{+7.08}_{-5.34}$	-
	ATLAS_TESDETECTOR	-	-	-	-	$^{+3.83}_{-3.24}$ †	$^{+4.87}_{-2.81}$	-
	ATLAS_TESINSITU	$^{+8.59}_{-5.30}$	-	$^{+35.29}_{-2.28}$	-	±1.36 †	-	-
	ATLAS_TESMODEL	-	-	-	-	±1.41	-	-
b-tagging	ATLAS_btagEffSfEigen_B_0	±5.53	±4.26	±2.10	-	±2.61	±5.78	±5.39
	ATLAS_btagEffSfEigen_C_0	±9.69	±12.57	±18.26	-	-	-	±7.94
	ATLAS_btagEffSfEigen_C_1	±3.23	±4.46	±4.16	-	-	-	±2.77
	ATLAS_btagEffSfEigen_C_2	±1.49	±2.48	±1.75	-	-	-	±1.03
	ATLAS_btagEffSfEigen_Light_0	±4.20	±5.00	±8.33	-	-	-	±3.05
	ATLAS_btagEffSfEigen_Light_1	-	-	±2.00	-	-	-	-
	ATLAS_btagEffSfEigen_Light_2	-	-	±3.89	-	-	-	±1.21
	ATLAS_btagEffSfEigen_Light_3	±1.37	±1.49	±2.26	-	-	-	-
	ATLAS_btagEffSfEigen_Light_4	-	±1.05	-	-	-	-	-
Top (excl. XS)	ATLAS_TTBAR_RADIATION	-	-	-	-	±4.55 †	-	-
	ATLAS_TTBAR_SHOWERGEN	-	-	-	-	±6.68 †	-	-
Other	ATLAS_EGRESO	±1.23	-	-	-	-	-	-
	ATLAS_JERNP1	±14.99	±1.76	±19.45	-	-	±2.82	±4.43
	ATLAS_JETNP1	-	$^{+13.02}_{-2.68}$	-	-	†	-	-
	ATLAS_JETNP2	-	±1.56	-	-	-	-	-
	ATLAS_METSoftTrkResoPara	-	±2.37	-	-	†	-	±5.84
	ATLAS_METSoftTrkResoPerp	-	±1.48	±3.85	-	†	±2.23	-
	ATLAS_PRW	±5.60	-	$^{+8.31}_{-5.29}$	-	†	±2.90	$^{+15.12}_{-3.01}$

Table 6.9 Pre-fit uncertainty (in [%]) of NPs for the $m_{\mathrm{T}}^{\mathrm{tot}}$ distribution in the $\tau_\mu \tau_{\mathrm{had}}$ b-veto SR, as they are in the final workspace after smoothing and pruning. Shown are the total normalisation uncertainty, with † representing that a shape uncertainty is also considered. The normalisation effect is pruned if the uncertainty is below 1%, while shape effects are pruned if they do not have sufficient variations in neighbouring bins.

Type	Sample NP	$Z+$jets [%]	DYZ [%]	Diboson [%]	Fakes [%]	Top [%]	bbH300 [%]	ggH300 [%]
Signal	ATLAS_AU_bbH300	-	-	-	-	-	±2.57	-
	ATLAS_AU_ggH300	-	-	-	-	-	-	±3.88
XS	ATLAS_LPXKFACTORALPHAS	±2.58 †	±2.65	-	-	-	-	-
	ATLAS_LPXKFACTORPDF	±3.78	±3.86	-	-	-	-	-
	ATLAS_LPXKFACTORPI	†	-	-	-	-	-	-
	ATLAS_LUMI	±3.20	±3.20	±3.20	-	±3.20	±3.20	±3.20
	ATLAS_xsec_Diboson	-	-	±6.00	-	-	-	-
	ATLAS_xsec_Top	-	-	-	-	±6.00	-	-
Data driven	ATLAS_Fakes_Dphi_QCD_mh	-	-	-	±4.85 †	-	-	-
	ATLAS_Fakes_Dphi_Wjets_mh	-	-	-	±1.35	-	-	-
	ATLAS_Fakes_shape_QCD_mh	-	-	-	±2.42	-	-	-
	ATLAS_Fakes_shape_Wjets_mh	-	-	-	±5.62 †	-	-	-
	ATLAS_Fakes_shape_rQCDmuhad	-	-	-	±1.32 †	-	-	-
Tau	ATLAS_TAUIDAFII	-	-	-	-	-	±3.00	-
	ATLAS_TAUIDHighPt	†	-	-	-	-	-	-
	ATLAS_TAUIDTotal	±5.87	-	±5.48	-	±5.79	±5.83	±5.84
	ATLAS_TAURECOAFII	-	-	-	-	-	±4.99	-
	ATLAS_TAURECOHighPt	†	-	-	-	-	-	-
	ATLAS_TAURECOTauEleOLR	†	-	-	-	-	±1.25	±1.20
	ATLAS_TAURECOTauEleOLRAFII	-	-	-	-	-	±2.22	-
	ATLAS_TAURECOTotal	±3.94 †	-	±3.23	-	±2.92	±2.58	±2.60 †
	ATLAS_TESAFII	-	-	-	-	-	±3.71 †	-
	ATLAS_TESDETECTOR	†	-	±2.17	-	±1.48	±2.69 †	±2.40 †
	ATLAS_TESINSITU	±3.34 †	-	±1.56 †	-	±1.11	†	-
	ATLAS_TESMODEL	±1.76	-	±1.41	-	-	†	†
b-tagging	ATLAS_btagEffSfEigen_B_0	-	-	-	-	±7.89	±2.12 †	-
Top (excl. XS)	ATLAS_TTBAR_RADIATION	-	-	-	-	±1.04	-	-
	ATLAS_TTBAR_SHOWERGEN	-	-	-	-	±2.24	-	-
Other	ATLAS_JERNP1	±1.74	-	±1.70	-	±13.60	±1.14	±1.06
	ATLAS_JETNP1	±2.74 †	±2.91	†	-	±1.26	±2.69	±1.62 †
	ATLAS_METSoftTrkResoPara	-	±2.37 †	†	-	±1.23	†	†
	ATLAS_METSoftTrkResoPerp	-	±2.60 †	†	-	-	†	†
	ATLAS_METSoftTrkScale	-	$^{+2.82}_{-2.28}$	-	-	-	-	-
	ATLAS_MUONID	-	-	-	-	-	†	-
	ATLAS_MUONTRIGEFFSTAT	†	-	-	-	±1.00	±1.23	±1.27
	ATLAS_PRW	$^{+3.70}_{-2.37}$ †	-	$^{+3.51}_{-1.84}$	-	$^{+5.41}_{-4.34}$	-	$^{+3.42}_{-1.88}$

Table 6.10 Pre-fit uncertainty (in [%]) of NPs for the $m_{\mathrm{T}}^{\mathrm{tot}}$ distribution in the $\tau_\mu \tau_{\mathrm{had}}$ b-tagged SR, as they are in the final workspace after smoothing and pruning. Shown are the total normalisation uncertainty, with † representing that a shape uncertainty is also considered. The normalisation effect is pruned if the uncertainty is below 1%, while shape effects are pruned if they do not have sufficient variations in neighbouring bins.

Type	Sample NP	$Z+$jets [%]	DYZ [%]	Diboson [%]	Fakes [%]	Top [%]	bbH300 [%]	ggH300 [%]
Signal	ATLAS_AU_bbH300	-	-	-	-	-	±3.52	-
	ATLAS_AU_ggH300	-	-	-	-	-	-	±14.67
XS	ATLAS_LPXKFACTORALPHAS	±2.54	±2.67	-	-	-	-	-
	ATLAS_LPXKFACTORPDF	±3.74	±3.88	-	-	-	-	-
	ATLAS_LUMI	±3.20	±3.20	±3.20	-	±3.20	±3.20	±3.20
	ATLAS_xsec_Diboson	-	-	±6.00	-	-	-	-
	ATLAS_xsec_Top	-	-	-	-	±6.00	-	-
Data driven	ATLAS_Fakes_Dphi_QCD_mh	-	-	-	±5.74 †	-	-	-
	ATLAS_Fakes_Dphi_Wjets_mh	-	-	-	±1.24	-	-	-
	ATLAS_Fakes_shape_QCD_mh	-	-	-	±3.13 †	-	-	-
	ATLAS_Fakes_shape_WjetsBtag	-	-	-	±10.48	-	-	-
	ATLAS_Fakes_shape_Wjets_mh	-	-	-	±6.02	-	-	-
	ATLAS_Fakes_shape_rQCDmuhad	-	-	-	±1.63	-	-	-
Tau	ATLAS_TAUIDAFII	-	-	-	-	-	±2.99	-
	ATLAS_TAUIDTotal	±5.87	-	±5.84	-	±5.58	±5.83	±5.88
	ATLAS_TAURECOAFII	-	-	-	-	-	±4.99	-
	ATLAS_TAURECOTauEleOLR	-	-	±1.42	-	-	±1.21	±1.24
	ATLAS_TAURECOTauEleOLRAFII	-	-	-	-	-	±2.20	-
	ATLAS_TAURECOTotal	±3.93	-	±2.90	-	±3.08	±2.60 †	±2.47
	ATLAS_TESAFII	-	-	-	-	-	±3.87 †	-
	ATLAS_TESDETECTOR	-	-	-	†	±2.42 †	±1.83	-
	ATLAS_TESINSITU	$^{+6.06}_{-3.53}$	-	-	-	±1.58	-	-
	ATLAS_TESMODEL	$^{+5.31}_{-1.72}$	-	-	-	±1.57	-	-
b-tagging	ATLAS_btagEffSfEigen_B_0	±4.96	±3.58	±1.46	-	±2.56	±5.90 †	±1.72
	ATLAS_btagEffSfEigen_C_0	±7.90	±6.21	±13.95	-	-	-	±12.87
	ATLAS_btagEffSfEigen_C_1	±2.66	±2.43	±1.13	-	-	-	±2.67
	ATLAS_btagEffSfEigen_C_2	±1.18	±1.57	-	-	-	-	-
	ATLAS_btagEffSfEigen_Light_0	±8.49	±16.02	±14.29	-	-	-	±20.18
	ATLAS_btagEffSfEigen_Light_1	±1.60	±3.31	±3.78	-	-	-	±4.25
	ATLAS_btagEffSfEigen_Light_2	±1.24	±4.24	±5.19	-	-	-	±4.34
	ATLAS_btagEffSfEigen_Light_3	±1.15	±1.06	±4.14	-	-	-	±1.88
	ATLAS_btagEffSfEigen_Light_4	±1.26	±2.92	±1.08	-	-	-	±1.89
	ATLAS_btagEffSfextrapolation_charm	-	-	±2.07	-	-	-	-
Top (excl. XS)	ATLAS_TTBAR_RADIATION	-	-	-	†	±2.92 †	-	-
	ATLAS_TTBAR_SHOWERGEN	-	-	-	†	±4.81 †	-	-
Other	ATLAS_JERNP1	-	±4.51	±36.65	-	-	±2.13	±7.35
	ATLAS_JETNP1	±3.70	±10.72	-	-	-	±1.06	-
	ATLAS_JETNP2	$^{+2.77}_{-1.73}$	-	-	-	†	-	-
	ATLAS_METSoftTrkResoPara	±2.07	±5.89	-	-	-	-	-
	ATLAS_METSoftTrkResoPerp	±1.69	±3.04	±8.06	-	†	-	-
	ATLAS_MUONTRIGEFFSTAT	-	-	±2.00	-	±1.33	±1.31	±1.23
	ATLAS_PRW	±4.42	$^{+15.92}_{-10.54}$	-	-	-	-	$^{+9.97}_{-6.22}$

Table 6.11 Pre-fit uncertainty (in [%]) of NPs for the $m_{\mathrm{T}}^{\mathrm{tot}}$ distribution in the $\tau_{\mathrm{had}}\tau_{\mathrm{had}}$ b-veto SR, as they are in the final workspace after smoothing and pruning. Shown are the total normalisation uncertainty, with † representing that a shape uncertainty is also considered. The normalisation effect is pruned if the uncertainty is below 1%, while shape effects are pruned if they do not have sufficient variations in neighbouring bins.

Type	Sample NP	Multijet [%]	Others [%]	Top [%]	Wtaunu [%]	Ztautau [%]	bbH300 [%]	ggH300 [%]
Signal	ATLAS_AU_bbH300	-	-	-	-	-	±1.83	-
	ATLAS_AU_ggH300	-	-	-	-	-	-	±1.50
XS	ATLAS_LPXKFACTORALPHAS	-	-	-	-	±1.14	-	-
	ATLAS_LPXKFACTORPDF	-	-	-	-	±3.48 †	-	-
	ATLAS_LPXKFACTORPI	-	-	-	-	±1.38 †	-	-
	ATLAS_LUMI	-	±3.20	±3.20	±3.20	±3.20	±3.20	±3.20
	ATLAS_xsec_Top	-	-	±6.00	-	-	-	-
Data driven	ATLAS_QCDFF_EXTRAPO	±6.00	-	-	-	-	-	-
	HHFAKERATE	-	±4.39	$^{+9.89}_{-9.33}$	±7.72 †	-	-	-
	QCDFF_stat_data_1p_bin1	±2.17 †	-	-	-	-	-	-
	QCDFF_stat_data_1p_bin2	±1.73 †	-	-	-	-	-	-
	QCDFF_stat_data_1p_bin3	±1.77 †	-	-	-	-	-	-
	QCDFF_stat_data_1p_bin4	±1.93 †	-	-	-	-	-	-
	QCDFF_stat_data_1p_bin5	±1.37	-	-	-	-	-	-
	QCDFF_stat_data_3p_bin1	±1.13 †	-	-	-	-	-	-
	QCDFF_stat_data_3p_bin2	±1.24 †	-	-	-	-	-	-
	QCDFF_stat_data_3p_bin3	±1.12 †	-	-	-	-	-	-
Tau	ATLAS_TAUIDAFII	-	-	-	-	-	±5.05	-
	ATLAS_TAUIDHighPt	-	-	±1.09	-	±1.70 †	-	-
	ATLAS_TAUIDTotal	-	$^{+6.78}_{-3.82}$	$^{+8.73}_{-4.99}$	$^{+5.04}_{-2.95}$	$^{+10.46}_{-5.83}$	$^{+10.74}_{-5.98}$	$^{+10.75}_{-6.01}$
	ATLAS_TAURECOAFII	-	-	-	-	-	±10.24	-
	ATLAS_TAURECOHighPt	-	-	-	-	†	-	-
	ATLAS_TAURECOTotal	-	±2.82	±3.64	±2.22	±4.39	±4.80	±4.78
	ATLAS_TAUTRIGEFFSTATDATA2015	-	±12.64	±16.93	±7.07 †	±19.71 †	±18.84	±19.09
	ATLAS_TAUTRIGEFFSTATDATA2016	-	$^{+16.23}_{-15.70}$	$^{+21.55}_{-20.87}$	±8.56 †	$^{+25.16}_{-24.34}$ †	±22.45 †	±22.80 †
	ATLAS_TAUTRIGEFFSTATMC2015	-	±2.50	±3.45	±1.31	±3.88 †	±3.58 †	±3.68
	ATLAS_TAUTRIGEFFSTATMC2016	-	±3.82	$^{+5.26}_{-4.66}$	±2.07	$^{+5.88}_{-5.23}$ †	$^{+5.56}_{-5.02}$ †	$^{+5.69}_{-5.13}$
	ATLAS_TAUTRIGEFFSYST2015	-	±4.07	$^{+5.78}_{-5.20}$	±2.41	$^{+6.43}_{-5.83}$	$^{+7.12}_{-6.38}$	$^{+7.25}_{-6.48}$
	ATLAS_TAUTRIGEFFSYST2016	-	±3.97	±4.93	±2.08	±6.34 †	±5.72	±5.66
	ATLAS_TESAFII	-	-	-	-	-	±16.60	-
	ATLAS_TESDETECTOR	-	$^{+8.63}_{-6.44}$	±11.95	±7.16	$^{+9.61}_{-9.00}$ †	±14.13	±14.10
	ATLAS_TESINSITU	-	-	-	†	†	-	†
	ATLAS_TESMODEL	-	-	$^{+3.52}_{-1.84}$	-	†	±1.13	±1.38
b-tagging	ATLAS_btagEffSfEigen_B_0	-	-	±8.07	-	-	±2.47	-
	ATLAS_btagEffSfEigen_B_1	-	-	±1.76	-	-	-	-
Other	ATLAS_JERNP1	-	-	±2.18	-	-	±1.63	-
	ATLAS_METSoftTrkResoPerp	-	-	-	†	-	-	-
	ATLAS_PRW	-	$^{+3.50}_{-2.32}$	-	†	-	±1.13 †	†

Table 6.12 Pre-fit uncertainty (in [%]) of NPs for the $m_{\mathrm{T}}^{\mathrm{tot}}$ distribution in the $\tau_{\mathrm{had}}\tau_{\mathrm{had}}$ b-tagged SR, as they are in the final workspace after smoothing and pruning. Shown are the total normalisation uncertainty, with † representing that a shape uncertainty is also considered. The normalisation effect is pruned if the uncertainty is below 1%, while shape effects are pruned if they do not have sufficient variations in neighbouring bins.

Type	Sample NP	Multijet [%]	Others [%]	Top [%]	Wtaunu [%]	Ztautau [%]	bbH300 [%]	ggH300 [%]
Signal	ATLAS_AU_bbH300	-	-	-	-	-	±2.18	-
	ATLAS_AU_ggH300	-	-	-	-	-	-	±10.00
XS	ATLAS_LPXKFACTORALPHAS	-	-	-	-	±1.19	-	-
	ATLAS_LPXKFACTORPDF	-	-	-	-	±3.53	-	-
	ATLAS_LPXKFACTORPI	-	-	-	-	±1.33	-	-
	ATLAS_LUMI	-	±3.20	±3.20	±3.20	±3.20	±3.20	±3.20
	ATLAS_xsec_Top	-	-	±6.00	-	-	-	-
Data driven	ATLAS_QCDFF_EXTRAPO	±6.00	-	-	-	-	-	-
	HHFAKERATE	-	±2.75	±9.67	±7.16	-	-	-
	QCDFF_BTAG_syst	$^{+40.53}_{-16.07}$ †	-	-	-	-	-	-
	QCDFF_stat_data_1p_bin1	±2.35 †	-	-	-	-	-	-
	QCDFF_stat_data_1p_bin2	±1.73 †	-	-	-	-	-	-
	QCDFF_stat_data_1p_bin3	±1.58	-	-	-	-	-	-
	QCDFF_stat_data_1p_bin4	±1.84	-	-	-	-	-	-
	QCDFF_stat_data_1p_bin5	±1.36	-	-	-	-	-	-
	QCDFF_stat_data_3p_bin1	±1.30 †	-	-	-	-	-	-
	QCDFF_stat_data_3p_bin2	±1.17	-	-	-	-	-	-
	QCDFF_stat_data_3p_bin3	±1.06	-	-	-	-	-	-
Tau	ATLAS_TAUIDAFII	-	-	-	-	-	±5.05	-
	ATLAS_TAUIDHighPt	-	±5.26	±1.10	-	±1.76	-	-
	ATLAS_TAUIDTotal	-	$^{+8.72}_{-5.16}$	$^{+8.70}_{-4.95}$	$^{+5.18}_{-3.02}$	$^{+10.27}_{-5.78}$	$^{+10.74}_{-5.99}$	$^{+10.74}_{-5.98}$
	ATLAS_TAURECOAFII	-	-	-	-	-	±10.23	-
	ATLAS_TAURECOHighPt	-	±3.08	-	-	-	-	-
	ATLAS_TAURECOTotal	-	±3.94	±3.65	±2.23	±4.37	±4.74	±4.82
	ATLAS_TAUTRIGEFFSTATDATA2015	-	±17.18	±16.68	±10.77	±18.81	±19.35	±19.43
	ATLAS_TAUTRIGEFFSTATDATA2016	-	$^{+24.01}_{-22.64}$	$^{+21.36}_{-20.69}$	±13.60	$^{+23.69}_{-23.04}$	$^{+23.81}_{-23.30}$	±23.85
	ATLAS_TAUTRIGEFFSTATMC2015	-	±3.54	±3.33	±2.16	±3.69	±3.73	±3.65
	ATLAS_TAUTRIGEFFSTATMC2016	-	$^{+4.80}_{-4.30}$	$^{+5.10}_{-4.53}$	±3.22	$^{+5.65}_{-5.05}$	$^{+5.77}_{-5.17}$	$^{+5.88}_{-5.25}$
	ATLAS_TAUTRIGEFFSYST2015	-	±4.95	$^{+5.46}_{-4.93}$	±3.69	$^{+6.35}_{-5.74}$	$^{+6.85}_{-6.17}$	$^{+6.51}_{-5.88}$
	ATLAS_TAUTRIGEFFSYST2016	-	$^{+7.61}_{-6.90}$	±5.07	±3.40	±5.87	±5.96	±5.43
	ATLAS_TESAFII	-	-	-	-	-	$^{+18.61}_{-16.22}$	-
	ATLAS_TESDETECTOR	-	-	±10.73	±6.09	±6.38	±14.14	±11.61
	ATLAS_TESINSITU	-	-	-	-	-	†	-
	ATLAS_TESMODEL	-	-	-	±1.10	-	$^{+2.57}_{-1.77}$	±1.28
b-tagging	ATLAS_btagEffSfEigen_B_0	-	-	±2.49	±3.31	±3.81	±5.74	±4.38
	ATLAS_btagEffSfEigen_C_0	-	±4.31	-	$^{+7.49}_{-6.65}$	±8.96	-	±12.20
	ATLAS_btagEffSfEigen_C_1	-	-	-	±2.35	±1.86	-	±3.10
	ATLAS_btagEffSfEigen_Light_0	-	±22.76	-	±7.03	±9.94	-	±3.33
	ATLAS_btagEffSfEigen_Light_1	-	±2.55	-	±1.10	±1.83	-	-
	ATLAS_btagEffSfEigen_Light_2	-	±12.78	-	-	-	-	-
	ATLAS_btagEffSfEigen_Light_3	-	±8.86	-	±1.81	±1.30	-	-
	ATLAS_btagEffSfEigen_Light_4	-	±3.42	-	-	-	-	-
	ATLAS_btagEffSfextrapolation_charm	-	-	-	-	±1.11	-	-
Top (excl. XS)	ATLAS_TTBAR_RADIATION	-	-	$^{+22.42}_{-21.39}$	-	-	-	-
	ATLAS_TTBAR_SHOWERGEN	-	-	$^{+87.52}_{-45.58}$	-	-	-	-
Other	ATLAS_JERNP1	-	-	-	±3.50	-	±2.44	±8.55
	ATLAS_PRW	-	$^{+15.39}_{-1.25}$	-	-	$^{+3.41}_{-1.86}$	-	$^{+16.34}_{-3.68}$

6.5 Results

6.5.1 Analysis of the statistical model

The statistical model for the di-tau analysis is based on a binned likelihood function with a parameter of interest (POI) μ which scales the signal strength. Uncertainties in the model are implemented as nuisance parameters (NPs) in the function, the set of which is described in the previous section. More precisely, μ scales the combination of $b\bar{b}\phi$ and ggF signal histograms, which have each been normalised to represent the Higgs production with a cross-section of 1 pb. Normalisation factors `Norm_ggH` and `Norm_bbH` are applied to ggF and $b\bar{b}\phi$ histograms, respectively, such that there respective sum $\texttt{Norm\_ggH} + \texttt{Norm\_bbH} = 1$.

The combined statistical model consists of six signal regions (SRs): b-veto and b-tagged for each $\tau_e\tau_{had}$, $\tau_\mu\tau_{had}$ and $\tau_{had}\tau_{had}$; and two control regions (CRs): CR-T in the $\tau_e\tau_{had}$ and $\tau_\mu\tau_{had}$ channels. All NPs are fully correlated between regions unless otherwise stated in Section 6.4. The likelihood functions can be defined independently in each region, as well as in several combinations, in order to test the modelling in the different channels, as well as decouple the sensitivity from the different channels on the final result. The fits studied here include the CR-T only fit, the $\tau_{had}\tau_{had}$ only fit, the fit with CR-T and the $\tau_{lep}\tau_{had}$ region combined ($\tau_{lep}\tau_{had}$ + CR-T), and the fit with all regions included (CR-T, $\tau_{lep}\tau_{had}$ and $\tau_{had}\tau_{had}$), referred to as the *combined* fit. In order to test the likelihood model on the background-only hypothesis, conditional $\mu = 0$ fits are performed to both the data and Asimov (generated with $\mu = 0$) datasets. Figures 6.19 and 6.20 shows the NP pulls (see Section 5.5.2) for several fits to Asimov and observed datasets, respectively, in order of most constrained uncertainties. Figure 6.21 shows the correlations of sets of NPs for the combined fit to the observed data, where only correlations greater than 25% are plotted. Additional correlation plots and the corresponding correlation plots for the Asimov data fits, which show very similar correlations, and are documented in Figures B.1 and B.2 of Appendix B.1. The corresponding fit and correlation plots where the $\tau_{lep}\tau_{had}$ and $\tau_{had}\tau_{had}$ channels are further split into b-tagged and b-veto fits are shown in Appendix B.1. The subsequent discussions will make reference to these plots as needed.

6.5.1.1 Fit in the top control region

The CR-T is pure in $t\bar{t}$ events, and designed to constrain NPs which are large for this background. Table 6.13 shows the pre-fit and post-fit yields and uncertainties in the CR-T ($\tau_\mu\tau_{had}$+$\tau_e\tau_{had}$) only fit. It shows that CR-T is $\sim 89\%$ (86%) pure pre-fit (post-fit) in $t\bar{t}$ and

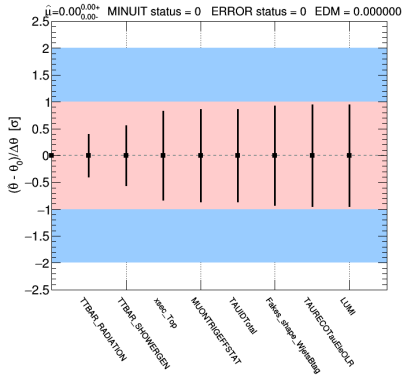

(a) CR-T

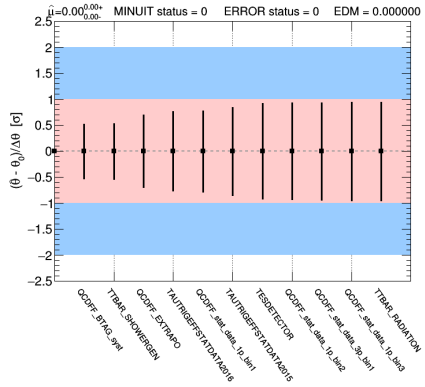

(b) $\tau_{\text{had}}\tau_{\text{had}}$

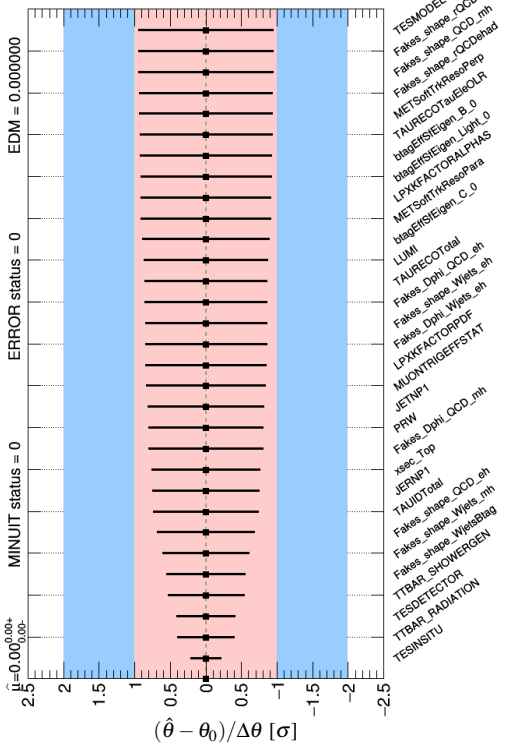

(c) $\tau_{\text{lep}}\tau_{\text{had}}$ + CR-T

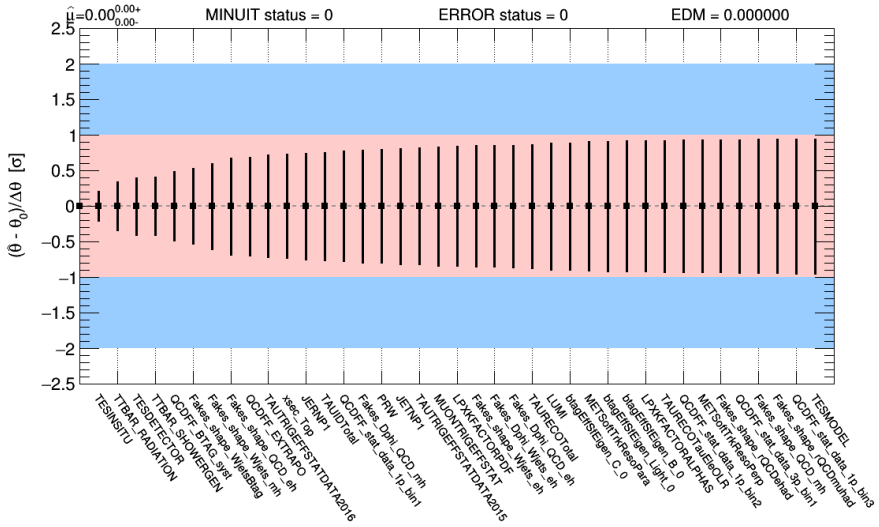

(d) combined

Figure 6.19 Nuisance parameter pulls for fits in different di-tau regions to the Asimov ($\mu = 0$) dataset. NPs are ordered in terms of the amount by which they are constrain. Pink (blue) bands show the area within 1σ (2σ) of the nominal.

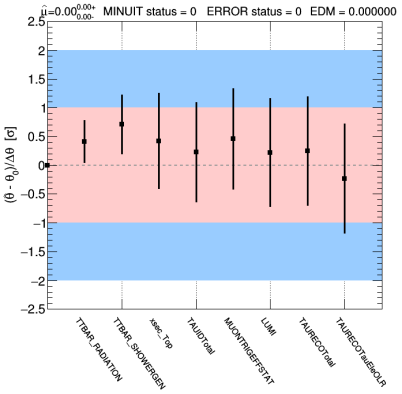

(a) CR-T

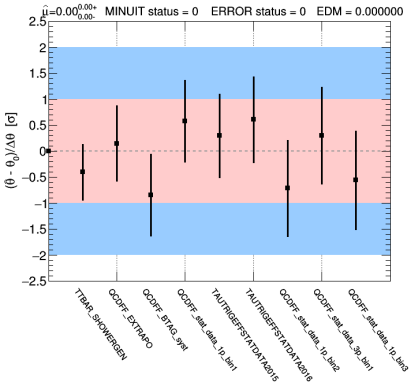

(b) $\tau_{\text{had}}\tau_{\text{had}}$

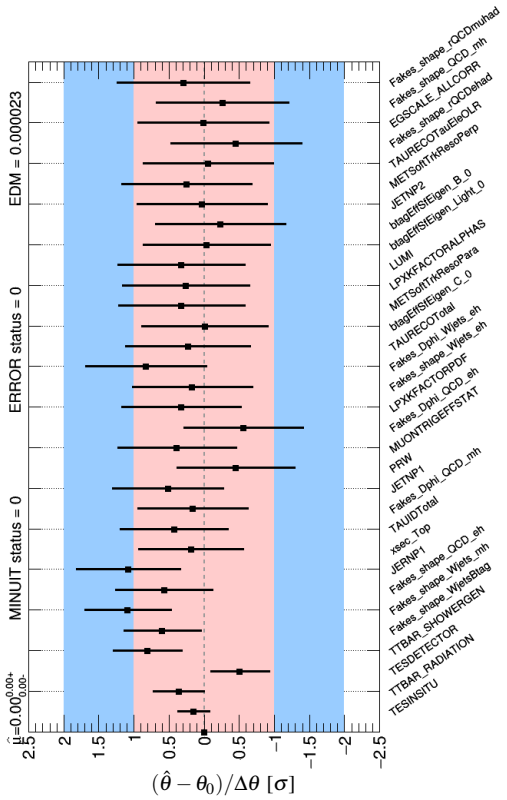

(c) $\tau_{\text{lep}}\tau_{\text{had}}$ + CR-T

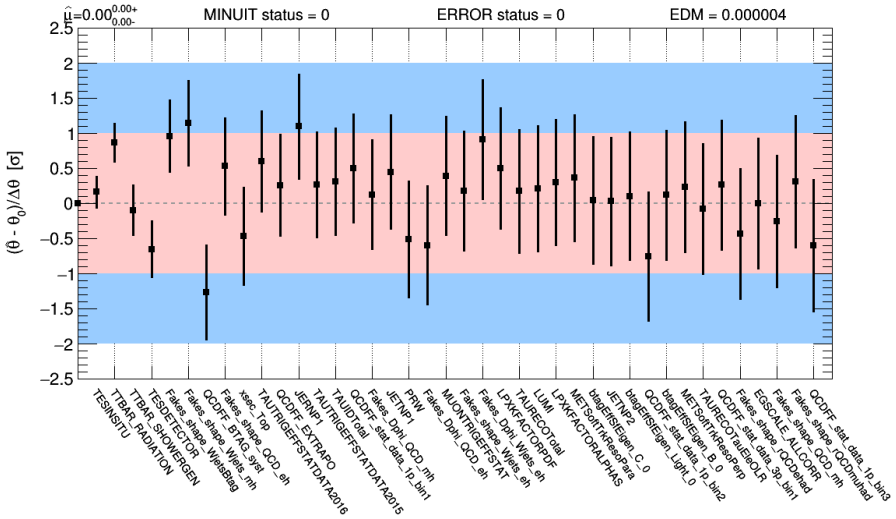

(d) combined

Figure 6.20 Nuisance parameter pulls for fits in different di-tau regions to the observed dataset. NPs are ordered in terms of the amount by which they are constrain. Pink (blue) bands show the area within 1σ (2σ) of the nominal.

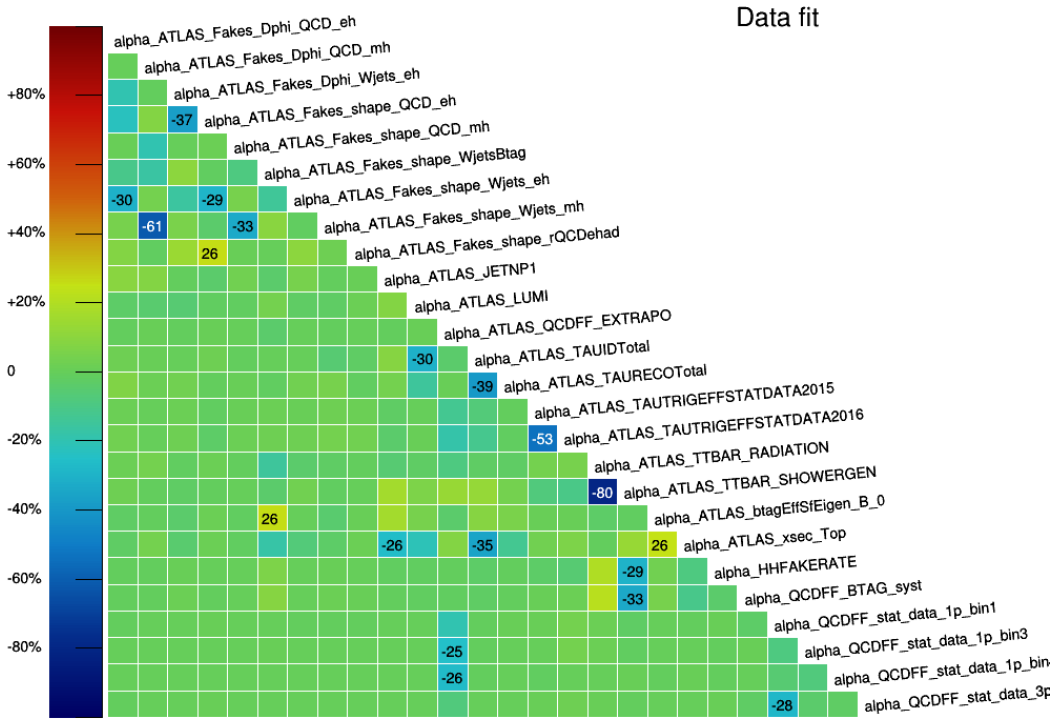

(a) Data fit, combined

Figure 6.21 Nuisance parameter correlations for fits in the combined di-tau regions to the observed dataset. Only pairs of NPs with a correlation greater that 25% are shown. Correlations for additional regions can be found in Figure B.1.

single top-quark contributions. Additionally, the total uncertainty on the top backgrounds is constrained from $\sim 16\%$ to $\sim 2\%$. Figures 6.19 (a) and 6.20 (a) show the pulls from the fit to Asimov data and observed data, respectively, with only the CR-T included. The $t\bar{t}$ radiation, showering and generator NPs are shown to be constrained to around 40% of their nominal uncertainty, and are found to be highly anti-correlated ($\sim 85\%$). This behaviour is expected in the CR-T due to the large fraction of true $\tau_{\text{had-vis}}$ background from $t\bar{t}$. To a lesser degree, uncertainties related to the $t\bar{t}$ normalisation, tau reconstruction and `ATLAS_Fakes_shape_Wjets_Btag`, which in CR-T is used to correct the jet $\rightarrow \tau_{\text{had-vis}}$ fakes normalisation, are also constrained. These NPs are pulled in the fit to data in order to correct for normalisation and shape in the $m_{\text{T}}^{\text{tot}}$ distribution. Figure 6.22 shows the post-fit plots for the $\tau_{\text{e}}\tau_{\text{had}}$ and $\tau_{\mu}\tau_{\text{had}}$ channels in CR-T, where the total pre-fit distributions are shown in red. The total statistical and post-fit uncertainties are also shown. Both channels show good modelling post-fit. Comparing the pre-fit and post-fit histograms to data shows

that the uncertainties on the top background are used to correct normalisation and shape mis-modelling in the high $m_{\mathrm{T}}^{\mathrm{tot}}$ bins. Uncertainties in the modelling of the fakes background are used in the low $m_{\mathrm{T}}^{\mathrm{tot}}$ bins (specifically the 2nd and 3rd bins) where this background can correct any residual mis-modelling. In particular, `ATLAS_Fakes_shape_Wjets_Btag`, which is treated as a normalisation uncertainty on the fake background of approximately 10% (shown in Table B.1), is pulled up by 1σ of its nominal value. This corresponds to the $\sim 10\%$ increase in the fakes background seen post-fit.

Table 6.13 Pre-fit and post-fit event yields and total uncertainties in CR-T. Post-fit results quoted are with regards to the CR-T only, background-only ($\mu = 0$), fit to data.

CR-T	Events in $\tau_\mu\tau_{\mathrm{had}}$				Events in $\tau_{\mathrm{e}}\tau_{\mathrm{had}}$			
Sample	Pre-fit		Post-fit		Pre-fit		Post-fit	
Diboson	15.01	$\pm$ 4.25	15.52	$\pm$ 4.21	14.55	$\pm$ 3.20	14.80	$\pm$ 3.11
Jet $\to \tau$ fake	699.08	$\pm$ 99.25	776.01	$\pm$ 92.66	640.93	$\pm$ 83.77	759.78	$\pm$ 81.72
$Z/\gamma^* \to ll$	1.80	$\pm$ 0.67	1.78	$\pm$ 0.65	3.28	$\pm$ 1.78	3.30	$\pm$ 1.80
$Z/\gamma^* \to \tau\tau$	11.34	$\pm$ 4.40	11.27	$\pm$ 4.01	4.15	$\pm$ 0.99	4.28	$\pm$ 0.96
Top	5594.69	$\pm$ 894.94	5371.44	$\pm$ 115.03	5221.88	$\pm$ 917.88	4881.86	$\pm$ 98.38
Total	6321.92	$\pm$ 880.55	6176.01	$\pm$ 73.16	5884.79	$\pm$ 899.50	5664.01	$\pm$ 68.46
Data	6205 $\pm$ 78.77				5653 $\pm$ 75.19			

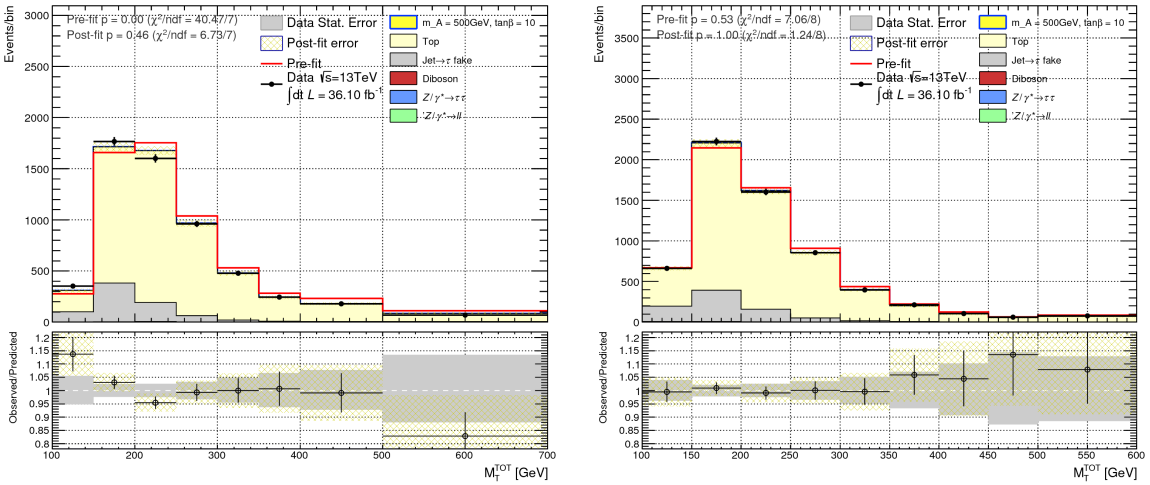

(a) $\tau_{\mathrm{e}}\tau_{\mathrm{had}}$ CR-T

(b) $\tau_\mu\tau_{\mathrm{had}}$ CR-T

Figure 6.22 Post-fit $m_{\mathrm{T}}^{\mathrm{tot}}$ distributions for the combined $\tau_{\mathrm{had}}\tau_{\mathrm{had}}$ + $\tau_{\mathrm{lep}}\tau_{\mathrm{had}}$ conditional ($\mu = 0$) background-only fit in the (a) $\tau_{\mathrm{e}}\tau_{\mathrm{had}}$ and (b) $\tau_\mu\tau_{\mathrm{had}}$ CR-T. The pre-fit histogram is shown in red and contains the total pre-fit background-only.

6.5.1.2 Combined fit results

A combined fit with all the SRs and the CR-T is used to extract the final result. A conditional fit with $\mu = 0$ is performed to assess the compatibility of the SM background modelling to the data. Table 6.14 shows the pre-fit and post-fit yield and total uncertainties for different samples in the $\tau_{\text{had}}\tau_{\text{had}}$ channel after the combined fit. Figure 6.23 shows the corresponding post-fit plot for the combined background-only fit in the $\tau_{\text{had}}\tau_{\text{had}}$ channel, with the total post-fit uncertainties propagated, and the pre-fit distributions shown by the red histogram. In the *b*-tagged $\tau_{\text{had}}\tau_{\text{had}}$ region the largest contributions are from multijet and top backgrounds with real $\tau_{\text{had-vis}}$. Due to the lack of statistics, this channel does not have large constraining power, and only the `QCDFF_BTAG_syst` (multijet) and `TTBAR_SHOWERGEN` (top background) are observed to be significantly constrained in the *b*-tagged $\tau_{\text{had}}\tau_{\text{had}}$ only fit (Figures B.3 (a) and (b)). The NPs are pulled to correct the over-estimation of the multijet background pre-fit, as well as some shape mis-modelling. The top related background is increased by $\sim 20\%$ by pulling the `TTBAR_SHOWERGEN` NP by[51] -0.07σ. The corresponding `TTBAR_SHOWERGEN` value in the combined fit is close to this, -0.1σ, suggesting that `TTBAR_SHOWERGEN` is still primarily correcting the top modelling in this region.

In the *b*-veto $\tau_{\text{had}}\tau_{\text{had}}$ channel the largest contributions are from the multijet and $Z/\gamma^* \to \tau\tau$ backgrounds. The pre-fit modelling is in general good, although the total normalisation uncertainty is initially large, on the order of 10%. This is reduced to 2% post-fit, predominantly though the constraint of several multijet fake-factor NPs which are shown to be constrained in the pull plots in Figures 6.19 (b) and 6.20 (b), and correct both the shape and normalisation mis-modelling in multijet. They are found to have some 25% correlation amongst themselves. Also constrained are single tau trigger NPs which have large initial uncertainties on the $Z/\gamma^* \to \tau\tau$ MC ($\sim 24\%$) and which affect both shape and normalisation of this sample. These NPs are $\sim 30\%$ correlated among themselves, and are both found to be pulled in the combined fit. The $\tau_{\text{had}}\tau_{\text{had}}$ *b*-veto channel is observed to have a slight deficit in data in the $m_{\text{T}}^{\text{tot}}$ range of 200–300 GeV, directly followed by a small excess in the range of 300–400 GeV range. The excess of data in these bins is partly corrected by the increase in the $Z/\gamma^* \to \tau\tau$ backgrounds by pulling tau trigger and reconstruction NPs. However, some residual mis-modelling remains, which will translate to stronger than expected cross-section limits on ggF production for the 200 GeV and 250 GeV mass points, and weaker limits at [52] around 500GeV. In the hMSSM parameter space this results in a reduced exclusion limit at

[51] The sign of the pulls are arbitrary since the direction of the uncertainties are not always indicative of the effect on the normalisation.

[52] The mass of the reconstructed boson in $m_{\text{T}}^{\text{tot}}$ is systematically lower than its true value.

Table 6.14 Pre-fit and post-fit event yields and total uncertainties in the $\tau_{\text{had}}\tau_{\text{had}}$ channel. Post-fit results quoted are with regards to the combined background-only ($\mu = 0$) fit to data.

		Events in b-veto		Events in b-tagging	
Channel	Process	pre-fit	post-fit	pre-fit	post-fit
$\tau_{\text{had}}\tau_{\text{had}}$	Multijet	3040 ± 240	3040 ± 90	106 ± 32	85 ± 10
	$Z/\gamma^* \to \tau\tau$	610 ± 230	770 ± 80	7.5 ± 2.9	8.6 ± 1.3
	$W(\to \tau\nu)$+jets	178 ± 31	182 ± 15	4.0 ± 1.0	4.1 ± 0.5
	$t\bar{t}$ and single top-quark	26 ± 9	29 ± 4	60 ± 50	74 ± 15
	Others	25 ± 6	27.4 ± 2.1	1.0 ± 0.5	1.1 ± 0.4
	SM Total	3900 ± 400	4050 ± 70	180 ± 60	173 ± 16
	Data	4059		154	

around $\tan\beta = 10$ and $m_A = 500$ GeV. When scaling the signal cross-section to the respective value at hMSSM $\tan\beta = 10$ and $m_A = 500$ GeV, the unconditional fit corresponds to a $\hat{\mu} = 1.02^{+1.10}_{-0.75}$, consistent with the signal hypothesis. It is however worth noting that the same signal hypothesis has a $\hat{\mu} = 0.58^{+0.71}_{-0.41}$ in the combined $\tau_{\text{had}}\tau_{\text{had}}$ fit, and a $\hat{\mu} = -0.07^{+0.33}_{-0.30}$ in the final combined fit. Furthermore, the merging of bins in the $m_{\text{T}}^{\text{tot}}$ range of 200–400 GeV was tested and found to eliminate the mis-modelling due to the down and up fluctuations in data cancelling each other.

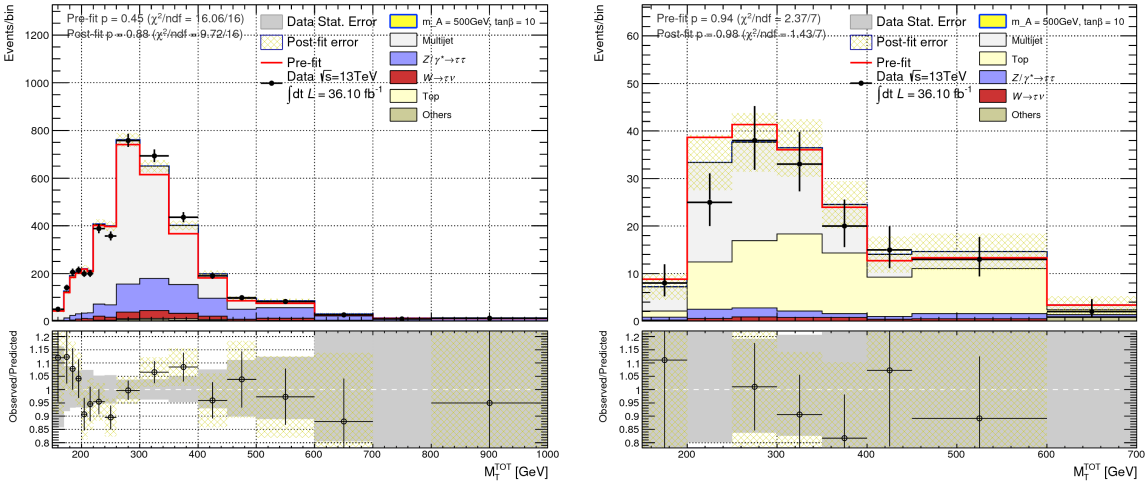

(a) $\tau_{\text{had}}\tau_{\text{had}}$ b-veto **(b)** $\tau_{\text{had}}\tau_{\text{had}}$ b-tagged

Figure 6.23 Post-fit $m_{\text{T}}^{\text{tot}}$ distributions for the combined $\tau_{\text{had}}\tau_{\text{had}}$ + $\tau_{\text{lep}}\tau_{\text{had}}$ conditional ($\mu = 0$) background-only fit for the four $\tau_{\text{had}}\tau_{\text{had}}$ SRs. The pre-fit histogram is shown in red and contains the total pre-fit background-only.

Table 6.15 shows the pre-fit and post-fit yield and total uncertainties for different samples in the $\tau_{\text{lep}}\tau_{\text{had}}$ channel ($\tau_{\text{e}}\tau_{\text{had}}$+$\tau_{\mu}\tau_{\text{had}}$) after the combined fit. Figure 6.24 shows the corresponding post-fit plots in each of the four regions. In both the $\tau_{\text{e}}\tau_{\text{had}}$ and $\tau_{\mu}\tau_{\text{had}}$ distributions, the pre-fit histogram is found to be below the data in the region at low $m_{\text{T}}^{\text{tot}}$. In this region there are considerable contributions from $t\bar{t}$, $Z/\gamma^{*} \to \tau\tau$, and the fakes backgrounds. Both the $Z/\gamma^{*} \to \tau\tau$ and the fakes background contributions are increased to compensate for the difference. The top NPs are predominantly constrained in CR-T, in which the $t\bar{t}$ contribution was reduced. Therefore they are not used to correct for the excess in data in the $\tau_{\text{lep}}\tau_{\text{had}}$ channel. The most constrained NPs in the b-tagged region are related to the $t\bar{t}$ modelling, TES and the W+jets fake-factors. The post-fit modelling of the background-only fits are shown to be in good agreement with the data. In the b-veto region there is a considerable contribution from Z/γ^{*}+jets and fakes background. The pre-fit modelling is in general already shown to be good in both $\tau_{\text{e}}\tau_{\text{had}}$ and $\tau_{\mu}\tau_{\text{had}}$. After performing the combined fit, all background contributions are increased. The uncertainties on $Z/\gamma^{*} \to \tau\tau$ are considerably constrained, from $\sim 12\%$ to $\sim 2\%$. The largest constraint is on the `ATLAS_TES_INSITU` NP which is used to fix both the shape and normalisation of the $Z/\gamma^{*} \to \tau\tau$ background. The reason for the large constraint of this NP is related to it being applied only to $\tau_{\text{had-vis}}$ candidates with $p_{\text{T}} < 70$ GeV. As such, the *in situ* component of the TES uncertainty only impacts the low $m_{\text{T}}^{\text{tot}}$ region, which is relatively pure in $Z/\gamma^{*} \to \tau\tau$ events. In particular, it is found to constrain the shape of the $Z/\gamma^{*} \to \tau\tau$ distribution, as it is not constrained when applied as a normalisation uncertainty only.

Table 6.15 Pre-fit and post-fit event yields and total errors in the $\tau_{\text{lep}}\tau_{\text{had}}$ channel. Post-fit results quoted are with regards to the combined background-only ($\mu = 0$) fit to data.

		Events in b-veto		Events in b-tagging	
Channel	Process	pre-fit	post-fit	pre-fit	post-fit
$\tau_{\text{lep}}\tau_{\text{had}}$	$Z/\gamma^{*} \to \tau\tau$	$92\,000 \pm 11\,000$	$96\,400 \pm 1600$	670 ± 140	690 ± 70
	Di-boson	880 ± 100	920 ± 70	6.3 ± 1.7	6.5 ± 1.4
	$t\bar{t}$ and single top-quark	1050 ± 170	1090 ± 130	2800 ± 400	2680 ± 80
	Jet $\to \tau$ fake	$83\,000 \pm 5000$	$88\,800 \pm 1700$	3000 ± 400	3390 ± 170
	$Z/\gamma^{*} \to ll$	$15\,800 \pm 1200$	$16\,200 \pm 700$	86 ± 21	89 ± 16
	SM Total	$193\,000 \pm 13\,000$	$203\,400 \pm 1200$	6500 ± 600	6850 ± 120
	Data	203 365		6843	

The final post-fit plots used in the analysis are shown in Figure B.8 in the $\tau_{\text{had}}\tau_{\text{had}}$ and $\tau_{\text{lep}}\tau_{\text{had}}$ channels, where the $\tau_{\text{e}}\tau_{\text{had}}$ and $\tau_{\mu}\tau_{\text{had}}$ channels have been merged into $\tau_{\text{lep}}\tau_{\text{had}}$ distributions. The plot for the CR-T distribution can be found in Figure B.4. The binning has undergone some minor modifications needed to combine the distributions. The combined prediction for A and H bosons with masses of 300, 500 and 800 GeV at $\tan\beta = 10$ in the

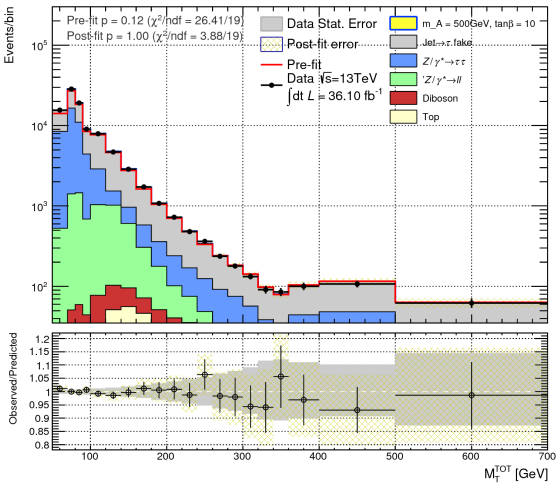

(a) $\tau_e\tau_{had}$ b-veto

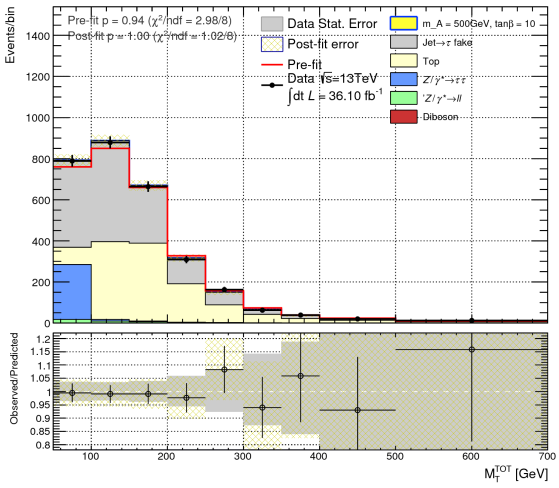

(b) $\tau_e\tau_{had}$ b-tagged

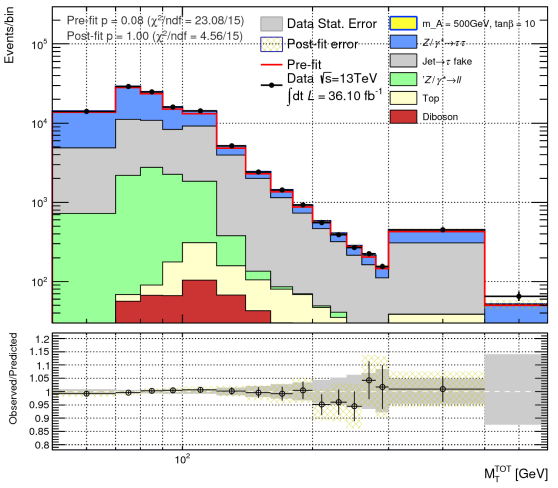

(c) $\tau_\mu\tau_{had}$ b-veto

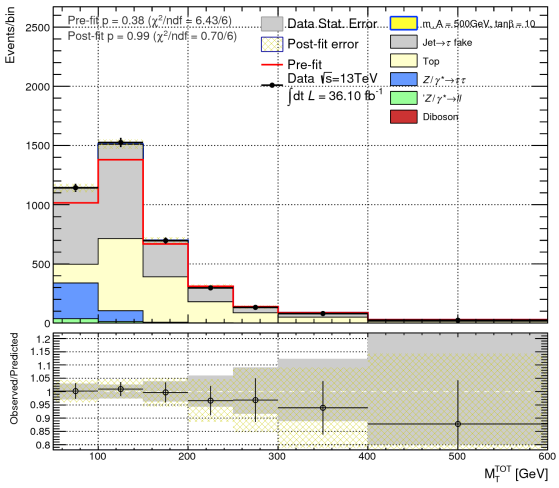

(d) $\tau_\mu\tau_{had}$ b-tagged

Figure 6.24 Post-fit m_T^{tot} distributions for the combined $\tau_{had}\tau_{had}$ + $\tau_{lep}\tau_{had}$ conditional ($\mu = 0$) background-only fit for the four $\tau_{lep}\tau_{had}$ SRs. The pre-fit histogram is shown in red and contains the total pre-fit background-only.

hMSSM scenario are superimposed. The statistical significance per-bin in the data with respect to the model and post-fit uncertainties is evaluated as described in Ref. [215], with the expected significance from the signals also shown. The data in each bin is found within the 2σ significance band. The post-fit plots are also evaluated for other representative distributions, shown in Appendix B.2.

6.5.2 Cross-section limits

The data is found to be in good agreement with the background-only hypothesis post-fit. Exclusion limits on the signal cross-section are set using the frequentist CLs method described in Section 5.2.2. They are calculated using the test statistic $\tilde{q}_\mu$ under the asymptotic approximation described in Section 5.3. The limits are calculated for two model-independent scenarios: a gluon-fusion or b-associated produced scalar resonance decaying to a pair of tau leptions. For the limits on gluon-fusion, the `Norm_ggH` normalisation factor is set to unity, while that of `Norm_bbH` is set to zero, and vice versa for the b-associated limits. The 95% CL upper limit on the scalar boson production times branching ratio to $\tau\tau$ is shown in Figure 6.26, for both $\tau_{\text{lep}}\tau_{\text{had}}$ and $\tau_{\text{had}}\tau_{\text{had}}$. The observed cross-section limits are shown for several mass points, with the median, 1σ and 2σ expected limits determined from fits to Asimov data. The median expected limits that are placed when the channels are split into b-tagged and b-veto categories are also shown. Comparisons to the respective expected limits from Ref. [216] are overlaid, where the shaded area shows the direction of the exclusion. In both the $\tau_{\text{had}}\tau_{\text{had}}$ and $\tau_{\text{lep}}\tau_{\text{had}}$ gluon-fusion limits, the b-tagged channel provides a negligible contribution to the total limit. The $\tau_{\text{had}}\tau_{\text{had}}$ cross-section limit is observed to be weaker than expected, and is outside the 2σ confidence interval for the 400 GeV mass point. This is caused by the slight excess observed in the b-veto $\tau_{\text{had}}\tau_{\text{had}}$ $m_{\text{T}}^{\text{tot}}$ distribution in the two bins between 300–400 GeV, as shown in Figure 6.23 (a). The observed limit is also stronger than expected for the 250 GeV mass point, attributed to the over-estimation of background in the bins between 200–300 GeV. Both effects are removed if the bins between 300–500 GeV are merged. Furthermore, when combined with the $\tau_{\text{lep}}\tau_{\text{had}}$ channel, the observed limits are within 2σ of the expectation. For the b-associated limits, the b-tagged region is found to provide competitive limits, at the level of, or stronger than, those from the b-veto channel. For the $\tau_{\text{had}}\tau_{\text{had}}$ channel the contribution from the b-veto channel still results in a stronger limit outside 2σ of the expected limit at the 250 GeV mass point, although the effect is reduced. The observed $\tau_{\text{lep}}\tau_{\text{had}}$ limits are all within the 2σ of the expected.

The combined cross-section limits in gluon-fusion and b-associated production are shown in Figure 6.27 and are found to be in the range 0.78–0.0058 pb (0.70–0.0037 pb) for

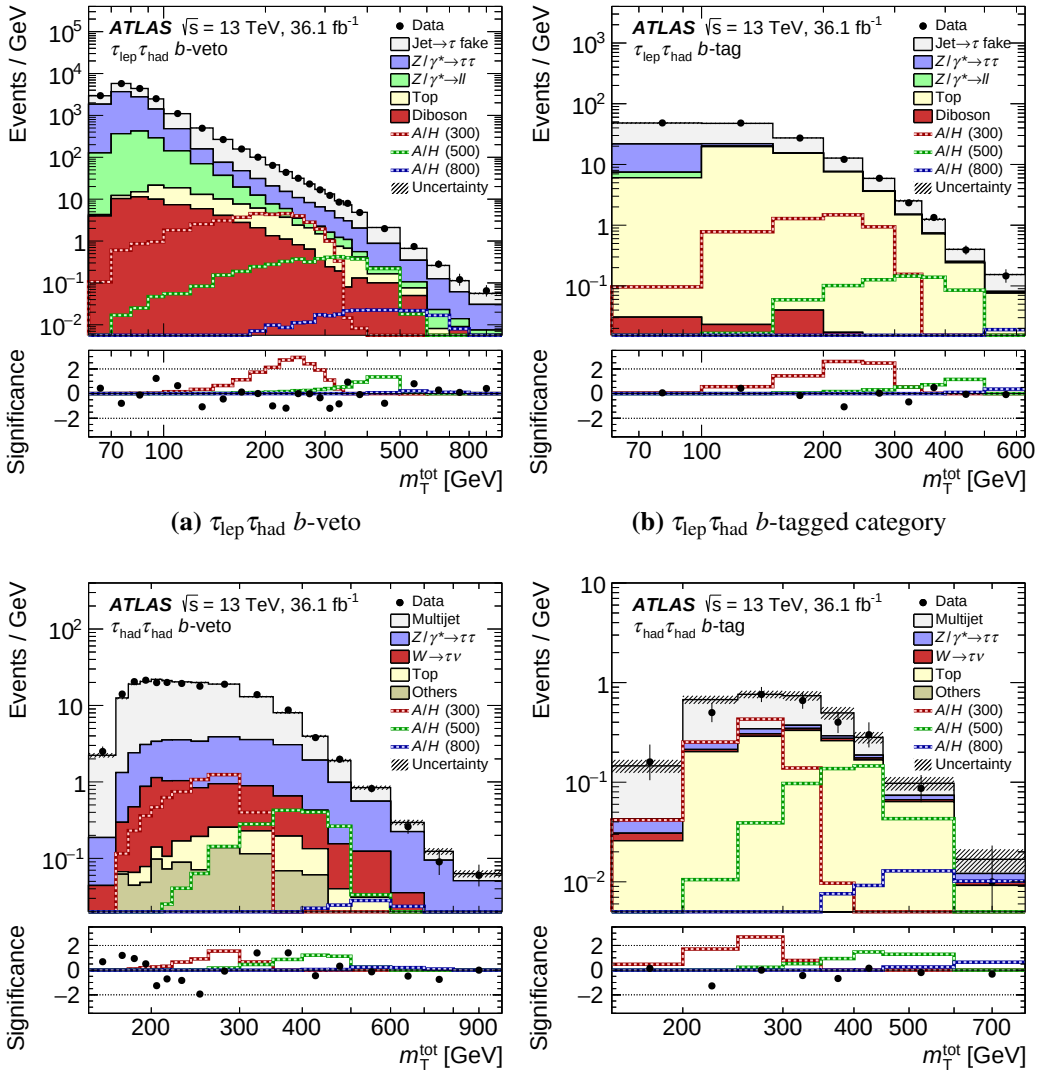

(a) $\tau_{\text{lep}}\tau_{\text{had}}$ b-veto **(b)** $\tau_{\text{lep}}\tau_{\text{had}}$ b-tagged category

(c) $\tau_{\text{had}}\tau_{\text{had}}$ b-veto category **(d)** $\tau_{\text{had}}\tau_{\text{had}}$ b-tagged category

Figure 6.25 Final post-fit distributions of $m_{\text{T}}^{\text{tot}}$ for the combined fit in the $\tau_{\text{lep}}\tau_{\text{had}}$ and $\tau_{\text{had}}\tau_{\text{had}}$ for b-tagged and b-veto categories [1]. Signal histograms are normalised to their respective cross-sections from $\tan\beta = 10$ in the hMSSM scenario. Shown are the per-bin statistical significance calculated as recommended in Ref. [215].

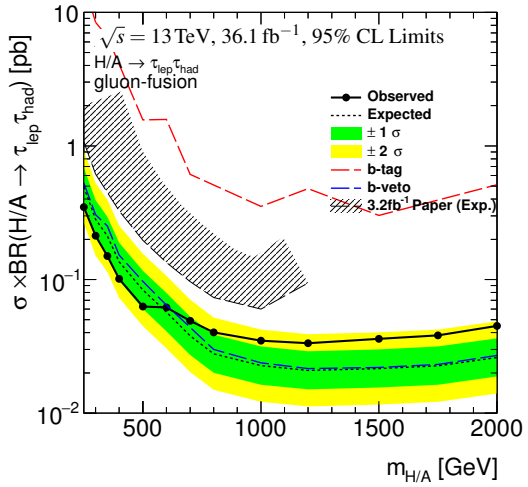

(a) $\tau_{\text{lep}}\tau_{\text{had}}$ gluon-fusion

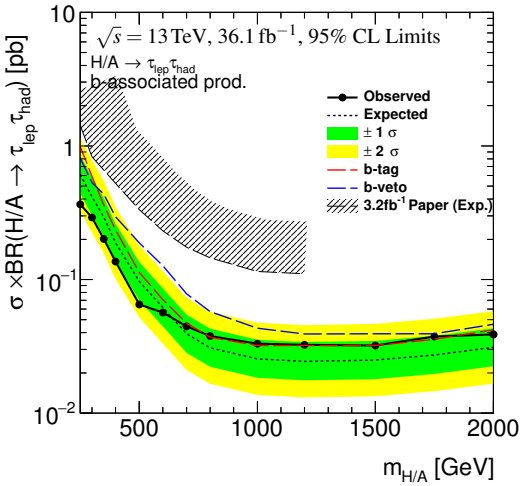

(b) $\tau_{\text{lep}}\tau_{\text{had}}$ b-associated

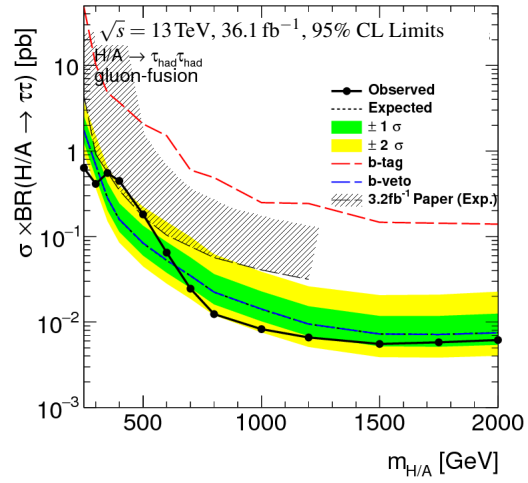

(c) $\tau_{\text{had}}\tau_{\text{had}}$ gluon-fusion

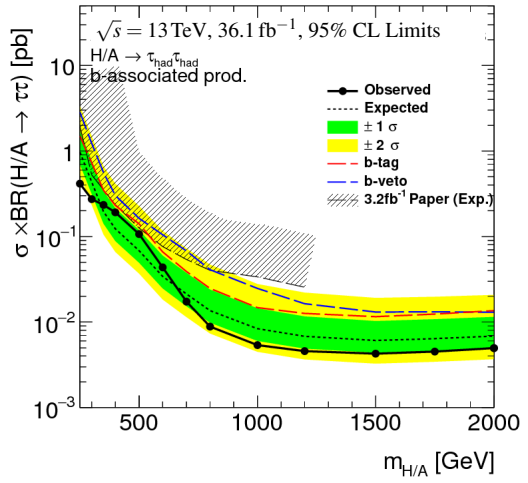

(d) $\tau_{\text{had}}\tau_{\text{had}}$ b-associated

Figure 6.26 The 95% CL upper limit on the production times branching ratio to $\tau\tau$ of a single scalar boson produced via gluon-fusion or b-associated production for 36.1 fb^{-1} of integrated luminosity at 13 TeV. Observed limits for channels split into b-tagged and b-veto categories, and a comparison to the expected limits from Ref. [216], are shown. Each category is shown separately.

gluon-fusion (b-associated production) for a resonance with mass between the 200 GeV and 2.25 TeV mass points, respectively. The small downward fluctuation is observed for mass points lower than ∼300 GeV in both limits. A small excess is present in the gluon-fusion limits. The model-independent limits are also explored with different mixtures of gluon-fusion and b-associated production. Figure 6.28 shows 2D scans of the observed and expected 95% CL upper limits as a function of the fractional contribution from b-associated production ($\sigma_{bb}/[\sigma_{bb}+\sigma_{gg}]$) and the scalar boson mass. The limits are extracted by scanning the $\sigma_{bb}/[\sigma_{bb}+\sigma_{gg}]$ ratio in steps of 10%, and linear interpolation is used between points. Contour lines are shown for fixed values of the cross-section times branching fraction to di-tau, $\sigma \times B(\phi \to \tau\tau)$. Additionally, the best fit point with regards to σ_{bb} vs σ_{gg} is extracted for each mass point. Figure 6.29 shows the 2D likelihood scans of gluon-fusion cross-section times branching fraction vs the b-associated production cross-section times branching fraction, for each signal point. For each mass point, 10^4 points are scanned, building a 2D grid of the likelihood function where the binned likelihood function is minimised. At each point in the scan the test statistic $t_\mu = -2\log\frac{\mathscr{L}(\boldsymbol{\mu},\hat{\hat{\boldsymbol{\theta}}})}{\mathscr{L}(\hat{\boldsymbol{\mu}},\hat{\boldsymbol{\theta}})}$ is calculated, where $\boldsymbol{\mu} = (\sigma_{bb},\sigma_{gg})$, and $\hat{\boldsymbol{\mu}}$ is the global minimum at that mass point. Using the asymptotic approximation, p-values are extracted[53] via Eq. (5.24) and 95% and 68% CL contours are extracted. Each point shows a best fit value consistent with the SM expectation (i.e., $\sigma_{bb}\times B(\phi\to\tau\tau) = \sigma_{gg}\times B(\phi\to\tau\tau) = 0$). The 400 GeV mass point has the largest deviation from the SM, with a best fit value at $\sigma_{gg}\times B(\phi\to\tau\tau) = 66$ fb (with $\sigma_{bb}\times B(\phi\to\tau\tau) = 0$).

6.5.3 Impact of uncertainties on the result

The impact of systematic uncertainties on the results are extracted by comparing the expected exclusion limits when including different sets of uncertainties in the model. The impact from different sources of uncertainties is determined separately for both the gluon-fusion and b-associated productions, and at each signal mass point. The expected 95% CL limits are calculated for the case where no NPs are included in the fit (μ^{95}_{stat}), and compared to the limit calculated when introducing a group of systematic uncertainties (μ^{95}_i). Figure 6.30 shows the impact of different groups of NPs on the limit as a function of the hypothesised boson mass. The major groups of uncertainties that are found to affect the limit performance are the TES, hadronic tau efficiency, and data-driven uncertainties. All other uncertainties are grouped into the *other* category. The impact of using the full set of NPs is also shown. In the low-mass range, where the sensitivity from the combined limits is dominated by the

[53] Under the asymptotic approximation, t_μ is χ^2 distributed with 2 DOF.

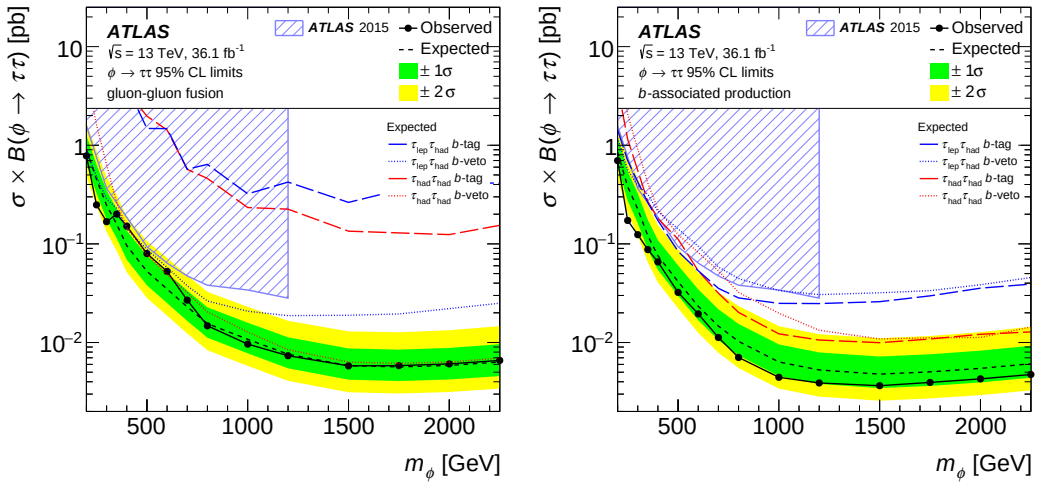

(a) $\phi \to \tau\tau$ gluon-fusion **(b)** $\phi \to \tau\tau$ b-associated

Figure 6.27 The combined 95% CL upper limit on the production times branching ratio to $\tau\tau$ of a single scalar boson produced via gluon-fusion or b-associated production for 36.1 fb^{-1} of integrated luminosity at 13 TeV [1]. Observed limits for channels split into b-tagged and b-veto, and $\tau_{\text{lep}}\tau_{\text{had}}$ and $\tau_{\text{had}}\tau_{\text{had}}$ categories, and a comparison to the expected limits from Ref. [216], are shown.

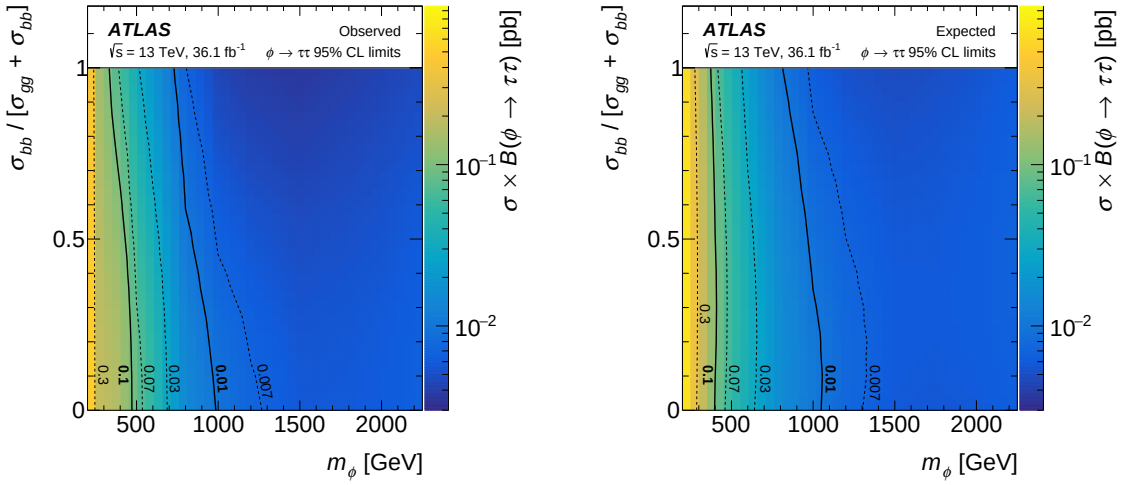

(a) Observed **(b)** Expected

Figure 6.28 The (a) observed and (b) expected 95% CL upper limit on the production cross-section times branching fraction as a function of the fractional contribution from b-associated production and the boson mass [1]. Contours represent fixed values of cross-section times branching fraction.

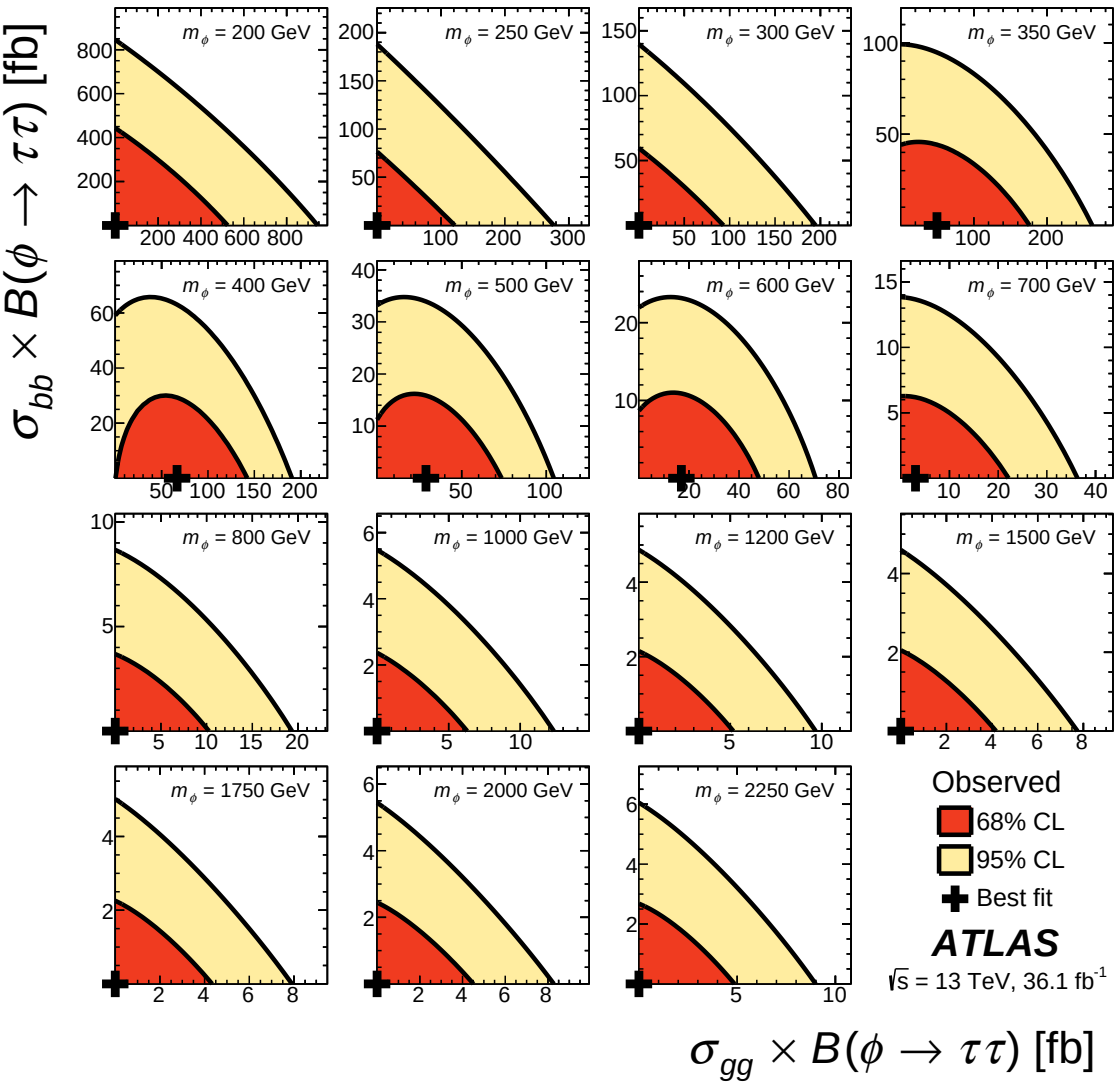

Figure 6.29 2D likelihood scans of gluon-fusion cross-section times branching fraction $\sigma_{gg} \times B(\phi \to \tau\tau)$ vs the b-associated production cross-section times branching fraction $\sigma_{bb} \times B(\phi \to \tau\tau)$ for each mass point [1]. The cross represents the best fit point at each mass point.

contribution from the $\tau_{\text{lep}}\tau_{\text{had}}$ channel, the dominant uncertainty comes from the data-driven background estimation in the $\tau_{\text{lep}}\tau_{\text{had}}$ channel. The TES quickly becomes dominant in the intermediate mass range, while at the high-mass range the tau identification uncertainty for high p_{T} $\tau_{\text{had-vis}}$ becomes dominant. The uncertainties on top backgrounds are found to contribute little to the final result, due to them being considerably constrained in CR-T.

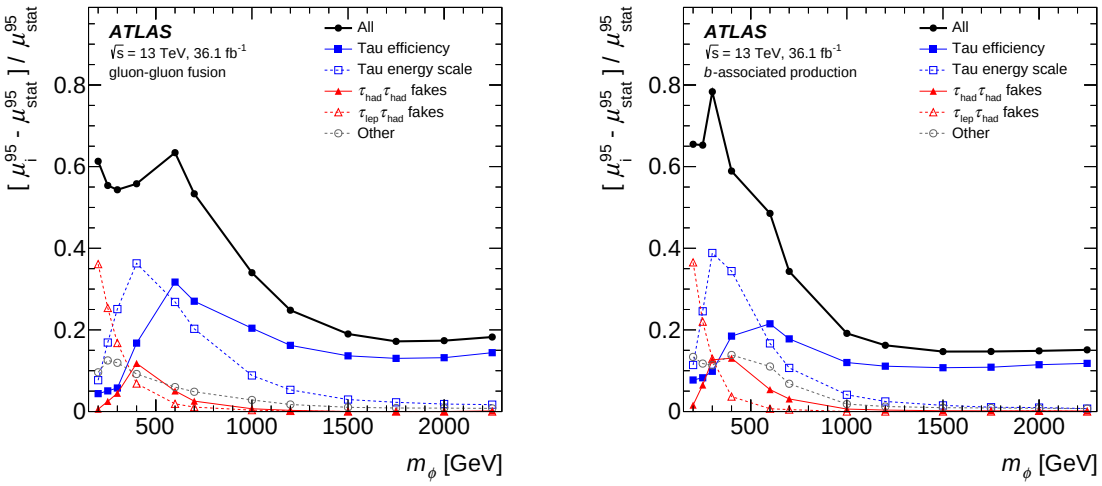

(a) gluon-fusion production

(b) b-associated production

Figure 6.30 Impact of major groups of systematic uncertainties on the 95% CL cross-section limits as a function of the scalar boson mass, separately for the (a) gluon-fusion and (b) b-associated production [1].

6.5.4 Interpretation in the MSSM

The limits set on the cross-section of a scalar boson decaying to di-tau can be reinterpreted in the context of the MSSM scenarios introduced in Section 2.3.1. For each case, the total cross-section times branching ratio,

$$\sigma_{\text{tot}}^{\text{MSSM}} \times B_{\phi\to\tau\tau}^{\text{MSSM}} = (\sigma_{b\bar{b}H}^{\text{MSSM}} + \sigma_{gg\to H}^{\text{MSSM}}) \times B_{H\to\tau\tau}^{\text{MSSM}} + (\sigma_{b\bar{b}A}^{\text{MSSM}} + \sigma_{gg\to A}^{\text{MSSM}}) \times B_{A\to\tau\tau}^{\text{MSSM}}, \quad (6.11)$$

is determined from the prediction, and compared to the 2D expected and observed 95% CL limits from Figure 6.28. If the predicted cross-section from the MSSM scenario is larger than the corresponding cross-section limit, the point is excluded. An example of the total hMSSM cross-section times branching fraction of the heavy Higgs bosons decaying to $\tau\tau$ is shown in Figure 6.31, calculated as described in Sections 2.4.1 and 2.4.2. The

cross-section times branching fraction for $\sigma_{ggA/H} \times B(\phi \to \tau\tau)$ and $\sigma_{b\bar{b}A\ H} \times B(\phi \to \tau\tau)$ are also shown. The b-associated production is shown to dominate the cross-section at high $\tan\beta$, while the gluon-fusion becomes dominant over the whole mass range at $\tan\beta \lesssim 5$. A local minima is observed for the gluon-fusion production, with a sharp increase at $2 \times m_t$ coming from an enhanced $gg \to A$ cross-section. It is more pronounced at lower $\tan\beta$ values where gluon-fusion dominates. The total cross-section times branching ratio in the $m_{\mathrm{h}}^{\mathrm{mod+}}$ scenario ($\sigma_{\mathrm{tot}}^{\mathrm{mod+}} \times B^{\mathrm{mod+}}(\phi \to \tau\tau)$) at the same value of $\tan\beta$ is overlaid. The predicted cross-section times branching ratio in the $m_{\mathrm{h}}^{\mathrm{mod+}}$ scenario is weaker than that of the hMSSM due to allowed Higgs decay modes to SUSY particles in $m_{\mathrm{h}}^{\mathrm{mod+}}$, which drops the heavy Higgs di-tau branching ratio. The local minima from $gg \to A$ in still observed, but to a very reduced degree.

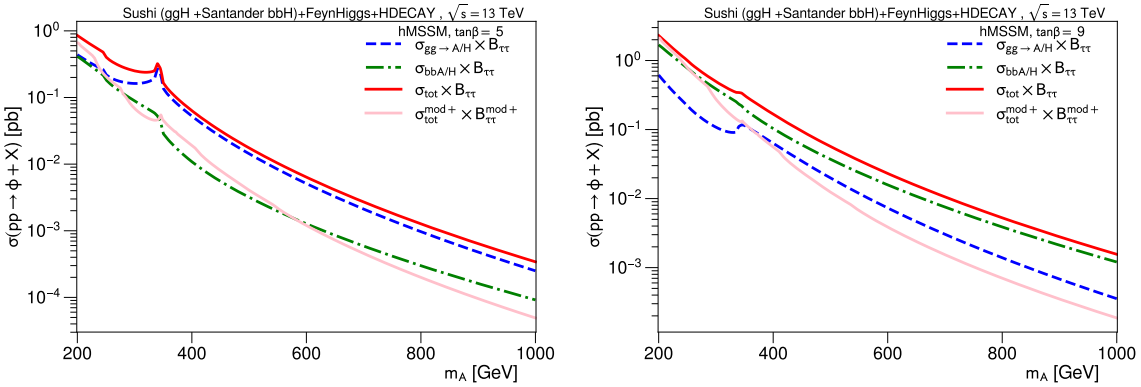

(a) hMSSM $\tan\beta$=5 **(b)** hMSSM $\tan\beta$=9

Figure 6.31 Predicted hMSSM total cross-section of the heavy Higgs bosons decaying to $\tau\tau$ at fixed $\tan\beta$ values (a) 5 and (b) 9 as a function of m_{A}. Also shown are the b-associated production and gluon-fusion components to the total cross-section times branching fraction, as well as the total $m_{\mathrm{h}}^{\mathrm{mod+}}$ cross-section times branching fraction.

The cross-section limits are interpreted in terms of the MSSM scenarios hMSSM, $m_{\mathrm{h}}^{\mathrm{max}}$, $m_{\mathrm{h}}^{\mathrm{mod+}}$ and $m_{\mathrm{h}}^{\mathrm{mod-}}$ described in Section 2.3.1. The interpretation assumes the widths of the A and H Higgs bosons are too narrow to be resolved in the final discriminant. Figure 6.32 shows the relative width of the signal hypothesis in the hMSSM model. From these plots it can be seen that the width is generally less than 6% of the Higgs boson mass, which is less than the resolution of the final discriminant, $m_{\mathrm{T}}^{\mathrm{tot}}$, and further off-shell effects on the signal samples can be ignored. Other MSSM scenarios are found to also be consistent with this conclusion.

Figure 6.33 shows the regions in the m_{A}–$\tan\beta$ plane that are excluded at 95% CL by the cross-section limits. The limits are in general stronger for the hMSSM scenario due to the

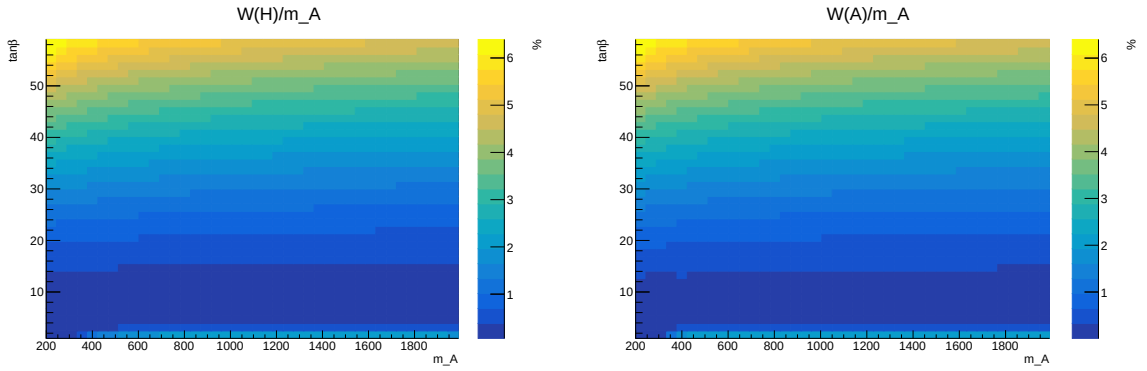

(a) H **(b)** A

Figure 6.32 The relative width of (a) H and (b) A for the hMSSM model as a function of $\tan\beta$ and m_{A}.

allowed SUSHI decays in the other scenarios. The hMSSM exclusion plot shows the overlaid constraints from the SM Higgs coupling measurements[54] from Ref. [17]. A comparison to the result from Ref. [216], as well as the contributions from the individual channels, are also shown. The exclusion contours for $m_{\mathrm{h}}^{\mathrm{max}}$, $m_{\mathrm{h}}^{\mathrm{mod}+}$ and $m_{\mathrm{h}}^{\mathrm{mod}-}$ are close to identical. In these scenarios the SM-like Higgs boson mass is not required to be at 125.09 GeV, and the m_h contours are overlaid to show the corresponding predicted mass at a particular m_{A}–$\tan\beta$ point. Large portions of the phase-space consistent with a $m_h = 125$ GeV still remain to be excluded at large values of m_{A}.

The final results in the di-tau analysis placed strong limits on the cross-section and branching fraction of a heavy resonance decaying to di-tau. While the results are interpreted here in the context of the MSSM, they are not limited to this interpretation. The analysis also placed limits on heavy Z' gauge bosons, which appear in many extensions of the SM [217–221]. The details are documented in the original publication [1] and are not repeated here.

[54]This was the state of the most up to date ATLAS constraint from the Higgs coupling measurement at the time of publication. They are now superseded by results presented in this thesis, in Section 8.3.2.

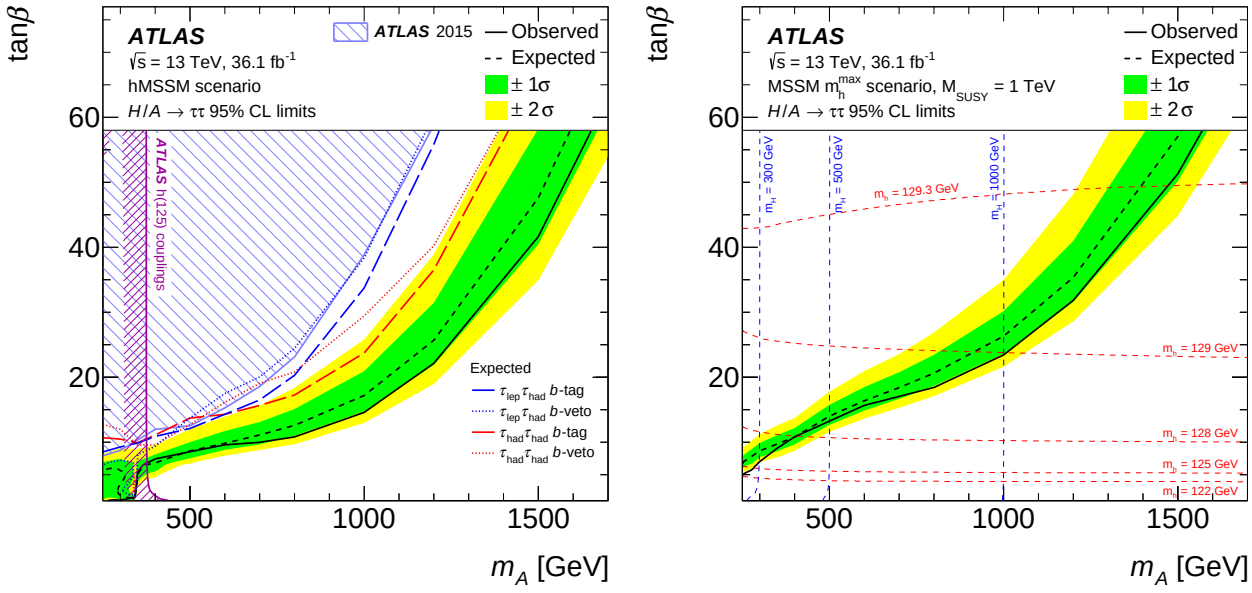

(a) hMSSM

(b) $m_{\mathrm{h}}^{\mathrm{max}}$

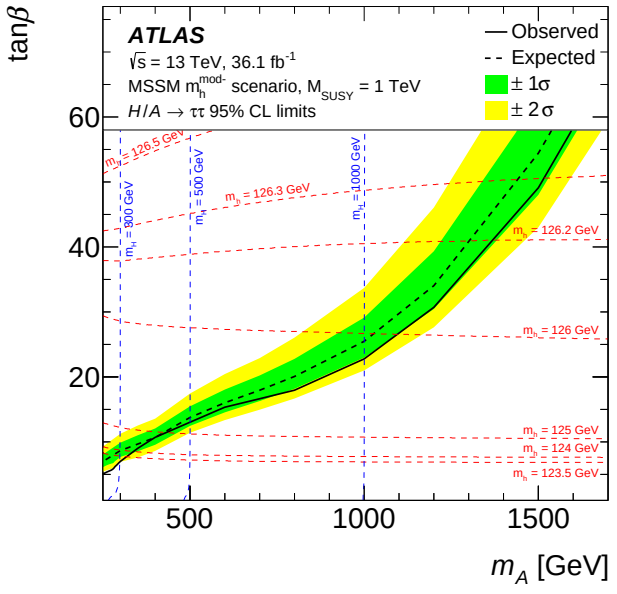

(c) $m_{\mathrm{h}}^{\mathrm{mod}-}$

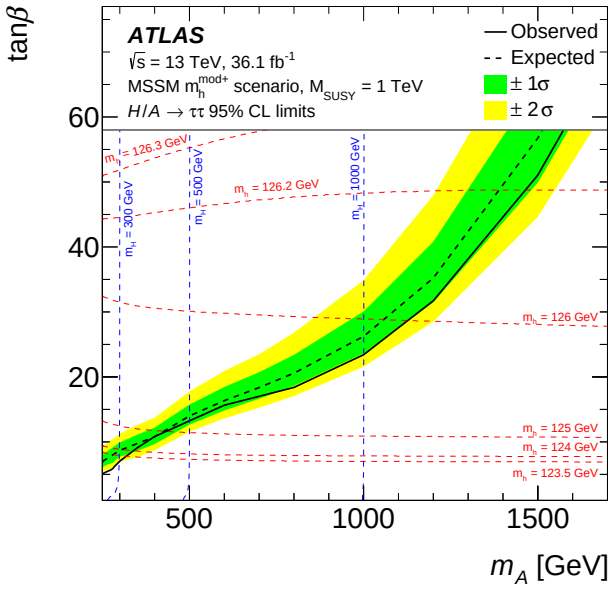

(d) $m_{\mathrm{h}}^{\mathrm{mod}+}$

Figure 6.33 The observed and expected 95% CL upper limits on $\tan\beta$ as a function of m_{A} in the (a) hMSSM, (b) $m_{\mathrm{h}}^{\mathrm{max}}$, (c) $m_{\mathrm{h}}^{\mathrm{mod}-}$ and (d) $m_{\mathrm{h}}^{\mathrm{mod}+}$ scenarios [1]. Dashed red and blue contours corresponding to constant values of the predicted m_h and m_H are shown for non-hMSSM scenarios: $m_{\mathrm{h}}^{\mathrm{max}}$, $m_{\mathrm{h}}^{\mathrm{mod}-}$ and $m_{\mathrm{h}}^{\mathrm{mod}+}$.

Chapter 7

Search for a charged Higgs boson decaying to a tau lepton and a neutrino

The observation of a charged Higgs boson ($H^{\pm}$) would immediately point to BSM physics. Charged Higgs bosons are a prediction of many BSM theories with extended Higgs sectors, such as the MSSM, and more generally 2HDMs, described in Section 2.4.3. In a Type-II 2HDM the production of the charged Higgs in pp collisions is dependant on the relationship between its mass and the mass of the top-quark. For light charged Higgs bosons with $m_{H^{\pm}} < m_t$ the production is driven by the decay of the top-quark as $t \to bH^+$ ($\bar{t} \to \bar{b}H^-$). In this case, the dominant decay mode of the charged Higgs is through a tau and a neutrino[55], $H^+ \to \tau^+\nu_\tau$. By contrast, if $H^{\pm}$ has a mass greater than the top mass, $m_{H^{\pm}} > m_t$, the dominant production is in association with a single-resonant top-quark, $gg \to H^+\bar{t}b$ ($H^-t\bar{b}$). This is also the dominant production mode for the MSSM at the decoupling limit, with $m_H^{\pm} \gtrsim 200$ GeV. In both the 2HDM and MSSM the decay of a heavy charged Higgs is determined by the particular parameters of the model, where $H^+ \to \tau\nu_\tau$ becomes important for large values of $\tan\beta$, as shown in Figure 2.10. When performing cross-section calculations in the intermediate mass range, i.e., $m_H^{\pm} \sim m_t$, non-resonant top-quark effects become relevant and need to be considered, as done in Ref. [92].

During Run-1 of the LHC, with 7–8 TeV centre-of-mass energy pp collisions, ATLAS and CMS performed searches for charged Higgs bosons below the top mass decaying to $\tau\nu_\tau$ and cs [97, 222–227], and above the top mass decaying to $\tau\nu_\tau$ or tb [97, 225, 228]. Additionally, searches for a charged Higgs boson decaying to $H^+ \to WZ$ were performed at

[55]The following process is also implied for the charge conjugate Higgs and its decay, i.e., $H^- \to \tau^-\bar{\nu}_\tau$. The charge conjugate process is implied by this notation in what follows.

$\sqrt{s}$ = 8 TeV and 13 TeV [229, 230]. Recent searches for a charged Higgs boson with data from $\sqrt{s}$ = 13 TeV collisions were performed in several decay modes by both ATLAS and CMS: $H^+ \to \ell\mu\mu$ with 15 GeV $\leq m_{H^\pm} \leq$ 75 GeV [231], $H^+ \to \tau\bar{\nu}_\tau$ with 90 GeV $\leq m_{H^\pm}$ [232, 233], $H^+ \to tb$ with 300 GeV $\leq m_{H^\pm}$ [234]. No evidence for a charged Higgs boson was observed in any of these searches.

This chapter presents the search documented in Ref. [2] for a charged Higgs boson in the mass range of 90 GeV $\leq m_{H^\pm} \leq$ 2000 GeV decaying to $\tau\nu_\tau$ in 36.1 fb^{-1} of pp collision data at $\sqrt{s}$ = 13 TeV recorded with the ATLAS detector. Only hadronically decaying tau leptons, τ_{had}, are considered. The analysis is split into two channels depending on the decay mode of the associated $W^\pm$ boson, i.e., either τ_{had}+jets where $W \to q\bar{q}$, or τ_{had}+lepton where the W decays into an electron or muon and neutrinos. The analysis places model-independent limits on the cross-section of a charged Higgs boson, which are interpreted in the context of the hMSSM model described in Sections 2.3.1 and 2.4.3.

This analysis shares several similarities with that of the di-tau search described in Chapter 6. In order to avoid duplication the subsequent sections are summarised briefly and only those areas of the analysis where the author made significant contributions are expanded upon. For additional details on the analysis, beyond what is described here, the reader is referred to the original publication [2].

7.1 Event samples

The analysis makes use of a dataset corresponding to an integrated luminosity of 36.1 fb^{-1} at $\sqrt{s}$ = 13 TeV [168]. The dataset is a collection of luminosity blocks recorded during 2015 and 2016 data-taking, filtered by the GRL to ensure good quality data for physics analyses. Backgrounds from calorimeter noise and non-collision sources are removed using the jet cleaning tool [141].

Signal events for the charged Higgs boson are generated differently for three distinct mass ranges. In the mass range below the top-quark mass (90–150 GeV) and for the intermediate-mass range (160–180 GeV) MadGraph 5 is used. In the low-mass range, $t\bar{t}$ events with a single top decaying to a charged Higgs and a b-quark are generated at LO. The corresponding contribution from single top-quark decay is negligible. In the intermediate-mass range the full $pp \to H^\pm W^\mp b\bar{b}$ process is generated at LO, as described in Section 2.4.3. For the high-mass range (200–2000 GeV), associated top-quark production of the charged Higgs is generated at NLO using MadGraph5_aMC@NLO. In all cases Pythia 8.186 is used for

the PS with the A14 tune of parameters. The NNPDF2.3 PDF set is used for ME and PS generators. A total of 31 samples at different masses are generated, summarised in Table 7.1. Samples are grouped into different BDT training sets used to train the final BDT discriminant described in Section 7.2.3.

Table 7.1 The masses for which the charged Higgs boson MC samples are generated. The samples are grouped into sets of samples used the training of the final BDT discriminant.

Mass range	BDT set	m_{H^+} [GeV]
low-mass	1	90, 100, 110, 120,
	2	130, 140, 150, 160
intermediate-mass	3	160, 165, 170, 175, 180
high-mass	4	200, 225, 250, 275, 300, 350,400,
	5	500, 600, 700, 800, 900,
		1000, 1200, 1400, 1600, 1800, 2000

The primary sources of SM background to the analysis is from $t\bar{t}$ events for the low- and intermediate-mass ranges, and multijet for the high-mass range. Additional backgrounds come from single top-quark production, $W+$jets, $Z+$jets and di-boson production. All backgrounds arising from a quark- or gluon-initiated jet misidentified as a $\tau_{\text{had-vis}}$ ($j \to \tau_{\text{had-vis}}$) are modelled via a data-driven technique described in Section 7.3.1, while backgrounds with real $\tau_{\text{had-vis}}$ candidates are modelled by MC simulation. This is also the case for events where a lepton is misidentified as a $\tau_{\text{had-vis}}$ candidate, referred to as $e/\mu \to \tau_{\text{had-vis}}$ fakes.

Background events from top-quark sources are generated with a set-up identical to that used in Section 6.1. $Z+$jets and $W+$jets samples are generated using up to NLO matrix-elements with COMIX [183] and OPENLOOPS [184], and are generated using the SHERPA 2.2.1 [185, 186] event generator. The PS is modelled with SHERPA using the ME+PS@NLO recommendation [187]. Di-boson samples are generated at NLO using the CT10 PDF set [173] with the POWHEG-BOX 2 [169–172] event generator, interfaced with PYTHIA v8.186 [174, 175] and using the AZNLO [176] tune and the CTEQ6L1 [177] PDF set for the PS model.

All simulated events are overlaid with minimum-bias events generated using PYTHIA 8 in order to model the effect of pileup. The resulting simulated events pass through the full detector simulation using GEANT 4 [132].

7.2 Analysis strategy

The analysis is split into two categories, τ_{had}+leptons and τ_{had}+jets, depending on the targeted decay mode of the associated final-state W boson. The baseline selection of objects in both categories is identical[56] to that described in Section 6.2.1. The corresponding signal regions are described below.

7.2.1 Event selection in the τ_{had}+jets channel

Events in the τ_{had}+jets channel are selected by $E_{\text{T}}^{\text{miss}}$ triggers with varying thresholds depending on the data-taking period: 70 GeV (2015), 90 GeV (2016) and 110 GeV (2016), all of which are seeded by a 50 GeV $E_{\text{T}}^{\text{miss}}$ L1 trigger[57]. The trigger efficiencies are measured in data and are used to reweight MC events [232]. Events passing these triggers are required to also pass the selection criterion detailed below.

Each event must have at least one $\tau_{\text{had-vis}}$ candidate passing the `medium` identification criterion with $p_{\text{T}} > 40$ GeV. Any event with at least one lepton (electron or muon) with $p_{\text{T}} > 20$ GeV and passing the `loose` identification is vetoed. The event must have at least three jets, each with $p_{\text{T}} > 25$ GeV, of which at least one must be b-tagged. Events with $E_{\text{T}}^{\text{miss}} > 150$ GeV are selected in order to reduce the multijet background. The transverse mass (m_{T}) of the highest p_{T} $\tau_{\text{had-vis}}$ candidate and the direction of $E_{\text{T}}^{\text{miss}}$ is determined as defined in Eq. (6.2) on page 107. In the absence of detector resolution effects, $m_{\text{T}} < m_W$ for $W \to \tau\nu$ background events and $m_{\text{T}} < m_{H^{\pm}}$ for signal events. The signature of the signal is the decay of $H^{\pm}$ into τ_{had} and ν_τ with back-to-back trajectories. The signal region therefore selects events with $m_{\text{T}} > 50$ GeV. This selection is used to reject events with mismeasured $E_{\text{T}}^{\text{miss}}$ and W+jets events, both of which have the $\tau_{\text{had-vis}}$ candidate nearly aligned with the direction of the $E_{\text{T}}^{\text{miss}}$. The m_{T} distribution in the τ_{had}+jets signal region is shown in Figure 7.1 using the 200–400 GeV BDT post-fit result. The dominant background at low m_{T} is from $t\bar{t}$ and single top-quark events, while at intermediate values of m_{T} the multijet background becomes important. Other backgrounds are less prominent. W+jets background events at low m_{T} have been removed by the selection criterion on m_{T}. Di-boson and $e\mu \to \tau_{\text{had-vis}}$ backgrounds are small.

[56] Objects such as electrons, muons, taus and b-jets are all selected with the same working points, except that the electron and muon isolation uses the `loose` working point instead of the `gradient`.

[57] The full trigger names are: `HLT_xe70_tc_lcw` in 2015 data, `HLT_xe90_mht_L1XE50` in 2016 for periods A-D3 and `HLT_xe110_mht_L1XE50` in 2016 data for periods D4-L.

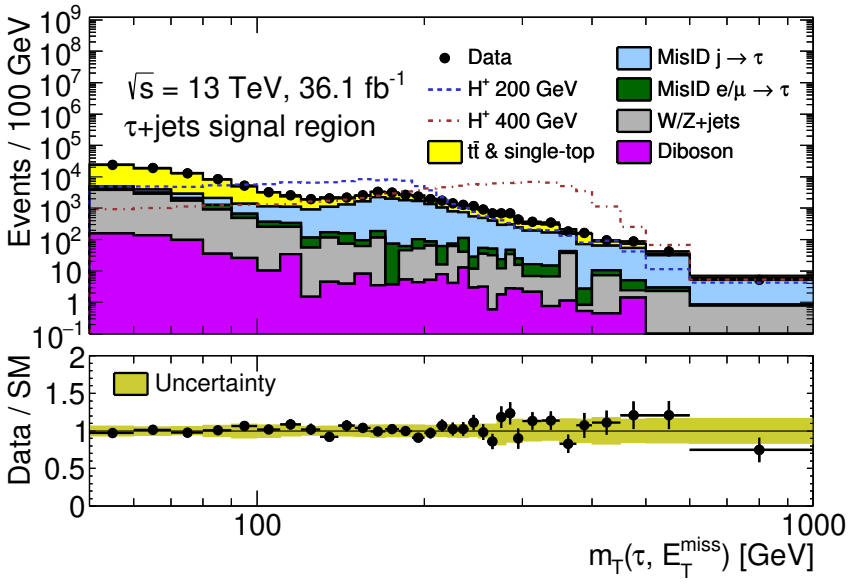

Figure 7.1 Post-fit plot of the m_{T} distribution in the τ_{had}+jets channel using the 200–400 GeV BDT post-fit result. The total statistical and systematic uncertainties, after being constrained by the fit, are shown. The normalisation of the signal distributions has been scaled to the background normalisation for illustration purposes.

The expected and observed numbers of events in the τ_{had}+jets SRs are quoted in Table 7.2, along with the total statistical and systematic uncertainties for the SM prediction. The total event yields are found to be compatible with the SM prediction within uncertainties. The predicted charged Higgs boson event yields for the hMSSM benchmark scenario at $\tan\beta = 40$ is shown for $H^{\pm} = 170$ GeV and $H^{\pm} = 1000$ GeV.

7.2.2 Event selection in the τ_{had}+leptons channel

Unprescaled single lepton triggers (electron or muon triggers) are used in the τ_{had}+leptons channel with thresholds dependant on the data-taking period. They are identical to the ones used in the $\tau_{\mathrm{lep}}\tau_{\mathrm{had}}$ channel of the di-tau analysis (see Table 6.1 on page 109). The τ_{had}+leptons channel is further split into the $\tau_{\text{had-vis}}$+electron and $\tau_{\text{had-vis}}$+muon sub-channels based on the trigger passed.

Events are selected with exactly one lepton with $p_{\mathrm{T}} > 30$ GeV matched to the single-lepton trigger object. This lepton is required to pass the `tight` identification criterion. Exactly one $\tau_{\text{had-vis}}$ candidate passing the `medium` identification criterion is selected with $p_{\mathrm{T}} > 30$ GeV and with opposite electric charge compared to the lepton candidate. At least

Table 7.2 Event yields in the τ_{had}+jets channel for the SM prediction and charged Higgs signal with a mass of 170 GeV and 1000 GeV in the hMSSM scenario with $\tan\beta = 40$ [2]. The total statistical and systematic uncertainties are quoted.

Sample	$\tau_{\text{had-vis}}$+jets		
	Events	(stat.)	(sys.)
$t\bar{t}$	6900	± 60	±1800
Single top-quark	750	± 20	± 100
W+jets	1050	± 30	± 180
Z+jets	84	± 42	± 28
Di-boson	63.2	± 4.6	± 7.2
$e, \mu \to \tau_{\text{had-vis}}$	265	± 12	± 35
jet $\to \tau_{\text{had-vis}}$	2370	± 20	± 260
All backgrounds	11500	± 80	±1800
Data	11021		
H^+ (170 GeV), hMSSM $\tan\beta = 40$	1400	± 10	± 170
H^+ (1000 GeV), hMSSM $\tan\beta = 40$	10.33	± 0.06	± 0.78

one b-tagged jet with $p_{\text{T}} > 25$ GeV is required. The event is required to have $E_{\text{T}}^{\text{miss}} > 50$ GeV to reject multijet events. The post-fit $E_{\text{T}}^{\text{miss}}$ distribution in the $\tau_{\text{had-vis}}$+electron channel using the 200–400 GeV BDT post-fit result are shown in Figure C.7. The dominant background is $t\bar{t}$ followed by multijet.

The expected and observed number of events in the τ_{had}+leptons SRs are quoted in Table 7.3, along with the total statistical and systematic uncertainties of the SM prediction and predicted number of charged Higgs events in the hMSSM. The total event yields are found to be compatible with the SM prediction within uncertainties.

Table 7.3 Event yields in the τ_{had}+leptons channel for the SM prediction and charged Higgs signal with a mass of 170 GeV and 1000 GeV in the hMSSM scenario with $\tan\beta = 40$ [2]. The total statistical and systematic uncertainties are quoted.

Sample	$\tau_{\text{had-vis}}$+electron			$\tau_{\text{had-vis}}$+muon		
	Events	(stat.)	(sys.)	Events	(stat.)	(sys.)
$t\bar{t}$	16000	± 80	±2500	14600	± 80	±2400
Single top-quark	1260	± 20	± 110	1260	± 20	± 110
W/Z+jets	433	± 27	± 80	352	± 48	± 43
Di-boson	39.3	± 2.1	± 4.5	32.3	± 1.7	± 3.6
$e, \mu \to \tau_{\text{had-vis}}$	626	± 27	± 59	454	± 16	± 27
jet $\to \tau_{\text{had-vis}}$	5640	± 40	± 450	5460	± 40	± 410
All backgrounds	24000	±100	±2600	22200	±100	±2500
Data	22645			21419		
H^+ (170 GeV), hMSSM $\tan\beta = 40$	850	± 12	± 65	852	± 11	± 66
H^+ (1000 GeV), hMSSM $\tan\beta = 40$	0.82	± 0.02	± 0.07	1.05	± 0.02	± 0.09

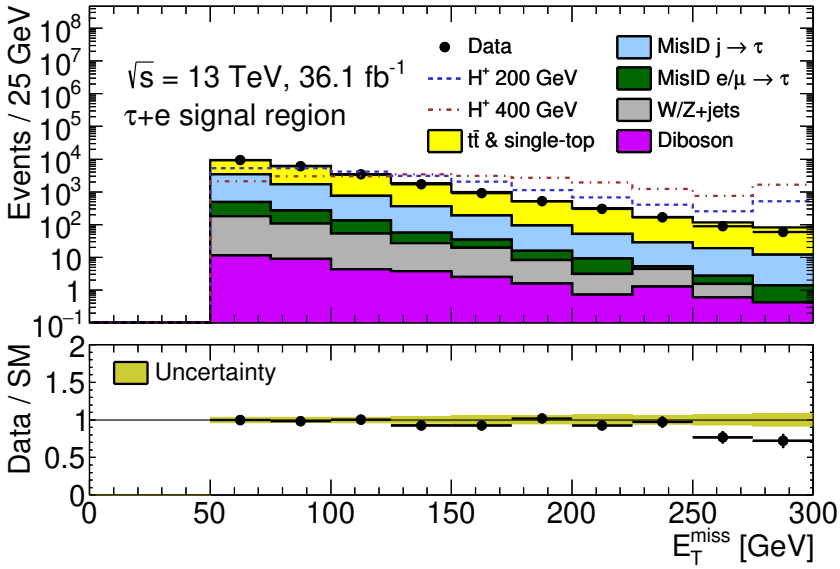

Figure 7.2 Post-fit plot of the $E_{\mathrm{T}}^{\mathrm{miss}}$ distribution in the $\tau_{\text{had-vis}}$+electron channel using the 200–400 GeV BDT post-fit result. The total statistical and systematic uncertainties, after being constrained by the fit, are shown. The normalisation of the signal distributions has been scaled to the background normalisation for illustration purposes.

7.2.3 Final discriminant

The analysis employs a multivariate BDT discriminant as the final discriminant for the statistical analysis. Different BDTs are trained depending on the signal mass, the number of tracks of the $\tau_{\text{had-vis}}$ candidate, and the channel considered. Signal samples are split into one of five BDT training sets, summarised in Table 7.1. Each set is designed to have signal samples with similar kinematic distributions for the input variables of the BDT. The samples in each set are normalised to the same event yield, in order to not bias the training, and combined into a single training sample. Different BDTs are trained for events in the τ_{had}+jets and τ_{had}+leptons channels, and for events where the $\tau_{\text{had-vis}}$ candidate has one ($\tau_{\text{1-prong}}$) or three ($\tau_{\text{3-prong}}$) charged tracks.

Each BDT is trained using the FastBDT [235] library via the TMVA toolkit [236] with a k-fold method for training and evaluation. The BDTs are trained to optimise the separation of the charged signal samples from the estimated background samples. The list of variables used as input to the BDT training is shown in Table 7.4. For low-mass signals the kinematics of $t \to bH^+$ and $t \to bW^+$ are similar, and the polarisation of the $\tau_{\text{had-vis}}$ is employed as a handle to discriminate against the background. For $\tau_{\text{1-prong}}$ the polarisation of the $\tau_{\text{had-vis}}$

candidate can be measured by the asymmetry of the energy carried by the charge and neutral pions in its decay. The analysis uses the variable Υ defined in Ref. [237] for $\tau_{\text{1-prong}}$ as,

$$\Upsilon = 2\frac{p_{\text{T}}^{\text{track}}}{p_{\text{T}}^{\tau}} - 1. \tag{7.1}$$

where p_{T}^{τ} and $p_{\text{T}}^{\text{track}}$ are the transverse momentum of the $\tau_{\text{had-vis}}$ candidate and the track of the $\tau_{\text{1-prong}}$ candidate, respectively. The variable Υ is employed as an input variable to the BDT training for both the τ_{had}+jets and τ_{had}+leptons channels and is ranked as the variable with highest discriminating power for low-mass signals. It however becomes less important for high-mass signals, and is removed from the training of the 500–2000 GeV signal set. This set is therefore trained inclusively for $\tau_{\text{1-prong}}$ and $\tau_{\text{3-prong}}$. The Υ distribution the $\tau_{\text{had-vis}}$+electron channel using the 200–400 GeV BDT post-fit result is shown in Figure C.8. The distributions of some key variables used in the BDT are documented in Appendix C.

Table 7.4 List of kinematic variables used as input to the BDT in the $\tau_{\text{had-vis}}$+jets and $\tau_{\text{had-vis}}$+lepton channels [2]. The Υ variable is not included for the BDT trained in the 500–2000 GeV mass range.

BDT input variable	$\tau_{\text{had-vis}}$+jets	$\tau_{\text{had-vis}}$+lepton
$E_{\text{T}}^{\text{miss}}$	✓	✓
p_{T}^{τ}	✓	✓
$p_{\text{T}}^{b\text{-jet}}$	✓	✓
p_{T}^{ℓ}		✓
$\Delta\phi(\tau_{\text{had-vis}}, E_{\text{T}}^{\text{miss}})$	✓	✓
$\Delta\phi(b\text{-jet}, E_{\text{T}}^{\text{miss}})$	✓	✓
$\Delta\phi(\ell, E_{\text{T}}^{\text{miss}})$		✓
$\Delta R(\tau_{\text{had-vis}}, \ell)$		✓
$\Delta R(b\text{-jet}, \ell)$		✓
$\Delta R(b\text{-jet}, \tau_{\text{had-vis}})$	✓	
Υ	✓	✓

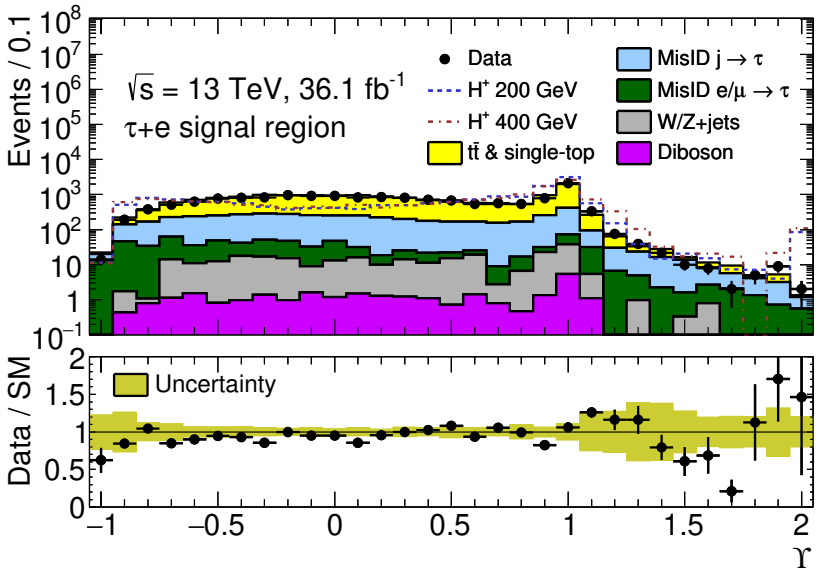

Figure 7.3 Post-fit plot of the Υ distribution in the $\tau_{\text{had-vis}}$+electron channel using the 200–400 GeV BDT post-fit result. The total statistical and systematic uncertainties, after being constrained by the fit, are shown. The normalisation of the signal distributions has been scaled to the background normalisation for illustration purposes.

7.3 Background estimation

The sources of backgrounds can be categorised according to the object that is identified as the $\tau_{\text{had-vis}}$ candidate. Events in which the $\tau_{\text{had-vis}}$ candidate is a real τ_{had}, or is a misidentified lepton[58], the backgrounds are estimated with simulation and normalised according to their predicted SM cross-sections. However, in the case of the $t\bar{t}$ background the normalisation is determined in a CR dominated by $t\bar{t}$ events, where the $t\bar{t}$ normalisation factor is left floating in the combined statistical fit[59].

Simulated events where the $\tau_{\text{had-vis}}$ candidate is as a result of a misidentified jet are removed from the background samples. Instead, a data-driven fake-factor method is employed to determine the jet $\rightarrow \tau_{\text{had-vis}}$ fakes contribution as described below.

[58] Electrons faking $\tau_{\text{had-vis}}$ candidates are not guaranteed to be well modelled in simulation. The modelling was checked in a dedicated CR enriched in $Z \rightarrow ee$ events. The modelling of electrons faking a $\tau_{\text{had-vis}}$ candidate after applying the recommended $e \rightarrow \tau_{\text{had-vis}}$ scale factors is found to be satisfactory [238].

[59] This is identical to what was done in the di-tau analysis, except that here a single bin CR is used, without any shape effect considered.

7.3.1 Backgrounds with jet $\rightarrow \tau_{\text{had-vis}}$ fakes

Events that contain quark- or gluon-initiated jets can enter the SR if one of these jets is reconstructed and identified as a $\tau_{\text{had-vis}}$ candidate. In the SR these events are predominantly from multijet and W+jets backgrounds, each with different proportions of quark- and gluon-initiated jets. The contribution from jet $\rightarrow \tau_{\text{had-vis}}$ fakes is estimated in the SR by using a fake-factor method. A control region (CR-1) is defined with the same event selection as the SR, except that the $\tau_{\text{had-vis}}$ candidate is required to pass the anti-$\tau_{\text{had-vis}}$ selection. The anti-$\tau_{\text{had-vis}}$ selection requires the $\tau_{\text{had-vis}}$ candidate to fail the `loose` tau identification, with a lower threshold on the tau identification BDT score that keeps the kinematics of the $\tau_{\text{had-vis}}$ candidate close to that of the SR.

The fake-factors are measured in two CRs. The first is the multijet CR, which utilises the same selection used in the τ_{had}+jets category with some exceptions: it is triggered by multijet triggers, has a veto on b-jets, and requires $E_{\text{T}}^{\text{miss}} < 80$ GeV. The second is the W+jets CR, which has the same selection as the τ_{had}+leptons category, except that it has a veto on b-jets, has no requirement of $E_{\text{T}}^{\text{miss}}$, and is defined in the region of 60 GeV $< m_{\text{T}}(\ell, E_{\text{T}}^{\text{miss}}) <$ 160 GeV.

The fake-factors are defined as the number of events in a particular CR that pass the `medium` $\tau_{\text{had-vis}}$ identification ($N^{\text{CR}}_{\tau-\text{id}}$), over the number that pass the anti-$\tau_{\text{had-vis}}$ selection ($N^{\text{CR}}_{\text{anti}-\tau-\text{id}}$),

$$FF = \frac{N^{\text{CR}}_{\tau-\text{id}}}{N^{\text{CR}}_{\text{anti}-\tau-\text{id}}}, \tag{7.2}$$

where the fake-factors are measured separately for one and three track $\tau_{\text{had-vis}}$ candidates, and are parameterised as function of the p_{T}. The fake-factors measured in the multijet and W+jets CRs are shown as a function of the p_{T} of the $\tau_{\text{had-vis}}$ in Figure 7.4 (a).

The relative proportions of the quark- and gluon-initiated jets from each fake-factor is determined using a template-fit approach, based on variables sensitive to the relative jet composition. For $\tau_{\text{3-prong}}$ candidates, the tau identification BDT score is used. For $\tau_{\text{1-prong}}$ candidates, the $\tau_{\text{had-vis}}$ width is used, defined as,

$$w_\tau = \frac{\sum \left[p_T^{\text{track}} \times \Delta R\left(\tau_{\text{had-vis}}, \text{track}\right) \right]}{\sum p_T^{\text{track}}} \tag{7.3}$$

for tracks satisfying $\Delta R\left(\tau_{\text{had-vis}}, \text{track}\right) < 0.4$. Templates, denoted as f_{multijet} and $f_{W\text{+jets}}$, of these distributions are obtained for anti-$\tau_{\text{had-vis}}$ candidates in the multijet and W+jets CRs, respectively. Templates are built for different bins of p_{T} and number of associated tracks. The

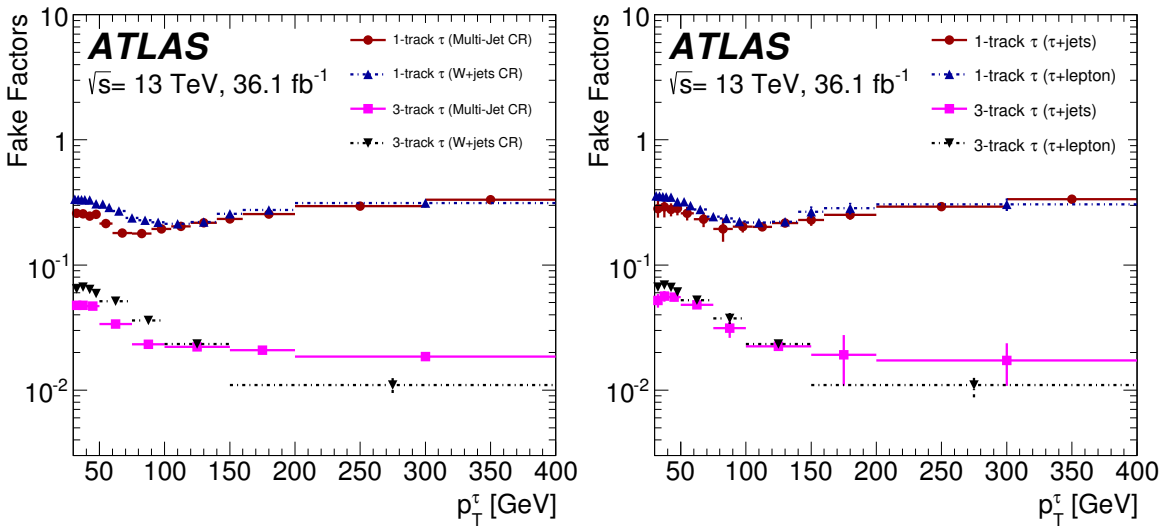

(a) **(b)**

Figure 7.4 Fake-factors parameterised as a function of p_{T}^{τ} and the number of charged τ decay products, as obtained (a) in the multijet and W+jets CRs, and (b) combined in the $\tau_{\text{had-vis}}$ +jets and $\tau_{\text{had-vis}}$ +lepton channels after reweighting by α_{MJ} [2].

templates are combined in a linear combination as $f(\alpha_{\mathrm{MJ}}) = \alpha_{\mathrm{MJ}} \times f_{\text{multijet}}(x) + (1-\alpha_{\mathrm{MJ}}) \times f_{W\text{+jets}}(x)$, where α_{MJ} is a free normalisation factor which scales the respective contribution of the multijet background and is anti-correlated with the W+jets bacground normalisation. The α_{MJ} parameter is measured in CR-1 by varying this parameter in a χ^2 fit to data while the simulated background contributions remain fixed.

From the best-fit values of α_{MJ}, combined fake factors can be determined as,

$$\mathrm{FF}^{\mathrm{comb}}(i) = \alpha_{\mathrm{MJ}}(i) \times \mathrm{FF}^{\mathrm{multijet}}(i) + [1-\alpha_{\mathrm{MJ}}(i)] \times \mathrm{FF}^{W\text{+jets}}(i),$$

where the index i refers to each bin in the parameterisation of the fake-factors, and where $\mathrm{FF}^{\mathrm{multijet}}$ and $\mathrm{FF}^{W\text{+jets}}$ indicate the fake-factors calculated in the two respective control regions. The combined fake-factors, used in the $\tau_{\text{had-vis}}$+jets and $\tau_{\text{had-vis}}$+lepton channels, are shown in Figure 7.4 (b). The final background estimation in the SR is determined by applying the combined fake-factor to events in CR-1 after subtracting contributions from simulation.

Finally, the Υ distribution is found to have some residual shape mis-modelling in a validation region after applying the fake-factors. This is due to differences in the shape of Υ following each of the $\tau_{\text{had-vis}}$ and anti-$\tau_{\text{had-vis}}$ selection criteria. A shape correction for Υ is

derived from the distributions, after applying the $\tau_{\text{had-vis}}$ and anti-$\tau_{\text{had-vis}}$ selection criterion in the fake-factor CRs, and applied to the Υ distribution in CR-1 following the technique described in Ref. [239]. The correction is only used for events with $\tau_{\text{1-prong}}$ candidates, as Υ is not used in the BDT for $\tau_{\text{3-prong}}$.

7.3.2 The top control region

The analysis incurs large uncertainties from the overwhelmingly large contribution of the $t\bar{t}$ background in the SR. In order to control the systematic uncertainties from this background, a CR pure in $t\bar{t}$ events is defined. The top CR adapts the same selection as the τ_{had}+leptons channel, except that it requires an $e+\mu$ pair in the final-state (instead of a $\tau+\mu$ or $\tau+e$ pair). Each lepton is required to have a p_{T} greater than 30 GeV. This region is pure in $t\bar{t}$ and single top-quark events, with the sub-dominant di-boson background contributing less than 0.5%. The top CR has $\sim$ 55k events in data is included in the combined fit as a single bin in the distribution, used both to determine the normalisation of the $t\bar{t}$ sample and constrain the $t\bar{t}$ uncertainties.

The normalisation factor for the $t\bar{t}$ background is extracted from the combined background-only fit in the five BDT sets. Since the normalisation factor is also included in the SRs, statistics from the BDT distributions in the SRs will also constrain the normalisation of the $t\bar{t}$ background. The $t\bar{t}$ normalisation factors in the five BDT sets, measured with background-only fits, are: 0.98 (set 1), 1.01 (set 2), 0.98 (set 3), 0.99 (set 4), 0.99 (set 5). They are compatible with the nominal normalisation used in the samples. The uncertainty on each normalisation factor is $\sim$ 3%.

7.4 Systematic uncertainties

The sources of systematic uncertainties to the analysis are summarised in this section. Tables 7.5–7.8 show the pre-fit uncertainties for the three SRs and the top CR which are included the fit for the 200–400 GeV BDT distribution. Some representative shape distributions are shown in Appendix C.2.

The theoretical uncertainties on the signal acceptance are evaluated for a few representative signal points. In each case, the uncertainty is determined by comparing the resulting SR distribution to the nominal case. The scale uncertainty is estimated by varying the factorisation and renormalisation scales by either a multiple of 0.5 (down) or 2.0 (up), for

a total of eight combinations (including combinations with nominal values). The largest uncertainty up or down for each mass point is symmetrised. Different PDF sets are used in the signal generation, in order to estimate the uncertainty on the signal acceptance from the choice of PDFs set, following the prescription from Ref. [211]. The uncertainties due to varying the PS and UE tunes are also evaluated and their resulting uncertainties are added in quadrature. The largest value determined from each or the three sources of signal acceptance uncertainty are added in quadrature to estimate a conservative signal acceptance uncertainty per mass point. The values are parameterised as a function of $m_{H^\pm}$ giving a conservative uncertainty of $\sim 10 \times e^{m_{H^\pm}/20}$ (in percent), where $m_{H^\pm}$ is in units of GeV. This translates to an uncertainty of $\sim 11\%$ and $\sim 30\%$ for the 90 GeV and 2 TeV mass points, respectively. The signal acceptance uncertainty is denoted as `ATLAS_AU_Hp` in the fit.

There are several sources that contribute to the uncertainty of the data-driven background estimation of Section 7.3.1. An uncertainty from the definition of the anti-$\tau_{\text{had-vis}}$ candidate selection (`Systau_ff_bdt`) is determined by varying the lower threshold used on the tau BDT score, thereby varying the proportions of quark- and gluon-initiated jets. The uncertainty associated with the subtraction of MC background in CR-1 (`Systau_ff_mcsub`) is evaluated by varying the normalisation of the MC samples by 50%. The statistical uncertainties entering into the calculation of the fake-factors (`Systau_ff_stat`) and statistical and fit uncertainties in the determination of α_{MJ} (`Systau_ff_alpha_MJ_L1`) are propagated to the final distributions. An additional uncertainty on using the fake-factor inclusively for light- and heavy-flavour initiated jets is determined from the difference in the distributions of their fake-factors (`tau_ff_HF_L1`). An uncertainty in the shape correction applied to the Υ distribution is included by comparing this distribution in the multijet and W+jets CRs (`Sysupsilon`).

Uncertainties affecting the normalisation and shape of MC samples are determined from generator-level studies. The uncertainties related to the modelling of $t\bar{t}$ events follow identical to those described in the di-tau analysis is Section 6.4.3, determined for scale (`Systtbar_model`), PDF (`Systtbar_model`), and PS and UE (`Systtbar_psue`) sources of uncertainty. Uncertainties on the W+jets (30%) and Z+jets (40%) MC normalisation are determined from studies varying the scales in the SHERPA generator. Uncertainties related to the modelling of heavy-flavour jets in W+jets and Z+jets samples (`Syswj_generator`) are evaluated by comparing to predictions using the MADGRAPH5_aMC@NLO generator interfaced with PYTHIA 5 and found to be 6% in the τ_{had}+jets and 14% in the τ_{had}+leptons channels. A conservative uncertainty of 50% is applied to di-boson samples (`Syswj_generator`) motivated from inclusive cross-section uncertainties [240].

An uncertainty of 2.1% is used for the integrated luminosity and is applied directly to the event yields of all simulated events [168]. All instrumental sources of systematic uncertainty, as described in the di-tau analysis in Section 6.4.1, are propagated through the analysis.

Table 7.5 Pre-fit uncertainty (in [%]) of NPs for the 200 GeV–400 GeV BDT distribution in the $\tau_{\text{had-vis}}$+electron SR, as they are in the final workspace after smoothing and pruning. Shown are the total normalisation uncertainty, with † representing that a shape uncertainty is also considered. The normalisation effect is pruned if the uncertainty is below 0.5%, while shape effects are pruned if they do not have sufficient variations in neighbouring bins.

Type	Sample NP	Z+jets [%]	$e/\mu \to \tau_{\text{had-vis}}$ [%]	Diboson [%]	$H^{\pm}$ (200GeV) [%]	single top-quark [%]	$t\bar{t}$ [%]	jet$\to \tau_{\text{had-vis}}$ [%]
Signal	ATLAS_AU_Hp200	-	-	-	±11.30	-	-	-
	ATLAS_LUMI	±2.10	±2.10	±2.10	±2.10	±2.10	-	-
XS	ATLAS_xsec_Diboson	-	-	±50.00	-	-	-	-
	ATLAS_xsec_Z	±40.00	-	-	-	-	-	-
	SysSingleTopNorm	-	-	-	-	±5.40	-	-
	Syszj_generator	±13.92 †	-	-	-	-	-	-
Data driven	Systau_ff_alpha_MJ_L1	-	-	-	-	-	-	±4.19 †
	Systau_ff_bdt	-	-	-	-	-	-	†
	Systau_ff_mcsub	-	-	-	-	-	-	±6.38
	Systau_ff_stat	-	-	-	-	-	-	±1.67 †
	Sysupsilon	-	-	-	-	-	-	†
	tau_ff_HF_L1	-	-	-	-	-	-	±5.00
Tau	SysTAUS_TRUEHADTAU_SME_TES_DETECTOR	-	-	±0.67	†	†	-	†
	SysTAUS_TRUEHADTAU_SME_TES_INSITU	±3.17	-	±2.58	±1.17 †	±3.63 †	±3.73 †	±0.63 †
	SysTAUS_TRUEHADTAU_SME_TES_MODEL	-	-	-	†	±0.86	±0.90 †	-
	Systau_eleolr_el	-	±2.29 †	-	-	-	-	-
	Systau_eleolr_tauhad	±0.99 †	-	±1.11 †	±1.10	±1.02 †	±0.95 †	-
	Systau_id_highpt	†	-	†	-	†	†	-
	Systau_id_total	±5.85	-	±5.82	±5.85	±5.84	±5.85	±0.78 †
	Systau_reco_highpt	†	-	-	-	-	-	-
	Systau_reco_total	±3.17 †	-	±3.17 †	±2.82 †	±3.20 †	±3.25 †	-
b-tagging	SysFT_EFF_Eigen_B_0	±1.98 †	±2.56 †	±1.28 †	±3.18	±2.73 †	±2.05 †	-
	SysFT_EFF_Eigen_B_1	±0.68 †	±0.57 †	†	±0.86	±0.94 †	±0.66 †	-
	SysFT_EFF_Eigen_B_2	-	-	-	±0.61	-	-	-
	SysFT_EFF_Eigen_C_0	±0.99 †	-	±0.73 †	-	-	-	-
	SysFT_EFF_Eigen_C_1	±1.03 †	-	±1.71 †	-	-	-	-
	SysFT_EFF_Eigen_C_2	†	-	†	-	-	-	-
	SysFT_EFF_Eigen_Light_0	±3.85 †	±1.91 †	±5.88 †	-	-	-	-
	SysFT_EFF_Eigen_Light_1	±0.72 †	±1.22 †	†	-	-	-	-
	SysFT_EFF_Eigen_Light_10	-	-	†	-	-	-	-
	SysFT_EFF_Eigen_Light_2	†	†	±0.76 †	-	-	-	-
	SysFT_EFF_Eigen_Light_3	†	-	±1.17 †	-	-	-	-
	SysFT_EFF_Eigen_Light_5	†	-	†	-	-	-	-
	SysFT_EFF_Eigen_Light_6	-	-	†	-	-	-	-
	SysFT_EFF_Eigen_Light_7	†	-	†	-	-	-	-
	SysFT_EFF_Eigen_Light_8	-	-	†	-	-	-	-
	SysFT_EFF_Eigen_Light_9	-	-	†	-	-	-	-
	SysFT_EFF_extrapolation	†	-	-	-	-	-	-
	SysFT_EFF_extrapolation_from_charm	-	-	±0.59 †	-	-	-	-
Top (excl. XS)	Systtbar_model	-	-	-	-	-	±6.33 †	-
	Systtbar_psue	-	-	-	-	-	±6.15 †	-
	Systtbar_scale	-	-	-	-	-	±10.80 †	-
Other	SysEG_RESOLUTION_ALL	†	†	-	-	-	-	-
	SysEG_SCALE_ALLCORR	-	†	-	†	-	†	-
	SysEG_SCALE_LARCALIB_EXTRA2015PRE	-	-	-	-	†	-	-
	SysEL_EFF_ID_TOTAL_1NPCOR_PLUS_UNCOR	±0.61	±0.66	±0.79	±0.64	±0.75	±0.71	-
	SysJET_EtaIntercalibration_NonClosure	±1.33	±2.41	-	±0.62 †	-	-	-
	SysJET_GroupedNP_1	$^{+13.02}_{-11.94}$ †	±4.65 †	±5.56 †	†	±2.14 †	±2.58 †	†
	SysJET_GroupedNP_2	$^{+3.86}_{-2.16}$ †	†	†	-	†	†	-
	SysJET_GroupedNP_3	$^{+6.91}_{-4.49}$ †	†	†	†	†	†	-
	SysJET_JER_SINGLE_NP	±4.29	±2.95	±0.87	±1.04 †	±0.54	±0.87 †	-
	SysJET_JvtEfficiency_central_jets	†	-	†	-	-	-	-
	SysMET_SoftTrk_ResoPara	±1.82 †	±1.43 †	±0.62 †	†	†	†	†
	SysMET_SoftTrk_ResoPerp	±4.19 †	±1.28 †	†	±1.38 †	†	†	†
	SysMET_SoftTrk_Scale	±4.45 †	±2.06 †	†	†	†	†	†

Table 7.6 Pre-fit uncertainty (in [%]) of NPs for the 200 GeV–400 GeV BDT distribution in the $\tau_{\text{had-vis}}$+muon SR, as they are in the final workspace after smoothing and pruning. Shown are the total normalisation uncertainty, with † representing that a shape uncertainty is also considered. The normalisation effect is pruned if the uncertainty is below 0.5%, while shape effects are pruned if they do not have sufficient variations in neighbouring bins.

Type	Sample NP	W+jets [%]	Z+jets [%]	$e/\mu \to \tau_{\text{had-vis}}$ [%]	Diboson [%]	$H^{\pm}$ (200GeV) [%]	single top-quark [%]	$t\bar{t}$ [%]	jet$\to \tau_{\text{had-vis}}$ [%]
Signal	ATLAS_AU_Hp200	-	-	-	-	±11.30	-	-	-
	ATLAS_LUMI	±2.10	±2.10	±2.10	±2.10	±2.10	±2.10	-	-
	ATLAS_xsec_Diboson	-	-	-	±50.00	-	-	-	-
XS	ATLAS_xsec_W	±35.00	-	-	-	-	-	-	-
	ATLAS_xsec_Z	-	±40.00	-	-	-	-	-	-
	SysSingleTopNorm	-	-	-	-	-	±5.40	-	-
	Syszj_generator	-	±8.48 †	-	-	-	-	-	-
	Systau_ff_alpha_MJ_L1	-	-	-	-	-	-	-	±4.19 †
	Systau_ff_bdt	-	-	-	-	-	-	-	±0.68 †
Data driven	Systau_ff_mcsub	-	-	-	-	-	-	-	±5.76
	Systau_ff_stat	-	-	-	-	-	-	-	±1.67
	Sysupsilon	-	-	-	-	-	-	-	†
	tau_ff_HF_L1	-	-	-	-	-	-	-	±5.00
	SysTAUS_TRUEHADTAU_SME_TES_DETECTOR	-	±1.13	-	-	†	-	†	-
	SysTAUS_TRUEHADTAU_SME_TES_INSITU	-	±0.93	-	±2.62	±1.54 †	±3.36	±3.69 †	±0.61
	SysTAUS_TRUEHADTAU_SME_TES_MODEL	-	-	-	-	†	±0.93	±0.82	-
	Systau_eleolr_el	-	-	±2.00 †	-	-	-	-	-
Tau	Systau_eleolr_tauhad	±1.15	±0.84 †	-	±0.98 †	±1.26	±1.01 †	±0.94 †	-
	Systau_id_highpt	-	†	-	†	-	†	†	-
	Systau_id_total	±5.61	±5.90	-	±5.85	±5.77	±5.83	±5.85	±0.72
	Systau_reco_highpt	-	†	-	†	-	†	-	-
	Systau_reco_total	±4.61	±3.08 †	-	±3.06 †	±2.76 †	±3.20 †	±3.27 †	-
	SysFT_EFF_Eigen_B_0	±2.30	±2.04 †	±2.26 †	±1.34 †	±3.05	±2.78 †	±2.16 †	-
	SysFT_EFF_Eigen_B_1	±0.98	±0.75 †	±0.65 †	†	±0.59	±0.81 †	±0.69 †	-
	SysFT_EFF_Eigen_B_2	±1.11	†	-	-	±0.55	†	-	-
	SysFT_EFF_Eigen_B_3	-	†	-	-	-	†	-	-
	SysFT_EFF_Eigen_C_0	-	±0.91 †	†	†	-	-	-	-
	SysFT_EFF_Eigen_C_1	-	±1.37 †	-	±1.49 †	-	-	-	-
	SysFT_EFF_Eigen_C_2	-	†	-	†	-	-	-	-
	SysFT_EFF_Eigen_Light_0	±0.50	±1.48 †	†	±6.38 †	-	-	-	-
	SysFT_EFF_Eigen_Light_1	-	†	†	±1.07 †	-	-	-	-
b-tagging	SysFT_EFF_Eigen_Light_11	-	-	-	†	-	-	-	-
	SysFT_EFF_Eigen_Light_13	-	-	-	†	-	-	-	-
	SysFT_EFF_Eigen_Light_2	-	±2.81 †	†	†	-	-	-	-
	SysFT_EFF_Eigen_Light_3	-	±2.98 †	-	±1.26 †	-	-	-	-
	SysFT_EFF_Eigen_Light_5	-	†	-	†	-	-	-	-
	SysFT_EFF_Eigen_Light_6	-	†	-	†	-	-	-	-
	SysFT_EFF_Eigen_Light_7	-	†	-	†	-	-	-	-
	SysFT_EFF_Eigen_Light_8	-	†	-	†	-	-	-	-
	SysFT_EFF_Eigen_Light_9	-	†	-	†	-	-	-	-
	SysFT_EFF_extrapolation	-	†	-	†	-	-	-	-
	SysFT_EFF_extrapolation_from_charm	-	-	-	±0.94 †	-	-	-	-
	Systtbar_model	-	-	-	-	-	-	±6.10 †	-
Top (excl. XS)	Systtbar_psue	-	-	-	-	-	-	±9.30 †	-
	Systtbar_scale	-	-	-	-	-	-	±11.53 †	-
	SysJET_EtaIntercalibration_NonClosure	-	±0.82	-	±0.97	-	†	-	†
	SysJET_GroupedNP_1	-	$^{+3.45}_{-2.68}$ †	±3.62 †	±1.41 †	±0.96 †	±2.18 †	±2.07 †	†
	SysJET_GroupedNP_2	-	†	±0.54 †	†	†	†	†	-
	SysJET_GroupedNP_3	-	±0.98 †	±1.31 †	†	†	±0.50 †	†	†
	SysJET_JER_SINGLE_NP	-	±6.29	±2.78 †	±1.25	±1.69 †	±0.69 †	†	†
	SysJET_JvtEfficiency_central_jets	-	†	-	-	-	-	-	-
	SysMET_SoftTrk_ResoPara	-	±3.44 †	±0.69 †	†	±0.67 †	†	†	†
Other	SysMET_SoftTrk_ResoPerp	-	±2.23 †	†	†	±0.58 †	†	†	†
	SysMET_SoftTrk_Scale	-	†	±0.64 †	†	†	†	†	†
	SysMUON_EFF_SYS	±1.89	±1.08	±1.18	±1.25	±1.18	±1.22	±1.19	-
	SysMUON_EFF_TrigStatUncertainty	±1.49	±0.58	±0.55	±0.58	±0.53	±0.58	±0.56	-
	SysMUON_EFF_TrigSystUncertainty	-	±0.95	±0.94	±0.93	±0.93	±0.93	±0.93	-
	SysMUON_ID	-	†	†	-	†	†	-	-
	SysMUON_MS	-	±0.69 †	†	-	±0.80 †	†	-	-
	SysMUON_SAGITTA_RESBIAS	-	-	†	†	†	-	†	-

Table 7.7 Pre-fit uncertainty (in [%]) of NPs for the 200 GeV–400 GeV BDT distribution in the $\tau_{\text{had-vis}}$+jets SR, as they are in the final workspace after smoothing and pruning. Shown are the total normalisation uncertainty, with † representing that a shape uncertainty is also considered. The normalisation effect is pruned if the uncertainty is below 0.5%, while shape effects are pruned if they do not have sufficient variations in neighbouring bins.

Type	Sample / NP	W+jets [%]	Z+jets [%]	$e/\mu \to \tau_{\text{had-vis}}$ [%]	Diboson [%]	$H^{\pm}$ (200GeV) [%]	single top-quark [%]	$t\bar{t}$ [%]	jet$\to \tau_{\text{had-vis}}$ [%]
Signal	ATLAS_AU_Hp200	-	-	-	-	±11.30	-	-	-
	ATLAS_LUMI	±2.10	±2.10	±2.10	±2.10	±2.10	±2.10	-	-
	ATLAS_xsec_Diboson	-	-	-	±50.00	-	-	-	-
XS	ATLAS_xsec_W	±35.00	-	-	-	-	-	-	-
	ATLAS_xsec_Z	-	±40.00	-	-	-	-	-	-
	SysSingleTopNorm	-	-	-	-	-	±5.40	-	-
Data driven	Systau_ff_alpha_MJ_L0	-	-	-	-	-	-	-	±7.23
	Systau_ff_bdt	-	-	-	-	-	-	-	±1.62 †
	Systau_ff_mcsub	-	-	-	-	-	-	-	±7.03
	Systau_ff_stat	-	-	-	-	-	-	-	±1.61
	Sysupsilon	-	-	-	-	-	-	-	†
	tau_ff_HF_L0	-	-	-	-	-	-	-	±5.00
Tau	SysTAUS_TRUEHADTAU_SME_TES_DETECTOR	-	±1.90	-	±0.52	±0.74 †	±0.89 †	±0.74	†
	SysTAUS_TRUEHADTAU_SME_TES_INSITU	±4.60 †	±2.77	-	±2.68	±4.72 †	±3.74 †	±4.95 †	±0.68
	SysTAUS_TRUEHADTAU_SME_TES_MODEL	±0.73	-	-	±1.09	±1.22 †	±0.89 †	±0.98 †	-
	Systau_eleolr_el	-	-	±2.21 †	-	-	-	-	-
	Systau_id_total	±5.87	±5.86	-	±5.75 †	±5.80	±5.85	±5.87	±0.85 †
	Systau_reco_total	±2.67 †	±2.63	-	±2.62	±2.80	±2.65 †	±2.77	-
b-tagging	SysFT_EFF_Eigen_B_0	±1.45 †	±1.31 †	±1.44 †	±1.30 †	±2.49	±2.20 †	±1.94 †	-
	SysFT_EFF_Eigen_B_1	-	±0.55 †	±0.71 †	†	±1.14 †	±0.97	±0.74 †	-
	SysFT_EFF_Eigen_B_2	-	-	†	-	-	-	-	-
	SysFT_EFF_Eigen_B_3	-	-	†	-	-	-	-	-
	SysFT_EFF_Eigen_C_0	±0.85 †	±2.53 †	-	†	-	-	†	-
	SysFT_EFF_Eigen_C_1	±1.71 †	±1.64 †	†	±2.00 †	-	-	-	-
	SysFT_EFF_Eigen_C_2	†	±0.62 †	-	†	-	-	-	-
	SysFT_EFF_Eigen_Light_0	±4.80 †	±4.02 †	±0.99 †	±4.08 †	-	†	†	-
	SysFT_EFF_Eigen_Light_1	†	±0.99 †	†	†	-	-	-	-
	SysFT_EFF_Eigen_Light_10	†	-	-	-	-	-	-	-
	SysFT_EFF_Eigen_Light_11	-	-	-	†	-	-	-	-
	SysFT_EFF_Eigen_Light_2	±0.61 †	±0.53 †	†	±0.51 †	-	-	†	-
	SysFT_EFF_Eigen_Light_3	±0.70 †	†	†	±1.06 †	-	-	†	-
	SysFT_EFF_Eigen_Light_5	†	†	-	†	-	-	-	-
	SysFT_EFF_Eigen_Light_6	†	-	-	†	-	-	-	-
	SysFT_EFF_Eigen_Light_7	†	-	-	†	-	-	-	-
	SysFT_EFF_Eigen_Light_8	†	-	-	†	-	-	-	-
	SysFT_EFF_Eigen_Light_9	-	-	-	†	-	-	-	-
	SysFT_EFF_extrapolation	±0.52	±0.62 †	†	±0.51 †	-	†	-	-
	SysFT_EFF_extrapolation_from_charm	-	±2.84 †	-	±1.10 †	-	-	-	-
Top (excl. XS)	Systtbar_model	-	-	-	-	-	-	±13.25 †	-
	Systtbar_psue	-	-	-	-	-	-	±14.02 †	-
	Systtbar_scale	-	-	-	-	-	-	±2.05 †	-
Other	SysJET_EtaIntercalibration_NonClosure	-	±1.18	-	-	±0.91	±0.88 †	±0.73 †	-
	SysJET_GroupedNP_1	±12.41 †	±3.19 †	±10.25 †	$^{+7.99}_{-5.99}$ †	±9.17 †	±8.86 †	±9.66 †	±1.67 †
	SysJET_GroupedNP_2	±1.13 †	±3.63 †	±0.95 †	†	±1.15 †	±1.30 †	±1.91 †	†
	SysJET_GroupedNP_3	$^{+3.42}_{-2.56}$ †	±1.79 †	±1.48 †	†	±1.52 †	$^{+2.35}_{-1.84}$ †	±1.98 †	†
	SysJET_JER_SINGLE_NP	±6.10 †	±5.32	±1.84	±0.90	±2.45	±5.20 †	±4.26	±0.73 †
	SysMET_SoftTrk_ResoPara	±1.65 †	±1.62 †	±1.50 †	±1.25 †	±1.09 †	±2.08 †	±1.30 †	†
	SysMET_SoftTrk_ResoPerp	±0.87 †	±3.02 †	±1.60 †	†	†	±1.78 †	±1.39 †	†
	SysMET_SoftTrk_Scale	±1.01 †	±0.92 †	±0.68 †	†	†	±1.48 †	±1.58 †	-
	Sysjet_sf_NOMINAL_central_jets_global_effSF_JVT	±0.68	±0.65	±0.78	±0.63	±0.74	±0.69	±0.78	-
	Sysjet_sf_NOMINAL_central_jets_global_ineffSF_JVT	†	-	-	-	-	-	-	-
	Sysjet_sf_NOMINAL_global_effSF_MVX	±0.63 †	±0.81 †	†	±0.62 †	-	±0.56 †	-	-
	Sysjet_sf_NOMINAL_global_ineffSF_MVX	-	-	-	†	-	†	-	-
	Systhree_jets_trig_eff	-	±0.59 †	±0.67	-	±0.60	±0.53 †	±0.63	-
	Syswj_generator	±6.40 †	-	-	-	-	-	-	-

Table 7.8 Pre-fit uncertainty (in [%]) of NPs for the 200 GeV–400 GeV BDT distribution in the top CR, as they are in the final workspace after smoothing and pruning. Shown are the total normalisation uncertainty, with † representing that a shape uncertainty is also considered. The normalisation effect is pruned if the uncertainty is below 0.5%, while shape effects are pruned if they do not have sufficient variations in neighbouring bins.

Type	Sample NP	Z+jets [%]	Diboson [%]	$H^{\pm}$ (200GeV) [%]	single top-quark [%]	$t\bar{t}$ [%]
Signal	ATLAS_AU_Hp200	-	-	±11.30	-	-
	ATLAS_LUMI	±2.10	±2.10	±2.10	±2.10	-
	ATLAS_xsec_Diboson	-	±50.00	-	-	-
XS	ATLAS_xsec_Z	±40.00	-	-	-	-
	SysSingleTopNorm	-	-	-	±5.40	-
	Syszj_generator	±26.76	-	-	-	-
	SysFT_EFF_Eigen_B_0	±2.14	±1.51	±3.64	±2.80	±2.18
	SysFT_EFF_Eigen_B_1	±0.78	-	±1.06	±0.85	±0.70
	SysFT_EFF_Eigen_C_0	±0.67	±1.26	-	-	-
	SysFT_EFF_Eigen_C_1	±1.37	±1.78	-	-	-
b-tagging	SysFT_EFF_Eigen_Light_0	±1.17	±6.72	±1.52	-	-
	SysFT_EFF_Eigen_Light_1	±0.96	±1.93	-	-	-
	SysFT_EFF_Eigen_Light_2	±0.85	-	-	-	-
	SysFT_EFF_Eigen_Light_3	±0.63	±0.68	-	-	-
	SysFT_EFF_Eigen_Light_5	-	±0.53	-	-	-
	Systtbar_model	-	-	-	-	±1.67
Top (excl. XS)	Systtbar_psue	-	-	-	-	±2.55
	Systtbar_scale	-	-	-	-	±3.16
	SysEL_EFF_ID_TOTAL_1NPCOR_PLUS_UNCOR	±0.76	±0.85	±0.62	±0.73	±0.68
	SysJET_EtaIntercalibration_NonClosure	±0.80	-	±0.55	-	-
	SysJET_GroupedNP_1	±12.93	±5.75	±2.58	±2.09	±1.79
	SysJET_GroupedNP_2	-	±0.58	-	-	-
	SysJET_GroupedNP_3	±3.67	-	±0.79	-	-
	SysJET_JER_SINGLE_NP	±1.01	±1.70	±5.59	-	±0.52
Other	SysMET_SoftTrk_ResoPara	±4.95	±0.76	-	-	-
	SysMET_SoftTrk_ResoPerp	±4.27	±0.79	±0.66	-	-
	SysMET_SoftTrk_Scale	±2.21	±0.90	-	-	-
	SysMUON_EFF_SYS	±1.08	±1.27	±1.14	±1.20	±1.18
	SysMUON_EFF_TrigStatUncertainty	±0.59	±0.54	±0.59	±0.57	±0.56
	SysMUON_EFF_TrigSystUncertainty	±0.92	±0.93	±0.93	±0.93	±0.93
	SysMUON_MS	±1.38	-	±0.69	-	-
	SysMUON_SAGITTA_RESBIAS	-	±0.50	±0.61	-	-

7.5 Results

The statistical analysis is based on a binned likelihood function with a parameter of interest (POI) μ which scales the signal strength. The signal strength corresponds to the normalisation of each signal sample such that $\mu = 1$ corresponds to a signal cross-section of 1 pb. The combined statistical model consists of the τ_{had}+jets, $\tau_{\text{had-vis}}$+electron and $\tau_{\text{had-vis}}$+muon SRs and the top CRs. All NPs are fully correlated between regions. The statistical analysis involves the combined simultaneous fit of the likelihood functions in each region to the data, where μ is allowed to float as a free parameter. The final discriminating variable used in the SRs is the BDT score, the binning of which is optimised prior to looking at the data by comparing the effect of different binning schemes on the expected cross-section limits.

In order to test the background-only modelling, the BDT distribution in each mass range is fit to data while $\mu = 0$ is fixed. The BDT distributions in the five mass ranges considered in the analysis are shown in Figure 7.5 ($\tau_{\text{had-vis}}$+jets), Figure 7.6 ($\tau_{\text{had-vis}}$+electron), and Figure 7.7 ($\tau_{\text{had-vis}}$+muon). The data are found to be consistent with the background-only hypothesis. Table 7.9 shows the compatibility of each mass point with the SM, where the p_0-values (Eq. (5.27)) are quoted for each $m_{H^\pm}$ point. The smallest p_0-value is 0.28 for both the $m_{H^\pm} = 350$ GeV and $m_{H^\pm} = 400$ GeV mass points.

Table 7.9 p_0-values for each $m_{H^\pm}$ point.

m_{H^+} [GeV]	p_0-value	m_{H^+} [GeV]	p_0-value	m_{H^+} [GeV]	p_0-value
90	0.92	175	0.66	600	0.77
100	0.83	180	0.62	700	0.80
110	0.96	200	0.54	800	0.82
120	0.97	225	0.50	900	0.82
130	0.61	250	0.38	1000	0.82
140	0.55	275	0.33	1200	0.81
150	0.66	300	0.34	1400	0.81
160	0.72	350	0.28	1600	0.81
165	0.69	400	0.28	1800	0.80
170	0.63	500	0.60	2000	0.79

Exclusion limits are set at the 95% confidence level (CL), by using the frequentist CLs method described in Section 5.2.2, on the total cross-section times branching fraction, $\sigma(pp \to tbH^+) \times B(H^+ \to \tau\nu)$, for the full mass range investigated. Figure 7.8 (a) shows the expected and observed exclusion limits as a function of the H^+ mass hypothesis. A comparison to results obtained with the Run-1 data at $\sqrt{s} = 8$ TeV [97] is also shown. The observed limits range from 4.2 pb to 2.5 fb over the mass range considered. Direct cross-

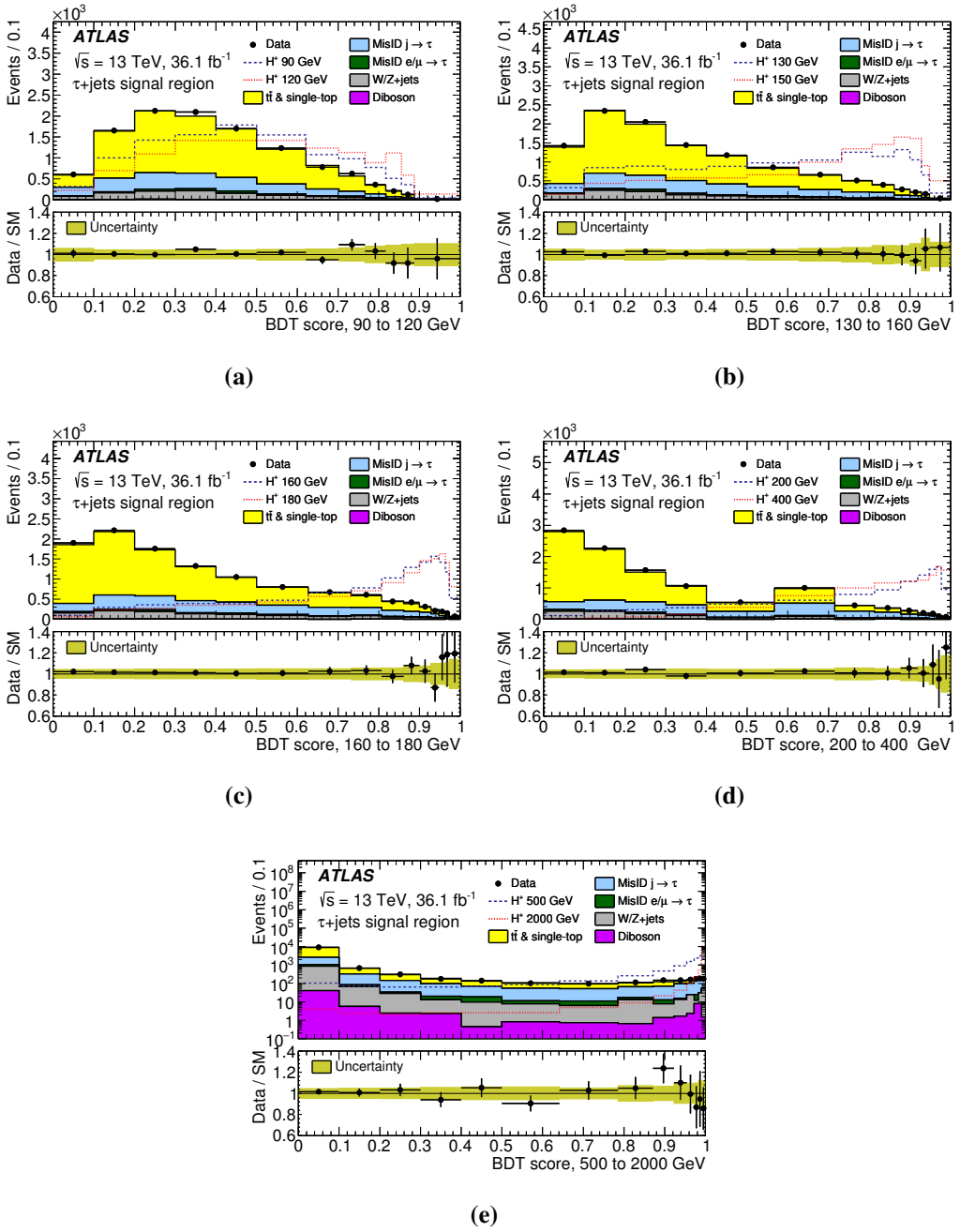

Figure 7.5 Post-fit BDT score distributions in the $\tau_{\text{had-vis}}$+jets SR from the combined background-only fit to data for the five mass ranges used in the BDT training [2]. Ratio plots shown the comparison of the observed data versus the SM background prediction, with the total post-fit uncertainties. The signal normalisation has been scaled for illustration purposes.

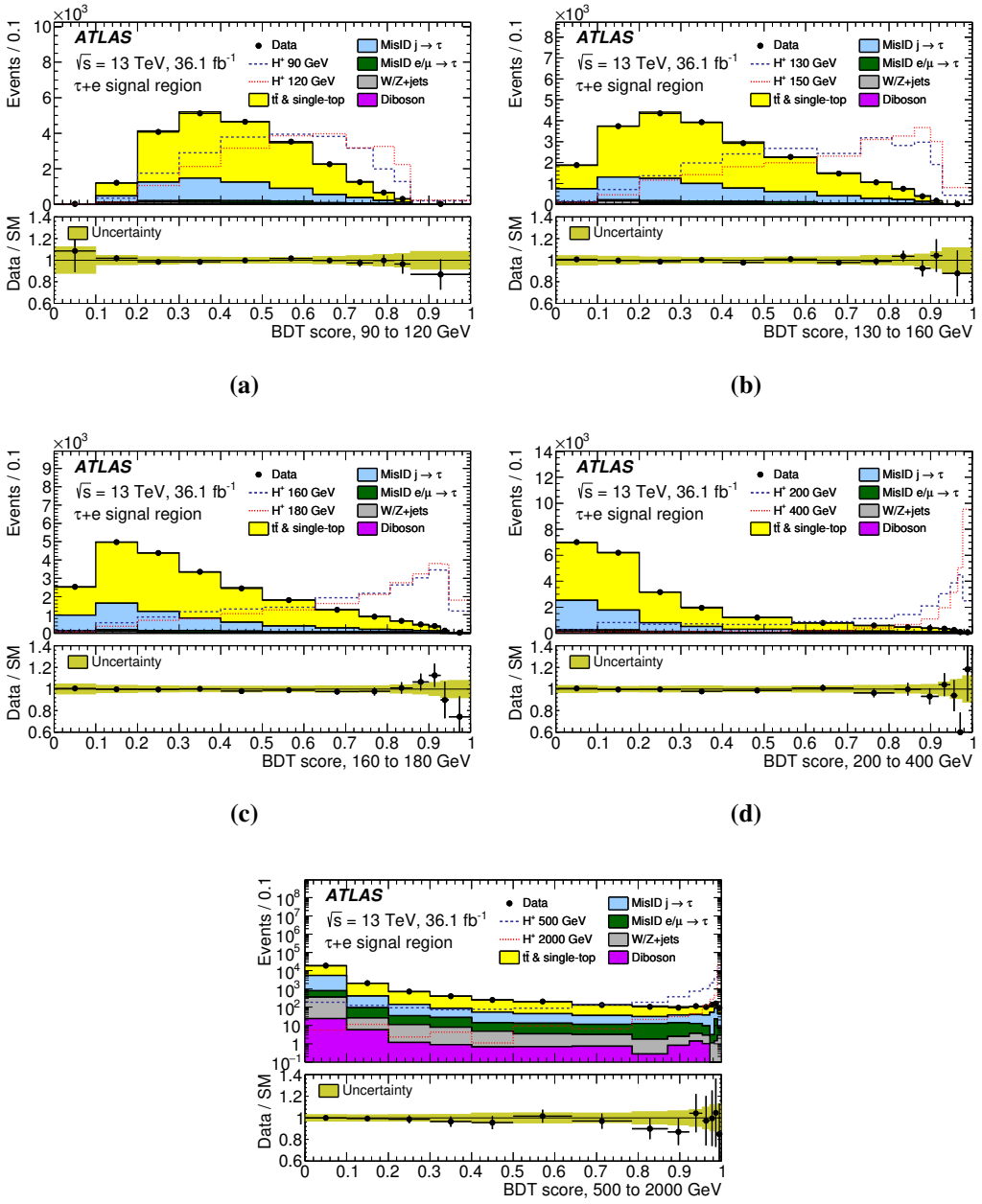

Figure 7.6 Post-fit BDT score distributions in the $\tau_{\text{had-vis}}$+electron SR from the combined background-only fit to data for the five mass ranges used in the BDT training [2]. Ratio plots shown the comparison of the observed data versus the SM background prediction, with the total post-fit uncertainties. The signal normalisation has been scaled for illustration purposes.

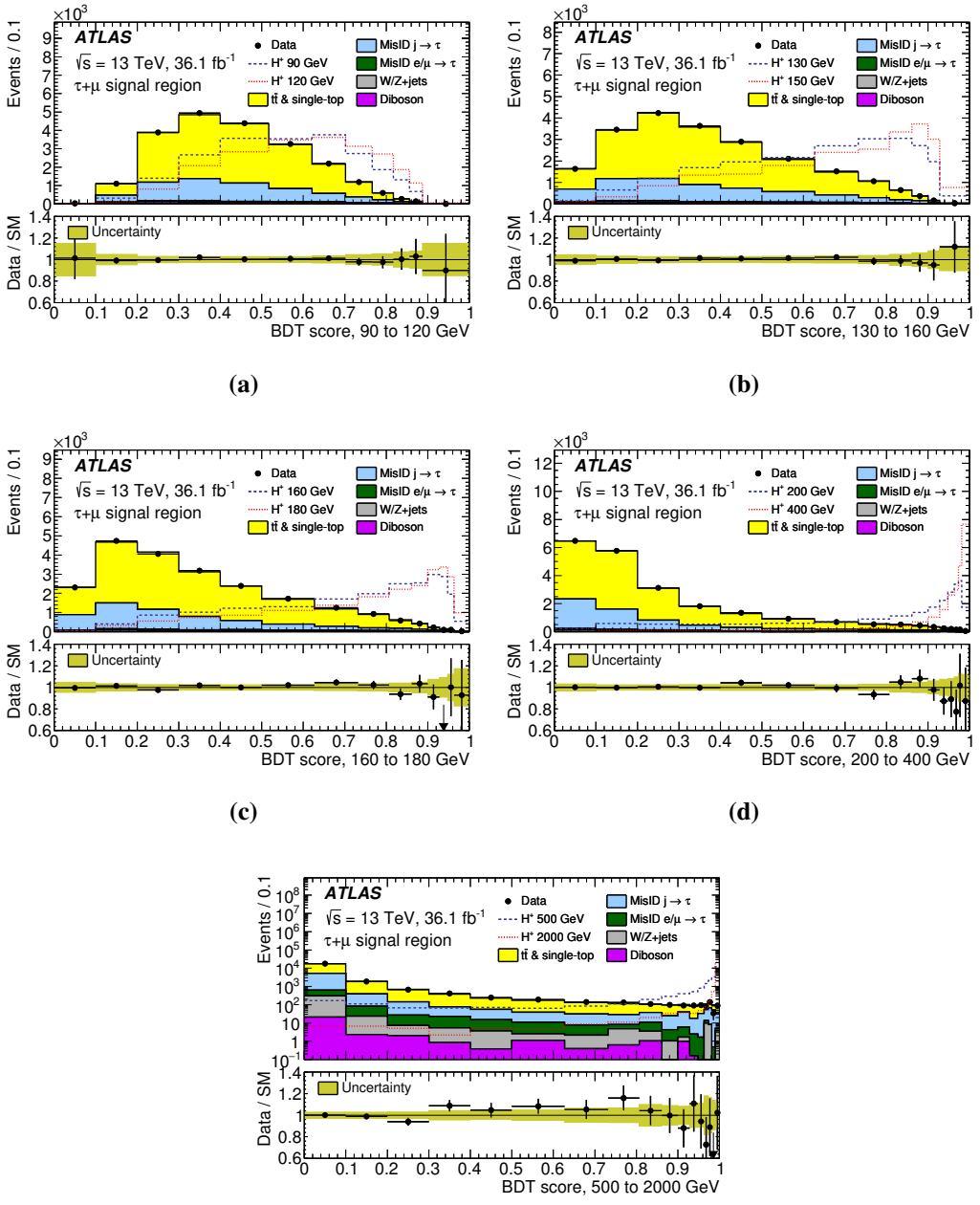

Figure 7.7 Post-fit BDT score distributions in the $\tau_{\text{had-vis}}$+muon SR from the combined background-only fit to data for the five mass ranges used in the BDT training [2]. Ratio plots shown the comparison of the observed data versus the SM background prediction, with the total post-fit uncertainties. The signal normalisation has been scaled for illustration purposes.

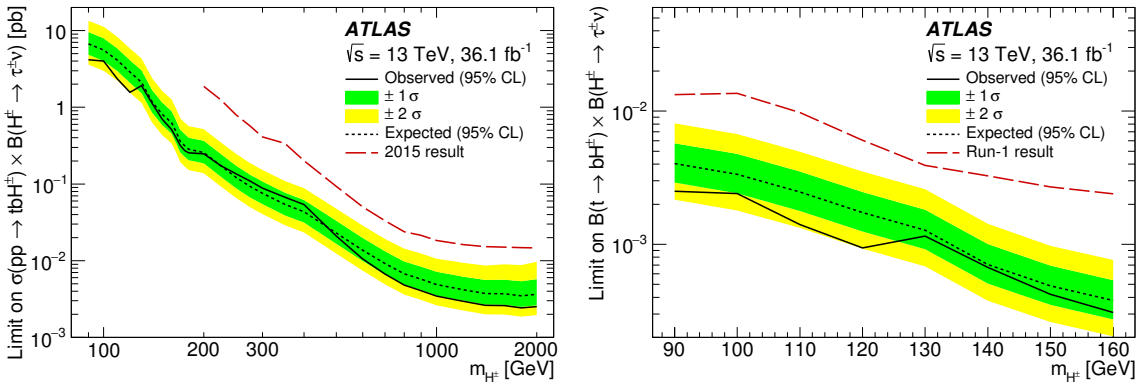

(a) **(b)**

Figure 7.8 Observed and expected 95% CL exclusion limits on (a) $\sigma(pp \to tbH^+) \times B(H^+ \to \tau\nu)$ and (b) $B(t \to bH^+) \times B(H^+ \to \tau\nu)$ as a function of the charged Higgs boson mass in 36.1 fb^{-1} of pp collision data at $\sqrt{s} = 13$ TeV [2]. Direct cross-section limits in the intermediate mass (160–180 GeV) range are placed for the first time. A comparison to previously observed exclusion limits on $B(t \to bH^+) \times B(H^+ \to \tau\nu)$ from Ref. [97] and on $\sigma(pp \to tbH^+) \times B(H^+ \to \tau\nu)$ from Ref. [232] are shown.

section limits in the intermediate mass (160–180 GeV) range are placed for the first time. The limits are interpolated between the signal points. The interpolation was tested at the boundary of each mass bin, where the alternative BDT distribution was used. The cross-section limits are found to be consistent with the default limit in each case. For the mass range between 90 and 160 GeV, the total cross-section limits can be used to extract limits on the branching fraction $B(t \to bH^+) \times B(H^+ \to \tau\nu)$ while assuming that the charged Higgs production cross-section is from $t\bar{t}$ events. Assuming the $t\bar{t}$ cross-section has the SM prediction, limits are set on $B(t \to bH^+) \times B(H^+ \to \tau\nu)$, shown in Figure 7.8 (b). The observed branching fraction limits range between 0.25% and 0.031% for the aforementioned masses, respectively.

The impact of systematic uncertainties on the result is extracted by comparing the expected exclusion limits when including different sets of uncertainties in the model, as was done for the di-tau analysis in Section 6.5.3. The impact from different sources of uncertainty is determined for two representative mass points and shown in Table 7.10. The expected 95% CL limits are calculated for the case where no NPs are included in the fit and compared to the limit calculated when introducing a group of systematic uncertainties. The largest impact on the result for low-mass points is from the uncertainties related to the data-driven background estimation ($\sim 20\%$), followed by reconstruction and identification related uncertainties ($\sim 17\%$). For the high-mass region the dominant uncertainties are

Table 7.10 Impact of systematic uncertainties on the expected 95% CL limit on $\sigma(pp \to tbH^+) \times B(H^+ \to \tau\nu)$, for two H^+ mass hypotheses: 170 GeV and 1000 GeV [2]. The impact is obtained by comparing the expected limit considering only statistical uncertainties (stat. only) with the expected limit when a certain set of systematic uncertainties is added in the limit-setting procedure.

Source of systematic uncertainty	Impact on the expected limit (stat. only) in %	
	$m_{H^+} = 170$ GeV	$m_{H^+} = 1000$ GeV
Experimental		
luminosity	2.9	0.2
trigger	1.3	<0.1
$\tau_{\text{had-vis}}$	14.6	0.3
jet	16.9	0.2
electron	10.1	0.1
muon	1.1	<0.1
$E_{\text{T}}^{\text{miss}}$	9.9	<0.1
Fake-factor method	20.3	2.7
Υ modelling	0.8	–
Signal and background models		
$t\bar{t}$ modelling	6.3	0.1
W/Z+jets modelling	1.1	<0.1
cross-sections ($W/Z/VV/t$)	9.6	0.4
H^+ signal modelling	2.5	6.4
All	52.1	13.8

related to statistical sources. The systematic uncertainties are therefore not as relevant, and the largest impact is from the uncertainty on the signal acceptance ($\sim 6\%$).

The category "All" in Table 7.10 is the difference of evaluating the charged Higgs cross-section limits with only statistical uncertainties, compared to applying all statistical and systematic uncertainties. It should be noted that the impacts are on the expected limit of the cross-section, and not on the signal strengths parameter itself. Due to correlations between nuisance parameters, the row "All" is not the trivial sum of individual contributions. In the case where statistical uncertainties dominate and there are no correlations between the groups of uncertainties, the row "All" would be approximately obtained by summing individual contributions in quadrature. In the same case, but with statistical uncertainties dominating, the row "All" would be approximately obtained by summing the individual contributions linearly. The correlation matrices between systematic uncertainties are shown in Appendix C.2, where large correlations between groups are seen, in particular with $t\bar{t}$ generator uncertainties.

The cross-section limits are interpreted in the context of two MSSM models. Figure 7.9 (a) and (b) show the 95% CL exclusion limits on $\tan\beta$ as a function of the charged Higgs boson mass in the context of the hMSSM and the $m_h^{\text{mod-}}$ benchmark scenarios, respectively. The cross-section predictions are determined as described in Section 2.4.3. The results are compared to the exclusion limits based on the previous Run-2 result with 3.2 fb^{-1} of $\sqrt{s} = 13\,\text{TeV}$ data [232].

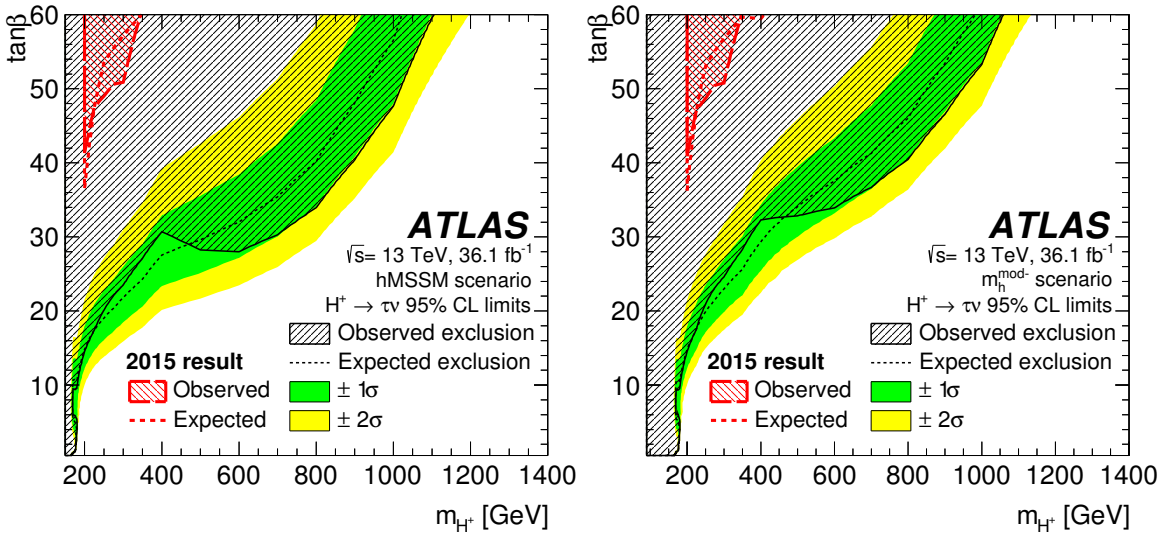

Figure 7.9 95% CL exclusion limits on $\tan\beta$ as a function of m_{H^+}, shown in the context of the (a) hMSSM and the (b) $m_{\text{h}}^{\text{mod}-}$ benchmark scenarios, for the regions in which reliable theoretical predictions exist ($1 \leq \tan\beta \leq 60$) [2]. As a comparison, the red curves show the observed and expected exclusion limits based on the dataset collected in 2015 at $\sqrt{s} = 13\,\text{TeV}$ [232].

Chapter 8

BSM interpretation of SM Higgs Couplings

The measurement of the Higgs boson production and decay rates are vital for probing the mechanism behind EWSB in the SM. As described in Section 1.4, there are a vast number of production and decay modes at the LHC which offer sensitivity to measurements of the 125 GeV Higgs boson. As such, there are several analyses targetting measurements of different Higgs boson topologies. The precision measurement of the Higgs boson fiducial and differential cross-sections are dependant not only on the individual analysis measurements, but benefit substantially from the combination of individual measurements. In particular, the combination of Higgs cross-section measurements gives a more powerful global statement on the state of Higgs measurements by probing their combined compatability with the SM.

One such combined measurement is that of the total inclusive cross-section (or signal strength) of the Higgs boson, which can be measured globally across all sub-channels in the combination. Another approach is to measure the total cross-sections of the dominant Higgs boson production and decay modes individually, which can be done inclusively as measurements of the production cross-section times branching fraction of individual processes. Yet another measurement is related to the compatability of the combined measurement to the expected SM coupling strengths, done in the so called κ-framework (detailed in Section 8.2), in which Higgs boson production cross-sections and branching fractions are parameterised in terms of the Higgs boson coupling strength to SM (and BSM) particles. The coupling strength measurements can be reinterpreted in the context of BSM models which have predefined Higgs gauge and Yukawa coupling predictions, as is the case with the 2HDM and MSSM introduced in Chapter 2.

One such combination of ATLAS and CMS analyses was performed with the full Run-1 datasets [31]. The combination measured the Higgs boson production cross-sections, decay rates, and couplings. More recent measurements are performed by the ATLAS experiment when combining measurement of Higgs cross-section analyses using up to 79.8 fb^{-1} of Run-2 data [241]. The most up to date ATLAS cross-section measurements using up to 79.8 fb^{-1} of Run-2 data are detailed in Ref. [3] and are presented here.

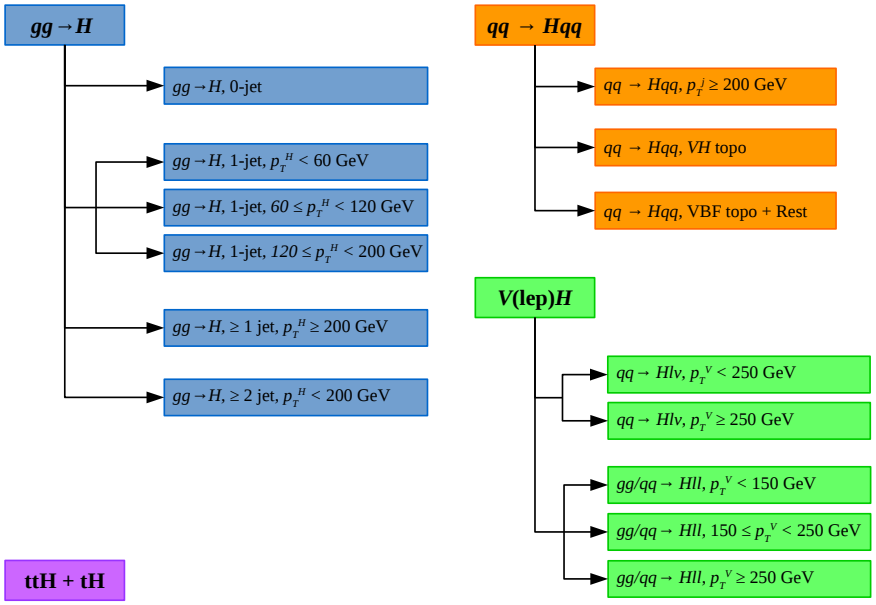

Figure 8.1 Definition of the simplified template cross section (STXS) measurement regions used in Ref. [3]. For each Higgs boson production process, the object selection for each region is shown, with regions nearer the top taking precedence in the case of overlap.

Input channels to the combination are constructed using the STXS regions as defined in Ref. [36]. The STXS regions serve as inputs to combined measurements of the total Higgs signal strength, production mode cross-sections and branching ratios, and the κ-framework interpretations. They are also measured in their own right. The STXS regions are defined in terms of the kinematics and topology of the Higgs production processes and decays such that: they maximise the sensitivity to deviations from the SM; they avoid large theory uncertainties with respect to the corresponding SM predictions; they approximately match the experimental acceptance so as to minimise model-dependent extrapolations. In light of this final criteria all regions are defined with the Higgs boson rapidity, y_H, satisfying $|y_H| < 2.5$, which corresponds to the region of experimental sensitivity. STXS regions are partitioned in terms of the Higgs boson transverse momentum, the number of associated jets,

and the transverse momentum of associated vector-bosons if present. Figure 8.1 shows the definition of the regions used in Ref. [3] with further details in the reference.

The regions included in the combined measurements are targetting the most prominent Higgs production modes (see Section 1.3) at the LHC: ggF, VBF, VH, and $t\bar{t}H$. The decay modes (Section 1.4.2) targeted are $H \to \gamma\gamma$, $H \to ZZ^*$, $H \to WW^*$, $H \to \tau\tau$, and $H \to b\bar{b}$. The $H \to \mu\mu$ analysis is also considered: since it is not yet sensitive to Higgs boson signal at the level of the SM prediction, it is only combined with other channels in the κ-framework measurement, and excluded from other measurements. A summary of the analyses included in the Higgs cross-section combination, along with the integrated luminosity of their respective Run-2 datasets [168], is given in Table 8.1.

Results from the inclusive Higgs signal strength measurement and Higgs production cross-sections and decays are summarised briefly in Section 8.1. The κ-framework is introduced in Section 8.2 along with the results for the parameterisation assuming a SM structure. The main focus in this section is on the results presented in Section 8.3 related to the reinterpretation of the κ-framework measurements in the context of 2HDMs and the MSSM. With each parameterisation considered, its compatability with the SM is quantified using the p_0-value from Eq. (5.27). The notation used in Ref. [3] is p_{SM} and is adopted here for consistency with the figures. The resulting p_{SM} approaches unity when the best fit values align with the SM prediction, i.e., the measurement is SM-like.

Table 8.1 Analyses included in the Higgs cross-section combination in Ref. [3] with up to 80fb^{-1} of Run-2 data.

Analysis	Integrated luminosity (fb^{-1})	Refs.
$H \to \gamma\gamma$	79.8	[33, 242]
$H \to ZZ^* \to 4\ell$	79.8	[33, 243]
$H \to WW^* \to e\nu\mu\nu$	36.1	[244]
$H \to \tau\tau$	36.1	[164]
VH,$H \to b\bar{b}$	79.8	[245]
VBF,$H \to b\bar{b}$	24.5-30.6	[246]
$t\bar{t}H$, $H \to b\bar{b}$ and $t\bar{t}H$ multilepton	36.1	[33, 247, 248]
$H \to \mu\mu$	79.8	[249]

8.1 Higgs signal strength and cross-section measurements

8.1.1 Measurement of the Higgs global signal strength

The measurement of the global signal strength is performed within the combination of Higgs cross-section measurements described above. For a specific Higgs production process i, with cross-section σ_i, and decay mode f, with branching fraction B_f, the Higgs signal yield may be expressed in terms of the signal strength μ_{if},

$$\mu_{if} = \mu_i \times \mu_f = \frac{\sigma_i}{\sigma_i^{\mathrm{SM}}} \times \frac{B_f}{B_f^{\mathrm{SM}}}, \tag{8.1}$$

were μ_i and μ_f are the signal strengths associated with production process i and decay mode f, respectively. Here σ_i^{SM} and B_f^{SM} are the SM predictions for σ_i and B_f, respectively. It follows that the SM expectation corresponds to $\mu_{if} = 1$.

In order to extract the global Higgs signal strength μ an unconditional fit is performed with every $\mu_{if} = \mu$. The likelihood function profiled against μ is shown in Figure 8.2. The observed signal strength is measured to be,

$$\mu = 1.11^{+0.09}_{-0.08} = 1.11^{+0.05}_{-0.05}\,(\text{stat.})\,^{+0.05}_{-0.04}\,(\text{exp.})\,^{+0.05}_{-0.04}\,(\text{sig. th.})\,^{+0.03}_{-0.03}\,(\text{bkg. th.}), \tag{8.2}$$

which is consistent with the SM with a two-sided p-value of $p_{\mathrm{SM}} = 18.0\%$. The uncertainty of the result is decomposed into its component sources: statistical uncertainties (stat.), experimental systematic uncertainties (exp.), and theory systematic uncertainties affecting background (bkg. th.) and signal (sig. th.) processes. This is done following the prescription outlined in Section 5.5.2 for the uncertainty breakdown. Here groups of uncertainties are fixed to their post-fit values, without replacement, and the fit is performed again to extract the uncertainty of that group. The order in which the groups are fixed is first background theory, then signal theory, and finally experimental systematic uncertainties, at which point one is left with only the statistical component. This process is detailed in Figure 8.2 where the likelihoods are shown with groups of NPs fixed, and the $-2\log\lambda = 1$ crossing corresponds to the uncertainties in Eq. 8.2.

The breakdown of groups of uncertainties[60] is extracted as described in Section 5.5.2 and is presented in Table 8.2. The up and down uncertainties are symmetrized into a single number, and the uncertainties are presented as relative to the measured signal strength $\Delta\mu/\mu$

[60] A list of the categories assigned to each NP in the workspace can be found in the internal documentation in Ref. [250] and has been excluded here for brevity.

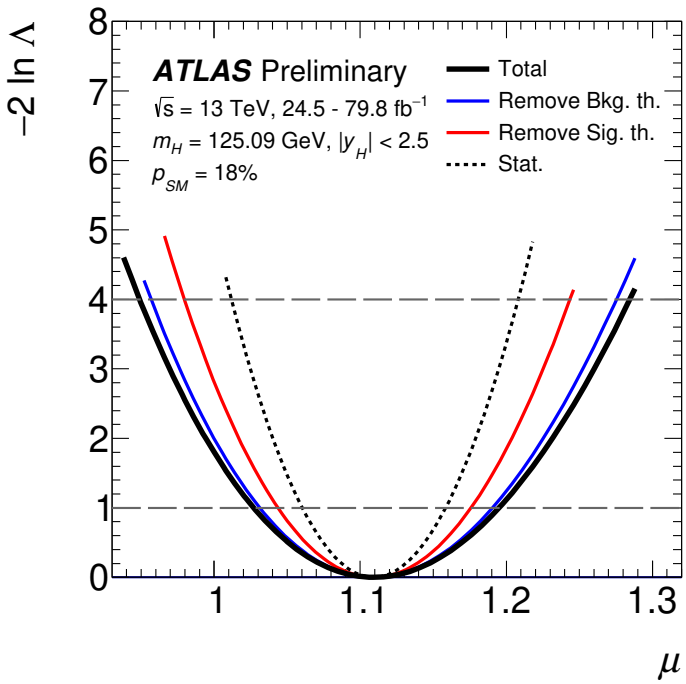

Figure 8.2 Negative log-likelihood scan of μ on the observed data [3]. Different lines show the effect of of removing different groups of uncertainties from the fit.

in percent. The corresponding ranking plot of the top 20 systematic uncertainties is shown in Figure 8.3. The pre-fit and post-fit impact $\Delta\hat{\mu}/\Delta\hat{\mu}_{\text{tot}}$ of each NP on $\hat{\mu}$ is obtained from Eq. (5.38), while their pull is obtained from Eq. (5.37). The total statistical uncertainty is around 4.4%, comparable to the total experimental and theoretical uncertainties. The largest source of systematic uncertainty is attributed to the Higgs signal theoretical uncertainty which by itself is around 4.2%. This can be attributed primarily to QCD scale uncertainties related to ggF, as evident from the highest (and 4th highest) ranked NP in the ranking plot. The most important source of experimental uncertainty can be attributed to uncertainties in the luminosity calculation (the luminosity NP is 2nd highest rank), and sources of uncertainties attributed to electrons and photons (NP with the 3rd highest rank).

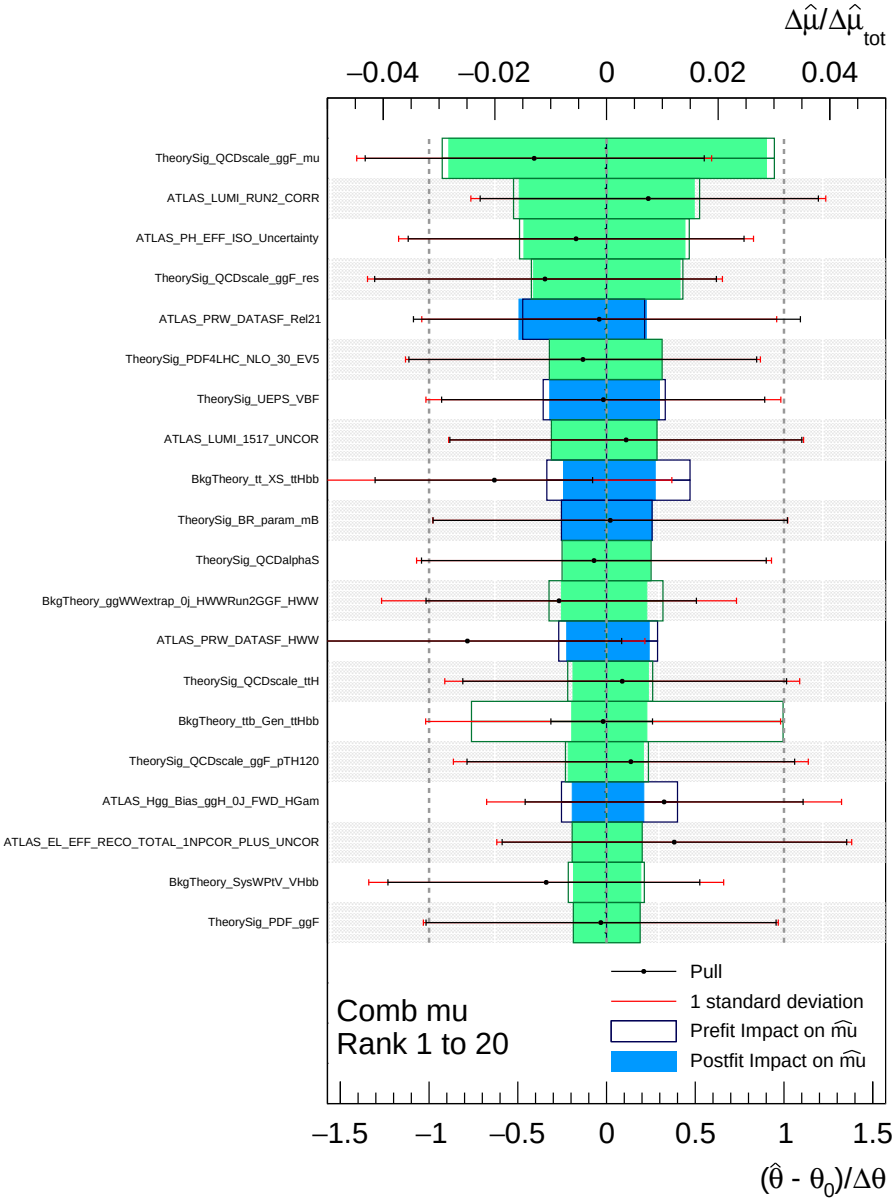

Figure 8.3 Ranking of systematic uncertainties for inclusive μ measurement of the 125 GeV Higgs boson.

Table 8.2 Breakdown of sources of uncertainties for the inclusive Higgs boson μ measurement [3].

Uncertainty group	$\Delta\mu/\mu$ [%]
Total	7.62
Statistical uncertainties	4.42
Systematic uncertainties (w/o MC stat.)	5.95
Experimental uncertainties	4.06
Bkg. modelling	1.55
Luminosity	2.00
Flavor tagging	1.08
Jets, $E_{\mathrm{T}}^{\mathrm{miss}}$	1.40
Electrons, photons	2.19
Muons	0.24
Taus	0.39
Other	1.58
Theoretical uncertainties	4.78
Signal	4.15
Background	2.57
MC stat. uncertainties	1.67

8.1.2 Higgs production cross-section measurements

Inclusive Higgs production cross-sections are measured directly from a fit to data where all Higgs branching fractions are fixed to their SM values. The production cross-sections considered are ggF, VBF, WH, ZH (including $ggZH$), and the combination of $t\bar{t}H$ and tH ($t\bar{t}H+tH$) referred to here as $t\bar{t}H$. The relative fractions of $t\bar{t}H$ and tH are fixed to their SM expectation. Similarly, the ggF cross-section includes a small contribution from $b\bar{b}H$, the proportion of which is set to the SM prediction. The five parameters of interest summarised in Table 8.3 are simultaneously profiled in an unconditional fit of the likelihood function.

Table 8.3 Parameters of interest for the measurement of production cross-sections.

POI	Name in workspace	Description
ggF	r_ggF	cross-section for ggF and $b\bar{b}H$
VBF	r_VBF	cross-section for VBF
ttH	r_ttH	cross-section for $t\bar{t}H$ and tH
WH	r_WH	cross-section for WH
ZH	r_ZH	cross-section for ZH and $ggZH$

The best fit values of the production cross-sections, as well as their uncertainties and SM predictions, are shown in Table 8.4. The results are summarised in Figure 8.4 with the cross-sections normalised to their SM predictions. The significance of rejecting the H_0 hypothesis (no SM Higgs) in favour of H_{SM} are calculated with the prescription presented in Eqs. (5.27) and (5.30), using the $\mu' = 0$ Asimov dataset for the expected significance[61]. The VBF process has an observed (expected) significance of 6.5σ (5.3σ). The observed (expected) significance of the combined VH measurement is 5.3σ (4.7σ), while for individual modes WH and ZH are 3.5σ (2.7σ) and 3.6σ (3.6σ), respectively. The observed (expected) significance for $t\bar{t}H$ production is 5.8σ (5.4σ). The compatability with the SM is calculated using Eq. (5.27) with 5 DOFs and has a p-value of $p_{\text{SM}} = 76\%$.

Table 8.4 Results from the Higgs production cross-section measurements [3]. Shown are the total cross-section and uncertainty for each process in [pb]. The uncertainties are broken down into their statistical, experimental and theoretical components, as described in the text. The most recent theoretical predictions are shown for comparison.

Cross-section [pb]								
	Measured						SM Predicted	
Production	total	tot. unc.	stat.	exp.	th.	bkg. th.	total	tot. unc.
ggF	46.5	4.0	3.1	2.2	0.9	1.13	44.7	2.2
VBF	4.25	$^{+0.84}_{-0.77}$	$^{+0.63}_{-0.60}$	$^{+0.35}_{-0.32}$	$^{+0.42}_{-0.32}$	$^{+0.14}_{-0.11}$	3.515	0.075
WH	1.57	$^{+0.48}_{-0.46}$	$^{+0.34}_{-0.33}$	$^{+0.25}_{-0.24}$	$^{+0.11}_{-0.07}$	0.20	1.204	0.024
ZH	0.84	$^{+0.25}_{-0.23}$	0.19	0.09	$^{+0.07}_{-0.04}$	0.10	0.797	$^{+0.033}_{-0.026}$
$t\bar{t}H$	0.71	$^{+0.15}_{-0.14}$	0.10	0.07	$^{+0.05}_{-0.04}$	$^{+0.08}_{-0.07}$	0.586	$^{+0.034}_{-0.049}$

The production cross-section fits are studied extensively in order to validate the fitting procedure. The correlations between POIs, and ranking plots of the most relevant NPs, are documented in Appendix D.1 and discussed here. The correlations between the measured cross-sections are summarised in Figure D.1, showing a 15% anti-correlation between the ggF and VBF cross-sections attributed to non-negligible contamination of ggF in VBF signal regions. The symmetrised breakdown of systematic uncertainties is presented in Table 8.5 for each production mode. The ranking results for the measurement of the five production cross-sections are presented in Figures D.2 and D.3. With the exception of ggF, the highest ranked uncertainties all come from theoretical sources. Sources of theory uncertainties related to the Higgs signal affect the VBF result at a level of approximately 9%. The highest ranked systematic in the VBF result is attributed to uncertainties in the underlying event

[61] The ggF process is well established and has an arbitrarily large significance (over 10 σ). It is not quoted in the result.

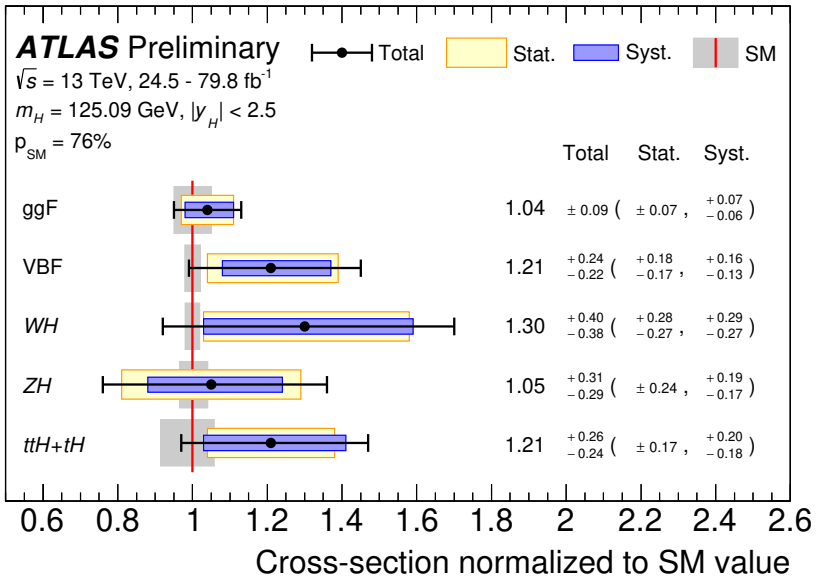

Figure 8.4 Summary of likelihood scan results for the Higgs production cross-section measurement [3].

parton shower (UEPS). Theory uncertainties related to background processes dominate in VH and $t\bar{t}H$ at a level of approximately 13% and 10%, respectively. Both WH and ZH have their highest ranked uncertainties related to the kinematics of the vector boson in background processes. Similarly the highest ranked $t\bar{t}H$ uncertainty is related to $t\bar{t}$ background modelling.

Alternative parameterisations for the cross-section results are presented in Ref. [3]. Those details are not relevant to the discussion of the κ-framework that follow but their results are briefly summarised in Appendix D.2.

Table 8.5 Breakdown of groups of uncertainties for the Higgs production cross-section [3].

Uncertainty group	$\frac{\Delta\sigma_{ggF}}{\sigma_{ggF}}$[%]	$\frac{\Delta\sigma_{VBF}}{\sigma_{VBF}}$[%]	$\frac{\Delta\sigma_{WH}}{\sigma_{WH}}$[%]	$\frac{\Delta\sigma_{ZH}}{\sigma_{ZH}}$[%]	$\frac{\Delta\sigma_{ttH}}{\sigma_{ttH}}$[%]
Total	8.86	18.90	30.02	28.65	20.93
Statistical uncertainties	6.36	14.55	20.97	22.89	14.17
Systematic uncertainties (w/o MC stat.)	5.97	11.04	19.74	15.42	14.79
Experimental uncertainties	5.01	6.49	9.93	9.56	9.20
Bkg. modelling	2.50	2.19	4.69	2.90	5.68
Luminosity	2.14	1.81	1.75	1.76	3.05
Flavor tagging	0.94	1.27	7.85	7.95	1.76
Jets, $E_{\mathrm{T}}^{\mathrm{miss}}$	0.90	5.38	2.97	3.26	4.02
Electrons photons	2.52	1.73	1.78	1.51	3.77
Muons	0.39	0.29	0.11	0.20	0.51
Taus	0.21	1.34	0.32	0.14	2.44
Other	2.49	1.19	0.28	1.08	0.80
Theoretical uncertainties	3.36	9.18	14.43	13.89	11.93
Signal	2.01	8.68	5.81	6.71	6.26
Background	2.66	3.03	13.20	11.94	10.03
MC stat. uncertainties	1.55	4.80	8.77	7.85	4.35

8.2 Higgs cross-section in the κ-framework

The κ-framework is used to express the SM Higgs cross-sections in terms of multiplicative modifiers which effectively scale the SM Higgs cross-section and width. In this context the cross-section times branching fraction of a particular Higgs process (initial-state production i to final-state decay f) can be parameterised as [38],

$$(\sigma \times B)_{if} = \kappa_i^2 \sigma_i^{\mathrm{SM}} \frac{\kappa_f^2 \Gamma_f^{\mathrm{SM}}}{\kappa_H^2 \Gamma_H^{\mathrm{SM}}}, \tag{8.3}$$

where σ_i^{SM} is the SM Higgs production cross section via the initial process i, Γ_H^{SM} and Γ_f^{SM} are the respective SM values for the total Higgs width and the partial width into final-state f, and $\kappa_{i,f,H}$ are their multiplicative modifiers defined as,

$$\kappa_i^2 = \frac{\sigma_i}{\sigma_i^{\mathrm{SM}}}, \tag{8.4}$$

$$\kappa_f^2 = \frac{\Gamma_f}{\Gamma_f^{\mathrm{SM}}}, \text{ and} \tag{8.5}$$

$$\kappa_H^2 = \Sigma_f B_f^{\mathrm{SM}} \kappa_f^2. \tag{8.6}$$

Both κ_f and κ_i can be expressed as an effective coupling parameter κ_X related to the tree-level couplings of the Higgs boson to the respective SM particles. Under a SM like structure this results in a parameterisation of the Higgs production cross-sections in terms of modifiers related to the coupling of the Higgs to the SM particles. The total Higgs width is in effect also parameterised in the same way.

There are several processes in the parameterisation that arise as loop processes, the most important of which are the Higgs couplings to gluons (Hgg) and photons ($H\gamma\gamma$). Under SM assumptions one can relate their respective couplings to the other κ_X coupling modifiers. For example, t-quark and b-quark loops enter the effective coupling Hgg introducing an explicit dependence on κ_t and κ_b (the effects of lighter quark loops are generally considered negligible). Similarly the $H\gamma\gamma$ coupling is dependant on κ_W and κ_t through the decay loops in $H \to \gamma\gamma$ (see Figure 1.11 on page 24). In both cases interference effects should be considered. Alternatively these couplings can be assigned their own effective modifiers (κ_g and κ_γ) thereby dissociating the loop κ parameters from their SM dependencies. An additional parameter B_{BSM} can also be introduced to describe the effects of BSM on the total Higgs width from the branching fraction of Higgs to invisible decays and final-states that are currently undetected. The undetected states include decays into final-states that are undetectable by ATLAS, not covered in the Higgs cross-section combination, or have not been directly meassured as of yet. The B_{BSM} parameter directly affects the total Higgs width as

$$\Gamma_H = \frac{\Gamma_H^{\text{SM}}}{1 - B_{\text{BSM}}}, \tag{8.7}$$

which relates the Higgs boson width Γ_H to its SM value Γ_H^{SM}, with $B_{\text{BSM}} = 0$ under nominal SM assumptions. In the results presented in Ref. [3], B_{BSM} is decomposed further into Higgs to invisible $B_{\text{inv.}}$ and Higgs to undetectable $B_{\text{undet.}}$ branching fractions, such that,

$$B_{\text{BSM}} = B_{\text{inv.}} + B_{\text{undet.}}, \tag{8.8}$$

and

$$\Gamma_H = \frac{\Gamma_H^{\text{SM}}}{1 - (B_{\text{inv.}} + B_{\text{undet.}})}, \tag{8.9}$$

where $B_{\text{inv.}} \geq 0$ and $B_{\text{undet.}} \geq 0$. The measurement of the κ parameters are then performed under several assumptions pertaining to B_{BSM}. The nominal case assumes a SM structure to the coupling parameterisation with no BSM contribution to the Higgs width, i.e., $B_{\text{BSM}} = 0$. To probe the contribution from Higgs to invisible decays in the κ-framework three analyses

targetting Higgs to invisible [62] [251–253] are correlated to $B_{\text{inv.}}$, with $B_{\text{undet.}}$ allowed to vary or fixed to zero. Alternatively one can use the Higgs off-shell measurement[63] of $H^* \to ZZ$ [254] to constrain the Higgs total width and B_{BSM}.

Table 8.6 Parameterisation of Higgs boson production cross-sections in the κ-framework under SM assumptions [36, 38].

Production	Parameterisation
$\mu(\sigma_{\text{ggF}})$	$1.04\,\kappa_t^2 + 0.002\,\kappa_b^2 - 0.04\,\kappa_t\,\kappa_b$
$\mu(\sigma_{VBF})$	$0.73\,\kappa_W^2 + 0.27\,\kappa_Z^2$
$\mu(\sigma_{qq/qg\to ZH})$	κ_Z^2
$\mu(\sigma_{gg\to ZH})$	$2.46\,\kappa_Z^2 + 0.46\,\kappa_t^2 - 1.90\,\kappa_Z\,\kappa_t$
$\mu(\sigma_{WH})$	κ_W^2
$\mu(\sigma_{t\bar{t}H})$	κ_t^2
$\mu(\sigma_{tHW})$	$2.91\,\kappa_t^2 + 2.31\,\kappa_W^2 - 4.22\,\kappa_t\,\kappa_W$
$\mu(\sigma_{tHq})$	$2.63\,\kappa_t^2 + 3.58\,\kappa_W^2 - 5.21\,\kappa_t\,\kappa_W$
$\mu(\sigma_{b\bar{b}H})$	κ_b^2

A parameterisation scheme assuming a SM structure of the loop processes and no BSM contributions is assumed in what follows. Results from alternative parameterisations where the effective κ_γ and κ_g, and/or $B_{\text{BSM}}(B_{\text{inv.}}, B_{\text{undet.}})$ parameters are varied, are documented in Ref. [3]. Tables 8.6 and 8.7 show the signal strengths of Higgs boson cross-sections and Higgs boson decay widths, respectively, parameterised in terms of κ_X modifiers under SM assumptions as defined in Ref. [38] with updates from Ref. [36]. Here the parameters κ_W and κ_Z are the modifiers of Higgs couplings to the $W^\pm$ and Z, respectively. Fermionic coupling modifiers $\kappa_t, \kappa_b, \kappa_\tau,$ and κ_μ are defined, where κ_t and κ_b are for the b-quarks and t-quarks, respectively, and κ_t and κ_b are the respective modifiers for the τ and μ leptons. The couplings to all first generation fermions have no effect on the subsequent measurement due to the lack of current sensitivity in the direct measurement of their κ's and are all fixed to 1. Coupling modifiers to second generation quarks are set to their respective third generation values, i.e., $\kappa_c = \kappa_t$ and $\kappa_s = \kappa_b$. The cross-section signal strength $\mu(\sigma_i)$ for Higgs cross-section process

[62] Each Higgs to invisible analysis is performed with 36.1fb^{-1} of Run-2 data collected with the ATLAS experiment.

[63] The Higgs off-shell measurement of $H^* \to ZZ$ is performed with 36.1fb^{-1} of Run-2 data collected with the ATLAS experiment.

Table 8.7 Parameterisation of Higgs decay partial and total widths in the κ-framework under SM assumptions [36, 38].

Partial decay width	Parameterisation
$\mu(\Gamma_{\gamma\gamma})$	$1.59\,\kappa_W^2 + 0.07\,\kappa_t^2 - 0.67\,\kappa_W\,\kappa_t$
$\mu(\Gamma_{ZZ})$	κ_Z^2
$\mu(\Gamma_{WW})$	κ_W^2
$\mu(\Gamma_{\tau\tau})$	κ_τ^2
$\mu(\Gamma_{bb})$	κ_b^2
$\mu(\Gamma_{\mu\mu})$	κ_μ^2
$\mu(\Gamma_{gg})$	$1.11\,\kappa_t^2 + 0.01\,\kappa_b^2 - 0.12\,\kappa_t\,\kappa_b$
$\mu(\Gamma_{Z\gamma})$	$1.12\,\kappa_W^2 - 0.12\,\kappa_W\,\kappa_t$
Total width	**Parameterisation**
$\mu(\Gamma_H)$	$0.58\,\kappa_b^2 + 0.22\,\kappa_W^2 + 0.08\,\kappa_g^2 + 0.06\,\kappa_\tau^2 + 0.03\,\kappa_Z^2 + 0.03\,\kappa_c^2$ $+0.0023\,\kappa_\gamma^2 + 0.0015\,\kappa_{(Z\gamma)}^2 + 0.0004\,\kappa_s^2 + 0.00022\,\kappa_\mu^2$

i is given as

$$\mu(\sigma_i) = \frac{\sigma_i}{\sigma_i^{\mathrm{SM}}}, \tag{8.10}$$

while the Higgs width signal strength for the decay mode f is,

$$\mu(\Gamma_f) = \frac{\Gamma_f}{\Gamma_f^{\mathrm{SM}}}. \tag{8.11}$$

Tables 8.6 and 8.7 are calculated in terms of the LO κ-framework which: uses SM input parameters as defined in Ref. [36] for Higgs cross-sections and branching fractions calculations, including a Higgs mass of $m_h = 125.09$ GeV; uses the state of the art QCD corrections for a particular process (next-to-next-to-next-leading-order (N3LO)/NNLO/NLO/LO); and neglects EW corrections which are not assumed to factorise for κs. As an example, the calculation of σ_{ggF} in Table 8.6 in terms of the κ-framework is presented in Appendix D.3.

No invisible or undetectable contributions are assumed to contribute to the total Higgs width such that $B_{\mathrm{BSM}} = 0$ is fixed. The results from a global fit to data from the cross-section measurements performed in the κ-framework under SM assumptions are shown in Table 8.8. All parameters are assumed to be positive in the fit. Since no direct evidence of the $H\mu\mu$ coupling was observed and 95% CL upper limit on the coupling modifier are set for κ_μ:

the observed (expected) limit is found at 1.51 (1.79). The combined SM p-value of the measurement is found to be $p_{\mathrm{SM}} = 78\%$, computed for a model with 6 DOFs, and compatible with the SM predictions.

Table 8.8 Fit results in the κ-framework with a SM structure [3]. Parameters, κ_Z, κ_W, κ_b, κ_t, κ_τ and κ_μ, are all defined to be unity in the SM.

Parameter	Result
κ_Z	1.10 ± 0.08
κ_W	1.05 ± 0.08
κ_b	$1.06^{+0.19}_{-0.18}$
κ_t	$1.02^{+0.11}_{-0.10}$
κ_τ	1.07 ± 0.15
κ_μ	< 1.51 at 95% CL

When taking into account the effect of the mass of the SM particle on its effective coupling strength to the Higgs boson, one can rewrite the coupling modifiers as reduced coupling strength modifiers $\kappa_F \frac{m_F}{v}$, for fermions ($F = t, b, \tau, \mu$), and $\sqrt{\kappa_V}\frac{m_V}{v}$, for gauge bosons ($V = W, Z$), where $v = 246\,\mathrm{GeV}$ is the vacuum expectation value of the Higgs field. The SM prediction is given by m/v for which $\kappa_{F,V} \to 1$. Figure 8.5 shows the linear dependence of the reduced coupling strengths as a function of the particle mass, which is in accordance with the SM expectations.

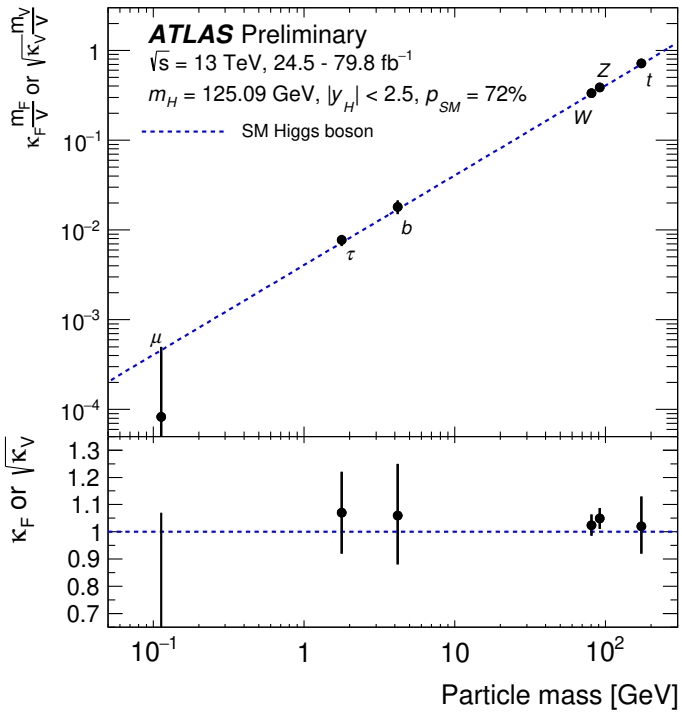

Figure 8.5 Measurement of reduced coupling strength modifiers $\kappa_F \frac{m_F}{v}$ for fermions ($F = t, b, \tau, \mu$) and $\sqrt{\kappa_V}\frac{m_V}{v}$ for weak gauge bosons ($V = W, Z$) as a function of their masses m_F and m_V, respectively, and the vacuum expectation value of the Higgs field $v = 246\,\text{GeV}$ [3]. The SM prediction for both cases is also shown (dotted line).

8.3 Reinterpretation of κ framework for BSM models

The coupling modifiers in the κ-framework presented in Section 8.2 offer a method to probe the SM-like (125 GeV) Higgs coupling strength to SM (and BSM) particles. As was shown in the result from Figure 8.5, all measured Higgs couplings scale with respect to the coupled particle mass in accordance with the SM expectation. Furthermore, the direct measurement of the κ's in Table 8.8 show good agreement of Higgs coupling modifiers under SM assumptions. While these results give a general status of the measured Higgs couplings and their agreement with the SM, more direct statements can be made with respect to BSM physics by probing particular models. Constraints on BSM physics via Higgs boson couplings were placed with the full Run-1 ATLAS dataset covering several BSM models [17]. These include constraints on 2HDM and MSSM models, which were discussed in Section 2.5, each of which have predefined Higgs coupling strengths. The coupling strength parameters (κ's) can therefore be reparameterised in terms of the free parameters of the BSM model. The results from the

reparameterisation of the κ-framework in Section 8.2 in the context of the 2HDM and the MSSM are presented in Sections 8.3.1 and 8.3.2, respectively. Since both models predict additional Higgs bosons, the earlier convention where h denotes the 125 GeV Higgs, while H is the heavy CP-even Higgs, is used in the remainder of the chapter.

8.3.1 Two Higgs doublet model

The Higgs sector in 2HDMs as described in Section 2.2 has well-defined Higgs couplings which are dependant on the level of mixing and vacuum expectation values of the two Higgs doublets. Following the same conventions established, we can consider the Yukawa couplings of the SM-like Higgs to be $Y_f^h = \sqrt{2} m_f \xi_f^h / v$, where h is the SM-like Higgs boson, $v = 246$ GeV, m_f is the mass of the desired fermion, and ξ_f^h is a scale factor for the coupling strength. The scaling factor is relative to the expected SM Yukawa coupling $\xi_f^h = \frac{Y_f^h}{Y_f^{H,SM}}$. Within the four different types of 2HDMs without FCNCs, the Yukawa coupling to up-type quarks, down-type quarks and leptons are affected in different ways. The coupling factors are therefore grouped as ξ_{up}^h, ξ_{down}^h, and ξ_ℓ^h for up-type quarks, down-type quarks, and leptons, respectively. Additionally, a scaling factor ξ_V^h for the SM-like Higgs couplings to vector bosons is introduced. The four types of 2HDMs without FCNCs (Type-I, Type-II, Lepton-specific and Flipped) are characterised by their couplings in the fermion sector (see Table 2.1 on page 29). All four 2HDMs have Higgs sectors defined by the free parameters $\tan\beta$ and α. The SM-like Higgs boson coupling scaling factors for the four different 2HDM types are summarised in Table 8.9.

Table 8.9 Relative coupling strength factors of the SM-like (h) 2HDM Higgs-fermion Yukawa couplings and vector boson couplings with respect to the SM [40].

Coupling factor	Type-I	Type-II	Lepton-specific	Flipped
ξ_V^h		$\sin(\beta-\alpha)$		
ξ_{up}^h		$\cos\alpha/\sin\beta$		
ξ_{down}^h	$\cos\alpha/\sin\beta$	$-\sin\alpha/\cos\beta$	$\cos\alpha/\sin\beta$	$-\sin\alpha/\cos\beta$
ξ_ℓ^h	$\cos\alpha/\sin\beta$	$-\sin\alpha/\cos\beta$	$-\sin\alpha/\cos\beta$	$\cos\alpha/\sin\beta$

8.3.1.1 Reparameterisation for 2HDM

The coupling scaling factors in Table 8.9 are directly compatible with the coupling modifiers of the κ-framework in Section 8.2. This allows the reparameterisation of the POIs in the

κ-framework workspace such that they are expressed in terms of the free parameters $\tan\beta$ and $\cos(\beta-\alpha)$. For example, both κ_Z and κ_W can be parameterised such that $\kappa_Z = \kappa_W = \xi_V^h = \sin(\beta-\alpha)$. Similarly $\kappa_t = \xi_{\text{up}}^h$, $\kappa_b = \xi_{\text{down}}^h$ and $\kappa_\tau = \kappa_\mu = \xi_\ell^h$. The code used to parameterise the coupling modifiers is documented in Appendix D.4. The SM structure assumed in Section 8.2 is considered here, with the observed Higgs boson being identified with the light CP-even neutral scalar h predicted by 2HDMs, and its accessible production and decay modes are assumed to be the same as those of the SM Higgs boson.

The parameterisation of the couplings in Table 8.9 are only approximate, and do not take into account BSM processes and various higher order corrections related to new physics. These effects may contribute substantially in the cross-section and branching fraction calculations of the SM-like Higgs boson. For example, the $h \to \gamma\gamma$ decay loops which are parameterised to include SM particles in Table 8.7 do not take into account the interference from non-SM particles like H^+ found in 2HDMs. Additionally, the effect from the heavy Higgs to h coupling, Hhh, could enhance the SM-like Higgs cross-section. In the context of 2HDMs both of these effects could become important. The proposed parameterisation is validated by comparing the predicted SM-like Higgs boson cross-sections and branching fractions to direct calculations. This allows us to make a statement on the validity of the parameterisation without testing the effects of charged and heavy Higgs contributions directly.

Tables 8.10 and 8.11 show these differences a for Type-I 2HDM at different values of $\tan\beta$ and $\cos(\beta-\alpha)$ assuming[64] $m_A = 1$ TeV. The corresponding study for a Type-II 2HDM is documented[65] in Tables D.1 and D.2. Here the h cross-sections via ggF (σ_{ggF}) and b-associated production[66] (σ_{bbh}) are calculated using the program SusHi [66] and the Santander matching [82] procedure described in Section 2.4.2, while its total width (Γ_h) and branching ratios (B_i for decay mode i) have been calculated with 2HDMC[255]. At the SM alignment limit, $\cos(\beta-\alpha) = 0$, the differences are below a few percent level. Generally the differences are within the theoretical uncertainties from a SM Higgs boson with $m_h = 125.09$ GeV, which are $O(10\%)$ for ggF, around 20% for b-associated production, and on the order of a few percent for branching fractions[67]. Exceptions are found at values in $|\cos(\beta-\alpha)| \to 1$ where Higgs couplings can vanish and the total cross-section becomes small. In these

[64]The parameterisation for the 2HDM generally assumes that all the additional Higgs bosons are heavy. However, even if the m_A is chosen to be 300 GeV the differences are qualitatively the same.

[65]Lepton-specific and Flipped models are special cases of Type-I and Type-II and do not require an independent study.

[66]Only shown for a Type-II where the contribution can be sizeable.

[67]The branching fraction with the largest theoretical uncertainty comes from $B_{Z\gamma}$ and is approximately 6% [36, 38].

cases the effect of radiative corrections which are not present in the parameterisation make sizeable contributions to the small total cross-section. These effects are however constrained to regions in the 2HDM parameter space sufficiently far away to those where the limits are set, and their impact on the exclusion contours will be marginal. The parameterisation is considered adequate for the purpose of setting exclusion limits on 2HDM models.

Table 8.10 The differences between the parameterised production cross sections and branching ratios of the SM-like Higgs compared to precision calculations using SUSHI and 2HDMC for 2HDM Type-I with $m_A = 1000$ GeV [250]. All the differences are quoted in percent.

$\tan\beta$	$\cos(\beta-\alpha)$	σ [pb]	$\Delta\sigma_{ggF}$ [%]	B_{ZZ} [%]	B_{WW} [%]	B_{bb} [%]	$B_{\tau\tau}$ [%]	$\frac{\Gamma_h}{\Gamma_h^{\mathrm{SM}}}$
0.5	-0.800	42.87	7.47	-1.02	-1.02	-1.02	-1.02	1.03
0.5	-0.300	6.21	-7.01	0.81	0.81	0.81	0.81	-0.81
0.5	-0.100	29.46	-1.18	-0.52	-0.52	-0.52	-0.52	0.52
0.5	0.000	46.11	-0.08	-0.81	-0.81	-0.81	-0.81	0.81
0.5	0.100	65.36	0.66	-0.99	-0.99	-0.99	-0.99	1.00
0.5	0.300	109.45	1.64	-1.19	-1.19	-1.19	-1.19	1.21
0.5	0.800	216.04	3.21	-1.40	-1.40	-1.40	-1.40	1.42
1.0	-0.800	1.52	21.21	1.35	1.35	1.35	1.35	-1.34
1.0	-0.300	20.11	-2.06	-0.28	-0.28	-0.28	-0.28	0.28
1.0	-0.100	37.11	-0.57	-0.68	-0.68	-0.68	-0.68	0.68
1.0	0.000	46.11	-0.08	-0.81	-0.81	-0.81	-0.81	0.81
1.0	0.100	55.06	0.32	-0.91	-0.91	-0.91	-0.91	0.91
1.0	0.300	71.74	0.98	-1.06	-1.06	-1.06	-1.06	1.07
1.0	0.800	88.10	2.49	-1.33	-1.33	-1.33	-1.33	1.34
2.0	-0.800	2.01	-8.15	1.12	1.12	1.12	1.12	-1.11
2.0	-0.300	30.04	-0.90	-0.58	-0.58	-0.58	-0.58	0.59
2.0	-0.100	41.27	-0.32	-0.74	-0.74	-0.74	-0.74	0.75
2.0	0.000	46.11	-0.08	-0.81	-0.81	-0.81	-0.81	0.81
2.0	0.100	50.24	0.13	-0.86	-0.86	-0.86	-0.86	0.87
2.0	0.300	55.86	0.52	-0.96	-0.96	-0.96	-0.96	0.97
2.0	0.800	45.30	1.70	-1.22	-1.21	-1.21	-1.21	1.23

Table 8.11 (continued from Table 8.10) The differences between the parameterised production cross sections and branching ratios of the SM-like Higgs compared to precision calculations using SUSHI and 2HDMC for 2HDM Type-I with $m_A = 1000$ GeV [250]. All the differences are quoted in percent.

$\tan\beta$	$\cos(\beta-\alpha)$	σ [pb]	$\Delta\sigma_{ggF}$ [%]	B_{ZZ} [%]	B_{WW} [%]	B_{bb} [%]	$B_{\tau\tau}$ [%]	$\frac{\Gamma_h}{\Gamma_h^{\mathrm{SM}}}$
5.0	-0.800	9.07	-1.65	-0.24	-0.24	-0.24	-0.24	0.24
5.0	-0.300	36.96	-0.38	-0.71	-0.71	-0.71	-0.71	0.71
5.0	-0.100	43.87	-0.17	-0.78	-0.78	-0.78	-0.78	0.78
5.0	0.000	46.11	-0.08	-0.81	-0.81	-0.81	-0.81	0.81
5.0	0.100	47.46	0.00	-0.83	-0.83	-0.83	-0.83	0.84
5.0	0.300	47.28	0.18	-0.89	-0.89	-0.89	-0.89	0.90
5.0	0.800	26.39	0.85	-1.08	-1.08	-1.08	-1.08	1.09
10	-0.800	12.55	-0.75	-0.39	-0.39	-0.39	-0.39	0.39
10	-0.300	39.42	-0.23	-0.73	-0.73	-0.73	-0.73	0.73
10	-0.100	44.75	-0.13	-0.78	-0.78	-0.78	-0.78	0.79
10	0.000	46.11	-0.08	-0.81	-0.81	-0.81	-0.81	0.81
10	0.100	46.55	-0.04	-0.83	-0.83	-0.83	-0.83	0.84
10	0.300	44.58	0.05	-0.88	-0.88	-0.88	-0.88	0.88
10	0.800	21.21	0.44	-1.05	-1.05	-1.05	-1.05	1.06

8.3.1.2 Results for 2HDM

Exclusion limits are produced for 2HDM models by parameterising the κ-framework workspace in terms of $\tan\beta$ and $\cos(\beta-\alpha)$ as described in Section 8.3.1.1. For each 2HDM type, a 2D grid of conditional likelihood fits in the parameter space of $\tan\beta \in [0.1, 10.0]$ and $\cos(\beta-\alpha) \in [-1.0, 1.0]$ is produced, resulting in a grid of negative log-likelihood values, $-\log\mathscr{L}(\tan\beta, \cos(\beta-\alpha), \hat{\hat{\boldsymbol{\theta}}})$. The global minimum of the log-likelihood function is determined by performing an unconditional fit where $\tan\beta$ and $\cos(\beta-\alpha)$ are allowed to vary freely. In order to speed up the minimisation the unconditional fit can be constrained to a region of phase-space motivated by the minimum points in the conditional fits. The 2D grid of the test statistic t_μ, is built and interpolation is used to predict interstitial points. Using the asymptotic approximation p-values are extracted via Eq. (5.24) with a χ^2 distribution with 2 DOF. Exclusion contours at 95% CL are set by applying a threshold value $p_\mu = 0.05$, corresponding to $t_\mu = 5.99$.

Figure 8.6 shows the 95 % CL exclusion limits, where regions of the $(\cos(\beta-\alpha), \tan\beta)$ plane are excluded for each of the four types of 2HDMs. The expected exclusion limits in the SM hypothesis are also overlaid, determined from fits of the Asimov dataset ($\boldsymbol{\kappa} = \mathbf{1}$). The data is consistent with the alignment limit at $\cos(\beta-\alpha) = 0$, in which the couplings of h match those of the SM Higgs boson. The allowed regions also include narrow, curved petal regions at positive $\cos(\beta-\alpha)$ and moderate $\tan\beta$ in the Type-II, Lepton-specific, and Flipped models. These correspond to regions with $\cos(\beta+\alpha) \approx 0$, for which some fermion couplings have the same magnitude as in the SM, but the opposite sign. The best fit values are shown in Table 8.12 for each 2HDM type, along with their respective coupling modifier values. The compatability with the SM is expressed in terms of the p-value p_{SM} and also shown. They are $p_{\text{SM}}^{\text{Type-I}} > 99\%$, $p_{\text{SM}}^{\text{Type-II}} = 67\%$, $p_{\text{SM}}^{\text{Type-III}} > 99\%$, and $p_{\text{SM}}^{\text{Type-IV}} = 71\%$. In all cases large deviations from the SM limit would imply a suppression of κ_V which is disfavoured by the data. Noticeably, Type-I and Type-III have a much better agreement with the SM prediction than Type-II and Type-IV. This is due to the best fit values of Type-I and Type-III found very close to the SM alignment limit, while those of Type-II and Type-IV are further away. The source of this difference is caused by correlations between coupling modifiers introduced in the parameterisation. All 2HDMs have the same κ_V and κ_{up} parameterisation, with $\kappa_V \leq 1$. However, the κ_{down} is parameterised in the same way as κ_{up} in Type-I and Type-III, while κ_{down} is anti-correlated with κ_{up} in Type-II and Type-IV. This difference results in both Type-I and Type-III having high compatibility with the SM, while Type-II and Type-IV less so.

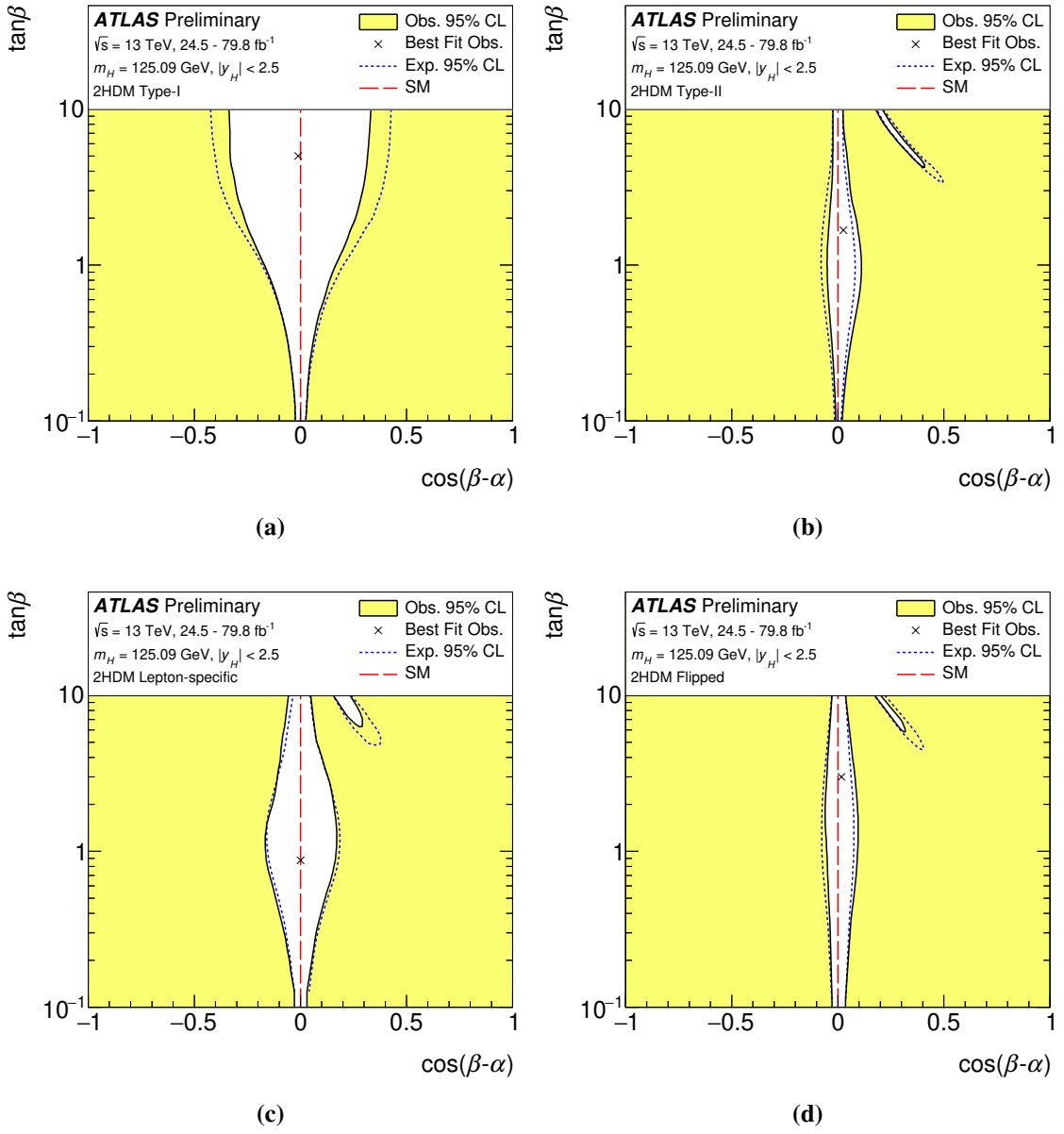

Figure 8.6 Regions of the $(\cos(\beta-\alpha), \tan\beta)$ plane of four types of 2HDMs excluded by fits to the measured rates of Higgs boson production and decays [3]. Contours at 95% CL, are shown for both the data and the expectation for the SM Higgs sector. The cross in each plot marks the observed best-fit value. The alignment limit at $\cos(\beta-\alpha)=0$, in which all Higgs boson couplings take their SM values, is indicated by the dashed red line.

Table 8.12 Best fit values in $\cos(\beta-\alpha)$ and $\tan\beta$ for the different types of 2HDM models with their respective coupling modifiers, as defined in Table 8.9. Their compatability with the SM are represented with the p-values p_{SM} defined in Eq. (5.27)

2HDM	$\cos(\beta-\alpha)$	$\tan\beta$	κ_V	κ_{up}	κ_{down}	κ_ℓ	$p_{\text{SM}}[\%]$
Type-I	-0.01	5.00	1.00	1.00	1.00	1.00	>99
Type-II	0.036	1.67	1.00	1.02	0.96	0.96	67
Type-III	-0.00	0.88	1.00	1.00	1.00	1.00	>99
Type-IV	0.02	3.00	1.00	1.01	0.95	1.01	71

8.3.2 Minimal Supersymmetric Standard Model

As discussed in Section 2.3.1 the hMSSM is different to other MSSM benchmark models in that it is not dependant on SUSY parameters that can drive the importance of certain radiative corrections. When only considering dominant radiative corrections primarily involving top quarks and stops, these corrections can be expressed in terms of m_{A} and $\tan\beta$ when assuming $m_h = 125.09\,\text{GeV}$. This approximation is limited as the hMSSM is not valid for low $\tan\beta$ values ($O(1)$ or lower). Furthermore, the missing radiative corrections also lower the precision of the approximation at high $\tan\beta$ values ($O(10)$ or larger) where bottom-quark corrections can become substantial. Due to the lowest order mass relation among the MSSM Higgs bosons the approximation breaks completely for low m_A and low $\tan\beta$. However, assuming the above assumptions are valid, SM-like Higgs boson couplings to vector bosons (κ_V), up-type fermions (κ_{up}), and down-type fermions (κ_{down}), relative to the corresponding SM predictions are expressed as functions of $\tan\beta$, and the masses of the CP-odd scalar (m_A), the Z boson (m_Z), and m_h,

$$\begin{aligned}
\kappa_V &= \frac{s_d(m_A,\tan\beta)+\tan\beta\; s_u(m_A,\tan\beta)}{\sqrt{1+\tan^2\beta}} \\
\kappa_{\text{up}} &= s_u(m_A,\tan\beta)\frac{\sqrt{1+\tan^2\beta}}{\tan\beta} \\
\kappa_{\text{down}} &= s_d(m_A,\tan\beta)\sqrt{1+\tan^2\beta},
\end{aligned} \tag{8.12}$$

where the functions s_u and s_d are given by:

$$\begin{aligned}
s_u &= \frac{1}{\sqrt{1+\frac{\left(m_A^2+m_Z^2\right)^2\tan^2\beta}{\left(m_Z^2+m_A^2\tan^2\beta-m_h^2\left(1+\tan^2\beta\right)\right)^2}}} \\
s_d &= \frac{\left(m_A^2+m_Z^2\right)\tan\beta}{m_Z^2+m_A^2\tan^2\beta-m_h^2\left(1+\tan^2\beta\right)}\,s_u.
\end{aligned} \tag{8.13}$$

8.3.2.1 Reparameterisation for hMSSM

The parameterisation in Eq. (8.12) is directly comparable to the coupling modifiers in the κ-framework. However, when reparemeterising the κ-framework workspaces, it is useful to rewrite the parameterisation so that the coupling modifiers are explicitly dependant on m_{A}^{-1}. The likelihood scan becomes dependant on parameters that converge to a certain value ($\kappa_i \to \kappa_i^{\mathrm{SM}}$ as $m_{\mathrm{A}}^{-1} \to 0$) at the SM limit, providing better closure and stability to the likelihood scan[68]. The exact parameterisation used is documented in Appendix D.4.

As with the discussion on the 2HDM parameterisation in Section 8.3.1.1, the hMSSM parameterisation in Eq. (8.12) is approximate and does not take into account several effects which could contribute to differences in the SM-like Higgs cross-sections and branching fractions. The parameterisation is validated against state of the art calculations of the SM-like Higgs boson cross-sections and branching fractions. Here the h cross-sections via ggF (σ_{ggF}) and b-associated production (σ_{bbh}) are calculated using SUSHI and the Santander matching procedure described in Section 2.4.2, while its total width (Γ_h) and branching ratios (B_i for decay mode i) have been calculated with the program HDECAY[256]. As with the 2HDMs, hMSSM effects to both $H \to hh$ production and $h \to \gamma\gamma$ branching fractions are not considered in the parameterisation. The parameterisation is compared to the hMSSM prediction, studied in Appendix D.6, where the parameterisation is found to not be sensitive to these effects in the region where the limits are set. Additionally the comparison of precise cross-section calculations and the parameterisation for some indicative m_A and $\tan\beta$ values are studied in Appendix D.6, and are found to be sufficiently compatible. An additional comparison is performed by comparing directly the Higgs boson couplings from SUSHI to the parameterised couplings. Table 8.13 shows a comparison of the SM-like Higgs couplings from SUSHI versus the parameterisation. The study has been performed for the top- and bottom-quark couplings, which are the most relevant in this model. The differences are of the order of 7% (3%) for the top (bottom) coupling at $m_A > 200$GeV and are within 1% in the mass range where the hMSSM limits are set.

[68] For example, calculating $p_{\mathrm{SM}}^{\mathrm{hMSSM}}$ can be done by evaluating the likelihood function at either $m_{\mathrm{A}} = \infty$ or $m_{\mathrm{A}}^{-1} = 0$. The former requires an arbitrarily large value to be used in the computation, while the latter avoids any ambiguity.

Table 8.13 Largest difference per m_A between κ values calculated with SUSHI versus the simplified MSSM parameterisation.

	top-quark coupling				bottom-quark coupling			
m_A[GeV]	$\tan\beta$	κ_t^{SusHi}	$\kappa_t^{\text{paramet.}}$	$\Delta\kappa$ [%]	$\tan\beta$	κ_b^{SusHi}	$\kappa_b^{\text{paramet.}}$	$\Delta\kappa$ [%]
130.0	10.0	0.443	0.426	3.915	6.4	6.041	6.250	3.449
140.0	2.8	0.295	0.308	4.396	2.8	2.767	2.846	2.840
150.0	1.3	0.091	0.133	46.280	1.3	1.558	1.631	4.668
160.0	1.3	0.222	0.265	19.387	1.3	1.539	1.603	4.179
170.0	1.3	0.333	0.375	12.739	1.3	1.510	1.566	3.695
180.0	1.3	0.424	0.465	9.561	1.3	1.477	1.525	3.249
190.0	1.3	0.500	0.538	7.633	1.3	1.442	1.483	2.857
200.0	1.3	0.563	0.598	6.316	1.3	1.409	1.444	2.517
210.0	1.3	0.615	0.648	5.351	1.3	1.377	1.408	2.227
220.0	1.3	0.658	0.689	4.612	1.3	1.348	1.374	1.979
230.0	1.3	0.695	0.723	4.029	1.3	1.321	1.344	1.768
240.0	1.3	0.726	0.752	3.557	1.3	1.297	1.317	1.588
250.0	1.3	0.752	0.776	3.168	1.3	1.275	1.293	1.433
260.0	1.3	0.775	0.797	2.844	1.3	1.255	1.271	1.299
270.0	1.3	0.795	0.815	2.569	1.3	1.237	1.252	1.183
280.0	1.3	0.812	0.831	2.335	1.3	1.221	1.234	1.082
290.0	1.3	0.827	0.845	2.132	1.3	1.206	1.218	0.993
300.0	1.3	0.841	0.857	1.956	1.3	1.193	1.204	0.915
310.0	1.3	0.852	0.868	1.802	1.3	1.181	1.190	0.846
320.0	1.3	0.863	0.877	1.666	1.3	1.169	1.179	0.784
330.0	1.3	0.872	0.886	1.546	1.3	1.159	1.168	0.729
340.0	1.3	0.881	0.893	1.439	1.3	1.150	1.158	0.680
350.0	1.3	0.888	0.900	1.342	1.3	1.142	1.149	0.635
360.0	1.3	0.895	0.907	1.256	1.3	1.134	1.141	0.595
370.0	1.3	0.902	0.912	1.178	1.3	1.127	1.133	0.559
380.0	1.3	0.907	0.917	1.107	1.3	1.120	1.126	0.526
390.0	1.3	0.912	0.922	1.043	1.3	1.114	1.120	0.496
400.0	1.3	0.917	0.926	0.984	1.3	1.108	1.114	0.468

8.3.2.2 Results for hMSSM

Exclusion limits are produced for the hMSSM by reparameterising the κ-framework workspace in terms of $\tan\beta$ and ${m_{\mathrm{A}}}^{-1}$ as described in Section 8.3.2.1. A 2D grid of conditional likelihood fits in values of the parameter space $\tan\beta \in [1.0, 10.0]$ and $m_{\mathrm{A}}^{-1} \in [0.0, 0.05]$ GeV^{-1} ($m_{\mathrm{A}} \in [200.0, \infty)$ GeV) is produced. The global minimum of the negative log-likelihood function is determined by performing an unconditional fit where $\tan\beta$ and m_{A}^{-1} are allowed to vary freely. The 2D grid of the test statistic t_μ is built and interpolation is used to predict interstitial points. Using the asymptotic approximation p-values are extracted via Eq. (5.24) with a χ^2 distribution with two degrees of freedom. Exclusion contours at 95% CL are set by applying a threshold value of $p_\mu = 0.05$, corresponding to $t_\mu = 5.99$. Figure 8.7 shows the regions of the hMSSM parameter space that are excluded by the measurement of the Higgs boson production and decay rates. The observed (expected) lower limit at 95% CL on the CP-odd Higgs boson mass is $m_A > 482$ GeV (403 GeV) for $2 \leq \tan\beta \leq 10$, with the limit increasing to 534 GeV (451 GeV) for $\tan\beta < 2$. The observed limit is stronger than expected since the measured rates in some channels, including the $h \to ZZ^* \to 4\ell$ channel[69], are higher than predicted by the SM. The hMSSM parameterisation has a physical boundary $\kappa_V \leq 1$ so the vector boson coupling cannot be larger than the SM value.

Table 8.14 The MSSM coupling modifier values for different particle types from points in $\tan\beta$ and m_A from the expected and observed limits.

$\tan\beta$	m_A [GeV]		κ_V		κ_{up}		κ_{down}	
	exp	obs	exp	obs	exp	obs	exp	obs
1.0	450.6	533.9	0.9968	0.9984	0.9172	0.9422	1.0765	1.0546
2.0	412.6	492.7	0.9979	0.9990	0.9655	0.9768	1.1274	1.0878
10.0	402.9	481.6	0.9999	0.9999	0.9983	0.9989	1.1603	1.1088

Table 8.14 shows the coupling modifier values along the expected and observed limits. As expected from the enhanced observed vector boson rates, κ_V approaches it's upper bound at unity. In the hMSSM κ_{up} and κ_{down} have an upper and lower bounds at 1, respectively, where $\kappa_{\mathrm{up}} \to 1$ (from below) and $\kappa_{\mathrm{down}} \to 1$ (from above) as $m_{\mathrm{A}} \to \infty$. There is therefore an anti-correlation between κ_{down} and κ_{up} which is dependant on $\tan\beta$, i.e., κ_{down} (κ_{up}) is enhanced (suppressed) at high $\tan\beta$. Accordingly the limit at high $\tan\beta$ shown in Table 8.14 has an observed $\kappa_{\mathrm{down}} \approx 1.11$ and $\kappa_{\mathrm{up}} \approx 1$. At low values of $\tan\beta$ less emphasis is given to the

[69] For example, the VBF cross-section times ZZ branching fraction measurement in Ref. [3] is $2.68^{+0.98}_{-0.83}$ times the SM prediction. Similarly, the VBF cross-section times $\gamma\gamma$ branching fraction measurement is $1.39^{+0.40}_{-0.35}$ times the SM prediction.

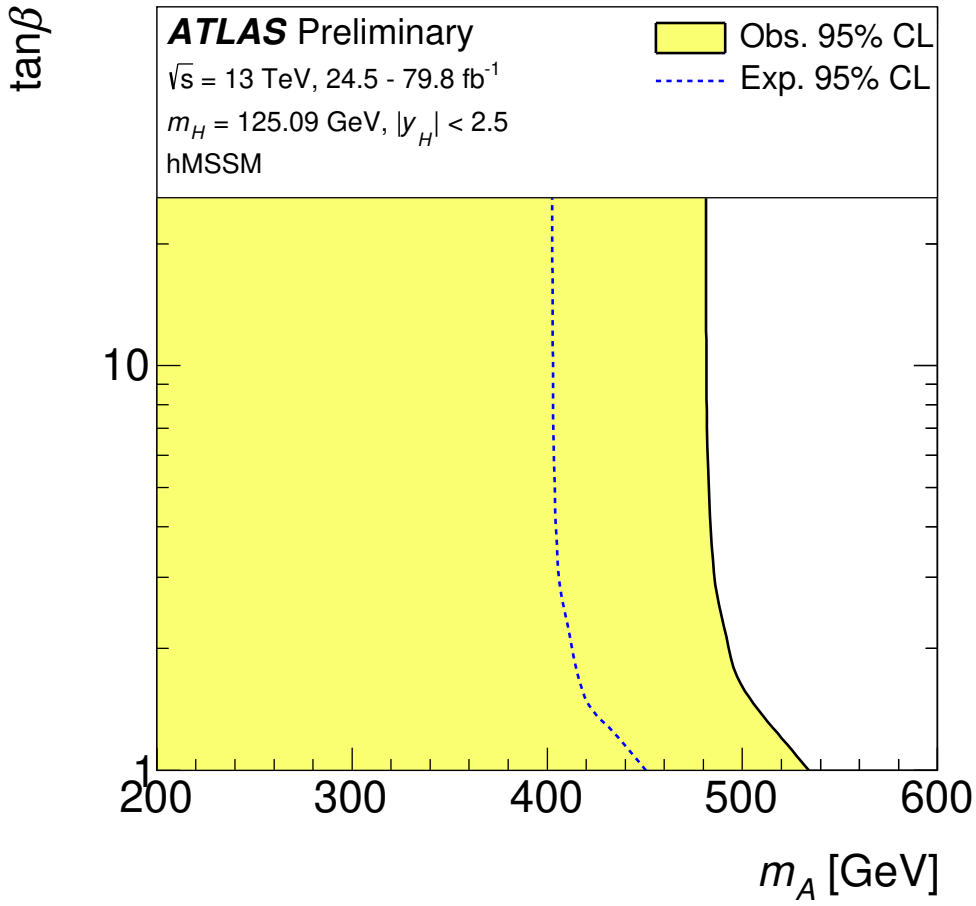

Figure 8.7 Regions of the $(m_A, \tan\beta)$ plane in the hMSSM excluded by fits to the measured rates of Higgs boson production and decays. Likelihood contours at 95% CL are drawn for both the data and the expectation of the SM Higgs sector. The regions to the left of the solid contour are excluded. The decoupling limit, in which all Higgs boson couplings tend to their SM value, corresponds to $m_A \to \infty$.

down-type couplings and at the exclusion limit κ_{down} becomes more SM-like, while the κ_{up} is allowed to fluctuate downwards. The observed compatability with the SM is $p_{\text{SM}} > 99\%$ due to the best fit value being arbitrarily close to ${m_{\text{A}}}^{-1} = 0$. A detailed comparison to the hMSSM limits to an intermediate result [241] is documented in Appendix D.7, and includes a study of the expected limits from different Asimov datasets. The limits presented here in the hMSSM show a compatible exclusion with that recently presented by CMS from Run-2 data in Ref. [35].

Part IV

Conclusion

Chapter 9

Summary of results

> ...the question is not whether bugs exist, but how many there are, and how critical their positions.
>
> PYTHIA 6.4 Physics and Manual [175]

The Higgs sector has been shown to provide a rich phenomenology for physics beyond the Standard Model. In the analyses described in this thesis, two approaches have been taken.

The first is the search for new physics by directly searching for resonant signatures which are compatible with Higgs bosons predicted by models with extended Higgs sectors. Two direct searches, one for a neutral Higgs boson, and one for a charged Higgs boson, were conducted with 36.1 fb^{-1} of $\sqrt{s} = 13$ TeV data collected with the ATLAS detector. The data was found in each case to be compatible with the SM background prediction, and no evidence of an additional Higgs boson was observed. Limits on the production cross-section times branching fractions of the additional Higgs bosons are placed in each case.

The second approach documented is that of the reinterpretation of the SM-like Higgs boson with $m_h = 125$ GeV in the context of BSM physics. Here the compatibility of BSM models with the various measured cross-section times branching ratios of the 125 GeV Higgs boson is tested. The cross-section measurements are found to be compatible with the SM prediction. The results are reinterpreted using the κ-framework for the SM couplings. The measurements are therefore used to exclude large portions of the BSM parameter space.

All three analyses presented in this thesis have been used to place limits in the parameter space of the hMSSM benchmark model. Figure 9.1 shows an overlay plot with the latest exclusion limits from direct searches for additional Higgs bosons using the ATLAS detector,

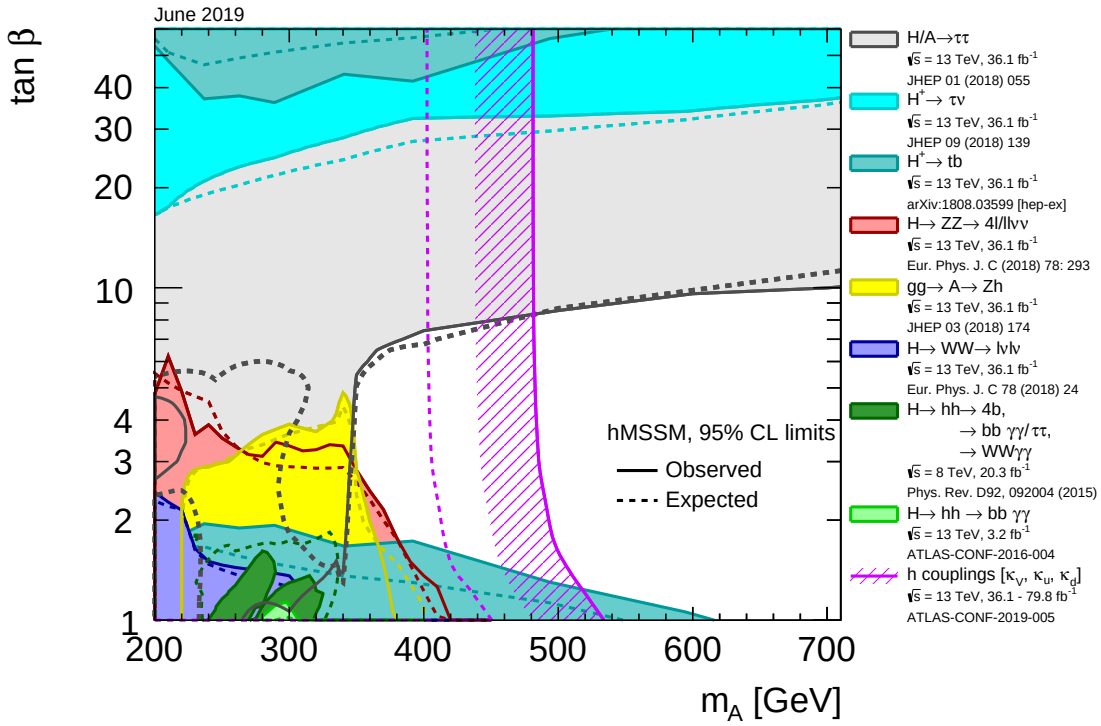

Figure 9.1 Regions of the m_{A}–$\tan\beta$ plane excluded in the hMSSM model via direct searches for heavy Higgs bosons and fits to the measured rates of observed 125 GeV Higgs boson production and decays [257]. Limits are quoted at the 95% CL and are indicated for the data (solid lines) and the expectation for the SM Higgs sector (dashed lines). The light shaded or hashed regions indicate the observed exclusions.

in the context of the hMSSM. The limits from the search for $H/A \to \tau\tau$ in Chapter 6 and $H^+ \to \tau\nu$ in Chapter 7 are shown. Also shown in Figure 9.1 are the limits from the direct searches for: a charged Higgs boson decaying via $H^+ \to tb$; a heavy CP-even Higgs boson decaying via either $H \to WW$, $H \to ZZ$ or $H \to hh$, and a heavy CP-odd Higgs boson decaying via $A \to Zh$. The $H/A \to \tau\tau$ analysis places stringent limits on the neutral heavy Higgs bosons, having excluded values above $\tan\beta \sim 10$ for a mass $m_{\mathrm{A}} < 700$ GeV. The analysis also places the only direct limits at intermediate values of $\tan\beta \sim 5$ at lower mass values, $200 \lesssim m_{\mathrm{A}} \lesssim 350$ GeV. The limits are compatible with recent results by CMS [81]. The direct limit from the $H^+ \to \tau\nu$ analysis excludes values greater than $\tan\beta \sim 20$ at $m_{\mathrm{A}} = 200$ GeV to around $\tan\beta \sim 35$ at $m_{\mathrm{A}} = 700$ GeV. Although the limits from $H^+ \to \tau\nu$ are considerably weaker than those placed by the $H/A \to \tau\tau$ analysis, they are currently the strongest limits placed from a direct search of a charged Higgs boson in the mass range considered.

The limits from the 125 GeV couplings reinterpretation are overlaid in Figure 9.1 and exclude $m_{\mathrm{A}} \lesssim 400$ GeV in the range $1.5 \lesssim \tan\beta \lesssim 7$ region, not otherwise covered by the direct searches. However, this limit should be considered to be slightly conservative since its confidence interval is defined by a χ^2 cutoff, which is know to lead to over-coverage near the physical boundaries of the limit. The limit is compatible with the recent limits placed by CMS using the same approach [35].

While the limits shown in the context of the hMSSM offer a concise and elegant summary of the current status of Higgs boson searches within the ATLAS experiment, the reader should keep in mind that the hMSSM itself is a simplified benchmark model of an already minimal model, the MSSM. The additional benchmark models described in Section 2.3.1 are designed to be physical over the entire phase-space in which they are defined. However, reinterpreting the 125 GeV coupling results in these additional benchmarks becomes non-trivial in the context of the κ-framework, and at present no simplified parameterisation of the SM-like couplings of these models exists, such as the one that was used for the hMSSM in Section 8.3.2.

As commented on in Section 2.3.1, the MSSM benchmark scenarios which are presented for the interpretation of the Higgs searches will undergo updates from Ref. [53], intended to be used for the final Run-2 searches. Improvements to the di-tau analysis can be made, in particular by expanding the studied mass range to values of $m_{\mathrm{A}} < 200$ GeV. Including the $\tau_{\mathrm{lep}}\tau_{\mathrm{lep}}$ channel could improve the sensitivity in this range. Additionally, improvements to the MSSM interpretation can be made by including the ggF Higgs p_{T} reweighting procedure discussed in Section 2.4.1. The current ggF signal generation does not account for the effects from BSM couplings in the virtual ggF loops, which could affect the Higgs p_{T} distribution. This reweighting procedure can be used to correct the signal acceptance and final discriminant distributions by taking into account the MSSM couplings that are currently neglected. It was recently shown by CMS [81] that the reweighting procedure has an effect on the gluon-fusion cross-section limits for mass points of $m_{\phi} \lesssim 150$ GeV.

Finally, the expected exclusion limits in the hMSSM and $m_{\mathrm{h}}^{\mathrm{mod}+}$ benchmark scenarios from a projection of the sensitivity of the $H/A \to \tau\tau$ search in Chapter 6 with the expected HL-LHC dataset, of 3000 fb^{-1} of $\sqrt{s} = 14$ TeV pp collisions, are shown in Figure 9.2 [258]. The projection is performed with both systematic and statistical uncertainties being reduced, as expected, with the increased dataset. "Unreduced sys." uses the same systematic uncertainties as the Run 2 analysis while "Stat. unc. only" represents the expected limit without considering systematic uncertainties. The 5 σ sensitivity shows the region with potential for the discovery of an additional Higgs boson. The full analysis details are presented in

Ref. [258]. The projection can be compared to the results from the search presented in Chapter 6. A considerably large portion of the MSSM phase-space will become available at large values of m_{A} throughout the lifetime of the LHC, during which the Higgs sector will continue to be probed, and there is still the possibility for the discovery of another Higgs boson.

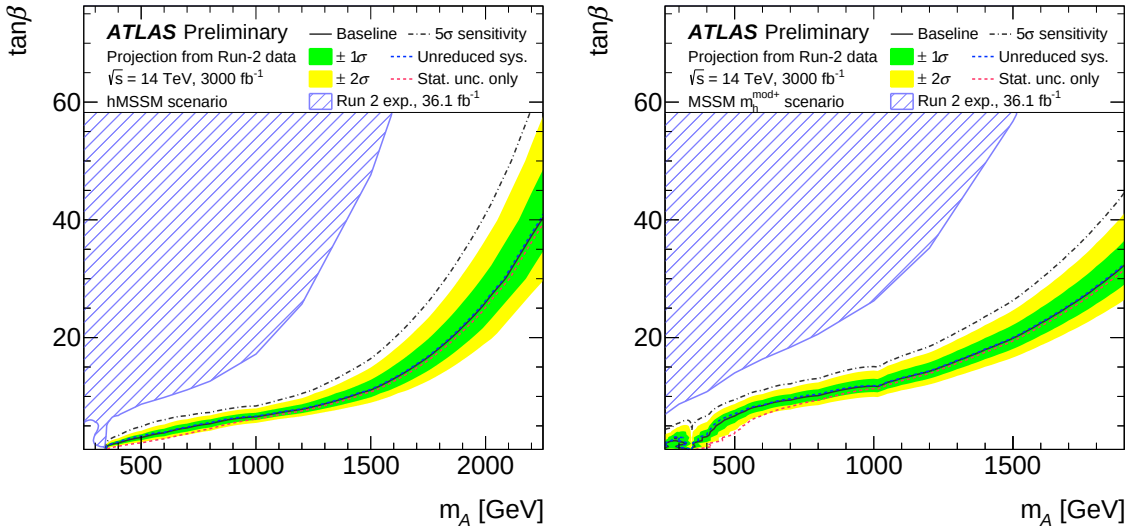

Figure 9.2 Projection of the excluded region in the m_{A}–tanβ plane of the (a) hMSSM and (b) $m_{\mathrm{h}}^{\mathrm{mod+}}$ benchmark models from the $H/A \to \tau\tau$ analysis with an expected HL-LHC dataset of 3000 fb^{-1} [258]. The nominal exclusion uses a reduced systematic uncertainties scenario.

Part V

Back Matter

References

[1] ATLAS Collaboration, *Search for additional heavy neutral Higgs and gauge bosons in the ditau final state produced in* $36 fb^{-1}$ *of pp collisions at* $\sqrt{s} = 13\,TeV$ *with the ATLAS detector*, JHEP **01** (2018) 055, arXiv:1709.07242 [hep-ex].

[2] ATLAS Collaboration, *Search for charged Higgs bosons decaying via* $H^{\pm} \to \tau^{\pm}\nu_{\tau}$ *in the* τ*+jets and* τ*+lepton final states with* $36 fb^{-1}$ *of pp collision data recorded at* $\sqrt{s} = 13\,TeV$ *with the ATLAS experiment*, JHEP **09** (2018) 139, arXiv:1807.07915 [hep-ex].

[3] ATLAS Collaboration, *Combined measurements of Higgs boson production and decay using up to* $80 fb^{-1}$ *of proton–proton collision data at* $\sqrt{s} = 13\,TeV$ *collected with the ATLAS experiment*, ATLAS-CONF-2019-005, 2019, https://cds.cern.ch/record/2668375.

[4] ATLAS Collaboration, *Technical Design Report for the ATLAS Inner Tracker Strip Detector*, Tech. Rep. CERN-LHCC-2017-005. ATLAS-TDR-025, CERN, Geneva, Apr, 2017. https://cds.cern.ch/record/2257755.

[5] W. N. Cottingham and D. A. Greenwood, *An Introduction to the Standard Model of Particle Physics*. Cambridge University Press, 2 ed., 2007.

[6] M. Thomson, *Modern particle physics*. Cambridge University Press, New York, 2013. http://www-spires.fnal.gov/spires/find/books/www?cl=QC793.2.T46::2013.

[7] J. F. Gunion, H. E. Haber, G. L. Kane, and S. Dawson, *The Higgs Hunter's Guide*, Front. Phys. **80** (2000) 1–404.

[8] A. Banfi, D. Cerdeño, C. Englert, D. Maître, C. Maxwell, and N. Knostantinidis, *Lecture notes for the 2016 HEP School for Experimental High Energy Physics Students*, Tech. Rep. RAL-TR-2016-007, 2016.

[9] F. Englert and R. Brout, *Broken symmetry and the mass of gauge vector mesons*, Phys. Rev. Lett. **13** (1964) 321.

[10] P. W. Higgs, *Broken symmetries, massless particles and gauge fields*, Phys. Lett. **12** (1964) 132.

[11] P. W. Higgs, *Broken symmetries and the masses of gauge bosons*, Phys. Rev. Lett. **13** (1964) 508.

[12] P. W. Higgs, *Spontaneous symmetry breakdown without massless bosons*, Phys. Rev. **145** (1966) 1156.

[13] G. Guralnik, C. Hagen, and T. Kibble, *Global conservation laws and massless particles*, Phys. Rev. Lett. **13** (1964) 585.

[14] L. Evans and P. Bryant, *LHC Machine*, JINST **3** (2008) S08001.

[15] ATLAS Collaboration, *The ATLAS Experiment at the CERN Large Hadron Collider*, JINST **3** (2008) S08003.

[16] CMS Collaboration, *The CMS experiment at the CERN LHC*, JINST **3** (2008) S08004.

[17] ATLAS Collaboration, *Constraints on new phenomena via Higgs boson couplings and invisible decays with the ATLAS detector*, JHEP **11** (2015) 206, arXiv:1509.00672 [hep-ex].

[18] S. L. Glashow, *Partial Symmetries of Weak Interactions*, Nucl. Phys. **22** (1961) 579–588.

[19] S. Weinberg, *A Model of Leptons*, Phys. Rev. Lett. **19** (1967) 1264–1266.

[20] A. Salam, *Weak and Electromagnetic Interactions*, Conf. Proc. **C680519** (1968) 367–377.

[21] Particle Data Group Collaboration, M. Tanabashi et al., *Review of Particle Physics*, Phys. Rev. **D98** (2018) 030001.

[22] M. Kobayashi and T. Maskawa, *CP-Violation in the Renormalizable Theory of Weak Interaction*, Progress of Theoretical Physics **49** (1973) 652–657, https://doi.org/10.1143/PTP.49.652.

[23] Z. Maki, M. Nakagawa, and S. Sakata, *Remarks on the Unified Model of Elementary Particles*, Progress of Theoretical Physics **28** (1962) 870–880, https://doi.org/10.1143/PTP.28.870.

[24] T. Kibble, *Symmetry breaking in non-Abelian gauge theories*, Phys. Rev. **155** (1967) 1554.

[25] ATLAS Collaboration, *Observation of a new particle in the search for the Standard Model Higgs boson with the ATLAS detector at the LHC*, Phys. Lett. B **716** (2012) 1, arXiv:1207.7214 [hep-ex].

[26] CMS Collaboration, *Observation of a new boson at a mass of 125 GeV with the CMS experiment at the LHC*, Phys. Lett. B **716** (2012) 30, arXiv:1207.7235 [hep-ex].

[27] ATLAS Collaboration, *Study of the spin and parity of the Higgs boson in diboson decays with the ATLAS detector*, Eur. Phys. J. C **75** (2015) 476, arXiv:1506.05669 [hep-ex].

[28] ATLAS Collaboration, *Measurements of the Higgs boson production and decay rates and coupling strengths using pp collision data at $\sqrt{s} = 7$ and 8 TeV in the ATLAS experiment*, Eur. Phys. J. C **76** (2016) 6, arXiv:1507.04548 [hep-ex].

[29] CMS Collaboration, *Precise determination of the mass of the Higgs boson and tests of compatibility of its couplings with the standard model predictions using proton collisions at 7 and 8 TeV*, Eur. Phys. J. C **75** (2015) 212, arXiv:1412.8662 [hep-ex].

[30] CMS Collaboration, *Constraints on the spin-parity and anomalous HVV couplings of the Higgs boson in proton collisions at 7 and 8 TeV*, Phys. Rev. D **92** (2015) 012004, arXiv:1411.3441 [hep-ex].

[31] ATLAS and CMS Collaborations, *Measurements of the Higgs boson production and decay rates and constraints on its couplings from a combined ATLAS and CMS analysis of the LHC pp collision data at $\sqrt{s} = 7$ and 8 TeV*, JHEP **08** (2016) 045, arXiv:1606.02266 [hep-ex].

[32] LHC Higgs Cross Section Working Group, S. Dittmaier, C. Mariotti, G. Passarino, and R. Tanaka (Eds.), *Handbook of LHC Higgs Cross Sections: 2. Differential Distributions*, arXiv:1201.3084 [hep-ph].

[33] ATLAS Collaboration, *Observation of Higgs boson production in association with a top quark pair at the LHC with the ATLAS detector*, arXiv:1806.00425 [hep-ex].

[34] CMS Collaboration, CMS Collaboration, *Observation of $\mathrm{t\bar{t}}H$ production*, Phys. Rev. Lett. **120** (2018) 231801, arXiv:1804.02610 [hep-ex].

[35] CMS Collaboration, *Combined measurements of Higgs boson couplings in proton–proton collisions at $\sqrt{s} = 13$ TeV*, Eur. Phys. J. (2018), arXiv:1809.10733 [hep-ex].

[36] LHC Higgs Cross Section Working Group, *Handbook of LHC Higgs Cross Sections: 4. Deciphering the Nature of the Higgs Sector*, arXiv:1610.07922 [hep-ph].

[37] ATLAS Collaboration,, *ATLAS Summary Plots*, https://atlas.web.cern.ch/Atlas/GROUPS/PHYSICS/CombinedSummaryPlots/.

[38] LHC Higgs Cross Section Working Group, *Handbook of LHC Higgs Cross Sections: 3. Higgs Properties*, arXiv:1307.1347 [hep-ph].

[39] Planck Collaboration, P. A. R. Ade et al., *Planck 2013 results. XVI. Cosmological parameters*, Astron. Astrophys. **571** (2014) A16, arXiv:1303.5076 [astro-ph.CO].

[40] G. C. Branco et al., *Theory and phenomenology of two-Higgs-doublet models*, Phys. Rept. **516** (2012) 1, arXiv:1106.0034 [hep-ph].

[41] P. Fayet, *Supersymmetry and Weak, Electromagnetic and Strong Interactions*, Phys. Lett. B **64** (1976) 159.

[42] P. Fayet, *Spontaneously Broken Supersymmetric Theories of Weak, Electromagnetic and Strong Interactions*, Phys. Lett. B **69** (1977) 489.

[43] S. P. Martin, *A Supersymmetry primer*, arXiv:hep-ph/9709356 [hep-ph], [Adv. Ser. Direct. High Energy Phys.18,1(1998)].

[44] M. Miura, *Search for the proton decay in Super-Kamiokande*, pp. , 525–530. 2009.

[45] S. L. Glashow and S. Weinberg, *Natural Conservation Laws for Neutral Currents*, Phys. Rev. **D15** (1977) 1958.

[46] ATLAS Collaboration, *SUSY Summary Plots, November 2018*, ATL-PHYS-PUB-2018-046, 2018, https://cds.cern.ch/record/2651265.

[47] CMS Collaboration,, *CMS Supersymmetry Run 2 Summary plots*, https://twiki.cern.ch/twiki/bin/view/CMSPublic/PhysicsResultsSUS.

[48] A. Djouadi, *The Anatomy of electro-weak symmetry breaking. II. The Higgs bosons in the minimal supersymmetric model*, Phys. Rept. **459** (2008) 1, arXiv:hep-ph/0503173.

[49] M. Carena, S. Heinemeyer, C. E. M. Wagner and G. Weiglein, *Suggestions for benchmark scenarios for MSSM Higgs boson searches at hadron colliders*, Eur. Phys. J. C **26** (2003) 601, arXiv:hep-ph/0202167.

[50] S. Myers, *The LEP Collider, from design to approval and commissioning*. John Adams' Lecture. CERN, Geneva, 1991. https://cds.cern.ch/record/226776. Delivered at CERN, 26 Nov 1990.

[51] ALEPH, DELPHI, L3, and OPAL Collaborations, *Search for neutral MSSM Higgs bosons at LEP*, Eur. Phys. J. C **47** (2006) 547, arXiv:hep-ex/0602042.

[52] M. Carena, S. Heinemeyer, O. Stål, C. Wagner, and G. Weiglein, *MSSM Higgs boson searches at the LHC: benchmark scenarios after the discovery of a Higgs-like particle*, Eur. Phys. J. C **73** (2013) 2552, arXiv:1302.7033 [hep-ph].

[53] H. Bahl, E. Fuchs, T. Hahn, S. Heinemeyer, S. Liebler, S. Patel, P. Slavich, T. Stefaniak, C. E. M. Wagner, and G. Weiglein, *MSSM Higgs Boson Searches at the LHC: Benchmark Scenarios for Run 2 and Beyond*, arXiv:1808.07542 [hep-ph].

[54] A. Djouadi, L. Maiani, G. Moreau, A. Polosa, J. Quevillon, and V. Riquer, *The post-Higgs MSSM scenario: Habemus MSSM?*, Eur. Phys. J. C **73** (2013) 2650, arXiv:1307.5205 [hep-ph].

[55] A. Djouadi, L. Maiani, A. Polosa, J. Quevillon, and V. Riquer, *Fully covering the MSSM Higgs sector at the LHC*, JHEP **06** (2015) 168, arXiv:1502.05653 [hep-ph].

[56] S. Heinemeyer, W. Hollik, and G. Weiglein, *FeynHiggs: A Program for the calculation of the masses of the neutral CP even Higgs bosons in the MSSM*, Comput. Phys. Commun. **124** (2000) 76, arXiv:hep-ph/9812320.

[57] S. Heinemeyer, W. Hollik, and G. Weiglein, *The Masses of the neutral CP - even Higgs bosons in the MSSM: Accurate analysis at the two loop level*, Eur. Phys. J. C **9** (1999) 343, arXiv:hep-ph/9812472.

[58] G. Degrassi, S. Heinemeyer, W. Hollik, P. Slavich, and G. Weiglein, *Towards high precision predictions for the MSSM Higgs sector*, Eur. Phys. J. C **28** (2003) 133, arXiv:hep-ph/0212020.

[59] M. Frank, T. Hahn, S. Heinemeyer, W. Hollik, H. Rzehak, and G. Weiglein, *The Higgs boson masses and mixings of the complex MSSM in the Feynman-diagrammatic approach*, JHEP **02** (2007) 047, arXiv:hep-ph/0611326.

[60] T. Hahn, S. Heinemeyer, W. Hollik, H. Rzehak, and G. Weiglein, *High-Precision Predictions for the Light CP -Even Higgs Boson Mass of the Minimal Supersymmetric Standard Model*, Phys. Rev. Lett. **112** (2014) 141801, arXiv:1312.4937 [hep-ph].

[61] K. E. Williams, H. Rzehak, and G. Weiglein, *Higher order corrections to Higgs boson decays in the MSSM with complex parameters*, Eur. Phys. J. C **71** (2011) 1669, arXiv:1103.1335 [hep-ph].

[62] A. Djouadi, J. Kalinowski, and M. Spira, *HDECAY: A Program for Higgs boson decays in the standard model and its supersymmetric extension*, Comput. Phys. Commun. **108** (1998) 56, arXiv:hep-ph/9704448.

[63] A. Djouadi, M. M. Muhlleitner, and M. Spira, *Decays of supersymmetric particles: The Program SUSY-HIT (SUspect-SdecaY-Hdecay-InTerface)*, Acta Phys. Polon. B **38** (2007) 635–644, arXiv:hep-ph/0609292.

[64] A. Bredenstein, A. Denner, S. Dittmaier, and M. M. Weber, *Precise predictions for the Higgs-boson decay H —> WW/ZZ —> 4 leptons*, Phys. Rev. D **74** (2006) 013004, arXiv:hep-ph/0604011.

[65] A. Bredenstein, A. Denner, S. Dittmaier, and M. Weber, *Radiative corrections to the semileptonic and hadronic Higgs-boson decays $H \to W W / Z Z \to 4$ fermions*, JHEP **02** (2007) 080.

[66] R. V. Harlander, S. Liebler, and H. Mantler, *SusHi: A program for the calculation of Higgs production in gluon fusion and bottom-quark annihilation in the Standard Model and the MSSM*, Comp. Phys. Commun. **184** (2013) 1605, arXiv:1212.3249 [hep-ph].

[67] M. Spira, A. Djouadi, D. Graudenz, and P. M. Zerwas, *Higgs boson production at the LHC*, Nucl. Phys. B **453** (1995) 17, arXiv:hep-ph/9504378.

[68] R. V. Harlander and M. Steinhauser, *Supersymmetric Higgs production in gluon fusion at next-to-leading order*, JHEP **09** (2004) 066, arXiv:hep-ph/0409010.

[69] R. Harlander and P. Kant, *Higgs production and decay: Analytic results at next-to-leading order QCD*, JHEP **12** (2005) 015, arXiv:hep-ph/0509189.

[70] G. Degrassi and P. Slavich, *NLO QCD bottom corrections to Higgs boson production in the MSSM*, JHEP **11** (2010) 044, arXiv:1007.3465 [hep-ph].

[71] G. Degrassi, S. Di Vita, and P. Slavich, *NLO QCD corrections to pseudoscalar Higgs production in the MSSM*, JHEP **08** (2011) 128, arXiv:1107.0914 [hep-ph].

[72] G. Degrassi, S. Di Vita, and P. Slavich, *On the NLO QCD corrections to the production of the heaviest neutral Higgs scalar in the MSSM*, Eur. Phys. J. C **72** (2012) 2032, arXiv:1204.1016 [hep-ph].

[73] R. V. Harlander and W. B. Kilgore, *Next-to-Next-to-Leading Order Higgs Production at Hadron Colliders*, Phys. Rev. Lett. **88** (2002) 201801, arXiv:hep-ph/0201206.

[74] C. Anastasiou and K. Melnikov, *Higgs boson production at hadron colliders in NNLO QCD*, Nucl. Phys. B **646** (2002) 220, arXiv:hep-ph/0207004.

[75] V. Ravindran, J. Smith, and W. L. van Neerven, *NNLO corrections to the total cross-section for Higgs boson production in hadron hadron collisions*, Nucl. Phys. B **665** (2003) 325, arXiv:hep-ph/0302135.

[76] R. Harlander and W. B. Kilgore, *Production of a pseudoscalar Higgs boson at hadron colliders at next-to-next-to leading order*, JHEP **10** (2002) 017, arXiv:hep-ph/0208096.

[77] C. Anastasiou and K. Melnikov, *Pseudoscalar Higgs boson production at hadron colliders in NNLO QCD*, Phys. Rev. D **67** (2003) 037501, arXiv:hep-ph/0208115.

[78] U. Aglietti, R. Bonciani, G. Degrassi, and A. Vicini, *Two loop light fermion contribution to Higgs production and decays*, Phys. Lett. B **595** (2004) 432, arXiv:hep-ph/0404071.

[79] R. Bonciani, G. Degrassi, and A. Vicini, *On the generalized harmonic polylogarithms of one complex variable*, Comput. Phys. Commun. **182** (2011) 1253, arXiv:1007.1891 [hep-ph].

[80] E. Bagnaschi and A. Vicini, *The Higgs transverse momentum distribution in gluon fusion as a multiscale problem*, JHEP **01** (2016) 056, arXiv:1505.00735 [hep-ph].

[81] CMS Collaboration, *Search for additional neutral MSSM Higgs bosons in the $\tau\tau$ final state in proton-proton collisions at $\sqrt{s} = 13$ TeV*, arXiv:1803.06553 [hep-ex].

[82] R. Harlander, M. Krämer, and M. Schumacher, *Bottom-quark associated Higgs-boson production: reconciling the four- and five-flavour scheme approach*, 2011, arXiv:1112.3478 [hep-ph].

[83] R. Harlander and W. B. Kilgore, *Higgs boson production in bottom quark fusion at next-to-next-to-leading order*, Phys. Rev. D **68** (2003) 013001, arXiv:hep-ph/0304035.

[84] S. Dittmaier, M. Krämer and M. Spira, *Higgs radiation off bottom quarks at the Tevatron and the LHC*, Phys. Rev. D **70** (2004) 074010, arXiv:hep-ph/0309204.

[85] S. Dawson, C. B. Jackson, L. Reina, and D. Wackeroth, *Exclusive Higgs boson production with bottom quarks at hadron colliders*, Phys. Rev. D **69** (2004) 074027, arXiv:hep-ph/0311067.

[86] M. Bonvini, A. S. Papanastasiou, and F. J. Tackmann, *Resummation and matching of b-quark mass effects in $b\bar{b}H$ production*, JHEP **11** (2015) 196, arXiv:1508.03288 [hep-ph].

[87] M. Bonvini, A. S. Papanastasiou, and F. J. Tackmann, *Matched predictions for the $b\bar{b}H$ cross section at the 13 TeV LHC*, JHEP **10** (2016) 053, arXiv:1605.01733 [hep-ph].

[88] C. Degrande, M. Ubiali, M. Wiesemann, and M. Zaro, *Heavy charged Higgs boson production at the LHC*, JHEP **10** (2015) 145, arXiv:1507.02549 [hep-ph].

[89] M. Flechl, R. Klees, M. Kramer, M. Spira, and M. Ubiali, *Improved cross-section predictions for heavy charged Higgs boson production at the LHC*, Phys. Rev. D **91** (2015) 075015, arXiv:1409.5615 [hep-ph].

[90] S. Dittmaier, M. Kramer, M. Spira, and M. Walser, *Charged-Higgs-boson production at the LHC: Next-to-leading-order supersymmetric QCD correction*, Phys. Rev. D **83** (2011) 055005, arXiv:0906.2648 [hep-ph].

[91] E. L. Berger, T. Han, J. Jiang, and T. Plehn, *Associated production of a top quark and a charged Higgs boson*, Phys. Rev. D **71** (2005) 115012, arXiv:hep-ph/0312286 [hep-ph].

[92] C. Degrande, R. Frederix, V. Hirschi, M. Ubiali, M. Wiesemann, and M. Zaro, *Accurate predictions for charged Higgs production: Closing the $m_{H^\pm} \sim m_t$ window*, Phys. Lett. B **772** (2017) 87–92, arXiv:1607.05291 [hep-ph].

[93] ATLAS Collaboration, *Search for neutral Higgs bosons of the minimal supersymmetric standard model in pp collisions at $\sqrt{s} = 8$ TeV with the ATLAS detector*, JHEP **11** (2014) 056, arXiv:1409.6064 [hep-ex].

[94] ATLAS Collaboration, *Search for a CP-odd Higgs boson decaying to Zh in pp collisions at $\sqrt{s} = 8$ TeV with the ATLAS detector*, Phys. Lett. B **744** (2015) 163, arXiv:1502.04478 [hep-ex].

[95] ATLAS Collaboration, *Search for a high-mass Higgs boson decaying to a W boson pair in pp collisions at $\sqrt{s} = 8$ TeV with the ATLAS detector*, JHEP **01** (2016) 032, arXiv:1509.00389 [hep-ex].

[96] ATLAS Collaboration, *Search for an additional, heavy Higgs boson in the $H \to ZZ$ decay channel at $\sqrt{s} = 8$ TeV in pp collision data with the ATLAS detector*, Eur. Phys. J. C **76** (2016) 45, arXiv:1507.05930 [hep-ex].

[97] ATLAS Collaboration, *Search for charged Higgs bosons decaying via $H^\pm \to \tau^\pm \nu$ in fully hadronic final states using pp collision data at $\sqrt{s} = 8$ TeV with the ATLAS detector*, JHEP **03** (2015) 088, arXiv:1412.6663 [hep-ex].

[98] LHCb Collaboration, A. A. Alves, Jr. et al., *The LHCb Detector at the LHC*, JINST **3** (2008) S08005.

[99] ALICE Collaboration, K. Aamodt et al., *The ALICE experiment at the CERN LHC*, JINST **3** (2008) S08002.

[100] ATLAS Collaboration,, *ATLAS Luminosity Public Results, Run-II*, https://atlas.web.cern.ch/Atlas/GROUPS/PHYSICS/CombinedSummaryPlots/.

[101] G. Apollinari, O. Brüning, T. Nakamoto, and L. Rossi, *High Luminosity Large Hadron Collider HL-LHC*, CERN Yellow Rep. (2015) 1–19, arXiv:1705.08830 [physics.acc-ph].

[102] J. Goodson, *Search for Supersymmetry in States with Large Missing Transverse Momentum and Three Leptons including a Z-Boson*. PhD thesis, Stony Brook University, May, 2012. Presented 17 Apr 2012.

[103] J. Pequenao, *Computer generated image of the whole ATLAS detector*, Mar, 2008. https://cds.cern.ch/record/1095924.

[104] ATLAS Collaboration,, *ATLAS inner detector: Technical Design Report, 1*. Technical Design Report ATLAS. CERN, Geneva, 1997. https://cds.cern.ch/record/331063.

[105] ATLAS Collaboration, S. Haywood, L. Rossi, R. Nickerson, and A. Romaniouk, *ATLAS inner detector: Technical Design Report, 2*. Technical Design Report ATLAS. CERN, Geneva, 1997. http://cds.cern.ch/record/331064.

[106] G. Aad et al., *ATLAS pixel detector electronics and sensors*, JINST **3** (2008) P07007.

[107] ATLAS TRT Collaboration, E. Abat et al., *The ATLAS Transition Radiation Tracker (TRT) proportional drift tube: Design and performance*, JINST **3** (2008) P02013.

[108] ATLAS Collaboration,, *ATLAS liquid-argon calorimeter: Technical Design Report*. Technical Design Report ATLAS. CERN, Geneva, 1996. https://cds.cern.ch/record/331061.

[109] ATLAS Collaboration,, *ATLAS tile calorimeter: Technical Design Report*. Technical Design Report ATLAS. CERN, Geneva, 1996. https://cds.cern.ch/record/331062.

[110] ATLAS Collaboration,, *ATLAS muon spectrometer: Technical design report*,.

[111] ATLAS TDAQ Collaboration, *The ATLAS Data Acquisition and High Level Trigger system*, Journal of Instrumentation **11** (2016) P06008–P06008.

[112] ATLAS Collaboration, ATLAS Collaboration, *Performance of the ATLAS Trigger System in 2015*, Eur. Phys. J. **C77** (2017) 317, arXiv:1611.09661 [hep-ex].

[113] ATLAS Collaboration, *Track Reconstruction Performance of the ATLAS Inner Detector at* $\sqrt{s} = 13$ *TeV*, ATL-PHYS-PUB-2015-018, 2015, https://cds.cern.ch/record/2037683.

[114] ATLAS Collaboration, *ATLAS insertable B-layer technical design report*, Atlas-tdr-19, 2010, http://cds.cern.ch/record/1291633.

[115] ATLAS Collaboration, *ATLAS insertable B-layer technical design report addendum*, Atlas-tdr-19-add-1, 2012, http://cds.cern.ch/record/1451888.

[116] J. Pequenao, *Computer generated image of the ATLAS inner detector*, Mar, 2008. https://cds.cern.ch/record/1095926.

[117] *ATLAS silicon microstrip detector system (SCT)*, Nucl. Instrum. Methods Phys. Res. A **511** (2003) 58 – 63, Proceedings, 11th Int. Workshop on Vertex Detectors.

[118] ATLAS Collaboration, M. Aaboud et al., *Reconstruction of primary vertices at the ATLAS experiment in Run 1 proton–proton collisions at the LHC*, Eur. Phys. J. **C77** (2017) 332, arXiv:1611.10235 [physics.ins-det].

[119] ATLAS Collaboration, M. Aaboud et al., *Performance of the ATLAS Track Reconstruction Algorithms in Dense Environments in LHC Run 2*, Eur. Phys. J. **C77** (2017) 673, arXiv:1704.07983 [hep-ex].

[120] ATLAS Collaboration, *Performance of the ATLAS Inner Detector Track and Vertex Reconstruction in High Pile-Up LHC Environment*, ATLAS-CONF-2012-042, 2012, https://cds.cern.ch/record/1435196.

[121] ATLAS Collaboration, *Performance of primary vertex reconstruction in proton–proton collisions at $\sqrt{s} = 7$ TeV in the ATLAS experiment*, ATLAS-CONF-2010-069, 2010, https://cds.cern.ch/record/1281344.

[122] ATLAS Collaboration, *Early Inner Detector Tracking Performance in the 2015 Data at $\sqrt{s} = 13$ TeV*, ATL-PHYS-PUB-2015-051, 2015, https://cds.cern.ch/record/2110140.

[123] ATLAS Collaboration,, *Basic Inner Detector Tracking Performance at 13 TeV*, https://atlas.web.cern.ch/Atlas/GROUPS/PHYSICS/PLOTS/IDTR-2015-007/.

[124] J. Pequenao, *Computer Generated image of the ATLAS calorimeter*, Mar, 2008. https://cds.cern.ch/record/1095927.

[125] ATLAS Collaboration, *The ATLAS experiment at the CERN Large Hadron Collider*, JINST **3** (2008) S08003.

[126] ATLAS Collaboration, *Topological cell clustering in the ATLAS calorimeters and its performance in LHC Run 1*, Eur. Phys. J. C **77** (2017) 490, arXiv:1603.02934 [hep-ex].

[127] ATLAS Collaboration,, *ATLAS Fact Sheet : To raise awareness of the ATLAS detector and collaboration on the LHC*, 2010. https://cds.cern.ch/record/1457044.

[128] ATLAS Collaboration,, *Trigger Operation Public Results*, https://twiki.cern.ch/twiki/bin/view/AtlasPublic/TriggerOperationPublicResults#2016_pp_at_13_TeV.

[129] A. Collaboration, *ATLAS Computing: technical design report*. Technical Design Report ATLAS. CERN, Geneva, 2005. https://cds.cern.ch/record/837738.

[130] M. Elsing, M. Goossens, A. Nairz, and G. Negri, *The ATLAS Tier-0: Overview and operational experience*, J. Phys.: Conf. Ser. **219** (2010) 072011, https://cds.cern.ch/record/1270548.

[131] I. Antcheva et al., *ROOT — A C++ framework for petabyte data storage, statistical analysis and visualization*, Computer Physics Communications **180** (2009) 2499 – 2512.

[132] GEANT4 Collaboration, S. Agostinelli et al., *GEANT4 – a simulation toolkit*, Nucl. Instrum. Meth. A **506** (2003) 250–303.

[133] ATLAS Collaboration, *The simulation principle and performance of the ATLAS fast calorimeter simulation FastCaloSim*, ATL-PHYS-PUB-2010-013, 2010, https://cds.cern.ch/record/1300517.

[134] J. Pequenao, *Event Cross Section in a computer generated image of the ATLAS detector.*, Mar, 2008. https://cds.cern.ch/record/1096081.

[135] ATLAS Collaboration, *Electron efficiency measurements with the ATLAS detector using the 2015 LHC proton-proton collision data*, ATLAS-CONF-2016-024, 2016, https://cds.cern.ch/record/2157687.

[136] ATLAS Collaboration, *Measurement of the photon identification efficiencies with the ATLAS detector using LHC Run 2 data collected in 2015 and 2016*, Eur. Phys. J. C **79** (2019) 205, arXiv:1810.05087 [hep-ex].

[137] ATLAS Collaboration, *Muon reconstruction performance of the ATLAS detector in proton–proton collision data at* $\sqrt{s} = 13\,TeV$, Eur. Phys. J. C **76** (2016) 292, arXiv:1603.05598 [hep-ex].

[138] G. P. Salam, *Towards Jetography*, Eur. Phys. J. **C67** (2010) 637–686, arXiv:0906.1833 [hep-ph].

[139] M. Cacciari, G. P. Salam, and G. Soyez, *The anti-k_t jet clustering algorithm*, JHEP **04** (2008) 063, arXiv:0802.1189 [hep-ph].

[140] M. Cacciari, G. P. Salam, and G. Soyez, *FastJet user manual*, Eur. Phys. J. C **72** (2012) 1896, arXiv:1111.6097 [hep-ph].

[141] ATLAS Collaboration, *Jet energy scale measurements and their systematic uncertainties in proton–proton collisions at* $\sqrt{s} = 13\,TeV$ *with the ATLAS detector*, Phys. Rev. D **96** (2017) 072002, arXiv:1703.09665 [hep-ex].

[142] M. Cacciari and G. P. Salam, *Pileup subtraction using jet areas*, Phys. Lett. **B659** (2008) 119–126, arXiv:0707.1378 [hep-ph].

[143] ATLAS Collaboration, *Tagging and suppression of pileup jets with the ATLAS detector*, ATLAS-CONF-2014-018, 2014, https://cds.cern.ch/record/1700870.

[144] ATLAS Collaboration, *Selection of jets produced in* 13 *TeV proton–proton collisions with the ATLAS detector*, ATLAS-CONF-2015-029, 2015, https://cds.cern.ch/record/2037702.

[145] ATLAS Collaboration, *Performance of b-jet identification in the ATLAS experiment*, JINST **11** (2016) P04008, arXiv:1512.01094 [hep-ex].

[146] ATLAS Collaboration, *Optimisation of the ATLAS b-tagging performance for the 2016 LHC Run*, Atl-phys-pub-2016-012, 2016, https://cds.cern.ch/record/2160731.

[147] ATLAS Collaboration, *Expected performance of the ATLAS b-tagging algorithms in Run-2*, ATL-PHYS-PUB-2015-022, 2015, https://cds.cern.ch/record/2037697.

[148] ATLAS Collaboration, *Identification and energy calibration of hadronically decaying tau leptons with the ATLAS experiment in pp collisions at* $\sqrt{s} = 8$ *TeV*, Eur. Phys. J. C **75** (2015) 303, arXiv:1412.7086 [hep-ex].

[149] ATLAS Collaboration, *Measurement of the tau lepton reconstruction and identification performance in the ATLAS experiment using pp collisions at* $\sqrt{s} = 13$ TeV, Atlas-conf-2017-029, 2017, https://cds.cern.ch/record/2261772.

[150] ATLAS Collaboration, *Reconstruction of hadronic decay products of tau leptons with the ATLAS experiment*, Eur. Phys. J. C **76** (2016) 295, arXiv:1512.05955 [hep-ex].

[151] ATLAS Collaboration, *Reconstruction, Energy Calibration, and Identification of Hadronically Decaying Tau Leptons in the ATLAS Experiment for Run-2 of the LHC*, ATL-PHYS-PUB-2015-045, 2015, https://cds.cern.ch/record/2064383.

[152] ATLAS Collaboration, *Performance of missing transverse momentum reconstruction with the ATLAS detector in the first proton–proton collisions at* $\sqrt{s} = 13$ *TeV*, ATL-PHYS-PUB-2015-027, 2015, https://cds.cern.ch/record/2037904.

[153] ATLAS Collaboration, *Expected performance of missing transverse momentum reconstruction for the ATLAS detector at* $\sqrt{s} = 13$ *TeV*, ATL-PHYS-PUB-2015-023, 2015, https://cds.cern.ch/record/2037700.

[154] J. Neyman and E. Pearson, *On the Problem of the Most Efficient Tests of Statistical Hypotheses*, Philosophical Transactions of the Royal Society, A **231** (1933) 289–337.

[155] G. Cowan, K. Cranmer, E. Gross, and O. Vitells, *Asymptotic formulae for likelihood-based tests of new physics*, Eur. Phys. J. C **71** (2011) 1554, arXiv:1007.1727 [physics.data-an], [Erratum: Eur. Phys. J. C 73 (2013) 2501].

[156] A. L. Read, *Presentation of search results: the* CL_s *technique*, J. Phys. G **28** (2002) 2693–2704.

[157] S. S. Wilks, *The Large-Sample Distribution of the Likelihood Ratio for Testing Composite Hypotheses*, Ann. Math. Statist. **9** (1938) 60–62, https://doi.org/10.1214/aoms/1177732360.

[158] A. Wald, *Tests of statistical hypotheses concerning several parameters when the number of observations is large*, 1943.

[159] L. Moneta, K. Belasco, K. S. Cranmer, S. Kreiss, A. Lazzaro, et al., *The RooStats Project*, PoS **ACAT2010** (2010) 057, arXiv:1009.1003 [physics.data-an].

[160] ATLAS Collaboration, *Evidence for the Higgs-boson Yukawa coupling to tau leptons with the ATLAS detector*, JHEP **04** (2015) 117, arXiv:1501.04943 [hep-ex].

[161] CMS Collaboration, *Evidence for the direct decay of the* 125 *GeV Higgs boson to fermions*, Nature Phys. **10** (2014) 557, arXiv:1401.6527 [hep-ex].

[162] CMS Collaboration, *Evidence for the 125 GeV Higgs boson decaying to a pair of τ leptons*, JHEP **05** (2014) 104, arXiv:1401.5041 [hep-ex].

[163] CMS Collaboration, *Observation of the Higgs boson decay to a pair of τ leptons*, Phys. Lett. B **779** (2018) 283, arXiv:1708.00373 [hep-ex].

[164] ATLAS Collaboration, *Cross-section measurements of the Higgs boson decaying into a pair of τ-leptons in proton–proton collisions at $\sqrt{s} = 13$ TeV with the ATLAS detector*, Phys. Rev. (2018), arXiv:1811.08856 [hep-ex].

[165] ATLAS Collaboration, *Test of CP Invariance in vector-boson fusion production of the Higgs boson using the Optimal Observable method in the ditau decay channel with the ATLAS detector*, Eur. Phys. J. C **76** (2016) 658, arXiv:1602.04516 [hep-ex].

[166] CMS Collaboration, *Search for neutral MSSM Higgs bosons decaying to a pair of tau leptons in pp collisions*, JHEP **10** (2014) 160, arXiv:1408.3316 [hep-ex].

[167] CMS Collaboration,, *Search for a low-mass $\tau^+\tau^-$ resonance in association with a bottom quark in proton-proton collisions at $\sqrt{s} = 13$ TeV*, arXiv:1903.10228 [hep-ex].

[168] ATLAS Collaboration, ATLAS Collaboration, *Luminosity determination in pp collisions at $\sqrt{s}$ = 8 TeV using the ATLAS detector at the LHC*, Eur. Phys. J. C **76** (2016) 653, arXiv:1608.03953 [hep-ex].

[169] P. Nason, *A New method for combining NLO QCD with shower Monte Carlo algorithms*, JHEP **11** (2004) 040, arXiv:hep-ph/0409146.

[170] S. Frixione, P. Nason, and C. Oleari, *Matching NLO QCD computations with parton shower simulations: the POWHEG method*, JHEP **11** (2007) 070, arXiv:0709.2092 [hep-ph].

[171] S. Alioli, P. Nason, C. Oleari, and E. Re, *A general framework for implementing NLO calculations in shower Monte Carlo programs: the POWHEG BOX*, JHEP **06** (2010) 043, arXiv:1002.2581 [hep-ph].

[172] S. Alioli, P. Nason, C. Oleari, and E. Re, *NLO Higgs boson production via gluon fusion matched with shower in POWHEG*, JHEP **04** (2009) 002, arXiv:0812.0578 [hep-ph].

[173] H.-L. Lai et al., *New parton distributions for collider physics*, Phys. Rev. D **82** (2010) 074024, arXiv:1007.2241 [hep-ph].

[174] T. Sjöstrand, S. Mrenna and P. Skands, *A brief introduction to PYTHIA 8.1*, Comput. Phys. Commun. **178** (2008) 852, arXiv:0710.3820 [hep-ph].

[175] T. Sjöstrand, S. Mrenna and P. Skands, *PYTHIA 6.4 physics and manual*, JHEP **05** (2006) 026, arXiv:hep-ph/0603175.

[176] ATLAS Collaboration, *Measurement of the Z/γ^* boson transverse momentum distribution in pp collisions at $\sqrt{s}$ = 7 TeV with the ATLAS detector*, JHEP **09** (2014) 55, arXiv:1406.3660 [hep-ex].

[177] J. Pumplin et al., *New generation of parton distributions with uncertainties from global QCD analysis*, JHEP **07** (2002) 012, arXiv:hep-ph/0201195.

[178] N. Davidson, T. Przedzinski, and Z. Was, *PHOTOS Interface in C++: Technical and Physics Documentation*, Comput. Phys. Commun. **199** (2016) 86–101, arXiv:1011.0937 [hep-ph].

[179] C. Anastasiou, L. J. Dixon, K. Melnikov, and F. Petriello, *High precision QCD at hadron colliders: Electroweak gauge boson rapidity distributions at NNLO*, Phys. Rev. D **69** (2004) 094008, arXiv:hep-ph/0312266.

[180] S. Dulat, T. J. Hou, J. Gao, M. Guzzi, J. Huston, P. Nadolsky, J. Pumplin, C. Schmidt, D. Stump, and C. P. Yuan, *New parton distribution functions from a global analysis of quantum chromodynamics*, Phys. Rev. D **93** (2016) 033006, arXiv:1506.07443 [hep-ph].

[181] S. G. Bondarenko and A. A. Sapronov, *NLO EW and QCD proton-proton cross section calculations with mcsanc-v1.01*, Comput. Phys. Commun. **184** (2013) 2343–2350, arXiv:1301.3687 [hep-ph].

[182] A. D. Martin, R. G. Roberts, W. J. Stirling, and R. S. Thorne, *Parton distributions incorporating QED contributions*, Eur. Phys. J. C **39** (2005) 155–161, arXiv:hep-ph/0411040.

[183] T. Gleisberg and S. Höche, *Comix, a new matrix element generator*, JHEP **12** (2008) 039, arXiv:0808.3674 [hep-ph].

[184] F. Cascioli, P. Maierhofer, and S. Pozzorini, *Scattering Amplitudes with Open Loops*, Phys. Rev. Lett. **108** (2012) 111601, arXiv:1111.5206 [hep-ph].

[185] S. Schumann and F. Krauss, *A Parton shower algorithm based on Catani-Seymour dipole factorisation*, JHEP **03** (2008) 038, arXiv:0709.1027 [hep-ph].

[186] T. Gleisberg, S. Höche, F. Krauss, M. Schönherr, S. Schumann, et al., *Event generation with SHERPA 1.1*, JHEP **02** (2009) 007, arXiv:0811.4622 [hep-ph].

[187] S. Höche, F. Krauss, M. Schönherr, and F. Siegert, *QCD matrix elements + parton showers: The NLO case*, JHEP **04** (2013) 027, arXiv:1207.5030 [hep-ph].

[188] K. Melnikov and F. Petriello, *Electroweak gauge boson production at hadron colliders through $O(\alpha_s^2)$*, Phys. Rev. D **74** (2006) 114017, arXiv:hep-ph/0609070.

[189] R. Gavin, Y. Li, F. Petriello, and S. Quackenbush, *FEWZ 2.0: A code for hadronic Z production at next-to-next-to-leading order*, Comput. Phys. Commun. **182** (2011) 2388, arXiv:1011.3540 [hep-ph].

[190] ATLAS, CMS, CDF, D0 Collaboration, R. Schwienhorst, *Top cross-sections and single top*, Int. J. Mod. Phys. Conf. Ser. **31** (2014) 1460277, arXiv:1403.0513 [hep-ex].

[191] P. Skands, *Tuning Monte Carlo generators: The Perugia tunes*, Phys. Rev. D **82** (2010) 074018, arXiv:1005.3457 [hep-ph].

[192] M. Czakon and A. Mitov, *Top++: A program for the calculation of the top-pair cross-section at hadron colliders*, Comput. Phys. Commun. **185** (2014) 2930, arXiv:1112.5675 [hep-ph].

[193] P. Kant, O. M. Kind, T. Kintscher, T. Lohse, T. Martini, S. Mbitz, P. Rieck, and P. Uwer, HATHOR *for single top-quark production: Updated predictions and uncertainty estimates for single top-quark production in hadronic collisions*, Comput. Phys. Commun. **191** (2015) 74, arXiv:1406.4403 [hep-ph].

[194] M. Aliev et al., HATHOR*: HAdronic Top and Heavy quarks crOss section calculatoR*, Comput. Phys. Commun. **182** (2011) 1034, arXiv:1007.1327 [hep-ph].

[195] N. Kidonakis, *Two-loop soft anomalous dimensions for single top quark associated production with a W- or H-*, Phys. Rev. D **82** (2010) 054018, arXiv:1005.4451 [hep-ph].

[196] T. Sjöstrand, S. Ask, J. R. Christiansen, R. Corke, N. Desai, P. Ilten, S. Mrenna, S. Prestel, C. O. Rasmussen, and P. Z. Skands, *An introduction to PYTHIA 8.2*, Comput. Phys. Commun. **191** (2015) 159, arXiv:1410.3012 [hep-ph].

[197] J. Alwall, R. Frederix, S. Frixione, V. Hirschi, F. Maltoni, et al., *The automated computation of tree-level and next-to-leading order differential cross sections, and their matching to parton shower simulations*, JHEP **07** (2014) 079, arXiv:1405.0301 [hep-ph].

[198] M. Wiesemann, R. Frederix, S. Frixione, V. Hirschi, F. Maltoni, and P. Torrielli, *Higgs production in association with bottom quarks*, JHEP **02** (2015) 132, arXiv:1409.5301 [hep-ph].

[199] ATLAS Collaboration, *ATLAS Run 1 Pythia8 tunes*, ATL-PHYS-PUB-2014-021, 2014, https://cds.cern.ch/record/1966419.

[200] R. D. Ball et al., *Parton distributions with LHC data*, Nucl. Phys. B **867** (2013) 244–289, arXiv:1207.1303 [hep-ph].

[201] ATLAS Collaboration, *Summary of ATLAS Pythia 8 tunes*, ATL-PHYS-PUB-2012-003, 2012, https://cds.cern.ch/record/1474107.

[202] A. D. Martin et al., *Parton distributions for the LHC*, Eur. Phys. J. C **63** (2009) 189, arXiv:0901.0002 [hep-ph].

[203] ATLAS Collaboration, *The ATLAS simulation infrastructure*, Eur. Phys. J. C **70** (2010) 823, arXiv:1005.4568 [physics.ins-det].

[204] A. Elagin, P. Murat, A. Pranko, and A. Safonov, *A New Mass Reconstruction Technique for Resonances Decaying to di-tau*, Nucl. Instrum. Meth. **A654** (2011) 481, arXiv:1012.4686 [hep-ex].

[205] D. Alvarez Piqueras et al., *Search for neutral MSSM Higgs bosons $H/A \to \tau_{lep}\tau_{had}$ and $Z' \to \tau_{lep}\tau_{had}$ produced in 13 TeV collisions with the ATLAS detector*, Tech. Rep. ATL-COM-PHYS-2015-604, CERN, Geneva, Jul, 2015. https://cds.cern.ch/record/2030187.

[206] ATLAS Collaboration, *Trigger Menu in 2016*, ATL-DAQ-PUB-2017-001, 2017, https://cds.cern.ch/record/2242069.

[207] L. Zhang et al., *Search for Neutral MSSM Higgs Bosons H/A and Z' decaying to $\tau_\ell\tau_{had}$ produced in 13 TeV proton-proton collisions with the data collected by the ATLAS Detector in full 2015 and 2016*, Tech. Rep. ATL-COM-PHYS-2016-1458, CERN, Geneva, Oct, 2016. https://cds.cern.ch/record/2223254.

[208] H. Lorenz et al., *Search for Neutral MSSM Higgs Bosons H/A and Z' decaying to $\tau_h\tau_h$ produced in 13 TeV proton-proton collisions with the data collected by the ATLAS Detector in full 2015 and 2016*, Tech. Rep. ATL-COM-PHYS-2016-1459, CERN, Geneva, Oct, 2016. https://cds.cern.ch/record/2223255.

[209] ATLAS Collaboration, *Search for high-mass new phenomena in the dilepton final state using proton–proton collisions at $\sqrt{s} = 13$ TeV with the ATLAS detector*, Phys. Lett. B **761** (2016) 372, arXiv:1607.03669 [hep-ex].

[210] W. Davey, J. Dingfelder, D. Duschinger, W. Mader, M. Morgenstern, F. Scutti, A. Straessner, and S. Wahrmund, *Search for neutral MSSM Higgs bosons in the decay mode $H \to \tau^+\tau^- \to \tau_{\text{had}}\tau_{\text{had}}$ + 2 neutrinos in proton-proton collisions at $\sqrt{s}$=8 TeV with the ATLAS Experiment.*, ATL-COM-PHYS-2013-238 (2013), https://cds.cern.ch/record/1520112.

[211] J. Butterworth et al., *PDF4LHC recommendations for LHC Run II*, arXiv:1510.03865 [hep-ph].

[212] A. Buckley, J. Ferrando, S. Lloyd, K. Nordstr, B. Page, M. Renacht, M. Schherr, and G. Watt, *LHAPDF6: parton density access in the LHC precision era*, Eur. Phys. J. C **75** (2015) 132, arXiv:1412.7420 [hep-ph].

[213] The ATLAS Collaboration, *ATLAS Pythia8 tunes to 7 TeV data*, ATL-PHYS-PUB-2014-0021 [https://cds.cern.ch/record/1966419] (2014).

[214] ATLAS Collaboration, *A study of optimal parameter setting for* MADGRAPH5_AMC@NLO + PYTHIA *8 matched setup*, ATL-PHYS-PUB-2015-048, 2015, https://cds.cern.ch/record/2103221.

[215] G. Choudalakis and D. Casadei, *Plotting the differences between data and expectation*, Eur. Phys. J. Plus **127** (2012) 25, arXiv:1111.2062 [physics.data-an].

[216] ATLAS Collaboration, *Search for Minimal Supersymmetric Standard Model Higgs bosons H/A and for a Z' boson in the $\tau\tau$ final state produced in pp collisions at $\sqrt{s} = 13$ TeV with the ATLAS Detector*, Eur. Phys. J. C **76** (2016) 585, arXiv:1608.00890 [hep-ex].

[217] J. L. Hewett and T. G. Rizzo, *Low-energy phenomenology of superstring-inspired* E_6 *models*, Phys. Rept. **183** (1989) 193–381.

[218] M. Cvetic and S. Godfrey, *Discovery and identification of extra gauge bosons*, arXiv:hep-ph/9504216.

[219] A. Leike, *The Phenomenology of extra neutral gauge bosons*, Phys. Rept. **317** (1999) 143–250, arXiv:hep-ph/9805494.

[220] R. Diener, S. Godfrey, and T. A. Martin, *Unravelling an extra neutral gauge boson at the LHC using third generation fermions*, Phys. Rev. D **83** (2011) 115008, arXiv:1006.2845 [hep-ph].

[221] P. Langacker, *The Physics of Heavy Z′ Gauge Bosons*, Rev. Mod. Phys. **81** (2009) 1199–1228, arXiv:0801.1345 [hep-ph].

[222] ATLAS Collaboration, ATLAS Collaboration, *Search for charged Higgs bosons decaying via $H^+ \to \tau\nu$ in top quark pair events using pp collision data at $\sqrt{s} = 7$ TeV with the ATLAS detector*, JHEP **06** (2012) 039, arXiv:1204.2760 [hep-ex].

[223] ATLAS Collaboration, ATLAS Collaboration, *Search for charged Higgs bosons through the violation of lepton universality in $t\bar{t}$ events using pp collision data at $\sqrt{s} = 7$ TeV with the ATLAS experiment*, JHEP **03** (2013) 076, arXiv:1212.3572 [hep-ex].

[224] CMS Collaboration, CMS Collaboration, *Search for a light charged Higgs boson in top quark decays in pp collisions at $\sqrt{s} = 7$ TeV*, JHEP **07** (2012) 143, arXiv:1205.5736 [hep-ex].

[225] CMS Collaboration, CMS Collaboration, *Search for a charged Higgs boson in pp collisions at $\sqrt{s} = 8$ TeV*, JHEP **11** (2015) 018, arXiv:1508.07774 [hep-ex].

[226] ATLAS Collaboration, ATLAS Collaboration, *Search for a light charged Higgs boson in the decay channel $H^+ \to c\bar{s}$ in $t\bar{t}$ events using pp collisions at $\sqrt{s}$ = 7 TeV with the ATLAS detector*, Eur. Phys. J. C **73** (2013) 2465, arXiv:1302.3694 [hep-ex].

[227] CMS Collaboration, CMS Collaboration, *Search for a light charged Higgs boson decaying to $c\bar{s}$ in pp collisions at $\sqrt{s} = 8$ TeV*, JHEP **12** (2015) 178, arXiv:1510.04252 [hep-ex].

[228] ATLAS Collaboration, ATLAS Collaboration, *Search for charged Higgs bosons in the $H^\pm \to tb$ decay channel in pp collisions at $\sqrt{s} = 8$ TeV using the ATLAS detector*, JHEP **03** (2016) 127, arXiv:1512.03704 [hep-ex].

[229] ATLAS Collaboration, ATLAS Collaboration, *Search for a Charged Higgs Boson Produced in the Vector-Boson Fusion Mode with Decay $H^\pm \to W^\pm Z$ using pp Collisions at $\sqrt{s} = 8$ TeV with the ATLAS Experiment*, Phys. Rev. Lett. **114** (2015) 231801, arXiv:1503.04233 [hep-ex].

[230] CMS Collaboration, CMS Collaboration, *Search for Charged Higgs Bosons Produced via Vector Boson Fusion and Decaying into a Pair of W and Z Bosons Using pp Collisions at $\sqrt{s} = 13$* TeV, Phys. Rev. Lett. **119** (2017) 141802, arXiv:1705.02942 [hep-ex].

[231] CMS Collaboration, S. M. Albert et al., *Search for a light charged Higgs boson decaying to a W boson and a CP-odd Higgs boson in final states with $e\mu\mu$ or $\mu\mu\mu$ in proton-proton collisions at $\sqrt{s} = 13$ TeV*, Tech. Rep. arXiv:1905.07453.

CMS-HIG-18-020-003, CERN, Geneva, May, 2019.
https://cds.cern.ch/record/2675010.

[232] ATLAS Collaboration, *Search for charged Higgs bosons produced in association with a top quark and decaying via $H^{\pm} \to \tau\nu$ using pp collision data recorded at $\sqrt{s} = 13\,TeV$ by the ATLAS detector*, Phys. Lett. B **759** (2016) 555, arXiv:1603.09203 [hep-ex].

[233] CMS Collaboration, *Search for charged Higgs bosons in the $H^{\pm} \to \tau^{\pm}\nu_{\tau}$ decay channel in proton–proton collisions at $\sqrt{s} = 13\,TeV$*, arXiv:1903.04560 [hep-ex].

[234] ATLAS Collaboration, *Search for charged Higgs bosons in the $H^{\pm} \to tb$ decay channel in pp collisions at $\sqrt{s} = 13$ TeV using the ATLAS detector*, ATLAS-CONF-2016-089, 2016, https://cds.cern.ch/record/2206809.

[235] T. Keck, *FastBDT: A Speed-Optimized Multivariate Classification Algorithm for the Belle II Experiment*, Comput. Softw. Big Sci. **1** (2017) 2.

[236] A. Hoecker, P. Speckmayer, J. Stelzer, J. Therhaag, E. von Toerne, and H. Voss, *TMVA: Toolkit for Multivariate Data Analysis*, PoS **ACAT** (2007) 040, arXiv:physics/0703039.

[237] ATLAS Collaboration, ATLAS Collaboration, *Measurement of τ polarization in $W \to \tau\nu$ decays with the ATLAS detector in pp collisions at $\sqrt{s} = 7$ TeV*, Eur. Phys. J. C **72** (2012) 2062, arXiv:1204.6720 [hep-ex].

[238] M. Pitt et al., *Search for charged Higgs bosons in the τ+jets and τ+lepton final states with 36.1 fb^{-}1 of pp collision data recorded at sqrt(s) = 13 TeV with the ATLAS experiment*, Tech. Rep. ATL-COM-PHYS-2016-1452, CERN, Geneva, Oct, 2016. https://cds.cern.ch/record/2222104.

[239] L. Devroye, *Non-Uniform Random Variate Generation*. published by Springer, New York, 1986.

[240] ATLAS Collaboration, *Multi-Boson Simulation for 13 TeV ATLAS Analyses*, Atl-phys-pub-2016-002, 2016, https://cds.cern.ch/record/2119986.

[241] ATLAS Collaboration, *Combined measurements of Higgs boson production and decay using up to 80 fb^{-1} of proton–proton collision data at $\sqrt{s} = 13$ TeV collected with the ATLAS experiment*, ATLAS-CONF-2018-031, 2018, https://cds.cern.ch/record/2629412.

[242] ATLAS Collaboration, *Measurements of Higgs boson properties in the diphoton decay channel with 36fb^{-1} of pp collision data at $\sqrt{s} = 13\,TeV$ with the ATLAS detector*, Phys. Rev. D **98** (2018) 052005, arXiv:1802.04146 [hep-ex].

[243] ATLAS Collaboration, *Measurement of the Higgs boson coupling properties in the $H \to ZZ^* \to 4\ell$ decay channel at $\sqrt{s} = 13\,TeV$ with the ATLAS detector*, JHEP **03** (2018) 095, arXiv:1712.02304 [hep-ex].

[244] ATLAS Collaboration, *Measurements of gluon-gluon fusion and vector-boson fusion Higgs boson production cross-sections in the $H \to WW^* \to e\nu\mu\nu$ decay channel in pp collisions at $\sqrt{s} = 13$ TeV with the ATLAS detector*, Phys. Lett. B **789** (2019) 508, arXiv:1808.09054 [hep-ex].

[245] ATLAS Collaboration, *Observation of $H \to b\bar{b}$ decays and VH production with the ATLAS detector*, Phys. Lett. B **786** (2018) 59, arXiv:1808.08238 [hep-ex].

[246] ATLAS Collaboration, *Search for Higgs bosons produced via vector-boson fusion and decaying into bottom quark pairs in $\sqrt{s} = 13$ TeV pp collisions with the ATLAS detector*, Phys. Rev. D **98** (2018) 052003, arXiv:1807.08639 [hep-ex].

[247] ATLAS Collaboration, *Evidence for the associated production of the Higgs boson and a top quark pair with the ATLAS detector*, Phys. Rev. D **97** (2018) 072003, arXiv:1712.08891 [hep-ex].

[248] ATLAS Collaboration, *Search for the standard model Higgs boson produced in association with top quarks and decaying into a $b\bar{b}$ pair in pp collisions at $\sqrt{s} = 13$ TeV with the ATLAS detector*, Phys. Rev. D **97** (2018) 072016, arXiv:1712.08895 [hep-ex].

[249] ATLAS Collaboration, *Search for the Dimuon Decay of the Higgs Boson in pp Collisions at $\sqrt{s} = 13$ TeV with the ATLAS Detector*, Phys. Rev. Lett. **119** (2017) 051802, arXiv:1705.04582 [hep-ex].

[250] ATLAS Collaboration, *Combined measurements of Higgs boson production and decay using up to 80 fb^{-1} of proton–proton collision data at $\sqrt{s} = 13$ TeV collected with the ATLAS experiment*, Tech. Rep. ATLAS-COM-CONF-2019-008, CERN, Geneva, Mar, 2019. https://cds.cern.ch/record/2666980.

[251] ATLAS Collaboration, *Search for invisible Higgs boson decays in vector boson fusion at $\sqrt{s} = 13$ TeV with the ATLAS detector*, Phys. Lett. (2018), arXiv:1809.06682 [hep-ex].

[252] ATLAS Collaboration, *Search for an invisibly decaying Higgs boson or dark matter candidates produced in association with a Z boson in pp collisions at $\sqrt{s} = 13$ TeV with the ATLAS detector*, Phys. Lett. B **776** (2018) 318, arXiv:1708.09624 [hep-ex].

[253] ATLAS Collaboration, *Search for dark matter in events with a hadronically decaying vector boson and missing transverse momentum in pp collisions at $\sqrt{s} = 13$ TeV with the ATLAS detector*, JHEP **10** (2018) 180, arXiv:1807.11471 [hep-ex].

[254] ATLAS Collaboration, *Constraints on off-shell Higgs boson production and the Higgs boson total width in $ZZ \to 4\ell$ and $ZZ \to 2\ell 2\nu$ final states with the ATLAS detector*, Phys. Lett. B **786** (2018) 223, arXiv:1808.01191 [hep-ex].

[255] D. Eriksson, J. Rathsman, and O. Stal, *2HDMC: Two-Higgs-Doublet Model Calculator Physics and Manual*, Comput. Phys. Commun. **181** (2010) 189–205, arXiv:0902.0851 [hep-ph].

[256] A. Djouadi, J. Kalinowski, M. Mühlleitner, and M. Spira, *An update of the program HDECAY*, in *The Les Houches 2009 workshop on TeV colliders: The tools and Monte Carlo working group summary report*. 2010. arXiv:1003.1643 [hep-ph].

[257] ATLAS Collaboration,, *HMSSM working group hMSSM summary plots*, https://atlas.web.cern.ch/Atlas/GROUPS/PHYSICS/PUBNOTES/ATL-PHYS-PUB-2019-034/.

[258] ATLAS Collaboration, *Prospects for the search for additional Higgs bosons in the ditau final state with the ATLAS detector at HL-LHC*, ATL-PHYS-PUB-2018-050, 2018, https://cds.cern.ch/record/2652284.

[259] C. Anastasiou, C. Duhr, F. Dulat, E. Furlan, T. Gehrmann, F. Herzog, A. Lazopoulos, and B. Mistlberger, *High precision determination of the gluon fusion Higgs boson cross-section at the LHC*, JHEP **1605** (2016) 058, arXiv:1602.00695 [hep-ph].

Appendix A

Theory appendix

A.1 Gluon-fusion produced Higgs p_{T} reweighting

The gluon-fusion (ggF) produced Higgs boson generation in the MSSM is sensitive to top-quark and bottom-quark interference effects which are sensitive to $\tan\beta$, as discussed in Section 2.4.1. The kinematic distributions of the generated Higgs boson should therefore be corrected. The corresponding shape effects of the interference term (e.g., on the Higgs p_{T}) depends only on the scalar mass (m_ϕ) while the relative yield of the effect is dependant on $\tan\beta$. These effects can be taken into account by implementing resummation scheme which takes into account the interference as $p_{\mathrm{T}}^{\phi} \to 0$. The resummation can be performed for a generic 2HDM and re-scaled to the corresponding MSSM by using the Yukawa coupling of the model which depends on $\tan\beta$. Gluon-fusion produced neutral Higgs boson events are generated with POWHEG-BOX 2 [171] using the 2HDM implementation [36, 80]. matrix-element (ME) events are generated at a particular mass m_ϕ with $\tan\beta = 15$ for the

- top-quark-only loop contribution, σ_t^{2HDM}, at the top-quark resummation scale, $Q_t(m_\phi)$,
- bottom-quark-only loop contribution, σ_b^{2HDM}, at the bottom-quark resummation scale, $Q_b(m_\phi)$
- top-bottom interference loop contribution, $\sigma_{\mathrm{int}}^{\mathrm{2HDM}}$, at the interference scale, $Q_{\mathrm{int}}(m_\phi)$,
- top-quark-only loop contribution, σ_t^{2HDM}, at the interference scale, $Q_{\mathrm{int}}(m_\phi)$,
- bottom-quark-only loop contribution, σ_b^{2HDM}, at the interference scale, $Q_{\mathrm{int}}(m_\phi)$.

The resummation scales used in each case is dependant on the mass of the resonant ϕ considered, and are shown in Figure A.1 [80]. The renormalisation and factorisation scales are chosen at half the Higgs pole mass ($m_\phi/2$). The resummation, and renormalisation and factorisation, scales are varied to half and two-times their nominal values, and event weights for the variations are stored in the ME output. The ME events are interfaced with PYTHIA 8 [174] for the PS and the resulting Higgs p_{T} distribution is extracted. The components histograms (top-only, bottom-only, and interference) are normalised to their total cross-section as determined from the event generation and summed to extract the total ${p_{\mathrm{T}}}^{\phi}$ distribution. The distributions are summed as,

$$\sigma_{\text{total}}^{\text{2HDM}} = \sigma_t^{\text{2HDM}}(Q_t) + \sigma_b^{\text{2HDM}}(Q_b) + \overbrace{\sigma_{\text{int}}^{\text{2HDM}}(Q_{\text{int}}) - \sigma_t^{\text{2HDM}}(Q_{\text{int}}) - \sigma_b^{\text{2HDM}}(Q_{\text{int}})}^{\text{interference}}. \tag{A.1}$$

An example p_{T}^{H} distribution is shown in Figure A.2 where the top-only, bottom-only and interference histograms are shown. The resulting total distribution, as well as the scale uncertainties are shown. The final scale uncertainties would be taken as the envelope of the uncertainties.

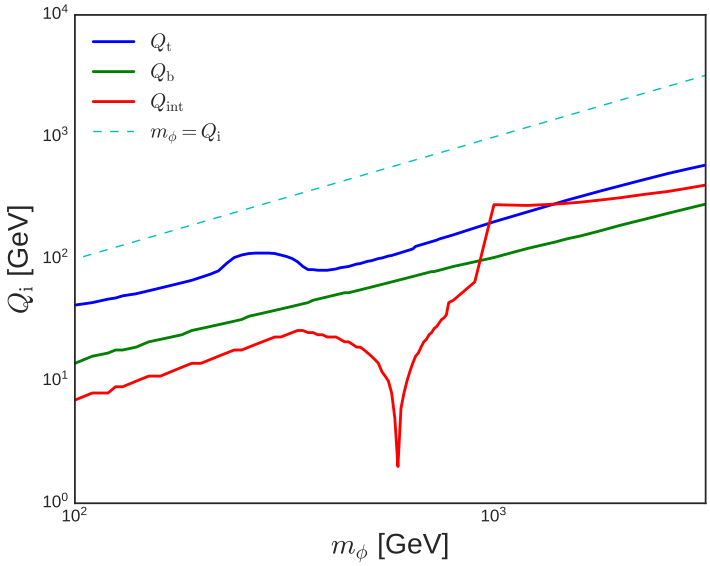

Figure A.1 Gluon-fusion resummation scales as determined in Ref. [80]

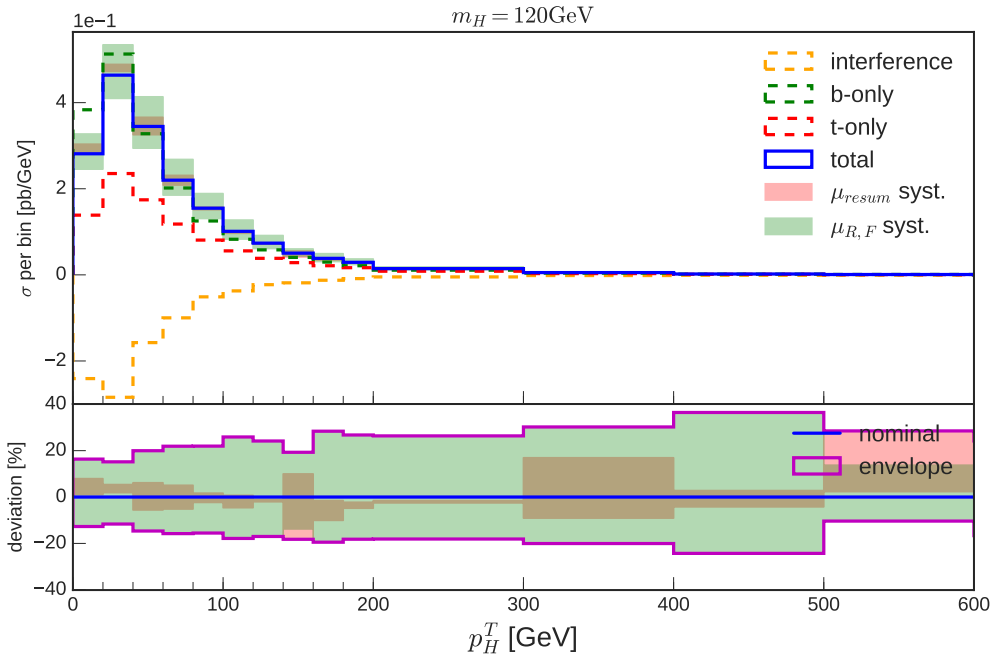

Figure A.2 p_{T} distribution of a 2HDM Higgs (H) with mass $m_H = 120$ GeV when taking into account the top-bottom loop interference effects. Shown are the top-only, bottom-only and interference histograms, as well as the total distribution with corresponding scale uncertainties. μ_{resum} and $\mu_{R,F}$ are the resummation, and renormalisation and factorisation scales, respectively.

Appendix B

Appendix for the di-tau analysis

B.1 Fit diagnostics

The pre-fit uncertainty tables of the $\tau_{\text{lep}}\tau_{\text{had}}$ CR-T are shown in Tables B.1 and B.2 Additional pull and correlation plots for the individual fits in the di-tau analysis, as discussed in Section 6.5.1 are shown in Figures B.1–B.3.

Table B.1 Pre-fit uncertainty (in [%]) of NPs for the $m_{\mathrm{T}}^{\mathrm{tot}}$ distribution in the $\tau_{\mathrm{e}}\tau_{\mathrm{had}}$ CR-T, as they are in the final workspace after smoothing and pruning. Shown are the total normalisation uncertainty, with † representing that a shape uncertainty is also considered. The normalisation effect is pruned if the uncertainty is below 1%, while shape effects are pruned if they do not have sufficient variations in neighbouring bins.

Type	Sample NP	Z+jets [%]	DYZ [%]	Diboson [%]	Fakes [%]	Top [%]	bbH300 [%]	ggH300 [%]
Signal	ATLAS_AU_bbH300	-	-	-	-	-	±3.52	-
	ATLAS_AU_ggH300	-	-	-	-	-	-	±14.67
XS	ATLAS_LPXKFACTORALPHAS	±1.16	±1.82	-	-	-	-	-
	ATLAS_LPXKFACTORPDF	±3.34	±3.24	-	-	-	-	-
	ATLAS_LPXKFACTORPI	±1.40	-	-	-	-	-	-
	ATLAS_LUMI	±3.20	±3.20	±3.20	-	±3.20	±3.20	±3.20
	ATLAS_xsec_Diboson	-	-	±6.00	-	-	-	-
	ATLAS_xsec_Top	-	-	-	-	±6.00	-	-
Data driven	ATLAS_Fakes_Dphi_QCD_eh	-	-	-	±1.41	-	-	-
	ATLAS_Fakes_Dphi_Wjets_eh	-	-	-	±3.23 †	-	-	-
	ATLAS_Fakes_shape_QCD_eh	-	-	-	±3.81	-	-	-
	ATLAS_Fakes_shape_WjetsBtag	-	-	-	±9.47	-	-	-
	ATLAS_Fakes_shape_Wjets_eh	-	-	-	±5.88 †	-	-	-
	ATLAS_Fakes_shape_rQCDehad	-	-	-	±1.45	-	-	-
Tau	ATLAS_TAUIDAFII	-	-	-	-	-	±3.00	-
	ATLAS_TAUIDTotal	±5.82	-	±5.65	±1.50	±5.69	±5.73	±5.82
	ATLAS_TAURECOAFII	-	-	-	-	-	±5.01	-
	ATLAS_TAURECOEleEleOLR	-	±1.14	-	-	-	-	-
	ATLAS_TAURECOTauEleOLR	±1.18	-	±1.53	-	±1.05	±1.18	±1.07
	ATLAS_TAURECOTauEleOLRAFII	-	-	-	-	-	±2.63	-
	ATLAS_TAURECOTotal	±2.83	-	±2.86	-	±3.16	±3.11	±2.74
	ATLAS_TESAFII	-	-	-	-	-	±10.96	-
	ATLAS_TESDETECTOR	-	-	-	-	-	$^{+10.11}_{-7.93}$	-
b-tagging	ATLAS_btagEffSfEigen_B_0	±2.47	±2.67	±2.22	-	±2.55	±4.61	±3.16
	ATLAS_btagEffSfEigen_C_0	±10.76	±16.47	±9.58	-	-	-	$^{+7.73}_{-7.07}$
	ATLAS_btagEffSfEigen_C_1	±1.23	±2.96	±1.09	-	-	-	±3.22
	ATLAS_btagEffSfEigen_C_2	-	±1.62	-	-	-	-	±2.20
	ATLAS_btagEffSfEigen_Light_0	±11.73	±5.89	±13.41	-	-	-	±15.56
	ATLAS_btagEffSfEigen_Light_1	±2.63	±1.86	±2.58	-	-	-	±4.33
	ATLAS_btagEffSfEigen_Light_2	±4.73	±1.91	±2.08	-	-	-	±10.93
	ATLAS_btagEffSfEigen_Light_3	±1.42	-	-	-	-	-	±4.83
	ATLAS_btagEffSfEigen_Light_4	±1.42	±2.82	-	-	-	-	±2.47
Top (excl. XS)	ATLAS_TTBAR_RADIATION	-	-	-	±2.37	±9.11 †	-	-
	ATLAS_TTBAR_SHOWERGEN	-	-	-	±2.94	±11.24 †	-	-
Other	ATLAS_ELEISO	-	-	-	-	†	-	-
	ATLAS_JERNP1	±3.69	±50.79	±3.95	-	-	±3.50	±12.23
	ATLAS_JETNP1	$^{+15.22}_{-12.55}$	-	±2.85	-	±1.74	±7.18	±1.64
	ATLAS_JETNP2	-	-	$^{+1.89}_{-1.12}$	-	-	-	-
	ATLAS_JvtEffSf	-	-	-	-	-	-	±1.01
	ATLAS_METSoftTrkResoPara	±1.11	-	-	-	†	±3.08	-
	ATLAS_METSoftTrkResoPerp	±1.09	-	-	-	†	-	-
	ATLAS_PRW	-	-	±1.38	-	-	-	$^{+10.72}_{-1.27}$

Table B.2 Pre-fit uncertainty (in [%]) of NPs for the $m_{\mathrm{T}}^{\mathrm{tot}}$ distribution in the $\tau_\mu \tau_{\mathrm{had}}$ CR-T, as they are in the final workspace after smoothing and pruning. Shown are the total normalisation uncertainty, with † representing that a shape uncertainty is also considered. The normalisation effect is pruned if the uncertainty is below 1%, while shape effects are pruned if they do not have sufficient variations in neighbouring bins.

Type	Sample / NP	$Z+$jets [%]	DYZ [%]	Diboson [%]	Fakes [%]	Top [%]	bbH300 [%]	ggH300 [%]
Signal	ATLAS_AU_bbH300	-	-	-	-	-	±3.52	-
	ATLAS_AU_ggH300	-	-	-	-	-	-	±14.67
XS	ATLAS_LPXKFACTORALPHAS	±1.91	±1.89	-	-	-	-	-
	ATLAS_LPXKFACTORPDF	±3.24	±3.19	-	-	-	-	-
	ATLAS_LUMI	±3.20	±3.20	±3.20	-	±3.20	±3.20	±3.20
	ATLAS_xsec_Diboson	-	-	±6.00	-	-	-	-
	ATLAS_xsec_Top	-	-	-	-	±6.00	-	-
Data driven	ATLAS_Fakes_Dphi_QCD_mh	-	-	-	±1.56	-	-	-
	ATLAS_Fakes_Dphi_Wjets_mh	-	-	-	±2.64	-	-	-
	ATLAS_Fakes_shape_QCD_mh	-	-	-	±3.13	-	-	-
	ATLAS_Fakes_shape_WjetsBtag	-	-	-	±10.64	-	-	-
	ATLAS_Fakes_shape_Wjets_mh	-	-	-	±6.14	-	-	-
	ATLAS_Fakes_shape_rQCDmuhad	-	-	-	±1.59	-	-	-
Tau	ATLAS_TAUIDAFII	-	-	-	-	-	±3.00	-
	ATLAS_TAUIDTotal	±5.63	-	±5.62	±1.80	±5.70	±5.72	±5.61
	ATLAS_TAURECOAFII	-	-	-	-	-	±5.00	-
	ATLAS_TAURECOTauEleOLR	±1.23	-	-	-	-	±1.18	±1.27
	ATLAS_TAURECOTauEleOLRAFII	-	-	-	-	-	±2.64	-
	ATLAS_TAURECOTotal	±4.04	-	±2.98	±1.17	±3.28	±3.23	±3.59
	ATLAS_TESAFII	-	-	-	-	-	$^{+9.59}_{-6.93}$	-
	ATLAS_TESDETECTOR	-	-	±1.30	-	-	$^{+6.70}_{-4.55}$	-
b-tagging	ATLAS_btagEffSfEigen_B_0	±3.11	±1.04	±1.58	-	±2.55	±5.01	±1.20
	ATLAS_btagEffSfEigen_C_0	±2.82	±34.76	±20.21	-	-	-	±18.23
	ATLAS_btagEffSfEigen_C_1	-	±6.58	-	-	-	-	±3.44
	ATLAS_btagEffSfEigen_C_2	-	±3.85	±1.58	-	-	-	±2.71
	ATLAS_btagEffSfEigen_C_3	-	±2.19	-	-	-	-	±1.48
	ATLAS_btagEffSfEigen_Light_0	±21.24	-	±6.74	-	-	-	±15.88
	ATLAS_btagEffSfEigen_Light_1	±4.93	-	-	-	-	-	±3.55
	ATLAS_btagEffSfEigen_Light_2	±9.92	-	-	-	-	-	±4.32
	ATLAS_btagEffSfEigen_Light_3	±2.55	-	±1.41	-	-	-	±1.64
	ATLAS_btagEffSfEigen_Light_4	±4.23	-	-	-	-	-	±1.74
Top (excl. XS)	ATLAS_TTBAR_RADIATION	-	-	-	±2.00	±7.52 †	-	-
	ATLAS_TTBAR_SHOWERGEN	-	-	-	±2.70	±9.74 †	-	-
Other	ATLAS_JERNP1	±7.40	-	±10.67	-	-	±9.46	±31.93
	ATLAS_JETNP1	±21.69	-	±4.56	-	±1.94	±2.33	-
	ATLAS_METSoftTrkResoPara	±5.78	-	-	-	-	±3.88	-
	ATLAS_METSoftTrkScale	-	-	-	-	-	±2.07	-
	ATLAS_MUONEFFSYS	-	-	±1.07	-	-	-	-
	ATLAS_MUONSAGITTARESBIAS	-	-	-	-	-	±1.22	-
	ATLAS_MUONSAGITTARHO	-	-	-	-	†	-	-
	ATLAS_MUONTRIGEFFSTAT	±1.15	±4.16	±1.64	-	±1.64	±1.71	±1.41
	ATLAS_PRW	-	-	$^{+5.92}_{-1.24}$	$^{+1.59}_{-1.02}$	-	$^{+3.09}_{-1.49}$	±7.67

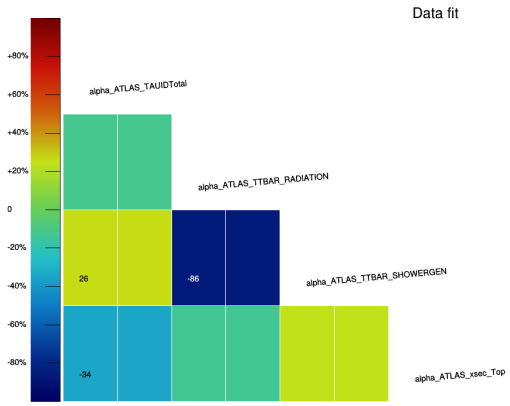

(a) Data fit, CR-T

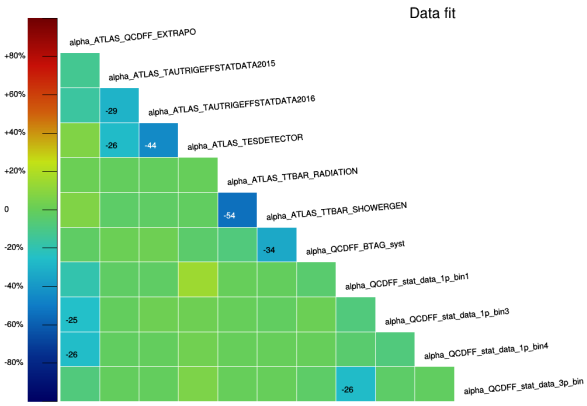

(b) Data fit, $\tau_{\text{had}}\tau_{\text{had}}$

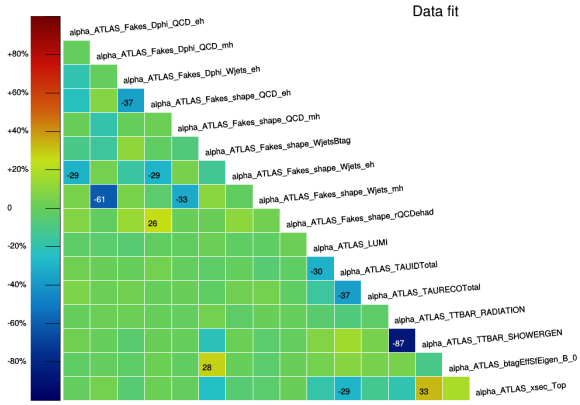

(c) Data fit, $\tau_{\text{lep}}\tau_{\text{had}}$ + CR-T

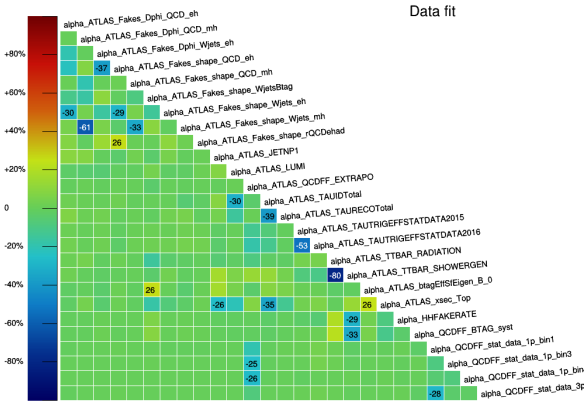

(d) Data fit, combined

Figure B.1 Nuisance parameter correlations for fits in different di-tau regions to the observed dataset. Only pairs of NPs with a correlation greater that 25% are shown.

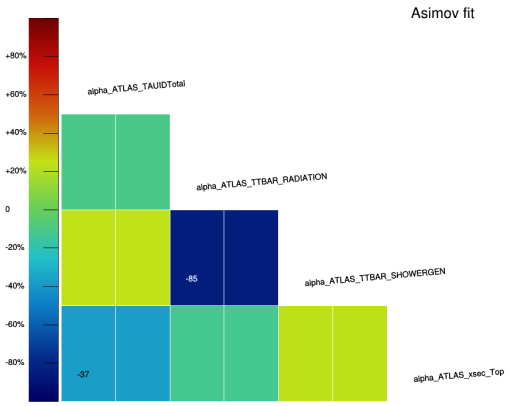

(a) Asimov, CR-T

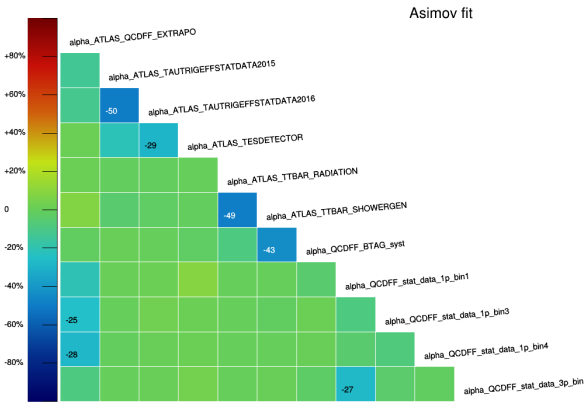

(b) Asimov, $\tau_{\text{had}}\tau_{\text{had}}$

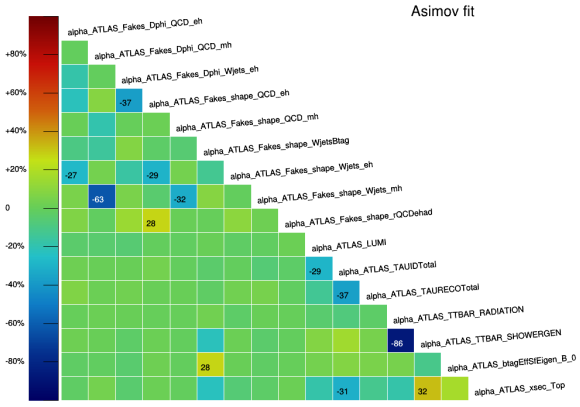

(c) Asimov, $\tau_{\text{lep}}\tau_{\text{had}}$ + CR-T

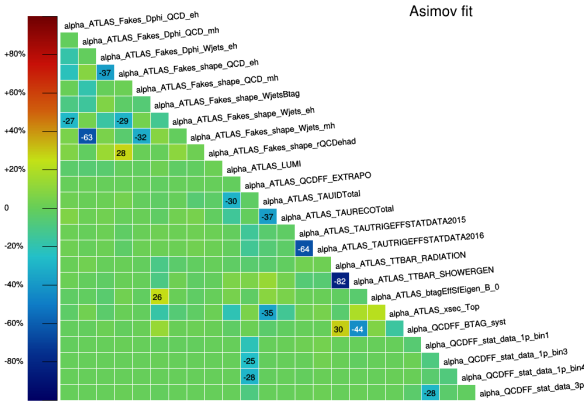

(d) Asimov, combined

Figure B.2 Nuisance parameter correlations for fits in different di-tau regions to the Asimov dataset. Only pairs of NPs with a correlation greater that 25% are shown.

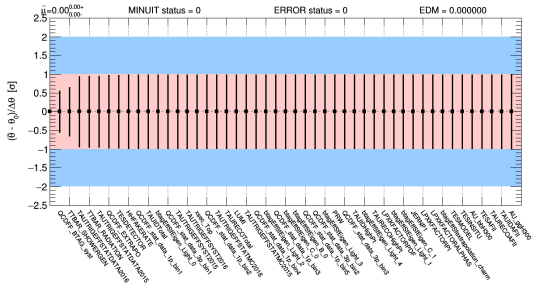

(a) Asimov, $\tau_{\text{had}}\tau_{\text{had}}$ b-tagged

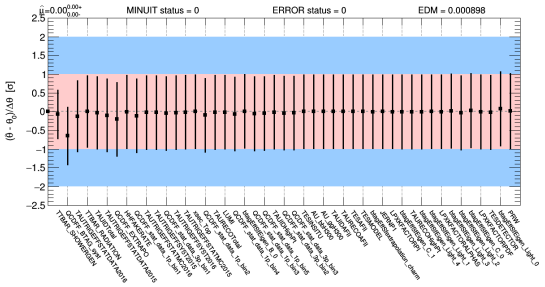

(b) Data, $\tau_{\text{had}}\tau_{\text{had}}$ b-tagged

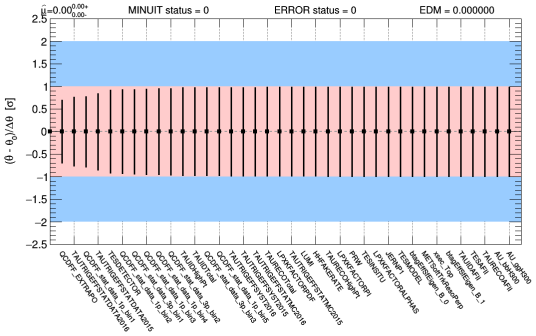

(c) Asimov, $\tau_{\text{had}}\tau_{\text{had}}$ b-veto

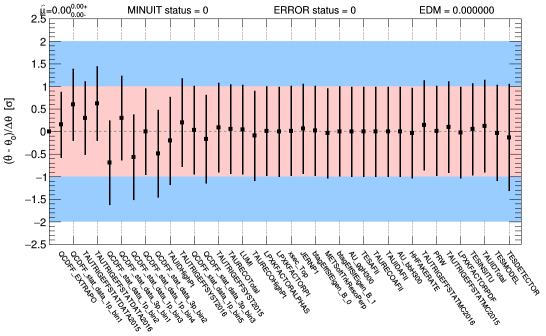

(d) Data, $\tau_{\text{had}}\tau_{\text{had}}$ b-veto

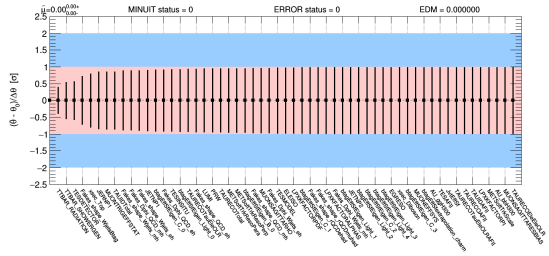

(e) Asimov, $\tau_{\text{lep}}\tau_{\text{had}}$ b-tagged

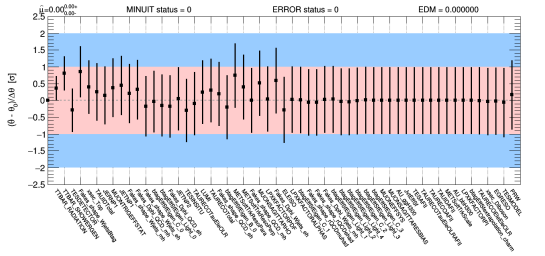

(f) Data, $\tau_{\text{lep}}\tau_{\text{had}}$ b-tagged

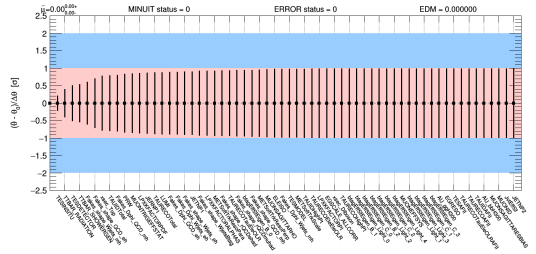

(g) Asimov, $\tau_{\text{lep}}\tau_{\text{had}}$ b-veto

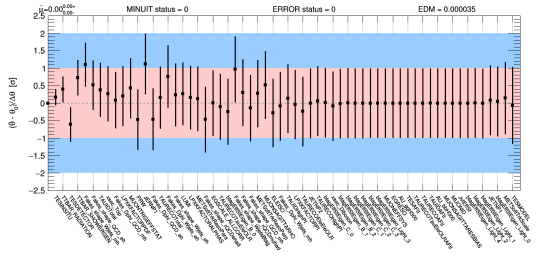

(h) Data, $\tau_{\text{lep}}\tau_{\text{had}}$ b-veto

Figure B.3 Nuisance parameter pulls for fits in different di-tau regions to the Asimov and data dataset. NPs are ordered in terms of the amount by which they are constrain.

B.2 Post-fit plots of additional variables

The fit results obtained from the fit in the $m_{\mathrm{T}}^{\mathrm{tot}}$ distributions in Section 6.5.1.2 are applied to templates in additional representative distributions. Since the fits are performed in $m_{\mathrm{T}}^{\mathrm{tot}}$, they are not expected to accurately model additional distributions. These distributions are however useful reference material when studying areas where mis-modelling might still be present post-fit.

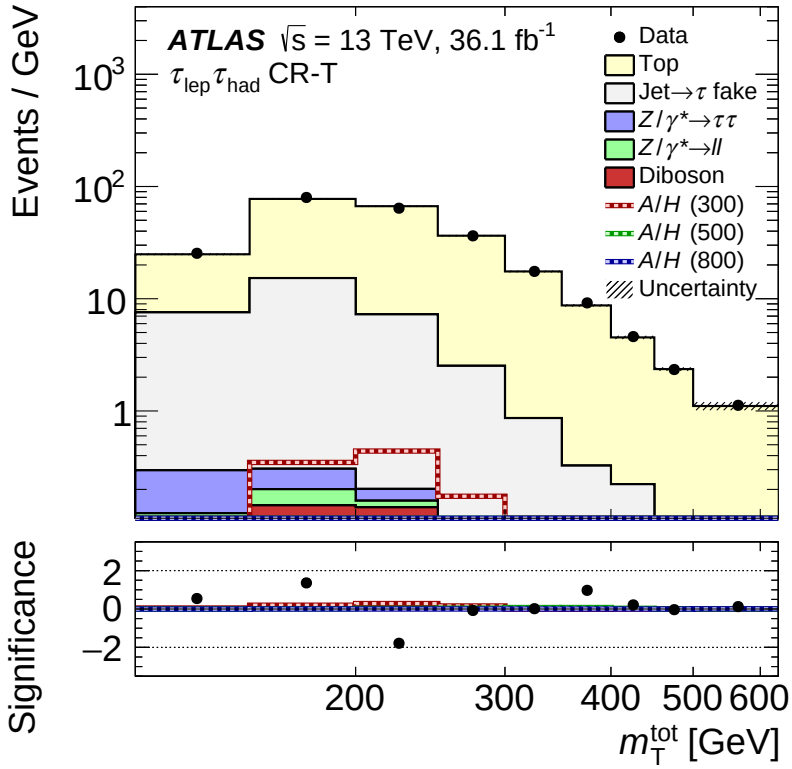

(a) CR-T

Figure B.4 Final post-fit distributions of $m_{\mathrm{T}}^{\mathrm{tot}}$ for the combined fit in the CR-T [1]. Signal histograms are normalised to their respective cross-sections from $\tan\beta = 10$ in the hMSSM scenario. Shown are the per-bin statistical significance calculated as recommended in Ref. [215].

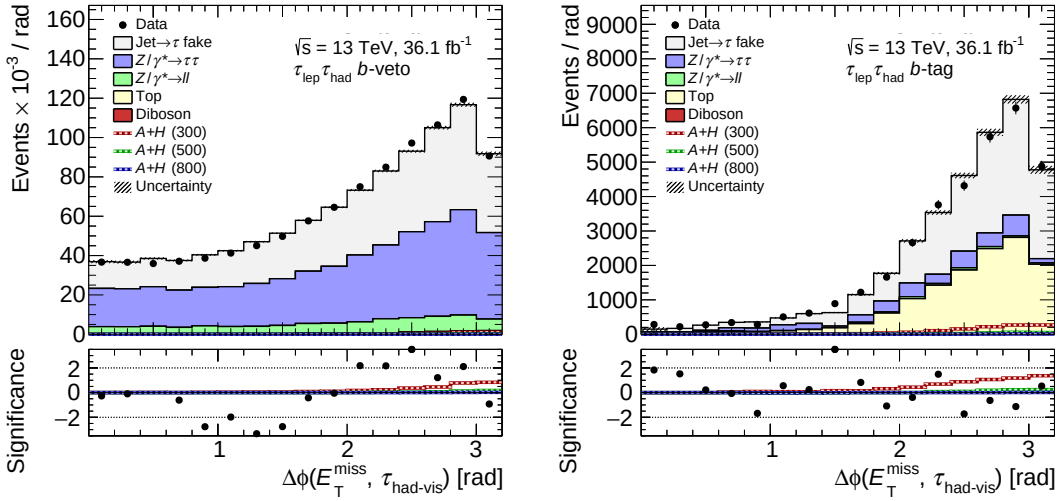

Figure B.5 Final post-fit distributions of additional variables for the combined fit in the $\tau_{\text{lep}}\tau_{\text{had}}$, $\tau_{\text{had}}\tau_{\text{had}}$ and CR-T for the $\tau_{\text{lep}}\tau_{\text{had}}$ b-tagged and b-veto categories [1]. Signal histograms are normalised to their respective cross-sections from $\tan\beta = 10$ in the hMSSM scenario. Shown are the per-bin statistical significance calculated as recommended in Ref. [215].

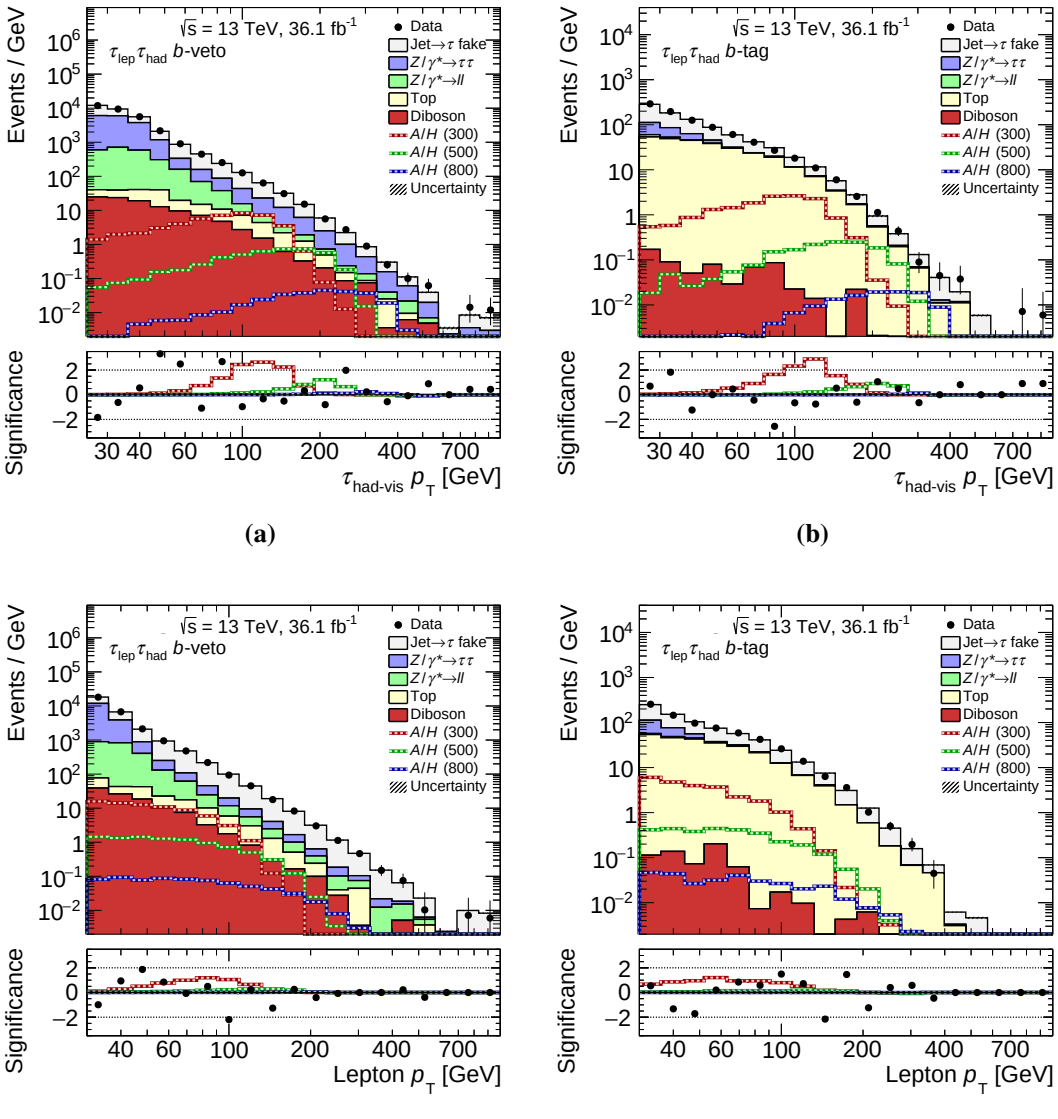

Figure B.6 Final post-fit distributions of additional variables for the combined fit in the $\tau_{\text{lep}}\tau_{\text{had}}$, $\tau_{\text{had}}\tau_{\text{had}}$ and CR-T for the $\tau_{\text{lep}}\tau_{\text{had}}$ b-tagged and b-veto categories [1]. Signal histograms are normalised to their respective cross-sections from $\tan\beta = 10$ in the hMSSM scenario. Shown are the per-bin statistical significance calculated as recommended in Ref. [215].

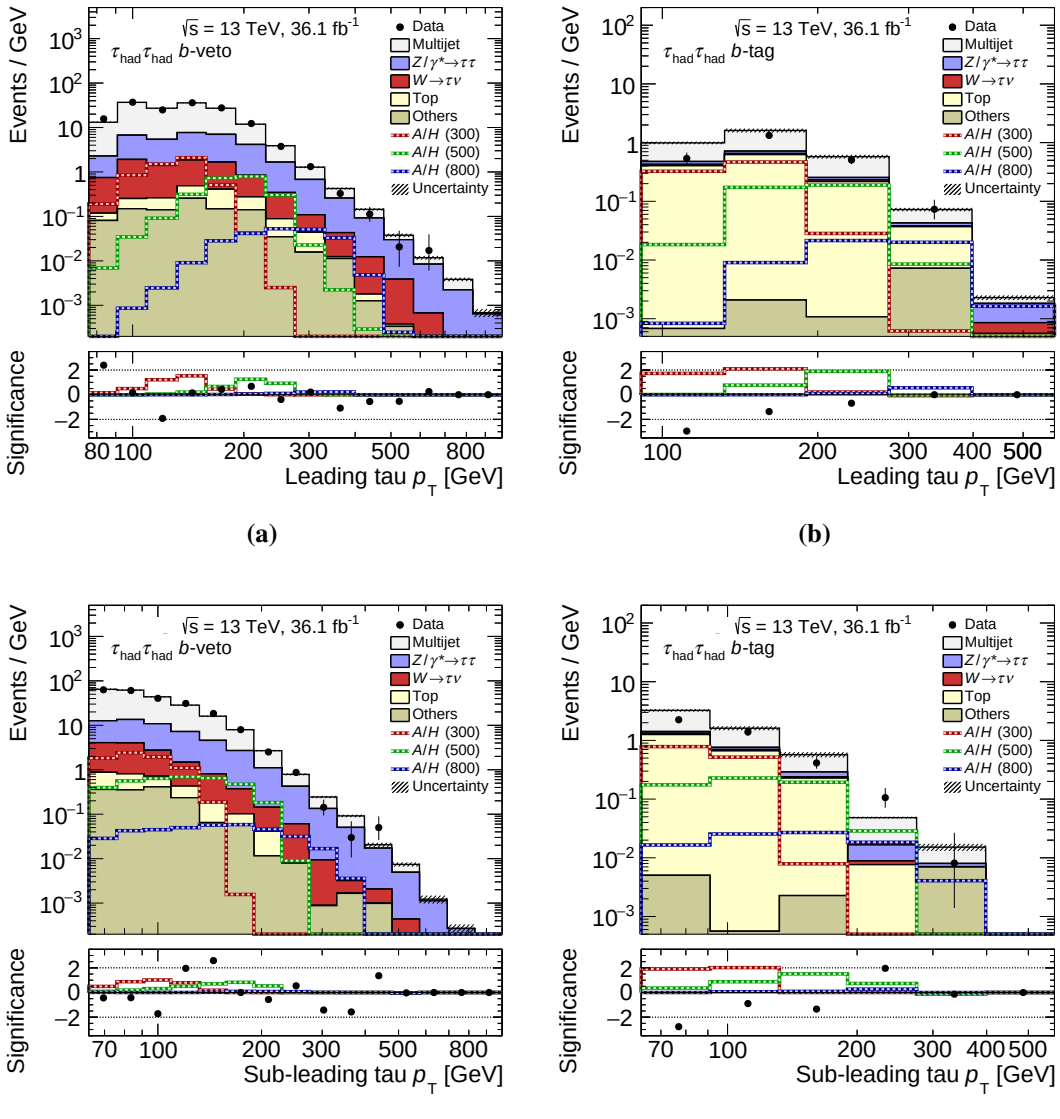

Figure B.7 Final post-fit distributions of additional variables for the combined fit in the $\tau_{\text{lep}}\tau_{\text{had}}$, $\tau_{\text{had}}\tau_{\text{had}}$ and CR-T for the $\tau_{\text{had}}\tau_{\text{had}}$ b-tagged and b-veto categories [1]. Signal histograms are normalised to their respective cross-sections from $\tan\beta = 10$ in the hMSSM scenario. Shown are the per-bin statistical significance calculated as recommended in Ref. [215].

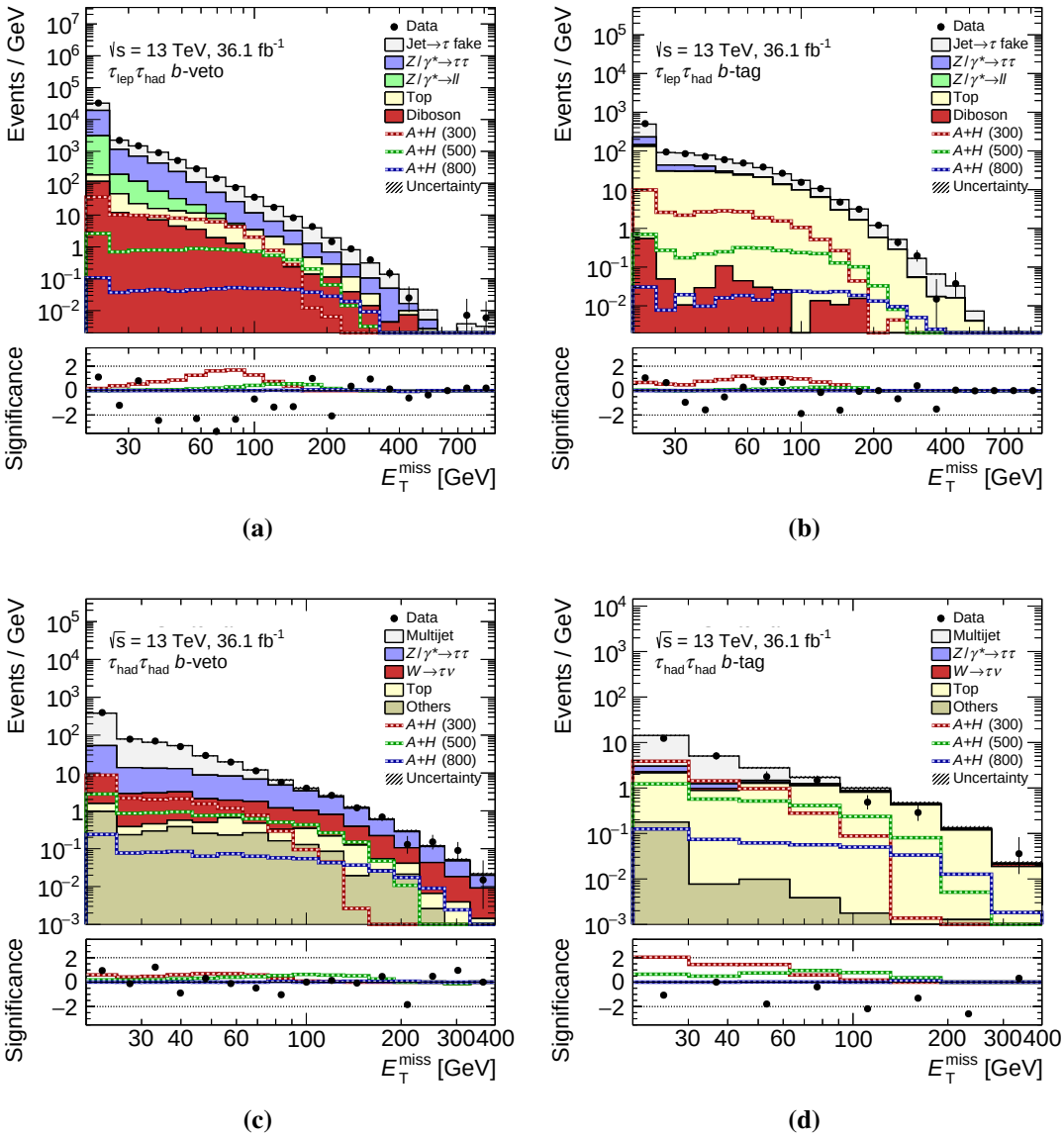

Figure B.8 Final post-fit distributions of additional variables for the combined fit in the $\tau_{\text{lep}}\tau_{\text{had}}$, $\tau_{\text{had}}\tau_{\text{had}}$ and CR-T for the $\tau_{\text{had}}\tau_{\text{had}}$ b-tagged and b-veto categories [1]. Signal histograms are normalised to their respective cross-sections from $\tan\beta = 10$ in the hMSSM scenario. Shown are the per-bin statistical significance calculated as recommended in Ref. [215].

Appendix C

Appendix for the charged Higgs analysis

C.1 Input distributions for the multivariat discriminant

The post-fit results from the fit in the 200 GeV–400 GeV BDT distribution is applied to variables used in the training of Section 7.2.3. Post-fit results for variables used in the BDT training are show in Figures C.1 to C.8.

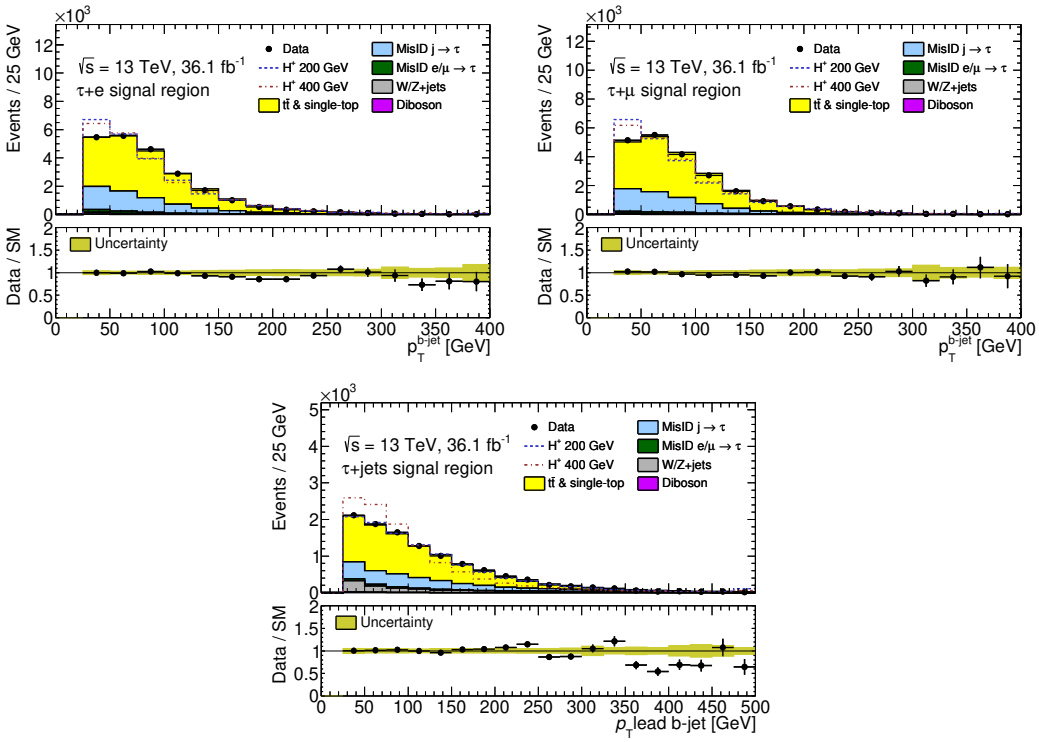

Figure C.1 Plot of p_{T} of leading b-jet using 200 GeV–400 GeV BDT post-fit result. The total statistical and systematic uncertainties, after being constrained by the fit, are shown. The normalisation of the signal distributions has been scaled to the background normalisation for illustration purposes.

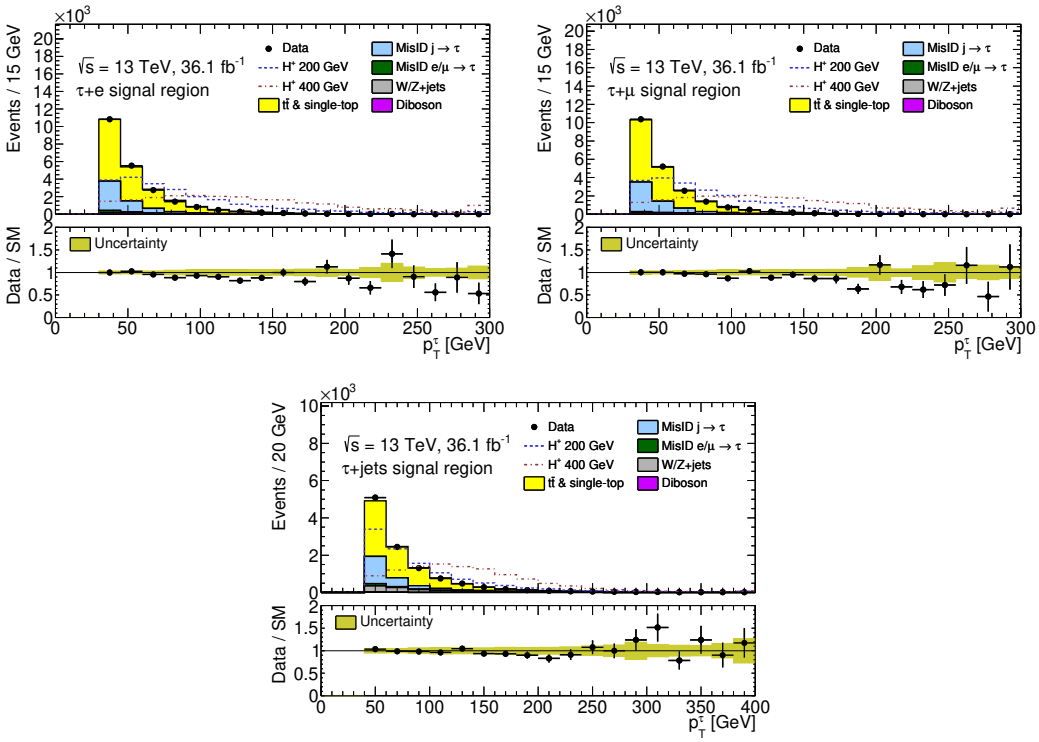

Figure C.2 Plot of p_{T} of leading τ-lepton using 200 GeV–400 GeV BDT post-fit result. The total statistical and systematic uncertainties, after being constrained by the fit, are shown. The normalisation of the signal distributions has been scaled to the background normalisation for illustration purposes.

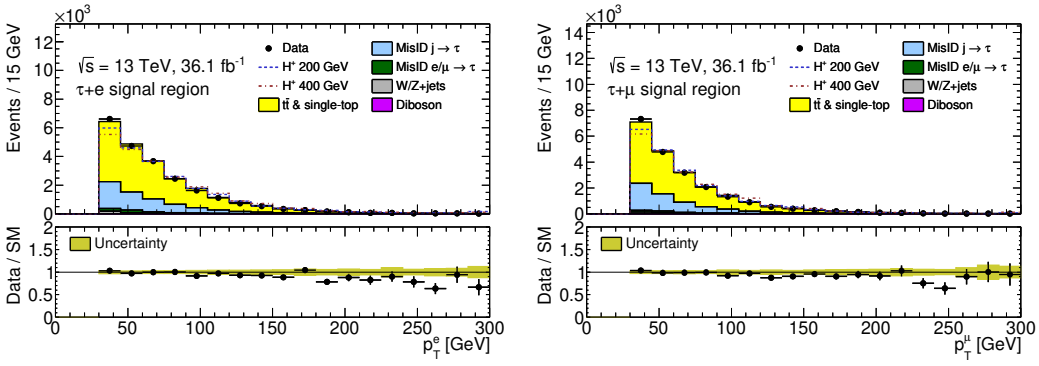

Figure C.3 Plot of p_{T} of leading e/μ-lepton using 200 GeV–400 GeV BDT post-fit result. The total statistical and systematic uncertainties, after being constrained by the fit, are shown. The normalisation of the signal distributions has been scaled to the background normalisation for illustration purposes.

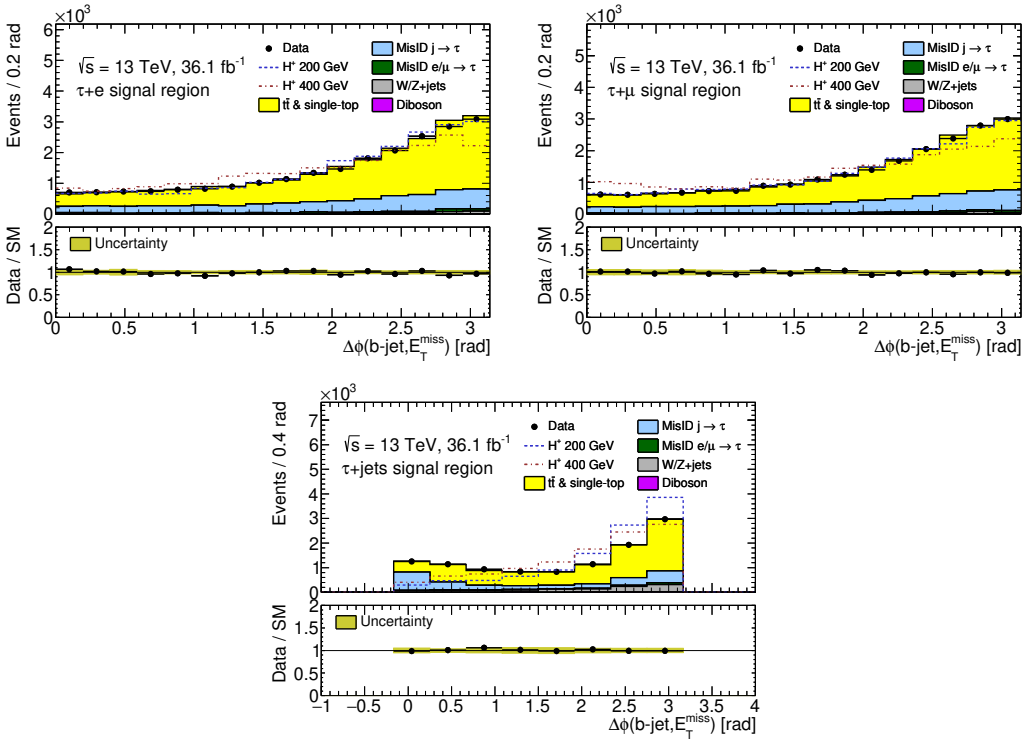

Figure C.4 Plot of $\Delta\phi(\mathrm{b-jet}, E_{\mathrm{T}}^{\mathrm{miss}})$ using 200 GeV–400 GeV BDT post-fit result. The total statistical and systematic uncertainties, after being constrained by the fit, are shown. The normalisation of the signal distributions has been scaled to the background normalisation for illustration purposes.

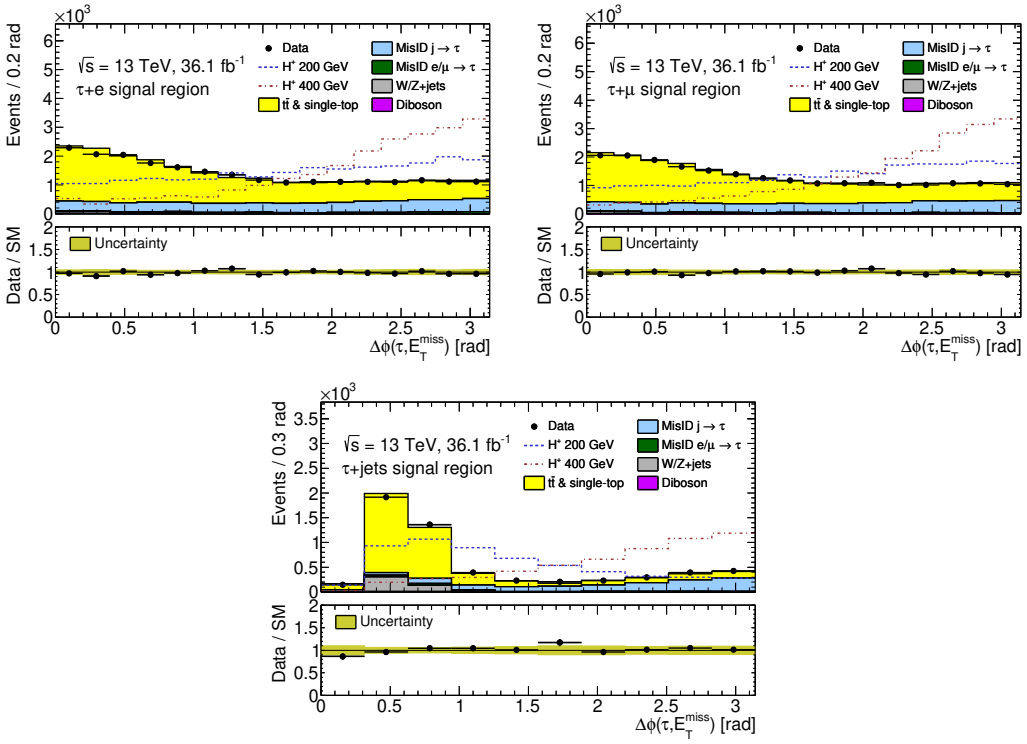

Figure C.5 Plot of $\Delta\phi(\tau, E_{\mathrm{T}}^{\mathrm{miss}})$ using 200 GeV–400 GeV BDT post-fit result. The total statistical and systematic uncertainties, after being constrained by the fit, are shown. The normalisation of the signal distributions has been scaled to the background normalisation for illustration purposes.

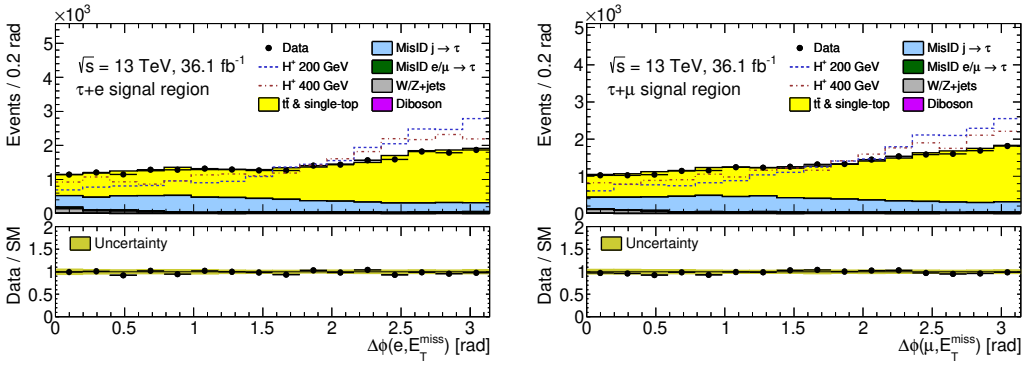

Figure C.6 Plot of $\Delta\phi(\ell, E_{\mathrm{T}}^{\mathrm{miss}})$ using 200 GeV–400 GeV BDT post-fit result. The total statistical and systematic uncertainties, after being constrained by the fit, are shown. The normalisation of the signal distributions has been scaled to the background normalisation for illustration purposes.

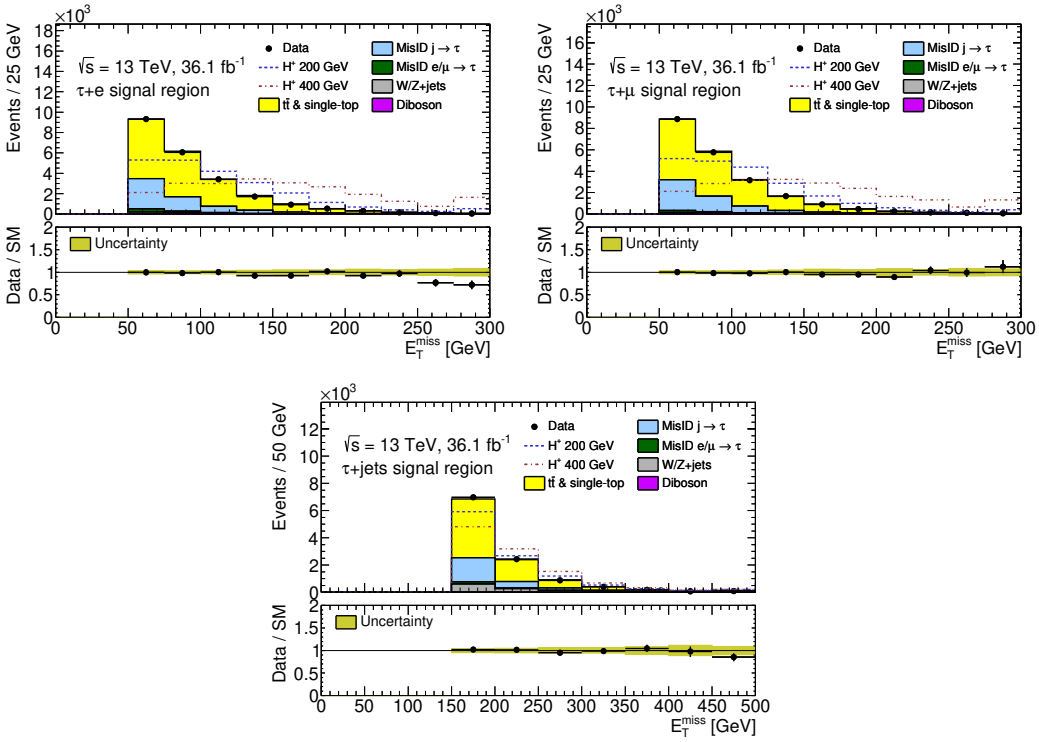

Figure C.7 Plot of $E_{\mathrm{T}}^{\mathrm{miss}}$ using 200 GeV–400 GeV BDT post-fit result. The total statistical and systematic uncertainties, after being constrained by the fit, are shown. The normalisation of the signal distributions has been scaled to the background normalisation for illustration purposes.

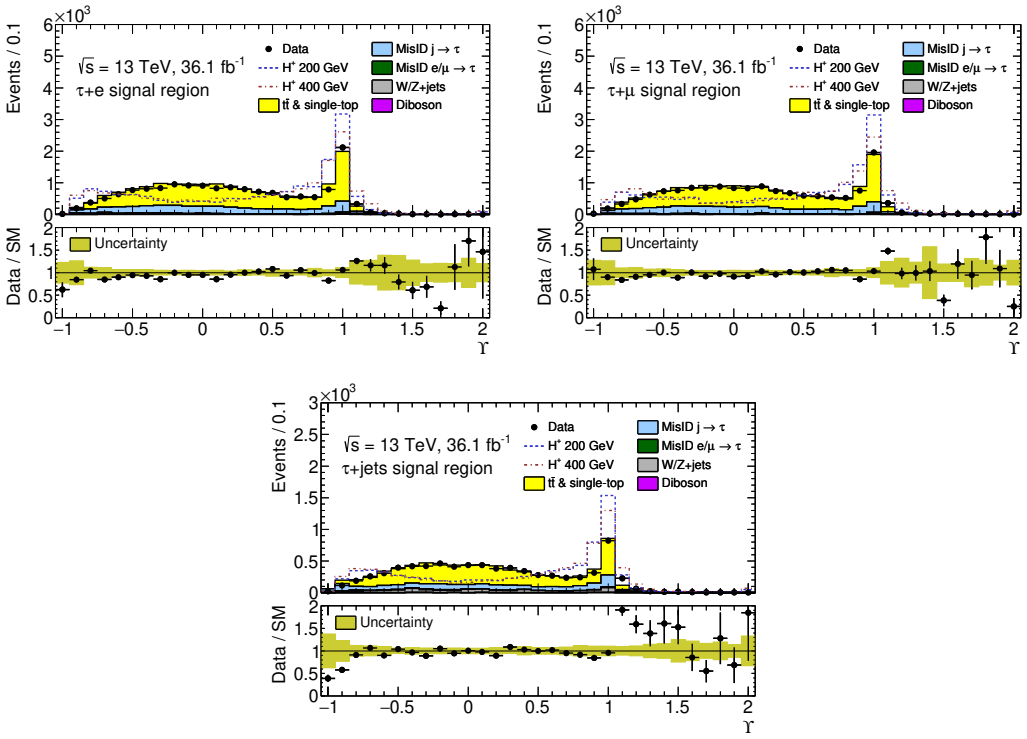

Figure C.8 Plot of Υ using 200 GeV–400 GeV BDT post-fit result. The total statistical and systematic uncertainties, after being constrained by the fit, are shown. The normalisation of the signal distributions has been scaled to the background normalisation for illustration purposes.

C.2 Fit studies

Shape distributions of systematics

Some representative shape uncertainty distributions are shown in this section related to data-driven (Figure C.9), Z + jets (Figure C.10) and $t\bar{t}$ (Figure C.11) modelling.

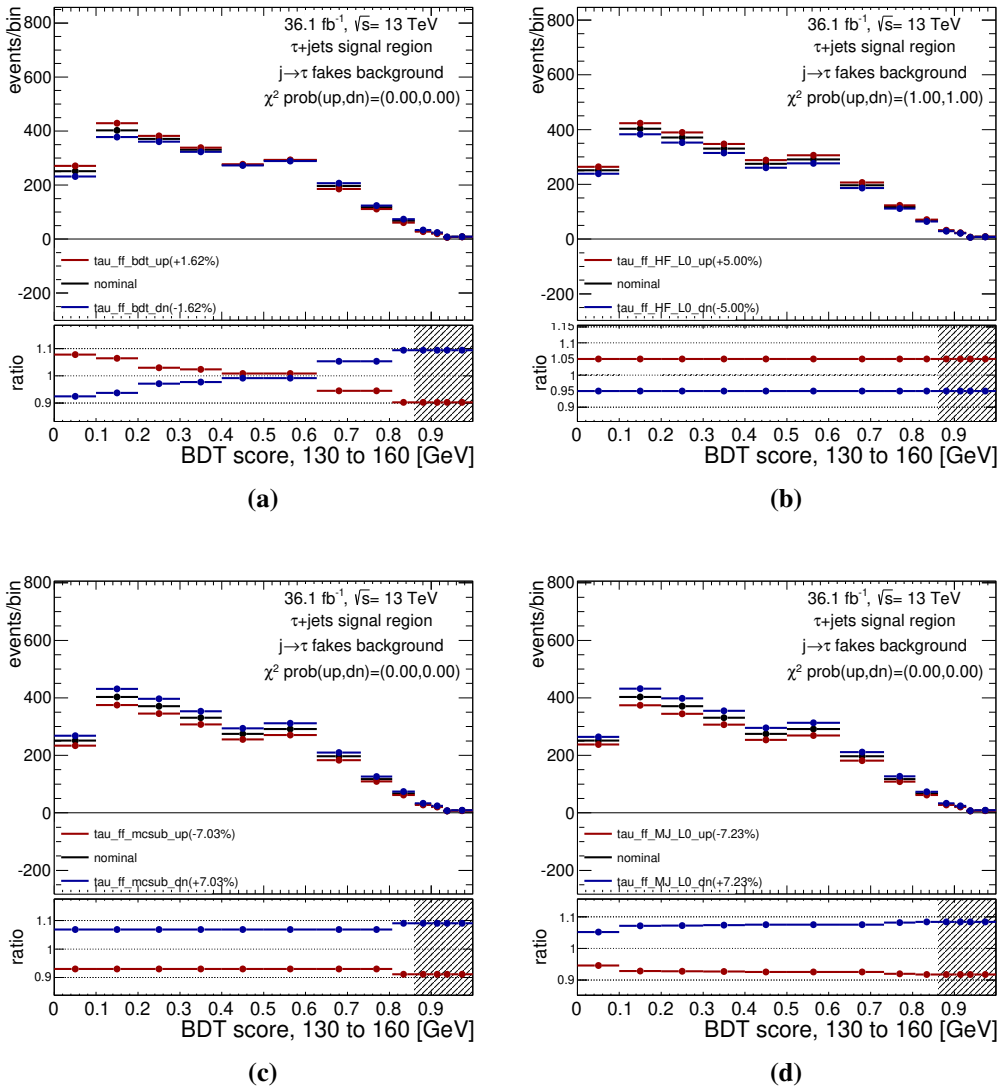

Figure C.9 Effect of systematic variations on the BDT score in the H^+ mass range 130–160 GeV for the $\tau_{\text{had-vis}}$ +jets signal region: (a) lower cut of the $\tau_{\text{had-vis}}$ BDT score, (b) HF$\rightarrow\tau$ fakes uncertainty, (c) prompt-τ contamination in the anti-τ control region, (d) error on α_{MJ} in the template-fit method. The dashed area in the ratio plots comes from the statistical error in every bin of the BDT score.

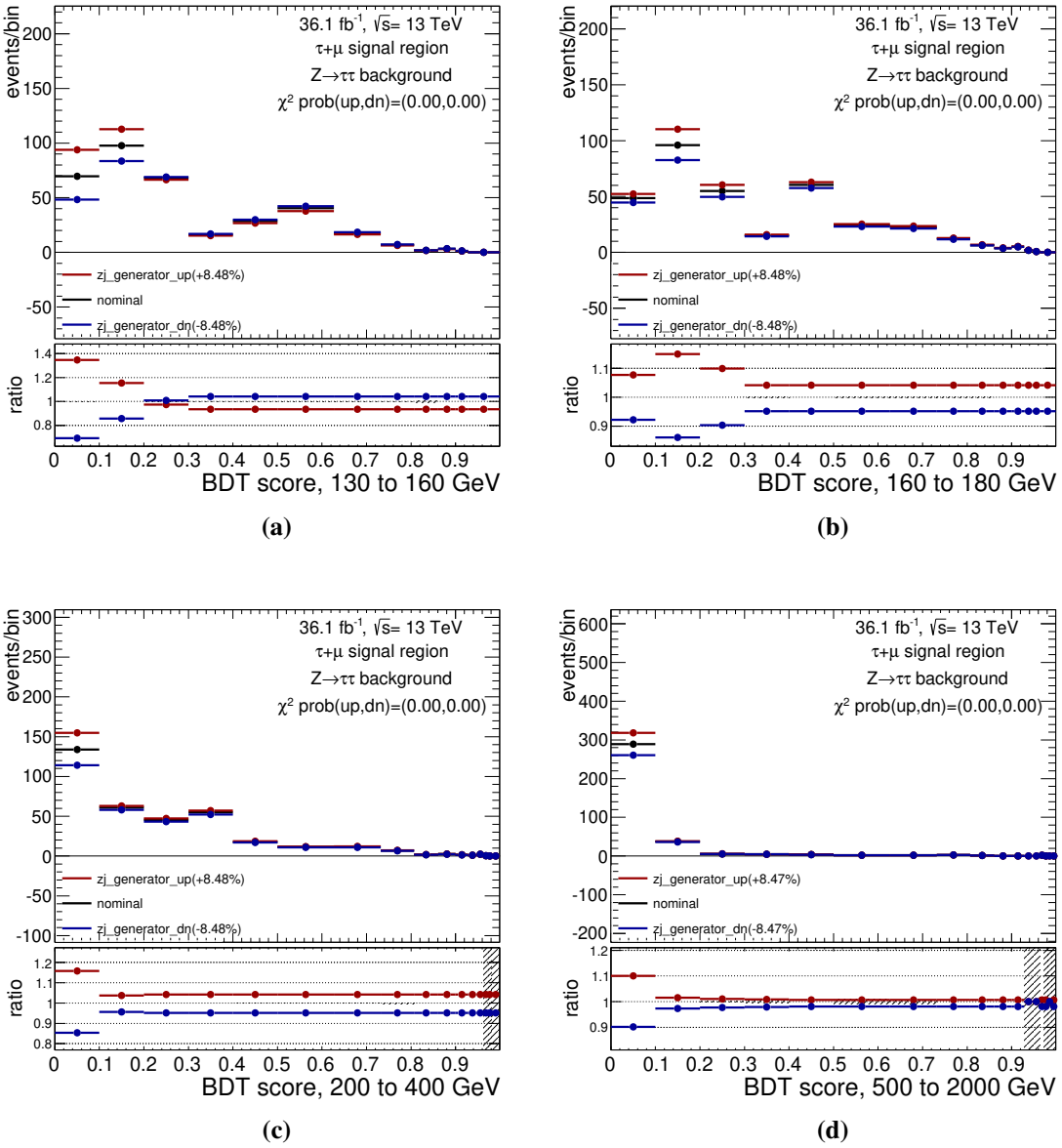

Figure C.10 Effect of systematic variations on the final BDT shape of the Z + jets background for the $\tau_{\text{had-vis}}$ +muon signal region, for 4 different BDT variables, due to the modelling. The dashed area in the ratio plots comes from the statistical error in every bin of the BDT score.

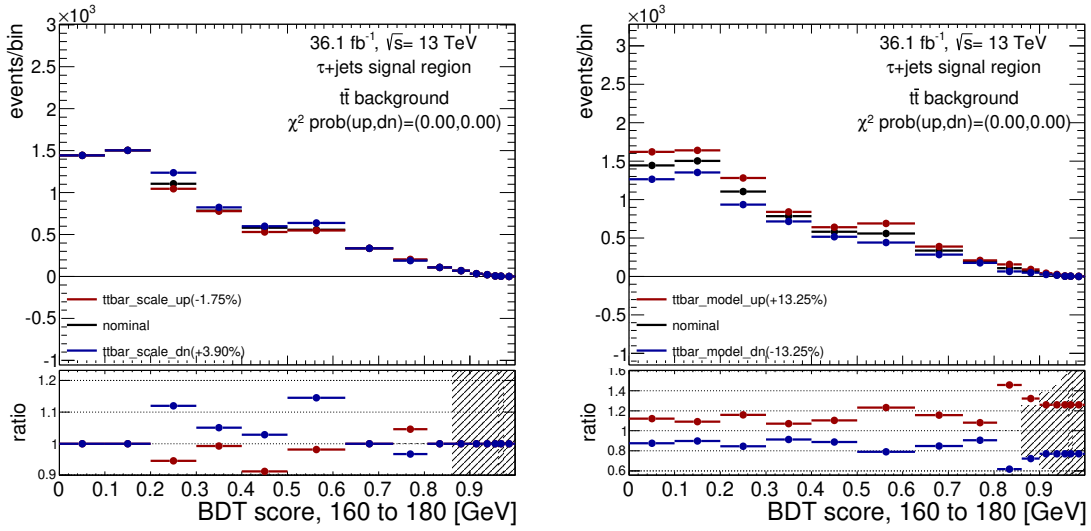

(a) **(b)**

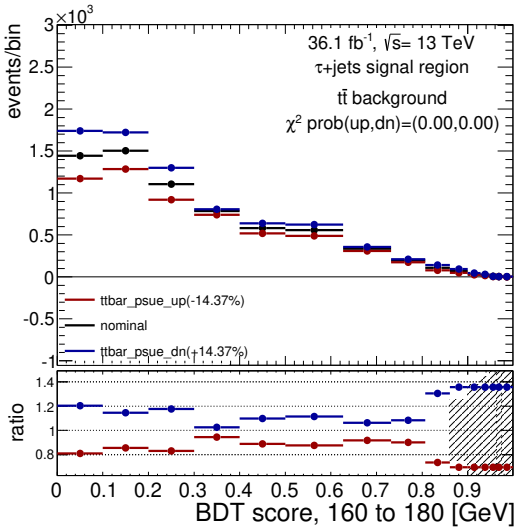

(c)

Figure C.11 Effect of systematic variations on the final BDT shape of the $t\bar{t}$ background for the $\tau_{\text{had-vis}}$ +jets signal region due to (a) scale, (b) ME, and (c) PS and UE. The dashed area in the ratio plots comes from the statistical error in every bin of the BDT score.

Correlation matrices

Correlation matrices are shown in Figures C.12 and C.13 for the Asimov $\mu = 0$ fit and the unblinded fit, respectively. Only correlations which are greater than 10% are kept.

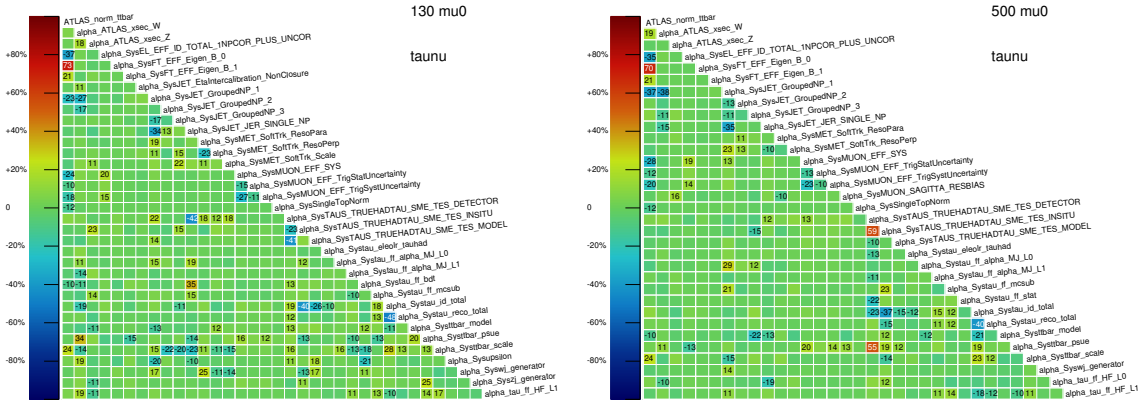

(a) **(b)**

Figure C.12 Systematic covariance matrix for the BDT-based fit trained for the mass ranges (a) 160–180 GeV and (b) 500–2000 GeV (left) using the Asimov dataset. Only correlations which are greater than 10% are kept.

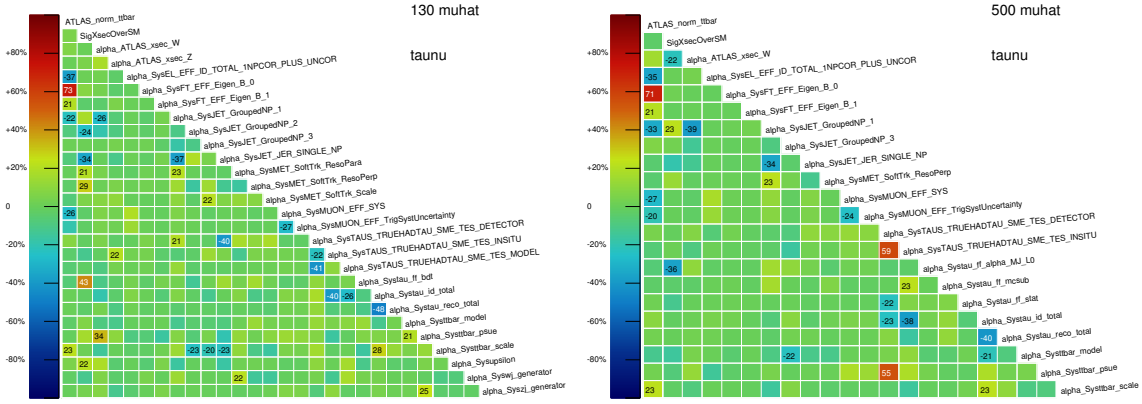

(a) **(b)**

Figure C.13 Systematic covariance matrix for the BDT-based fit trained for the mass ranges (a) 160–180 GeV and (b) 500–2000 GeV (left) using the Asimov dataset. Only correlations which are greater than 10% are kept.

Fit diagnostics

Pull plots for the 170 GeV combined fit in the charged Higgs analysis is shown in Figure C.14, determined as discussed in Section 6.5.1.

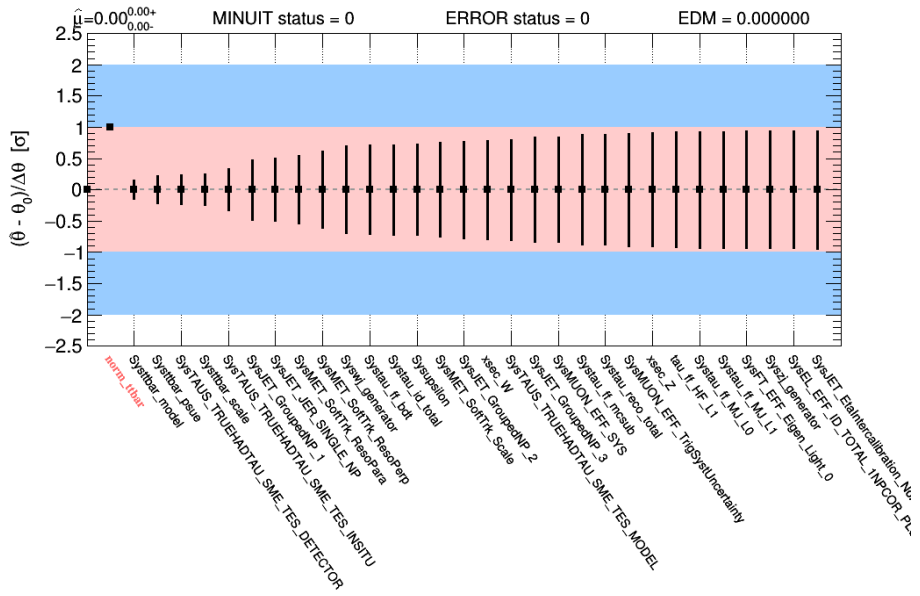

(a)

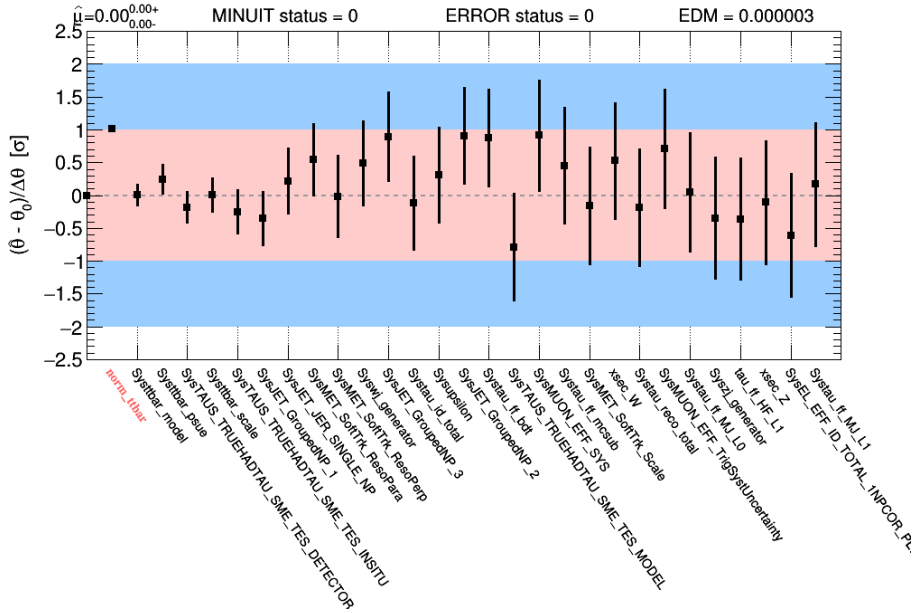

(b)

Figure C.14 Profiling of the NPs in the (a) Asimov data and (b) the observed data for $H^{\pm}$ mass of 170 GeV in combined signal region with control region top CR, showing only the most constrained NPs. The $t\bar{t}$ normalisation factor is highlighted, and is constrained to $\sim$3%.

The pull results demonstrated several pulled NPs related to $t\bar{t}$ and $\tau_{\text{had-vis}}$ uncertainties. In order to validate the fitting model, the results are cross checked against a fit with additional DOFs. Each channel is given an independed transfer factor from the Top CR to the signal region. Additionaly, the following TES and Top theory NPs were decorrelated between the signal regions: `Systtbar_psue`, `Systtbar_model`, `Systtbar_scale`, `SysTAUS_TRUEHADTAU_SME_TES_DETECTOR`, `SysTAUS_TRUEHADTAU_SME_TES_INSITU`, and `SysTAUS_TRUEHADTAU_SME_TES_MODEL`.

Figure C.15 shows the comparison of the expected and observed limits using the nominal fit model and model with decorrelated nuisance parameters. The small difference was observed in the first BDT training bin (90–120 GeV). The limits for the tested model are slightly higher (worse). Nevertheless, the difference is small and the observed limits are within experimental uncertainties with respect to expected limits. For higher BDT training bins, the difference is negligible. It is therefore concluded that dicorrelating the pulled NPs would have negligable impact on the result, and the fit is maintained with the default configuration.

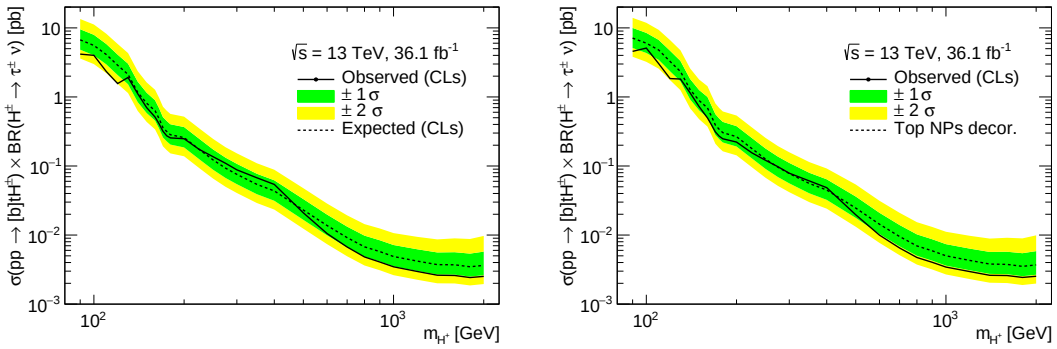

(a) **(b)**

Figure C.15 Comparison of the observed and expected 95% CL combined exclusion limits on $\sigma(pp \to [b]tH^+) \times B(H^+ \to \tau\nu)$ for charged Higgs boson production as a function of $m_{H^\pm}$ for (a) nominal fit model and (b) model with decorrelated nuisance parameters.

Appendix D

Appendix for the coupling combination

D.1 Fit diagnostics for the production cross-section measurement

Correlation between POIs (Figure D.1), and ranking plots of the most relevant NPs (Figures D.2 and D.3), for the Production cross-section measurement of Section 8.1.2, following the discussion on page 199.

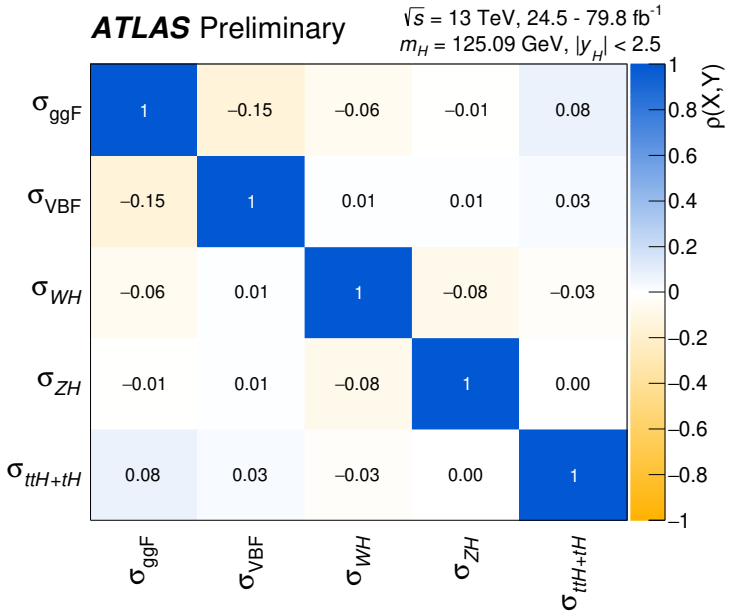

Figure D.1 Correlations between the five measured Higgs production cross-sections for observed data Ref. [3].

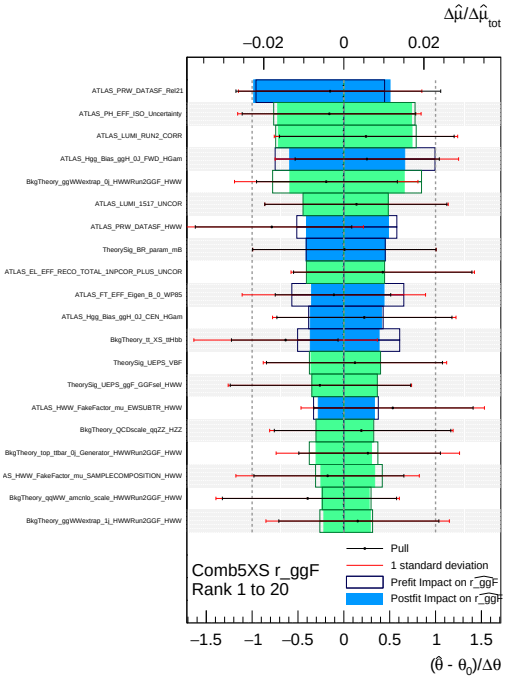

(a) ggF

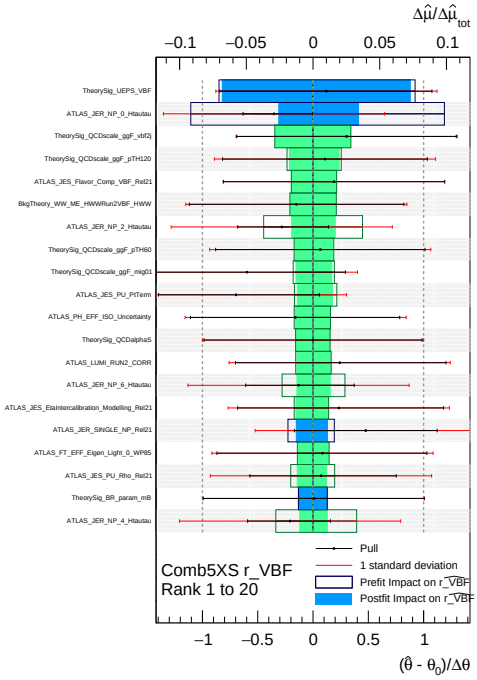

(b) VBF

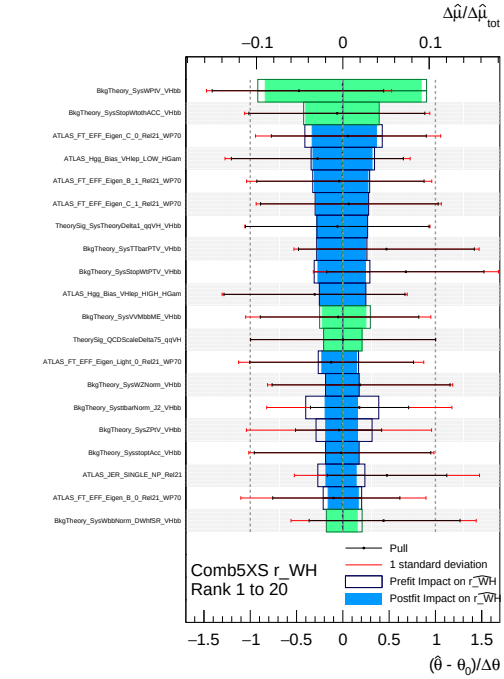

(c) WH

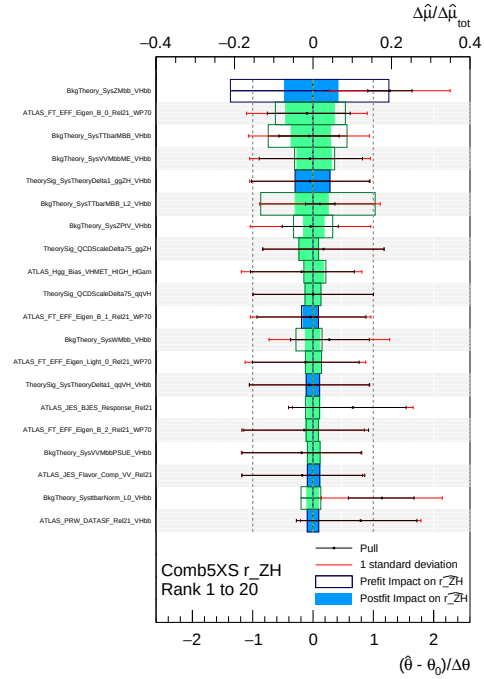

(d) ZH

Figure D.2 Ranking of systematic uncertainties for the (a) ggF, (b) VBF, (c) WH and (d) ZH Higgs production cross-section from the Higgs production cross-section fit.

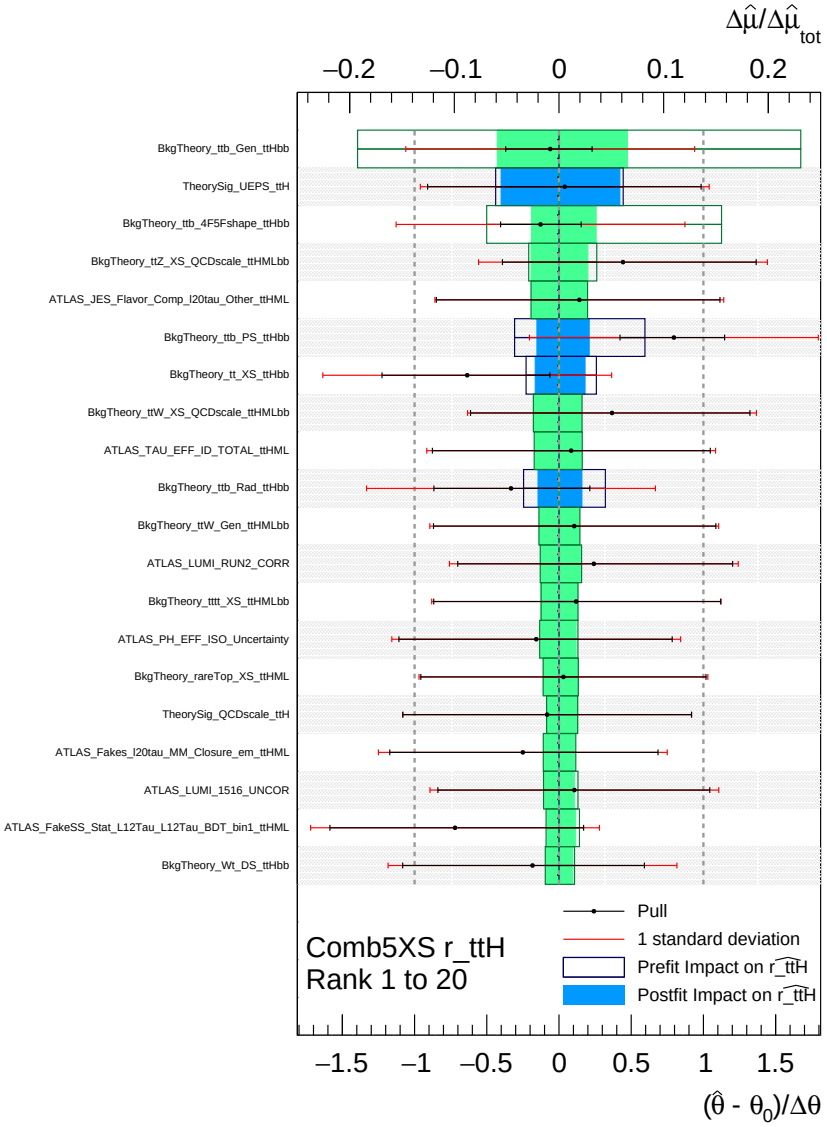

Figure D.3 Ranking of systematic uncertainties for the $t\bar{t}H$ Higgs production cross-section from the Higgs production cross section fit.

D.2 Additional cross-section measurement results

Additional parameterisations for the cross-section results in Section 8.1.2 are presented in Ref. [3]. Their subsequent description here is brief, and the presentation of their results have been limited to only quoting their respective compatability with the SM predictions. A parameterisation in terms of the products $(\sigma \times B)_{if}$ for each Higgs production process i times branching fraction to final-state f is considered. The WH and ZH production modes are merged into VH due to their lack of sensitivity. The model has 20 DOFs[70] and is compatible with the SM with a p-value of $p_{\text{SM}} = 71\%$. An additional parameterisation is considering the ratio of Higgs cross-sections and branching fractions. The products $(\sigma \times B)_{if}$ can be expressed in terms of a reference process, chosen to be $gg \to H \to ZZ^*$, as,

$$(\sigma \times B)_{if} = \sigma_{ggF}^{ZZ} \times \frac{\sigma_i}{\sigma_{ggF}} \times \frac{B_f}{B_{ZZ}}, \tag{D.1}$$

where σ_{ggF}^{ZZ} represents the $gg \to H \to ZZ^*$ cross-section. Considering the ratios $\frac{\sigma_i}{\sigma_{ggF}}$ and $\frac{B_f}{B_{ZZ}}$ allows us to decouple the cross-sections and branching fractions in the measurement. This feature was not available in the preceding prameterisations, which either measured cross-sections and branching fractions inclusively, or directly fixed the Higgs branching fractions to SM predictions. The likelihood model has 9 POIs defined as σ_{ggF}^{ZZ}, $\frac{\sigma_i}{\sigma_{ggF}}$ where $i \in (\text{VBF}, ZH, WH, t\bar{t}H)$, and $\frac{B_f}{B_{ZZ}}$ where $f \in (\gamma\gamma, WW, \tau\tau, bb)$. The measured compatability with the SM corresponds to $p_{\text{SM}} = 93\%$. Finally, the STXS introduced at the start of Section 8 measures the Higgs production cross sections in granular bins defined from the Higgs production kinematics and topology. Similar to the previous parameterisation, the Higgs branching fractions are decoupled from the cross-section bins. The products $(\sigma \times B)_{if}$ can be expressed in terms of the Higgs production cross-section in STXS region i times the branching fraction of $H \to ZZ^*$, $(\sigma \times B)_{i,ZZ}$, and the ratio of Higgs branching fractions $\frac{B_f}{B_{ZZ}}$,

$$(\sigma \times B)_{if} = \sigma_{i,ZZ} \times \frac{B_f}{B_{ZZ}}. \tag{D.2}$$

The resulting STXS model has 19 DOF and is compatible with the SM prediction corresponding to $p_{\text{SM}} = 88\%$.

[70] The list of measured POIs is: ggF, $H \to \gamma\gamma$; ggF,$H \to ZZ^*$; ggF, $H \to WW^*$; ggF, $H \to \tau\tau$; VBF, $H \to \gamma\gamma$; VBF, $H \to ZZ^*$; VBF, $H \to WW^*$; VBF, $H \to \tau\tau$;VBF, $H \to b\bar{b}$; VH, $H \to \gamma\gamma$; VH, $H \to ZZ^*$; VH, $H \to b\bar{b}$; $t\bar{t}H$, $H \to \gamma\gamma$; $t\bar{t}H$, $H \to VV*$; $t\bar{t}H$, $H \to \tau\tau$; and $t\bar{t}H$, $H \to b\bar{b}$.

D.3 Example parameterisation in the κ-framework

As an example the calculation of σ_{ggF} (Table 8.6) in terms of the κ-framework is presented. The σ_{ggF}^{SM} cross-sections are calculated at N3LO QCD [259]. The total inclusive ggF cross-section σ_{ggF} is dependant on individual contribution of cross-sections from the top loop, bottom loop, and top-bottom loop interference, denoted as σ_{tt}, σ_{bb} and σ_{tb}, respectively. Additional corrections to the ggF cross-section from c-quark related loops are present, with σ_{cc}, σ_{tc} and σ_{bc} as the cross-sections of ggF via charm loops, and the top-charm and bottom-charm loop interference, respectively. The total ggF cross-section, ignoring EW and light quark contributions, is therefore,

$$\sigma_{ggF} = \sigma_{tt} + \sigma_{bb} + \sigma_{tb} + \sigma_{tc} + \sigma_{bc} + \sigma_{cc}. \tag{D.3}$$

Making the substitution in Eq. (8.4) into Eq. (D.3) leads to,

$$\sigma_{ggF} = \kappa_t^2\sigma_{tt}^{\text{SM}} + \kappa_b^2\sigma_{bb}^{\text{SM}} + \kappa_t\kappa_b\sigma_{tb}^{\text{SM}} + \kappa_t\kappa_c\sigma_{tc}^{\text{SM}} + \kappa_b\kappa_c\sigma_{bc}^{\text{SM}} + \kappa_c^2\sigma_{cc}^{\text{SM}}. \tag{D.4}$$

Under the SM the subsequent ggF cross-sections at 13TeV pp collisions with N3LO QCD are $\sigma_{tt}^{\text{SM}} = 47.94$ [pb], $\sigma_{bb}^{\text{SM}} = 0.10$ [pb], $\sigma_{tb}^{\text{SM}} = -1.73$ [pb], $\sigma_{cc}^{\text{SM}} = 0.0009$ [pb], $\sigma_{tc}^{\text{SM}} = -0.22$ [pb] and $\sigma_{bc}^{\text{SM}} = 0.02$ [pb]. Substituting the SM cross-sections into Eq. (D.4) yields,

$$\sigma_{ggF} = 47.94\kappa_t^2 + 0.10\kappa_b^2 - 1.73\kappa_t\kappa_b - 0.22\kappa_t\kappa_c + 0.02\kappa_b\kappa_c + 0.0009\kappa_c^2. \tag{D.5}$$

The NLO EW contribution to the total ggF cross section, σ_{EW}^{SM}, is determined to be $\sigma_{EW}^{\text{SM}} = 2.39$ [pb] so that the total ggF cross-section is $\sigma_{ggF,\text{ incl. EW}}^{\text{SM}} = 48.50$ [pb]. However, as mentioned above, one ignores EW corrections in the LO κ-framework which leads to a total ggF cross-section of $\sigma_{ggF}^{\text{SM}} = 46.11$ [pb]. Taking the ratio $\frac{\sigma_{ggF}}{\sigma_{ggF}^{\text{SM}}}$, and ignoring contributions from charm quark loops, the expression in Table 8.6 is recovered,

$$\mu(\sigma_{\text{ggF}}) = \frac{\sigma_{\text{ggF}}}{\sigma_{\text{ggF}}^{\text{SM}}} = 1.04\,\kappa_t^2 + 0.002\,\kappa_b^2 - 0.04\,\kappa_t\kappa_b. \tag{D.6}$$

D.4 Higgs cross-section reparemeterisation

Reparameterisation code snippets for the BSM κ-framework in Section 8.3 are shown in Listing D.1, Listing D.2, Listing D.3, Listing D.4 and Listing D.5 for MSSM and 2HDM type I, type II, type III, and type IV models, respectively. The reference cards are written

in XML code and used to build a new PDF from the Higgs couplings workspace with the κ parameters paremetrized in terms of $\tan\beta$, and m_A or $\cos(\beta-\alpha)$. The model is represented using RooStats classes and the coupling modifiers are represented in the code as CW, CZ, Cto, Cb, Cta, and Cmu for κ_W, κ_Z, κ_t, κ_b, κ_τ, and κ_μ, respectively.

Listing D.1 MSSM parameterisation card

```
<!DOCTYPE Organization SYSTEM 'Organization.dtd'> <Organization
InFile="WS.root" OutFile = "MSSM-WS_v8.root" ModelName = "MSSM-WS"
POINames = "mAinv,tanB" > <!-- Set POI MA^-1 for closure in global
fit--> <Item Name="mAinv[0.002,0.,0.005]"/> <Item
Name="tanB[5.0,0.0,1000.0]"/> <!-- Use 125.09 GeV as Higgs mass
where possible --> <Item Name="mZ[91.1876]"/> <Item
Name="mh[125.09]"/> <!-- MSSM parameterisation --> <Item
Name="prod::mAinv2(mAinv,mAinv)"/> <Item
Name="prod::tanB2(tanB,tanB)"/> <Item Name="prod::mZ2(mZ,mZ)"/>
<Item Name="prod::mh2(mh,mh)"/> <!-- These lines where the previous
parameterisation and did not converge as ma->inf --> <Item
Name="expr::shu('1/sqrt(1+pow(1+@0*@2,2)*@1/pow(@2*@0+@1-@3*@0*(1+@1),2))',mAinv2,
    tanB2,mZ2,mh2)"/>
<Item
Name="expr::shd('(1+@0*@2)*@4/(@2*@0+@1-@3*@0*(1+@1))*@5',mAinv2,tanB2,mZ2,mh2,
    tanB,shu)"/>
<!-- Vector boson couplings --> <Item
Name="expr::CV_MSSM_reduced('sqrt(1/(1+@0))*@2+@1*sqrt(1/(1+@0))*@3',tanB2,tanB,shd,shu)"/
    >
<!-- Up type quarks --> <Item
Name="expr::Cu_MSSM_reduced('sqrt(1+@0)/@1*@2',tanB2,tanB,shu)"/>
<!-- Down type fermions --> <Item
Name="expr::Cd_MSSM_reduced('sqrt(1+@0)*@1',tanB2,shd)"/> <!-- PDF
--> <Item Name="EDIT::NEWPDF(OLDPDF, CW=CV_MSSM_reduced,
CZ=CV_MSSM_reduced, Cto=Cu_MSSM_reduced, Cb=Cd_MSSM_reduced,
Cta=Cd_MSSM_reduced, Cmu=Cd_MSSM_reduced,)"/> </Organization>
```

Listing D.2 2HDM type I parameterisation card

```
<!DOCTYPE Organization SYSTEM 'Organization.dtd'> <Organization
InFile="WS.root" OutFile = "THDM-I-WS_v8.root" ModelName =
"THDM-I-WS" POINames = "cosBmA,tanB" > <Item
Name="cosBmA[0.0,-1.0,1.0]"/> <Item Name="tanB[5.0,0.0,200.0]"/>
<Item Name="expr::sinBmA('sin(acos(@0))',cosBmA)"/> <Item
Name="expr::cotB('1/@0',tanB)"/> <Item
Name="expr::Cu_reduced('@0+@1*@2',sinBmA,cosBmA,cotB)"/> <Item
Name="expr::Cd_reduced('@0+@1*@2',sinBmA,cosBmA,cotB)"/>
```

```
<!−− PDF −−> <Item Name="EDIT::NEWPDF(OLDPDF, CW=sinBmA, CZ=sinBmA,
Cto=Cu_reduced, Cb=Cd_reduced, Cta=Cd_reduced, Cmu=Cd_reduced ,)"/>
</Organization>
```

Listing D.3 2HDM type II parameterisation card

```
<!DOCTYPE Organization SYSTEM 'Organization.dtd'> <Organization
InFile="WS.root" OutFile = "THDM−II−WS_v8.root" ModelName =
"THDM−II−WS" POINames = "cosBmA,tanB" > <Item
Name="cosBmA[0.0,−1.0,1.0]"/> <Item Name="tanB[5.0,0.0,200.0]"/>
<Item Name="expr::sinBmA('sin(acos(@0))',cosBmA)"/> <Item
Name="expr::cotB('1/@0',tanB)"/> <Item
Name="expr::Cu_reduced('@0+@1∗@2',sinBmA,cosBmA,cotB)"/> <Item
Name="expr::Cd_reduced('@0−@1∗@2',sinBmA,cosBmA,tanB)"/>

<!−− PDF −−> <Item Name="EDIT::NEWPDF(OLDPDF, CW=sinBmA, CZ=sinBmA,
Cto=Cu_reduced, Cb=Cd_reduced, Cta=Cd_reduced, Cmu=Cd_reduced ,)"/>
</Organization>
```

Listing D.4 2HDM type III parameterisation card

```
<!DOCTYPE Organization SYSTEM 'Organization.dtd'> <Organization
InFile="WS.root" OutFile = "THDM−III−WS_v8.root" ModelName =
"THDM−III−WS" POINames = "cosBmA,tanB" > <Item
Name="cosBmA[0.0,−1.0,1.0]"/> <Item Name="tanB[5.0,0.0,200.0]"/>
<Item Name="expr::sinBmA('sin(acos(@0))',cosBmA)"/> <Item
Name="expr::cotB('1/@0',tanB)"/> <Item
Name="expr::Cu_reduced('@0+@1∗@2',sinBmA,cosBmA,cotB)"/> <Item
Name="expr::Cd_reduced('@0+@1∗@2',sinBmA,cosBmA,cotB)"/> <Item
Name="expr::Cl_reduced('@0−@1∗@2',sinBmA,cosBmA,tanB)"/>

<!−− PDF −−> <Item Name="EDIT::NEWPDF(OLDPDF, CW=sinBmA, CZ=sinBmA,
Cto=Cu_reduced, Cb=Cd_reduced, Cta=Cl_reduced, Cmu=Cl_reduced, )"/>
</Organization>
```

Listing D.5 2HDM type IV parameterisation card

```
<!DOCTYPE Organization SYSTEM 'Organization.dtd'> <Organization
InFile="WS.root" OutFile = "THDM−IV−WS_v8.root" ModelName =
"THDM−IV−WS" POINames = "cosBmA,tanB" > <Item
Name="cosBmA[0.0,−1.0,1.0]"/> <Item Name="tanB[5.0,0.0,200.0]"/>
<Item Name="expr::sinBmA('sin(acos(@0))',cosBmA)"/> <Item
Name="expr::cotB('1/@0',tanB)"/> <Item
Name="expr::Cu_reduced('@0+@1∗@2',sinBmA,cosBmA,cotB)"/> <Item
Name="expr::Cd_reduced('@0−@1∗@2',sinBmA,cosBmA,tanB)"/> <Item
```

```
Name="expr::Cl_reduced('@0+@1*@2',sinBmA,cosBmA,cotB)"/>

<!-- PDF --> <Item Name="EDIT::NEWPDF(OLDPDF, CW=sinBmA, CZ=sinBmA,
Cto=Cu_reduced, Cb=Cd_reduced, Cta=Cl_reduced, Cmu=Cl_reduced ,)"/>
</Organization>
```

D.5 Parameterisation validation tables for Type-II 2HDM

Table D.1 The differences between the parameterised production cross sections and branching ratios of the SM-like Higgs compared to precision calculations using SUSHI and 2HDMC for 2HDM Type-II with $m_A = 1000$ GeV [250]. All the differences are quoted in %.

$\tan\beta$	$\cos(\beta-\alpha)$	σ [pb]	$\Delta\sigma_{ggF}$ [%]	$\Delta\sigma_{bbh}$ [%]	B_{ZZ} [%]	B_{WW} [%]	B_{bb} [%]	$B_{\tau\tau}$	$\frac{\Gamma_h}{\Gamma_h^{\mathrm{SM}}}$
0.5	-0.800	47.96	3.20	-8.98	-0.07	-0.07	1.62	-0.07	0.07
0.5	-0.300	6.43	-7.57	-4.45	-0.36	-0.35	0.21	-0.35	0.36
0.5	-0.100	29.33	-1.00	-2.84	-0.64	-0.64	-0.44	-0.64	0.64
0.5	0.000	46.11	-0.08	-1.94	-0.81	-0.81	-0.81	-0.81	0.81
0.5	0.100	65.64	0.53	-0.93	-0.99	-0.99	-1.20	-0.99	1.00
0.5	0.300	110.96	1.14	1.72	-1.39	-1.39	-2.15	-1.39	1.41
0.5	0.800	223.31	1.99	59.83	-2.42	-2.42	-9.90	-2.42	2.48
1.0	-0.800	3.89	-10.06	-6.09	-0.41	-0.41	0.54	-0.41	0.41
1.0	-0.300	20.06	-1.84	-3.73	-0.63	-0.63	-0.23	-0.63	0.63
1.0	-0.100	36.98	-0.43	-2.63	-0.74	-0.74	-0.59	-0.74	0.74
1.0	0.000	46.11	-0.08	-1.94	-0.81	-0.81	-0.81	-0.81	0.81
1.0	0.100	55.12	0.48	-1.09	-0.88	-0.88	-1.07	-0.88	0.89
1.0	0.300	72.71	0.50	1.66	-1.08	-1.08	-1.83	-1.08	1.09
1.0	0.800	92.21	0.89	-25.10	-1.23	-1.23	5.79	-1.23	1.24
2.0	-0.800	4.79	-17.97	-5.27	-0.65	-0.65	0.11	-0.65	0.65
2.0	-0.300	29.96	-0.66	-3.74	-0.76	-0.76	-0.36	-0.76	0.76
2.0	-0.100	41.11	-0.15	-2.73	-0.79	-0.79	-0.62	-0.79	0.80
2.0	0.000	46.11	-0.08	-1.94	-0.81	-0.81	-0.81	-0.81	0.81
2.0	0.100	50.53	-0.07	-0.74	-0.81	-0.81	-1.07	-0.81	0.81
2.0	0.300	57.05	-0.21	6.80	-0.69	-0.69	-2.41	-0.69	0.69
2.0	0.800	50.33	-1.66	-8.98	-0.27	-0.27	1.41	-0.27	0.27

Table D.2 (continued from Table D.1) The differences between the parameterised production cross sections and branching ratios of the SM-like Higgs compared to precision calculations using SUSHI and 2HDMC for 2HDM Type-II with $m_A = 1000$ GeV [250]. All the differences are quoted in %.

$\tan\beta$	$\cos(\beta-\alpha)$	σ [pb]	$\Delta\sigma_{ggF}$ [%]	$\Delta\sigma_{bbh}$ [%]	B_{ZZ} [%]	B_{WW} [%]	B_{bb} [%]	$B_{\tau\tau}$	$\frac{\Gamma_h}{\Gamma_h^{\mathrm{SM}}}$
5.0	-0.800	21.24	-15.78	-5.26	-0.70	-0.70	0.05	-0.70	0.70
5.0	-0.300	37.69	-0.67	-4.30	-0.79	-0.79	-0.27	-0.79	0.80
5.0	-0.100	43.51	0.36	-3.25	-0.83	-0.83	-0.54	-0.83	0.84
5.0	-0.000	46.11	-0.08	-1.94	-0.81	-0.81	-0.81	-0.81	0.81
5.0	0.000	46.11	-0.08	-1.94	-0.81	-0.81	-0.81	-0.81	0.81
5.0	0.100	48.15	-0.49	2.21	-0.59	-0.59	-1.45	-0.59	0.59
5.0	0.300	50.67	-2.00	-11.69	0.16	0.16	2.59	0.16	-0.16
5.0	0.800	43.27	-11.32	-6.37	-0.52	-0.52	0.50	-0.52	0.53
10	-0.800	61.14	-21.80	-5.38	-0.69	-0.69	0.09	-0.69	0.69
10	-0.300	44.34	-2.88	-4.77	-0.76	-0.76	-0.13	-0.76	0.77
10	-0.100	44.68	0.11	-3.83	-0.83	-0.83	-0.41	-0.83	0.84
10	0.000	46.11	-0.08	-1.94	-0.81	-0.81	-0.81	-0.81	0.81
10	-0.000	46.11	-0.08	-1.94	-0.81	-0.81	-0.81	-0.81	0.81
10	0.100	48.28	-1.23	-88.76	0.11	0.11	0.00	0.11	-0.11
10	0.300	54.68	-5.69	-7.25	-0.34	-0.34	0.90	-0.34	0.34
10	0.800	79.17	-21.58	-5.92	-0.60	-0.60	0.31	-0.60	0.60

D.6 Additional details of the validation of the hMSSM parameterisation

Additional studies to validate the hMSSM parameterisation as discussed in Section 8.3.2.1 are documented. The easiest effect that can be checked is the effect of the di-Higgs boson production in the hMSSM. The fraction of the gluon-gluon fusion $H \to hh$ production can be compared to the Higgs boson production that the parameterisation takes into account. In Figure D.4 (a) this comparison is shown and it is clear that for the region relevant for the limit ($m_A > 400$GeV) the effect is well below the theory uncertainties. The effect of the charged Higgs boson can be best seen by comparing the Higgs boson to $\gamma\gamma$ branching ratio results of the parametrized values against the precision HDECAY calculated values. This is shown in Figure D.4 (b), where it is shown that the effect is at the few % level.

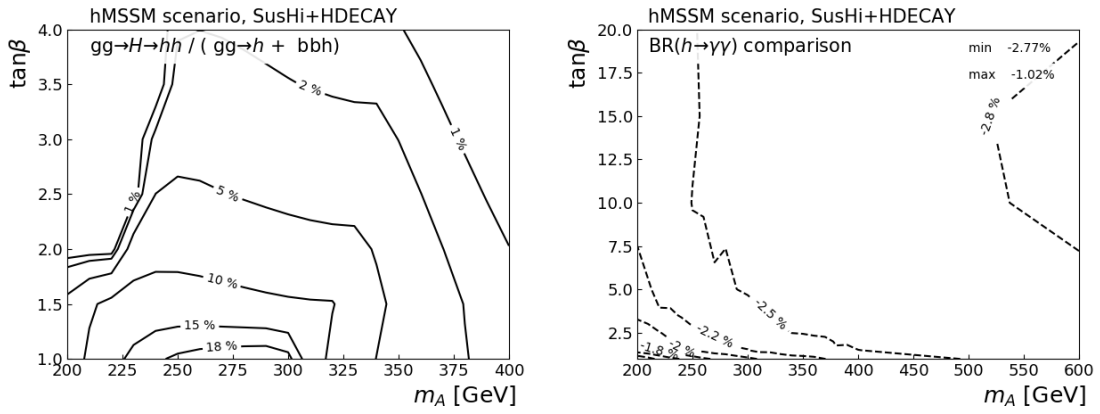

(a) **(b)**

Figure D.4 From Ref. [250]: (a) Fraction of the hh production versus single Higgs boson production in the hMSSM scenario. In the parameterisation that is employed here effects from hh production are ignored. (b) The difference between the parameterised $h \to \gamma\gamma$ branching ratio versus HDECAY calculations for the hMSSM scenario. The difference is sensitive to the charged Higgs boson, the effect of which is ignored in the parameterisation.

The comparison of precise calculations and the hMSSM parameterisation for some indicative m_A and $\tan\beta$ values are shown in Table D.3. The differences are found always to be below 6% for ggF, whereas for the b-associated production and the branching ratios the differences are at a few % level at most, all of which are within their respective theoretical uncertainties. An additional comparison is performed by comparing directly the Higgs boson couplings from SusHi to the parameterised couplings, discussed in Section 8.3.2.1.

Table D.3 The differences between the parameterised production cross-sections and branching ratios of the SM-like Higgs compared to precision calculations using SUSHI and HDECAY for the hMSSM scenario (Ref. [250]). All the differences are quoted in %.

$\tan\beta$	σ [pb]	$\Delta\sigma$ (%)	$\Delta\sigma_{ggF}$ (%)	$\Delta\sigma_{bbh}$ (%)	B_{ZZ} (%)	B_{WW} (%)	B_{bb} (%)	$B_{\tau\tau}$ (%)	$\frac{\Gamma_h}{\Gamma_h^{\mathrm{SM}}}$
$m_A = 200$ GeV									
1.0	11.13	-5.99	-6.44	-0.90	0.42	2.31	-0.02	-2.48	1.03
1.5	20.48	-1.52	-1.61	-0.01	-0.12	1.84	-0.05	-2.43	1.58
2.0	27.15	-0.75	-0.80	0.10	-0.08	1.85	-0.06	-2.43	1.59
4.0	39.11	0.02	0.01	0.20	-0.08	1.84	-0.08	-2.42	1.59
6.0	42.66	0.17	0.16	0.22	-0.08	1.83	-0.08	-2.42	1.55
10.0	44.83	0.09	0.09	0.12	-0.08	1.84	-0.09	-2.42	1.55
20.0	45.72	0.27	0.28	0.24	-0.08	1.83	-0.09	-2.42	1.62
$m_A = 300$ GeV									
1.0	29.64	-1.42	-1.47	0.70	0.27	2.19	-0.12	-2.29	1.21
1.5	36.06	-0.34	-0.37	1.08	0.12	2.02	-0.11	-2.26	1.39
2.0	39.48	-0.16	-0.19	1.13	0.11	2.04	-0.11	-2.24	1.39
4.0	44.00	0.05	0.03	1.19	0.13	2.06	-0.12	-2.23	1.39
6.0	45.04	0.10	0.08	1.20	0.13	2.08	-0.11	-2.23	1.39
10.0	45.63	0.08	0.06	1.18	0.14	2.05	-0.11	-2.23	1.38
20.0	45.86	0.13	0.11	1.21	0.13	2.04	-0.11	-2.22	1.39
$m_A = 500$ GeV									
1.0	40.34	-0.47	-0.50	1.61	0.32	2.26	-0.11	-2.11	1.19
1.5	42.85	-0.15	-0.18	1.74	0.28	2.20	-0.11	-2.10	1.24
2.0	44.05	-0.10	-0.12	1.77	0.26	2.23	-0.10	-2.09	1.24
4.0	45.50	-0.03	-0.05	1.79	0.25	2.21	-0.10	-2.09	1.24
6.0	45.81	-0.02	-0.04	1.79	0.27	2.21	-0.10	-2.08	1.23
10.0	45.98	-0.02	-0.04	1.78	0.28	2.23	-0.09	-2.09	1.23
20.0	46.05	-0.00	-0.03	1.79	0.28	2.19	-0.11	-2.08	1.24

D.7 hMSSM comparison to intermediate result

Ref. [241] provides a preliminary combination of the SM Higgs cross-sections, referred to here as the ICHEP combination. The main difference between the ICHEP result and the result presented in this section is the addition of data for VBF and VH channels in the latter. A comparison of the hMSSM limits compared to previous ICHEP result is shown in Figure D.5. Noticeably, the ICHEP result has stronger observed limits, while the expected limits remain comparable. The cause of this feature is studied via fits to Asimov datasets with injected signal strengths.

The observed hMSSM limit is found to be closer to the expected limit with comparison to the ICHEP result. The decrease in the observed limit exclusion can be explained by an increase in the observed bottom quark coupling, which has increased by 5% with respect to ICHEP result. This difference is directly attributed to the addition of data from $H \to bb$ channels targetting VBF and VH production. As alluded to earlier, the hMSSM has increased down-type fermion couplings at low m_A and high $\tan\beta$. Since $\kappa_{\text{down}} \to 1$ from above as $m_{\text{A}} \to \infty$, the higher observed bottom coupling pushes the limit to lower values of m_A. The effects of the SM couplings on the observed limit is studied by creating datasets with injected signal strengths. The datasets are created by profiling the NPs while all particle couplings are set to 1. The coupling of interest is then set to 1.1 (an additional 10%) and the pseudo-data is extracted. Exclusion limits at 95% CL are extracted from the pseudo-data and shown in Figure D.6[71]. When compared to the expected limit, they show the effect of having data that pulls the relative SM couplings up by 10%. Clearly shown is the effect of fitting a dataset with increased κ_b coupling, which pushes the limit to lower values of m_{A} as expected from the preceding discussion.

[71] The expected and observed limits shown are created with a close to final version of the workspace used in Ref. [3]. Although not an exact match, the limits (and conclusions derived) are practically the same.

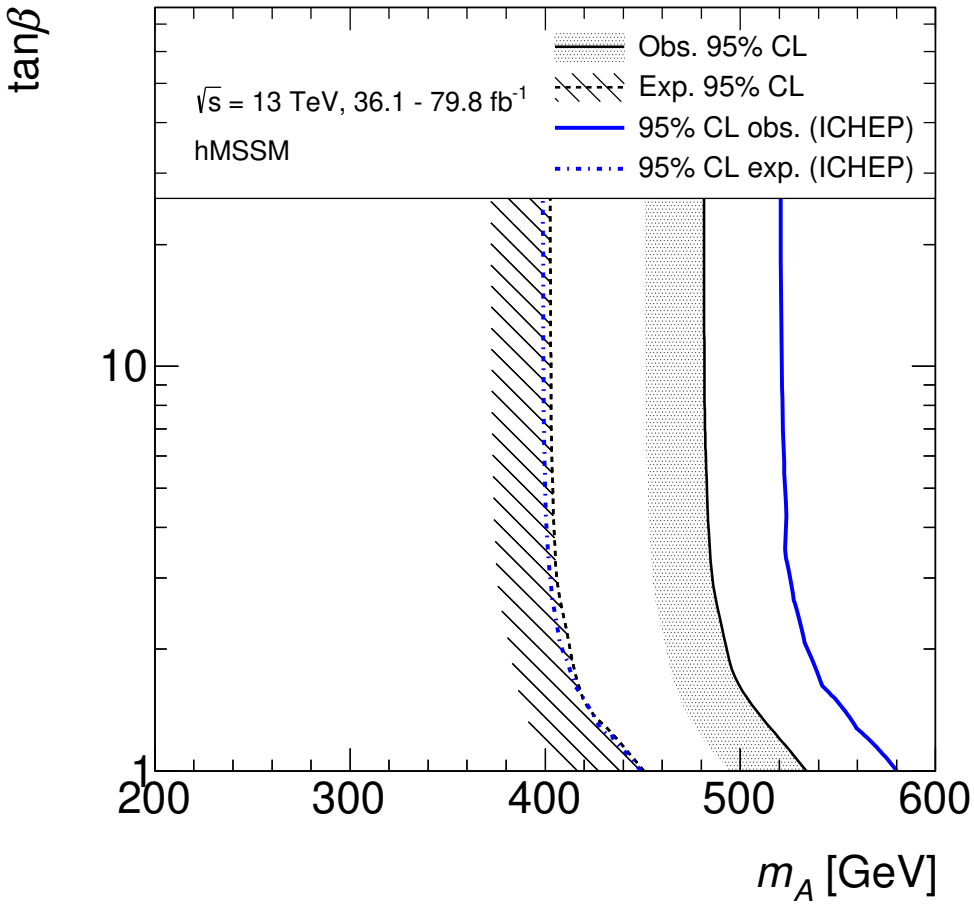

Figure D.5 Comparison of the hMSSM limits to the intermediate (ICHEP) result from Ref. [241].

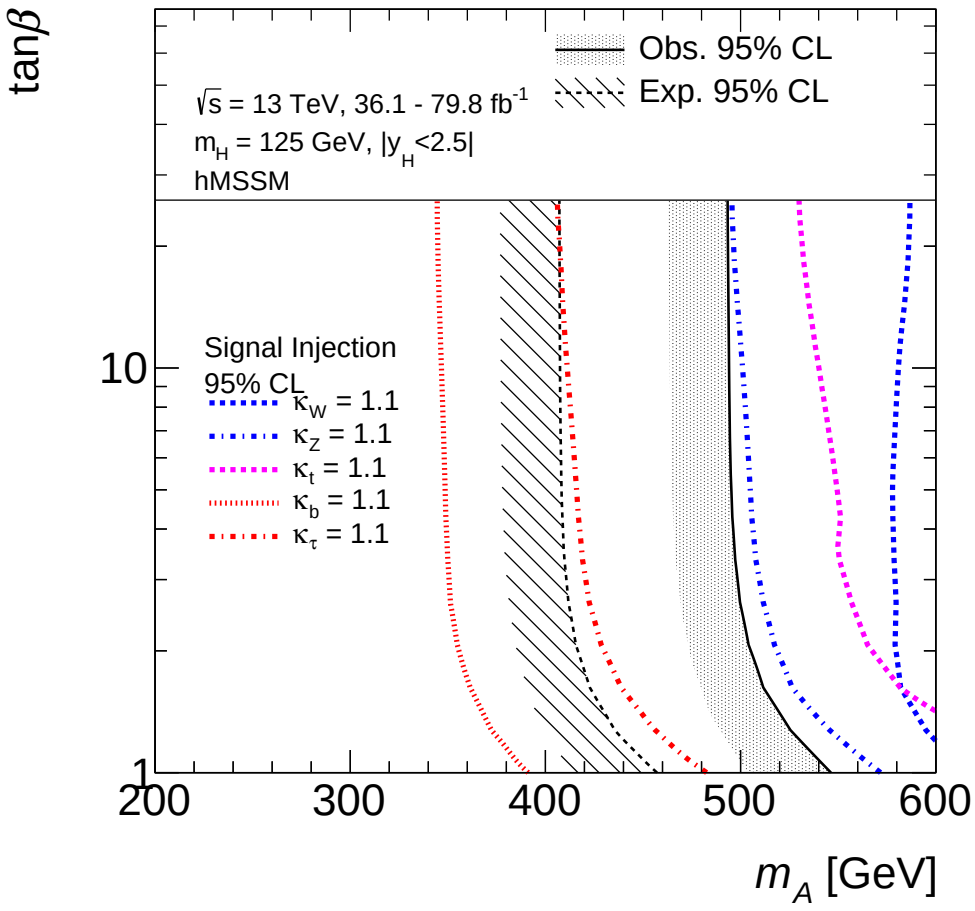

Figure D.6 Comparison of the expected and observed hMSSM limits and limits created from fits to signal injected Asimov data sets. Asimov datasets are created where a particular POI (κ_W, κ_Z, κ_t, κ_b, or κ_τ) is increased by 10% from its nominal value.

List of figures

List of tables

Abbreviations

A Large Ion Collider Experiment (ALICE)

51

A Toroidal LHC Apparatus (ATLAS)

20, 21, 24, 25, 33, 46, 48, 51–54, 59, 61, 62, 68–71, 73, 74, 76, 78, 79, 82, 83, 99, 102–104, 166, 169, 173, 182, 183, 187, 267

Analysis Object Data (AOD)

69

b-associated Higgs boson production ($b\bar{b}H$)

21, 34

beyond the Standard Model (BSM)

2, 3, 7, 27, 47, 54, 78, 79, 169, 173, 182, 183, 187, 188, 256

boosted decision tree (BDT)

78, 81, 82, 114–116

Cabibbo–Kobayashi–Maskawa (CKM)

8, 27, 30

Cathode Strip Chambers (CSCs)

60, 74

Central Trigger Processor (CTP)

62, 64

Clustering Processor (CP)

63

Compact Muon Solenoid (CMS)

20, 33, 39, 51, 99, 167, 169, 173

confidence level (CL)

46, 48, 85, 89, 92, 94, 192, 199

control region (CR)

114–116, 122, 127, 128, 149

degree of freedom (DOF)

17, 18, 28, 29, 92, 160, 179, 185, 192, 199, 255

Effective Field Theory (EFT)

36

electromagnetic (EM)

7, 8, 12, 27, 58–60, 74, 77, 103

electromagnetic barrel calorimeter (EMB-Cal)

59

electromagnetic calorimeter (EM-Cal)

55, 58, 59, 63, 64, 71–74, 81, 268

electromagnetic end-cap calorimeter (EME-Cal)

59, 60

electroweak (EW)

8, 10, 11, 13, 17, 21, 27, 32, 39, 101, 135, 185, 256

electroweak symmetry breaking (EWSB)

17, 19, 29, 173

Event Data (EVNT)

69

68, 69

favour-changing charged current (FCCC)

30

favour-changing neutral current (FCNC)

28–30, 187, 273

final-state radiation (FSR)

140

first long shutdown (LS1)

52, 56

five-flavour scheme (5FS)

40–43, 45

forward calorimeter (FCal)

59, 60

four-flavour scheme (4FS)

40–43, 45, 102

front-end (FE)

62

gluon-fusion (ggF)

20–22, 34, 36–39, 99, 100, 102, 108, 111, 112, 140, 141, 149, 155, 167, 174, 177, 179, 180, 189, 195, 223, 255, 256, 262, 267, 268, 273

good run list (GRL)

100

Grand Unified Theory (GUT)

27, 28, 36

hadronic calorimeter (Had-Cal)

55, 58–60, 63, 64, 72–74, 268

hadronic end-cap calorimeter (HEC)

60

High Luminosity Large Hadron Collider (HL-LHC)

3, 52, 93

High-Level trigger (HLT)

62, 65, 66, 72, 74, 78, 81, 82, 106

infra-red and collinear (IRC)

76

initial-state radiation (ISR)

140

inner detector (ID)

55, 57–59, 61, 62, 65–67, 71, 73–75, 81

Insertable B-layer (IBL)

56, 78

jet energy scale (JES)

77, 78, 103

jet vertex tagger (JVT)

78, 103

jet/$\sum E$ processor (JEP)

63, 84

Large Electron-Positron Collider (LEP)

34

Large Hadron Collider (LHC)

2, 3, 20–22, 44, 46, 51, 52, 54, 68, 79, 174, 267

Large Hadron Collider beauty experiment (LHCb)

51

Large Hadron Collider Cross Section Working Group (LHCXSWG)

43

leading-order (LO)

20, 21, 40–42, 45, 184, 185, 256

Level-1 calorimeter trigger (L1Calo)

62–64, 268

Level-1 muon trigger (L1Muon)

62–65, 268

Level-1 topological trigger (L1Topo)

64

Level-1 trigger (L1)

62–64, 66, 72, 74, 81, 84

lightest supersymmetric particle (LSP)

28, 33, 36–38, 268

Linear Accelerator (LINAC)

52

liquid-argon (LAr)

55, 59, 60

matrix-element (ME)

70, 140, 223, 224

Matrix-element Oriented Sampling Calculator (MOSAIC)

105

maximum-likelihood estimator (MLE)

87–89, 93–96

Minimal Supersymmetric extension to the Standard Model (MSSM)

3, 28, 33–36, 39–41, 45–47, 99, 100, 108, 169, 175, 187, 194, 223, 256, 268

Missing Mass Calculator (MMC)

105

Monitored Drift Tubes (MDTs)

60, 66, 74

Monte Carlo (MC)

69, 77, 80, 95, 103, 106, 108–111, 114, 115, 118, 119, 121–123, 126–129, 131–133, 135, 136, 142, 155, 227–231

muon spectrometer (MS)

60, 61, 65–67, 74, 75, 77, 83, 268

next-to-leading-order (NLO)

39, 41–43, 45, 46, 101, 102, 185, 256, 268

next-to-next-leading-logarithm (NNLL)

101

next-to-next-to-leading-order (NNLO)

39, 41, 42, 101, 185

next-to-next-to-next-leading-order (N3LO)

185, 256

nuisance parameter (NP)

87, 94–96, 133, 134, 143–156, 164, 176, 177, 179, 243, 244, 246–248, 252, 264, 270, 272–275

parameter of interest (POI)

87–89, 92, 94, 95, 149, 175, 179, 188, 252, 255, 266, 272

parton distribution function (PDF)

See also probability distribution function below. 70, 72, 101, 102, 135, 140, 256

parton shower (PS)

70, 101, 102, 135, 136, 224

Pontecorvo–Maki–Nakagawa–Sakata (PMNS)

8, 27

probability distribution function (PDF)

88, 90, 91

Proton Synchroton (PS)

52

Proton Synchrotron Booster (PSB)

52

Quantum Chromodynamincs (QCD)

8, 10, 25, 40, 45, 70, 73, 76, 101, 140, 185, 256

Quantum Electrodynamincs (QED)

11, 12, 70

Quantum Field Theory (QFT)

7, 10

Read-Out Driver (ROD)

62

Read-Out System (ROS)

62

Region-of-Interest (RoI)

62–67, 71, 73, 78, 81, 82, 268

Resistive Plate Chambers (RCPs)

60, 63, 65, 268

second long shutdown (LS2)

52

the European Organization for Nuclear Research (CERN)

51

Thin Gap Chambers (TGCs)

60, 63–65, 268

third long shutdown (LS3)

52

transition radiation tracker (TRT)

55, 57, 58, 71–73

Trigger and Data Acquisition (TDAQ)

55, 62, 65, 68–70

Two-Higgs-Doublet-Model (2HDM)

3, 28–33, 35, 40, 41, 45–48, 99, 100, 169, 175, 187–189, 192, 194, 195, 223, 225, 256, 268, 271, 273

underlying event (UE)

69, 72, 75, 77, 140

underlying event parton shower (UEPS)

181

vacuum expectation value (VEV)

15, 16, 18, 20, 29, 187

vector-boson associated Higgs boson production (VH)

21, 23, 174, 181, 255, 264, 267

vector-boson-fusion (VBF)

21, 22, 174, 179–181, 255, 264, 267

Worldwide LHC Computing Grid (WLCG)

68